

V. Advanced Battery Materials Research (BMR)

V.A. Introduction

The Vehicle Technologies Office (VTO) supports focused fundamental research to identify, develop and analyze new materials for high-performance, next-generation, rechargeable batteries for use in HEVs, PHEVs, and EVs. Over the last few years the focus has shifted to EV applications. The goal of the BMR Program is to develop long-life batteries that are superior to commercial lithium-ion systems (graphitic anode and metal oxide cathodes) in terms of cost, vehicle range, and safety.

Background and Program Context

The BMR Program addresses the fundamental challenges of electrode chemical and mechanical instabilities that have slowed the development of affordable, high performance, automotive batteries. The aim is to identify electrode/electrolyte materials that yield enhanced battery performance and lead to greater acceptance of electric vehicles. The Program not only supports research that leads to improvements to existing materials, but also investigations into high-risk “leap-frog” technologies that might have a tremendous impact in the marketplace. Novel diagnostics and modeling methods are employed to gain a better understanding of key factors that limit cell and material performance and to provide guidance in designing next-generation materials. Once promising materials are identified, materials are then evaluated in small prototype research-cells. If good cell performance is validated, novel materials and preliminary cell designs are then transitioned to the Advanced Battery Research (ABR) Program within the VTO for further development, scale-up and assessment. An overview of the approach used in the BMR program is shown in Figure V-1.

Solving applied problems using a fundamental approach

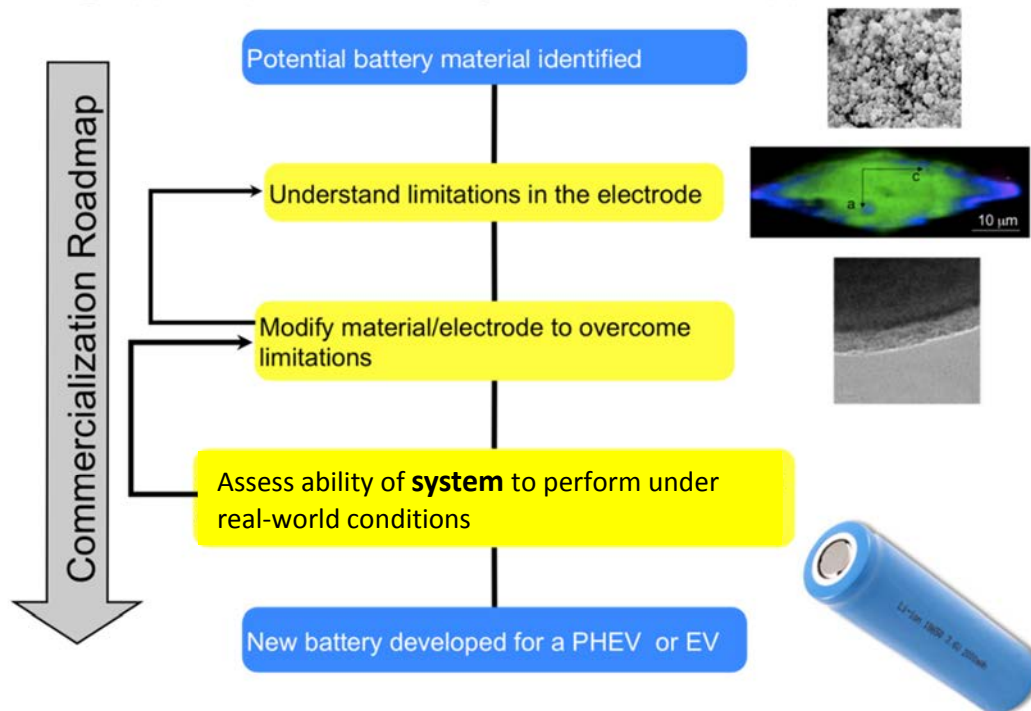


Figure V-1: BMR approach overview

The BMR program has a portfolio of topics to ensure success in the short, intermediate, and long term. The focus is on optimizing all three components of the battery, namely, the anode, cathode and electrolyte. To aid in these activities, the BMR program integrates three cross-cutting techniques: (i) advanced mathematical modeling, including tools across multiple length scales, (ii) diagnostics, especially *in situ* techniques to understand the behavior of the materials, and (iii) electrochemical characterization, to ensure that material level understanding can be translated into device-level performance. The program funds a multidisciplinary team of world-renown researchers using state-of-the-art equipment and facilities. In the pursuit of their activities, the BMR investigators push the boundaries on advanced battery technology by developing better tools and techniques to address the challenges. The structure of the BMR program and the areas of focus are illustrated in Figure V-2. A summary of the individual focus areas is listed below.

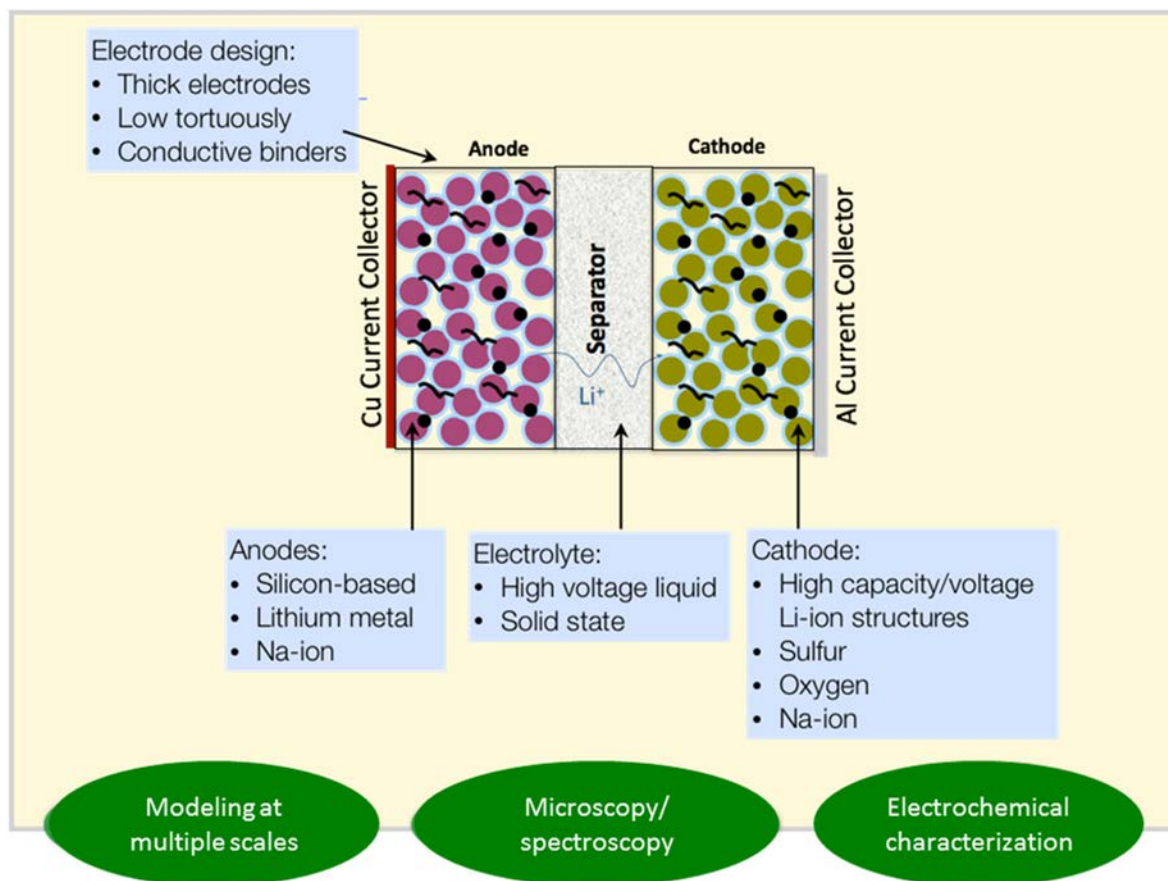


Figure V-2: Areas of focus in the BMR program with materials discovery aided by modeling and diagnostics

Advanced Electrode Architectures involve understanding the performance, life, and abuse tolerance of battery electrodes using innovative electrochemical techniques. In addition, the tasks also focus on finding ways to redesign the electrode architecture to extract more energy and power from existing materials, for example, by increasing the thickness of the electrodes. Emphasis is placed on understanding how electrodes behave and using this knowledge to decrease the tortuosity and increase the thickness of the electrodes. Projects are presently concentrating on graphite and silicon-based anodes, and on metal oxide cathodes. This effort contains four projects: (1) *Higher Energy Density via Inactive Components and Processing Conditions* (Lawrence Berkeley National Laboratory), (2) *Assembly of Battery Materials and Electrodes* (HydroQuebec), (3) *Design and Scalable Assembly of High-Density, Low-Tortuosity Electrodes* (Massachusetts Institute of Technology), and (4) *Hierarchical Assembly of Inorganic/Organic Hybrid Si Negative Electrodes* (Lawrence Berkeley National Laboratory).

Silicon Anodes focus on finding ways to enable the use of silicon as an anode material to take advantage of the order of magnitude extra capacity compared to currently-used graphite anodes. A big issue with this system is the large first-cycle irreversible capacity loss due to the formation of the solid electrode interface (SEI) and the large volume expansion when intercalating silicon. This effort consists of two projects: (1) *Development of*

Silicon-Based High-Capacity Anodes (Pacific Northwest National Laboratory, University of Pittsburgh) and (2) *Pre-Lithiation of Silicon Anode for High-Energy Lithium-Ion Batteries* (Stanford University). In project 1, a low-cost Si-graphite-carbon composite and a nanoscale silicon and lithium-ion conducting lithium oxide composite will be developed to improve the long-term cycling performance while maintaining reasonably high capacity. Project 2 explores developing facile and practical methods to increase first-cycle Coulombic efficiency of silicon anodes, and will seek to synthesize fully lithiated silicon and other lithium compounds for pre-storing lithium.

High Energy Density Cathodes for Advanced Lithium-Ion Batteries aim to find novel cathode materials and processing methods that offer significant improvements in volumetric and specific energy and/or power over current state-of-the-art materials, like $\text{Li}(\text{NiCoMn})_{1/3}\text{O}_2$. Previous efforts focused on developing high-voltage cathode materials including NMC and Ni-Mn spinels. In our present program, four projects are directed toward new syntheses and modifications of existing materials to improve cathode stability under high-voltage cycling conditions ($> 4.4 \text{ V}$) for Ni-rich NMC and Li-Mn-rich NMC [Pacific Northwest National Laboratory (*Development of High-Energy Cathode Materials*), Argonne National Laboratory (*Novel Cathode Materials*), (*Processing Methods, Exploring Cobalt and Nickel Spinels in Structurally Integrated Composite Electrodes*), Lawrence Berkeley National Laboratory (*Advanced Cathode Materials for High-Energy Lithium-Ion Batteries*)]. Another four projects are directed toward synthesis and structural stabilization of high-capacity polyanionic cathodes that can have > 1 lithium per transition metal and be in crystalline or amorphous phases [Oak Ridge National Laboratory (*Studies of High Energy Density Cathodes for Advanced Lithium-ion Batteries*), Lawrence Berkeley National Laboratory (*Discovery of High-Energy Battery Materials*), Brookhaven National Laboratory (*In situ Solvothermal Synthesis of Novel High Capacity Cathodes*) and State University of New York at Binghamton (*High Energy Density Lithium Battery*)] and one project is developing membranes to stabilize lithium metal anodes and eventually enable high-capacity cathodes in full-cell configurations [UT Austin (*Lithium Batteries with Higher Capacity and Voltage*)].

Diagnostics involve the use of advanced techniques, such as Fourier transform infrared (FTIR), X-ray absorption fine structure (XAFS), X-ray diffraction (XRD), and nuclear magnetic resonance (NMR) to investigate interfacial and micro-scale failure mechanisms in lithium-ion batteries. Projects often use DOE user facilities and include *in situ* diagnostic techniques. Several projects are tackling the chemical processes and reactions at the electrode/electrolyte interface. Researchers at Lawrence Berkeley National Laboratory are using *in situ* and *ex situ* vibrational spectroscopy, far- and near-field scanning probe spectroscopy, and laser-induced breakdown spectroscopy to understand the composition, structure, and formation/degradation mechanisms of the SEI at the silicon anode and high-voltage cathodes (*Design and Synthesis of Advanced High-Energy Cathode Materials, Interfacial Processes-Diagnostics, Advanced in situ Diagnostic Techniques for Battery Materials, Analysis of Film Formation Chemistry on Silicon Anodes by Advanced in situ and Operando Vibrational Spectroscopy*). The University of California at San Diego is combining scanning transmission electron microscopy/ electron energy loss spectroscopy (STEM/EELS), XPS, and ab initio computation for surface and interface characterization and to identify the cause of electrode instability (*Optimization of Ion Transport in High-Energy Composite Cathodes*). Cambridge University is employing NMR to identify the major SEI components, their spatial proximity, and how they change during cycling (*NMR and Pulse Gradient Studies of SEI and Electrode Structure*). At Brookhaven National Laboratory and Pacific Northwest National Laboratory efforts (*Advanced in situ Diagnostic Techniques for Battery Materials, Microscopy Investigation on the Fading Mechanism of Electrode Materials*) are concentrating on elucidating the fading mechanisms of electrode materials, using synchrotron based X-ray techniques (diffraction and hard/soft X-ray absorption) and high-resolution transmission electron microscopy (HRTEM). Finally, Argonne National Laboratory is developing model systems of electrode materials that will be used for advanced diagnostic and mechanistic studies at both bulk and single-crystal levels (*Characterization and Computational Modeling of Structurally Integrated Electrode*).

Advanced Electrode Material Modeling provides a mathematical perspective to the challenges confronting next generation battery materials such as high-capacity lithium-ion intercalation and sulfur cathodes, and silicon and lithium metal anodes. Knowledge gained in understanding the failure modes will lead to potential solutions that can be investigated by the material synthesis and electrode architecture groups. Three projects at Lawrence Berkeley National Laboratory are focusing on understanding the working principles of high capacity lithium-excess cathode materials (*Predicting and Understanding Novel Electrode Materials from First Principles, First Principles Calculations of Existing and Novel Electrode Materials*) and the Li/S system

(*Electrode Materials Design and Failure Prediction*). In the area of silicon anodes, efforts are underway to understand the interfacial instability of Si and suggest methods to improve the cyclability at General Motors and Michigan State University (*A Combined Experimental and Modeling Approach for the Design of High Current Efficiency Silicon Electrodes*). In addition, Texas A&M University is focusing on designing artificial SEI layers that can accommodate the volume change (*First Principles Modeling of SEI Formation on Bare and Surface/Additive Modified Silicon Anode*). Finally, efforts at Brigham Young University (*Predicting Microstructure and Performance for Optimal Cell Fabrication*) are focused on understanding conduction within the electrode and on simulating the full electrode that describes the intricate physics inside the battery electrode.

Metallic Lithium and Solid Electrolytes aim to solve the long-standing problems of lithium metal anodes: dendritic growth and poor efficiency during cycling. For the liquid electrolyte batteries, Pacific Northwest National Laboratory is examining the use of dual Li salts and organic additives to the typical organic carbonate electrolytes to impede Li corrosion and dendrite formation at both the lithium and graphite anodes (*Lithium Dendrite Suppression for Lithium-Ion Batteries*). At Stanford University, novel coatings and 3D structures are being developed to suppress lithium surface roughening and lengthen cycle life (*Nanoscale Interfacial Engineering for Stable Lithium-Metal Anodes*). For solid electrolyte batteries, four programs are investigating a relatively new family of solid electrolytes utilizing a garnet crystal structure that demonstrates superionic conductivity and good electrochemical stability. Aspects of the processing of the ceramic garnet electrolyte are being addressed at the University of Maryland (*Overcoming Interfacial Impedance in Solid-State Batteries*) and at the University of Michigan (Solid Electrolytes for Solid-State and Lithium-Sulfur Batteries), with attention to effect of flaws on critical current density. Computational models will complement these experiments to better understand interfaces and guide reduction of the lithium and cathode area specific resistance. At Oak Ridge National Laboratory, composite electrolytes composed of ceramic and polymer phases are being investigated, anticipating that the mixed phase structures may provide additional means to adjust the mechanical and transport properties (*Composite Electrolytes to Stabilize Metallic Lithium Anodes*). Lastly, Oak Ridge National Laboratory and Michigan Technological University are teaming to use nano-indentation methods to measure the mechanical properties of the solid electrolyte, the Li-metal anode, and the interface of an active electrode (*Mechanical Properties at the Protected Interface*).

Lithium Sulfur Batteries focus on solving the problems related to the sulfur cathode, especially the migration of polysulfides to the anode. These include: limited inherent electronic conductivity of sulfur and sulfur compound based cathodes, volumetric expansion and contraction of both the sulfur cathode and lithium anode, soluble polysulfide formation/dissolution and sluggish kinetics of subsequent conversion of polysulfides to Li_2S resulting in poor cycling life, particle fracture and delamination as a result of the repeated volumetric expansion and contraction, irreversible loss of lithium at the sulfur cathode, resulting in poor Coulombic efficiency, and high diffusivity of polysulfides in the electrolyte, resulting in plating at the anode and consequent loss in cell voltage. To address these issues, this effort focuses on (i) encapsulating the sulfur in polymer, carbon matrices, (ii) protecting the Li metal to prevent side reactions with polysulfides, (iii) changing the cathode by additives and other substitutions, and (iv) understanding the reactions using x-ray spectroscopy and *ab initio* and mesoscale modeling. The goal is to ensure stable cycling without the detrimental effects of the dissolution/precipitation reaction. The Team includes University of Pittsburgh, Lawrence Berkeley National Laboratory, Argonne National Laboratory, Brookhaven National Laboratory, Pacific Northwest National Laboratory, Stanford University, Texas A&M University, University of Wisconsin and University of Texas Austin).

Li-Air Batteries have an estimated practical energy density of ~ 800 Wh/kg and has the potential to be extremely beneficial for long-range EVs. Although significant progress has been made in this area in recent years, the research in this field is still in an early stage, and many barriers must be overcome before practical applications are observed. The main barriers include: instability of electrolytes and air electrode during charge/discharge processes in an O-rich environment, limited cyclability, low energy efficiency associated with large over-potential and poor cyclability, low power rate capability due to electrode blocking by the reaction products, and absence of a low-cost, high-efficiency oxygen supply system (such as oxygen selective membrane). In this focus area, Pacific Northwest National Laboratory seeks to provide a better understanding on the fundamental reaction mechanisms of Li-O₂ batteries and identify the required components (especially electrolytes and electrodes) for stable operation of Li-O₂ batteries (*Rechargeable Lithium-Air Batteries*). Argonne National Laboratory is developing new cathode materials and electrolytes with long cycle life, high

capacity, and high efficiency (*Lithium-Air Batteries*) and Liox is replacing traditional organic and aqueous electrolytes with a nonvolatile, inorganic molten salt (*Efficient Rechargeable Li/O₂ Batteries Utilizing Inorganic Molten Salt Electrolytes*).

Na-Ion Batteries have attracted increasing attention due to the more abundant and less expensive nature of the sodium resource. Due to the high-risk nature of the project, the BMR program uses this effort to ensure that it stays abreast of the challenges confronting this novel system. Brookhaven National Laboratory is employing synchrotron-based *in situ* X-ray techniques and other diagnostic tools to evaluate new materials and redox couples, in order to gain a fundamental understanding of the mechanisms governing the performance of these materials, and provide guidance for new material developments (*Exploratory Studies of Novel Sodium-Ion Battery Systems*).

V.B. Advanced Electrode Architectures

V.B.1. Higher Energy Density *via* Inactive Components and Processing Conditions (LBNL)

Vincent Battaglia, Principal Investigator

Lawrence Berkeley National Laboratory
1 Cyclotron Road
Berkeley, CA 94960
Phone: 510-486-7172; Fax: 510-486-4260
E-mail: vsbattaglia@lbl.gov

Tien Q. Duong, DOE Program Manager

U.S. Department of Energy
Advanced Battery Materials Research (BMR)
Vehicle Technologies Office
1000 Independence Avenue, SW
Washington, DC 20585
Phone: 202-586-7836
E-mail: Tien.Duong@ee.doe.gov

Start Date: October 1, 2016
End Date: September 30, 2018

Abstract

Objectives

- To determine how thick of an electrode can be produced via standard processing conditions and materials.
- To determine how thick of an electrode can be produced through modifications of the components and the processing conditions.
- To determine how thick and to what minimum porosity an electrode can be cast and still achieve the EV energy and power requirements.
- To determine the effect of material distribution on performance and cycling characteristics.
- To determine the effect of rheological properties and drying rates on material distribution.
- To determine the effect of material properties on rheological properties.
- Develop engineering principles that guide electrode formulations.

Accomplishments

- Verified that binder from a new supplier functions as well and is as processible as the binder from our original supplier.
- Fabricated thick electrodes at different casting speeds.
- Fabricated thick electrodes at different doctor blade heights.
- Fabricated thick electrodes from slurries of at different viscosity.
- Fabricated electrodes with binders of two different molecular weights from the same supplier.
- Calendered electrodes to different porosities and measured their capacity density, average voltage, and resistance at 80% DOD.

- Developed a technique for measuring the binder, carbon, and active material distribution of a cross section of an electrode from current collector to surface.

Future Achievements

- Fabricate electrodes with binders of a third molecular weight.
- Fabricate electrode with a different carbon additive.
- Measure the rheological properties of our slurries.
- Measure the mechanical properties of our dried laminates.
- Assess effect of drying rates.
- Assess cycleability of electrodes.

Technical Discussion

Background

Improvements in battery energy density have been attempted in the past. Typically, the approach has been to see how thick an electrode one can make using standard processing conditions and standard materials. In this research, we shall investigate the effect of making moderately small but significant changes to materials that make up a lithium-ion battery electrode and determine how to select material for making electrodes of any thick-ness.

Introduction

Battery energy density is one of the key factors limiting the widespread uptake of EVs in the United States. There are three approaches to addressing this issue: 1) new chemistries with higher capacity and/or voltage, 2) extracting more capacity and higher voltages out of present materials, and 3) improved cell and electrode engineering. This project adopts the third approach of taking today's state of the art lithium-ion chemistry (NCM/Graphite) and attempting to improve the energy density by increasing the ratio of active material to inactive material. But instead of investigating the ability to make thicker electrodes from the standard materials used in lithium-ion batteries, this project will investigate small but significant changes to the electrode components, for example, changing the molecular weight of the binder, changing the morphology of the conductive additive, changing the size distribution of the active material, and testing the effectiveness of pre-coating the current collector with binder and conductive agent. As we have found, the suggested changes affect the rheology of the slurry. The rheology of the slurry impacts the initial height of the cast slurry and the quality of the dried laminate. It also affects the distribution of the materials during the drying step and may impact the cohesion and adhesion of the laminate.

Approach

The approach is primarily experimental. Systematic changes to the electrode materials and processing conditions will be made and the rheology of the slurry measured. Electrodes will then be cast to different thicknesses and calendered to different porosities. Electrode physical characteristics will be measured such as material distribution, Young's modulus, cohesion, and adhesion, along with its electrochemical characteristics such as energy vs. discharge rate, pulse power at 80% depth of discharge, and cycleability. Relationships between starting materials, rheological properties, and electrode properties will be developed.

Results

In the quarter before the project officially started, the results of casting films using our standard materials and processes but at varying doctor blade heights were reported. To summarize: laminates were drawn with the doctor blade set as high as 750 microns; the laminates set to about a 1/3 of the doctor blade height after drying;

it was found that laminates cast at doctor blade heights greater than 500 microns easily delaminated from the current collector.

During the first quarter of the project, laminates were cast using a powder binder of PVDF provided by Arkema (761 - considered a standard binder for lithium-ion cells and has a molecular weight of ca. 400,000.) The first discovery in switching to this new binder is that when added to NMP, the solution is clear. The standard binder utilized up to then, which is available in powder and solution form (dissolved in NMP), produced a yellow to brown tint when in solution form. It is believed that this is probably some impurity that, for now, does not warrant further investigation but is notable. The second discovery to switching to the Arkema binder is that the processing with this binder is simpler: slurries mixed faster and more uniformly with the Arkema binder, despite the fact that the Arkema binder has a higher molecular weight than the original baseline binder (molecular weight ca. 250,000).

Up until now our group has been responsible for making electrodes for Focus Groups and evaluating new materials for their capacity and cycleability under galvanostatic conditions – typical conditions familiar to the scientific community. For this project, testing is shifting to be more consistent with the EV Battery Test Procedures Manual published by the DOE and USABC. Possessing less familiarity with this manual, the HPPC test was conducted, but was done so with the profile consistent for evaluating HEVs, not EVs, and therefore, the test did not include a 30-second current pulse. (Electrodes are presently under test with the proper load curve.) Below (Figure V-3) is a plot of the 10-s pulse resistance versus depth of discharge data for laminates ranging in loadings from 1.875 to 4.887 mAh/cm². One sees in this plot that there is a maximum in the resistance for electrodes cast at 2.655 mAh/cm². This is somewhat of a surprise. It has been long believed that the resistance should start high for thin electrodes, drop down as the electrodes get thicker, and start to rise again as the electrodes get thicker still. The reason being, for thin electrodes, the ohmic resistance is low but all of the ionic current in the electrolyte has to cross through a small total surface area of active material in the transition to electronic current. This small surface area results in large superficial-area based resistance. Why the resistance drops down for our thinnest electrodes is still unclear but is likely attributable to the unstable resistance of the lithium side of the cell.

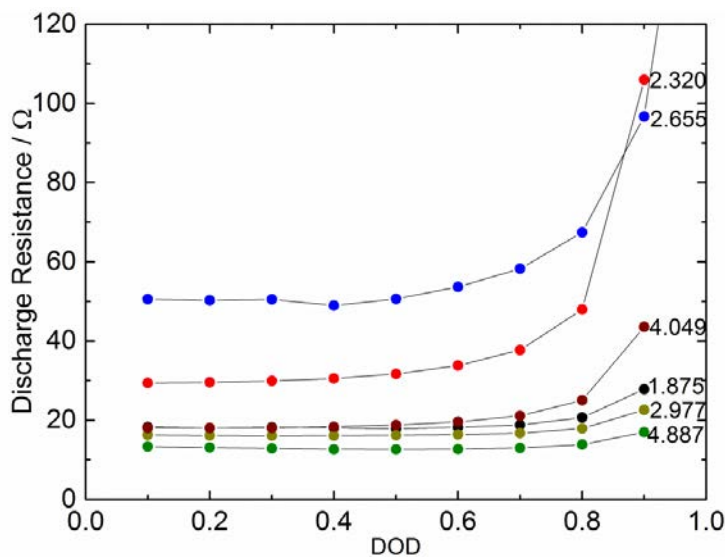


Figure V-3: The resistance from 10-second current pulses at every 10% DOD. The cell had an area of approximately 1.6 cm². The numbers listed next to each curve are the mAh/cm² of the electrode. Ignoring the lowest loading electrode, in general, the resistance is dropping with increase in loading

In the 2nd quarter, electrodes were cast using a high molecular-weight PVdF binder (HMW, ca. 1,000,000 g/mol). The difference in preparing a slurry with high molecular weight binder and low molecular weight binder (LMW) is that more NMP is needed for the former. Despite the need for more NMP, the slurry has a relatively higher viscosity. A higher viscosity appears beneficial for two reasons: 1) thick castings require higher viscosity to prevent them from collapsing and running off the current collector, and 2) higher viscosities appear to help prevent the accumulation of conductive agent on the surface of the electrode as the laminate dries.

SEMs of the cross sections of 200 micron thick electrodes fabricated from binders of two different molecular weights are provided in Figure V-4. In the figure on the left, one observes a thin film (*ca.* 40 microns thick) on the top of the electrode produced when using a LMW. The figure on the right shows no such film with the HMW.

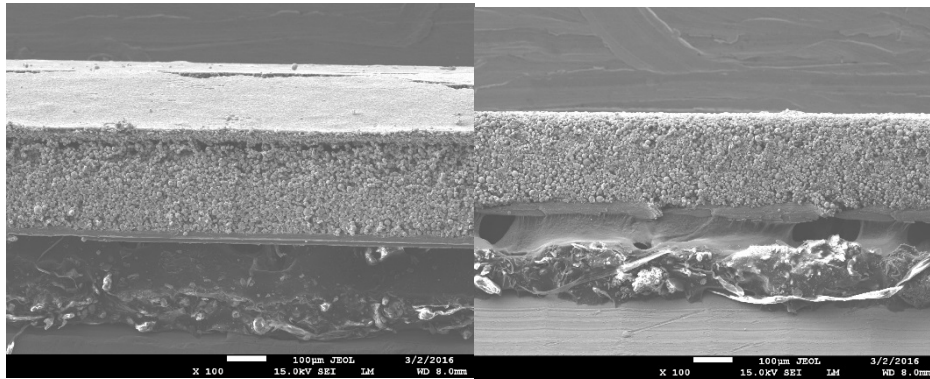


Figure V-4: SEMs of the cross section of electrodes prepared with two different molecular weights: left) low molecular weight binder, right) high molecular weight binder

Figure V-5 provides the results of EDX performed on the cross sections of these two electrodes from the current collector up to the surface. Here one observes in the figure on the left (LMW) a varying distribution, with oxygen (from the cathode) increasing up from the current collector to just before the surface, where it plunges, and carbon content (from conductive carbon and binder) decreasing up from current collector to just below the surface where it escalates. The figure on the right (HMW) displays a more uniform distribution from top to bottom.

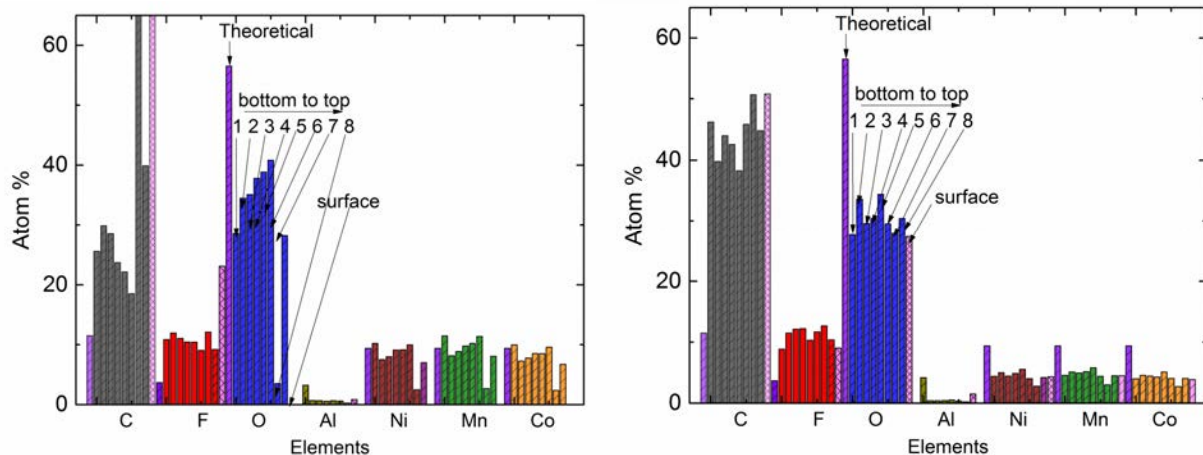


Figure V-5: EDX results of the cross section of the two laminates of an earlier figure. The numbers embedded in the figures refer to the composition in order from current collector up to the surface

Figure V-6 shows the performance of electrodes made with a LMW binder and a HMW binder. None of the electrodes were calendered. On the ordinate, the pulse power capability is plotted based on the resistance measured at 80% depth-of-discharge. On the abscissa is plotted 80% of the energy of the cell measured at a C-rate of C/3. The capacity per cm^2 is listed next to each data point on the graph.

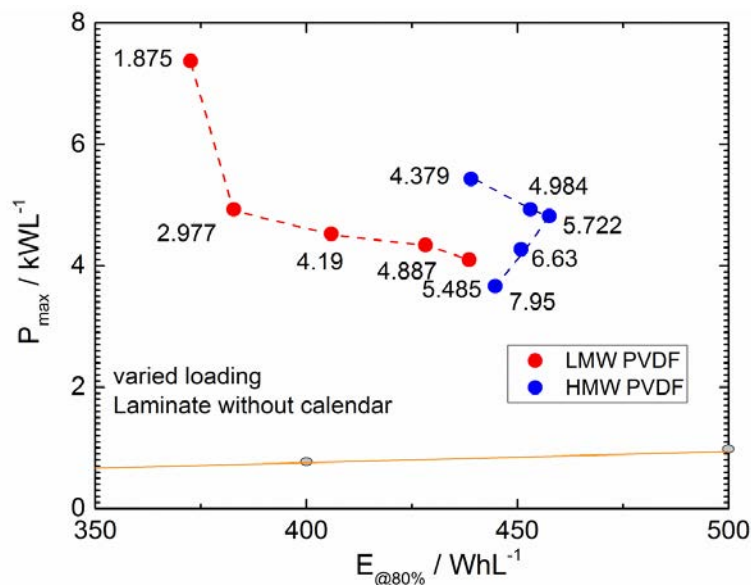


Figure V-6: Electrode performance data for uncalendered electrodes of two different molecular weight binders (red for LMW, blue for HMW). Numbers indicate the area specific capacity (mAh/cm²) of each electrode

One sees that for the LMW electrode, the data stops at a loading of 5.485 mAh/cm². This is because electrodes of higher loading could not be produced as the laminate fell off of the current collector. One also sees that for electrodes of comparable loadings, the electrodes with the HMM binder provide both a higher energy density and a higher power density. This was a pleasant surprise. The electrode with a HWM binder was feared to show less energy and power but would allow one to produce thicker electrodes which would surpass that of the LMW electrodes. Demonstrating better overall performance may be due to the fact that the carbon additive and binder migrate to the surface of thick LMW electrodes during drying forming a film of carbon and binder. Thus, perhaps, either the film is diminishing the performance at C/3 and the resistance of the 30-second pulses or the lack of carbon throughout the bulk of the electrode is limiting access to the energy and creating more resistance to power pulses.

Another point of interest is that electrodes with HMW binder do eventually show a maximum in energy density. Apparently, for electrodes produced at greater than 5.7 mAh/cm² loading with this binder and are not calendered, all of the material in the electrode is not accessible at discharge rates of C/3.

Figure V-7 shows the power *versus* energy density (times 2 to include the anode) for electrodes of loading from 4.5 to 11 mAh/cm² and porosities from *ca.* 45% to as low as 8.4%. Except for the electrodes that are 11 mAh/cm², the electrodes at a given porosity show a slight increase in energy density with loading. More impressive is the increase in energy as a function of porosity. Since the current collectors and separators are not that thick when compared to electrodes that are *ca.* 200 microns, one sees little value in increasing their size; however, when these thick electrodes are compressed to low porosities, there is a much greater increase. Also impressive is that the energy can still be extracted at 8.4% porosity.

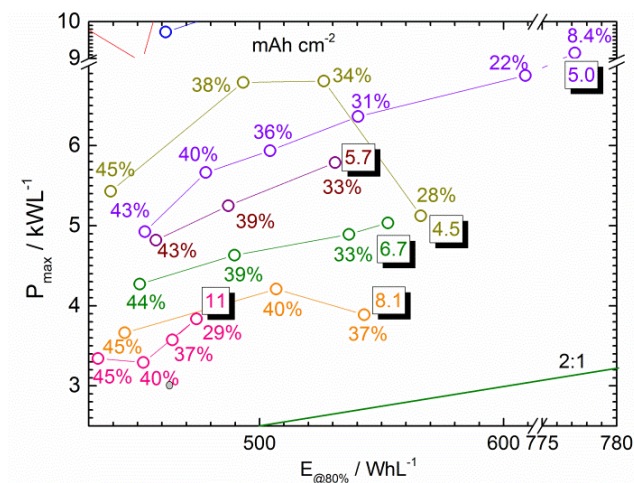


Figure V-7: Power vs. Energy densities x 2 for laminates at different loadings and porosities

Figure V-8 shows the energy density of electrodes at calendered to *ca.* 30% porosity at a C/3 discharge rate for different active material loadings. One sees that the energy density continues to increase up to about 8.1 mAh/cm² and then drops for electrodes at 11 mAh/cm². Questions that still remain: Does one see improved performance for even lower porosities? Do these electrodes cycle? Will they easily delaminate?

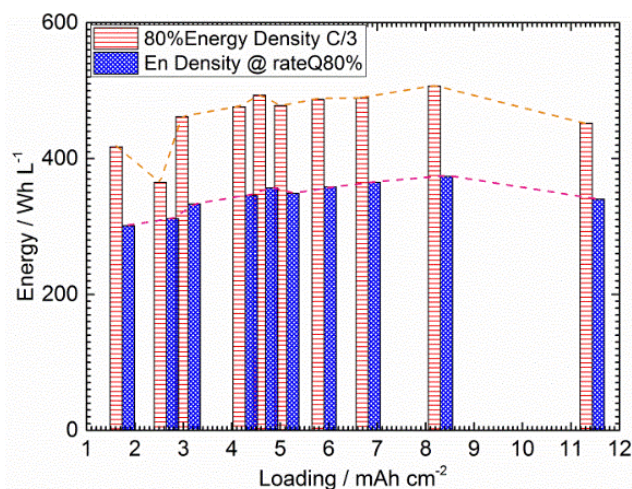


Figure V-8: Energy densities x 2 for laminates at different loadings and a porosity of ca. 30%

Conclusions

This year, we made tremendous progress on the project and accomplished the following:

- Switched to a new binder supplier.
- Discovered the binder from the new supplier is cleaner and easier to process.
- Laminates drawn and allowed to dry overnight with a standard molecular weight binder result in separation of the carbon additive from the active material and a thin coating of carbon on the electrode surface.
- Thick laminates produced with a high molecular weight binder (*ca.* 1 M g/mol) result in more uniform electrodes.
- Thick electrodes produced using a higher molecular weight binder have more power per cm² than those with a standard molecular weight binder.

- Early indications are that electrodes can be pressed to below 20% porosity and still meet the EV 30-sec pulse power requirement.
- Electrodes that are calendared with loadings as high as 8 mAh/cm² show higher energy density at a C/3 discharge rate than thinner electrodes.

The binder molecular weight matters. Is this due to its binding properties or its effect on the rheology? Do thicker electrodes have comparable cycling capability to standard electrodes? Moving forward, we will start investigating rheological properties and electrochemical cycling properties.

Products

Presentations/Publications/Patents

1. “Revealing and suppressing surface Mn(II) formation of Na_{0.44}MnO₂ electrodes for Na-ion batteries,” [Ruimin Qiao](#), [Kehua Dai](#), [Jing Mao](#), [Tsu-Chien Weng](#), [Dimosthenis Sokaras](#), Dennis Nordlunde, Xiangyun Song, Vince S. Battaglia, Zahid Hussain, Gao Liu, Wanli Yang, Nano Energy Volume 16, September 2015, Pages 186–195.
2. “The effect of cobalt doping on the morphology and electrochemical performance of high-voltage spinel LiNi_{0.5}Mn_{1.5}O₄ cathode material,” Jing Mao, Mengze Ma, Panpan Liu, Junhua Hu, Guosheng Shao, Vince Battaglia, Kehua Dai, Gao Liu, Solid State Ionics, Volume 292, September 2016, Pages 70–74.

V.B.2. Electrode Architecture-Assembly of Battery Materials and Electrodes (Hydro-Quebec)

Karim Zaghib

Hydro-Quebec (IREQ)
1800 Lionel Boulet
Varenes, QC J4X 1S1
Phone: 450-652-8019; Fax: 450-652-8566
E-mail: Zaghib.Karim@ireq.ca

Tien Q. Duong, DOE Program Manager

U.S. Department of Energy
Advanced Battery Materials Research (BMR)
Vehicle Technologies Office
1000 Independence Avenue, SW
Washington, DC 20585
Phone: 202-586-7836
E-mail: Tien.Duong@ee.doe.gov

Start Date: October 2012
End Date: September 2016

Abstract

Objectives

- Develop high-capacity, low-cost electrodes with good cycle stability and rate capability to replace graphite in lithium-ion batteries.
- Identify an alternative supplier of Si powder material as baseline for the BMR.
- Fabricate laminated pouch lithium-ion cells of < 2 Ah capacities based on Si-anode and NCM cathode.

Accomplishments

- The process has been optimized to produce low-cost nano-Si powders by a metallurgical process that considers milling time, bead size, solid content and agitating speed.
- Scale-up test completed to produce ~kg level of nano-Si/C composite.
- The cyclability at higher loading level was improved with new water-based acrylic resin binder.
- Laminated pouch-type 1.5Ah lithium-ion batteries based on nano-Si/C composite and NCM cathode were assembled and their electrochemical performance was explored.

Future Achievements

- To increase the loading level of nano-Si/C composite anode electrodes, and different types of binder will be developed.
- To increase the cycle stability of nano-Si/C composite anodes, heat-treatment will be explored with different condition.

Technical Discussion

Background

The technical barriers to overcome are the electrochemical capacity limitations (both gravimetric and volumetric) of conventional carbon anodes by developing low-cost electrode architectures based on silicon. One of the biggest challenges of silicon is its volume expansion and structural changes which lead to capacity fade and shorter cycle life. These failures are due in part to loss of electrolyte by reduction and a SEI layer that is not stable on the surface with repeated cycling because of exposure of fresh surfaces of Si particles that result in a continuous reaction to form more SEI.

Life: Poor cycle life.

Cost: High \$/kWh.

Introduction

The target of the DOE's Program is to identify the next generation of high-energy batteries. Achieving this target will require materials of higher capacity and improved coulombic efficiency or cells with higher voltage. High-capacity anode materials such as Si or Sn alloys have the potential to fulfill the energy density requirements for EV/PHEV applications. However, large volume expansion during the lithiation process of these materials usually leads to fast capacity fade that hinders its practical applications. Real-time SEM studies on charge/discharge of Si-anodes have demonstrated that decreasing the particle size to nanometer scale is an effective means of accommodating the volume change, and thus delaying its degradation.

HQ proposed a strategy to design the architecture of the Si-anode material that can tolerate the volumetric expansion and provide acceptable cycle life with low capacity fade. The particle size, binder type and electrode composition are the main parameters that define the formulation of the Si-anode. The porosity of the electrode has a direct impact on the performance, and therefore was optimized by investigating various mixing methods.

Approach

- Explore a variety of synthesis methods to produce low-cost nano-Si materials with controlled purity and particle morphology.
- Develop an appropriate silicon anode architecture that can tolerate volumetric expansion and provide an acceptable cycle life with low capacity fade.
- Identify a binder and electrode composition by investigating parameters that define the electrode structure such as porosity, loading and electrode density. The optimized Si-anode will be matched with high-voltage NMC cathode to fabricate large format lithium-ion cells.
- Use *in situ* techniques such as SEM and impedance spectroscopy to monitor the particle and electrode environment changes during cycling.
- Achieve cost reduction by moving from more costly Si (>\$50/kg) to metallurgical Si which is projected to be \$3~\$5/kg.

Results

During this year, Hydro-Québec focused on optimizing the milling process to produce low-cost nano-Si powders compare to expensive nano-Si powders made by a plasma process. More effort was focused on the particle design by investigating different techniques. The particle size was optimized at around ~100nm size distribution. With this information, we optimized the milling process and explored the electrochemical performance with different binders in coin half-cells and with different electrolytes in full cells. The type of binder and the electrolyte component are critical to the electrochemical performance of nano-Si anodes and more effort should be focused on the development of the binder and electrolyte for Si applications. Hydro-Québec has identified techniques to produce secondary particles with milled nano-Si powder using a spray-dry

process and explored the scale-up test of ~kg level of nano-Si/C composites. The electrochemical performance of the material was evaluated in 1.5Ah full cells to determine the feasibility of utilizing nano-Si/C composite anodes.

1. ~100nm size milled nano-Si powders

The metallurgical Si is obtained as big chunks, which were crushed by the following steps: jaw crusher ($d_{50} < 13\text{mm}$), roll crusher ($d_{50} < 1\text{mm}$) and jet mill ($d_{50} < 10\mu\text{m}$). Then the powder was sieved with 150 mesh before wet milling. To further reduce the particle size in the second step, several process parameters were controlled such as; beads size (1.0mm beads size vs. 0.3mm), solid content (25% solid content vs. 10%) and milling power (2200 rpm vs. 3000 rpm). Organic IPA (isopropyl alcohol) was used as the mixing media for wet milling.

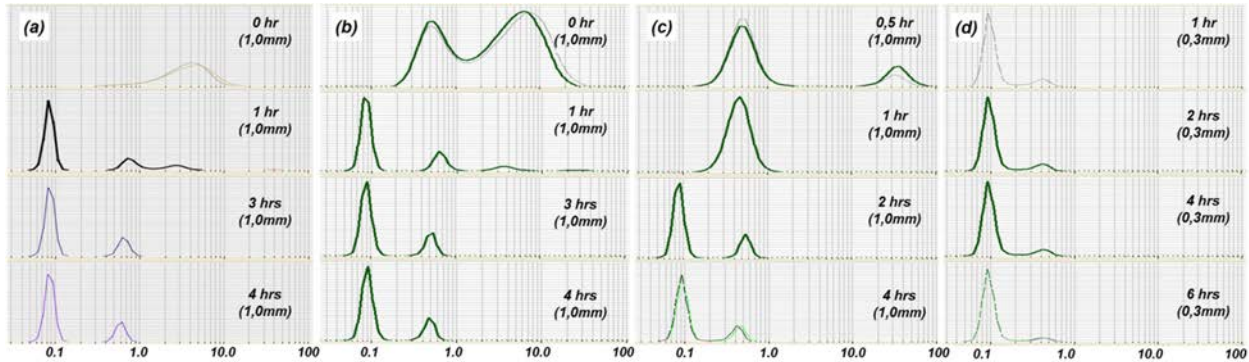


Figure V-9: Particle size distribution with different milling conditions (a) 1 mm dia./25%/2200rpm, (b) 1 mm dia./10%/2200 rpm, (c) 1 mm dia./10%/3000 rpm, and (d) 0.3mm dia./10%/3000 rpm; bead size/solid content/agitating speed

The particle size analysis shows clearly in Figure V-9 that at least 2 hours of milling time is required in all conditions. Reducing the solid content or increasing the power speed does not show any improvement in reducing the particle size. Nevertheless, using smaller beads of 0.3 mm shows some improvement regarding the second peak at 0.5 μm . The particles of this size are completely reduced after 6 hrs milling, approaching a monodispersed powder. In general, it seems that there is a limitation for particle reduction of this material at around 100 nm based on this technique.

2. Optimization of wet-milling time

With the information obtained in our previous work, we focused on the evaluation of electrochemical performance and characterization of materials obtained with different wet-milling times. We found that reducing the primary particle size obtained by the wet-milling process was limited to ~100 nm, and the electrochemical performance of the final product, especially obtained by more severe conditions (high energy, small beads, less solid content) showed low coulombic efficiency. The coulombic efficiency, especially 1st charge/discharge efficiency, should increase for the higher energy-density cell design.

On the other hand, the metallurgical Si powder obtained by jet milling and sieved with 100-mesh (~150 μm), was wet-milled in the circulation chamber filled with 1.0 mm diameter beads and IPA (isopropyl alcohol). The solid content was 20% and the samples were collected at different milling times (0, 3, 9 and 24 hrs) for physical characterization and electrochemical performance evaluation.

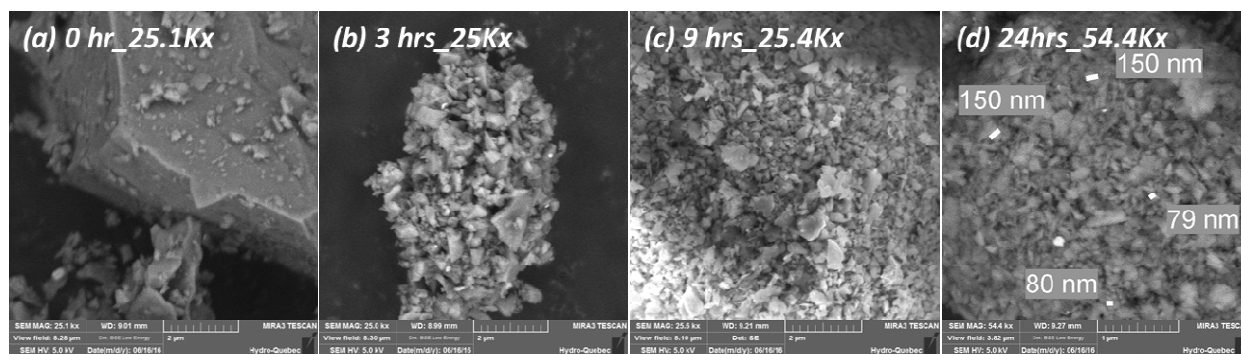


Figure V-10: SEM image of Si powder obtained with different milling times (a) 0 hr, (b) 3 hrs, (c) 9 hrs and (d) 24 hrs of wet-milling with 1 mm diameter beads and 2200 rpm agitating speed in the 20 wt% solid contents of IPA (isopropyl alcohol) solution

The SEM images (Figure V-10) show that the edge of the particles turned blunt and the particle size was reduced with milling time. The particle shape appears flake-like with longer milling time.

These powders were analyzed by XRD (Figure V-11) which showed that the peak intensity of Si(111) and the crystalline size decreased with milling time. In contrast, the FWHM of Si(111) and the peak intensity of Si-OH increased. The peak intensity ratio of Si-OH vs. Si(111) increased up to 48% with longer milling times, indicating an increased surface area.

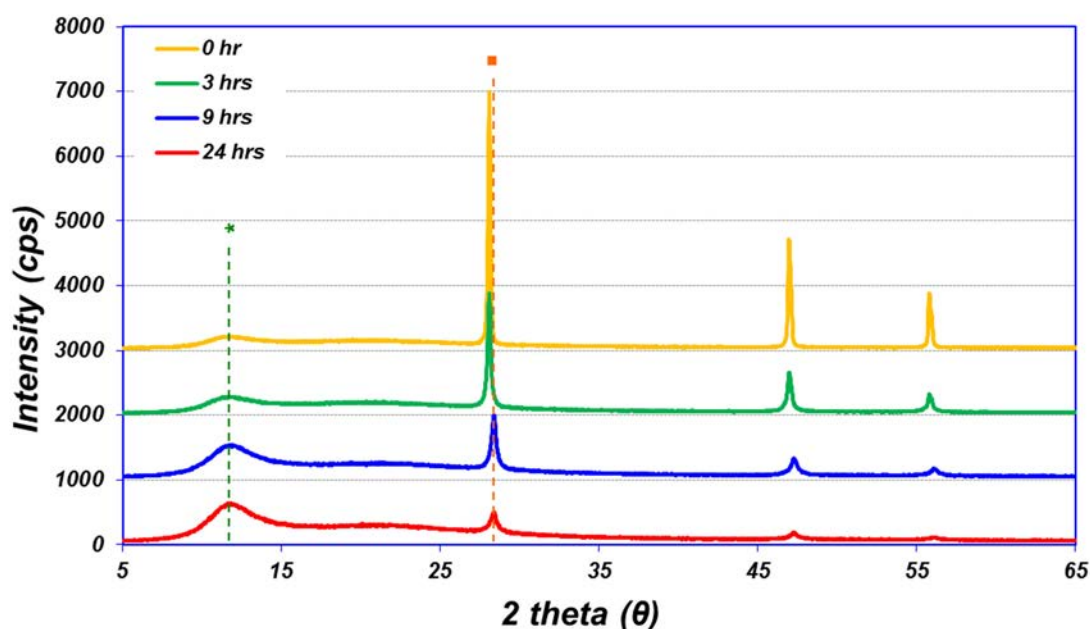


Figure V-11: X-ray diffraction patterns of Si powder milled with different time; (orange) 0 hr, (green) 3 hrs, (blue) 9 hrs and (red) 24 hrs

Figure V-12 shows the voltage profiles during the formation cycles along with 1st coulombic efficiency and discharge capacity. The initial (0 hr) sample (Figure V-12.a) showed a typical discharge profile of micro size Si powder with a plateau at around 0.4 V, and the 3 hrs milled sample (Figure V-12.b) still has around 40% of the plateau at 0.4 V. However, after 9 hrs of milling and higher (Figure V-12.c and d), the plateau at 0.4 V disappeared and the voltage profiles are nearly linear starting at around 0.1 V to around 0.6 V, which is a typical behavior we already observed with nano-Si powder produced by a plasma process.

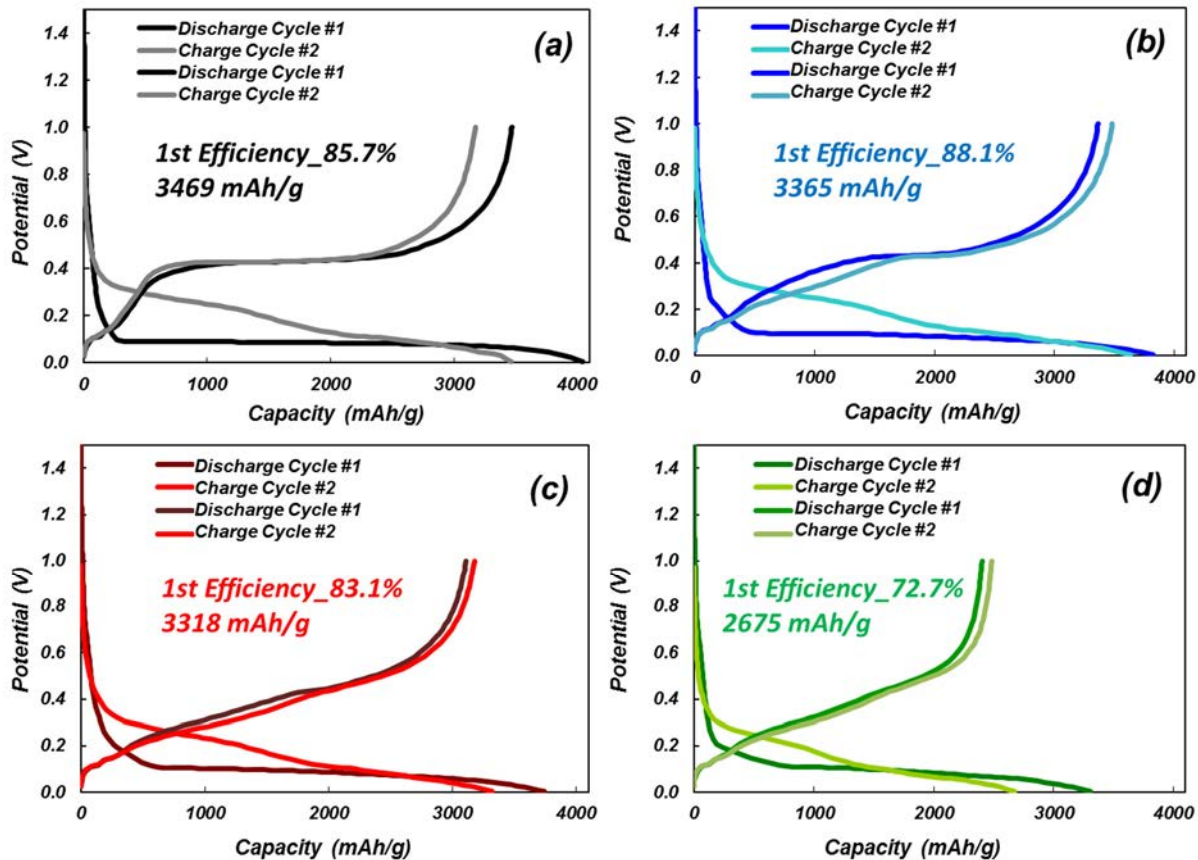


Figure V-12: Formation voltage profile of Si powder wet-milled with different times; (a) 0 hr, (b) 3 hrs, (c) 9 hrs and (d) 24 hrs

We observed that the 1st coulombic efficiency (CE) and discharge capacity decreased with milling time. The highest 1st CE (88.1%) was found with the sample milled for 3hrs, which also had a quite high discharge capacity of 3365 mAh/g. This confirms that the results obtained with the expensive nano-Si produced by a plasma technique can be duplicated by only optimizing the wet milling process.

3. Electrochemical performance with different binder and electrolyte

Hydro-Québec focused on improving the electrochemical performance of the Si materials by investigating different kinds of binders and electrolytes. Previously, the study was limited to improving the cycle life by optimizing the milling conditions, electrode structures and electrode formulations. In the case of the cycle performance of full-cells, cycle retention was always worse than that of half-cells because of the poor discharge/charge efficiency during cycling. The continuous formation and destruction of the unstable SEI (solid electrolyte interface) increases Li^+ consumption during cycling. Consequently, the formation of a stable SEI is a very important factor to improve the cycle life performance.

The voltage profiles of the formation cycles (Figure V-13) show the first discharge/charge efficiency obtained with different kinds of binders in coin half-cell tests. Acrylic resin (Figure V-13 (b)) shows the highest 1st cycle efficiency (84.2% with a capacity of 2973 mAh/g). On the other hand, the lowest 1st CE (72.8%) was found with the polyimide binder which shows the highest reversible capacity (3080mAh/g) during the first formation cycle.

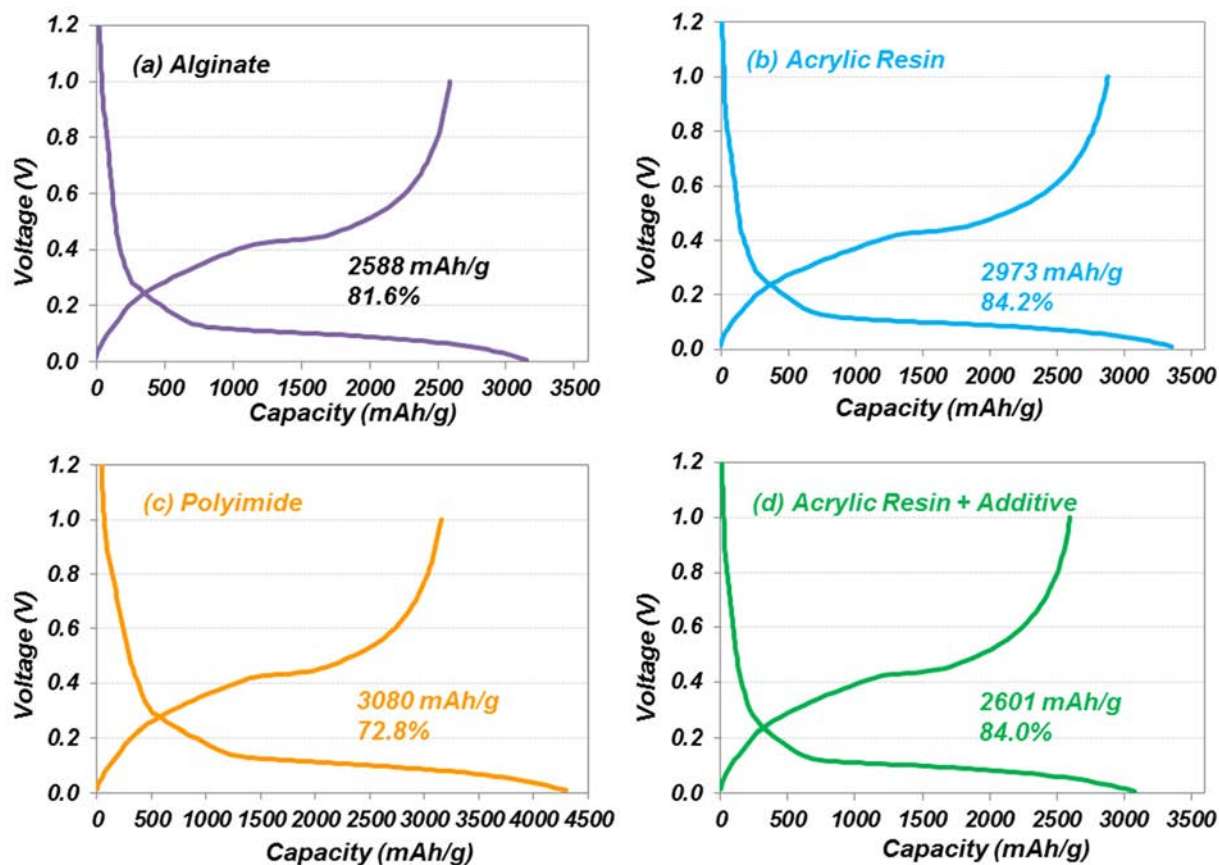


Figure V-13: Formation voltage profile of Si/C powder with different binders; (a) Alginate, (b) Acrylic Resins, (c) Polyimide and (d) Acrylic Resin + Additive

Figure V-14 shows the cycle performance with different binders in coin half-cells (Figure V-14.a) and with different electrolytes in full-cells (Figure V-14.b). Acrylic resin shows cycle retention of 2600 mAh/g after 60 cycles, while the lowest retention was found with polyimide (2000 mAh/g with 31% capacity fade). The alginate binder shows a capacity fade of 25%, with a capacity of 1900 mAh/g after 60 cycles. Based on these data, we selected the acrylic resin to make the electrode for full-cell tests to evaluate the effect of different kinds of electrolytes.

Figure V-14.b shows the cycle retention and efficiency during the cycle test in full-cells containing different electrolytes; EL-2 shows better cycle retention with better efficiency than the other electrolytes. However, the cycle life performance is not acceptable compared with that of commercial anodes.

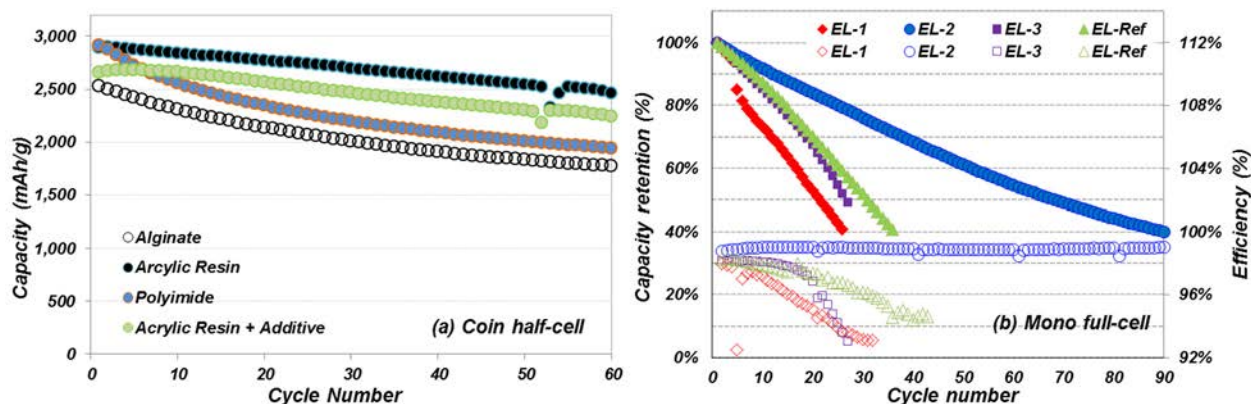


Figure V-14: Cycle retention of (a) different kinds of binders in coin half-cell level test with low loading level electrode and (b) different kinds of electrolytes in mono full-cell level test

In addition, we evaluated different electrolyte additives in the full cells composed of a Si-anode with an acrylic resin binder and NCM cathode.

4. Scale-up test for nano-Si/C composite

The nano-Si powder that was milled to 100 nm was used in the spray dry process with carbon and polymer to produce secondary particles in the nano-Si/C composite Figure V-15 shows photographs of the equipment used in the process.

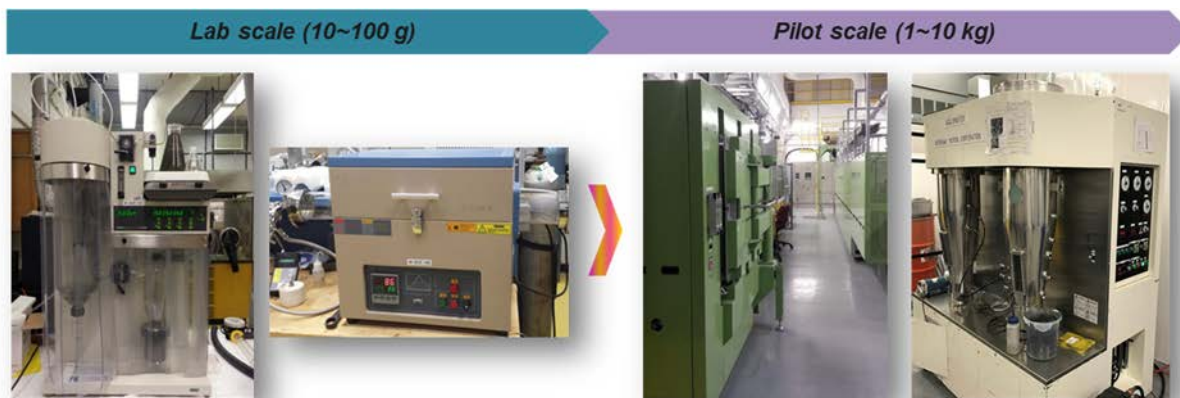


Figure V-15: Photos of (left) spray-dryer and tubular furnace for lab scale production of 10~100 g level and (right) simulator and agglomerator for pilot scale production of 1~10 kg level

The spray-dry process allows us to produce secondary particles of nano-Si/C composite with 5~60 μm particle size. (see Figure V-16.a). The cross section of particle obtained by ion-beam show that the secondary particles consist of hollow nano-Si particles, with an interior that contains a mixture of polymer, carbon black and a large fraction of void space (Figure V-16.b). For large-scale production using this technique (1-10kg), we used an Agglomerator machine and piloting furnace., and the secondary particles of nano-Si/C composite are shown in Figure V-16.c.

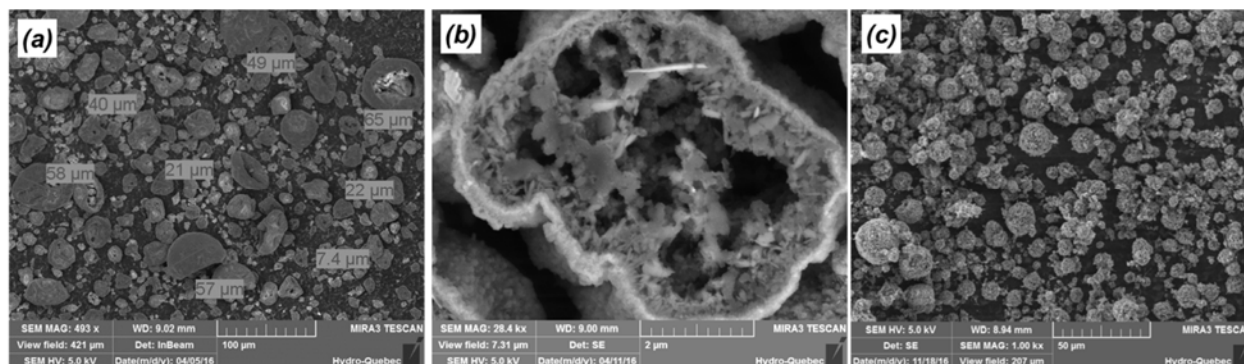


Figure V-16: SEM images (a) nano-Si/C composite made by spray-dryer, (b) the cross section view of (a) and nano-Si/C composite made by agglomerator (~kg level)

5. Full cell performance of 1.5Ah laminated-pouch cell

We assembled pouch cells containing NMC//nano-Si/C composite with a capacity of 1.5Ah (Figure V-17.a). The electrochemical performance (formation capacity, rate capability and cycle stability) was evaluated. The measurements at 0.2C rate revealed a discharge capacity around 1400 mAh and 95% of designed cell capacity between 2.75V and 4.4V voltage window (Figure V-17.b).

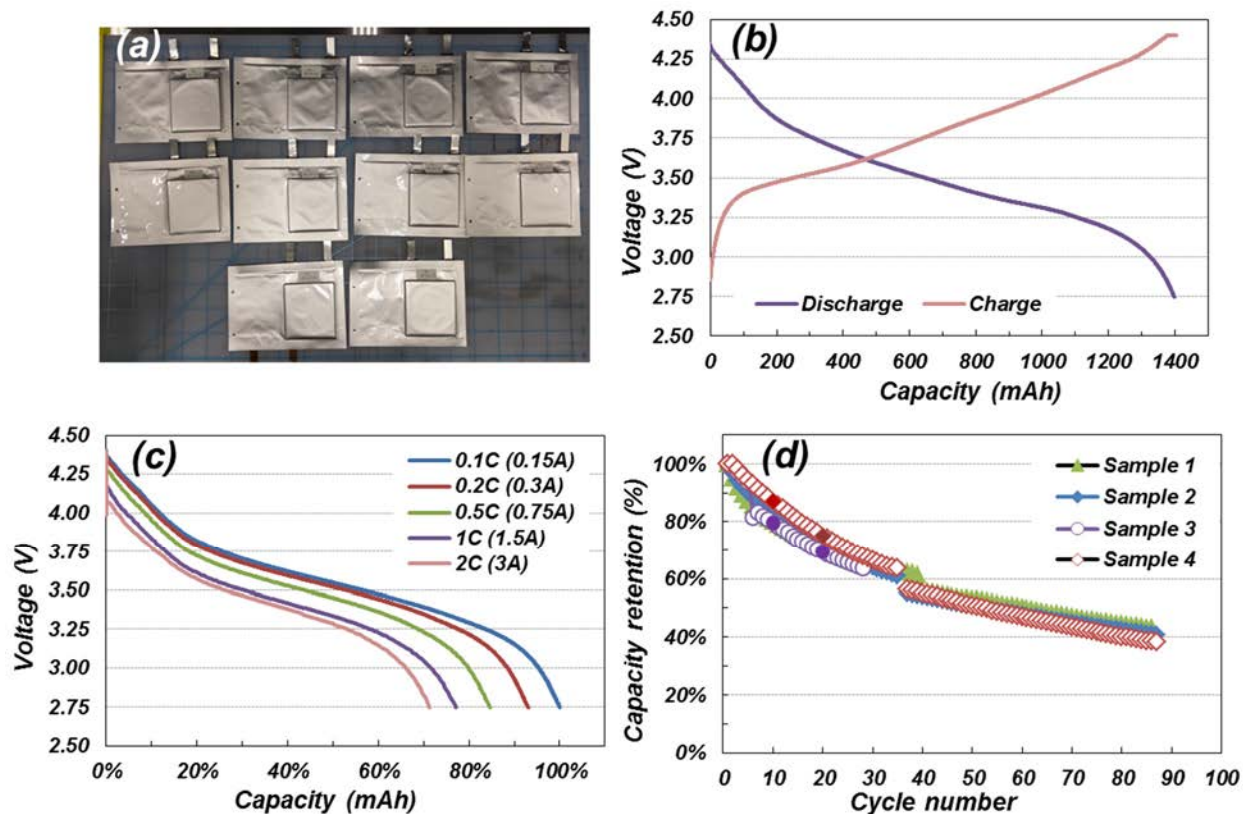


Figure V-17: Full cell performance of 1.5 Ah pouch-type cell (a) assembled cell (b) voltage profile during charge-discharge between 2.75 V and 4.4 V with 0.2 C rate (c) rate capability with different current and (d) cycle ability at RT

The rate capability with different current (0.1-2C) shows 70% of the capacity was delivered at 2C rate and low IR drop (Fig.9.c). However, cycling stability of these cells was not good. After 90 cycles, the capacity retention was only 40%, which we attribute to the stability of the anode material and its mechanical integrity.

6. Deliverables

- (1) 50 g nano-Si/C powder made by the spray dry process was supplied as 1st deliverable to LBNL for evaluation.
- (2) 2 films of nano-Si/C electrodes were supplied as 2nd deliverable to LBNL for evaluation.
- (3) 10 laminated-pouch full cells were supplied as 3rd deliverable to LBNL for evaluation.

Conclusions

During this year, Hydro-Québec focused on optimizing the milling process to produce low-cost nano-Si powders to replace the expensive nano-Si powders made by a plasma process. More effort was focused on the particle design (morphology and size) by investigating different techniques. The particle size was optimized at around ~100nm size distribution. Based on this data, we optimized the milling process and explored the electrochemical performance with different binders in coin half-cells and with different electrolytes in full cells. The type of binder and the electrolyte component play a critical role on the electrochemical performance of nano-Si anode. Consequently, more effort was focused on the development of alternative binders and electrolytes for Si application. Hydro-Québec explored the production of secondary particles with milled nano-Si powder using spray-dry process, and succeeded in scale-up to the ~kg level of nano-Si/C composites. With this material, The electrochemical performance of 1.5Ah full cells with the n composite materials was evaluated to determine the possibility of using nano-Si/C composite as anode in lithium-ion cells.

Products

Presentations/Publications/Patents

1. BMR 2016 1st Quarterly Report, January, 2016.
2. BMR 2016 2nd Quarterly Report, April, 2016.
3. U.S. DOE's 2016 Annual Merit Review, Washington D.C., June 6-10, 2016.
4. BMR 2016 3rd Quarterly Report, July, 2016.
5. BMR 2016 4th Quarterly Report, October, 2016.

References

1. Dominic Leblanc, Pierre Hovington, Chisu Kim, Abdelbast Guerfi, Daniel Bélanger, Karim Zaghbi "Silicon as anode for high-energy lithium-ion batteries: From molten ingot to nanoparticles", *Journal of Power Sources*, Volume 299, 20 December 2015, Pages 529-536.
2. Chapter under press "Silicon nanopowder synthesis by inductively-coupled plasma", in: *Silicon Nanomaterials Sourcebook*, edited by Klaus D. Sattler, Taylor & Francis.

V.B.3. Design and Scalable Assembly of High Density Low Tortuosity Electrodes (Massachusetts Institute of Technology)

Yet-Ming Chiang, MIT-Principal Investigator

Massachusetts Institute of Technology
77 Massachusetts Avenue
Cambridge, MA 02139
Phone: 617-253-6471; Fax: 617-253-6201
E-mail: ychiang@mit.edu

Tien Q. Duong, DOE Program Manager

U.S. Department of Energy
Advanced Battery Materials Research (BMR)
Vehicle Technologies Office
1000 Independence Avenue, SW
Washington, DC 20585
Phone: 202-586-7836
E-mail: Tien.Duong@ee.doe.gov

Start Date: May 22, 2013

End Date: April 3, 2017

Abstract

Objectives

- Develop scalable high density low-tortuosity electrode designs and fabrication processes to enable increased cell-level energy density compared to conventional lithium-ion technology.
- Maximize active material utilization and lower cost of lithium-ion cells for EV applications.
- Test electrochemical performance of fabricated electrodes in continuous and pulse modes representative of vehicle drive cycles.

Accomplishments

- Developed a directional-freezing approach for producing low-tortuosity porosity in electrodes that does not require subsequent sintering.
- Developed a novel magnetic alignment process for producing continuous low tortuosity porosity oriented in the normal direction of planar electrodes.
- Demonstrated sintered cathodes and anodes delivering more than 10 mAh/cm² area capacity under USABC's DST drive cycle.
- Demonstrated full cells in which the area capacity of both electrodes exceeds 10 mAh/cm².
- Developed a non-sintering approach for producing magnetically-aligned low tortuosity pores in battery electrodes.

Future Achievements

Demonstrate half-cells and full lithium-ion cells with >10 mAh/cm² area capacity for both cathode and anode, prepared by a non-sintering process.

Technical Discussion

Introduction

The high cost (\$/kWh) and low energy density of current automotive lithium-ion technology is in part due to the need for thin electrodes and associated high inactive materials content. The number of separator and current collector layers per Ah of cell capacity is inversely proportional to the area capacity (mAh/cm²) of the electrode. While area capacity (i.e., active materials loading) can be increased arbitrarily by increasing electrode thickness and/or density, increased loading does not contribute usable energy unless the capacity can be accessed at practical C-rates, or under realistic automotive drive cycles. Thus, concepts that can provide higher usable area capacity, e.g. during ~2C pulses in an EV or PHEV drive cycle, are needed. This project develops processes for producing low-tortuosity porosity in the primary transport direction of battery electrodes, i.e., normal to the electrode plane, thereby maximizing the usable area capacity. The electrodes produced use known families of cathode and anode actives, and are tested under representative drive cycles such as the dynamic stress test (DST). The new electrode architectures developed under the program deliver at least 3 times the areal capacity (mAh/cm²) of current technology under duty cycles representative of vehicle applications. At the cell and pack level, this approach enables higher active materials density and reduced inactive content, which will in turn enable higher energy density and lower-cost for EVs.

Approach

Over the duration of this project, two processing approaches for producing directional, low-tortuosity porosity have been developed. One is the directional freezing of aqueous suspensions, carried out as a collaboration between MIT and LBNL. For the cathode compounds, directional freezing and lyophilization is followed by sintering. For anode compounds, such as graphite, sintering would require excessively high temperatures and highly reducing conditions. Thus, one current goal is to develop a directional freezing approach that can be applied to electrode suspensions and which yields low tortuosity electrodes without further processing. During FY2015, this process has been demonstrated for graphite anodes.

The second process being explored is magnetic alignment of pore-forming entities such as polymer microrods that are subsequently removed by pyrolysis, or magnetic emulsion droplets that are removed simply by evaporation of the liquids. A key advantage of the magnetic alignment approach is that it is able to produce aligned porosity oriented in the primary transport direction of battery electrodes, namely, in the direction normal to the electrode plane. Magnetic processing also has the advantage of being relatively fast and potentially compatible with continuous electrode fabrication. This concept has now been realized in both variants and for both cathodes and anodes. Here also, the emphasis of this year's work has been on developing a process that does not require final sintering of the electrode.

The electrodes fabricated under this project are several times thicker than conventional lithium-ion electrodes, having thicknesses of 200–500 μm, and have areal capacities that are also several times higher, from 8-15 mAh/cm². It has been found that continuous discharge testing over a large SOC swing (e.g., from 100%-0% SOC) underestimates the power capability of the electrodes in more realistic drive cycles. Thus, a key element of the testing performed in this project is to use simplified industry-standard drive cycles for EV applications (with appropriate battery scaling factors).

Results

Graphite anodes prepared by directional freeze-casting without sintering

Unlike cathodes prepared by directional freezing, for which results have been previously reported, graphite anodes cannot be sintered in air for densification. Here, they are prepared and tested in the lyophilized but unheat-treated state, using the USABC Dynamic Stress Test (DST). Aqueous suspensions were prepared using battery-grade graphite and CMC binder (5 wt% relative to the graphite) and containing no conductive carbon additive. The formulations are similar to aqueous electrode suspensions developed for conventional lithium-ion processes. Directional freezing experiments were conducted in similar manner to previous work under this project, except for the absence of sintering. Figure V-18 shows an example of the highly oriented, low-

tortuosity pore channels that are obtained in the graphite electrode. The final porosity in the electrodes was 58-60 vol%. In order to have a theoretical area capacity of about 15 mAh/cm², approximately five times higher than a conventional lithium-ion anode, the anodes were sectioned to 800 μm thickness (about ten times thicker than a conventional graphite anode). Half-cells were built using these anodes and Li-metal counter-electrodes. In the following results, “charge” and “discharge” refer to the behavior of the graphite anode during cycling of a lithium-ion cell (lithiation of the graphite anode during cell charging and delithiation during cell discharging).

Beginning with a fully charged cell (fully lithiated anode), the DST cycle shown in Figure V-18 was repeatedly looped, each loop incrementally delithiating the anode (discharging a lithium ion cell). The DST cycle includes a maximum pulse delithiation rate of 2C and maximum pulse lithiation rate of 1C, and was repeated until a discharge voltage cutoff of 3V, or charge voltage cutoff of 10 mV was reached. During the first two DST cycles, the 10 mV charge cutoff was reached, but thereafter the charge voltage remains well above the cutoff. The test was terminated when the discharge voltage reached the 3.0V cutoff. The area capacity obtained is about 5 mAh/cm², well short of the 10 mAh/cm² values that have previously been demonstrated for similarly prepared cathodes in this project. The electrode kinetics limitations leading to the lower-than-expected capacity are currently being evaluated. However, it is believed that higher density, lower thickness anodes may exhibit similar performance to the cathodes previously demonstrated.

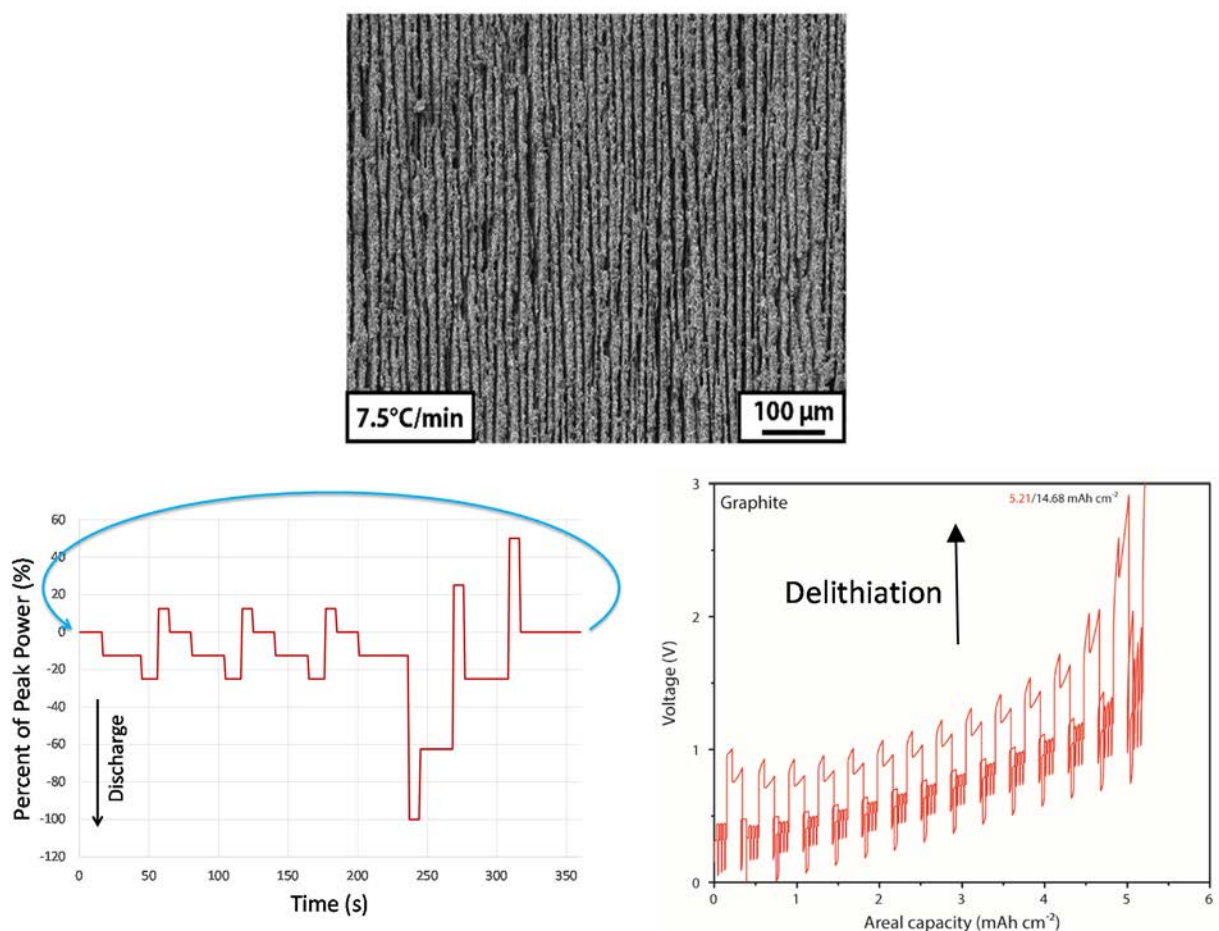


Figure V-18: Directionally-frozen graphite anode (top) subjected to DST testing (left) yielded voltage-area capacity results (right). The voltage limits reached on delithiation (discharge of a lithium-ion cell) become limiting as the graphite anode is systematically delithiated. Charge acceptance (lithiation of graphite) appears to have significantly faster kinetics than discharge. The anode tested has 14.7 mAh/cm² theoretical capacity and is 800 μm thick

Low-tortuosity electrodes prepared by magnetic alignment without sintering

A room-temperature, emulsion-based magnetic alignment approach was developed and applied to LiCoO₂ cathodes and MCMC graphite anodes. In this approach, an oil-in-water emulsion is used as the solvent phase

for an aqueous electrode formation. The oil droplets (~10 μm diameter) in the emulsion trap magnetite nanoparticles that are incorporated in the emulsion, producing magnetic emulsion droplets that respond to the application of a dc magnetic field produced by a permanent magnet. The remaining formulation of the starting electrodes consists of the electrode-active material (>95 wt%), carbon black, and an aqueous binder. Under the influence of the magnetic field, the oil droplets exhibit three distinct effects: 1) they each develop a magnetic moment and form linear chains aligned with the field. 2) The chained droplets extend through the entire thickness of the electrode, forming a continuous path that, when later evaporated, leaves a pore channel extending the entire distance across the electrode. 3) The chains exert a repulsive force on each other, causing the final pores to be uniformly separated, or even to form an ordered array if allowed to reach equilibrium. Upon drying and rinsing of the electrode, aligned porosity is created. The small amount of magnetite has no apparent effect on the electrochemical behavior of the electrodes.

Figure V-19 shows the vertically aligned low-tortuosity pore channels formed in a LiCoO_2 cathode and MCMB graphite anode. These channels are 3–15 μm in diameter and hundreds of microns in length, extending through the electrode thickness. The tortuosity of these electrodes was measured through DC-depolarization experiments; a LiCoO_2 cathode (43% porosity) and graphite anode (51% porosity) were found to have tortuosity of 1.9 and 2.1, respectively.

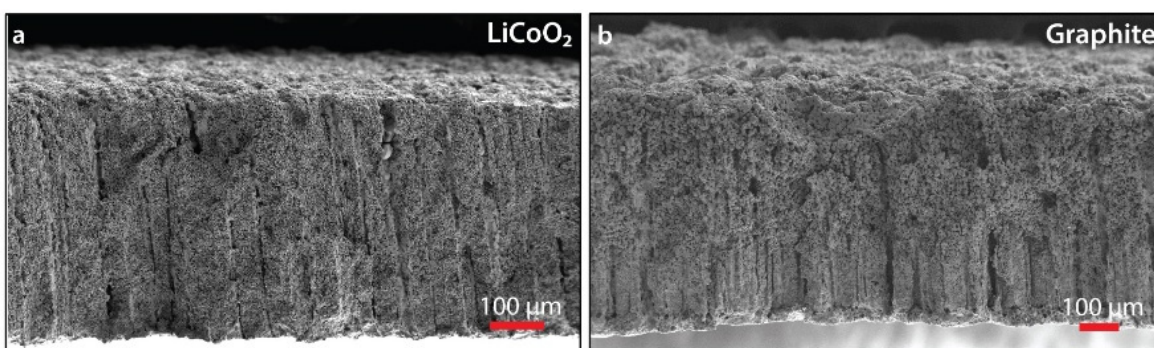


Figure V-19: SEM images of low-tortuosity LiCoO_2 cathode and MCMB graphite anode prepared by the magnetic alignment and drying of emulsion droplets

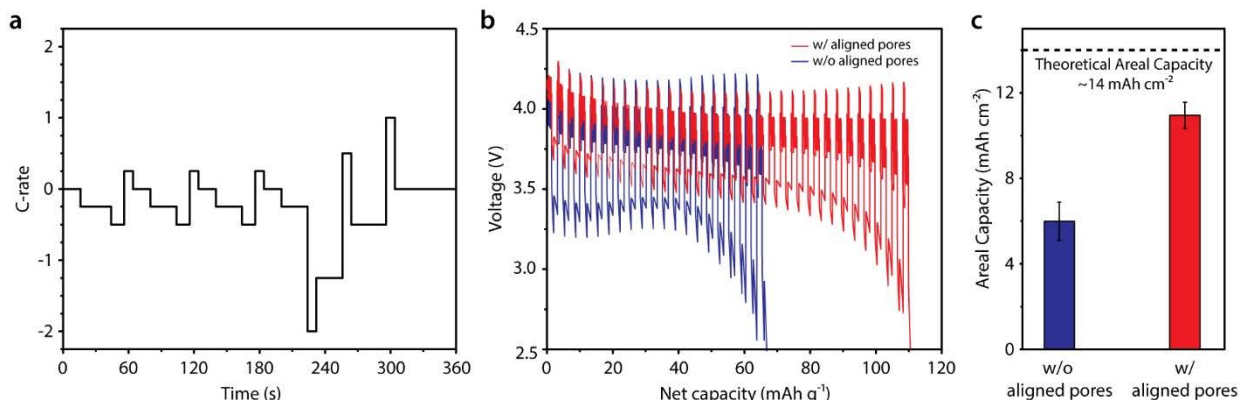


Figure V-20: a, DST protocol. b, Voltage-net capacity plots of LiCoO_2 electrodes with or without aligned pore channels under DST tests. c, Statistic results of areal capacity achieved under DST tests

Cathode half-cells were built using LiCoO_2 electrodes of 430–440 μm thickness and Li-metal counter electrodes, and tested using the DST protocol described earlier. Reference LiCoO_2 electrodes of similar thickness but without aligned porosity and thus high tortuosity ($\tau = 2.9$ based on DC-depolarization experiment) were prepared for testing via the same DST protocol. As shown in Figure V-20b, the DST protocol was run repeatedly on each electrode, beginning with a fully charged cell, until a lower cut-off voltage of 2.5 V was reached during pulse discharge. The sample with aligned pore channels exhibits almost twice the discharge capacity of the sample without aligned pore channels, and reaches an area capacity of $10.95 \pm 0.61 \text{ mAh/cm}^2$ (Figure V-20c).

The same emulsion-based approach was also carried out using mesocarbon microbead anode active material (MCMB 6-28, Osaka Gas Co.). Half-cells were built and tested under galvanostatic conditions. Figure V-21a compares the delithiation capacity vs. C-rate of an MCMB anode with aligned pores to that of a reference sample without aligned pores. These two electrodes have similar areal capacity of $\sim 13.8 \text{ mAh/cm}^2$ ($\sim 39.4 \text{ mg/cm}^2$ areal loading). The electrode with aligned pores is thicker but less dense compared to the reference sample without aligned pores (thickness of $485 \mu\text{m}$ vs $425 \mu\text{m}$ and porosity of 51% vs 44%). The MCMB anode with aligned pores clearly outperforms the reference sample, delivering $>11 \text{ mAh/cm}^2$ capacity at C/20 rate ($1\text{C} = 350 \text{ mA/g}$) and $>4 \text{ mAh/cm}^2$ at 1C (red circles in Figure V-21a). DC-polarization experiments revealed that the electrode with aligned pores has a low tortuosity of 2.0.

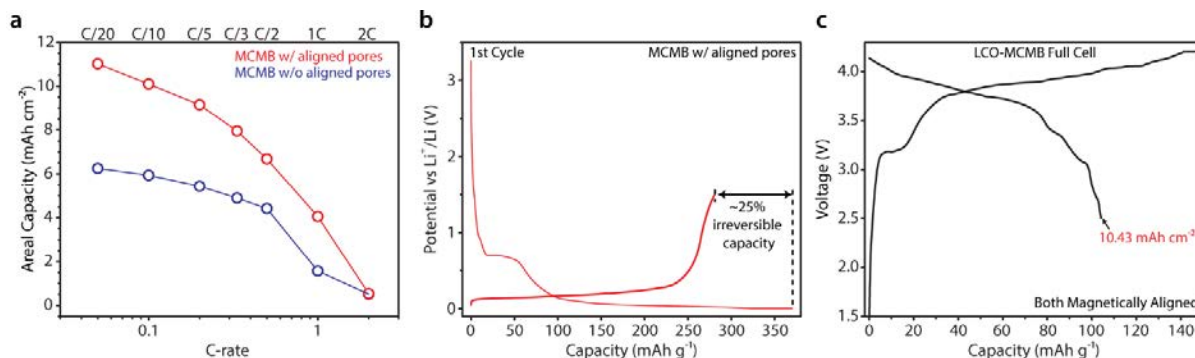


Figure V-21: a) Areal capacity vs. C-rate for the low-tortuosity MCMB anode in comparison with a high-tortuosity reference sample. b) 1st cycle lithiation-delithiation voltage profile of the low-tortuosity MCMB anode tested at 1/20 C. c) 1st cycle charge-discharge profile of a LiCoO₂-MCMB full cell tested at 1/20 C. Both electrodes are prepared by the emulsion-based magnetic alignment approach (theoretical areal capacity: LiCoO₂ cathode 13.7 mAh/cm², MCMB anode 14.4 mAh/cm²)

Figure V-21b shows the 1st cycle lithiation-delithiation voltage vs capacity profile of the low-tortuosity MCMB anode. This electrode was lithiated at C/20 to 10 mV and then delithiated to 1.5 V. After the 1st cycle, approximately 25% of the capacity is lost, possibly due to SEI formation at the MCMB graphite anode.

Finally, full cells were constructed using a LiCoO₂ cathode and a MCMB anode, which are both magnetically aligned. Figure V-21c shows the 1st charge-discharge voltage profile of the full cell at C/20 rate. The LiCoO₂ cathode is $\sim 440 \mu\text{m}$ in thickness and has a theoretical areal capacity of 13.7 mAh/cm^2 , while the MCMB anode is $\sim 500 \mu\text{m}$ in thickness and has a slightly higher theoretical areal capacity of 14.4 mAh/cm^2 , such that the AC ratio is $\sim 1.05:1$. Upon charge to 4.2 V (CC-CV charge, Figure V-21c), the LiCoO₂-MCMB full cell reaches a capacity of 146 mAh/g (calculated based on the active mass of the cathode). However, during discharge the full cell delivers a capacity of 105 mAh/g , $\sim 72\%$ of the charge capacity. Based on the MCMB-Li half-cell test (Figure V-21b), the 1st cycle capacity loss of the full cell can be mostly attributed to the loss at the MCMB anode. While the first-cycle loss clearly needs to be improved, the LiCoO₂-MCMB full cell is nonetheless able to deliver an area capacity on discharge of 10.43 mAh/cm^2 .

Conclusions

In the past year, we have developed an emulsion-based method for making low-tortuosity ultrahigh capacity electrodes through simple and efficient magnetic field processing. The approach uses the field-induced chaining of magnetic oil droplets to create, upon evaporation of all liquids, linear pores aligned in the thickness direction of a thin, plate-shaped electrode. Compared to the status of the project in the previous year (FY2015), the current process does not require high-temperature sintering, but instead, allows the electrodes to be used after drying without further post-processing. This ambient-temperature version of the magnetic alignment technique should be generally applicable to any cathode or anode material amenable to water-based processing. The electrode tortuosities achieved are $\tau = 1.9\text{-}2$, approximately one-half that of the same electrodes prepared without magnetic alignment. The non-sintered approach also provides greater flexibility in electrode design, permitting the incorporation of additives to improve mechanical properties or the electronic conductivity of the electrode, for example. The methods developed in this work may be adaptable to mass production methods in order to increase energy density and lower cost, and can be employed with any particle-based active material, including emerging higher energy density electrode compounds of interest for electric transportation.

Products

Presentations/Publications/Patents

1. J. Sander, R.M. Erb, L. Li, A. Gurijala, Y.-M. Chiang, “High-Performance Battery Electrodes via Magnetic Templating”, *Nature Energy*, 2016, 1, 16099.
2. L. Li, J. Sander, A. Gurijala, R.M. Erb, “Design and Scalable Assembly of High Density Low Tortuosity Electrodes”, 2016 DOE-AMR meeting, Washington, DC, June 8-9th, 2016.
3. L. Li and Y.-M. Chiang, “Processing of High Capacity Low Tortuosity Thick Electrodes for Lithium Ion Batteries,” U.S. Provisional Patent Application 62/347,475, filed June 8, 2016.

V.B.4. Hierarchical Assembly of Inorganic/Organic Hybrid Si Negative Electrodes (LBNL)

Gao Liu, Principal Investigator

Lawrence Berkeley National Laboratory
1 Cyclotron Road, MS 70R0108B
Berkeley, CA 94720
Phone: 510-486-7207; Fax: 510-486-7303
E-mail: gliu@lbl.gov

Tien Q. Duong, DOE Program Manager

U.S. Department of Energy
Advanced Battery Materials Research (BMR)
Vehicle Technologies Office
1000 Independence Avenue, SW
Washington, DC 20585
Phone: 202-586-7836
E-mail: Tien.Duong@ee.doe.gov

Start Date: October 1, 2012
End Date: September 30, 2016

Abstract

Objectives

This proposed work aims to enable Si as a high-capacity and long cycle-life material for negative electrode to address two of the barriers of lithium-ion chemistry for EV/PHEV application: insufficient energy density and poor cycle life performance. The proposed work will combine material synthesis and composite particle formation with electrode design and engineering to develop high-capacity, long-life, and low cost hierarchical Si-based electrode. State of the art lithium-ion negative electrodes employ graphitic active materials with theoretical capacities of 372 mAh/g. Silicon, a naturally abundant material, possesses the highest capacity of all lithium-ion anode materials. It has a theoretical capacity of 4200 mAh/g for highest Li-Si alloy to the $\text{Li}_{22}\text{Si}_5$ phase. However, Si volume change disrupts the integrity of electrode and induces excessive side reactions, leading to fast capacity fade. This work addresses the adverse effects of Si volume change and minimizes the side reactions to significantly improve capacity and lifetime to develop negative electrode with lithium-ion storage capacity over 2000 mAh/g and significantly improve the coulombic efficiency. The research and development activity will provide an in-depth understanding of the challenges associated with assembling large volume change materials into electrodes and will develop a practical hierarchical assembly approach to enable Si materials as negative electrodes in lithium-ion batteries.

Accomplishments

- Developed functional conductive and adhesive polymer binders for Si based electrode.
- Quantified the adhesion forces based on different adhesion functional groups.
- Understood the limiting factors of Si electrode loading and developed strategies to improve Si electrode loading to 4 mAh/cm².
- Fabricated NMC/Si full cell and quantified the cell performance.

Future Achievements

Lawrence Berkeley National Laboratory is in the process of negotiating a technology transfer agreement of the technology developed by this project with Zepton Inc., a battery start up company, to commercialize our functional binders and SiO electrode technology.

Technical Discussion

Background

State-of-the-art lithium ion electrode has used polymer binder to ensure integrity of the composite electrode for a dimensionally stable laminate. The polymer binder plays a critical function in maintaining the mechanical stability and electrical conduction during the lithium insertion and removal process. Classic electrode materials such as LiCoO_2 , graphite powders and acetylene black (AB) conductive additives are dimensional stable materials during the electrochemical processes. The polymer binder materials such as PVDF are suitable to adhere these particles together and keep the physical contacts for electrical connection within the laminate. State of the art approach has worked fairly well, until the introduction of higher capacity electrode materials such as Si in the composite electrode. Si volume change during cycling has created excessive stress and movement in the composite electrode and increased surface reactions. In order to use Si material, a new method to assemble Si-active material particles, along with Si surface stabilization has to be put in place. With the in-depth knowledge of the Si surface properties and increased commercial supply of Si for battery application, there is an opportunity/demand to investigate better Si assembly and stabilization for electrode application. Under the BATT program funding, a new approach has been developed to use electrically conductive polymer binder to connect and stabilize Si composite electrode to achieve unparalleled capacity retention during cycling. An underlining principle to use conductive polymer as a negative electrode binder was developed and implemented in the synthesis of the new binders. These binders are cathodically (reduction) doped in the Si electrode environment to achieve electrical conductivity. Adhesion groups have been incorporated into the polymer binder to improve the integrity of the electrode. The conductive polymer binders have opened a new paradigm of electrode design for Si materials, providing molecular level electrical interaction between the electrode matrix and active materials and accommodating to volume expansion of high capacity alloy materials.

Introduction

Si is a naturally abundant material. It possesses the highest capacity of any lithium-ion anode material. Recent research on electrochemical alloying of Li with Si resulted in a slightly lower practical capacity of 3580 mAh/g at $\text{Li}_{15}\text{Si}_4$ as the final electrochemical lithiation state. Si and Li alloy also has low potential plateau at around 0.45V (Li/Li^+) during delithiation process. Si anode combined with 4 V and above cathode materials can offer higher-energy density storage for EV/PHEV. However, despite its remarkable high-storage-capacity and the intensive research done in this field, there have been no widespread applications of Si in lithium-ion cells. The main issue is the high volume change associated with lithium ion insertion into Si. Almost 280% volume expansion occurs as the material transitions from the pure Si phase to the $\text{Li}_{15}\text{Si}_4$ phase. This high volume change tends to disrupt the electronic integrity of the composite electrode and induce high and continuous surface side reaction leading to drastic capacity fade.

Approach

This proposed hierarchically electrode design is aimed to uncover the principles to fabricate high active material loading ($>3\text{mAh}/\text{cm}^2$) and high coulombic efficiency ($>99\%$) Si-based negative electrode, and apply these principles to fabricate electrodes. First, use Si/conductive polymer composite particles to stabilize the volume change in the secondary particle level, minimizing electrode movement and maintaining the mechanical stability and electrical conductivity of the electrode - this *bulk assembly* approach will be investigated for improving Si loading. Second, form *in situ* compliant barrier coating on Si surface and electrode surface to minimize the Si new surface exposure to electrolyte during each charge and discharge cycles - this *surface stabilization* approach will be investigated for increasing CE. The hierarchical assembly of Si electrode will have both stable physical dimension and chemical surface to ensure high capacity and long lifetime performance for EV application.

Results

Hierarchical design is achieved through several levels of materials and electrode designs. Highly adhesive functional conductive polymer binders through covalent chemical bonding are developed to improve mechanical integrity of the electrode. High-tap-density silicon nanomaterials are highly desirable as anodes for lithium-ion batteries, due to their small surface area and minimum first-cycle loss. However, this material poses formidable challenges to polymeric binder design. This study developed a new binder, Poly(1-pyrenemethyl methacrylate-co-methacrylic acid) (PPyMAA), for a high-tap-density nano-silicon electrode cycled in a stable manner with a first cycle efficiency of 82%. The content of MAA is limited to 30 mol% to enhance the adhesion of the binder while not disturbing the conjugation of the PPy unit. Wide angle X-ray scattering (WAXS) of the PPy and PPyMAA polymers exhibit very similar pattern (Figure V-22b), indicating that the ordered phase characteristic of the pyrene is still maintained in the synthesized PPyMAA copolymer. Figure V-22c shows the sXAS spectra of PPy and PPyMAA. It is obvious that incorporating the MAA group does not change the lowest-energy features in sXAS, indicating the LUMO of the PPy polymer is intact in PPyMAA. The consistency of the overall lineshape also implies that the electron states close to the Fermi level are dominated by the pyrene-based PPy states. SEM indicates that the high tap-density nanoSi has a regular round shape with a median size of 200 nm (Figure V-22d). Although this Si particle is in nano-size, Brunauer-Emmett-Teller (BET) analysis indicates a surface area of only 12 m²/g, with a tap-density of 0.51 g/cm³. The cycling performance of high tap density nanoSi with PPyMAA is shown in Figure V-22f, which indicates a long-term stable electrochemical performance with a high specific capacity above 2500 mAh/g with high first cycle coulombic efficiency. The high tap-density nanoSi-based high capacity anodes enabled by the PPyMAA binder show great promise toward a commercial product.

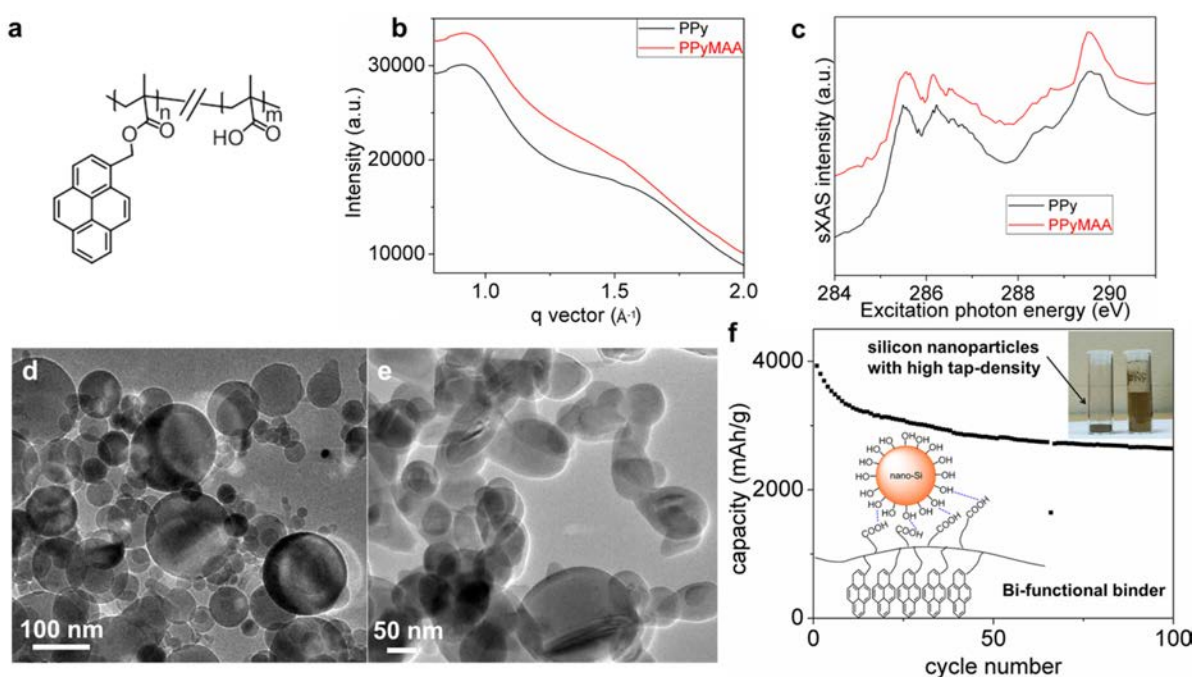


Figure V-22: (a) Chemical structure of PPyMAA conductive polymer binder. (b) Wide angle X-ray scattering (WAXS) of PPy and PPyMAA polymers. (c) Carbon K-edge sXAS of PPy and PPyMAA shows that the LUMO energy is intact in PPyMAA, although non-conductive methacrylic acid groups are introduced. TEM morphology of (d) high-tap-density nanoSi and (e) regular nanoSi produced by chemical vapor deposition (right). (f) cycling performance of PPyMAA/high tap density nanoSi
Nano Letters. 2015, 15, 7927-7932

Controlling porous electrode microstructure is also critical for the continued improvement of lithium-ion batteries. A convenient and economical method for controlling electrode porosity was developed, thereby enhancing material loading and stabilizing the cycling performance of lithium ion electrodes. Sacrificial NaCl is added to a SiO based electrode, which demonstrates an areal capacity of ~4 mAh/cm² at a C/10 rate (0.51 mA/cm²) and an areal capacity of 3 mAh/cm² at a C/3 rate (1.7 mA/cm²), one of the highest material loadings reported for a Si-based anode at such a high cycling rate (Figure V-23). X-ray microtomography confirmed the

improved porous architecture of the SiO electrode with NaCl (Figure V-24). This versatile method was also successfully applied to nanoSi and lithium iron phosphate electrodes. The method developed here is expected to be compatible with the state-of-the-art lithium-ion battery industrial fabrication processes, and therefore holds great promise as a practical technique for boosting the electrochemical performance of lithium-ion batteries without changing material systems.

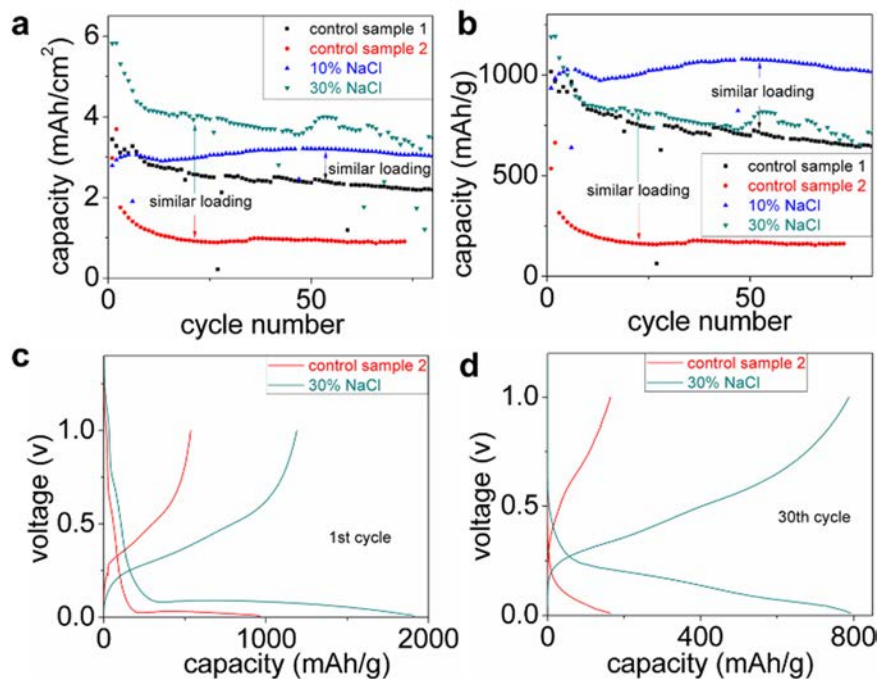


Figure V-23: Cycling performance of the SiO/PFM electrodes with or without NaCl. (a) Areal capacity vs. cycle number, (b) Specific capacity vs. cycle number. (c) First and (d) thirtieth cycle voltage curves of samples with or without NaCl

Nano Letters, 2016, 16 (7), 4686–4690

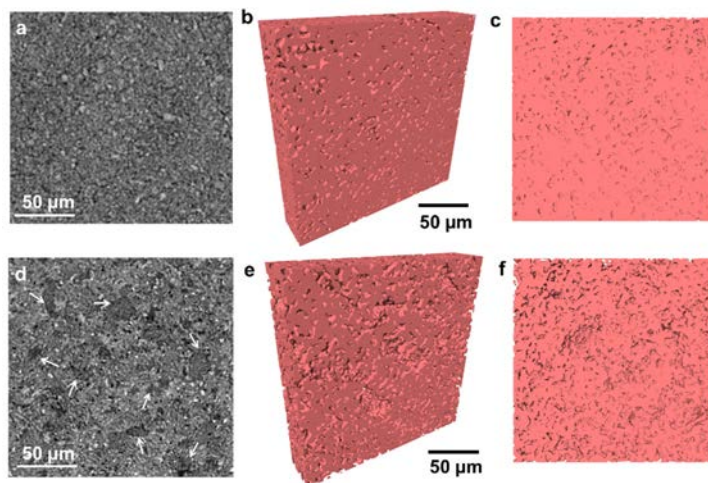


Figure V-24: Tomographically reconstructed cross-section and volume rendering of (a) (b) (c) the control SiO/PFM electrode and (d) (e) (f) the SiO/PFM electrode with porosity generation. The pores induced by NaCl are marked with arrows in the cross-section

Nano Letters, 2016, 16 (7), 4686–4690

Conclusions

A multifunctional conductive polymer binder with both electronic conductivity and adhesion functionalities is synthesized and used for a high tap density nanoSi anode. The high tap-density nanoSi-based high capacity

anodes enabled by the PPyMAA binder show great promise toward a commercial product. A convenient and economical method was developed to control electrode porosity, enhancing the material loading and stabilizing the cycling performance of lithium ion electrodes. Hierarchical design is achieved through several levels of novel materials and electrode designs. Highly adhesive functional conductive polymer binders through covalent chemical bonding are developed to improve mechanical integrity of the electrode. Controlling over porous electrode microstructure is also critical for the continued improvement of lithium-ion batteries. In combination of enhanced binder adhesion, electrode porosity and micro structure control, and minimized materials interface, a high loading, and long cycled life Si based electrode can be designed and fabricated.

Products

Presentations/Publications/Patents

Selected invited presentations

1. Development of High Area Loading and Stable Sulfur Electrode Through Interfaces Functionality Design for Lithium Sulfur Battery, The 12th Biannual China International Battery Fair (CIBF), Shengzhen, China, May **2016**.
2. *Device Making and Testing*, Industry Day at Berkeley Lab, Berkeley, CA, May **2016**.
3. *Functional Conductive Polymer Binders Enabled High Stability Cycling of Alloy Anodes*. The 66th Annual Meeting of the International Society of Electrochemistry. Oct. 4th-9th, Taipei, Taiwan, **2015**.
4. Investigation of surface effects through the application of the functional binders in lithium sulfur batteries, The 10th International Forum on Li Battery Technology & Industrial Development, Beijing, China, Oct. **2015**.
5. Functional Conductive Polymer Binders for High-Performance Silicon-Based Anodes in Lithium-Ion Batteries, ECS Fall Meeting, Phoenix. Oct. 11th-15th, **2015**.

Selected Peer-reviewed publications

1. The effect of cobalt doping on the morphology and electrochemical performance of high-voltage spinel $\text{LiNi}_{0.5}\text{Mn}_{1.5}\text{O}_4$ cathode material Jing Mao, Mengze Ma, Panpan Liu, Junhua Hu, Guosheng Shao, Vince Battaglia, Kehua Dai, Gao Liu, *Solid State Ionics*, **2016**, 292, 70–74.
2. Hui Zhao, Qing Yang, Neslihan Yuca, Min Ling, Kenneth Higa, Vincent Battaglia, Dilworth Parkinson, Venkat Srinivasan, and Gao Liu. A convenient and versatile method to control the electrode microstructure toward high-energy lithium-ion batteries. *Nano Letters*, **2016**, 16 (7), 4686–4690.
3. Hui Zhao, Allen Du (**co-first author**), Min Ling, Vincent Battaglia, and Gao Liu. Conductive polymer binder for nano-silicon/graphite composite electrode in lithium-ion batteries towards a practical application. *Electrochimica Acta*, **2016**, 209, 159-162.
4. Guo Ai, Zhihui Wang, Hui Zhao, Wenfeng Mao, Yanbao Fu, Vincent Battaglia, Sergey Lopatin, and Gao Liu. Scalable process for application of stabilized lithium metal powder in Lithium-ion batteries. *Journal of Power Sources*. **2016**, 309, 33-41.
5. Hui Zhao, Wei Yang, Ruimin Qiao, Chenhui Zhu, Ziyang Zheng, Min Ling, Zhe Jia, Ying Bai, Yanbao Fu, Jinglei Lei, Xiangyun Song, Vincent Battaglia, Wanli Yang, Phillip Messersmith, and Gao Liu. Conductive polymer binder for high-tap-density nano-silicon material for lithium-ion battery negative electrode application. *Nano Letters*. **2015**, 15, 7927-7932.

Granted patents

1. U.S. patent No. US9,153,353 B2, “Electrically Conductive Polymer Binder for Lithium-Ion Battery Electrode” Gao Liu, Vince Battaglia, Sang-Jae Park, Granted Oct 6th, 2015.
2. U.S. patent No. US9,214,668 B2, “Si Composite Electrode with Li Metal Doping for Advanced Lithium-ion Battery” Gao Liu, Shidi Xun, Vince Battaglia, Granted Dec 15th, 2015.

References

1. Hui Zhao, et al. *Nano Today*, **2015**, 10(2), 193-212.

2. Wen Yuan, et al. *J. Power Sources*, **2015**, 282, 223-227.
3. Sangjae Park, et al. *J. Am. Chem. Soc.*, **2015**, 137, 2565-2571.
4. Mingyan et al. *J. Mater. Chem. A*, **2015**, 3, 3651-3658.
5. Hui Zhao, et al. *ACS App. Mater. & Inter.* **2015**, 7(1), 862-866.
6. Hui Zhao, et al. *Nano Letters*, **2014**, 14(11), 6704-6710.
7. Gu, M. et al. *Scientific Report* **2014**,4, 3684-3688.
8. Wu, M., et al. *J. Am. Chem. Soc.* **2013**, 132, 12048-12056.
9. Liu, G., et al. *Adv. Mater.* **2011**, 23, 4679-4683.

V.C. Silicon Anode Research

V.C.1. Development of Si-Based High-Capacity Anodes (PNNL)

Ji-Guang Zhang, Principal Investigator

Pacific Northwest National Laboratory
902 Battelle Boulevard, Mail Stop K2-44
Richland, WA 99352
Phone: 509-372-6515; Fax: 509-375-2186
E-mail: Jiguang.Zhang@pnnl.gov

Jun Liu, Co- Principal Investigator

Pacific Northwest National Laboratory
902 Battelle Boulevard, Mail Stop K2-44
Richland, WA 99352
Phone: 509-375-4443; Fax: 509-351-6242
E-mail: Jun.Liu@pnnl.gov

Prashant Kumta, Co-Principal Investigator

University of Pittsburgh
815C Benedum Hall, 3700 O'Hara Street
Pittsburgh, PA 15261
Phone: 412-648-0223 Fax: 412-624-3699
E-mail: pkumta@pitt.edu

Tien Q. Duong, DOE Program Manager

U.S. Department of Energy
Advanced Battery Materials Research (BMR)
Vehicle Technologies Office
1000 Independence Avenue, SW
Washington, DC 20585
Phone: 202-586-7836
E-mail: Tien.Duong@ee.doe.gov

Start Date: October 2014

End Date: September 2016

Abstract

Objectives

- Develop high-capacity, low-cost silicon (Si)-based anodes with good cycle stability and rate capability.
- Reduce the first-cycle irreversible capacity loss and improve coulombic efficiencies during cycling.
- Advance the fundamental understanding of the degradation mechanism of Si-based anodes, including their mechanical and electrochemical stability.

Accomplishments

- Developed a low-cost approach to synthesize the active/inactive Si-based nanocomposite with a specific capacity of $\sim 800 \text{ mAh g}^{-1}$.
- Achieved 80% capacity retention over 200 cycles for a graphite-supported nano-Si-carbon-shell composite.

- Developed interface control agents and surface electron conducting additives to reduce the first-cycle irreversible loss and improve the Coulombic efficiency of the Si-based anode.
- Optimized the cost-effective, scalable high energy mechanical milling (HEMM) and solid-state synthesis techniques for the generation of active/inactive composites with capacities of $\sim 1000\text{--}1200\text{ mAh g}^{-1}$.
- Achieved $>80\%$ capacity retention over 300 cycles for thick electrodes ($>2\text{ mAh cm}^{-2}$) through optimization of the Si electrode structure and binder.
- Synthesized a suitable active/inactive nanocomposites containing Li_2O matrix ($\text{Si}+\text{Li}_2\text{O}$) or intermetallic matrix ($\text{Si}+\text{MnBm}$) with specific capacity of $\sim 1000\text{--}1200\text{ mAh g}^{-1}$.

Future Achievements

- Synthesize micron-sized Si with the desired porosity and *in situ*-grown graphene coating.
- Synthesize low-cost Si-based nanocomposite anode materials using HEMM and other economical template derived methods.
- Fabricate and characterize Si-based anodes with the desired electrode capacity ($\sim 3\text{ mAh cm}^{-2}$).

Technical Discussion

Background

Most lithium-ion batteries (LIBs) used in state-of-the-art electric vehicles (EVs) contain graphite as their anode material. The limited capacity of graphite (LiC_6 , 372 mAh g^{-1}) is one of the main barriers to long-range operation of EVs. In this regard, silicon (Si) is one of the most promising candidates for an alternative anode for LIB applications.¹ Si is environmentally benign and ubiquitous. The theoretical specific capacity of silicon is 4212 mAh g^{-1} ($\text{Li}_{12}\text{Si}_5$), which is 10 times the specific capacity of graphite. However, the high specific capacity of silicon is associated with large volume changes (more than 300%) when alloyed with lithium. These extreme volume changes can cause severe cracking and disintegration of the electrode and lead to significant capacity loss.

Introduction

Significant scientific research has been conducted to circumvent the deterioration of silicon-based anode materials during cycling.²⁻⁷ Various strategies, such as reduction of particle size, generation of active/inactive composites, fabrication of silicon-based thin films, use of alternative binders, and the synthesis of one-dimensional silicon nanostructures, have been implemented by a number of research groups. Fundamental mechanistic research also has been performed to better understand the electrochemical lithiation and delithiation processes during cycling in terms of crystal structure, phase transitions, morphological changes, and reaction kinetics. Although significant progress has been made in the development of the silicon-based anodes, there are still many obstacles that prevent their practical application. Long-term cycling stability remains the foremost challenge for Si-based anodes, especially for the high-loading electrodes ($>3\text{ mAh cm}^{-2}$) required for many practical applications. The cyclability of full cells using Si-based anodes is also complicated by multiple factors, such as diffusion-induced stress and fracture, loss of electrical contact among Si particles and between Si and the current collector, and the breakdown of solid-electrolyte interphase (SEI) layers during volume expansion/contraction processes. Several nanostructured Si materials have demonstrated excellent performance, but most of them work well only for low active-material loadings. In addition, the electrode performance degrades quickly with the increased loadings required for practical applications. Another barrier in this field is that most high-capacity Si-based electrodes have to be prepared using expensive processes that are difficult to scale up. Therefore, to achieve practical application of this technology, a cost-effective and scalable approach needs to be developed to produce Si-based anodes that can retain excellent performance under highly loaded conditions.

Approach

The following approaches have been used in this project:

- Synthesize a composite of nano-Si, hard carbon, and graphite using a low-cost hydrothermal method to improve the long-term cycling performance while maintaining a reasonably high capacity.
- Optimize the electrode composition and structure of porous Si/graphite composite to limit the electrode swelling.
- Use HEMM of silicon oxides with different reducing agents to generate a composite material of nanoparticle Si in a lithium conducting metal matrix by *in situ* mechano-chemical reduction of silicon oxides.

Results

1. Hard carbon coated nano-Si/graphite composite as a high performance anode for LIBs

A cost-effective hydrothermal-carbonization approach has been developed to synthesize a hard-carbon-coated nano-Si/graphite (HC-nSi/G) composite as a high performance anode for LIBs. In this hierarchical structured composite, the hard carbon coating layer not only provides an efficient pathway for electron transfer, but also alleviates the volume variation of silicon during charge/discharge processes. Figure V-25a shows a schematic illustration of the synthesis process of HC-nSi/G composite; Figure V-25(b)-(e) show scanning electron microscope (SEM) images, C/Si energy-dispersive X-ray spectroscopy (EDX) elemental maps, and X-ray spectra of the HC-nSi/G composite.

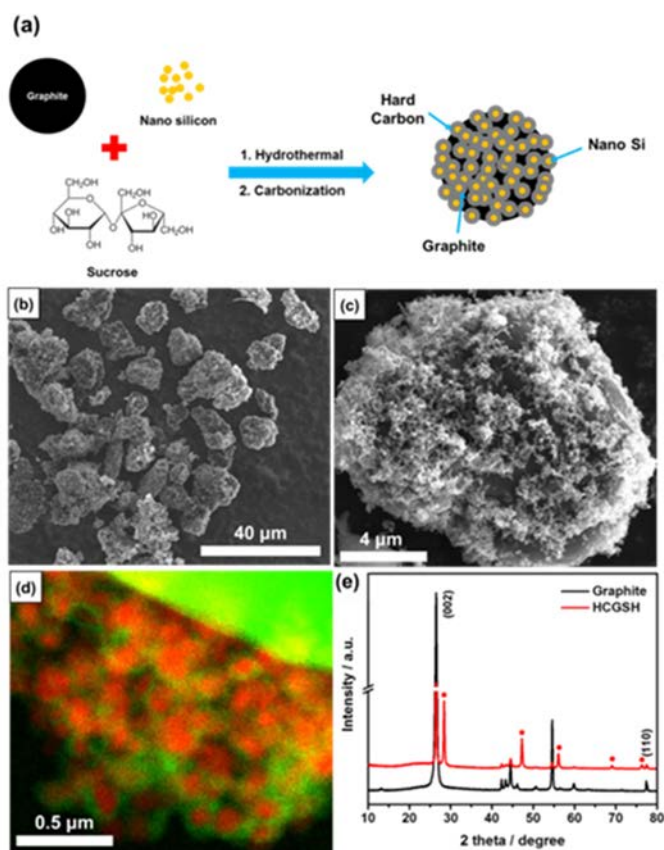


Figure V-25: (a) Schematic illustration of the synthesis of the HC-nSi/G. (b and c) SEM images of the HC-nSi/G composite. (d) C/Si EDX elemental map: (green: carbon; red: silicon). (e) X-ray diffraction (XRD) patterns

The electrochemical performance of the HC-nSi/G composite was evaluated. Figure V-26 shows the charge-discharge curves, cycling stability, and rate performance of the samples. The specific capacity was calculated

based on the active material (Si/graphite/hard carbon). The electrode loading was $1.5\sim 2.0\text{ mg cm}^{-2}$. A sample of HC-nSi/G with 10% binder and 11.4% silicon (designated E1) exhibits a high reversible capacity of 659.1 mAh g^{-1} with a first-cycle reversible capacity of 75.5%. With an increase of Si content to 14.6% (retaining the weight ratio of active materials, carbon black, and binder at 8:1:1), the electrode (designated E2) delivers a capacity of 764.1 mAh g^{-1} with a first-cycle reversible capacity of 78.7%. Increasing the binder content to 20% (E3) significantly increased the specific capacity of the electrode (878.6 mAh g^{-1}) and improved first-cycle reversible capacity to 80.5%. Figure V-26b presents the effects of binder and silicon content on the cycling performance of the composite electrodes. Sample E3 showed a capacity of 864.1 mAh g^{-1} in the 4th cycle and a capacity retention of 84.1% after 150 cycles. Rate capabilities of the HC-nSi/G composite electrodes with different compositions were further evaluated. A sample of HC-nSi/G with 10% binder and 11.4% silicon (E1) exhibited a higher discharge capacity than E2 and E3, delivering 860, 806, 797, 669, and 398 mAh g^{-1} at rates of 0.2, 0.5, 1, 2, and 4 C, respectively. After the rate test, a high discharge capacity of 874.5 mAh g^{-1} was recovered in the E1 electrode when the discharge current density was returned to 0.2C, further evidencing the good reversibility of the E1 electrode. Moreover, the coulombic efficiency of the E1 electrode increased to $>99.0\%$ during long-term cycling.

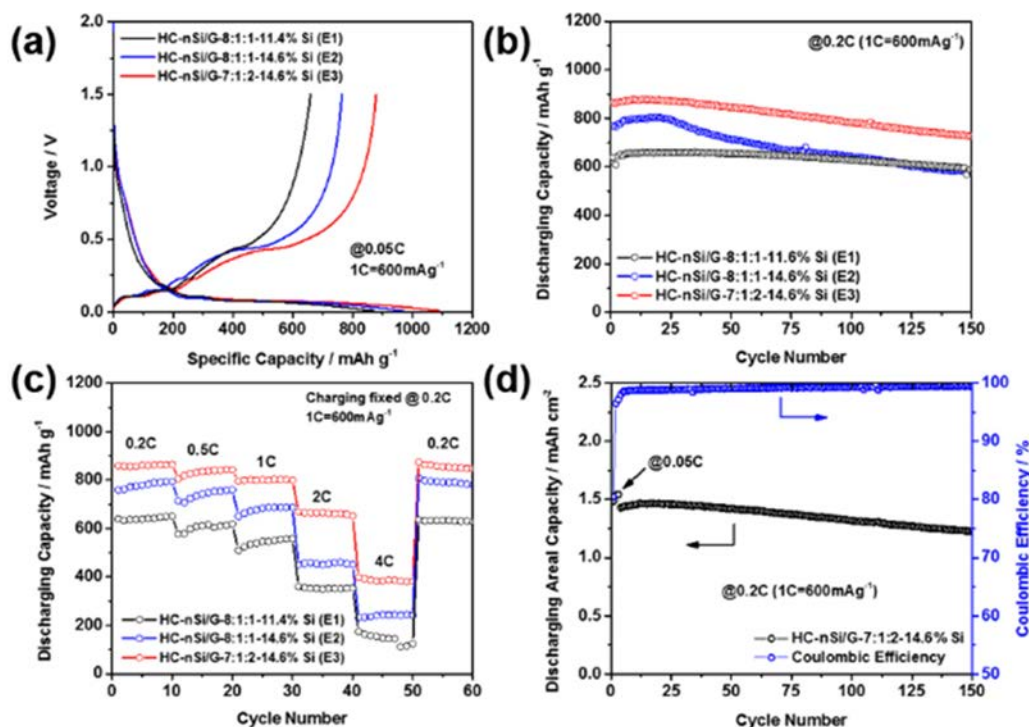


Figure V-26: (a) Initial lithiation/delithiation voltage profiles at 0.05 C, (b) Specific capacity as a function of cycle number at 0.2 C, and (c) Rate capability of HC-nSi/G at various discharging C-rates (charging C-rate fixed at 0.2 C) for HC-nSi/G. (d) Plot of areal capacity retention and coulombic efficiency of HC-nSi/G with an electrode composition ratio of active material:carbon black:binder = 7:1:2

2. Optimization of Si-based anode consisting of mesoporous-Si and graphite composite

The Si-based anode consisting of a composite of mesoporous Si (prepared by the anodization method) and graphite was further investigated at high loading and in full-cell configurations suitable for practical applications. Figure V-27a shows the cycling stability of a typical electrode with a porous-Si to graphite ratio of 1:3. The specific capacity was calculated based on the active material (porous Si and graphite). The electrode loading was $\sim 3\text{ mAh cm}^{-2}$ at a low current density of $\sim 0.06\text{ mA cm}^{-2}$. The areal capacity was $\sim 2.5\text{ mAh cm}^{-2}$ at a charge-discharge current density of $\sim 0.4\text{ mA cm}^{-2}$. The specific capacity was $\sim 610\text{ mAh g}^{-1}$. The capacity retention was $\sim 88\%$ after 500 cycles. Figure V-27b shows the cycling stability of a typical electrode with a porous-Si to graphite ratio of 1:2. The areal capacity was $\sim 2.5\text{ mAh cm}^{-2}$ at a charge-discharge current density of $\sim 0.4\text{ mA cm}^{-2}$. The specific capacity was $\sim 640\text{ mAh g}^{-1}$. The capacity retention was $\sim 80\%$ after 450 cycles.

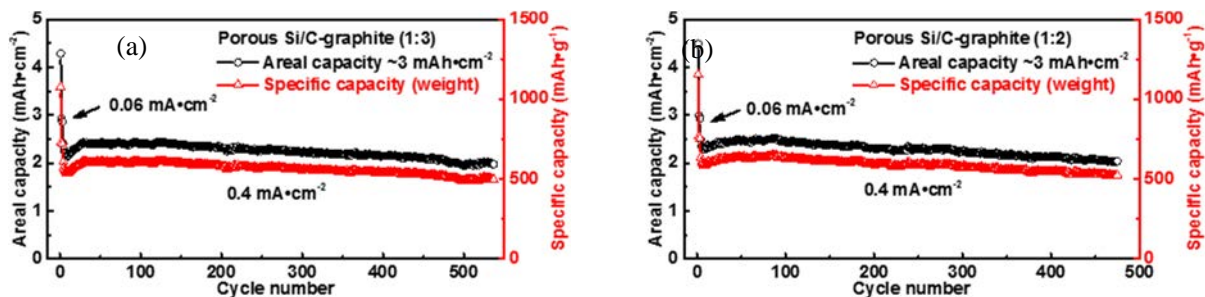


Figure V-27: Cycling stability of porous-Si-graphite electrode with porous Si:graphite ratio of (a) 1:3 and (b) 1:2

After prelithiation, the porous-Si-graphite electrodes were assembled into full cells with NMC electrodes. The full cell was cycled at 0.08 mA cm^{-2} for two formation cycles, then charged at 0.5 mA cm^{-2} and discharged at 0.75 mA cm^{-2} . Good cycling stability was obtained; Figure V-28 shows the typical cycling performance of an NMC-porous Si-graphite full cell with $\sim 83\%$ capacity retention over 300 cycles. The effect of Ge coating on the performance of a porous-Si-graphite electrode was also investigated. Figure V-28b shows the typical cycling result of the electrode with and without Ge coating. The electrode without Ge coating shows stable cycling of ~ 170 cycles with a capacity retention of $\sim 97\%$. The electrode with 10 nm Ge coating, however, shows faster capacity fade. The capacity retention after 100 cycles is $\sim 89\%$. It is believed that the Ge layer sputtered onto the Si electrode degraded the interface impedance of the Si electrode, causing the faster capacity fade.

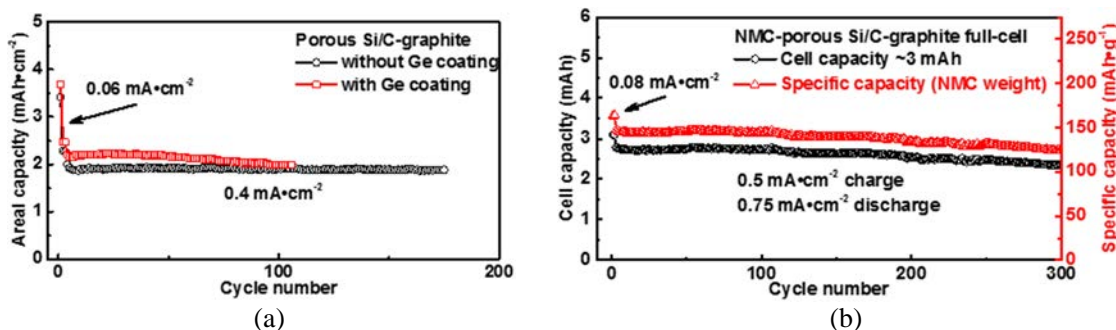


Figure V-28: (a) Cycling stability of NMC-porous-Si-graphite full cell. (b) The cycling stability of porous-Si-graphite electrodes with and without Ge coating

In another effort, a low temperature thermite approach was developed to synthesize porous Si from porous SiO_2 . A group of metal salts was developed as molten media for the thermite reaction. Preliminary results indicate that the porous structure of the silica precursor can be largely maintained and hence the porous Si can deliver good cycling stability. Further investigation is in progress.

3. Production of nanostructured silicon using economical water-soluble templates

Generation of Si nanoflakes and Si nanorods by using low-pressure chemical vapor deposition of Si on a low-cost, water-soluble template and modification of the milling time of the template was reported previously, and their long-term cycling performance in LIBs was studied. The Si nanorods had a more crystalline nature than nanoflakes as indicated by the Raman spectra. Transmission electron microscope analysis of Si nanorods showed nanorods of $\sim 80\text{--}120 \text{ nm}$ diameter. Si nanoflakes and nanorods generated by this method were tested at current rates of 0.3 mA g^{-1} , 0.4 mA g^{-1} , 0.5 mA g^{-1} , 0.05 A g^{-1} , 0.1 A g^{-1} , 0.2 A g^{-1} , 1 A g^{-1} , and 2 A g^{-1} . Si nanoflakes show stable performance along with higher capacities ($\sim 780 \text{ mAh g}^{-1}$) even at high cycling rates of 2 A g^{-1} as compared to Si nanorods ($\sim 470 \text{ mAh g}^{-1}$ @ 2 A g^{-1}). Si nanorods showed stable performance up to current rates of 0.5 A g^{-1} ; however, at higher current rates of 1 A g^{-1} and 2 A g^{-1} , the specific discharge capacity and normalized capacity decreased to values below those of nanoflakes under the same conditions. The specific discharge capacity and normalized capacity at different current rates are shown in Figure V-29. Si nanoflakes showed a high capacity of $\sim 1260 \text{ mAh g}^{-1}$ while the nanorods showed a capacity of $\sim 900 \text{ mA g}^{-1}$ at a current rate of 1 A g^{-1} . The normalized capacity of nanorods declined at higher current rates of 1 A g^{-1} and 2 A g^{-1} , while the nanoflakes showed a better rate capability. The amorphous nature of the Si nanoflakes

contributes to the stability in the cycling performance, and the lower Li⁺ diffusion distances contribute to their better rate capability.

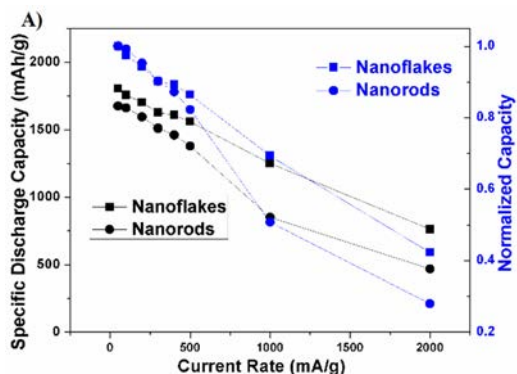


Figure V-29: Specific discharge and normalized capacity vs. current density of Si flakes and rods

4. Carbon nanofiber matrix based nc-Si/metal oxide nanocomposites

HEMR of SiO with metal alloy: Flexible nanofiber (NF) electrodes based on an active/inactive composite comprising nanocrystalline Si (*nc*-Si) and metal oxide (MM')_nO_x [*nc*-Si+(MM')_nO_x] impregnated on carbon nanofibers (CNFs) were fabricated using a combination of high energy mechano-chemical reduction (HEMR) and solution spinning. The [*nc*-Si+(MM')_nO_x] nanocomposite powder was obtained by HEMR using high energy ball milling of SiO_x with reducing metal alloy (MM') after 20 h of ball milling. The ball-milled powder was subsequently heat treated at 550°C to complete the reduction of SiO_x and crystallization of the (MM')_nO_x matrix (see Eq. (1)). XRD study showed evolution of *nc*-Si during HEMR and the formation of [*nc*-Si+(MM')_nO_x] composite after heat treatment. In order to form a flexible nanofiber [*nc*-Si+(MM')_nO_x]/CNF electrode, the nanostructured composite [*nc*-Si+(MM')_nO_x] was impregnated on the polymer-derived CNF (~10 wt%) by solution coating followed by carbonization. The electrochemical performance and response of the [*nc*-Si+(MM')_nO_x]/CNF electrode as an anode for LIBs showed first-cycle discharge and charge capacities of ~1650 mAh g⁻¹ and ~1045 mAh g⁻¹, respectively, with a first-cycle irreversible (FIR) loss of ~20% (Figure V-30a). The differential capacity plot (inset of Figure V-30a) shows an alloying/dealloying reaction of Si with Li, and the conversion of *nc*-Si into α-Si upon lithiation and delithiation of the composite. The NF electrode of [*nc*-Si+(MM')_nO_x]/CNF exhibits higher specific capacity on subsequent cycling (~1325 mAh g⁻¹ during the second discharge cycle) and lower FIR loss as compared to a slurry-coated [*nc*-Si+(MM')_nO_x] composite (Figure V-30b).

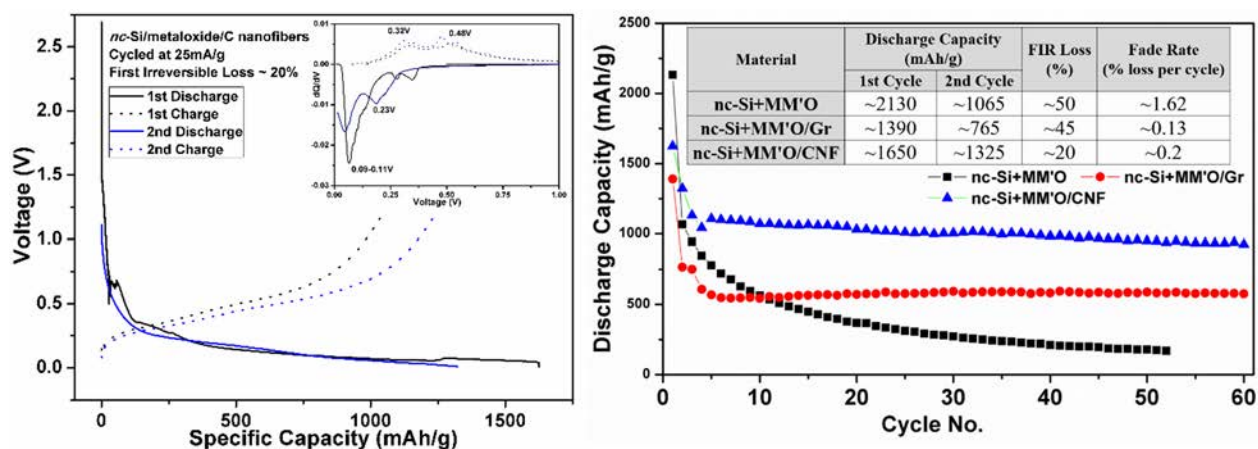


Figure V-30: (a) Voltage vs. specific capacity plot for a [*nc*-Si+(MM')_nO_x]/CNF electrode tested in a LIB. Inset: differential capacity plots of [*nc*-Si+(MM')_nO_x]/CNF nanofiber electrode. (b) Specific discharge capacity vs. cycle numbers for different active electrodes based on *nc*-Si/MM'O composite. Inset table shows the summary of performance of the materials

During the long-term testing of the nanocomposite-based electrode, bare nanocomposite powder $\text{Si}+(\text{MM}')_n\text{O}_x$ delivered first- and second-cycle discharge capacities of $\sim 2130 \text{ mAh g}^{-1}$ and $\sim 1065 \text{ mA g}^{-1}$, respectively, with a FIR loss of $\sim 50\%$ (Figure V-30b). However, it showed a rapid fade in capacity (1.62% loss per cycle) on subsequent cycling. In order to improve the cyclability, the nanocomposite was ball milled with 20 wt.% graphite (Gr) to generate an “intra” type composite of $[\text{nc-Si}+(\text{MM}')_n\text{O}_x]$ and graphite. The $[\text{nc-Si}+(\text{MM}')_n\text{O}_x]/\text{Gr}$ composite showed significantly lower first- and second-cycle discharge capacities of $\sim 1390 \text{ mAh g}^{-1}$ and $\sim 765 \text{ mA g}^{-1}$, respectively, in comparison to bare nanocomposite $[\text{nc-Si}+(\text{MM}')_n\text{O}_x]$ with FIR loss of $\sim 45\%$. However, it showed a significant improvement in the cyclability in comparison to $[\text{nc-Si}+(\text{MM}')_n\text{O}_x]$ with a fade in capacity of $\sim 0.13\%$ loss per cycle (Figure V-30b). The electrochemical performance of $[\text{nc-Si}+(\text{MM}')_n\text{O}_x]/\text{CNF}$ flexible fiber showed first- and second-cycle discharge capacities of $\sim 1650 \text{ mAh g}^{-1}$ and $\sim 1325 \text{ mAh g}^{-1}$, respectively, with a FIR loss of $\sim 20\%$ (Figure V-30b). Notably, the second-cycle discharge capacity of $[\text{nc-Si}+(\text{MM}')_n\text{O}_x]/\text{CNF}$ is comparable to/higher than that of the nanocomposite $[\text{nc-Si}+(\text{MM}')_n\text{O}_x]$ with a significant decrease in FIR loss. In addition, $[\text{nc-Si}+(\text{MM}')_n\text{O}_x]/\text{CNF}$ shows a significant improvement in the cyclability up to 60 cycles in comparison to bare $[\text{nc-Si}+(\text{MM}')_n\text{O}_x]$ with a fade in capacity of $\sim 0.2\%$ loss per cycle (Figure V-30b).

The poor electrochemical performance of the bare nanocomposite powder can be attributed to the formation of an SEI layer and loss of material from the matrix due to volumetric expansion, both contributing to higher FIR loss and fade rate. The graphite-based electrodes show a reduction in FIR loss due to the conductive graphite matrix. However, there is an initial capacity loss as a result of active material loss due to the volumetric changes. In the case of CNF-based electrodes, the formation of an SEI layer is minimized, and the nanofibers provide both electrical continuity and superior mechanical stability to the nanocomposite material, hence improving the electrochemical performance in LIBs.

5. HEMR of SiO with metal-based reductant

A *nc-Si*/metal-oxide/carbon nanofiber composite (*nc-Si*/ M_1O /CNF) was synthesized and studied as a promising anode material for LIBs. Initially, a *nc-Si*/ M_1O composite was prepared using HEMR of SiO_x using a metal-based reductant (M_1X) as a reducing agent for 40 h in argon atmosphere. The ball-milled powder was then heat treated at 500°C for 4 h to enable completion of the reduction reaction to form the *nc-Si*/ M_1O composite (see Eq. (2)). The XRD pattern of the composite shows the evolution of the *nc-silicon* during HEMR of SiO with M_1X followed by heat treatment of the milled material at 500°C for 4 h to form the *nc-Si*/ M_1O composite. The obtained *nc-Si*/ M_1O composites were then embedded in carbon nanofibers (CNFs) using a solution-coating technique followed by thermally induced carbonization. Figure V-31 shows the cycling performance of the *nc-Si*/ M_1O /CNF with an active-material loading density of $\sim 3\text{--}5 \text{ mg cm}^{-2}$. The *nc-Si*/ M_1O /CNF system shows first- and second-cycle discharge capacities of $\sim 1500 \text{ mAh g}^{-1}$ and $\sim 1340 \text{ mAh g}^{-1}$, respectively, at a current rate of $\sim 50 \text{ mA g}^{-1}$, with a FIR loss of $\sim 25\text{--}35\%$. The obtained capacities were in accordance with the theoretical calculated specific capacity of the *Si*/ M_1O /CNF composite. Following long-term cycling, the system showed a stable specific capacity of $\sim 730 \text{ mAh g}^{-1}$ at the end of 120 cycles at a charge/discharge rate of $\sim 500 \text{ mA g}^{-1}$ with a coulombic efficiency of $\sim 99.65\text{--}99.82\%$ and a fade rate of $\sim 0.15\%$ capacity loss per cycle. Retention of the metal oxide matrix in the HEMR-generated composite coupled with the interconnected CNF allows it to act as an efficient buffer to relieve the stresses generated during alloying/dealloying and also maintain electrical continuity during expansion of the *nc-Si*. This results in improved electrochemical performance and cycling stability of the *Si*-composite electrode when tested in LIBs. The synthesis involves a combination of scalable existing commercial technologies to synthesize *nc-Si*/metal oxide composites on a large scale and their stabilization in an interconnected CNF matrix system.

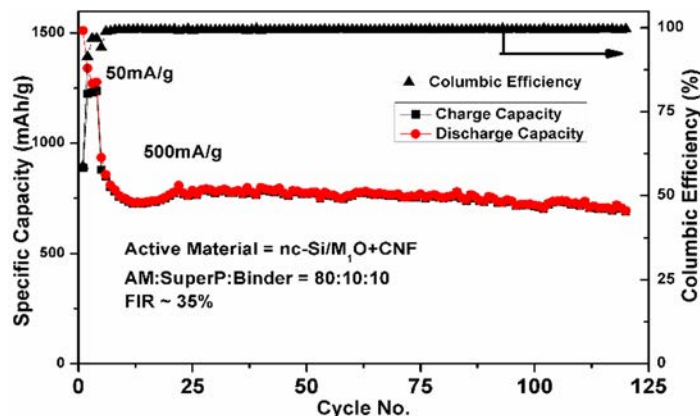
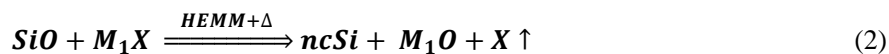


Figure V-31: Specific discharge capacity vs. cycle number for *nc-Si/M₁O/CNF* tested in a LIB. The current rate for the first 3 cycles was 50 mA g⁻¹ and the remaining cycles were tested at a rate of 500 mA g⁻¹ (~1.4 C)

Conclusions

In summary, we have reached the milestones in demonstration of long term cycling stability of high loading Si electrodes and gained substantial understanding on the failing of thick electrodes. We demonstrate a cost-effective hydrothermal carbonization approach to prepare a hard carbon coated nano-Si/graphite (HC-nSi/G) composite as a high performance anode for lithium-ion batteries. In this hierarchical structured composite, the hard carbon coating not only provides an efficient pathway for electron transfer, but also alleviates the volume variation of Si during charge/discharge processes. The HC-nSi/G composite electrode shows excellent performance, including a high specific capacity of 878.6 mAh g⁻¹ based on the total weight of composite, good rate performance, and a decent cycling stability, which is promising for practical applications. We also optimized Si based anode consists of meso porous-Si and graphite composite and investigated their performance at high loading and full cell conditions suitable for practical applications. Good cycling stability of Si/NMC full cells was obtained with ~83% capacity retention over 300 cycles. In addition, we have demonstrated generation of nanostructured silicon (nc-Si) in a Li-conducting metal oxide matrix by high energy mechanochemical reduction (HEMR) of silicon oxides using various metals, metal alloys and compounds. The resultant nc-Si/metal oxide nanocomposite obtained was further stabilized in a conducting flexible carbon nanofiber matrix resulting in stable capacities of ~1000 mAh g⁻¹. Electrodes with an active material loading of ~3-5 mg cm⁻² indicate stable capacity of ~730 mAh g⁻¹ at 500 mA g⁻¹ currents for 120 cycles with a fade rate of ~0.15% capacity loss per cycle. Finally, economic and completely recyclable green abundant template methods have been used to develop nc-Si morphologies exhibiting capacities of ~780 mAhg⁻¹ at 2Ag⁻¹.

Products

Presentations/Publications/Patents

1. Sookyung Jeong, Xiaolin Li, Jianming Zheng, Pengfei Yan, Ruiguo Cao, Hee Joon Jung, Chongmin Wang, Jun Liu, and Ji-Guang Zhang, "Hard carbon coated nano-Si/graphite composite as a high performance anode for Lithium-ion batteries," *Journal of Power Sources*, 329, 323-329.
2. Rigved Epur, Madhumati Ramanathan, Moni K. Datta, Dae Ho Hong, Prashanth H. Jampani, Bharat Gattu, Prashant N. Kumta, "Scribable multi-walled carbon nanotube-silicon nanocomposites: a viable lithium-ion battery system," *Nanoscale*, 2015, 7, 3504-3510.
3. Rigved Epur, Prashanth H. Jampani, Moni K. Datta, Dae Ho Hong, , Bharat Gattu, Prashant N. Kumta, "A simple and scalable approach to hollow silicon nanotube (h-SiNT) anode architectures of superior electrochemical stability and reversible capacity," *J. Mater. Chem. A*, 2015, 3, 11117-11129.

4. B. Gattu, P. P. Patel, P. Jampani, M. K. Datta and P. N. Kumta, "Nano Silicon (SiNP) Based Carbon Composite: Flexible Anode System in Lithium Ion Batteries," 228th ECS Meeting, Oct 2015, Phoenix, Arizona.
5. B. Gattu, P. Jampani, P. P. Patel, M. K. Datta, and P. N. Kumta, "High Performing Hollow Silicon Nanotube Anodes for Lithium Ion Batteries," 227th ECS Meeting, Chicago, Illinois, May 2015.
6. Sookyung Jeong, Xiaolin Li, Jianming Zheng, Pengfei Yan, Ruiguo Cao, Hee Joon Jung, Chongmin Wang, Jun Liu, and Ji-Guang Zhang, "Hard Carbon Coated Nano-Si/Graphite Composite as a High Performance Anode For Lithium-ion Batteries," presentation at 18th International Meeting on Lithium Batteries, June 19-24, 2016, Chicago, Illinois.
7. B. Gattu, P. M. Shanthi, P. Jampani, M. K. Datta, and P. N. Kumta, "Synthesis of High Performance Si Nanoflakes and Nanorod Anode Morphologies Using Water Soluble Recyclable Templates for Lithium Ion Batteries," 229th ECS Meeting, May 2016, San Diego, California.

References

1. Kasavajjula, U.; Wang, C. S.; Appleby, A. J. Nano- and bulk-silicon-based insertion anodes for lithium-ion secondary cells. *J. Power Sources* **2007**, *163*, , 1003.
2. Chan, C. K.; Peng, H. L.; Liu, G.; McIlwrath, K.; Zhang, X. F.; Huggins, R. A.; Cui, Y. High-performance lithium battery anodes using silicon nanowires. *Nature Nanotechnology* **2008**, *3*, , 31.
3. Wu, H.; Chan, G.; Choi, J. W.; Ryu, I.; Yao, Y.; McDowell, M. T.; Lee, S. W.; Jackson, A.; Yang, Y.; Hu, L.; Cui, Y. Stable cycling of double-walled silicon nanotube battery anodes through solid-electrolyte interphase control. *Nat Nano* **2012**, *7*, 310-315.
4. Liu, N.; Wu, H.; McDowell, M. T.; Yao, Y.; Wang, C.; Cui, Y. A Yolk-Shell Design for Stabilized and Scalable Lithium-ion Battery Alloy Anodes. *Nano Letters* **2012**, *12*, 3315-3321.
5. Li, X.; Meduri, P.; Chen, X.; Qi, W.; Engelhard, M. H.; Xu, W.; Ding, F.; Xiao, J.; Wang, W.; Wang, C.; Zhang, J.-G.; Liu, J. Hollow core-shell structured porous Si-C nanocomposites for Lithium-ion battery anodes. *Journal of Materials Chemistry* **2012**, *22*, 11014-11017.
6. Liu, N.; Lu, Z.; Zhao, J.; McDowell, M. T.; Lee, H.-W.; Zhao, W.; Cui, Y. A pomegranate-inspired nanoscale design for large-volume-change lithium battery anodes. *Nat Nano* **2014**, *9*, 187-192.
7. Li, X.; Gu, M.; Hu, S.; Kennard, R.; Yan, P.; Chen, X.; Wang, C.; Sailor, M. J.; Zhang, J.-G.; Liu, J. Mesoporous silicon sponge as an anti-pulverization structure for high-performance lithium-ion battery anodes. *Nat Commun* **2014**, *5*.

V.C.2. Pre-Lithiation of Silicon Anode for High Energy Li Ion Batteries (Stanford University)

Yi Cui, Principal Investigator

Stanford University
Department of Materials Science and Engineering
Stanford, CA 94305
Phone: 650-723-4613; Fax: 650-736-1984
E-mail: yicui@stanford.edu

Tien Q. Duong, DOE Program Manager

U.S. Department of Energy
Advanced Battery Materials Research (BMR)
Vehicle Technologies Office
1000 Independence Avenue, SW
Washington, DC 20585
Phone: 202-586-7836
E-mail: Tien.Duong@ee.doe.gov

Start Date: October 1, 2015
End Date: September 30, 2016

Abstract

Objectives

This study aims to develop high-capacity prelithiation additives that can work as a secondary lithium source and compensate the initial lithium loss in lithium-ion batteries. This study pursues two main directions: 1) developing different anode prelithiation and cathode prelithiation additives to increase first-cycle Coulombic efficiency of lithium-ion batteries, and 2) increase the stability of prelithiation additives in the electrode fabrication environments.

Accomplishments

- Synthesize $\text{Li}_x\text{Si}/\text{Li}_2\text{O}$ composites for anode prelithiation with improved stability in ambient air with 40% relative humidity.
- Explore a class of high-capacity cathode prelithiation materials based nanocomposites of lithium oxide and metal (e.g., $\text{Li}_2\text{O}/\text{Co}$, $\text{Li}_2\text{O}/\text{Ni}$ and $\text{Li}_2\text{O}/\text{Fe}$), nanocomposites of lithium fluoride and metal (e.g., LiF/Co and LiF/Fe), and nanocomposites of lithium sulfide and metal (e.g., $\text{Li}_2\text{S}/\text{Co}$ and $\text{Li}_2\text{S}/\text{Fe}$).
- Develop a surface-passivated high-capacity Li_3N as cathode prelithiation material.

Future Achievements

- Modified structure design for more stable prelithiation materials.
- Modified surface design to improve the stability of prelithiation materials in industrial battery fabrication conditions.
- Stable full-cell operation with prelithiation materials.

Technical Discussion

Background

There is unrelenting demand for rechargeable lithium-ion batteries (LIBs) with higher energy density to address the ever-increasing energy needs of modern society for wide applications such as extended-range electric vehicles and grid-scale storage. The electrodes of batteries largely decide their lithium storage capacity and energy density. In existing lithium-ion technology, lithium is provided by lithium-intercalated cathode materials, such as LiCoO_2 (LCO), $\text{LiNi}_{0.6}\text{Co}_{0.2}\text{Mn}_{0.2}\text{O}_2$ (NCM) and LiFePO_4 (LFP). Graphite has been as the most commonly used commercial anode material for LIBs since 1991 due to its high reversibility and low cost. On the other hand, various alternative high-capacity anode materials such as silicon, with a theoretical capacity more than ten times that of graphite, have been well studied and have already shown promise in potential applications. The formation of a solid electrolyte interphase (SEI) layer on the anode surfaces is a critical process that occurs prior to regular battery operations and consumes a significant amount of lithium, irreversibly reducing the overall capacity of batteries. Graphite anodes exhibit an irreversible capacity loss of 5–10% from the initial battery charging process, while for high-capacity anode materials, the first-cycle lithium loss is even higher (e.g., 15–35% for Si). Such lithium loss in the so-called “formation process” appreciably reduces the energy density of LIBs.

Introduction

Electrochemical prelithiation is an effective route to solve the issue of initial lithium loss in LIBs; however, it needs an extra process of electrochemical cell building. To improve the overall energy density of LIBs, it is vitally important to pre-store lithium into electrodes to compensate the initial lithium loss by using high-capacity, low-cost, and air-stable prelithiation materials. For anode prelithiation, we develop ambient-air stable $\text{Li}_x\text{Si}/\text{Li}_2\text{O}$ composites with the capacity of 2120 mAh/g, which can be mixed with various anode materials to achieve high first cycle Coulombic efficiency (CE) of >100%. In terms of cathode prelithiation, our group demonstrate that conversion reaction based nanocomposites (e.g., $\text{Li}_2\text{O}/\text{metal}$, LiF/metal and $\text{Li}_2\text{S}/\text{metal}$ composites) could be attractive cathode prelithiation materials with high lithium-ion donating capacities in the range of 500 to 700 mAh/g, good stability and compatibility with existing battery processing conditions. Moreover, we develop a surface-passivated Li_3N material with a higher “donor” lithium-ion specific capacity of 1761 mAh/g.

Approach

For anode prelithiation, ambient-air stable $\text{Li}_x\text{Si}/\text{Li}_2\text{O}$ composites were developed. SiO or SiO_2 NPs were heated to 250°C followed by the addition of Li metal foil. The mixture was kept at 250°C under mechanical stir at 200 rpm for at least 1 d in an Ar glove box. This one-pot thermal alloying process obtained a unique composite with homogeneously dispersed active Li_xSi nanodomains embedded in a robust Li_2O matrix, which gave the $\text{Li}_x\text{Si}/\text{Li}_2\text{O}$ composites an unparalleled stability in both dry air and ambient air conditions.

For cathode prelithiation, nanocomposites of lithium oxide and metal (e.g., $\text{Li}_2\text{O}/\text{Co}$, $\text{Li}_2\text{O}/\text{Ni}$ and $\text{Li}_2\text{O}/\text{Fe}$), nanocomposites of lithium fluoride and metal (e.g., LiF/Co and LiF/Fe), and nanocomposites of lithium sulfide and metal (e.g., $\text{Li}_2\text{S}/\text{Co}$ and $\text{Li}_2\text{S}/\text{Fe}$) were utilized. To synthesize the $\text{Co}/\text{Li}_2\text{O}$ composite, Co_3O_4 nanoparticles reacted with molten Li metal at 185 °C for 20 minutes and 200 °C for another 20 minutes under continuously mechanical stirring in an Argon-filled glove box. $\text{Ni}/\text{Li}_2\text{O}$ and $\text{Fe}/\text{Li}_2\text{O}$ composites were prepared with the same procedure using NiO and Fe_3O_4 nanoparticles as the starting materials. The molar ratios of metal oxides (M_xO_y) and Li were designed according to their reaction ($\text{M}_x\text{O}_y + 2y\text{Li} \rightarrow x\text{M} + y\text{Li}_2\text{O}$).

LiF/Co nanocomposite was synthesized through the chemical reaction between molten lithium and CoF_3 powder in an inert atmosphere. Molten lithium metal and CoF_3 powder were mixed together under mechanical stirring at 240 °C with a molar ratio of 3:1 according to the conversion reaction equation ($3\text{Li} + \text{CoF}_3 \rightarrow \text{Co} + 3\text{LiF}$). Meanwhile, LiF/Fe nanocomposite was also synthesized with the same procedure according to the reaction equation: $\text{FeF}_3 + 3\text{Li} \rightarrow \text{Fe} + 3\text{LiF}$. Moreover, we have successfully fabricated $\text{Li}_2\text{S}/\text{metal}$ ($\text{Li}_2\text{S}/\text{Co}$ and $\text{Li}_2\text{S}/\text{Fe}$) nanocomposites via a chemical conversion reaction using metal sulfide (CoS_2 and FeS_2) particles and Li metal as the starting materials.

We also present a simple and easily scalable synthetic route for the preparation of surface-passivated Li_3N . During the synthesis, pristine lithium metal foil was left in a nitrogen-filled glovebox with trace oxygen. The reaction between lithium metal and nitrogen gas to form Li_3N occurred spontaneously. After 3 days, the lithium metal foil transformed into a Li_3N flake, which was further heat-treated at 200 °C for 24 hours. Li_3N powder was obtained after grinding.

Results

$\text{Li}_x\text{Si}/\text{Li}_2\text{O}$ composites as high-capacity anode prelithiation materials

Here we developed $\text{Li}_x\text{Si}/\text{Li}_2\text{O}$ composites with excellent ambient air compatibility via a one-pot metallurgical process using low-cost SiO as the starting material to alloy thermally with molten Li metal. Figure V-32a shows the size of SiO NPs was in the range of 50-250 nm after ball-milling. The size of derived $\text{Li}_x\text{Si}/\text{Li}_2\text{O}$ composite was larger due to the volume expansion and some degree of particle aggregation during the alloying process (Figure V-32b). Compared with the STEM image, the corresponding EELS elemental mapping reveals that Li, Si and O elements were uniformly distributed as shown in Figure V-32c, indicating the formation of a homogeneous $\text{Li}_x\text{Si}/\text{Li}_2\text{O}$ composite. Furthermore, XRD confirms the complete transformation of amorphous SiO to crystalline $\text{Li}_{21}\text{Si}_5$ (PDF# 00-018-747) and Li_2O (PDF# 04-001-8930) (Figure V-32d). Figure V-32e shows thermally synthesized $\text{Li}_x\text{Si}/\text{Li}_2\text{O}$ composites exhibit excellent dry air stability. However, the electrochemically lithiated Si and SiO electrodes do not exhibit dry air stability, losing most of the capacity after in dry air for just 1 day. Figure V-32f shows the capacity retention of $\text{Li}_x\text{Si}/\text{Li}_2\text{O}$ composites, $\text{Li}_x\text{Si}/\text{Li}_2\text{O}$ core-shell NPs and artificial-SEI coated Li_xSi NPs in the air with different humidity levels for 6h, from which the superior stability of the $\text{Li}_x\text{Si}/\text{Li}_2\text{O}$ composites is evident. In our previous reports, little capacity was extracted for core-shell NPs with the humidity level higher than 10% RH. $\text{Li}_x\text{Si}/\text{Li}_2\text{O}$ composite still exhibited a high extraction capacity of 1383 mAh/g, after exposure to humid air with 20% RH. To further test whether $\text{Li}_x\text{Si}/\text{Li}_2\text{O}$ composite is stable enough for the whole battery fabrication process, the remaining capacities of $\text{Li}_x\text{Si}/\text{Li}_2\text{O}$ composite in ambient air with different durations were studied. The humidity range of the test room is from 35% RH to 40% RH. Although the XRD spectrum revealed small peaks belonging to LiOH (PDF# 00-032-0564), the intensity of Li_xSi peaks confirmed Li_xSi to be remained as the major component (Figure V-32h). Consistently, the red curve in Figure V-32g shows the $\text{Li}_x\text{Si}/\text{Li}_2\text{O}$ composite with an extraction capacity of 1240 mAh/g, indicating that the $\text{Li}_x\text{Si}/\text{Li}_2\text{O}$ composite is potentially compatible to the industrial battery fabrication environment.

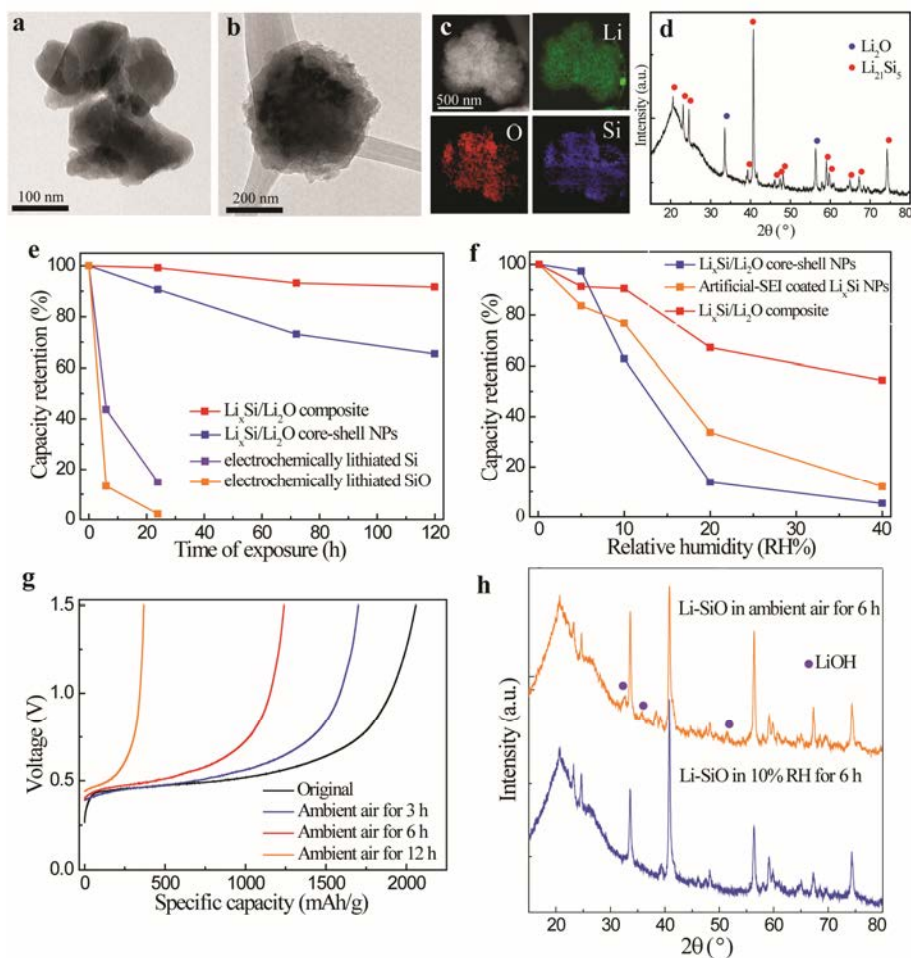


Figure V-32: Characterizations and stability of prelithiated SiO NPs. a, TEM image of ball-milled SiO NPs. b, TEM image of lithiated SiO NPs. c, STEM image of lithiated SiO NPs and the corresponding EELS maps of Li, O and Si distributions. d, XRD pattern of lithiated SiO NPs. e, Capacity retention of $\text{Li}_{1.5}\text{Si}/\text{Li}_2\text{O}$ composites (red), $\text{Li}_{1.5}\text{Si}/\text{Li}_2\text{O}$ core-shell NPs (blue), electrochemically lithiated Si electrode (purple) and electrochemically lithiated SiO electrode (orange) exposed to dry air with varying duration. f, Capacity retention of $\text{Li}_{1.5}\text{Si}/\text{Li}_2\text{O}$ composites (red), $\text{Li}_{1.5}\text{Si}/\text{Li}_2\text{O}$ core-shell NPs (blue) and artificial-SEI coated Li_xSi NPs (orange) after 6h storage in the air with different humidity levels. g, The remaining capacities of lithiated SiO NPs in ambient air ($\sim 40\%$ RH) with different durations. h, XRD patterns of lithiated SiO NPs exposed to ambient air for 6 h (upper) and to humid air (10% RH) for 6 h (bottom)

J. Zhao, Y. Cui et al. PNAS.

Previously, SiO_2 is not considered to be electrochemically active for lithium storage, due to the poor electrical and ionic conductivity. Here we demonstrated SiO_2 can also be used as starting materials for $\text{Li}_x\text{Si}/\text{Li}_2\text{O}$ composites. Figure V-33a shows SiO_2 NPs with a narrow size distribution around 90 nm. After metallurgical lithiation, the morphology of NPs remained while the size changed to 200 nm due to volume expansion (Figure V-33b). XRD pattern also confirms the formation of crystalline $\text{Li}_{12}\text{Si}_5$ and Li_2O during the alloying process (Figure V-33c). To measure the real capacity and eliminate the possible capacity loss during the slurry coating process, lithiated SiO_2 NPs were dispersed in cyclohexane and then drop casted on copper foil. The extraction capacities of lithiated SiO_2 were 1543 mAh/g, based on the mass of SiO_2 (Figure V-33d). The open circuit voltage (OCV) of lithiated SiO_2 NPs was below 0.1 V, confirming that the majority of SiO_2 has been successfully lithiated. Similar to lithiated SiO NPs, lithiated SiO_2 NPs can undergo slurry process with THF as slurry solvent and exhibit negligible capacity consumption. It is important to note that the galvanostatic discharge/charge profile of SiO_2 NPs (SiO_2 : Super P: PVDF=65:20:15 by weight, orange curve in Figure I-2d) showed little delithiation capacity after the first lithiation process, indicating that the sol-gel-synthesized SiO_2 NPs are electrochemically inactive. However, thanks to the thermal lithiation process, the inactive SiO_2 NPs can be successfully converted into high capacity anode. As the final products of lithiated SiO and SiO_2 are the same, lithiated SiO_2 also serves as a prelithiation reagent. Similarly, lithiated SiO_2 NPs were mixed with graphite and PVDF in a weight ratio of 6:84:10 to achieve high 1st CE of 99.7% (Figure V-33e). Due to the

nanoscale dimension and the small amount, prelithiation reagents tend to be embedded in the interstices of graphite microparticles. Therefore, graphite prelithiated with lithiated SiO_2 NPs follow the trend of the graphite control cell and exhibit stable cycling performance at C/20 for the first 3 cycles and C/5 for the following cycles ($1\text{C}=372\text{ mAh/g}$, Figure V-33f). The commercial graphite with $\text{Li}_x\text{Si/Li}_2\text{O}$ prelithiation reagents suppresses the undesired consumption of Li from cathode materials, which in turn increases the energy density of the full cell.

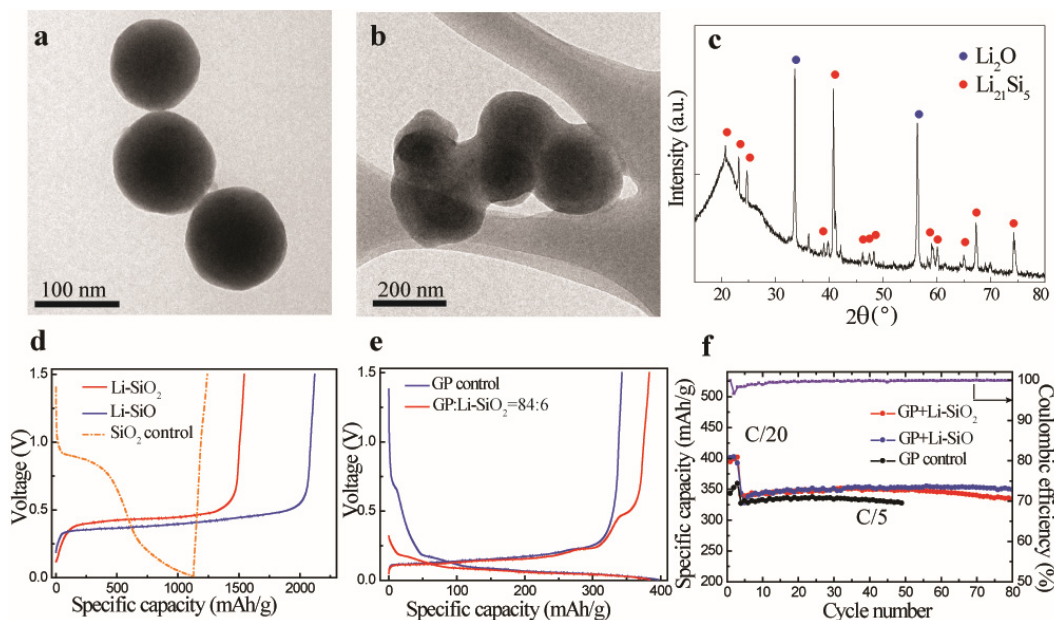


Figure V-33: Characterizations and electrochemical performance of SiO_2 NPs before and after thermal lithiation. a, b, TEM images of sol-gel synthesized SiO_2 NPs (a) and lithiated SiO_2 NPs (b). c, XRD pattern of lithiated SiO_2 NPs. d, First cycle delithiation capacity of lithiated SiO_2 NPs (red) and SiO NPs (blue). Galvanostatic lithiation/delithiation profile of SiO_2 NPs in 1st cycle (orange). The capacity is based on the mass of SiO or SiO_2 in the anode. e, First cycle voltage profiles of graphite/lithiated SiO_2 composite (84:6 by weight, red) and graphite control cell (blue). f, Cycling performance of graphite/lithiated SiO_2 composite (84:6 by weight, red), graphite/lithiated SiO composite (84:6 by weight, blue) and graphite control cell (black) at C/20 for first three cycles and C/5 for the following cycles ($1\text{C} = 0.372\text{ A/g}$, the capacity is based on the mass of the active materials, including graphite, SiO and SiO_2 in $\text{Li}_x\text{Si/Li}_2\text{O}$ composites). The purple line is the Coulombic efficiency of graphite/lithiated SiO_2 composite

J. Zhao, Y. Cui et al. PNAS.

Lithium oxide/metal nanocomposites as high-capacity cathode prelithiation materials

We develop a general one-step synthesis method of $\text{M/Li}_2\text{O}$ (M: Co, Fe, Ni, et al) nanocomposites (Figure V-34a) as cathode additives to effectively compensate the Li loss during the first charge process in lithium-ion batteries. As a typical example, the electrochemical performances of the nanometer-sized Co/nanometer-sized Li_2O (N-Co/N- Li_2O ; molar ratio, 3/4) composite were investigated (Figure V-34b,c). As expected, the as-prepared N-Co/N- Li_2O composite delivered a high charge specific capacity of 619 mAh/g and a low discharge specific capacity of 10 mAh/g for the first cycle in the potential range between 4.1 and 2.5 V, meeting the voltage criterion as a prelithiation additive. For comparison, electrochemical properties of two other Co/ Li_2O nanocomposites, including micrometer-sized Co/nanometer-sized Li_2O (M-Co/N- Li_2O) and sub-micrometer-sized Co/nanometer-sized Li_2O (SM-Co/N- Li_2O) composites were also investigated (Figure V-34b). They exhibited much higher charge potential ($\sim 4.1\text{ V}$) and lower specific charge capacity ($< 100\text{ mAh/g}$), due to the large particle size of Co and the loose contact between Li_2O and Co particles. Moreover, the N-Co/N- Li_2O electrode lost nearly all the capacity after the first cycle, suggesting that after providing lithium ion during the first charge, these nanocomposites did not contribute to the active electrochemical process in the cathode (Figure V-34c). Figure V-34d shows the charge potential profiles of LiFePO_4 cathode and Li metal anode half cells with different amounts of the N-Co/N- Li_2O cathode prelithiation material. The electrode made of pristine commercial LiFePO_4 powder delivers an initial charge capacity of 164 mAh/g. With a 4.8% N-Co/N- Li_2O additive (based on the entire cathode), the first-cycle specific charge capacity reaches 183 mAh/g (12% higher). When an 8% N-Co/N- Li_2O additive is used, the initial specific charge capacity is as

high as 195 mAh g (19% higher). As shown in Figure V-34e and f, the reversible discharge capacity of the as-made pristine LiFePO₄/graphite full cell without the N-Co/N-Li₂O cathode additive is only 120 mAh/g. In comparison, a LiFePO₄/graphite full cell with a 4.8 wt% N-Co/N-Li₂O cathode additive in the total cathode delivers a reversible discharge capacity of 133 mAh/g (11% higher) based on the weight of LiFePO₄ and the N-Co/N-Li₂O composite and stable cycling.

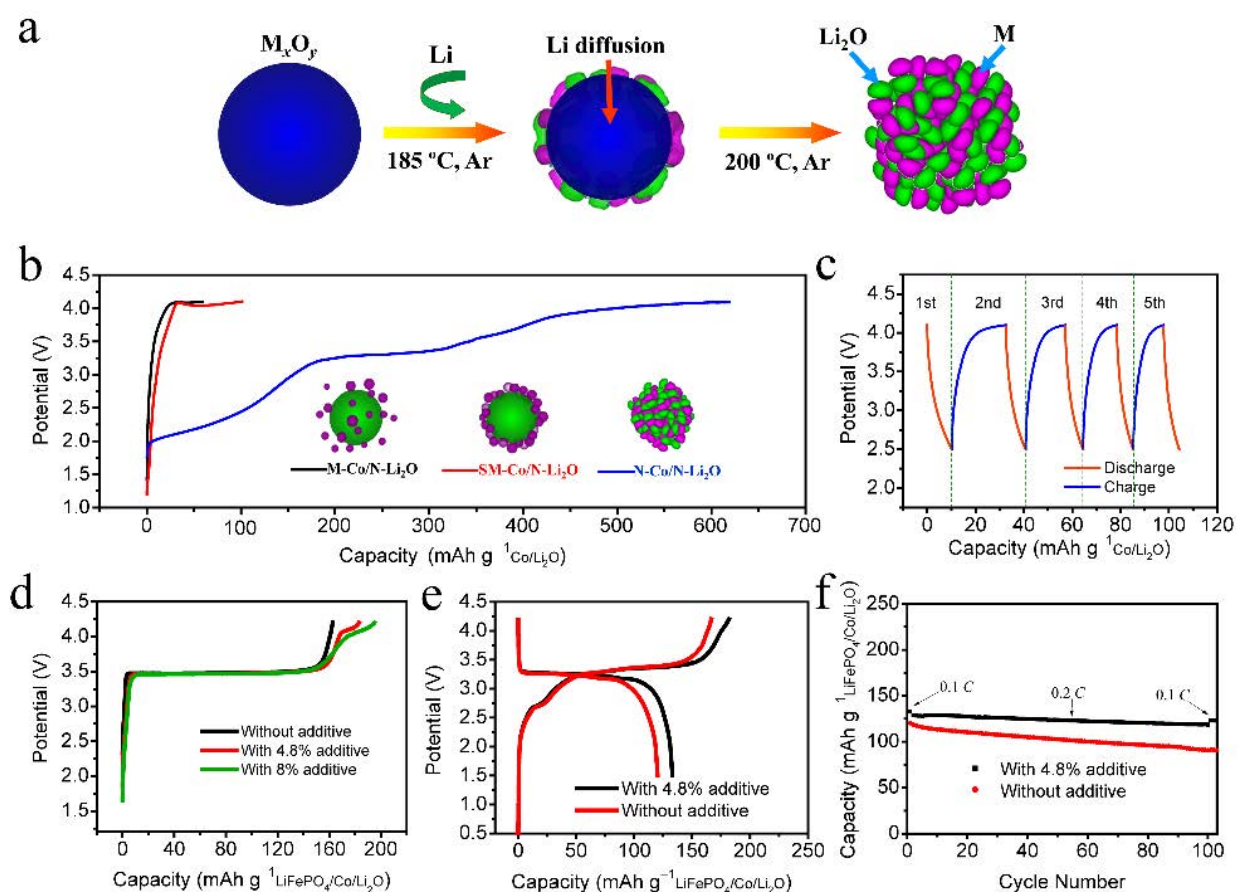


Figure V-34: Fabrication and electrochemical characteristics of the N-Co/N-Li₂O composite. a, Schematic of the fabrication process of the N-M/N-Li₂O composites. MOs are used as the starting materials and *in situ* converted into N-M/N-Li₂O composites via the chemical reaction with molten Li. b, The initial charge potential profiles of the electrodes made with various Co/Li₂O nanocomposites: M-Co/N-Li₂O composite, SM-Co/N-Li₂O and N-Co/N-Li₂O composites. c, The charge/discharge potential profiles of the N-Co/N-Li₂O electrode after the first charge process. d, The initial charge potential profiles of the LiFePO₄ electrodes with different amounts of the N-Co/N-Li₂O additive in half cell configurations. e, f, The initial charge/discharge potential profiles (e) and cycling performance (f) of LiFePO₄/graphite full cells with and without the N-Co/N-Li₂O additive. The specific capacities of the cathodes are evaluated based the weight of LiFePO₄ and the N-Co/N-Li₂O additive

Y. Sun, Y. Cui et al. *Nature Energy*.

To gain insight into the distribution of metallic Co particles and Li₂O in the composite, scanning transmission electron microscopy (STEM) was carried out. As shown in Figure V-35a, the dark/light contrast in a STEM image is clearly observed. The gray area can be assigned to Li₂O. The light patches suggest the existence of numerous Co nanoparticles. It is worth noting that the metallic Co nanocrystals are uniformly embedded in the Li₂O matrix. The crystallinity of metallic Co is confirmed by HRTEM (Figure V-35b, c).

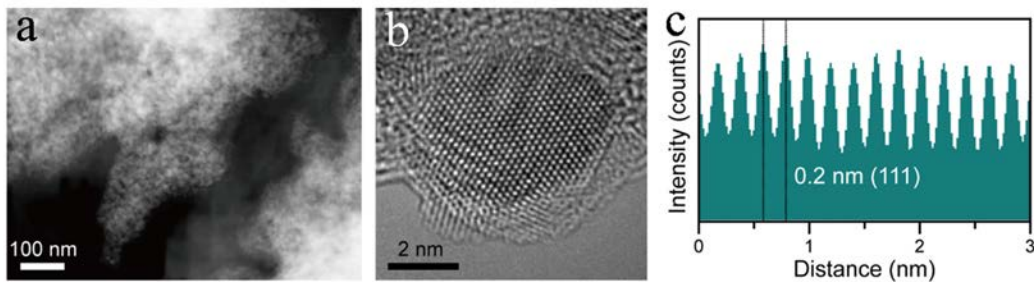


Figure V-35: Structure of the N-Co/N-Li₂O composite. a, STEM image of the N-Co/N-Li₂O composite, showing that Co nanoparticles are uniformly embedded in a Li₂O matrix. b,c, A HRTEM image (b) and the corresponding fringes of a Co particle (c), showing its crystallinity and the small particle size

Y. Sun, Y. Cui et al. Nature Energy.

To show the generality of using N-M/N-Li₂O composites as high-capacity cathode additives, we also prepared N-Ni/N-Li₂O and N-Fe/N-Li₂O composites using the same synthesis procedure. Working electrodes were prepared for N-Ni/N-Li₂O and N-Fe/N-Li₂O composites, respectively. As shown in Figure V-36a,b, the N-Ni/N-Li₂O and N-Fe/N-Li₂O electrodes exhibit different potential profiles upon the first-cycle charge process, probably due to the difference of M atoms and particle size. Similar to the N-Co/N-Li₂O composite, they possess high initial OCV (higher than 1.5 V) and deliver high charge capacities of 506 and 631 mAh/g, respectively, and very low discharge capacity of 11 and 19 mAh/g, respectively (Figure V-36a,b). The LiFePO₄ electrodes with the two additives were both subject to cycling (Figure V-36c,d). As expected, their first-cycle charge capacities are improved significantly. The initial charge capacities are 180 mAh/g for the electrode with a 4.8% N-Ni/N-Li₂O additive and 178 mAh/g for that with a 4.8% N-Fe/N-Li₂O composites, respectively. These capacity are ~10% higher than that of LiFePO₄ electrodes without any prelithiation additive. Moreover, these electrodes also show very good cycling stability (Figure V-36e,f).

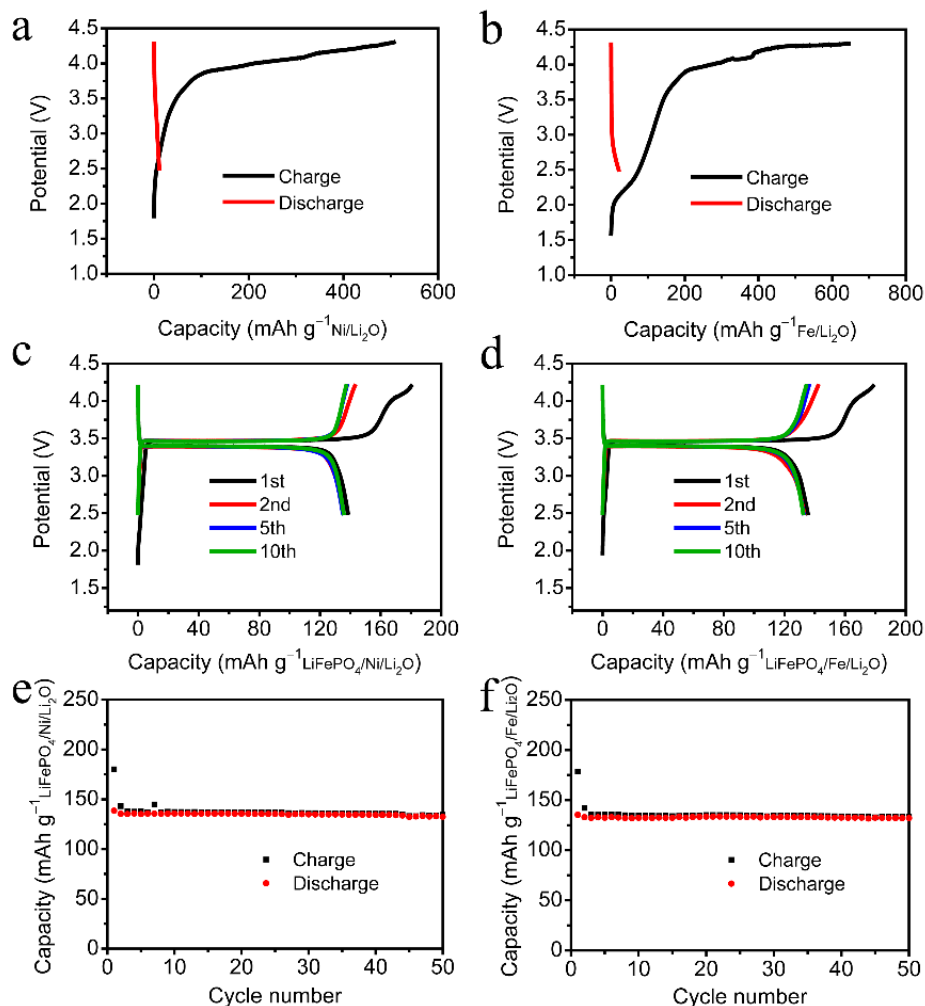


Figure V-36: Generalization to other N-M/N-Li₂O composites. a,b, The initial charge/discharge potential profiles of the pristine N-Ni/N-Li₂O (a) and N-Fe/N-Li₂O electrodes (b). c,d, The discharge/charge potential profiles of LiFePO₄ electrodes with 4.8% N-Ni/N-Li₂O (c) and N-Fe/N-Li₂O (d) additives in half cell configurations, respectively. e,f, Cycling performance of LiFePO₄ electrodes with 4.8% N-Ni/N-Li₂O (e) and N-Fe/N-Li₂O (f) additives, respectively
Y. Sun, Y. Cui et al. Nature Energy.

Lithium fluoride/metal nanocomposites as high-capacity cathode prelithiation materials

The X-ray diffraction (XRD) patterns for the starting CoF₃ and Co/LiF product are shown in Figure V-37b and c, respectively. The starting CoF₃ exhibits sharp XRD peaks with strong intensities, indicating its big particle size and high crystallinity (Figure V-37b). After the reaction, the XRD peaks for CoF₃ (JCPDS no. 09-0033) disappear and new peaks are observed, suggesting the chemical reaction-induced phase change (Figure V-37c). Clearly, these peaks can be readily indexed to mixed phases of Co (JCPDS no. 15-0806) and LiF (JCPDS no. 04-0857), in agreement with the product of the conversion-reaction equation. The significant broadening and reduced intensity of the XRD peaks confirm the nanocrystalline nature for the LiF/Co product. Despite the structure change, scanning electron microscopy (SEM) images show that the overall morphology of the starting CoF₃ is preserved after the reaction. Further evidence of the LiF/Co composite is found by the X-ray photoelectron spectroscopy (XPS) investigation. The high-resolution Co 2p XPS spectrum indicates the presence of Co with Co 2p 1/2 at 793.7 eV and Co 2p 3/2 at 778.4 eV (Figure V-37d).²⁴ The Li 1s peak is centered at 55.6 eV (Figure V-37e), whereas the F 1s peak is found at 684.8 eV (Figure V-37f), verifying the existence of LiF.

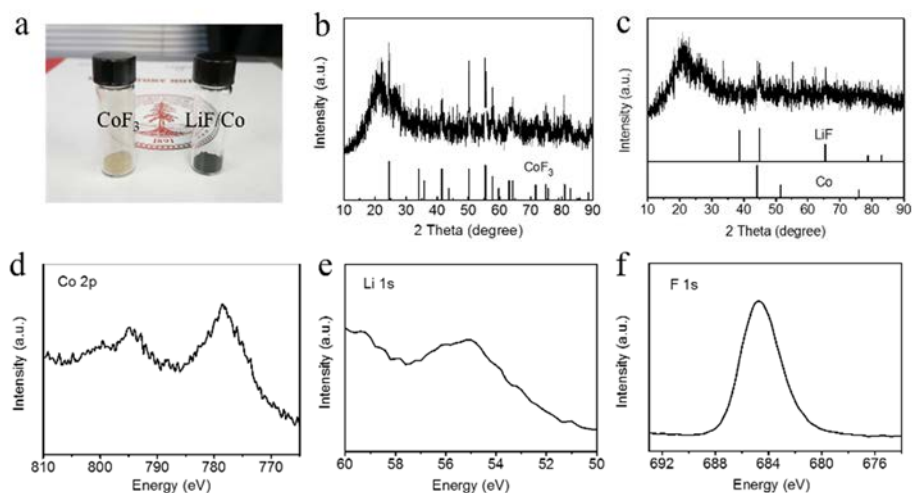


Figure V-37: (a) Digital images of the starting CoF_3 powder (left) and the LiF/Co product (right). XRD patterns of (b) the starting CoF_3 and (c) the LiF/Co product. High-resolution XPS spectra of (d) $\text{Co } 2p_3$, (e) $\text{Li } 1s$ and (f) $\text{F } 1s$. The XRD peaks at 21° and 27° arise from the Kapton tape

Y. Sun, Y. Cui et al. *Nano Letters*.

Transmission electron microscopy (TEM, Figure V-38a) and scanning TEM (STEM, Figure V-38b) images show that the LiF/Co composite has a unique nanostructure, where Co nanoparticles are uniformly embedded in a LiF matrix. The gray area in the STEM image is assigned to the LiF matrix, while the light patches suggest the existence of numerous Co nanoparticles with higher projected mass density. In the LiF/Co nanocomposite, the embedded Co nanoparticles enhance the electrical conductivity and the small dimension of LiF nanoparticles reduces the diffusion distance of lithium ions during their extraction process. Also, the Co nanoparticles make the nanocomposite electrically connected to the cathode during the first-cycle charge process. More importantly, the lithium exaction mechanism changes from the direct decomposition to a conversion reaction after the introduction of Co. This reduces the lithium-exaction potential within the cut-off voltage range of existing cathode materials and avoids the production of toxic fluorine gas. A high-resolution TEM (HRTEM) image was shown in Figure V-38c. The nanocrystalline nature and an ultrafine crystallite size of Co and LiF nanoparticles (~ 5 nm) are confirmed. In comparison, the initial individual CoF_3 particles have dimensions ranging from 100 to 300 nm with high crystallinity. A typical Co nanoparticle shows two sets of the lattices with an equal lattice plane spacing of 0.20 nm and a plane angle of 60° , corresponding to (111) and (-111) lattice planes of cubic Co. Two sets of lattices with an equal lattice plane spacing of 0.20 nm and angle of 90° are observed for a representative LiF nanoparticle, consistent with its (200) and (020) lattice planes. The lattice fringes of selected Co and LiF nanoparticles labeled in Figure V-38c are shown in Figure V-38d. The ability of extracting lithium from LiF/metal composites is related with the particle size and uniformity of the components. Due to the intimate nanoscale mixing of LiF and Co, as well as their small dimensions, the as-prepared nanostructure may deliver a high specific capacity during the first-cycle charge process in the cut-off potential range of existing cathodes.

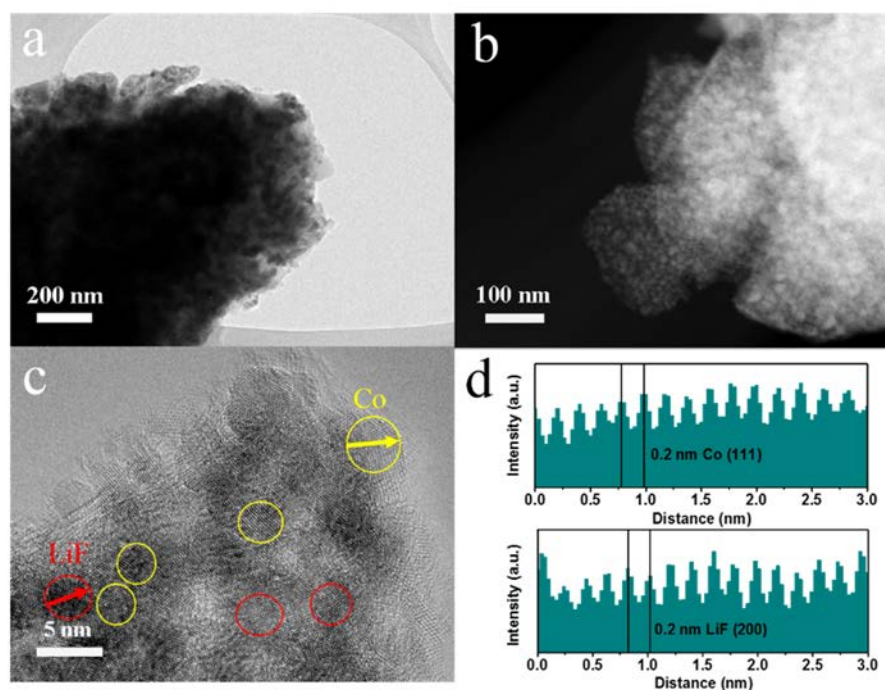


Figure V-38: (a) TEM and (b) STEM images of the LiF/Co nanocomposite. (c) A HRTEM image and (d) the corresponding fringes of se-lected Co and LiF nanoparticles, showing their crystallinity and the small particle size. The HRTEM image shows two sets of equal lattice plane spacing of 0.20 nm with a plane angle of 60° for Co [111], and two sets of equal lattice plane spacing of 0.20 nm with a plane angle 90° for LiF [200]

Y. Sun, Y. Cui et al. *Nano Letters*.

Experimentally, a wide cut-off potential range of 4.2–0.7 V and a low current density of 50 mA/g were applied to investigate the delithiation and lithiation electrochemical windows for the LiF/Co composite. The first-cycle galvanostatic charge/discharge profiles of a pristine LiF/Co electrode are shown in Figure V-39a. The LiF/Co electrode has a reasonably high OCV of 1.5 V, which makes no negative effects on the stability of cathode materials. It is observed that its potential range for lithium extraction is 3.2–4.2 V. Its initial specific charge capacity reaches as high as 520 mAh/g, while the specific discharge capacity is only 4 mAh/g between 4.2–2.5 V, showing a high “donor” lithium-ion specific capacity of 516 mAh/g. The intake of amount of lithium happens below 2.2 V, which is lower than that of the cut-off discharge potential for existing cathodes (> 2.5 V). These electrochemical characteristics meet the requirements of working potential and “donor” lithium-ion capacity as a superior cathode prelithiation material. Thus, when used as a cathode prelithiation additive, almost all the lithium in the LiF/Co nanocomposite can be extracted during the cathode charge process but does not transform back to the initial state during the discharge process. Here, we highlight the success of our LiF/Co nanocomposite as an effective structure design for the lithium extraction. To further evaluate its electrochemical compatibility with cathode materials and lithium compensation effect, the LiF/Co nanocomposite was used as a prelithiation additive to the commercial LiFePO_4 cathode material and the galvanostatic charge/discharge measurement of the composite electrode was carried out versus lithium metal counter/reference electrodes in half cells. Compared with the pristine LiFePO_4 electrode, the LiFePO_4 electrode with 4.8 wt% LiF/Co additive exhibits an obvious voltage slope above the charge plateau of the pristine LiFePO_4 , arising from the lithium extraction process from the additive (Figure V-39b). As predicted, The LiFePO_4 electrode with 4.8 wt% LiF/Co additive indeed delivers an increased initial charge specific capacity of 197 mAh/g at 0.1 C, which is 33 mAh/g (or 20.1%) higher than that (164 mAh/g) of the pristine LiFePO_4 electrode based on the mass of LiFePO_4 (Figure V-39b). This discharge capacity is very similar (145.9 and 146.6 mAh/g with and without prelithiation, respectively). Moreover, the hybrid electrode shows stable cyclability, verifying that the LiF/Co nanocomposite does not have any negative effect on the cathode materials (Figure V-39c).

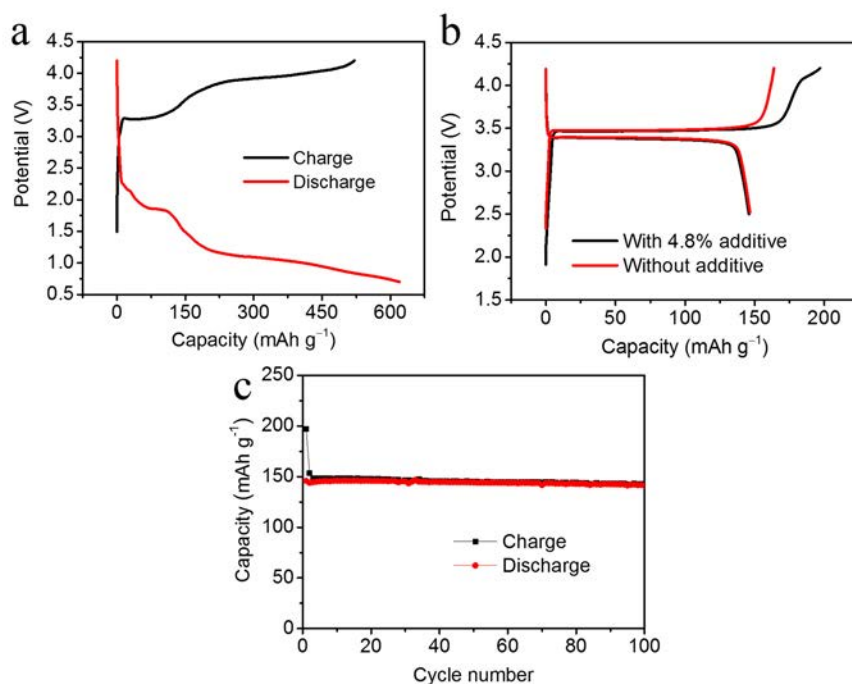


Figure V-39: (a) The initial charge and discharge curves for the LiF/Co electrode within the potential range of 4.2–0.7 V at the current density of 50 mA/g. (b) The comparison of the first-cycle charge and discharge curves of LiFePO₄ electrodes versus lithium metal in half cells with and without LiF/Co additive within the potential range of 4.2–2.5 V at 0.1 C. (c) Cycling stability for the LiFePO₄ electrode with 4.8% LiF/Co additive.

Y. Sun, Y. Cui et al. *Nano Letters*.

To show the generality of preparing the conversion-reaction based LiF/metal nanocomposites and their applications as efficient cathode prelithiation materials, we also synthesized LiF/Fe nanocomposite. TEM and STEM results indicate Fe nanoparticles are embedded in the LiF matrix uniformly, and both the Fe and LiF particles are ranging from 5 to 10 nm (Figure V-40a). Figure V-40b displays the voltage profiles of the as-synthesized LiF/Fe nanocomposite for the first cycle. As expected, the LiF/Fe nanocomposite exhibits a high OCV of 1.8 V. The first-cycle charge specific capacity reaches 565 mAh/g with a cut-off charge potential of 4.5 V, indicating most of the lithium in the LiF/Fe composite is extracted. Below the cut-off charge potential of existing cathodes (4.3V), a high capacity of 532 mAh/g is still achieved. Meanwhile, the LiF/Fe nanocomposite delivers a negligible discharge specific capacity of 26 mAh/g with the cut-off discharge potential of 2.5 V. Thus, a high donor lithium-ion capacity (506 mAh/g) is obtained for the as-prepared LiF/Fe nanocomposite within the potential range of existing cathodes.

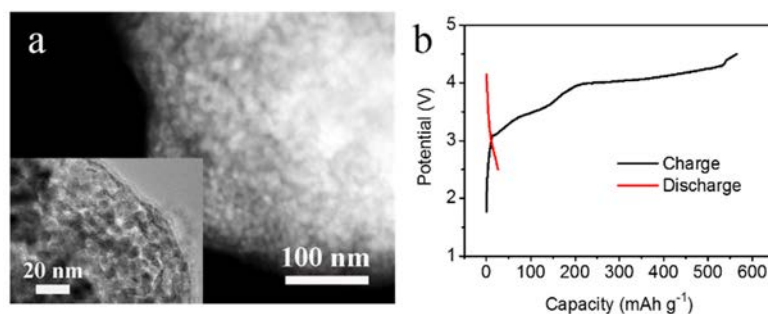


Figure V-40: (a) STEM and high-magnification TEM images (inset of a prior figure) of the LiF/Fe nanocomposite and (b) the initial charge and discharge curves for the pristine LiF/Fe electrode with the potential range of 4.5–2.5 V vs. Li⁺/Li at the current density of 50 mA/g. The STEM image shows that Fe particles are uniformly embedded in the LiF matrix. The TEM image at high magnification indicates that the particle size of the LiF and Fe nanodomains is 5–10 nm

Y. Sun, Y. Cui et al. *Nano Letters*.

Lithium sulfide/metal nanocomposites as high-capacity cathode prelithiation materials

A $\text{Li}_2\text{S}/\text{Co}$ nanocomposite was first prepared as a high-capacity cathode prelithiation material through the reaction between lithium metal and CoS_2 powder ($\text{CoS}_2 + 4\text{Li} \rightarrow \text{Co} + 2\text{Li}_2\text{S}$) at 220 °C for 2 hours. TEM was carried out to investigate the microstructure of the $\text{Li}_2\text{S}/\text{Co}$ nanocomposite (Figure V-41). After the chemical transformation reaction, the initial CoS_2 particles with a size ranging 300 to 600 nm transformed to a uniform composite with much smaller particles (Figure V-41a). The light/dark contrast in the STEM image is clearly observed (Figure V-41b). The light region can be assigned to the Li_2S matrix, while, the dark area suggests the presence of Co nanoparticles with higher mass density. The formed Li_2S and Co nanodomains are densely packed without cracks/pores. Therefore, the formation of a nanocomposite with Co nanoparticles embedded in a Li_2S matrix is verified. A high-magnification TEM image further confirms the finely dispersed Co nanoparticles in the Li_2S matrix (Figure V-41c). High resolution TEM (HRTEM) image shows that both the Co and Li_2S domains are crystalline with particle sizes of ~ 5 nm (Figure V-41d). Compared to the free CoS_2 , the introduction of metallic Co nanoparticles in the composite enhances the electronic conductivity. The intimate mixing of Li_2S and Co nanocrystal domains can maximize the extracted lithium-ion capacity via an inverse conversion reaction upon battery charging. The dense Co domains in the structure might help to insulate Li_2S from the ambient air and thus improve the ambient stability of the $\text{Li}_2\text{S}/\text{Co}$ composite.

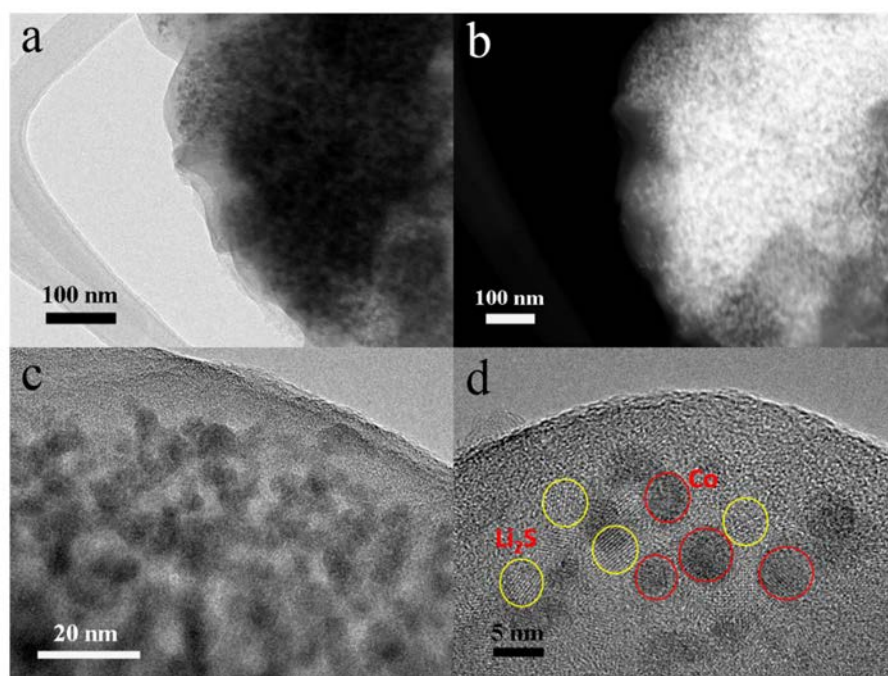


Figure V-41: a) Low-magnification TEM, (b) STEM, (c) high-magnification TEM and (d) HRTEM images of the $\text{Li}_2\text{S}/\text{Co}$ nanocomposite, showing the intimate mixing of Li_2S and Co nanocrystal domains with particle sizes of ~ 5 nm
Y. Sun, Y. Cui et al. *Advanced Energy Materials*.

To investigate the “donor” lithium-ion specific capacity of the as-made $\text{Li}_2\text{S}/\text{Co}$ nanocomposites, galvanostatic discharge/charge measurement of the pristine $\text{Li}_2\text{S}/\text{Co}$ electrode was carried out in the voltage range of 4.0–2.5 V at the current density of 50 mA/g. To match their application in current LIBs, a carbonate-based electrolyte was used instead of ether-based electrolytes usually used for Li_2S -based electrodes. A reasonably high OCV is observed (1.5 V), compatible with the existing cathodes. The lithium extraction from the $\text{Li}_2\text{S}/\text{Co}$ nanocomposite occurs in the potential range of 3.2–4.0 V during the charge process and its initial specific charge capacity reaches 683 mAh/g, close to its theoretical specific capacity of 711 mAh/g (Figure V-42a). During the discharge process, due to the large potential hysteresis of the conversion reaction, the additive does not transform back to its initial lithiated state above the cut-off discharge potential of the current cathodes. The specific discharge capacity of the $\text{Li}_2\text{S}/\text{Co}$ nanocomposite is only 13 mAh/g above the cut-off potential of 2.5 V (Figure V-42a). Therefore, the $\text{Li}_2\text{S}/\text{Co}$ nanocomposite has a noticeable high “donor” lithium-ion specific capacity of 670 mAh/g in the first cycle, which is more than three times that of the existing cathodes. To study compatibility with existing industrial battery processing conditions and the lithium compensation

effect of the $\text{Li}_2\text{S}/\text{Co}$ additive, the $\text{Li}_2\text{S}/\text{Co}$ nanocomposite was added as a prelithiation reagent to a commercial LiFePO_4 material for electrode fabrication. The electrochemical performances of the LiFePO_4 electrode with the $\text{Li}_2\text{S}/\text{Co}$ additive were performed in half cells with lithium metal as the counter/reference electrodes. During the first charge process, the LiFePO_4 with 4.8% $\text{Li}_2\text{S}/\text{Co}$ additive shows obvious potential slops and increased charge specific capacity in comparison to the pristine LiFePO_4 electrode (Figure V-42b), indicating the additive does not lose the lithium-ion activity during the electrode fabrication process. Notably, the LiFePO_4 electrode with 4.8% $\text{Li}_2\text{S}/\text{Co}$ additive delivers a high initial charge specific capacity of 204 mAh/g at 0.1 C, 42 mAh/g higher than that of the pristine LiFePO_4 electrode. Meanwhile, stable cyclability is achieved, indicating that such an additive does not have negative effect to the cathode materials (Figure V-42c, d).

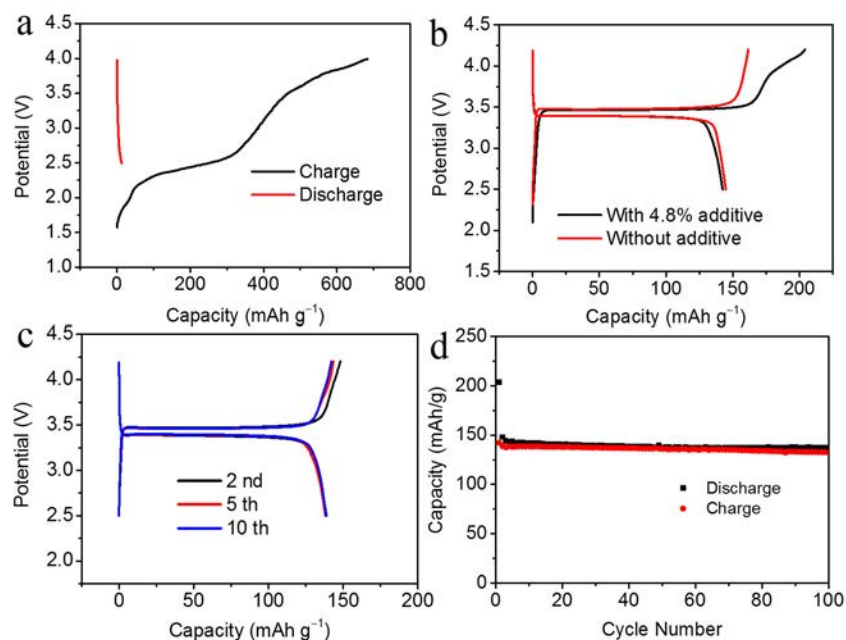


Figure V-42: (a) Voltage profiles of the 1st charge/discharge for pristine $\text{Li}_2\text{S}/\text{Co}$ electrode at the current density of 50 mA/g with the potential range of 4.0–2.5 V. (b) The comparison of the first-cycle charge and discharge curves of LiFePO_4 electrode with and without the $\text{Li}_2\text{S}/\text{Co}$ additive at 0.1 C in the potential range of 4.2–2.5 V. (c) Voltage profiles and (d) cyclability of a LiFePO_4 electrode with 4.8% $\text{Li}_2\text{S}/\text{Co}$ additive

Y. Sun, Y. Cui et al. *Advanced Energy Materials*.

Surface-passivated Li_3N as high-capacity cathode prelithiation material

We present a simple and easily scalable synthetic route for the preparation of surface-passivated Li_3N through the spontaneous reaction between lithium metal and nitrogen gas followed by an annealing process at 200 °C for 24 hours. XPS was carried out to investigate the surface electronic state of the as-prepared Li_3N . The binding energies were corrected by referencing the C 1s peak to 284.5 eV. The survey XPS spectrum of a Li_3N flake verifies the chemical composition of O, N and Li (Figure V-43a). A strong O1s peak and a weak N1s peak are observed, suggesting the surface of the Li_3N flake is strongly oxidized. To test the stability of the Li_3N after the annealing treatment, a Li_3N flake was exposed in ambient conditions for 30 days. XRD result shows that the main phase of the sample is still alpha- Li_3N (Figure V-43b), although peaks of LiOH and Li_2CO_3 are detected, indicating the good stability of the surface-passivated Li_3N material. XPS investigations on the ground Li_3N powder were also performed. Figure V-43c shows the survey and high-resolution N 1s XPS spectra of the Li_3N powder. The N peak in the survey almost disappears, suggesting the further oxidation of Li_3N during the mechanical grinding. In contrast, when probing beyond the surface of the Li_3N powder using EDX, a strong N peak and a weak O peak are observed in the spectrum (Figure V-43d). These results indicate that only the surface of the Li_3N powder is oxidized, and the main composition of the product is Li_3N . In fact, the passivation layer on the surface of Li_3N particles may prevent the further oxidation of Li_3N during the material processing. The passivation layer on the Li_3N might help to suppress the penetration of moisture from ambient air deep into the entire particles, protecting the powder during handling and electrode preparation process. The SEM images show that the Li_3N powder is composed of micrometer-size secondary

particles built from interconnected particles with the size of ~300 nm (Figure V-43e,f). TEM, HRTEM and EELS were performed to investigate the structure and composition of the passivation layer of Li_3N particles at a low temperature of ~100 K. It is confirmed that there exists a dense layer of highly crystalline Li_2O and Li_2CO_3 on the surface of Li_3N particles (Figure V-43g,h). Moreover, the surface oxidation of Li_3N particles was verified by Oxygen K-edge EELS spectrum (Figure V-43i). The dense and highly crystalline Li_2O and Li_2CO_3 isolates the active composition of materials from air and thus enable active prelithiation materials to have enhanced stability in ambient conditions.

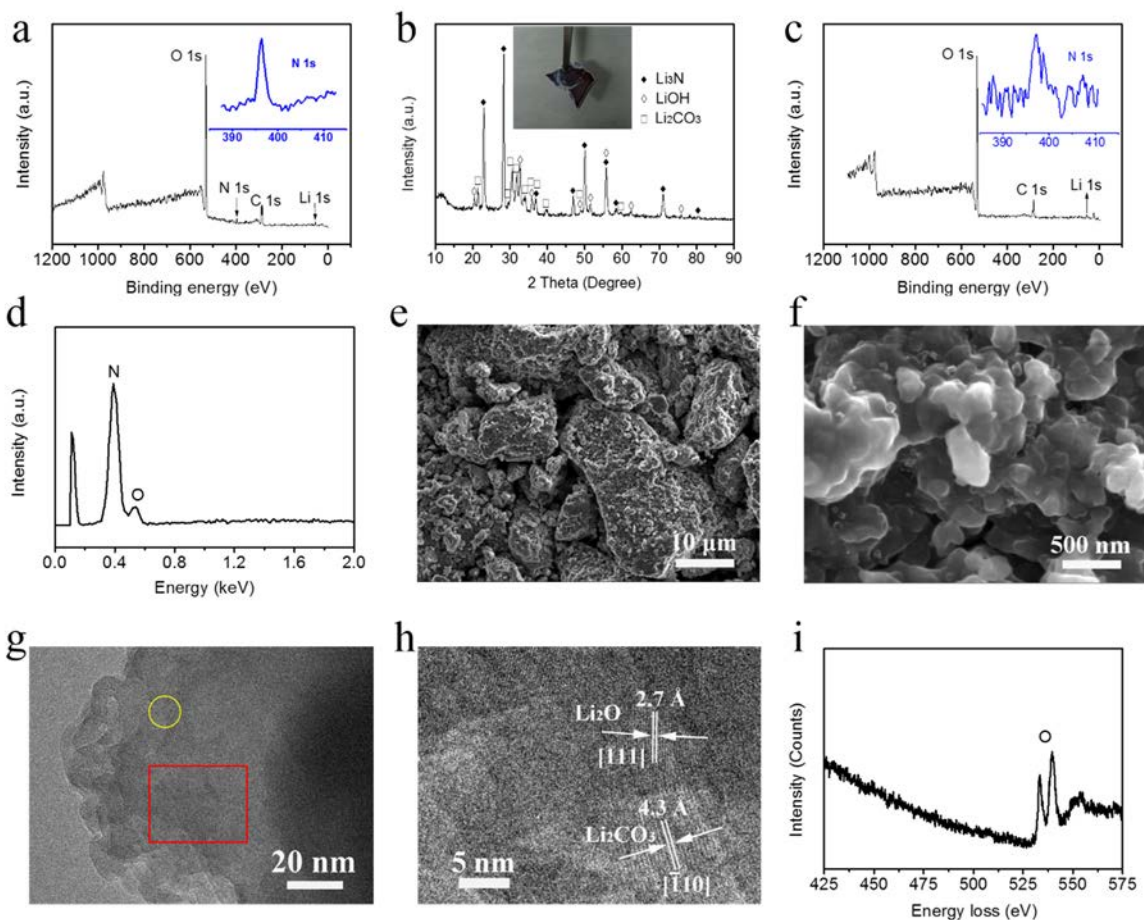


Figure V-43: Structure and stability characterizations of the as-achieved Li_3N flake and powder. a) Survey and high-resolution N 1s XPS spectra of a Li_3N flake, indicating that the surface of Li_3N is oxidized/passivated during the synthesis. b) XRD result of a Li_3N flake after exposure to ambient conditions for 30 days. The main phase of the sample is still Li_3N , although LiOH and Li_2CO_3 are detected. This result indicates that the as-formed Li_3N has good environmental stability. c) Survey and high-resolution N 1s XPS spectra of the Li_3N powder. The N peak in the survey almost disappears, suggesting the further oxidation of Li_3N during the mechanical grinding. d) EDX spectrum of the Li_3N powder. The strong O and weak N signals in survey XPS spectra, and the weak O and strong N signals in EDX spectrum indicate that only the surface of the Li_3N powder is oxidized, and the main composition of the product is Li_3N . e,f) SEM images of the Li_3N powder for slurry casting process, showing that the Li_3N powder consists of secondary Li_3N particles. g,h) TEM image (g) taken at the edge area of a Li_3N particle and HRTEM image (h) taken at the area labelled by a rectangle in (g). i) Oxygen K-edge EELS spectrum collected at the yellow circle in (g). The TEM and EELS results confirm that the surface of the Li_3N particles is passivated by a dense layer consisting of crystalline Li_2O and Li_2CO_3 .

Y. Sun, Y. Cui et al. *Energy Storage Materials*.

The as-prepared Li_3N electrodes exhibit a relatively high OCV of 1.16 V and a high decomposition potential above 4 V. Impressively, a high specific capacity of 1761 mAh/g is achieved with a charge cut-off potential of 4.8 V, which is ~10 times that of current cathode materials. When the charge cut-off potential is limited to 4.5 V, the specific capacity still reaches 1163 mAh/g (Figure V-44a). This extremely high “donor” capacity demonstrates that although a small amount of capacity is sacrificed to form a passivation layer on the surface of Li_3N , the final capacity of the surface-passivated Li_3N can be improved relative to the pristine Li_3N due to its

better stability. Meanwhile, cyclic voltammetry (CV) measurements were also performed for Li_3N electrodes. Consistent with the potential profile, a strong oxidation peak starting from 4.30 V is clearly observed (Figure V-44b), suggesting the high decomposition potential of Li_3N electrodes. This high decomposition potential of Li_3N electrodes compared to 0.9 V in the literature study may be caused by the insulating nature of the surface passivation layer on Li_3N formed during the material processing. After confirming the lithium compensation effect of the as-synthesized Li_3N material, we investigated the electrochemical performance of LCO cathodes with the addition of various amounts of Li_3N powder. Compared with the pristine LCO electrode, the potential profile of the LCO cathode with Li_3N additive extends above 3.8 V in the charge process, arising from the decomposition of Li_3N during charging (Figure V-44c). With the addition of 2.5% Li_3N , the initial charge capacity of the LCO cathode reaches 246 mAh/g, 51 mAh/g higher than the pristine LCO electrode. This increased capacity corresponds to 1782 mAh/g from Li_3N , indicating that high utilization of Li_3N is achieved in LCO cathodes. When 5% Li_3N is included into a LCO electrode, the cathode delivers an even higher initial charge capacity of 291 mAh/g with an extra lithium-ion capacity supply of 96 mAh/g from Li_3N . Furthermore, after the initial cycle, both the LCO electrodes with and without Li_3N display similar discharge capacities (based on the mass of LCO, ~150 mAh/g) and stable cycling (Figure V-44d). This good cycling performance confirms that the Li_3N additive does not have obvious negative effects on the stability of cathodes. To show the generality of using Li_3N as a prelithiation additive for various cathodes, we also prepared NCM and LFP cathodes with Li_3N additives using the same electrode fabrication procedures. As expected, their initial charge capacities increase significantly. The initial charge capacity of a NCM electrode with 2.5% Li_3N is 273 mAh/g, while a pristine NCM electrode delivers an initial charge capacity of 229 mAh/g (Figure V-44e). After adding 2.5% Li_3N in a LFP electrode, the first charge profile shows two obvious plateaus. The first plateau is around 3.48 V with a capacity of ~170 mAh/g, while the second plateau is around 4.1 V, delivering a capacity of 62 mAh/g, corresponding to the extraction of Li from Li_3N (Figure V-44f).

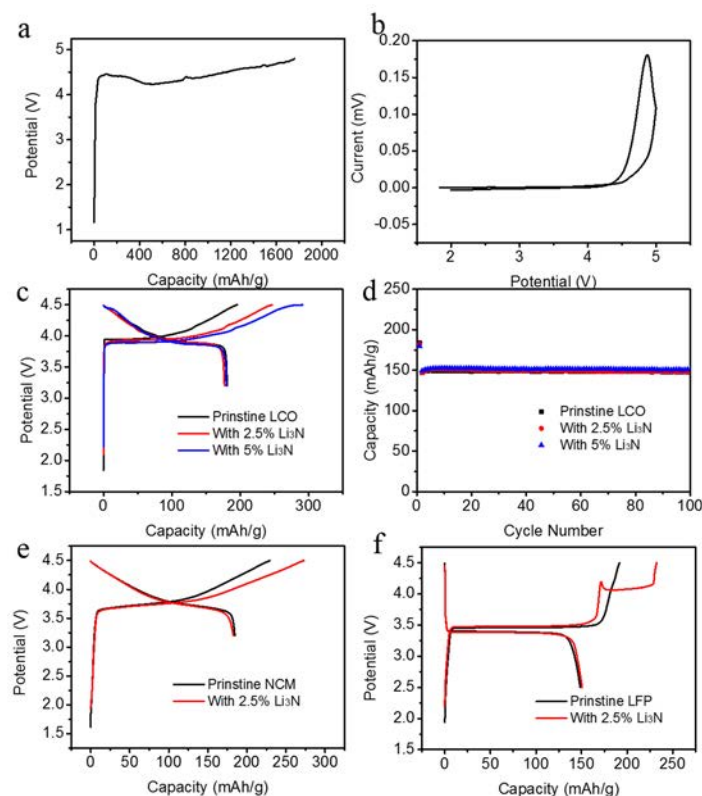


Figure V-44: Electrochemical properties of the as-prepared Li_3N electrodes. a,b) Charge potential profile (a) and CVs (b) of a Li_3N electrode prepared by a slurry manufacturing process. c,d) Initial charge and discharge curves (c) and cycling (d) of LCO cathodes with and without the addition of Li_3N . e) The comparison of initial charge and discharge potential profiles of NCM electrodes with and without the addition of Li_3N . f) The initial charge and discharge potential profiles of LFP electrodes with and without the Li_3N additive. With the additive of Li_3N , the initial charge capacities of cathodes increase, indicating the lithium “donor” effect of Li_3N . Stable cycling performances are achieved for the LCO electrodes with various amounts of the Li_3N additive. This result shows that the Li_3N additive has negligible negative effect on the stability of the cathode materials
Y. Sun, Y. Cui et al. Energy Storage Materials.

Conclusions

In all, in the past one year, we have made exciting progress in designing high-capacity prelithiation materials to offset the initial lithium loss in lithium-ion batteries. For anode prelithiation, we developed a one-pot metallurgical process to synthesize $\text{Li}_x\text{Si}/\text{Li}_2\text{O}$ composites by using low-cost SiO or SiO_2 as the starting material. The resulting composites consist of homogeneously dispersed Li_xSi nanodomains embedded in a highly crystalline Li_2O matrix, providing the composite excellent stability even in ambient air with 40% RH. The composites are readily mixed with various anode materials to achieve high first cycle CE of >100%.

We also demonstrate a novel and facile cathode prelithiation method that offers high prelithiation efficacy, and good compatibility with ambient air, regular solvent, binder and the thermal processes used in current lithium-ion battery manufacturing. We have developed cathode additives, nanoscale mixtures of transition metal (M) and lithium compounds (Li_2O , LiF and Li_2S), which are the reaction products of transition metal oxide (M_xO_y), fluoride (M_xF_y) and sulfide (M_xS_y), and Li metal via a well-known conversion reaction mechanism. The nanocomposites afford a high theoretical prelithiation capacity (typically up to 800 mAh/g, 2700 mAh/cm³) when converted back to M_xO_y (M_xF_y , M_xS_y) and lithium ions during cathode charge. As an example, we demonstrate that in a full cell configuration, the LiFePO_4 electrode with a 4.8% $\text{Co}/\text{Li}_2\text{O}$ additive shows 11% higher overall capacity than that of the pristine LiFePO_4 electrode.

To achieve prelithiation with higher donor lithium ion capacity, a surface-passivated Li_3N material was prepared by the reaction of lithium metal with nitrogen followed by an annealing process. A dense surface passivation layer consisting of crystalline Li_2O and Li_2CO_3 isolates the active composition of materials from air and thus enables good stability of Li_3N particles. A high “donor” lithium-ion specific capacity of 1761 mAh/g is achieved for a pristine Li_3N electrode. As a typical example, with a 2.5% Li_3N additive, a LCO electrode delivers a 51 mAh/g higher capacity than that of the pristine LCO electrode in the first charge process and shows stable cycling behavior.

Products

Presentations/Publications/Patents

Presentations

1. (Plenary) “Nanomaterials Design for Energy Conversion and Storage” 1st International Symposium on Energy Chemistry and Materials”, October 29-31, 2015, Fudan University, Shanghai, China.
2. (Plenary) “Electrochemical Nanotechnology: Batteries and Electrocatalysts” International Conference on Innovative Electrochemical Energy Materials and Technologies (EEMT2015), Nanning, China, November 8-11, 2015.
3. (Invited) “Nanomaterials Design of Batteries Guided by In-Operando Characterization and Atomistic Simulation”, Gordon Research Conference on Batteries, Feb. 21-26, 2016, Ventura, California.

Patents

1. Y. Cui, J. Zhao, Z. Lu. “High capacity prelithiation reagents and lithium-rich anode materials.” Patent Application No. 14/869,800.
2. Y. Cui, Y. M. Sun. “Nanocomposites of lithium compounds and metals as cathode additives for lithium-ion batteries.” Patent Application No. 15/179545.

References

1. J. Zhao, H.-W. Lee, J. Sun, K. Yan, Y. Liu, W. Liu, Z. Lu, D. Lin, G. Zhou, Y. Cui, Proc. Natl. Acad. Sci. U.S.A. 2016, 113, 7408.
2. Y. Sun, H. -W. Lee, Z. W. Seh, N. Liu, J. Sun, Y. Z. Li, Y. Cui, Nature Energy, 2016, 1, 15008.
3. Y. Sun, H. -W. Lee, Z. W. Seh, G. Y. Zheng, J. Sun, Y. Li, Y. Cui, Adv. Energy Mater., 2016, 6, 1600154.
4. Y. Sun, H. -W. Lee, G. Y. Zheng, Z. W. Seh, J. Sun, Y. Li, Y. Cui, Nano Lett., 2016, 16, 1497.
5. Y. Sun, Y. Li, J. Sun, Y. Li, A. Pei, Y. Cui, Energy Storage Materials, 2016, 6, 119.

V.C.3. Novel Non-Carbonate Based Electrolytes for Silicon Anodes (Wildcat Discovery Technologies)

Dee Strand, Principal Investigator

Wildcat Discovery Technologies
6985 Flanders Drive
San Diego, CA 92121
Phone: 858-550-1980; Fax: 858-638-7533
E-mail: dstrand@wildcatdiscovery.com

Walter Parker, Project Officer/Manager

National Energy Technology Laboratory
Phone: 412-386-7357
E-mail: walter.parker@netl.doe.gov

Start Date: October 1, 2013
End Date: June 30, 2016

Abstract

Objectives

Develop non-carbonate electrolytes that form a stable solid electrolyte interphase (SEI) on silicon alloy anodes, enabling substantial improvements in energy density and cost relative to current lithium-ion batteries (LIBs)

Accomplishments

- Identified anode SEI additives that improved cycle life performance over baseline formulations containing either ethylene carbonate or propylene carbonate.
- Effectively used promising additives to screen a wide range of noncarbonate solvents.
- Identified the most effective solvent replacements for cyclic and linear carbonates.
- Optimized salt composition and concentration in novel solvent systems to provide improved cycle life relative to a control electrolyte.
- Achieved over 300 cycles to 80% capacity retention in full cells with a carbonate-free solvent system with a single SEI additive.
- Achieved improved performance relative to the control with novel additives in carbonate based systems.
- Demonstrated that formulations with improved cycle life did not decrease 1st cycle capacity or coulombic efficiency.
- Performed initial screening of gas formation in noncarbonate or EC-free formulations which did not show increased gassing over the carbonate control formulations.
- Tested several of the carbonate-free and EC-free formulations which showed improved cycle life at higher voltage than the control electrolyte.

Future Achievements

- This project was completed by June 30, 2016.

Technical Discussion

Background

The objective of this project is to develop non-carbonate electrolytes that form a stable solid electrolyte interphase (SEI) on silicon alloy anodes, enabling substantial improvements in energy density and cost relative to current lithium-ion batteries (LIBs). These improvements are vital for mass market adoption of electric vehicles. At present, commercial vehicle batteries employ cells based on LiMO_2 ($M = \text{Mn, Ni, Co}$), LiMn_2O_4 , and/or LiFePO_4 coupled with graphite anodes. Next generation cathode candidates include materials with higher specific capacities or higher operating voltages, with a goal of improving the overall cell energy density. However, to achieve substantial increases in cell energy density, a higher energy density anode material is also required. Silicon anodes demonstrate very high specific capacities, with a theoretical limit of 4,200 mAh/g and state-of-the-art electrodes exhibiting capacities greater than 1,000 mAh/g. While these types of anodes can help achieve target energy densities, their current cycle life is inadequate for automotive applications. In graphite anodes, carbonate electrolyte formulations reductively decompose during the first cycle lithiation, forming a passivation layer that allows lithium transport, yet is electrically insulating to prevent further reduction of bulk electrolyte. However, the volumetric changes in silicon upon cycling are substantially larger than graphite, requiring a much more mechanically robust SEI film.

Introduction

Silicon-based anodes suffer from major disadvantages relative to graphite. First, during cycling, silicon exhibits a volume change of up to 300% (vs. 5-10% for graphite), causing severe mechanical stress and electrical disconnection of particles. This mechanical stress can be managed by careful control of particle size/morphology, including that for nanoparticles, nanowires, and nano-pillared materials. Such nanostructured materials have high surface areas (e.g., $>10 \text{ m}^2/\text{g}$) and often require a composite matrix to prevent electrochemical sintering. Second, carbonate-based electrolyte formulations do not form a stable SEI on silicon, with subsequent high irreversible capacity loss and poor cycle life (typically $>15\%$ and <100 cycles, respectively).

3M has developed several prospective silicon alloy anodes that provide a 100% increase in the composite electrode energy density compared to graphite coatings. In 18650 test cells using a fluorinated ethylene carbonate (FEC)-based electrolyte, 3M has demonstrated a full cell energy increase of 15% to 20% against a standard NMC cathode, with charge-depleting cycling for 500+ cycles resulting in 67% capacity retention at a C/2 charge/discharge rate from 2.8V to 4.35V. Catastrophic failure still occurs with long-term cycling due to parasitic reactions consuming the electrolyte. This project focuses on the development of formulations that provide stable SEIs using additives in a non-carbonate formulation. Linear and cyclic carbonate solvents do not yield suitably stable SEIs on silicon. In order to avoid simultaneous reduction with the new SEI additives, carbonates need replacement.

Approach

Wildcat is using a three stage approach to the development of noncarbonate electrolytes for silicon anodes (Figure V-45). In the first, an additive package was developed in a propylene carbonate (PC) based system. PC does not form a stable SEI on the anode, so the effect of additives on the resulting SEI will be measurable. Once a promising additive package was identified, new solvent candidates were enabled. Therefore, the second stage consisted of the identification of novel solvents that provide high ionic conductivity, good low temperature performance, improved thermal stability/safety, and adequate oxidative stability. The development of an effective additive package to form an SEI practically enables electrolyte solvents that might not otherwise be considered, and substantially increases the number of potential candidates. Finally, optimization of the electrolyte is necessary in the final stage of the project to ensure that the final solution can meet all of the PHEV/EV cell level goals, including ionic conductivity and oxidative stability to 4.6V.

In the design and development of novel SEI additives, several factors were taken into consideration, as shown in Table V-1. The approach uses molecular design concepts to create an SEI with improved mechanical and electrochemical performance, enabling longer cycle life for silicon anodes.

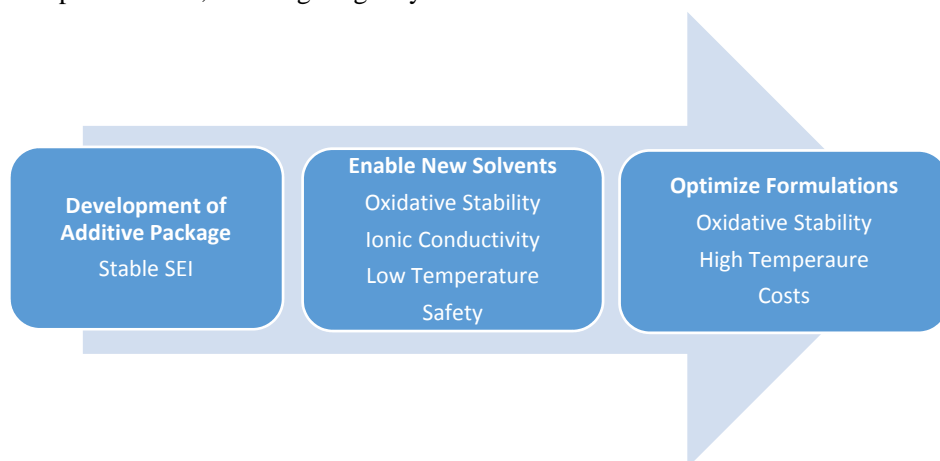


Figure V-45: Systematic approach to electrolyte development

Table V-1: Molecular Design Approach for Anode SEI Additives

Approach	Factor
Control SEI thickness	Influenced by the relative amount of polymer additive relative to surface area of anode, and the reduction potential of the additive
Control SEI modulus and/or glass transition temperature (Tg)	Property of polymer influenced by 1) average molecular weight and distribution, 2) chemical composition, 3) effective crosslink density, 4) degree of swelling by solvent.
Control amount of more brittle non-polymeric species	Influenced by other components of the electrolyte such as solvent, other additives, and salts
Control ionic conductivity of SEI	Influenced by polymer composition and other electrolyte components such as the salt

Results

Phase 1: Identification of SEI Additives for EC-Free Electrolyte Formulations

Today’s electrolyte formulations most often contain a blend of a high dielectric constant solvent and a low viscosity solvent. The most common high dielectric constant solvent is ethylene carbonate (EC), which solvates the Li⁺ cations and also, fortuitously, participates in SEI formation on graphite anodes. Propylene carbonate (PC) is another commonly used high dielectric constant solvent. However, it cannot form effective SEI layers on graphite. However, EC (and many other high dielectric constant solvents) tend to have high viscosities, requiring dilution with a low viscosity solvent to work effectively in a battery. Linear carbonates such as ethyl methyl carbonate (EMC) are often used as the low viscosity solvents.

Today’s common SEI additives, such as vinylene carbonate (VC) are used within electrolyte formulations that contain a blend of EC with various linear carbonate solvents. We, therefore, tested the electrochemical performance of hundreds of SEI additives from different chemical categories in the presence of EC, which participates in the SEI formation on graphite/silicon, and PC, which does not participate in SEI formation. This allows us to elucidate those additives that can form an effective SEI on their own vs. those that require co-reaction with EC to form an SEI. Figure V-46 shows a subset of the data, including three categories (Cat) of additives tested in two different base formulations. All additives were tested at two different concentrations (open and closed circles).

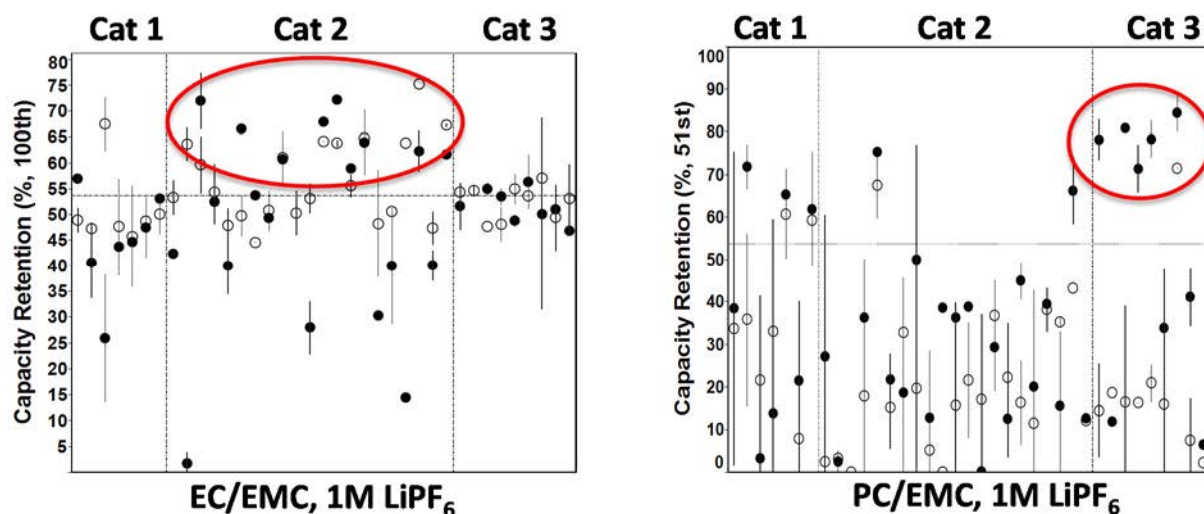


Figure V-46: Additives show synergies with differing solvent formulations

In EC-based formulations, Category 2 additives tended to show improved capacity retention relative to the baseline (dashed line). Yet these same additives showed detrimental performance relative to the baseline in PC based formulations. Instead, Category 3 additives improved the cycle life performance when used with PC. Category 2 additives were reactive monomer species, such as VC, which appear to form an SEI in a cooperative fashion with EC to form higher molecular weight species. In the absence of the EC, they are unable to create an effective SEI. Category 3 based additives are polymer/oligomeric in nature, providing the necessary higher molecular weight species to the SEI film. Several other promising categories of additives were also identified that resulted in improved cycle life in PC-based formulations.

Phase 2: Identification of Promising Solvents for Noncarbonate or EC-Free Electrolyte Formulations

Solvent Selection

Using the additives identified in Phase 1 of the project, we evaluated the performance of large numbers of solvent combinations in full cells containing NMC and 3M silicon alloy anode. Approximately 25 high dielectric (HD) constant solvents and 25 low viscosity (LV) solvents were selected that met criteria of electrochemical stability, physical properties, salt solubility, etc. for use as lithium-ion battery electrolytes. Initial screening consisted of blending all the HD solvents with a linear carbonate, EMC, and evaluating with 1M LiPF₆ and one of five different SEI additives. Cycle life results for the best performing formulations are shown in Figure V-47.

The most promising HD solvents were then blended with all LV solvents, 1M LiPF₆, and a single SEI additive for evaluation in full cells. The first cycle discharge capacity and capacity retention of these formulations are shown in a correlation plot in Figure V-48. In this graph, the baseline performance for both metrics is shown as the gray band (vertical and horizontal). The data points in different colors represent varying combinations of HD and LV solvents. A number of combinations showed performance similar to the standard carbonate control formulation, which are circled in red.

These formulations provided the basis for further iteration and optimization. These best noncarbonate or EC-free formulations were then improved by optimization of solvent ratios, salts (concentration and combinations), and additives (concentrations and combinations).

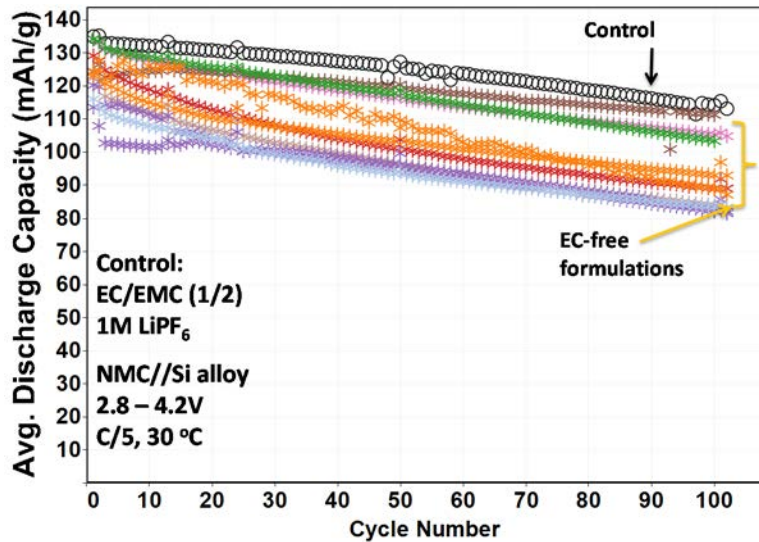


Figure V-47: Best performing high dielectric constant solvents were identified in EMC blends

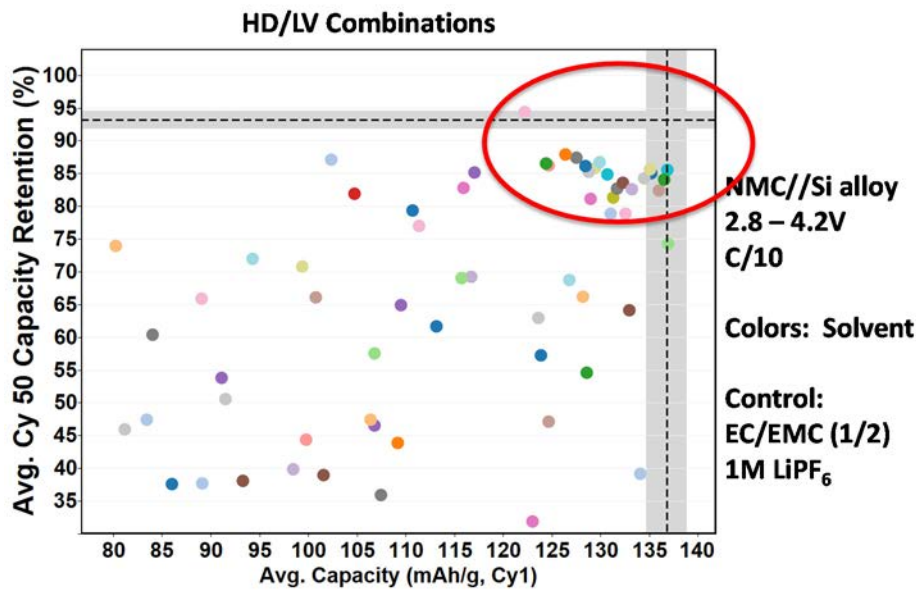


Figure V-48: Evaluation of best performing high dielectric constant solvents with a variety of low viscosity solvents

Salt Optimization

While a wide variety of solvents were evaluated as described above, other formulation variables were kept constant. For example, all formulations contained 1M LiPF₆. However, there was no reason to expect that this salt or this concentration would be optimal for entirely new solvent systems. Therefore, optimization was required. Results for an example of the initial salt optimization experiments are summarized in Table V-2. In the experimental design, each of the best combinations of HD solvents and LV solvents is tested with five different salts. For example, LV solvent A is blended with HD solvents 1, 2, and 3; LV solvent B is blended with HD solvents 1, 2, and 4; etc. For each formulation, the cycle 1 capacity and cycle 100 capacity retention is determined. Results are visualized by color coding the box green if the performance is improved relative to the control, gray if the results are unchanged from the control, and red if the results are worse than the control. In this way, it is easy to see that, for example, Salt 5 tends to be beneficial to LV solvent B blended with HD solvents 1, 2, and 4. These results are the basis for further optimization of salt composition, concentration, and salt combinations to further improve full cell cycle life.

Table V-2: Salt Efficacy is Very Solvent Dependent

		LiPF ₆		Salt 1		Salt 2		Salt 3		Salt 4		Salt 5	
LV	HD	Cy1 Capa. mAh/g	Capa. Reten (%)										
Control		134.2	83.6	134.2	83.6	134.2	83.6	134.2	83.6	134.2	83.6	134.2	83.6
A	1	132.4	72.0	122.4	30.3	129.4	21.7	133.1	0.47	129.1	92.1	123.8	82.4
	2	134.1	80.2	122.6	33.0	131.6	33.9	132.7	0.34	129.8	93.3	123.2	80.1
	3	122.9	71.8	80.3	41.5	131.4	53.3	128.7	1.9	125.9	89.0	122.4	82.3
B	1	124.5	78.4	31.1	59.4	125.9	26.3	134.5	76.7	127.3	15.1	131.3	88.2
	2	131.6	75.7	116.6	62.5	131.9	73.9	131.5	84.6	102.3	6.9	127.2	89.6
	4	123.1	86.9	126.1	54.2	131.1	76.0	134.0	79.8	131.9	43.0	132.9	86.3
C	5	133.8	80.8	90.6	54.5	121.6	0.1	137.7	0.1	103.6	1.2	131.8	87.7
	6	131.7		-	-	118.6		135.7		120.4		129.2	
	7	136.5		-	-	118.5		135.1		133.7		129.5	
D	3	134.0	86.9	122.1	66.2	121.2	90.4	135.7	88.8	133.9	81.7	130.4	88.4
E	2	135.5		-	-	130.6		127.3		134.3		125.4	

Capacity Retention @ 100 cycles

Example cycle life results for optimized salts in the novel solvent formulations are shown in Figure V-49, where cycle life of the noncarbonate or EC-free formulations exceeds that of the control. Cycle life results after further optimization are shown in Figure V-50, where 300 cycles are achieved to 80% capacity retention in carbonate-free formulations. Thus far, all of the formulations contain only a single SEI additive - leaving much headroom for optimization of additives, additive concentrations, and combinations of additives.

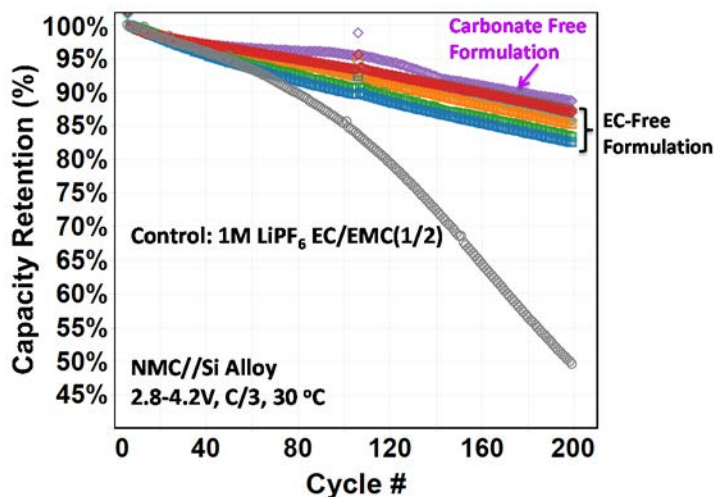


Figure V-49: Carbonate-free formulations exceed performance of control electrolyte

In parallel to the optimization experiments in novel solvent formulations, we continued to screen additional SEI additives in both EC and PC based formulations. These experiments provided additional options to include new additives in combination with those previously identified. Throughput multiple rounds of high throughput screening, Wildcat achieved further improvement in cycle life while building knowledge on structure property relationships as we expanded upon promising additives by structural modifications.

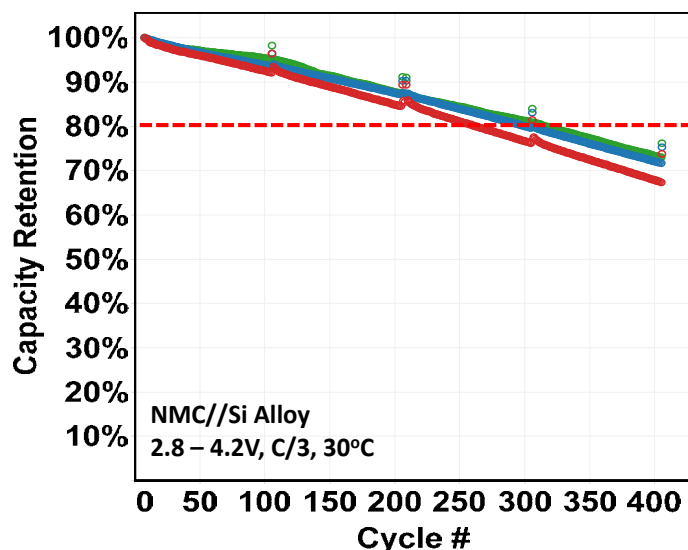


Figure V-50: Carbonate-free formulations achieve 300 cycles to 80% capacity retention

Phase 3: Formulation Optimization

The final optimization consisted of combinations of additives and co-solvents in both noncarbonate and carbonate solvents to yield a good balance of performance across multiple metrics. Thus, the formulations with the absolute best cycle life were not necessarily the best overall electrolytes – as they may have had a severe shortfall that could not be corrected with additional additives. Table V-3 summarizes final formulations that were identified for further testing.

Table V-3: Summary of Final Formulations

Formulation	Solvents	Additives
Control	EC/EMC (1:2 by volume)	10% FEC
2	EC/EMC (1:2 by volume)	2% LiBOB, 2% WDT-2317
3	EC/EMC (1:2 by volume)	2% WDT-2320
4	Noncarbonate combination	2% VC, 0.5% WDT-2094
5	Noncarbonate combination	2% WDT-2320, 2% WDT-2094
6	Noncarbonate combination	2% VC, 2% WDT-2093

Figure V-51 shows the room temperature cycle life of formulations 2-6 compared to the control electrolyte. All of the formulations identified by Wildcat improved capacity retention relative to the control. However, the two noncarbonate formulations (4, 5) had lower initial capacity. The best performing electrolyte in terms of capacity retention extrapolates to approximately double the cycle life of the control – 320 cycles. While the project goal was 500 cycles, our post-mortem work suggests that electrode failure mechanisms occurred around 300 cycles that were unrelated to true lithium loss due to SEI formation. If active material utilization decreases due to electrical isolation of particles or delamination from current collector, these problems cannot be solved by electrolyte improvements. Addressing these types of failure mechanisms was outside the scope of this project, but suggests that future achievements must address multiple failure mechanisms in parallel. Nevertheless, the new formulations show improved cycle life in full cells without the use of FEC.

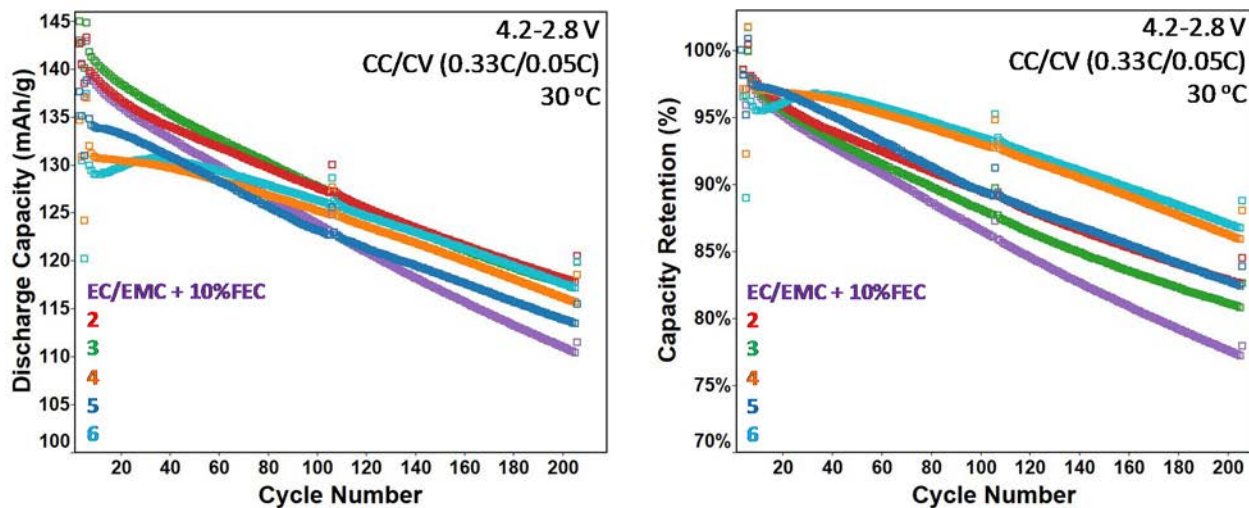


Figure V-51: Room temperature cycle life improved with Wildcat formulations

The high temperature cycle life of formulations 2-5 is shown in Figure V-52. All the final formulations outperform the control electrolyte containing 10% FEC. High temperature performance of FEC is known to be problematic. Wildcat formulations offer significant value at high temperature due to replacement of FEC with other additives.

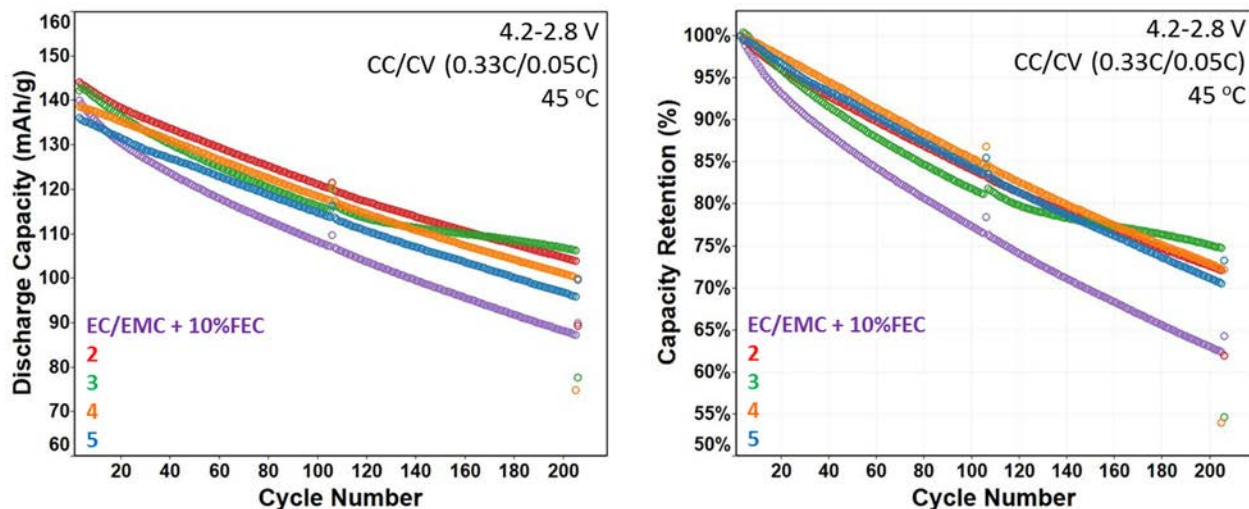


Figure V-52: New formulations outperform control with 10% FEC

High temperature storage (60C) experiments for two weeks were performed. The capacities remaining after the high temperature storage, as well as the recovered capacities are shown in Figure V-53. Both the remaining capacities and recovered capacities were measured at 30C at C/10 discharge rate. Several of the new electrolytes (3, 4, and 5) showed lower capacities after high temperature storage than the control. This self-discharge could probably be minimized with further optimization of the formulations. All formulations showed similar or better recovered capacities compared to the control formulation containing 10% FEC. The cell impedance growth after high temperature storage (60C) for two weeks was also measured for these formulations. Figure V-54 shows that the initial impedance of the four final (non-carbonate and carbonate-based) formulations is similar or lower to that of the control electrolyte with 10% FEC. After high temperature storage, three of four formulations maintain similar area specific impedances.

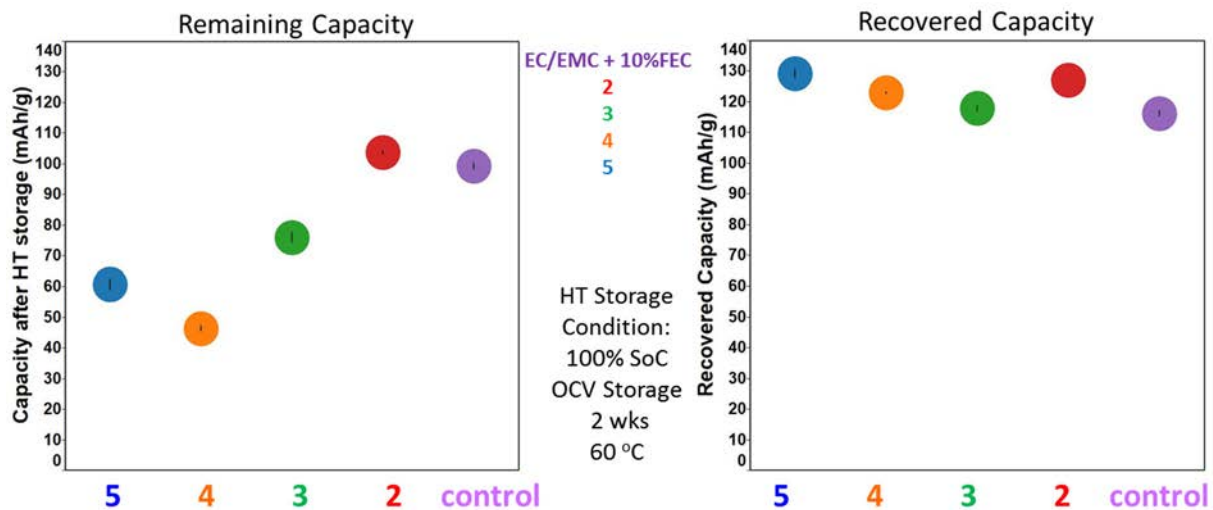


Figure V-53: Capacity after high temperature storage experiment

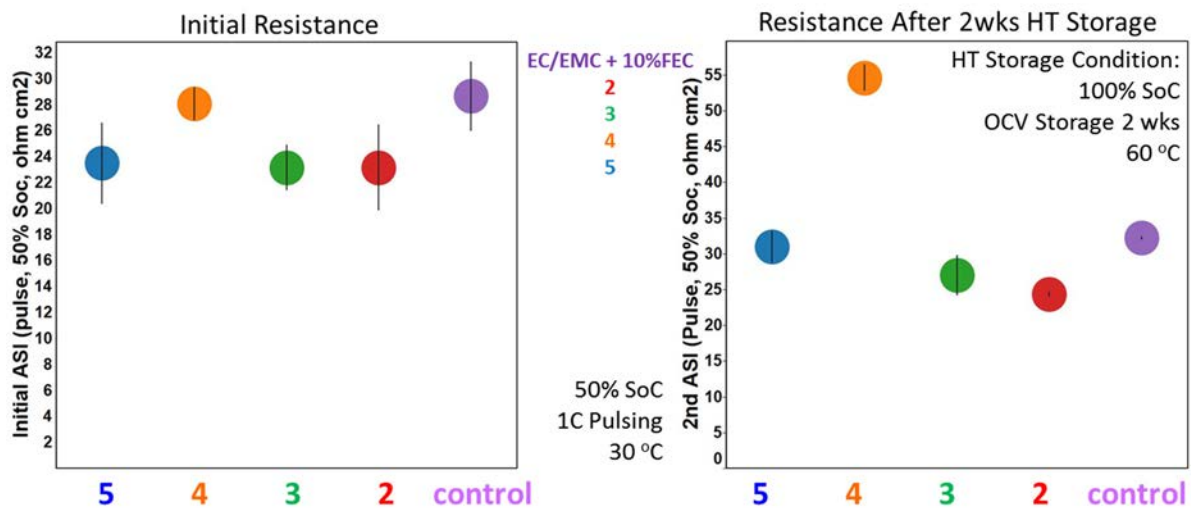


Figure V-54: Area specific impedance of formulations after 60 °C storage for two weeks

The new formulations would be expected to have similar performance at high voltage as standard carbonate formulations, but benefit from elimination of the FEC. One of the new formulations was tested and optimized with high voltage additives to demonstrate feasibility at higher voltages, as shown in Figure V-55. In this case, the FEC content in the control electrolyte was reduced to 2% as we know this additive does not perform well at high voltage. The formulations could not be tested above 4.45V, as we did not have electrodes balanced for higher voltages. However, the results at 4.45V show that with the addition of high voltage additives, this new formulation can cycle better than the FEC-based control.

The low temperature (-20C) area specific impedance (ASI) and capacity retention on C/10 discharge were also measured for the formulations. As shown in Figure V-56, the new formulations all showed similar or lower ASI and similar or higher discharge capacity (C/10) at -20C compared to the 10% FEC control electrolyte.

Ionic conductivity results for the formulations are summarized in Table V-4. While the room temperature ionic conductivities is less for the noncarbonate formulations (4,5,6), the low temperature ionic conductivity is similar. In general, silicon anodes cannot be cycled at high rates, so room temperature ionic conductivity can tolerate some decrease. However, in order to pass low temperature cold crank tests, it is important not to significantly decrease the low temperature ionic conductivity.

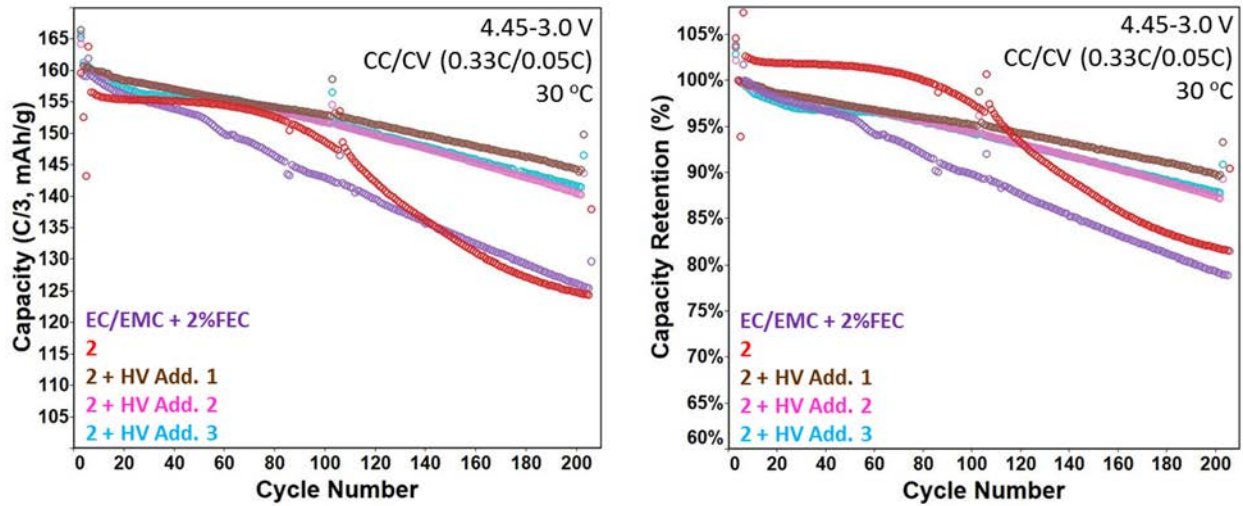


Figure V-55: Wildcat noncarbonate formulation demonstrates feasibility at higher voltage

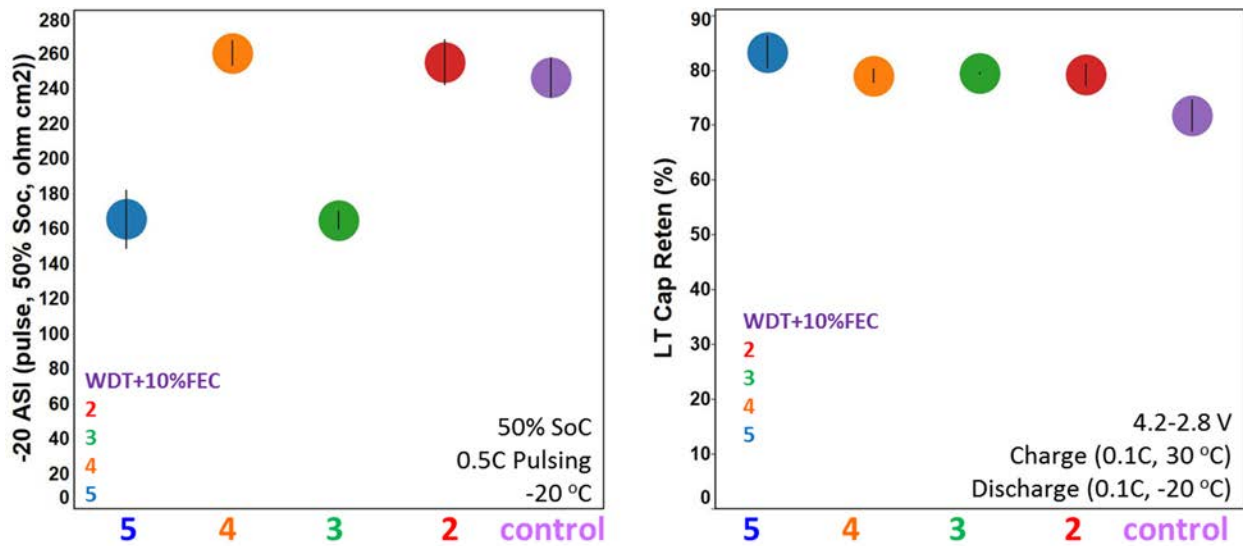


Figure V-56: Low temperature performance of formulations

Table V-4: Room Temperature and Low Temperature Ionic Conductivities of Formulations

Formulation	25C Ionic Conductivity (mS/cm)	-30C Ionic Conductivity (mS/cm)
Control (10% FEC)	8.5	1.8
Control (2% FEC)	7.5	1.4
2	9.1	1.7
3	9.2	1.8
4	5.4	1.6
5	5.0	1.4
6	5.8	1.7

In an effort to help ensure translation of results from Wildcat small format cells to larger format cells, we prepared single layer pouch cells using the same NMC//Si alloy electrodes. Variables such as the electrolyte amount and stack pressure were varied to determine the effect on cell performance for a selection of electrolytes. Samples of the results are shown in Figure V-57 and Figure V-58.

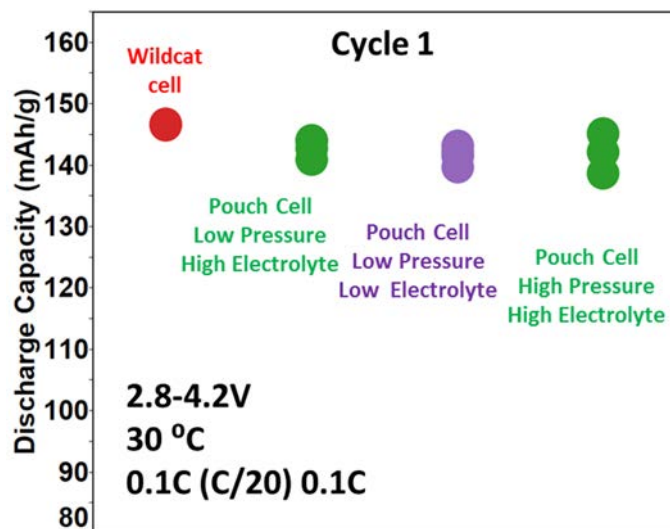


Figure V-57: Wildcat pouch cells perform similarly to high throughput cells on Cycle 1

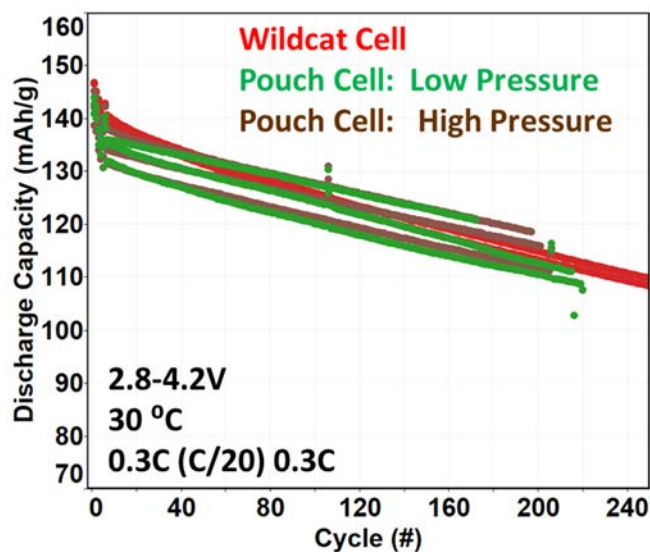


Figure V-58: Cycle life in Wildcat pouch cells is similar to high throughput cells

A cost comparison of the electrolytes was also performed. According to Avicenne Energy (4/2015, 24th Edition), carbonate solvents for battery use have an average selling price of \$3.9/kg (2013 data, Figure V-59). Common additives such as FEC have an average selling price of \$80/kg. Most electrolytes used with silicon anodes today contain high concentrations (10 – 30 weight %) of FEC, resulting in significant cost increases.

Wildcat developed both carbonate and non-carbonate based formulations with improved performance over the course of this project. The carbonate-based formulations use typical carbonate solvents expected to match the average selling price of \$3.9/kg. Formulations 2 and 3 (carbonate) shown in preceding graphs contained no FEC, and contained much lower additive quantities. Formulation 2 contains 4 weight % total additive concentration, and formulation 3 contains 2 weight %. The specific additive packages used are combinations of common additives used today and newly discovered Wildcat additives. The common additives (used at 2 weight % or less) would compare in cost to those in Avicenne report, so should not impart a cost increase in the new formulations relative to a standard carbonate formulation. Prices for the new additives can be found on

line for small volumes on the order of \$5-10/kg, well under the average selling price of \$80/kg. The new additives are also used at typical concentrations of 2 weight % or less.

Similar additives are used in the noncarbonate formulations, so the cost comparison will depend upon the relative costs of the solvents. Online prices for higher volume high purity anhydrous solvents used for the new formulations were on the order of \$3-5/kg (\$3000-\$5000/metric ton). Of course, the actual cost comparison will depend upon many factors including purity of the starting components and any additional purification that might be required. Materials used in this project were used as received and were not subjected to further purification.

In summary, the high level cost analysis of Wildcat new formulations do not show any obvious cost increases over today's state of the art silicon electrolyte formulations – which contain high levels (10-30 weight %) of expensive FEC.

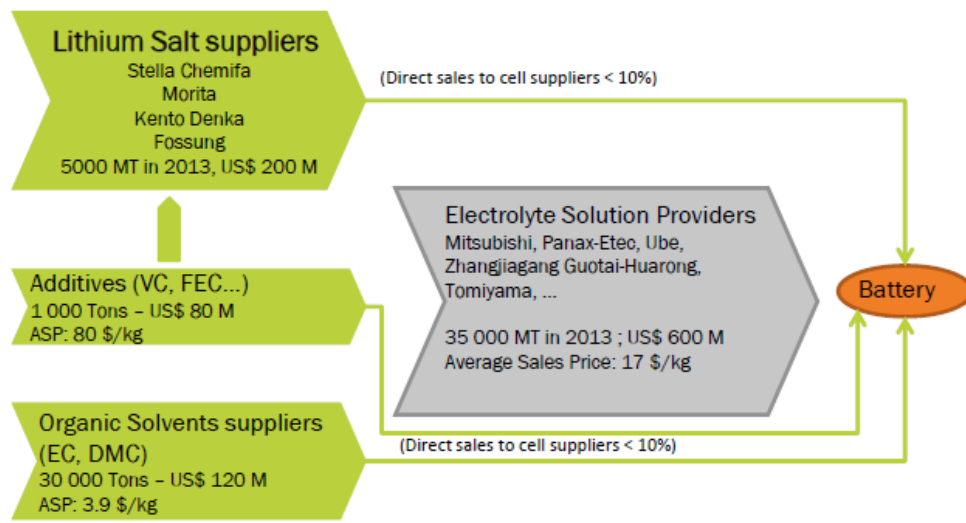


Figure V-59: Electrolyte component costs

Conclusions

We have made dramatic progress in the identification of non-carbonate solvents for use with silicon anodes in lithium-ion batteries. The current cycle life of 350 cycles to 80% capacity retention outperforms the control electrolyte containing significant quantities of expensive FEC. It should be pointed out that further improvements could be made to the carbonate based control electrolyte – which may make it a better selection in the long run. However, this project will result in alternatives to carbonates that may provide other advantages such as high voltage stability, lower volatility, etc. Furthermore, the electrolyte additives being discovered may be valuable across a range of solvent systems.

Products

Presentations/Publications/Patents

1. Strand, D.A., Caldwell, M., DOE Annual Merit Review poster (Jun., 2014, Washington, DC).
2. Strand, D.A., Zhu, Y., Cheng, G., Caldwell, M., "Development of Novel Electrolytes for Silicon Anodes," The Battery Show, (Sept., 2014, Novi, MI).
3. Strand, D.A., Zhu, Y., Cheng, G., Caldwell, M., "Review: Development of Novel Electrolytes for Silicon Anodes," BATT Review, (Jan., 2015, Berkeley, CA).
4. Strand, D.A., Zhu, Y., Cheng, G., Caldwell, M., "Novel Noncarbonate Electrolytes for Silicon Anodes," 32nd International Battery Conference, (Mar., 2015, Ft. Lauderdale, FL).

5. Li, B., Strand, D.A., Zhu, Y., Cheng, G., Caldwell, M., "Novel Noncarbonate Electrolytes for Silicon Anodes," 2nd International Forum on Cathode & Anode Materials for Advanced Batteries, (Apr., 2015, Hangzhou, China).
6. Zhu, Y., Strand, D.A., Cheng, G., "Development of Novel Lithium Ion Battery Electrolytes for Silicon Anodes," 227th ECS Meeting, (May, 2015, Chicago, IL).
7. Strand, D.A., Zhu, Y., Cheng, G., Caldwell, M., "Novel Noncarbonate Electrolytes for Silicon Anodes," DOE AMR, (Jun., 2015, Washington, D.C.).
8. Cheng, G., Zhu, Y., Strand, D.A., "Development of Novel Electrolytes for Silicon Anodes," 4th China LIB Electrolytes Conference 2015, (Jun., 2015, Hangzhou, China).
9. Cheng, G., Zhu, Y., Strand, D.A., "Novel Noncarbonate Electrolytes for Silicon Anodes," AABC USA 2015, (Jun., 2015, Troy, MI).
10. Strand, D.A., Zhu, Y., Cheng, G., "Development of Novel Electrolytes for Silicon Anodes," ABAA8, September/2015, Bilbao, Spain.
11. Strand, D.A., Zhu, Y., Cheng, G. "Development of Novel Electrolytes for Silicon Anodes," Batteries 2015, October/2015, Nice, France.
12. Li, B., Zhu, Y., Strand, D., Cheng, G., "Development of Electrolytes for Silicon Anodes," 12th China International Battery Fair (CIBF), May, 2016, Shenzhen, China.
13. Zhu, Y., Strand, D., "Development of Electrolytes for Silicon Anodes," 229th ECS Meeting (June, 2016, San Diego, CA).
14. Zhu, Y., Strand, D., "Development of Electrolytes for Silicon Anodes," IMLB (June, 2016, Chicago, IL).
15. Six (6) patent applications.

V.D. High Energy Density Cathodes for Advanced Lithium-Ion Batteries

V.D.1. Studies on High Capacity Cathodes for Advanced Lithium-Ion Batteries (ORNL)

Jagjit Nanda, Principal Investigator

Oak Ridge National Laboratory
1 Bethel Valley Road
Oak Ridge, TN 37831-6124
Phone: 865-241-8361; Fax: 865-574-4357
E-mail: nandaj@ornl.gov

Tien Q. Duong, DOE Program Manager

U.S. Department of Energy
Advanced Battery Materials Research (BMR)
Vehicle Technologies Office
1000 Independence Avenue, SW
Washington, DC 20585
Phone: 202-586-7836
E-mail: Tien.Duong@ee.doe.gov

Start Date: October 1, 2015
End Date: September 30, 2018

Abstract

Objectives

- Design and synthesis of high capacity multi-lithium cathodes belonging to $\text{Li}_2\text{M}^{\text{I}}_x\text{M}^{\text{II}}_{1-x}\text{O}_2$, where M^{I} and M^{II} are transition metals (TM) such as Ni, Cu, Fe, and Mo.
- Target cathode capacities > 250 mAh/g with stable cycle life in the range of 100s of cycles by avoiding irreversible structural transitions and minimizing voltage hysteresis.
- Develop synthesis strategies to prevent oxygen evolution by anionic substitution or surface stabilization methods.
- Stabilize TM cations such as Cu and Ni in higher oxidation states to achieve higher redox potential using both crystalline and disordered polyanionic structures.

Accomplishments

- 50% Ni substitution in Li_2CuO_2 structure improves the electrochemical stability and raises the voltage plateau.
- HRTEM, TXM-XANES, and Raman analysis maps the structural transitions $\text{Li}_2\text{Ni}_{0.5}\text{Cu}_{0.5}\text{O}_2$ undergoes during cycling including the formation of intermediate LiNiO_2 and NiO phases.
- Gas evolution analysis at different state-of-charge (SoC) combined with XANES studies show loss of lattice oxygen > 3.9 V responsible for irreversible capacity loss.

Future Achievements

- Structurally stabilize Ni-rich compositions of $\text{Li}_2\text{Cu}_x\text{Ni}_{1-x}\text{O}_2$ ($x = 0.2-0.4$) to provide higher voltage and capacity by utilizing higher oxidation states of Cu and Ni.
- Transition from oxides to polyanionic groups to stabilize Cu in higher oxidation state.

Technical Discussion

Introduction

The project is directed towards developing high-capacity cathodes for advanced lithium-ion batteries. This is at present the most critical barrier for developing high-energy-density lithium-ion cells. Chemistries with more than one lithium per transition metal are one approach for increasing the capacity of lithium-ion cathodes. Recent examples include lithium-rich NMCs ($x\text{Li}_2\text{MnO}_3 \cdot (1-x)\text{LiMO}_2$ where $M=\text{Mn, Ni, Co}$), anti-fluorite type oxides, [ENREF 2](#) and several poly-anionic compounds. While many of these cathodes have very high theoretical capacities, none have proven practical for commercial cells due to a number of materials and interfacial issues. For example, lithium-rich NMCs lose both lithium and oxygen during the initial charge, and they undergo slow phase transformations during subsequent cycling. These structural changes lead to capacity loss, voltage fade, and impedance rise. The anti-fluorite type oxides such as Li_5FeO_4 also lose oxygen (as Li_2O) during charge. Generally, only one or fewer Li^+ per formula unit can be cycled reversibly. Successful cycling of more than one Li^+ per formula unit has been demonstrated with polyanionic compounds, although typically only one redox couple of the transition metal is within a useful voltage range. $\text{Li}_2\text{MnSiO}_4$ is a notable exception, but this material suffers from poor transport and structural instability.

Recently, we characterized the electrochemical performance of $\text{Li}_2\text{Cu}_{0.5}\text{Ni}_{0.5}\text{O}_2$ cathodes, which have a very high theoretical capacity of 250 mAh/g per Li^+ .¹ Nearly 400 mAh/g of capacity is obtained during the first charge, but only ~125 mAh/g is reversible. The large first-cycle irreversible loss was attributed to oxygen evolution and structural transformations. Gas evolution measurements, *in situ* Raman spectroscopy, and *in situ* X-ray absorption spectroscopy were used to track the chemical and structural changes.

Approach

We employ a number of synthesis methods for cathode materials including solid state, hydrothermal, solvothermal, and sol-gel. Various doping and surface coating methods are employed to address interfacial stability and surface reactivity. The cathode compositions and phases are selected based on (1) phase diagram analysis and modelling from work by Ceder and others (2) materials availability and cost (3) thermal safety. When appropriate, we use ORNL's expertise in thin film batteries to prepare the same materials as thin films. Thin film electrodes do not require polymer binders or conductive carbon additives, and can therefore facilitate our understanding of the intrinsic properties of the cathode material. We also have an active interest in developing coatings that can improve cathode properties such as conductivity or interfacial stability. Recently, we successfully demonstrated coating a nanometer-thick layer of the solid-ion conductor lithium phosphorous oxynitride (LiPON) on high voltage lithium-manganese rich NMC (LMR-NMC) and spinel compounds. For optimizing our cathode synthesis process and improving cell level performance, we apply various electrochemical, multi-scale advanced X-ray, optical spectroscopy, and microscopy techniques. These techniques include EIS, micro-Raman, transmission X-ray microscopy combined with X-ray absorption near edge spectroscopy (TXM-XANES), aberration corrected electron microscopy combined with EELS, X-ray photoelectron spectroscopy (XPS), ICP-AES, and X-ray and neutron diffraction to refine structures.

Results

Redox activity of Li_2CuO_2 and $\text{Li}_2\text{Cu}_{0.5}\text{Ni}_{0.5}\text{O}_2$ solid solution

We compare the redox activity of Li_2CuO_2 and $\text{Li}_2\text{Cu}_{0.5}\text{Ni}_{0.5}\text{O}_2$ cathodes during the first couple of cycles where they undergo substantial structural transformations, which have significant effect on their electrochemical properties. The cathode compositions were synthesized using the solid state route as reported in our previous publication.¹ Figure V-60 shows the cyclic voltammetry of Li_2CuO_2 and $\text{Li}_2\text{Cu}_{0.5}\text{Ni}_{0.5}\text{O}_2$ compared under identical scan rates and electrode parameters. The CV scans were between 2.25 and 4.3 V. Both Li_2CuO_2 and $\text{Li}_2\text{Cu}_{0.5}\text{Ni}_{0.5}\text{O}_2$ CVs show significant changes during the 1st charge, implying an irreversible phase transformation. This aspect is common to lithium-rich and conversion compounds during delithiation. Most often this activity is accompanied by oxygen (or gas) evolution. It is clear from CV that from the 2nd cycle onwards, $\text{Li}_2\text{Cu}_{0.5}\text{Ni}_{0.5}\text{O}_2$ shows redox activity in a higher voltage region compared to pure copper phases.

Discharge profiles also show a greater capacity contribution at higher voltage for $\text{Li}_2\text{Cu}_{0.5}\text{Ni}_{0.5}\text{O}_2$ compared to Li_2CuO_2 . In the subsequent sections, we investigate the details related to the nature of the structural transformations and their effect on the electrochemical performance and capacity loss.

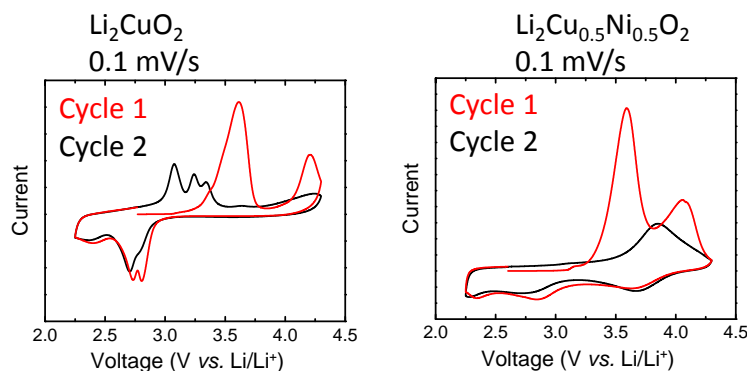


Figure V-60: CV of Li_2CuO_2 and $\text{Li}_2\text{Cu}_{0.5}\text{Ni}_{0.5}\text{O}_2$ cathode composition during 1st and 2nd cycle

Characterizing the intermediate phases formed at different states of charge (SoC) for $\text{Li}_2\text{Cu}_{0.5}\text{Ni}_{0.5}\text{O}_2$

For a more complete analysis of the phases that form, we performed XRD on cathodes harvested from cells charged (and discharged) to different cut-off voltages. The XRD pattern of $\text{Li}_2\text{Cu}_{0.5}\text{Ni}_{0.5}\text{O}_2$ powder shows that the material is nearly phase pure (Figure V-61). All of the most intense reflections are attributed to the expected *Immm* orthorhombic phase. Lithium carbonate is present as a minor impurity. The diffraction lines for the pristine material disappear during the first charge. In fact, the structure appears to transform completely during the first voltage plateau from OCV to 3.4 V. Charging to 3.4 V requires about 120 mAh/g of capacity or 0.5 Li^+ per formula unit. Several new phases emerge during charge. The peak near 19 degrees two-theta is characteristic of LiNiO_2 with a layered *R3m* structure. The transformation from orthorhombic to layered has been predicted computationally for *Immm* Li_2NiO_2 . Broad peaks centered near 38, 44, and 63 two-theta are a good match for $\text{Li}_x\text{Ni}_{1-x}\text{O}$ with the cubic, rocksalt-type lattice ($x \leq 0.3$). In addition to the nickel oxide phases, LiCuO , Li_2CO_3 , and Li_2O are also formed, as indicated in Figure V-61. $\text{Li}_2\text{Cu}_{0.5}\text{Ni}_{0.5}\text{O}_2$ is a solid solution of orthorhombic Li_2NiO_2 and Li_2CuO_2 . The structural changes in $\text{Li}_2\text{Cu}_{0.5}\text{Ni}_{0.5}\text{O}_2$ closely resemble those of the parent Li_2NiO_2 composition during charge.²⁻⁴

Immm Li_2NiO_2 also showed weak diffraction peaks for layered LiNiO_2 and rocksalt NiO after charging.³ The structure collapsed forming amorphous material (or very small crystallites), which were not detected by XRD. $\text{Li}_2\text{Cu}_{0.5}\text{Ni}_{0.5}\text{O}_2$ must also form phase(s) amorphous to XRD. The diffraction patterns show no significant change after the initial charging plateau at 3.4 V. Besides the layered LiNiO_2 , none of the crystalline phases are expected to be electrochemically active over the voltage range studied. Much of the electrochemical capacity must come from intercalation and deintercalation in amorphous or nanocrystalline material.

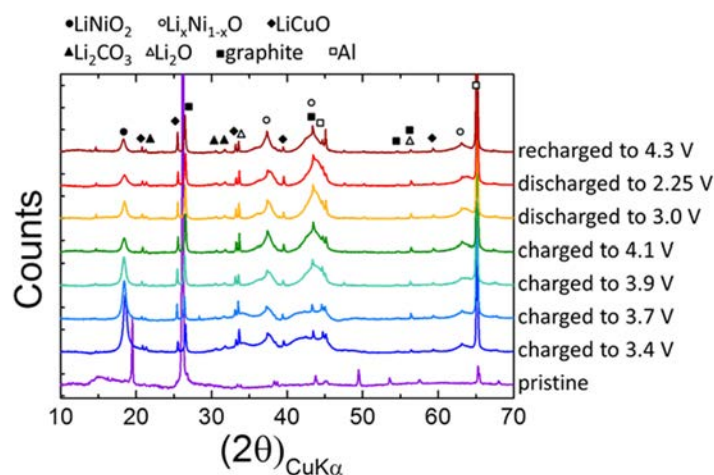


Figure V-61: XRD patterns of cathodes taken from cells charged (and discharged) to different endpoints during the first full cycle (charge to 4.3 V and discharge to 2.25 V). The top trace is from a cathode that underwent one full charge/discharge cycle and was recharged to 4.3 V

The crystallographic phase of the pristine material was also confirmed using TEM (Figure V-62a-c). Selective area electron diffraction (SAED) patterns and scanning TEM-high angle annular dark field (STEM-HAADF) lattice images confirm that the crystal symmetry is *Immm* orthorhombic. The structural evolution was further investigated by TEM (Figure V-62d-f). The pristine particles are uniformly dense (Figure V-62d). After one charge-discharge cycle the particle morphology converts to a form with exfoliated layers (Figure V-62e). The XRD patterns (Figure V-61) suggested layered LiNiO_2 and rocksalt NiO phases formed during the first cycle.

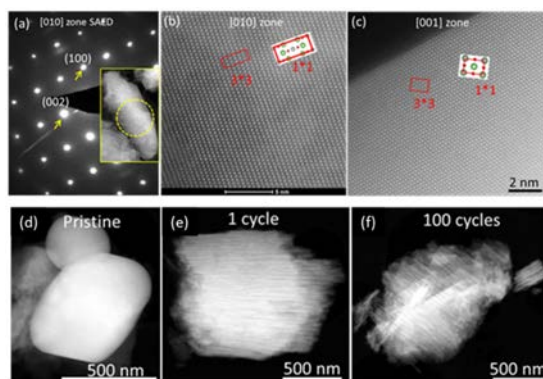


Figure V-62: (Top) TEM characterization of the pristine $\text{Li}_2\text{Cu}_{0.5}\text{Ni}_{0.5}\text{O}_2$ sample. (a) A [010] zone axis SAED pattern from a pristine particle (inset image). (b) STEM-HAADF lattice image from the [010] zone axis. (c) STEM-HAADF lattice image from the [001] zone axis. (Bottom) STEM-HAADF images showing the change in particle morphology after charge-discharge cycling. (d) pristine particles (e) particle after one charge-discharge cycle (f) particle after 100 charge-discharge cycles

TEM investigations confirmed the transformation from orthorhombic to layered and rocksalt structures (Figure V-63). An SAED pattern (Figure V-63b) was obtained from the layered region of a $\text{Li}_2\text{Cu}_{0.5}\text{Ni}_{0.5}\text{O}_2$ particle after one cycle (Figure V-63a). The 0.47 nm spacing is a good match for the (003) plane of LiNiO_2 , while the rings at 0.21 and 0.24 nm correspond to the (200) and (111) planes of NiO . HRTEM images also confirmed the formation of the LiNiO_2 phase characterized by the 0.47 nm lattice spacing (Figure V-63c). Nanoscale domains of the LiNiO_2 phase are embedded within rocksalt-type nanocrystals. Exfoliation of the pristine particles into layers accommodates the significant change in density that occurs when the particles transform from orthorhombic (3.7 g/cm^3) to trigonal (4.8 g/cm^3 for LiNiO_2) and cubic (6.7 g/cm^3 for NiO). After 100 charge-discharge cycles, no further evolution in particle morphology or structure was observed compared to the cathode particles cycled only once. This is consistent with the CV plot (Figure V-60), which shows that the voltage profiles also stabilize after the initial cycle.

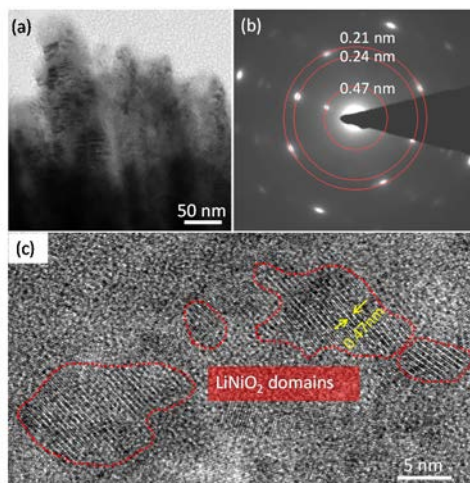


Figure V-63: TEM observation of a $\text{Li}_2\text{Cu}_{0.5}\text{Ni}_{0.5}\text{O}_2$ particle after 1 cycle. (a) Low magnification bright field image showing layered morphology. (b) A SAED pattern from the particle showing different lattice spacings. (c) HRTEM image showing the embedded LiNiO_2 nanodomains highlighted by dashed red circles

TXM-XANES maps semicrystalline and amorphous phases in pristine and cycled $\text{Li}_2\text{Cu}_x\text{Ni}_{1-x}\text{O}_2$

To gain additional insights into the chemical and structural changes that occur in $\text{Li}_2\text{Cu}_{0.5}\text{Ni}_{0.5}\text{O}_2$, we undertook TXM-XANES studies. TXM-XANES does not require long-range order, and is therefore ideally suited for characterizing both nanocrystalline and bulk crystalline phases. Surprisingly, we found multiple phases in pristine electrodes before electrochemical cycling. The phases were easily separated using k-means cluster analysis in the TXM-Wizard software package (Figure V-64). The XANES of each cluster are shown in Figure V-64 a and b for the Cu and Ni K-edges. The main phase shown in blue corresponds to $\text{Li}_2\text{Cu}_{0.5}\text{Ni}_{0.5}\text{O}_2$ where both Cu and Ni are in the 2+ oxidation state. A second, minor phase appears in both the Cu and Ni XANES where the absorption edge is shifted towards lower energy. The XANES spectra at both the Cu and Ni K-edges changes significantly with cycling. For lack of space, we do not show the detailed *ex situ* voltage dependent XANES spectra for the Cu and Ni K-edges. The absorption edge for Cu shifts towards lower binding energy after one full cycle. The absorption peak for Ni broadens and shifts towards lower energy after 1 cycle, similar to Cu. Similar changes in the shape of the absorption edge were observed for Li_2NiO_2 and attributed to different coordination environments of the transition metals before and after cycling.⁵ In the pristine *Immm* $\text{Li}_2\text{Cu}_{0.5}\text{Ni}_{0.5}\text{O}_2$ the transition metals are coordinated by four oxygen atoms in a square planar geometry. The square planar coordination is not expected to be stable against delithiation.² After cycling the XANES features more closely match copper and nickel coordinated by oxygen with octahedral symmetry. This change in coordination would be consistent with a transformation from the orthorhombic phase to a layered structure similar to the LiNiO_2 or 1T- Li_2NiO_2 phases. To characterize the uniformity of the structural changes that occur during cycling, phase maps were generated for the cells cycled once and 43 times *ex situ* (Figure V-65). The XANES spectrum of each pixel was fit to a linear combination of the bulk XANES. None of the pristine phase remains after the first cycle (Figure V-65a-b). For the sample cycled 43 times, linear combination fitting suggests a small region of one of the particles most closely resembles the pristine phase (Figure V-65c-d). However, the fitting error is larger for this region than for the rest of the sample. The maps after one and 43 cycles are not perfectly uniform. Each map in Figure V-65 is fit to a mixture of the bulk XANES after 1 (blue) and 43 (red) cycles, although the XANES after 1 and 43 cycles are very similar and therefore difficult to deconvolute. Overall, the changes in the Cu and Ni chemistry are largely homogenous after cycling, despite the large particle size ($\sim 10 \mu\text{m}$).

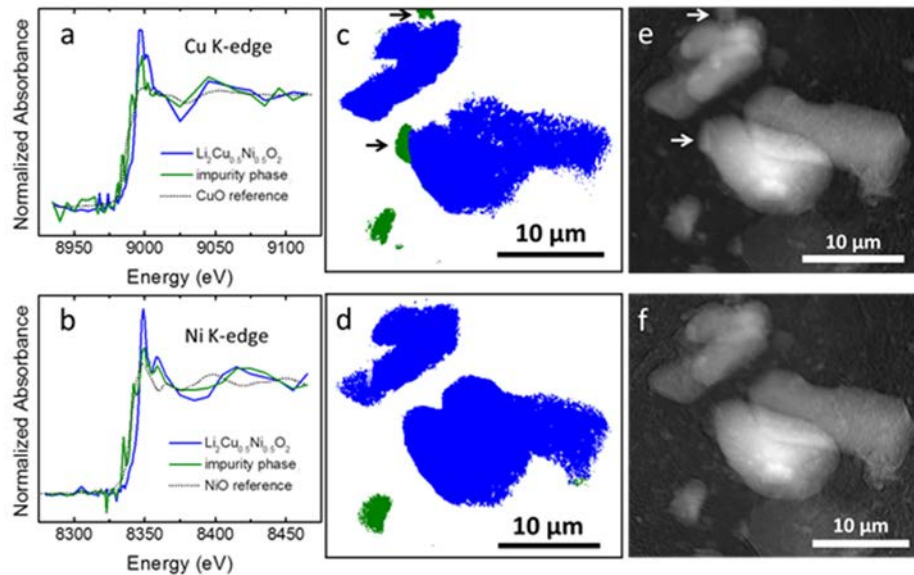


Figure V-64: XANES of clusters at the (a) Cu K-edge and (b) Ni K-edge used to generate cluster maps (c) and (d). Dashed lines in (a) and (b) show XANES of CuO and NiO for reference. Absorption images at (e) 9115 eV after the Cu K-edge and (f) 8465 eV after the Ni K-edge. Cu-rich particles are indicated with arrows

While the *ex situ* measurements are informative, they only capture the chemistry under equilibrium (or near equilibrium) conditions. Gradients in the lithium concentration or phase distribution have time to relax. In order to capture the phase changes *in situ* we also performed TXM-XANES imaging on pouch cells during cycling. TXM-XANES maps were acquired during the initial charge by alternating across six different locations on the electrode (three positions each for the Cu and Ni K-edges). Figure V-66a and b show the average (bulk) XANES at the Cu K-edge from region 1 for a cell charged *in situ*. No systematic change is observed in the XANES below 4.0 V. At 4.0 V and above the absorption edge shifts to lower binding energy. The direction of the shift is opposite what would be expected if Cu^{2+} were oxidized to Cu^{3+} . The shift likely reflects a change in coordination or structure, and not a change in the formal oxidation state of Cu. This is consistent with our earlier work, where we concluded that copper was not oxidized up to 4.3 V vs. Li/Li^+ .¹

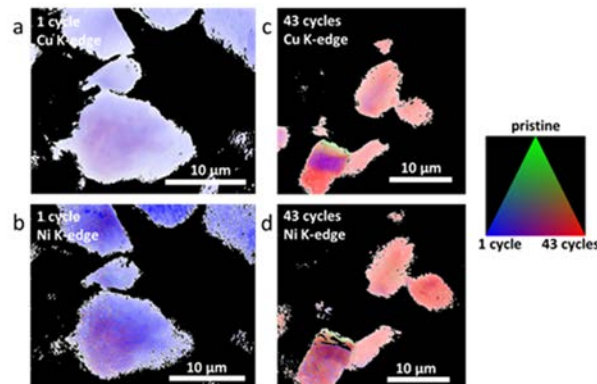


Figure V-65: Phase maps generated by linear combination fitting using the bulk XANES shown in the previous figure. Phase maps are from XANES at the (a) Cu K-edge after one full charge/discharge cycle. (b) Ni K-edge after one full charge/discharge cycle (c) Cu K-edge after 43 charge/discharge cycles and (d) Ni K-edge after 43 charge/discharge cycles

Figure V-66c shows the average (bulk) XANES spectrum at OCV along with XANES from a cell that was fully charged *ex situ*. The *in situ* and *ex situ* XANES for fully charged cathodes show good agreement. The XANES from Figure V-66c were used to create the phase maps shown in Figure V-66d by linear combination fitting. Absorption images at 9115 eV are also shown in Figure V-66d for the three different electrode positions where the Cu K-edge was scanned. Due to a slight drift in the pouch cell position relative to the beam, parts of the particles move out of the frame during the scan. At each of the three electrode positions, the phase maps show a significant change in the Cu chemistry above 4.

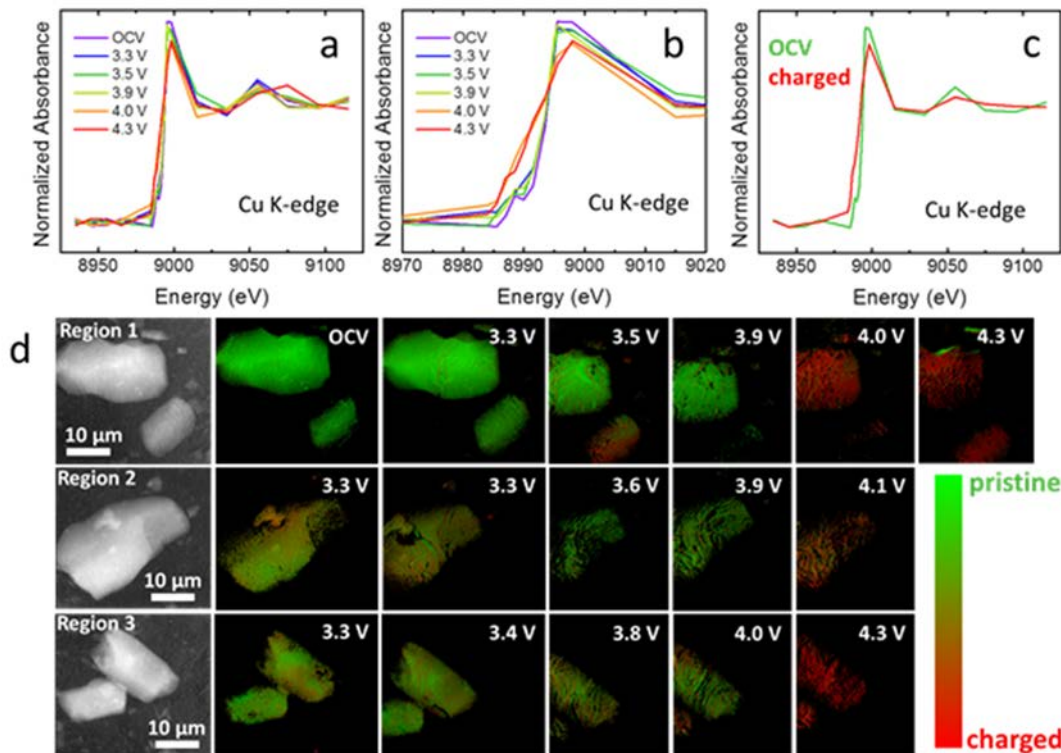


Figure V-66: (a) Average (bulk) XANES at the Cu K-edge from a cell charged *in situ*. (b) Magnified view of the absorption edge in (a). (c) Average (bulk) Cu K-edge XANES from an uncycled cell and cell charged *ex situ*. (d) Phase maps from TXM-XANES data collected *in situ* during charge at three different regions of the electrode. Phase maps were generated by linear combination fitting using the bulk XANES shown in panel c. Transmission images at 9115 eV are also shown

TXM-XANES maps collected *in situ* at the Ni K-edge during charge closely follow the results from the Cu K-edge and are not shown here. It is surprising that no change in the XANES is apparent at lower voltages given the significant change in the X-ray diffraction pattern at 3.4 V. Instead, the changes in the XANES spectra correlate better with the voltage at which significant gas evolution occurs as described in the next section.

Oxygen and gas evolution studies

From the CV and XANES results it is clear that during the first charge of $\text{Li}_2\text{Cu}_{0.5}\text{Ni}_{0.5}\text{O}_2$, significant capacity is extracted at the top of the charge without noticeable changes in the oxidation states of copper or nickel. This strongly suggests that oxygen participates in the redox chemistry, consistent with previous experimental and theoretical work on Li_2CuO_2 and related copper oxides.^{2, 4} Since both Li_2CuO_2 and Li_2NiO_2 parent compositions evolve oxygen at high voltage, we undertook quantitative measurements of the gas generation in

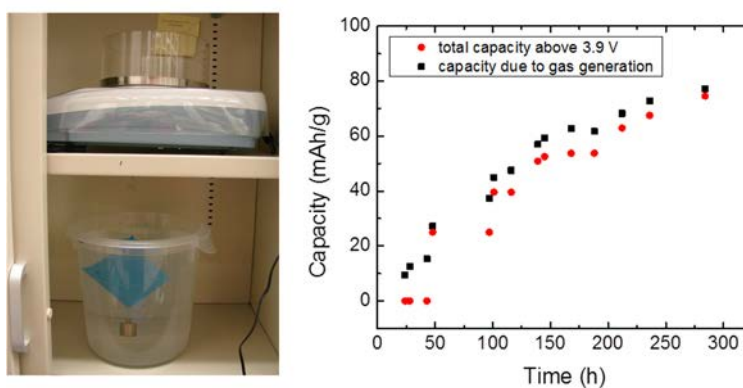


Figure V-67: Comparison of the total electrochemical capacity extracted from $\text{Li}_2\text{Cu}_{0.5}\text{Ni}_{0.5}\text{O}_2$ with the capacity that can be attributed to the evolution of oxygen gas

$\text{Li}_2\text{Cu}_{0.5}\text{Ni}_{0.5}\text{O}_2$ pouch cells (Figure V-67). Charging the cell from the OCP to 3.9 V did not yield any measurable amount of gas. However, significant amounts of gas were generated when the cell was charged above 3.9 V. In fact, we observed that after each charging step above 3.9 V, the OCP of the cell relaxed to ~ 3.9 V. Figure V-67 compares the total capacity that was extracted from the cell during charging steps between 3.9 and 4.3 V with the capacity that can be attributed to gas evolution. The capacity due to gas evolution was calculated assuming that all of the evolved gas is O_2 . This assumption is reasonable, since the carbonate electrolyte is known to be quite stable within this voltage range. Also, no measurable quantity of gas was evolved in a control cell resting at OCP (2.4 V) for a period of one month. Figure V-67 shows that virtually all of the capacity extracted from $\text{Li}_2\text{Cu}_{0.5}\text{Ni}_{0.5}\text{O}_2$ above 3.9 V is due to oxygen evolution. However, oxygen evolution appears to be necessary to activate the higher voltage redox reactions at 3.9 V (oxidation) and 3.6 V (reduction).

Conclusions

The *Immm* orthorhombic structure of $\text{Li}_2\text{Cu}_{0.5}\text{Ni}_{0.5}\text{O}_2$ collapses with the extraction of $<0.5 \text{ Li}^+$ per formula unit. After one electrochemical cycle, the particles transform from a bulk orthorhombic phase to a nanocrystalline form with both layered LiNiO_2 and rocksalt NiO domains. The phase change is accompanied by a significant change in the particle morphology, from uniformly dense to exfoliated layers. TXM-XANES mapping shows the Cu and Ni chemistry also change above 4.0 V. The transformation in the Cu and Ni K-edges correlates with the potential at which significant oxygen evolution occurs. The chemical, structural, and morphological changes are largely homogeneous, despite the large particle size (10 – 30 μm). The changes in particle morphology and crystalline phase are not reversible upon delithiation. This study broadly demonstrates the challenges associated with multi-lithium transition metal oxides, where there is close interplay between structure, transport, and oxygen loss that limits their use as high capacity cathodes for advanced lithium-ion systems.

Products

Presentations/Publications/Patents

1. Synthesis, Structure, and Electrochemical Performance of High Capacity $\text{Li}_2\text{Cu}_{0.5}\text{Ni}_{0.5}\text{O}_2$ Cathodes, R. Ruther, H. Zhou, C. Dhital, K. Saravanan, A. K. Kercher, G. Chen, A. Huq, Frank M. Delnick, and J. Nanda, *Chem. Mater.* **227**, 6746-6754 (2015).
2. Correlating Local Structure with Electrochemical Activity in Li_2MnO_3 , R. Ruther, H. Dixit, A. Pezesheki, R. Sacci, V. Cooper, J. Nanda and G. Veith, *J. Phys. Chem. C*, **119**, 18022-18029 (2015).
3. Quantifying Chemical and Morphological Heterogeneities in High Capacity Battery Materials: From Micro to Mesoscale, J. Nanda, IBM Almaden, 3rd Feb 2016, San Jose CA, USA. (Invited)
4. Studies on high energy density cathodes for advanced Lithium-ion, BMR review meeting, January 21st 2016, LBNL, Berkeley, CA.
5. Annual Merit Review, Washington DC, June 9-14th 2016, Poster presentation “Studies on high capacity lithium-ion Cathodes for Advance Lithium-ion, Jagjit Nanda & Rose Ruther
6. Meso and microscale chemical and morphological heterogeneities in high capacity battery materials, IMRC Meeting, Cancun, August 2016. (Invited)
7. Charge transfer across lithium-garnet solid electrolyte interface, Telluride Science Workshop, Telluride, Colorado, July 2016. (Invited)

References

1. Ruther, R. E.; Zhou, H.; Dhital, C.; Saravanan, K.; Kercher, A. K.; Chen, G. Y.; Huq, A.; Delnick, F. M.; Nanda, J., Synthesis, Structure, and Electrochemical Performance of High Capacity $\text{Li}_2\text{Cu}_{0.5}\text{Ni}_{0.5}\text{O}_2$ Cathodes. *Chem. Mater.* **2015**, *27* (19), 6746-6754.
2. Kang, K.; Chen, C. H.; Hwang, B. J.; Ceder, G., Synthesis, Electrochemical Properties, and Phase Stability of Li_2NiO_2 with the *Immm* Structure. *Chem. Mater.* **2004**, *16* (13), 2685-2690.

3. Back, C. K.; Yin, R.-Z.; Shin, S.-J.; Lee, Y.-S.; Choi, W.; Kim, Y.-S., Electrochemical Properties and Gas Evolution Behavior of Overlithiated Li_2NiO_2 as Cathode Active Mass for Rechargeable Li Ion Batteries. *J. Electrochem. Soc.* **2012**, *159* (6), A887-A893.
4. Imanishi, N.; Shizuka, K.; Ikenishi, T.; Matsumura, T.; Hirano, A.; Takeda, Y., Preparation and Electrochemical Properties of a Li_2CuO_2 - Li_2NiO_2 Solid Solution as a Lithium-Intercalation Electrode. *Solid State Ion.* **2006**, *177* (15-16), 1341-1346.
5. Kim, M. G.; Cho, J., Air Stable Al_2O_3 -Coated Li_2NiO_2 Cathode Additive as a Surplus Current Consumer in a Lithium-ion Cell. *J. Mater. Chem.* **2008**, *18* (48), 5880-5887.

V.D.2. High Energy Density Lithium Battery (Binghamton University)

M. Stanley Whittingham, Distinguished Professor, Principal Investigator

Binghamton University
85 Murray Hill Road
Vestal, NY, 13850
Phone: 607-777-4673
E-mail: stanwhit@binghamton.edu

Tien Q. Duong, DOE Program Manager

U.S. Department of Energy
Advanced Battery Materials Research (BMR)
Vehicle Technologies Office
1000 Independence Avenue, SW
Washington, DC 20585
Phone: 202-586-7836
E-mail: Tien.Duong@ee.doe.gov

Start Date: October 2014
End Date: September 2017

Abstract

Objectives

We propose to develop the anode and cathode materials for high-energy density cells for use in plug-in hybrid electric vehicles (PHEVs) and in electric vehicles (EV) that offer substantially enhanced performance over current batteries used in PHEVs and with reduced cost. Specifically the primary objectives are to:

- Increase the volumetric capacity of the anode by a factor of 1.5 over today's carbons by using a SnFeC composite conversion reaction anode.
- Increase the capacity of the cathode by using a high capacity conversion reaction cathode, CuF_2 , and/or using a high capacity 2 Li intercalation cathodes, VOPO_4 .
- Enable cells with an energy density exceeding 1 kWh/liter.

Accomplishments

- We have demonstrated more than 500 cycles of the $\text{Sn}_2\text{Fe}/\text{C}$ anode composite at a volumetric capacity exceeding 1.5 times that of carbon. Developed a chemical approach to forming the Sn/Fe anode material as an alternative to our original mechano-chemical synthesis. These materials exhibit excellent rate capabilities.
- We have demonstrated the discharge rate capability of the CuF_2 conversion reaction cathode. Shown that the mixed $\text{Cu}_{1-y}\text{Fe}_y\text{F}_2$ cathode can be discharged in a solid electrolyte cell.
 - Shown that the Fe redox couple is reversible.
 - Shown that cuprous ions are transported through both solid and liquid electrolytes.
- We have determined the optimum composition of the intercalation reaction cathode, Li_xVOPO_4 , as being LiVOPO_4 prepared by a high temperature synthesis or by a polyol approach
 - We have determined the rate capability of LiVOPO_4 , and shown that it has a capacity exceeding 250 mAh/g at the C/10 rate and 200 mAh/g at a C rate.
 - Demonstrated over 50 cycles of this Li-based 2 electron redox cathode, with an energy density substantially higher than the alternative Mg technology.

- We have demonstrated lithiation methods to incorporate lithium into either or both electrodes of the battery cell: $\text{Sn}_y\text{Fe}/\text{VOPO}_4$.

Future Achievements

- We will demonstrate the cyclability of a cell based on a Sn/Fe/C composite anode and a VOPO_4 Intercalation cathode.
 - Different approaches for incorporating lithium into these cells will be evaluated and the optimum couple and approach determined.
 - A comparison of these cells will be achieved against baseline cells (graphite// LiFePO_4)
- We will demonstrate extended cycling of the Li_xVOPO_4 cathode comparable to that of the Sn/Fe anode composite.
- The feasibility of finding answers to the charging of copper fluoride based cathodes will be determined, in collaboration with our electrolyte partners.

Technical Discussion

Background

Lithium-ion batteries are the dominant storage medium for electric-based transportation, and most other portable electric devices and are becoming important for grid storage. However, at the cell level they achieve less than 20% of their theoretical volumetric energy density, and 25% of their gravimetric energy density. The graphite anode is the major limitation to increasing the volumetric capacity and needs to be replaced. On the cathode side the gravimetric capacity in commercial cells using intercalation cathodes does not much exceed 170 Ah/kg, for either the layered oxide or the LiFePO_4 olivine. The latter is inherently safer than the layered oxides, because it does not release oxygen after charging and temperature runaway, but has a much lower volumetric energy density than the layered oxides. Alternative materials for the anode and cathode are required.

Introduction

The project objectives are to develop the anode and cathode materials for high-energy density cells for use in plug-in hybrid electric vehicles (PHEVs) and in electric vehicles (EV) that offer substantially enhanced performance over current batteries used in PHEVs and with reduced cost. Specifically, the goal of this project is to enable cells with an energy density exceeding 1 kWh/liter. The carbon anode in today's lithium-ion cells will be replaced with a tin-based anode with double the volumetric capacity of carbon. Similarly, the present intercalation cathodes will be replaced by materials, which are capable of reacting with up to two lithium ions per redox ion. Moreover, these cell reactions will occur within the stability limit of today's electrolytes, leading to longer-lived batteries.

Approach

Innovative Approach

The approach of this “beyond lithium-ion” battery concept is (a) to remove the volume intensive intercalation-based carbon anode in today's lithium-ion batteries, and replace it with a conversion reaction based material, and (b) to replace the present cathodes that mostly react with less than one lithium ion per transition metal ion with cathode materials that can react with more than one lithium ion. This latter is similar to the concept of using the divalent magnesium with its two-electron transfer. However, we believe that moving two of the much more mobile singly charged lithium ions is more viable, and moreover today's electrolytes, SEI additives and cell technology can be used. Attainment of the goals proposed here will lead to a 50-100% increase in the volumetric and gravimetric energy storage capability of both the anode and the cathode, which will allow for the realistic attainment of the next generation batteries for PHEV vehicles. At the same time, the

science generated will be applicable to other energy storage systems, such as anodes for Li/S. The anode and cathode components in this approach are:

1. A SnFeC composite for the anode which reacts by a conversion mechanism giving Li_xSn and Fe.
2. A CuF_2 containing material for the cathode which reacts with 2 lithium ions by a conversion mechanism giving Cu and LiF.
3. A VOPO_4 containing cathode which reacts with up to 2 lithium ions by an intercalation mechanism giving Li_2VOPO_4 .

Results

The Fe/Sn/C anode

Last year we showed that a mechanochemically formed Sn/Fe/C composite attained more than 1.5 times the volumetric capacity of a graphite anode for more than 100 cycles. We have developed a chemical synthesis approach for the formation of FeSn_2 and FeSn_5 materials, and characterized this material. The goal was to determine the rate capability of this tin-iron anode over 500 cycles and achieve a volumetric capacity of at least 1.5 times that of graphite, 0.8 Ah/cc. The results are shown in Figure V-68 (top) for the first 550 cycles in the voltage window 0.01-1.5V. The first 10 cycles were performed at a rate of C/10 on both lithium insertion and removal (discharge and charge); the next 10 were carried at C/5 on both charge and discharge; for the next 20 cycles the discharge rate was increased to C/2 and the remaining cycles were all at C discharge, whilst the charge rate was maintained at a C/5 rate. After 500 cycles the gravimetric capacity was 414 mAh/g. This translates into a final volumetric capacity of 1.2 Ah/cc, 1.5 times the 0.8 Ah/cc of graphite. The rate capability is also shown in Figure V-68 (bottom). This data is comparable to that of the mechano-chemically synthesized Sn_2FeC composite recently reported by us (see under publications) and shows the feasibility of these tin based materials as anodes for advanced lithium batteries.

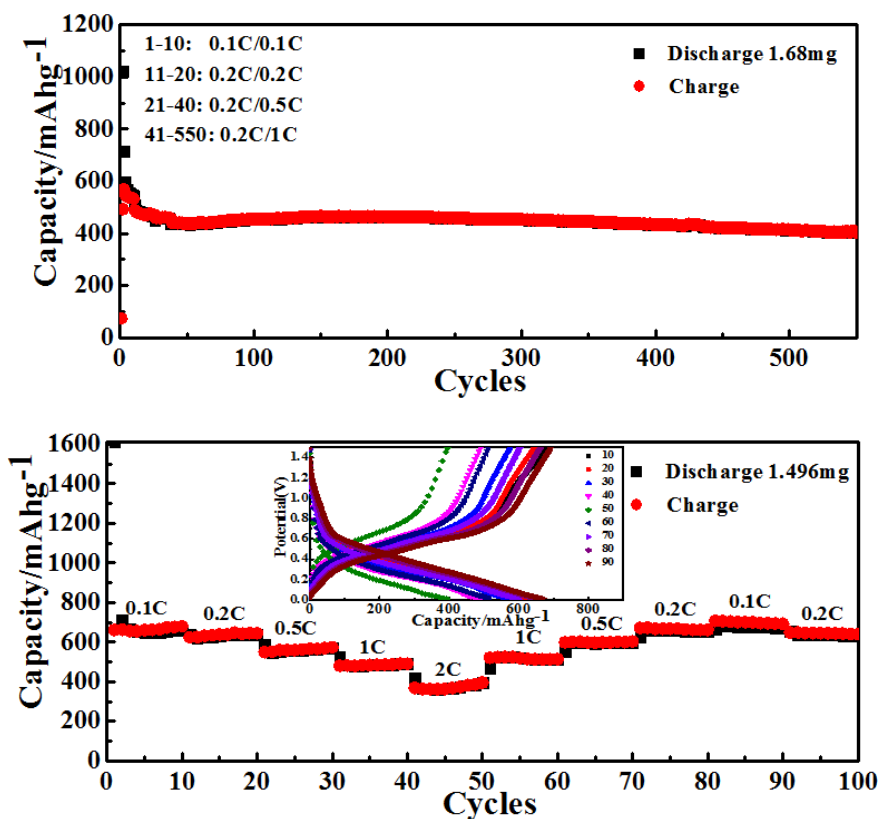


Figure V-68: The electrochemical behavior of the Sn_7Fe anode vs Li metal: (top) capacity over 500+ cycles. (bottom) capacity as a function of rate (the insert shows the voltage profile); charge and discharge with the same current rate. The weight of active material is given at the top right

The CuF₂ Cathode

Copper fluoride reacts by a conversion mechanism, which leads to a theoretical capacity of over 500 Ah/kg. On discharge copper metal and lithium fluoride are formed. We determined its rate capability and the reversibility of the reaction. The discharge capacity over a range of rates is shown in Figure V-69 for a CuF₂/C composite and a CuF₂/VOPO₄/C composite. Although the latter shows a higher capacity, the former shows a higher energy density. We have also shown conclusively that Cu⁺ ions diffuse readily in the common battery liquid electrolytes and in some solid electrolytes. This results in some copper metal being plated on the anode during charge, rather than the active CuF₂ compound being reformed. Thus, extended high capacity cycling of the CuF₂ cathode is not feasible at this time. Supporting this conclusion Figure V-70 shows the reversibility of the FeF₂ and Cu_{0.5}Fe_{0.5}F₂ electrodes using the PEO solid electrolyte. Whereas the FeF₂ electrode is fully reversible and the copper-based electrode discharges as expected (i.e. showing both the Fe and Cu redox potentials), on recharge completion of charging is incomplete due to the transport of Cu⁺ ions through the electrolyte (or possibly to the breakdown of the PEO). The search for electrolytes that do not transport Cu species continues in a collaborative effort with colleagues at U. Colorado at Boulder, University of Michigan, Oak Ridge National Laboratory and Toyota Research Institute of North America.

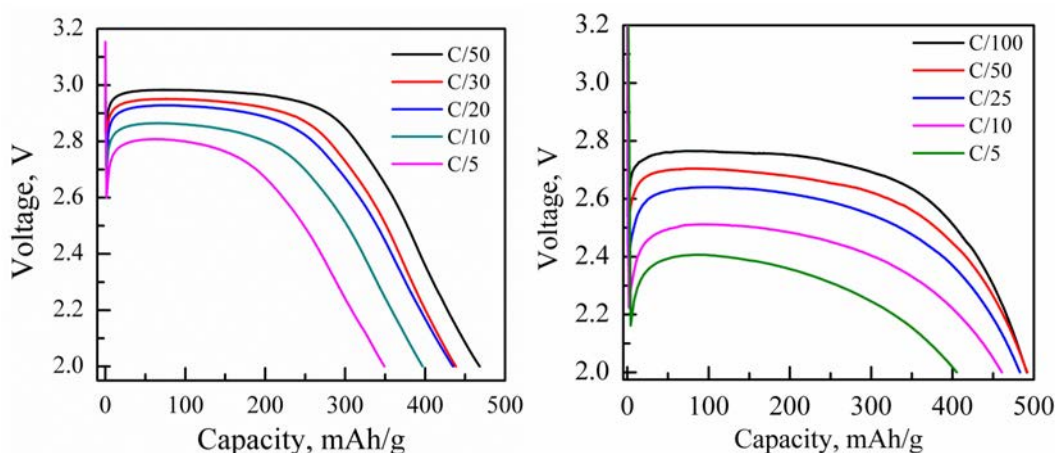


Figure V-69: The capacity vs rate of (left) a Li//CuF₂ cell and (right) a Li//CuF₂-VOPO₄ cell

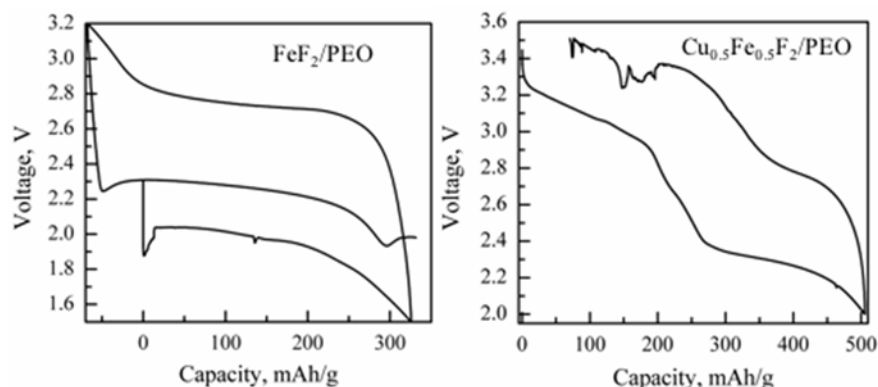


Figure V-70: Electrochemical cycling of FeF₂ and Cu_{0.5}Fe_{0.5}F₂ vs Li metal using the PEO solid electrolyte

The VOPO₄ Intercalation Cathode

Vanadyl phosphate reacts by an intercalation reaction, incorporating up to lithium ions per vanadium redox center. We have determined that the optimum composition of the starting cathode is ϵ -LiVOPO₄, i.e. a material containing some lithium rather than the Li-free ϵ -VOPO₄. The best synthetic approach is a solid-state reaction at 750°C. Hydrothermal synthesis results in the incorporation of protonic species into the lattice. The material made has however particles in the range of 2-5 μ m in size, so must be ground down to sub-micron to ensure effective reaction with lithium. This was accomplished by high energy

ball-milling. The cyclability of such LiVOPO_4 materials is shown in Figure V-71 under ambient conditions for two rates, C/20 and C/50. Through the first 20 cycles the C/50 materials show minimal capacity loss, and the highest capacity is seen for a ball-milling time of 0.5 hours. After this time the particles are around 200 nm in size.

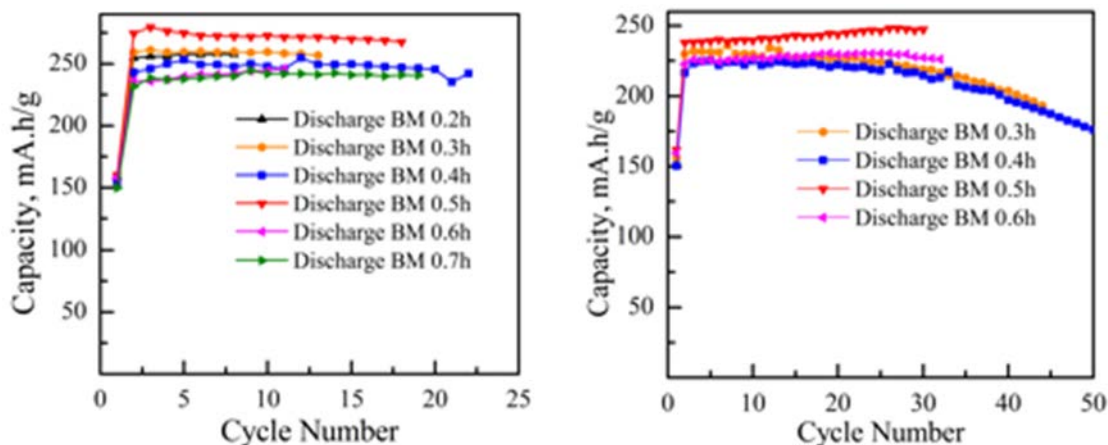


Figure V-71: Cycling capacity of a LiVOPO_4 electrode as a function of ball-milling time in hours and rate of charge/discharge: (left) C/50. (right) C/20

The rate capability of the LiVOPO_4 electrode is presented in Figure V-72. This cathode is an electronic insulator just like the olivine LiFePO_4 , so must be nanosized and covered with a conductive coating. However, unlike LiFePO_4 it cannot be carbon coated at elevated temperatures using a material such as sucrose, because the oxidation state of the vanadium is reduced under such conditions. Thus, the material was coated by high energy ball-milling with carbon; this ball-milling also resulted in the reduction of the particle size of the LiVOPO_4 .

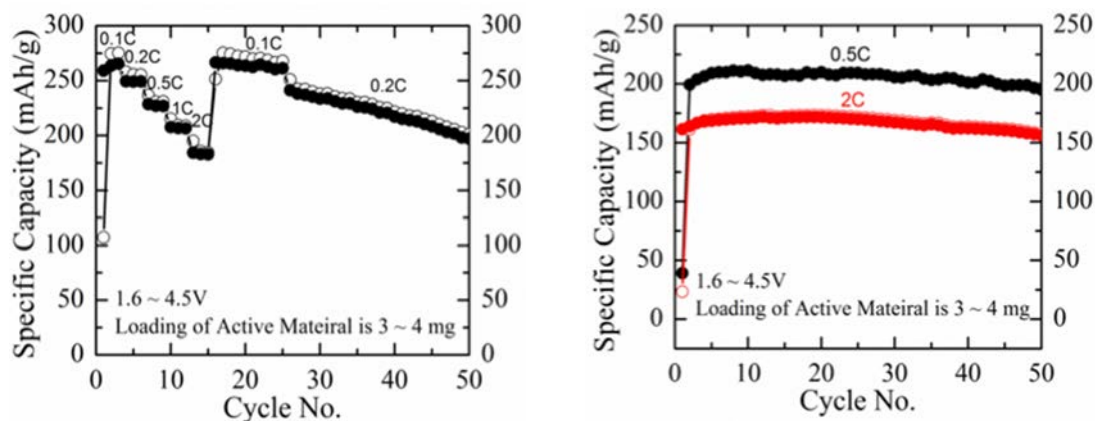


Figure V-72: Cycling behavior (left) and rate capability (right) of a LiVOPO_4 electrode

Demonstration of lithiation method

As none of the proposed electrode materials contain lithium it is necessary to incorporate lithium in a full cell. Several methods are under study to lithiate either one or both of the anode and the cathode. The techniques evaluated included pre-lithiation of the electrodes, addition of lithium or lithiating agents to the anode and addition of compounds like Li_2O to the cathode that will provide lithium on the first charge. Figure V-73 demonstrates that constructing a cell of electrochemically lithiated Sn/Fe/C and VOPO_4 allows a functional cell. Further work is necessary to optimize the electrochemical behavior

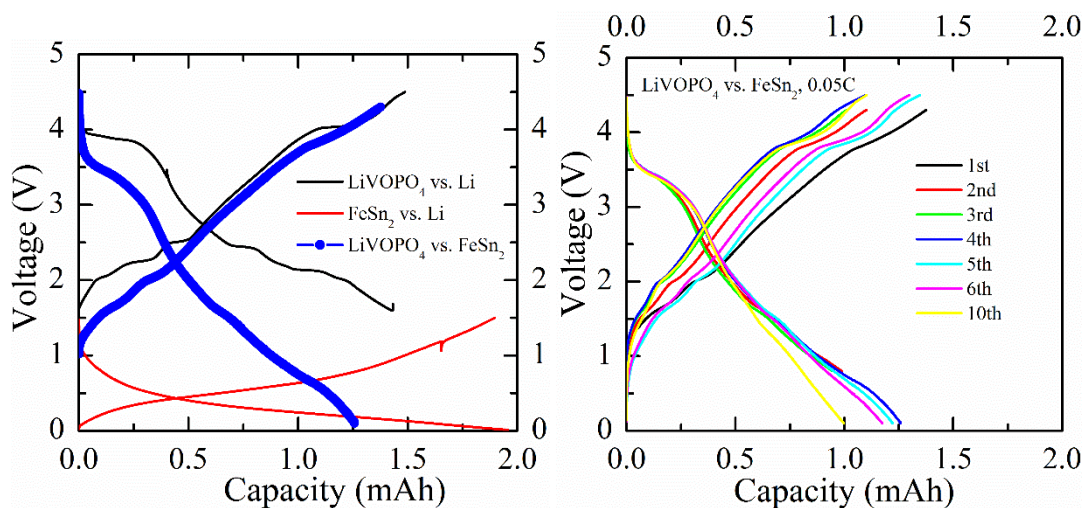


Figure V-73: (left) First cycle of the individual electrodes vs Li metal, and of the full cell, and (right) charge and discharge curves for the first 10 cycles of a lithiated Sn-Fe//VOPO₄ cell

Conclusions

We have made significant progress in both the cathode and anode conversion materials. The Sn₂Fe/C composite has achieved well over 1.5 times the volumetric capacity of the graphitic anode based on the lithiated product. This has been achieved for over 500 full cycles and over a range of C rates.

We have shown that copper fluoride electrodes have capacities up to 500 Ah/kg on the first discharge at low rates, and that even at rates as high as C/5 the capacity remains above 400 Ah/kg. We have shown that on charging the Cu/LiF product of the discharge reaction, cuprous ions are transported through the electrolyte, whether liquid or solid, leading to plating of copper metal at the anode. A search is continuing for electrolytes that show a higher selectivity for lithium transport over copper.

We have shown that the 2 electron redox cathode, lithium vanadyl phosphate, LiVOPO₄, can be readily cycled at rates up to 2C. It shows a substantially higher energy density than the alternative approach using magnesium.

Products

Presentations/Publications/Patents

1. Zhixin Dong, R. Zhang, D. Ji, N. A. Chernova, K. Karki, S. Sallis, L. Piper, M. S. Whittingham: The anode challenge for lithium-ion batteries: a mechanochemically synthesized Sn-Fe-C composite anode surpasses graphitic carbon. *Advanced Science*, 3, 1500229, 2016.
2. "High Energy Density Lithium Battery", ES231_Whittingham_2015_p, US DOE Vehicle Technologies AMR, June 9th, 2016.
3. Fredrick Omenya, M. Stanley Whittingham, "High Energy Density Lithium Battery – an update", DOE-EERE-NETL Visit to Binghamton, Binghamton, NY, September 24th, 2015.
4. FeSn₂ and FeSn₅ alloy with high and stable capacity as anodes in lithium-ion batteries. ACS NERM, Binghamton, NY, October 7th, 2016. Fengxia Xin.
5. Intrinsic challenges in creating a reversible copper (II) fluoride cathode for lithium-ion batteries, ACS NERM, Binghamton, NY, October 6th, 2016. Nik Zagarella.
6. Synthesis, characterization and organization of vanadium phosphates as cathode material for lithium-ion batteries. ACS NERM, Binghamton, NY, October 6th, 2016. Yong Shi.

V.D.3. Development of High-Energy Cathode Materials (PNNL)

Ji-Guang Zhang, Principal Investigator

Pacific Northwest National Laboratory
Energy & Environment Directorate
902 Battelle Boulevard
Richland, WA 99354
Phone: 509-372-6515; Fax: 509-375-2186
E-mail: jiguang.zhang@pnnl.gov

Jianming Zheng, Co-Principal Investigator

Pacific Northwest National Laboratory
902 Battelle Boulevard
Richland, WA 99354
Phone: 509-372-4762; Fax: 509-375-2186
E-mail: jianming.zheng@pnnl.gov

Tien Q. Duong, DOE Program Manager

U.S. Department of Energy
Advanced Battery Materials Research (BMR)
Vehicle Technologies Office
1000 Independence Avenue, SW
Washington, DC 20585
Phone: 202-586-7836
E-mail: Tien.Duong@ee.doe.gov

Start Date: October 1, 2015
End Date: September 30, 2018

Abstract

Objectives

- Develop high-energy cathode materials with improved safety for plug-in hybrid electric vehicle (PHEV) and electric vehicle (EV) applications.
- Develop low-cost synthesis routes for environmentally benign cathode materials with long cycle life.

Accomplishments

- Identified NMC candidates that can deliver more than 200 mAh g⁻¹ at high voltage.
- Identified the behavior of Co, Ni, and Mn in NMC cathodes during battery charge/discharge processes and their correlation with battery fading characteristics.
- Revealed the structural/chemical evolution of modified NMC cathodes during cycling at high charge-cutoff voltages.
- Identified the compositions of NMC materials to achieve improved electrochemical performance (90% capacity retention after 100 cycles).

Future Achievements

- Complete lattice doping to enhance the cycling stability of NMC at high charge-cutoff voltages.
- Identify appropriate solvents for surface modification of NMC and determine the related structure changes.
- Complete surface modification to enhance the cycling stability of NMC at high charge-cutoff voltages.

- Further improve the electrochemical performance of NMC cathodes.

Technical Discussion

Background

The lithium-ion battery (LIB) is the most promising energy storage technology for EVs, which can help to reduce environmental pollution and support energy security in the United States. However, the large-scale market penetration of EVs has been hindered by several barriers, including limited energy density, high cost, and safety concern of cathodes in LIBs.

Introduction

Conventional layered oxide LiCoO_2 (LCO) has been widely used in LIBs developed for portable electronic devices and power tools. However, the high cost of cobalt and limited lithium utilization (~ 0.5 Li) has hindered application of LCO in EVs, especially PHEVs. To meet the requirements for large-scale commercialization of PHEVs/EVs, low-cost electrode materials with high tap densities, high energy densities, good rate capabilities, and long cycle lives must be developed. The ternary layered oxides $\text{LiNi}_x\text{Mn}_y\text{Co}_z\text{O}_2$ (NMC) are promising cathode materials, because they combine the advantages of Ni, Co, and Mn in the structure.^[1] Replacement of Co with high Mn/Ni content also leads to a significant reduction in the production cost. NMC cathode materials that have been successfully adopted in commercial LIBs, including $\text{LiNi}_{1/3}\text{Mn}_{1/3}\text{Co}_{1/3}\text{O}_2$ (NMC333), and $\text{LiNi}_{0.4}\text{Mn}_{0.4}\text{Co}_{0.2}\text{O}_2$ (NMC442), can deliver a reversible capacity of about 155 mAh g^{-1} if they are charged to a voltage of 4.3 V vs. Li^+/Li . However, these capacities are still not sufficient to satisfy the needs of high-energy lithium-ion batteries to be deployed in PHEVs and EVs. Two efficient approaches can be employed to further improve the energy density of NMC cathode materials: (1) extend the charge-cutoff voltage,^[2] and/or (2) develop NMC materials with higher Ni content.^[3,4]

Approach

1. Extending the charge-cutoff voltage is an effective way to achieve higher lithium utilization with NMC layered materials. Electrochemical results show that the discharge capacity of NMC442 was considerably increased, from ca. 140 to more than 200 mAh g^{-1} , with an increase in charge-cutoff voltage from 4.2 to 4.7 V. In this case, new approaches need to be adopted to provide stability of NMC at higher voltages.
2. Another strategy to achieve higher discharge capacity is to develop NMC layered materials with higher Ni content, because Ni can operate between $\text{Ni}^{2+/3+}$ and $\text{Ni}^{3+/4+}$, which offers higher discharge capacity without severe variation in discharge voltage profiles. For instance, the discharge capacities of $\text{LiNi}_{0.6}\text{Co}_{0.2}\text{Mn}_{0.2}\text{O}_2$ (NMC622) were over 10% higher than those of NMC442 at the same charge cutoff, 4.5 V or 4.8 V.

Results

1. High-voltage stability of NMC cathodes

To achieve higher discharge capacity of NMC cathode materials, the effects of high charge-cutoff voltage on the structural/interfacial stability of several NMC cathodes was first investigated. Figure V-74a and d compare the initial charge/discharge voltage profiles of different NMC cathodes at charge-cutoff voltages of 4.5 and 4.8 V. With the increase of charge-cutoff voltage from 4.5 to 4.8 V, these NMC cathodes were able to deliver greatly enhanced discharge capacities of over 200 mAh g^{-1} , representing a significant improvement in energy density of NMC cathodes. The long-term cycling performance of different NMC cathodes has been found to be very sensitive to the compositions of the materials. The high-voltage stability of the four NMCs follows the trend of $\text{NMC442} > \text{NMC532} \sim \text{NMC622} \sim \text{NMC333}$ at a charge-cutoff voltage of 4.5 V (Figure V-74b, c), and $\text{NMC442} > \text{NMC532} \sim \text{NMC622} > \text{NMC333}$ at a charge-cutoff voltage of 4.8 V (Figure V-74e, f). The capacity degradation mechanism of NMC532 charged to a high cutoff voltage of 4.8 V has already been reported by Kang and coworkers.^[5] In FY16, the detailed capacity fading mechanisms of NMC442 and

NMC333 during high-voltage cycling were studied in detail using advanced characterization techniques including scanning transmission electron microscopy (STEM) and electron energy loss spectroscopy (EELS).

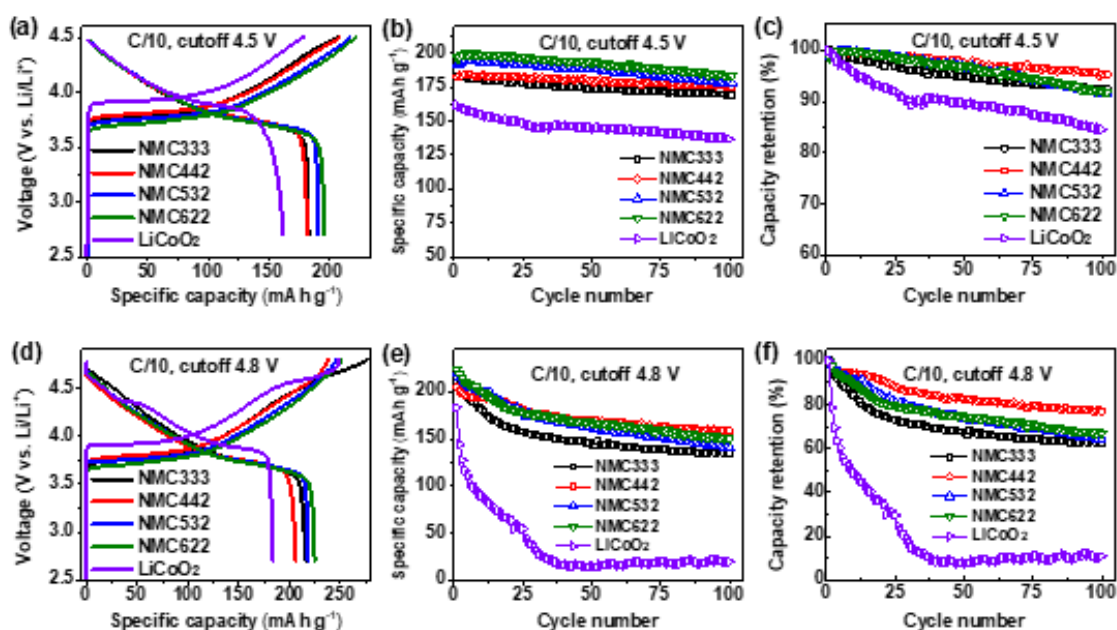


Figure V-74: (a, d) Initial charge/discharge profiles, (b, e) discharge capacity vs. cycle number, and (c, f) capacity retention vs. cycle number of different NMC cathode materials at C/10 in the voltage range of (a-c) 2.7~4.5 V and (d-f) 2.7~4.8 V.

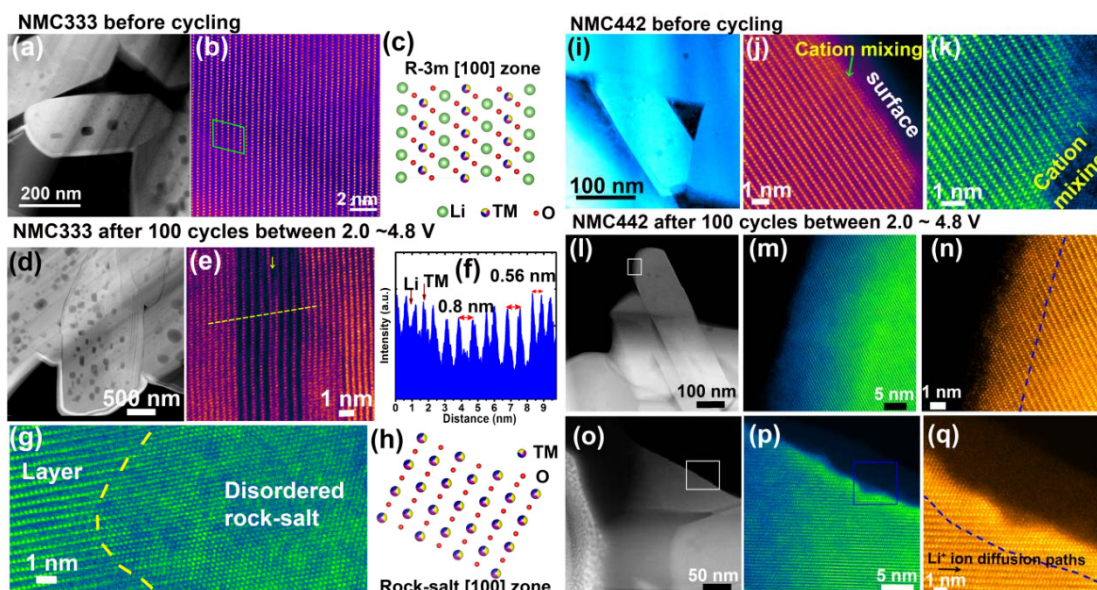


Figure V-75: (a-c) Crystal structure of pristine NMC333 cathode. (a) High-angle annular dark-field (HAADF) Z-contrast image. (b) STEM image and (c) atomic model showing the layered structure viewed down the [100] zone axis. (d-h) Crystal structure of NMC333 particle after 100 cycles in the range of 2.0~4.8 V at C/10. (d, e) HAADF Z-contrast image and STEM images showing significant microcracks and lattice expansion in the cycled particle. (f) Intensity plot along the yellow dashed line shown in (e). (g) STEM image showing the disordered rock-salt phase formation at the surface region of the cycled particles. (h) Atomic model of the Fm-3m disordered rock-salt phase in [110] zone projection. (i-k) Crystal structure of pristine NMC442 cathode. (i) HAADF Z-contrast image. (j, k) STEM images showing the layered structure at the surface terminated with (j) a transition metal (TM) layer and (k) a mix of cations and anions viewed down the [100] zone axis. (l-n) Crystal structure of NMC442 after 100 cycles in the range of 2.0~4.8 V at C/10. (l) HAADF Z-contrast image. (m, n) STEM images showing disordered rock-salt phase formation at the surface region of cycled particle. (o-q) Crystal structure of another cycled NMC442 particle (after 100 cycles in the range of 2.0~4.8 V at C/10)

All the NMC materials showed improved cycling stability as compared to LiCoO₂, at both charge-cutoff voltages of 4.5 and 4.8 V, evidencing the advantage of NMC materials. In comparison, NMC333 exhibited the poorest cycling stability because of its inferior structural/interfacial stability when charged to 4.8 V (Figure V-75a-h). This could be ascribed to the higher Co content in NMC333 (33% Co) and the considerable overlap between the Co^{3+/4+} : 3d band with the top of the O²⁻ : 2p band, which induced significant oxygen extraction when charged to a voltage ≥ 4.5 V. The continuous oxygen extraction at high voltage gave rise to the formation of a significant quantity of oxygen vacancies inside the particle, greatly weakening the electrical attraction between the TM ions and the reduced oxygen coordinates. Furthermore, the buildup of internal microstrain associated with the anisotropic volume variation at deep lithium de/intercalations resulted in microcrack formation inside the primary particles (Figure V-75d-f). Also, oxygen loss at the particle surface caused significant phase transformation from layered to disordered rock-salt structure (Figure V-75g, h). The microcrack region and the disordered rock-salt region may not be capable of reversible lithium-ion storage, resulting in fast capacity fading of NMC333 when cycled under such a high charge-cutoff voltage. These fundamental findings indicate that effects of material composition (especially Co content) should be carefully considered for the development of next-generation NMC cathode materials for high voltage battery systems. Among the materials tested, NMC442 showed the best cycling performance due to its superior structural/interfacial stability at high charge-cutoff voltage of 4.8 V. Although the NMC442 shows slightly more cation disorder in the material before cycling (Figure V-75i-k), its layered structure is better preserved during cycling, as confirmed by the limited evolution of the surface reconstruction layer (disordered rock-salt phase, only 2~3 nm) and the well maintained layered structure inside the particle bulk (Figure V-75l-q).

2. Synthesis condition optimization of Ni-rich NMC cathodes

Another approach to achieve higher discharge capacity is to develop NMC cathode materials with higher Ni content. The synthesis conditions, such as co-precipitation pH value, particle size, lithium content, calcination temperature, calcination atmosphere (O₂, air, etc.), heating/cooling rates, play an important role in manipulating the material structural properties and thus influencing the electrochemical performance of prepared Ni-rich cathode materials. In FY16, the effects of calcination temperature on the primary particle size, cation mixing, and the electrochemical performances of Ni-rich cathode materials were systematically investigated. The electrochemical performance of the Ni-rich LiNi_{0.76}Mn_{0.14}Co_{0.10}O₂ cathode was found to be very sensitive to the calcination temperature. The initial charge/discharge voltage profiles demonstrated that high discharge capacities of ca. 215 mAh g⁻¹ were achieved at calcination temperatures of 750~850°C (Figure V-76a). The capacity retentions after 200 cycles decreased with increasing calcination temperature; they were 80.1%, 79.0%, 78.7%, 72.9%, 56.4% and 41.9% for materials prepared at 725, 750, 775, 800, 850 and 900°C, respectively (Figure V-76b). The data also demonstrate that the LiNi_{0.76}Mn_{0.14}Co_{0.10}O₂ cathode prepared at calcination temperatures of 750°C exhibited only a very small fade of 0.055 V in average discharge voltage after 200 cycles (Figure V-76c). This voltage fade is much less than the 0.105, 0.242, and 0.399 V, respectively, for materials prepared at calcination temperatures of 800, 850, and 900°C, respectively.

The LiNi_{0.76}Mn_{0.14}Co_{0.10}O₂ sample prepared at 750°C shows higher discharge capacities at various C rates (Figure V-76d). In particular, the sample delivers the highest discharge capacity of 168 mAh g⁻¹ at a 10C rate, which is much higher than the values of 152, 164, 163, 125, and 47 mA h g⁻¹ for those prepared at 725, 775, 800, 850 and 900°C, respectively. When cycled at high temperature of 60°C, the capacity retentions after 100 cycles of these materials are calculated to be 79.8%, 81.4%, 86.2%, 78.4%, 58.2% and 59.6% for materials prepared at 725, 750, 775, 800, 850 and 900°C, respectively (Figure V-76e). The material prepared at 775°C exhibited the best capacity retention and the highest discharge capacity (194 mAh g⁻¹) after 100 cycles. All of these results indicate that the optimal calcination temperature for LiNi_{0.76}Mn_{0.14}Co_{0.10}O₂ was 750~775°C based on the achievable discharge capacity and the cyclability. The electrochemical performance of the LiNi_{0.76}Mn_{0.14}Co_{0.10}O₂ sample prepared at 750°C was also evaluated in a thick electrode with a loading of ca. 2.5 mAh cm⁻² (~12 mg active material per cm²), as shown in Figure V-76f. The thick LiNi_{0.76}Mn_{0.14}Co_{0.10}O₂ electrode still delivered a high discharge capacity of ca. 210 mAh g⁻¹ during the formation cycles, which is similar to that obtained in a thin electrode with a low loading of ~4 mg cm⁻² as shown in Figure V-76a-e, indicating good electrode kinetics of the prepared materials. During cycling at a C/3 charge rate and a 1C discharge rate, the thick LiNi_{0.76}Mn_{0.14}Co_{0.10}O₂ electrode behaved similarly to the thin-electrode counterpart, demonstrating a decent cycling stability with a high capacity retention of 92% after 100 cycles.

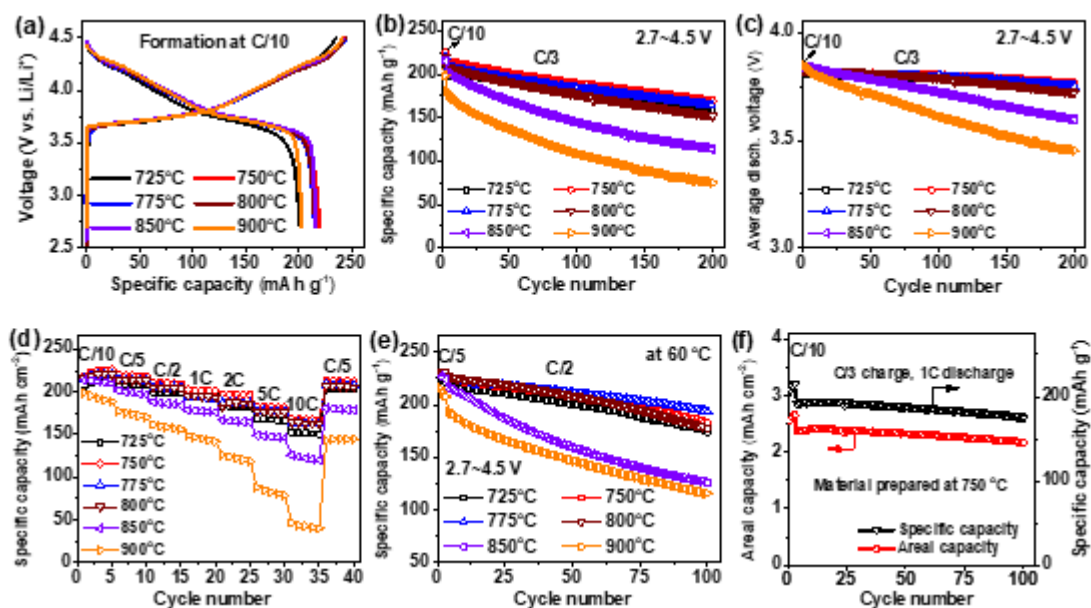


Figure V-76: (a) Initial charge/discharge profiles at C/10, (b) cycling performance, and (c) average discharge voltage of the $\text{LiNi}_{0.76}\text{Mn}_{0.14}\text{Co}_{0.10}\text{O}_2$ cathodes prepared at different calcination temperatures at C/3 after 3 formation cycles at C/10 over the voltage range of 2.7~4.5 V. (d) Rate performance and (e) high temperature (60°C) performance of $\text{LiNi}_{0.76}\text{Mn}_{0.14}\text{Co}_{0.10}\text{O}_2$ cathodes prepared at different calcination temperatures. (a-e) Electrode loading is about 4 mg active material per cm^2 . (f) Performance of thick $\text{LiNi}_{0.76}\text{Mn}_{0.14}\text{Co}_{0.10}\text{O}_2$ cathode prepared at the optimal condition of 750°C. Thick electrode loading is ~12 mg active material per cm^2

The cells were disassembled after 200 cycles and the cathode were retrieved for further characterization, focusing on examination of the microstrain and microcrack formation in the cycled particles. Cross-sectional scanning electron microscope (SEM) images of the pristine (Figure V-77a-f) and cycled (Figure V-77g-k) particles demonstrated the formation of microcracks and void space inside the cycled particles. The materials prepared at higher temperature i.e., 800~900°C, exhibited severe formation of cracks and voids inside the secondary particles, because of substantial microstrain caused by the anisotropic volume variation. The crack formation is believed to be closely related to the size of the primary particles constituting the secondary particles of each material. The electrolyte penetrated into the interior of secondary particles along the crack network, leading to the formation of a resistive solid electrolyte interphase layer at the grain boundaries. Crack formation and the degradation of particle interfacial stability resulted in the loss of electrical contact between the primary particles, leading to quick buildup of electrode resistance (Figure V-77l-p) and fast capacity fading. This is believed to be the primary reason for the poor cycling stability of the materials prepared at calcination temperatures higher than 800°C. In this regard, mitigation of the microstrain and crack formation inside the secondary particles is critically important for achieving improved long-term cycling performance.

The effect of calcination temperature on the electrochemical performance of another Ni-rich NMC cathode material, $\text{LiNi}_{0.68}\text{Mn}_{0.22}\text{Co}_{0.10}\text{O}_2$, was further investigated. Calcination temperature was expected to significantly affect the cycling performance and rate performance of $\text{LiNi}_{0.68}\text{Mn}_{0.22}\text{Co}_{0.10}\text{O}_2$. The optimal calcination temperature was identified to be 775°C based on the superior capacity retention of 93.8% after 100 cycles as shown in Figure V-78. The optimal temperature for $\text{LiNi}_{0.68}\text{Mn}_{0.22}\text{Co}_{0.10}\text{O}_2$ (775°C) is higher than that for $\text{LiNi}_{0.76}\text{Mn}_{0.14}\text{Co}_{0.10}\text{O}_2$ (750°C). This finding is consistent with that summarized in our recent review paper published in Nano Today.^[6] Generally, NMC with higher Mn content requires a higher calcination temperature to achieve enhanced crystallinity, while NMC with higher Ni content needs to be calcined at a lower temperature to avoid the formation of impurity phase. This general finding provides a useful guide for the selection of optimal calcination temperature for Ni-rich NMC cathode materials with different compositions.

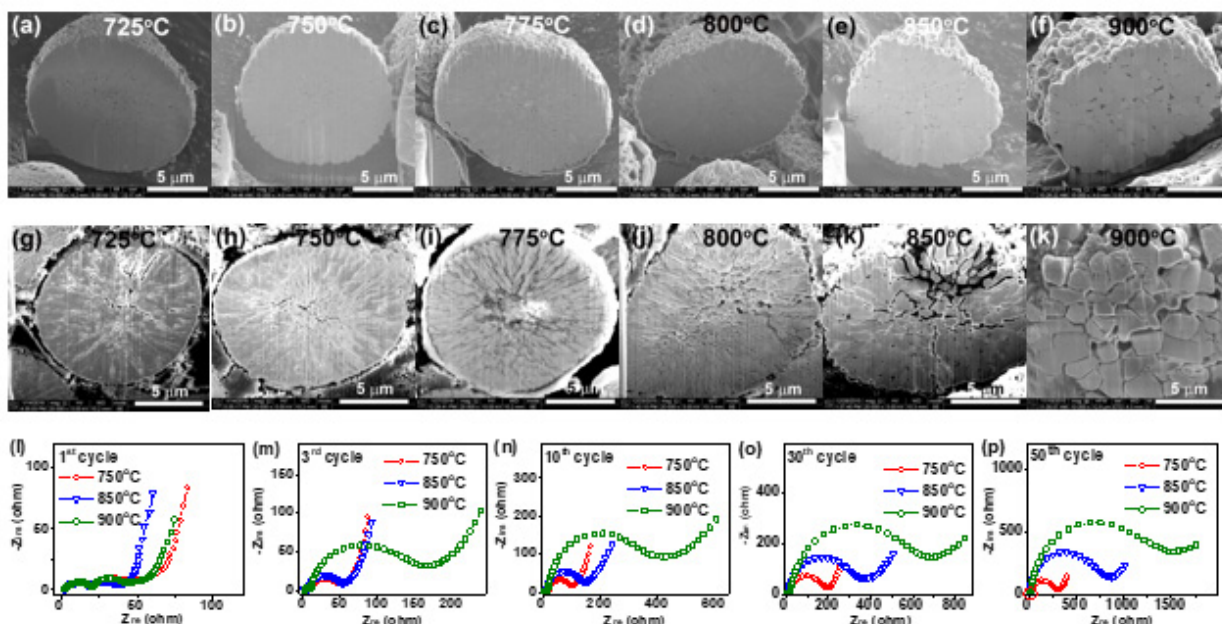


Figure V-77: (a-k) Cross-sectional SEM images of $\text{LiNi}_{0.76}\text{Mn}_{0.14}\text{Co}_{0.10}\text{O}_2$ cathodes prepared at different calcination temperatures ranging from 725 to 900°C (a-f) before and (g-k) after 200 cycles at C/3 after 3 formation cycles at C/10. (l-p) Nyquist plots of $\text{LiNi}_{0.76}\text{Mn}_{0.14}\text{Co}_{0.10}\text{O}_2$ cathodes prepared at different calcination temperatures in the charged state of 4.3 V during cycling. (l) 1st cycle; (m) 3rd cycle; (n) 10th cycle; (o) 30th cycle; (p) 50th cycle

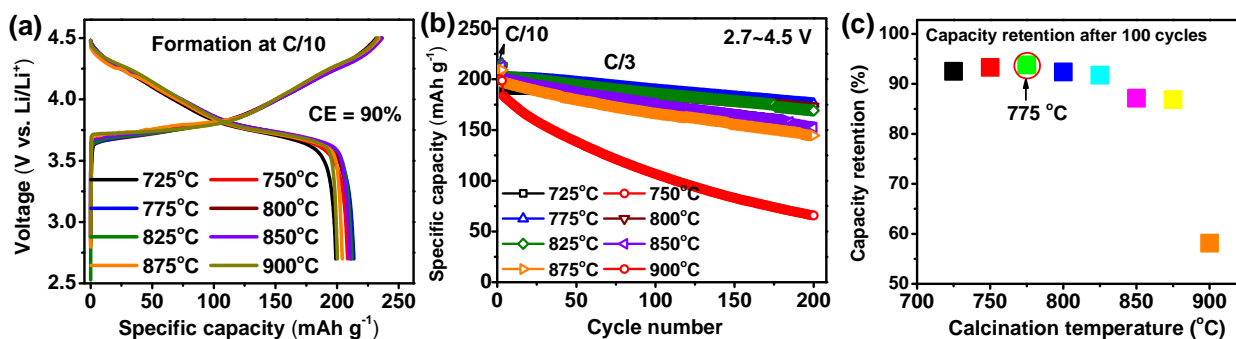


Figure V-78: (a) Initial charge/discharge profiles at C/10, (b) cycling performance, and (c) capacity retention after 100 cycles of the $\text{LiNi}_{0.68}\text{Mn}_{0.22}\text{Co}_{0.10}\text{O}_2$ cathodes prepared at different calcination temperatures at C/3 after 3 formation cycles at C/10 over the voltage range of 2.7~4.5 V. Electrode loading is about 4 mg active material per cm^2

3. Composition optimization of Ni-rich NMC cathodes

With the findings obtained from the optimization of calcination temperature, the compositions of NMC materials with respect to their Ni, Co, and Mn contents have been also optimized to achieve improved electrochemical performance. Ni-rich NMC cathode materials that were synthesized include $\text{LiNi}_{0.76}\text{Mn}_{0.14}\text{Co}_{0.10}\text{O}_2$ (750°C), $\text{LiNi}_{0.68}\text{Mn}_{0.22}\text{Co}_{0.10}\text{O}_2$ (775°C), $\text{LiNi}_{0.62}\text{Mn}_{0.25}\text{Co}_{0.13}\text{O}_2$ (800°C), and $\text{LiNi}_{0.5}\text{Mn}_{0.3}\text{Co}_{0.2}\text{O}_2$ (800°C). Their electrochemical performance is shown in Figure V-79, in which the performance of a commercial low-Ni-content material, $\text{LiNi}_{1/3}\text{Mn}_{1/3}\text{Co}_{1/3}\text{O}_2$, is also shown for comparison.

The initial charge/discharge voltage curves demonstrated that discharge capacities of 200 mAh g^{-1} or higher could be achieved at a Ni content ≥ 0.5 with charge-cutoff voltage of 4.5 V (Figure V-79a). The long-term cycle life of these NMC cathodes, as presented in Figure V-79b, was found to be very sensitive to the Ni content in the prepared materials. The capacity retention of the NMCs after 100 cycles follows the trend of $\text{Ni}_{0.33}$ (97.7%) > $\text{Ni}_{0.50}$ (97.6%) > $\text{Ni}_{0.62}$ (97.2%) > $\text{Ni}_{0.68}$ (93.8%) > $\text{Ni}_{0.76}$ (88.5%) during cycling at C/3. The comparison of voltage profiles of $\text{LiNi}_{0.68}\text{Mn}_{0.22}\text{Co}_{0.10}\text{O}_2$ (Figure V-79c) and $\text{LiNi}_{0.76}\text{Mn}_{0.14}\text{Co}_{0.10}\text{O}_2$ (Figure V-79d) illustrates that the material with higher Ni content showed faster capacity decay, as labeled by

the red arrows in Figure V-79c and d. This could be attributed to the poor interfacial stability of high-Ni NMC materials due to parasitic reactions between Ni^{4+} and the electrolyte as well as the structural instability owing to large volume variation upon deep delithiation.

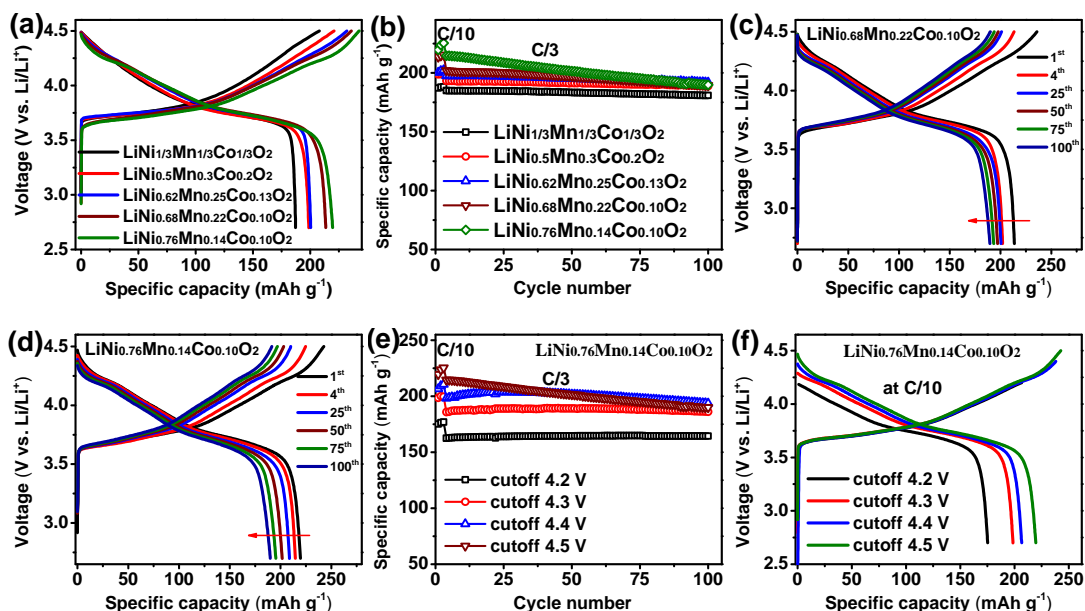


Figure V-79: (a) Initial charge/discharge profiles and (b) cycling performance of different NMC cathodes at C/3 after 3 formation cycles at C/10 in the voltage range of 2.7~4.5 V. (c, d) Charge/discharge profile evolution of (c) $\text{LiNi}_{0.68}\text{Mn}_{0.22}\text{Co}_{0.10}\text{O}_2$ and (d) $\text{LiNi}_{0.76}\text{Mn}_{0.14}\text{Co}_{0.10}\text{O}_2$. (e) Cycling performance of $\text{LiNi}_{0.76}\text{Mn}_{0.14}\text{Co}_{0.10}\text{O}_2$ with different charge-cutoff voltages at C/3 after 3 formation cycles at C/10. (f) Charge/discharge profiles of $\text{LiNi}_{0.76}\text{Mn}_{0.14}\text{Co}_{0.10}\text{O}_2$ with different charge-cutoff voltages at C/10

The effect of charge-cutoff voltage on the cycling stability of the Ni-rich cathode material $\text{LiNi}_{0.76}\text{Mn}_{0.14}\text{Co}_{0.10}\text{O}_2$ was also investigated in detail (Figure V-79e, f). Decreased charge-cutoff voltage significantly improved the cycling stability of the material (Figure V-79e). The capacity retention after 100 cycles was improved from 88.5% to 97.6% when the charge-cutoff voltage was reduced from 4.5 V to 4.4 V. Furthermore, there was almost no capacity fade observed at charge-cutoff voltages of 4.3 V and 4.2 V. This could be ascribed to fewer side reactions occurring at electrode surfaces at lower charge voltage along with the decreased extraction of lithium ions during each charge, which mitigated the structural degradation. However, considerably decreased accessible discharge capacity was obtained at lower cutoff voltages, especially when 4.2 V was used as the cutoff. The initial discharge capacities at charge-cutoff voltages of 4.5 V, 4.4 V, 4.3 V, and 4.2 V were 219, 207, 200, and 176 mAh g^{-1} , respectively (Figure V-79f). In this regard, a good trade-off between discharge capacity and cycling stability was achieved at a charge cutoff of ~4.4 V. In future study, additional lattice doping, surface modification, and electrolyte additives will be adopted for high-Ni NMC cathodes in order to achieve both high discharge capacity and improved long-term cycling stability.

Conclusions

In summary, two approaches have been adopted to improve the discharge capacity and thus the energy density of modified NMC cathode materials for LIBs.

High charge-cutoff voltage could significantly improve the energy density of NMC cathode materials, albeit at the expense of accelerated capacity decay. The capacity degradation mechanism of NMC333 and NMC442 has been investigated in detail. The material composition shows significant effects on the performance of NMC materials under high voltage operation. The primary reason behind the poor structural and interfacial stability of NMC333 is believed to be its higher Co content and the significant overlap between the $\text{Co}^{3+/4+} t_{2g}$ band and the $\text{O}^{2-} 2p$ band, resulting in oxygen removal and consequent structural changes at high voltages, including obvious microcrack formation, and transformation from layered to disordered rock-salt phase. Therefore, NMC333 shows much faster capacity degradation than NMC442 during cycling at a charge-cutoff voltage of 4.8 V. These fundamental findings indicate that the intrinsic structural stability and its relation to material

composition (Co, Ni, Mn) of NMC cathodes should be taken into account in future development of cathode materials for high voltage battery systems.

To develop Ni-rich NMC cathode materials with optimized electrochemical performance, the effects of calcination temperature on the structure, morphology, and electrochemical performance of Ni-rich cathode materials at a high charge-cutoff voltage of 4.5 V have been systematically investigated. The findings highlight the importance of optimizing the synthesis conditions for preparing the Ni-rich cathode materials. The results demonstrated that the electrochemical performance of Ni-rich cathodes is very sensitive to the calcination temperature. The optimum calcination temperature for a typical Ni-rich NMC $\text{LiNi}_{0.76}\text{Mn}_{0.14}\text{Co}_{0.10}\text{O}_2$ cathode was determined to be 750~775°C. This material exhibits a capacity above 160 mAh g^{-1} even at 10C rate and retains ca. 79% of its initial capacity after 200 cycles at C/3 rate. Higher calcination temperature ($\geq 800^\circ\text{C}$) led to inferior long-term cycling stability and rate capability, because of severe microstrain and microcrack formation upon deep lithium ion de/intercalation in the cathodes prepared from material with large primary particle size. The optimum calcination temperature is closely related to the compositions of the Ni-rich cathodes, which need to be carefully considered for the synthesis of other Ni-rich cathode materials in order to achieve optimum electrochemical performance.

The compositions of NMC materials with respect to their Ni, Co, and Mn contents and the effect of charge-cutoff voltage have been systematically optimized to achieve improved electrochemical performance. An initial discharge capacity of more than 200 mAh g^{-1} and capacity retention above 90% after 100 cycles have been achieved for Ni-rich NMCs (including $\text{LiNi}_{0.68}\text{Mn}_{0.22}\text{Co}_{0.10}\text{O}_2$, $\text{LiNi}_{0.62}\text{Mn}_{0.25}\text{Co}_{0.13}\text{O}_2$, and $\text{LiNi}_{0.5}\text{Mn}_{0.3}\text{Co}_{0.2}\text{O}_2$). Although the high-Ni-content $\text{LiNi}_{0.76}\text{Mn}_{0.14}\text{Co}_{0.10}\text{O}_2$ shows slightly faster capacity fading, its discharge capacity is 10% higher than that of the other materials during the early stage of cycling. Considering the high discharge capacity and high energy density of $\text{LiNi}_{0.76}\text{Mn}_{0.14}\text{Co}_{0.10}\text{O}_2$, future research will be focused on improving the cycling stability of $\text{LiNi}_{0.76}\text{Mn}_{0.14}\text{Co}_{0.10}\text{O}_2$ via additional lattice doping, surface modification, and the use of electrolyte additives.

Products

Presentations/Publications/Patents

Publications

1. “Li- and Mn-rich Cathode Materials: Challenges to Commercialization,” Jianming Zheng, Seungjun Myeong, Woongrae Cho, Pengfei Yan, Jie Xiao, Chongmin Wang, Jaephil Cho, and Ji-Guang Zhang, accepted for publication by *Advanced Energy Materials*.
2. Jianming Zheng, Jie Xiao, and Ji-Guang Zhang, “The roles of oxygen non-stoichiometry on the electrochemical properties of oxide-based cathode materials,” *Nano Today*, 2016, doi: 10.1016/j.nantod.2016.08.011.
3. Pengfei Yan, Jianming Zheng, Sarvanan Kuppan, Qiuyan Li, Dongping Lv, Jie Xiao, Guoying Chen, Ji-Guang Zhang and Chong-Min Wang, “Phosphorus Enrichment as a New Composition in the Solid Electrolyte Interphase of High-Voltage Cathodes and Its Effects on Battery Cycling,” *Chem. Mater.*, 2015, 27(21) 7447-7451.
4. P. Yan, J. Zheng, Z. Wang, G. Teng, S. Kuppan, J. Xiao, G. Chen, F. Pan, J.-G. Zhang, C.-M. Wang, “Ni and Co Segregations on Selective Surface Facets and Rational Design of Layered Lithium Transition-Metal Oxide Cathodes,” *Adv. Energy Mater.* 2016, 6(9), 201502455.
5. P. Yan, J. Zheng, X. Zhang, R. Xu, K. Amine, J. Xiao, J.-G. Zhang and C. Wang, “Atomic to Nanoscale Investigation of Functionalities of Al_2O_3 Coating Layer on Cathode for Enhanced Battery Performance,” *Chem. Mater.*, 2016, 28, 857-863.
6. W. Shi, J. Zheng, J. Xiao, X. Chen, B. J. Polzin, and J.-G. Zhang, “The Effect of Entropy and Enthalpy Changes on the Thermal Behavior of Li-Mn-rich Layered Composite Cathode Materials,” *J. Electrochem. Soc.*, 2016, 163, A571-A577.
7. Wei Shi, Jiulin Wang, Jianming Zheng, Jiuchun Jiang, Vilayanur Viswanathan, Ji-Guang Zhang, “Influence of memory effect on the state-of-charge estimation of large format Lithium-ion batteries based on LiFePO_4 cathode,” *J. Power Sources*, 2016, 312, 55-59.

Presentations

1. Jianming Zheng, Pengfei Yan, Jie Xiao, Chongmin Wang, Ji-Guang Zhang, "The effects of synthesis conditions on the performances of Ni-rich $\text{LiNi}_x\text{MnyCozO}_2$ cathode materials for lithium-ion batteries," 18th International Meeting on Lithium Batteries: IMLB 2016, Chicago, Illinois, June 19-24, 2016.
2. Jianming Zheng, Pengfei Yan, Jie Xiao, Mark Engelhard, Chongmin Wang, Ji-Guang Zhang, "Degradation mechanism of $\text{LiNi}_x\text{MnyCozO}_2$ cathodes at high charge-cutoff-voltages in lithium-ion batteries," Pacificchem 2015, Honolulu, HI, USA., December 2015.
3. Ji-Guang Zhang and Jianming Zheng, "Development of High-Energy Cathode Materials," DOE Annual Merit Review Meeting, Washington DC. June 6-10, 2016.

References

1. J. K. Ngala, N. A. Chernova, M. Ma, M. Mamak, P. Y. Zavalij, M. S. Whittingham, "The synthesis, characterization and electrochemical behavior of the layered $\text{LiNi}_{0.4}\text{Mn}_{0.4}\text{Co}_{0.2}\text{O}_2$ compound," *J. Mater. Chem.* 2004, 14, 214-220.
2. N. Yabuuchi, Y. Makimura, T. Ohzuku, "Solid-State Chemistry and Electrochemistry of $\text{LiCo}_{1/3}\text{Ni}_{1/3}\text{Mn}_{1/3}\text{O}_2$ for Advanced Lithium-Ion Batteries: III. Rechargeable Capacity and Cycleability," *J. Electrochem. Soc.* 2007, 154, A314-A321.
3. H.-J. Noh, S. Youn, C. S. Yoon, Y.-K. Sun, "Comparison of the structural and electrochemical properties of layered $\text{Li}[\text{Ni}_x\text{Co}_y\text{Mn}_z]\text{O}_2$ ($x = 1/3, 0.5, 0.6, 0.7, 0.8$ and 0.85) cathode material for lithium-ion batteries," *J. Power Sources* 2013, 233, 121-130.
4. W. Liu, P. Oh, X. Liu, M.-J. Lee, W. Cho, S. Chae, Y. Kim, J. Cho, "Nickel-Rich Layered Lithium Transition-Metal Oxide for High-Energy Lithium-Ion Batteries," *Angew. Chem. Int. Ed.* 2015, 54, 4440-4457.
5. S.-K. Jung, H. Gwon, J. Hong, K.-Y. Park, D.-H. Seo, H. Kim, J. Hyun, W. Yang, K. Kang, "Understanding the Degradation Mechanisms of $\text{LiNi}_{0.5}\text{Co}_{0.2}\text{Mn}_{0.3}\text{O}_2$ Cathode Material in Lithium Ion Batteries," *Adv. Energy Mater.* 2014, 4, 1300787.
6. J.M. Zheng, J. Xiao, and J.-G. Zhang, "The roles of oxygen non-stoichiometry on the electrochemical properties of oxide-based cathode materials," *Nano Today*, 2016, doi: 10.1016/j.nantod.2016.08.011.

V.D.4. *In situ* Solvothermal Synthesis of Novel High-Capacity Cathodes (BNL)

Feng Wang, Principal Investigator

Brookhaven National Laboratory
Sustainable Energy Technologies Department
Upton, NY 11973
Phone: 631-344-4388; Fax: 631-344-7905
E-mail: fwang@bnl.gov

Jianming Bai, Co-Principal Investigator

Brookhaven National Laboratory
National Synchrotron Light Source II
Upton, NY 11973
Phone: 631-344-2583
E-mail: jmbai@bnl.gov

Tien Q. Duong, DOE Program Manager

U.S. Department of Energy
Advanced Battery Materials Research (BMR)
Vehicle Technologies Office
1000 Independence Avenue, SW
Washington, DC 20585
Phone: 202-586-7836
E-mail: Tien.Duong@ee.doe.gov

Start Date: October 1, 2015
End Date: September 30, 2018

Abstract

Objectives

Develop novel high-capacity cathodes through precise control of the phase, stoichiometry and morphology.

Accomplishments

- Developed synthesis procedures for preparing Ni-Co-Mn (NCM) layered oxides.
- Identified the impact of synthesis conditions on the reaction kinetics and pathways for forming layered NCM oxides *via in situ* studies.
- Developed new capabilities for monitoring synthesis parameters (P , T , pH values) in real time during solvothermal synthesis of cathode materials.
- Identify synthetic approaches for stabilizing the layered structure of NCM cathodes.

Future Achievements

- Identify synthetic approach for making stoichiometric Ni-rich Ni-Co-Mn (NCM) layered oxides that deliver high capacity (~ 200 mAh/g).
- Develop new *in situ* synchrotron X-ray and neutron techniques for probing the dynamics of cation ordering in NCM layered oxides under real synthesis conditions.

Technical Discussion

Background

Present-day lithium-ion batteries are incapable of meeting the targeted miles of all-electric-range within the weight and volume constraints. New cathodes with higher energy density are needed for lithium-ion batteries so that they can be widely commercialized for plug-in electric vehicle applications. The effort will focus on increasing energy density (while maintaining the other performance characteristics of current cathodes) using synthesis methods that have the potential to lower cost.

Introduction

Despite considerable interest in developing new cathodes for lithium-ion batteries, only a small number of known materials show real promise for achieving significant improvement in capacity and/or a reduction in cost. The preparation of new compounds or materials with unique properties often relies on trial and error as there are a variety of synthesis parameters (precursor concentration, temperature, pressure, *pH* value, cation type and reaction time) that can have a strong influence on the material properties (crystal structure, morphology, particle size) and electrochemical performance (*e.g.*, capacity, rate capability, and durability). Most solution-based reactions are carried out in a sealed autoclave and therefore the reactor is a black box – the inputs and outputs are known, but little is known about intermediate phases and overall reaction pathways. *In situ*, *real-time* probing of synthesis reactions can provide the details of reactions, elucidating intermediate phases and how temperature, pressure, time and the precursor concentrations affect the reaction pathways. The results of such studies enable strategies to optimize synthesis reactions, particularly the formation of materials of desired phases and properties. With a more fundamental understanding of the correlation between synthesis conditions, crystallization processes, and material properties, a more rational design of advanced lithium electrode materials should emerge.

Approach

Building on the established capabilities for synthesis and characterization of battery materials, we continue to develop synchrotron X-ray, neutron-based *in situ* techniques and apply them to studies of synthesis reactions and involved structural ordering during preparation of high-capacity cathode materials, to gain access to the structural chemistry involving intermediate and short-lived phases. Insights obtained from *in situ* studies will provide knowledge on how the synthesis conditions (temperature, pressure, *pH*, precursor concentration, etc.) affect the kinetics and synthesis reaction pathways. *Ex situ* characterization conducted using synchrotron X-ray, neutron scattering, transmission electron microscopy (TEM), electron energy-loss spectroscopy (EELS) and various electrochemical techniques helps us to gain understanding of how structure, composition, and synthesis affect electrochemical performance. Together, *in situ* studies of synthesis process coupled with *ex situ* characterization of structural/electrochemical properties of the synthesized materials provide a basis for designing and synthesizing phase-pure cathodes of desired structure, stoichiometry and morphology.

Results

Development of New Capabilities for Monitoring Synthesis Parameters For *in situ* X-ray studies of synthesis reactions, several different types of micro-reactors have been developed under this project. Figure V-80a shows one of them, specified for *in situ* solvothermal synthesis, wherein the temperature (*T*) of the solution is precisely controlled and measured, allowing studies of *T* dependence of the kinetics and thermodynamics of reactions. It is also desirable to track other synthesis parameters, particularly pressure (*P*) and *pH* value that usually evolve with time (*t*) and/or *T*, and impact reaction kinetics/pathway; but they are neither measurable nor theoretically predicable due to the complexity of the synthesis reactions. In order to corroborate the results from *in situ* X-ray measurements, an autoclave-based reactor system was developed (Figure V-80b), with multiple meters/gauges to monitor *P*, *T* and *pH* online as synthesis reactions are progressing within the sealed reactor. In one hand, large quantities of materials (in ~ grams) can be synthesized using such a large autoclave reactor (as opposed to micro-reactors) for further electrochemical/structural analysis; on the other hand, the measured parameters from the autoclave reactor, *i.e.* *P* and *pH* and their correlation with *T*, can be used to

estimate the P , pH values in the micron-sized *in situ* reactor when the two types of reactors are set for the same reaction. Thus, the structural evolution during synthesis and its dependence on the full set of parameters (T , P and pH) can now be investigated for mechanistic understanding of the formation of intermediates (*e.g.* tendency towards forming various polymorphs) and the associated kinetic reaction pathways. Such complementary *ex situ/in situ* measurements (using two types of reactors) provide new avenues for synthetic control of the structure and electrochemical properties of cathode materials.

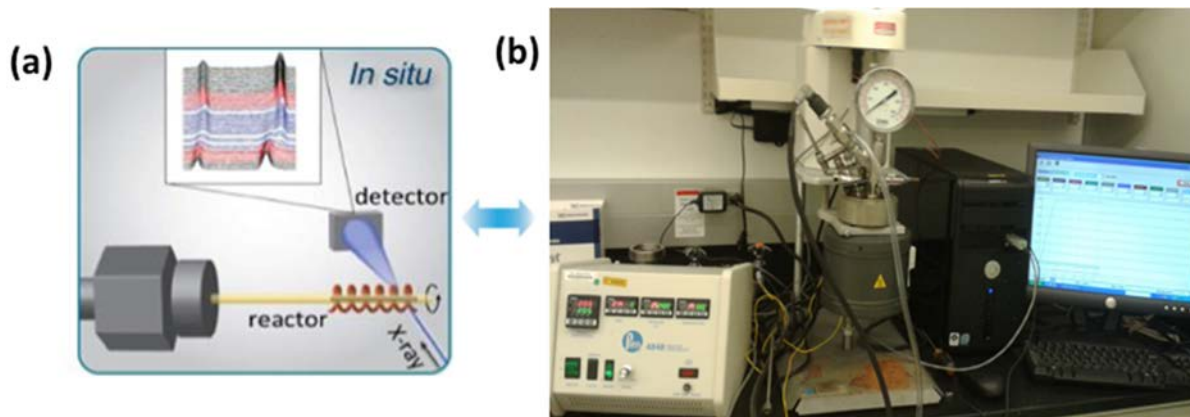


Figure V-80: Setup for *In situ* hydrothermal/solvothermal synthesis. (a) Illustration of a micro-reactor for t and T -resolved X-ray measurements. (b) Photograph of an autoclave-based reactor system, equipped with multiple gauges/meters for monitoring T , P , pH values online

The newly developed autoclave system has been applied to the solvothermal synthesis of Ni-rich layered cathodes under controlled conditions (with well-defined T , P and pH). In Figure V-81a, typical $T(t)$, $P(t)$ curves, both from the hydrothermal and solvothermal synthesis of the precursors of $\text{LiNi}_{0.5}\text{Mn}_{0.5}\text{O}_2$, are given to show how the auto-generated pressure evolved differently in the water vs. ethylene glycol (EG) solvent. During the hydrothermal process, an initial pH value was ~ 9 , and then gradually decreased to ~ 7 by the end of the reaction; in contrast, the pH value remained constant, being around 7 during the solvothermal reaction.

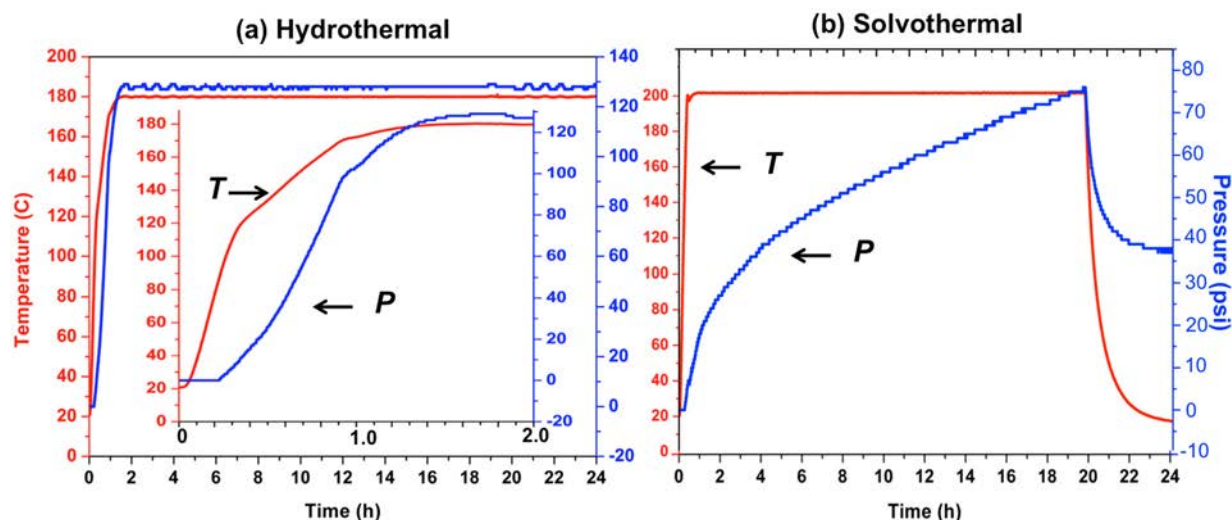


Figure V-81: Evolution of the temperature (T ; red) and pressure (P ; blue) during hydrothermal synthesis (a), and in the ethylene glycol (EG) solvent during solvothermal synthesis (b)

Development of Procedures for Synthesizing Ni-rich Layered Oxides Among NCM-based cathodes (Li-Ni-Co-Mn-O), Ni-rich layered oxides are most interesting for the application in lithium-ion batteries for electric vehicles, due to their high capacity (~ 200 mAh/g) and low cost. However, it is difficult to synthesize highly ordered layered oxides due to cation mixing, one critical issue (among many others) leading to reduced capacity and poor cycling performance of the electrodes. Synthesis procedures, based on a sol-gel process followed by high-temperature calcination, were developed to make $\text{LiNi}_{1-x}\text{M}_x\text{O}_2$ ($M=\text{Co, Mn}$) from lithium

acetate and transition metal acetate hydrates (with certain nominal molar ratios). The synthesis process and impact of synthesis conditions on the structural and electrochemical properties of the final phases were explored, using a combination of thermogravimetric analysis (TGA), X-ray/neutron diffraction and electrochemical measurements; some of the results were provided in Figure V-82. Clearly, when heated in the air the TGA response of the precursors for $\text{LiNi}_{0.8}\text{Co}_{0.2}\text{O}_2$ is different than that under highly oxidizing environment, e.g., under O_2 flow, which is better seen in a close view at the temperature range of 700-950°C (inset in Figure V-82): a continuous mass loss (indicated by sloped profile in the TGA curve) occurs in the air, in contrast to the flat plateau under O_2 flow -- indicating the probability of stabilizing a layered phase with subtle structural changes and weight loss. While heat treatment at too high temperature (above 800°C) leads to degradation of the layered structure, as indicated by the reduced ratio of the integrated intensity of diffraction peaks, (003) and (104), namely $R = I(003)/I(104)$ in Figure V-82b.

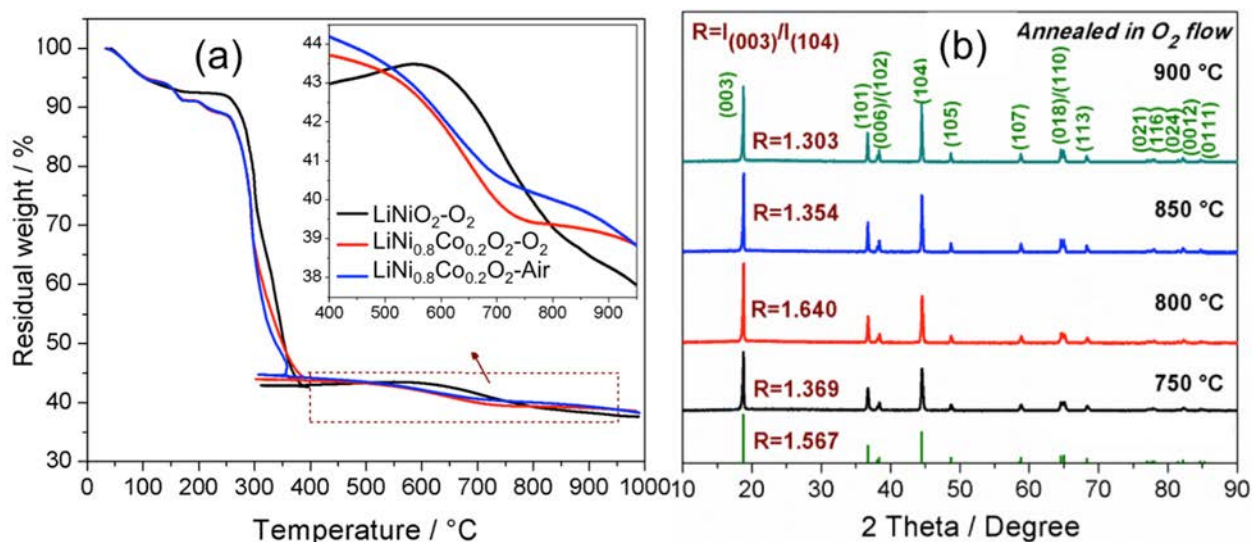


Figure V-82: Structural evolution in the intermediates with temperature during solid-state synthesis of Ni-rich layered oxides. (a) TGA curves of the precursors for synthesizing LiNiO_2 in O_2 flow (black line), $\text{LiNi}_{0.8}\text{Co}_{0.2}\text{O}_2$ in O_2 flow (red), $\text{LiNi}_{0.8}\text{Co}_{0.2}\text{O}_2$ in the air (blue). (b) XRD patterns of $\text{LiNi}_{0.8}\text{Co}_{0.2}\text{O}_2$ prepared at different sintering temperatures in O_2 flow

In situ Studies of Synthesis Reactions in Preparing Ni-rich Layered Oxides In order to better understand the impact of synthesis conditions on the reaction kinetics and pathways towards ordered layer oxides, *in situ* XRD studies were conducted on synthesis reactions in preparing LiNiO_2 and $\text{LiNi}_{0.8}\text{Co}_{0.2}\text{O}_2$ under pure O_2 environment. Some results from studying the $\text{LiNi}_{0.8}\text{Co}_{0.2}\text{O}_2$ system are given in Figure V-83. *In situ* XRD patterns were also recorded during synthesis of LiNiO_2 (not shown here), with a similar trend of phase evolution during synthesis of $\text{LiNi}_{0.8}\text{Co}_{0.2}\text{O}_2$; nevertheless, there is a subtle but distinguishable difference, indicating a different cationic ordering process towards forming the layered structure. At the initial stage of precursor decomposition during synthesis of $\text{LiNi}_{0.8}\text{Co}_{0.2}\text{O}_2$, no separated rock-salt phases of NiO , or CoO (or spinel Co_2O_3) were found but instead a solid solution $\text{Ni}(\text{Co})\text{O}$ was formed at low temperatures. Interestingly, a low-temperature layered phase, with lattice parameter close to that of LiCoO_2 , was found at a temperature as low as 500°C. It is likely that a Co-rich layered phase (containing Ni in a low concentration) has formed as a result of local segregation of Li^+ and Co^{3+} in octahedral sites since the two have large difference of their ionic radii (0.76 vs. 0.54 Å). The nucleation of this layered phase appears to be beneficial to the initial formation of Li-deficient layered phase. The crystal structure of the intermediates, and evolution towards the final product, were directly obtained from the changes in the diffraction patterns, e.g., changes in the intensity of (003) reflection, the splitting of (006)/(012) and (018)/(110) doublets. In Figure V-83b, the structural ordering of layered oxides is demonstrated by intensity evolution of the (003) reflection, or the ratio of the integrated intensity $R = I(003)/I(104)$ since the reflection from (104) planes is independent of the ordering. The maximum value of the ratio R is 1.29 in $\text{LiNi}_{0.8}\text{Co}_{0.2}\text{O}_2$, much higher than the value (0.92) found for LiNiO_2 , indicating a significant enhancement of structural ordering of the layered Ni-rich oxide due to Co substitution. In comparison to the rapid degradation of $\text{LiNi}_{0.8}\text{O}_2$ at high temperatures, $\text{LiNi}_{0.8}\text{Co}_{0.2}\text{O}_2$ can retain the layered structure up to 950°C, without transition to the rock-salt phase until 975°C, showing the remarkable enhancement of thermal stability by Co substitution.

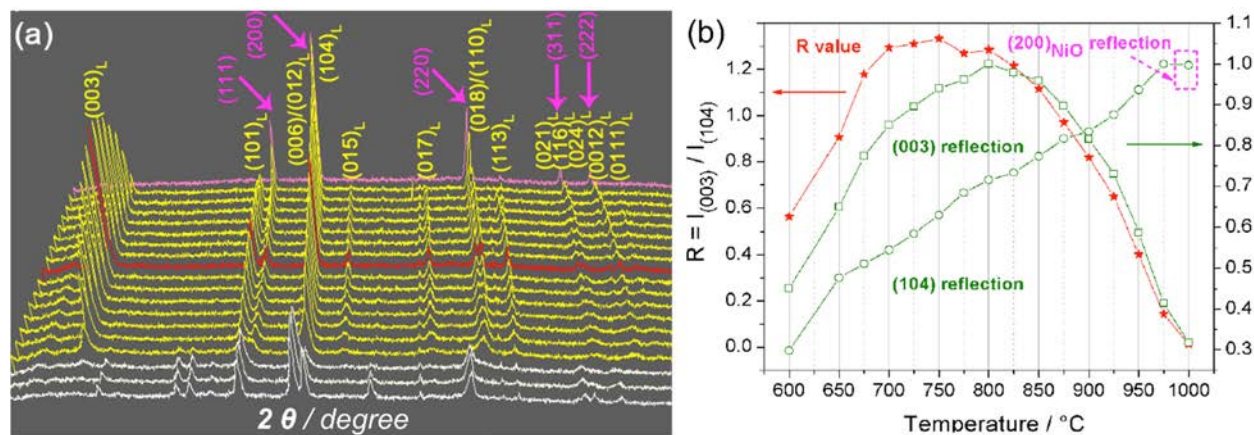


Figure V-83: Real time tracking of structural evolution in the intermediates during solid-state synthesis of Ni-rich layered oxides in O₂ flow. (a) *In situ* XRD patterns recorded during synthesis of LiNi_{0.8}Co_{0.2}O₂. (b) Evolution of the intensity of (003) and (104) reflections and the ratio of the two, $R = I_{(003)}/I_{(104)}$

Identifying the Evolution of Cationic Ordering in LiNi_{0.8}Co_{0.2}O₂ with Temperature Quantitative structure analysis *via* Rietveld refinement was made to individual diffraction patterns, to obtain structural information related to the cationic ordering, such as phase concentration, Li occupancy, local bonding, as given in Figure V-84). The results from *in situ* studies along with quantitative structure analysis indicate a direct phase transition from rock salt to the layered phase, followed by improving the cationic ordering of the layered structure with further lithiation. During the process, Co substitution facilitates the nucleation of a Co-rich layered phase at low temperatures and subsequent growth and stabilization of solid solution Li(Ni, Co)O₂ upon heat treatment. In addition, Co substitution considerably enhances the structural stability of Ni-rich layered oxides, resulting in retention of the layered structure of LiNi_{0.8}Co_{0.2}O₂ at high temperatures (up to 975 °C). The results indicated that the best ordered layered structure should be formed at around 800 °C.

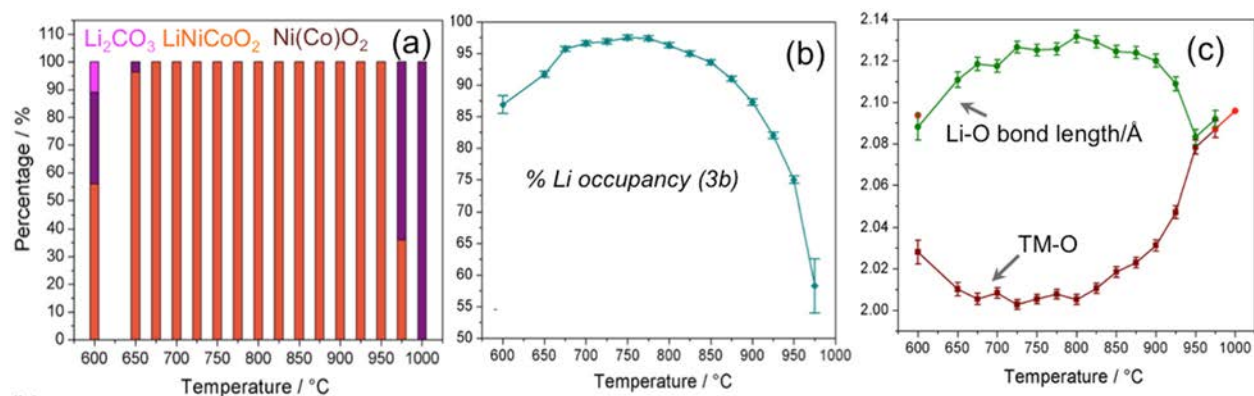


Figure V-84: Evolution of the involved phases, and structural ordering of LiNi_{0.8}Co_{0.2}O₂ with temperature during heat treatment in O₂ flow. a) Concentration of the involved phases, Ni(Co)O, Li₂CO₃, and LiNi_{0.8}Co_{0.2}O₂. b) Lithium occupancy at 3b sites (Li sites). c) Ni-O and Li-O bond lengths. Lines were used as a guide to the eye

Identifying the Evolution of Structural Ordering in LiNi_{0.8}Co_{0.2}O₂ with Time Further studies were made on the evolution of cationic ordering in LiNi_{0.8}Co_{0.2}O₂ with sintering time during heat treatment at 800 °C in O₂ flow, via combined TGA, scanning electron microscopy (SEM) and neutron powder diffraction (NPD) measurements. Some of the results are given in Figure V-85. As indicated in the TGA curve, a dynamically complex structural (dis)ordering process occurs during synthesis of LiNi_{0.8}Co_{0.2}O₂ due to the competition between cationic ordering with Li incorporation, and disordering arising from Li/O loss during heat treatment. As is evident, kinetic control of the cationic ordering is important to achieving high stoichiometry in LiNi_{0.8}Co_{0.2}O₂. According to the refinement of the NPD patterns, high structural ordering in LiNi_{0.8}Co_{0.2}O₂, with 98.0% Li occupancy at 3b sites, was achieved by heat treatment at 800 °C in O₂ flow for 5 hours.

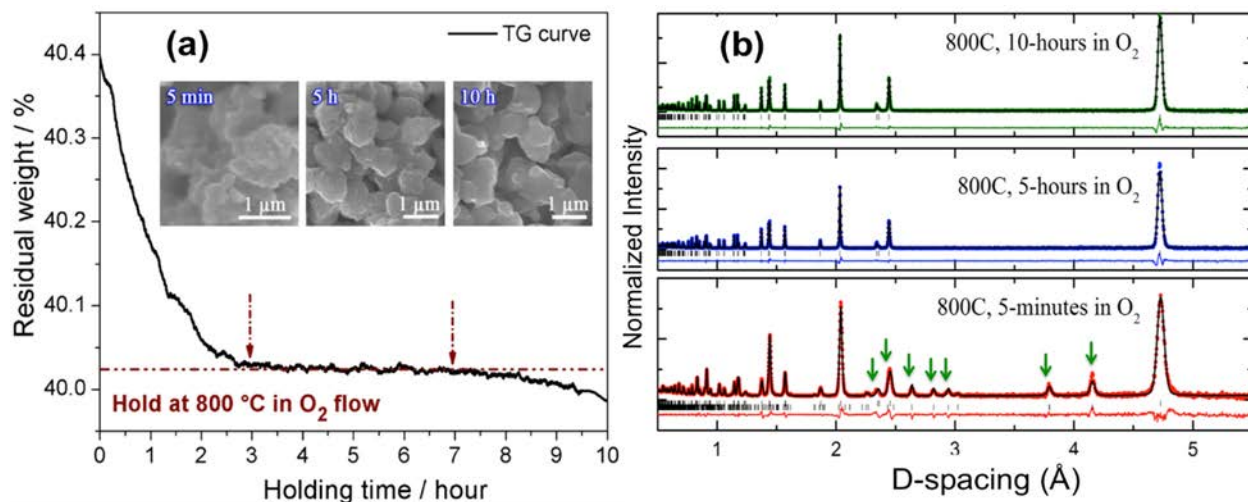


Figure V-85: Structural evolution of $\text{LiNi}_{0.8}\text{Co}_{0.2}\text{O}_2$ with time during sintering at 800°C in O_2 flow. (a) TGA curve during heat treatment, and SEM images from the samples after 5 min, 5 h and 10 h heat treatment (inset). (b) NPD patterns with Rietveld refinements from the samples prepared with different sintering time. The peaks associated with residual Li_2CO_3 were indicated by green arrows (bottom panel)

Structural Analysis of the Synthesized Layered Oxides $\text{LiNi}_{0.8}\text{Co}_{0.2}\text{O}_2$ powder was synthesized under the optimal condition (at 800°C in O_2 flow for 5 hours), as determined via *in situ* XRD measurements, and its structure was also examined using high resolution synchrotron XRD, along with Rietveld refinement (Figure V-86). Consistent with NPD measurements, the result shows high cationic ordering (98.0%), with desired occupation of Li ions and Ni/Co cation within the lithium and transition metal layers respectively, in contrast to the low cationic ordering in the synthesized LiNiO_2 under optimal condition (at 750°C in O_2 flow for 5 h), of about 96.5% (not shown here).

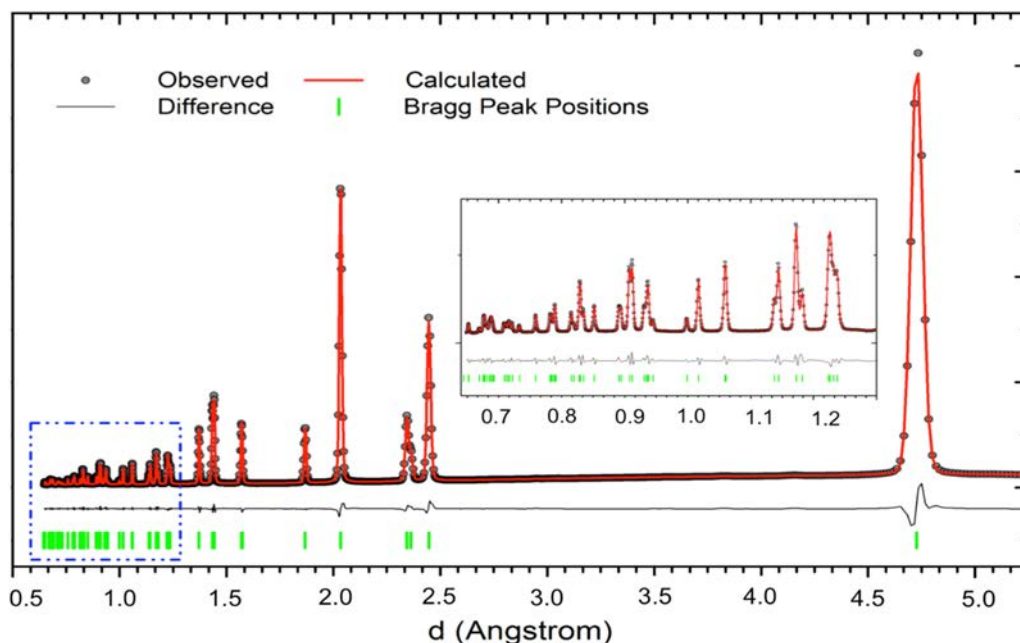


Figure V-86: Structural analysis of $\text{LiNi}_{0.8}\text{Co}_{0.2}\text{O}_2$ powder synthesized under optimized conditions (at 800°C in O_2 flow for 5 h), via synchrotron X-ray diffraction, in comparison to the calculated patterns by Rietveld refinement

Local structural/chemical analysis was also conducted on individual particles of the synthesized $\text{LiNi}_{0.8}\text{Co}_{0.2}\text{O}_2$, using TEM/STEM, EELS and electron diffraction, indicating highly ordered layer structure in the bulk, coated with a thin layer of rock-salt phase on the surface (Figure V-87).

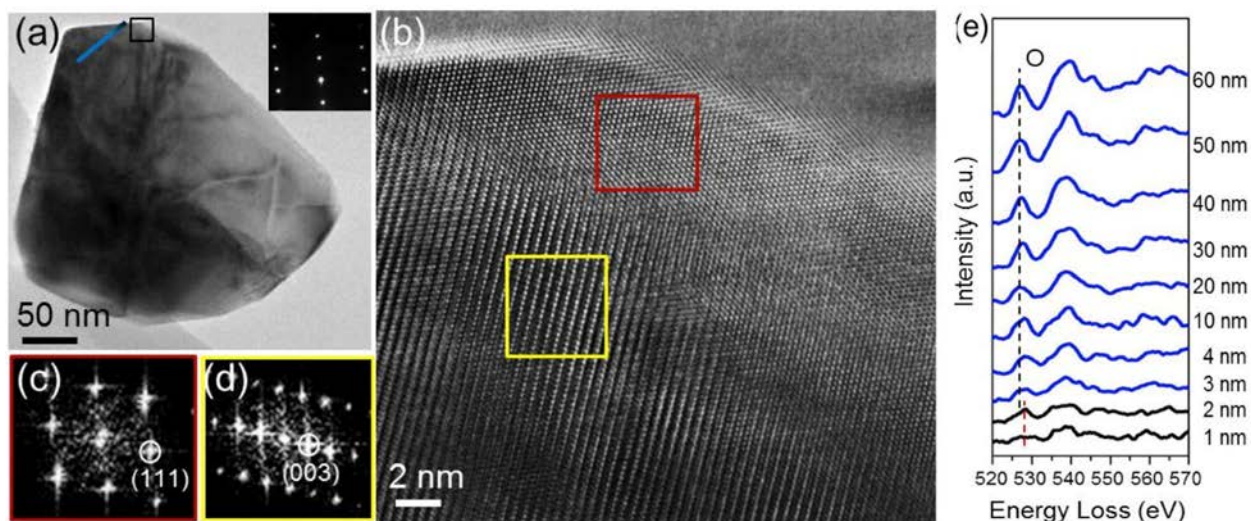


Figure V-87: Local structural/chemical analysis of individual $\text{LiNi}_{0.8}\text{Co}_{0.2}\text{O}_2$ particles. (a) A bright-field TEM image showing the typical morphology of $\text{LiNi}_{0.8}\text{Co}_{0.2}\text{O}_2$ particles, and the single-crystalline layered structure identified by selected area electron diffraction (from the whole particle; inset). (b) A HRTEM image obtained from the local region marked by black box in (a). (c, d) Fast Fourier transformation (FFT) patterns obtained from two local areas marked by red and yellow boxes in (b), indicating the different structure of surface area (rock-salt) than that of the bulk (layered). (e) EELS spectra of O K-edge recorded along the blue line in (a). The spectra generated from the surface region were drawn in black color, while the ones from the bulk region in blue color, showing formation of a thin layer of surface rock salt (~ 2 nm)

Electrochemical Characterization of the Synthesized Layered Oxides Figure V-88 shows the electrochemical performances of the electrodes made from the samples of $\text{LiNi}_{0.8}\text{Co}_{0.2}\text{O}_2$ synthesized at 800°C in O_2 flow for 5 hours ($\text{LiNi}_{0.8}\text{Co}_{0.2}\text{O}_2$ -800- O_2 -5h) in comparison to $\text{LiNi}_{0.8}\text{Co}_{0.2}\text{O}_2$ synthesized in the air at an optimal temperature of 900°C for 20 hours (marked as $\text{LiNi}_{0.8}\text{Co}_{0.2}\text{O}_2$ -900-A-20h), as well as LiNiO_2 (LiNiO_2 - O_2 -5h). The electrodes made from $\text{LiNi}_{0.8}\text{Co}_{0.2}\text{O}_2$ -800- O_2 -5h exhibited an initial capacity of ~ 180 mAh/g and 85% retention after 50 cycles under a moderate cycling condition (0.1 C rate; 2.7-4.3 V window), in contrast to poor cycling stability in LiNiO_2 and low capacity in $\text{LiNi}_{0.8}\text{Co}_{0.2}\text{O}_2$ synthesized in the air. When the $\text{LiNi}_{0.8}\text{Co}_{0.2}\text{O}_2$ electrode was cycled in extended voltage range, between 2.7-4.6 V, much higher capacity (>200 mAh/g) was achieved although the capacity retention is sacrificed somehow (compared to that cycled between 2.7-4.3 V).

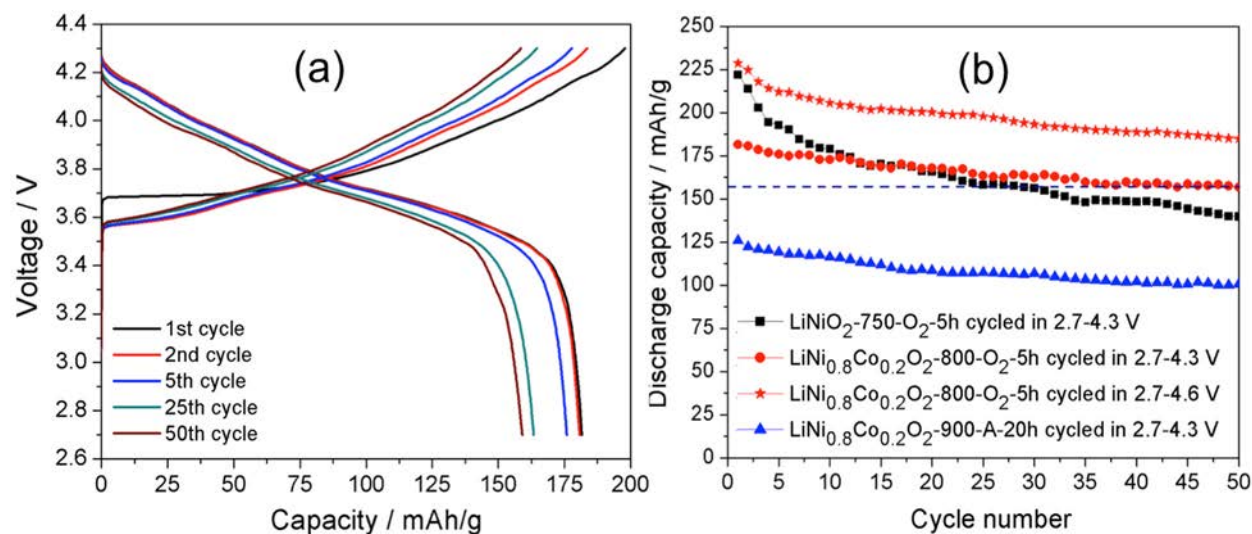


Figure V-88: Electrochemical performance of LiNiO_2 and $\text{LiNi}_{0.8}\text{Co}_{0.2}\text{O}_2$ synthesized under different conditions. (a) Voltage profiles of $\text{LiNi}_{0.8}\text{Co}_{0.2}\text{O}_2$ during charge/discharge at 0.1 C in the voltage range of 2.7–4.3 V (sample: $\text{LiNi}_{0.8}\text{Co}_{0.2}\text{O}_2$ -800- O_2 -5h, synthesized in O_2 , at 800°C for 5 h). (b) Cycling performance of the three samples, LiNiO_2 -750- O_2 -5h, $\text{LiNi}_{0.8}\text{Co}_{0.2}\text{O}_2$ -800- O_2 -5h, and $\text{LiNi}_{0.8}\text{Co}_{0.2}\text{O}_2$ -900-A-20 h at 0.1 C in the voltage range of 2.7–4.3 V, along with the performance of $\text{LiNi}_{0.8}\text{Co}_{0.2}\text{O}_2$ -800- O_2 -5 h in the voltage range of 2.7–4.6 V, demonstrating achievable higher capacity in the extended voltage range

In situ Synthetic Control of Structural/Electrochemical Properties of Layered Oxides As illustrated in Figure V-89, structural evolution of the intermediates (on the top panel), Li and Ni(Co) slab distances evolve with temperature (bottom panel) were extracted from *in situ* XRD measurements. The information may be used as guidance for synthetic control of the electrochemical properties of the electrode materials. For example, even a slight change in Li slab distance (*i.e.*, 4%) may cause considerable change in the activation energy for Li immigration (by more than 200%; or a few orders of magnitude reduction in Li diffusivity). Therefore, in order to meet the demands on high electrochemical activity of the layered oxides, precise control of the Li slab distance is needed and may be realized *via* fine-tuning the synthesis conditions, temperature in particular. The plot suggests that $\text{LiNi}_{0.8}\text{Co}_{0.2}\text{O}_2$ should be synthesized at the temperature range 750-850°C to maximize Li slab distance; in the materials synthesized at temperatures below or above the range, the slab distance is much reduced, so suppressing Li diffusivity, and resulting in sluggish Li intercalation kinetics of the synthesized materials. Another relevant parameter is Ni(Co) slab distance, which, despite its much smaller effect on Li mobility, is an important indicator of the oxidation state of Ni(Co) and very relevant to the specific capacity and redox potential of the synthesized materials.

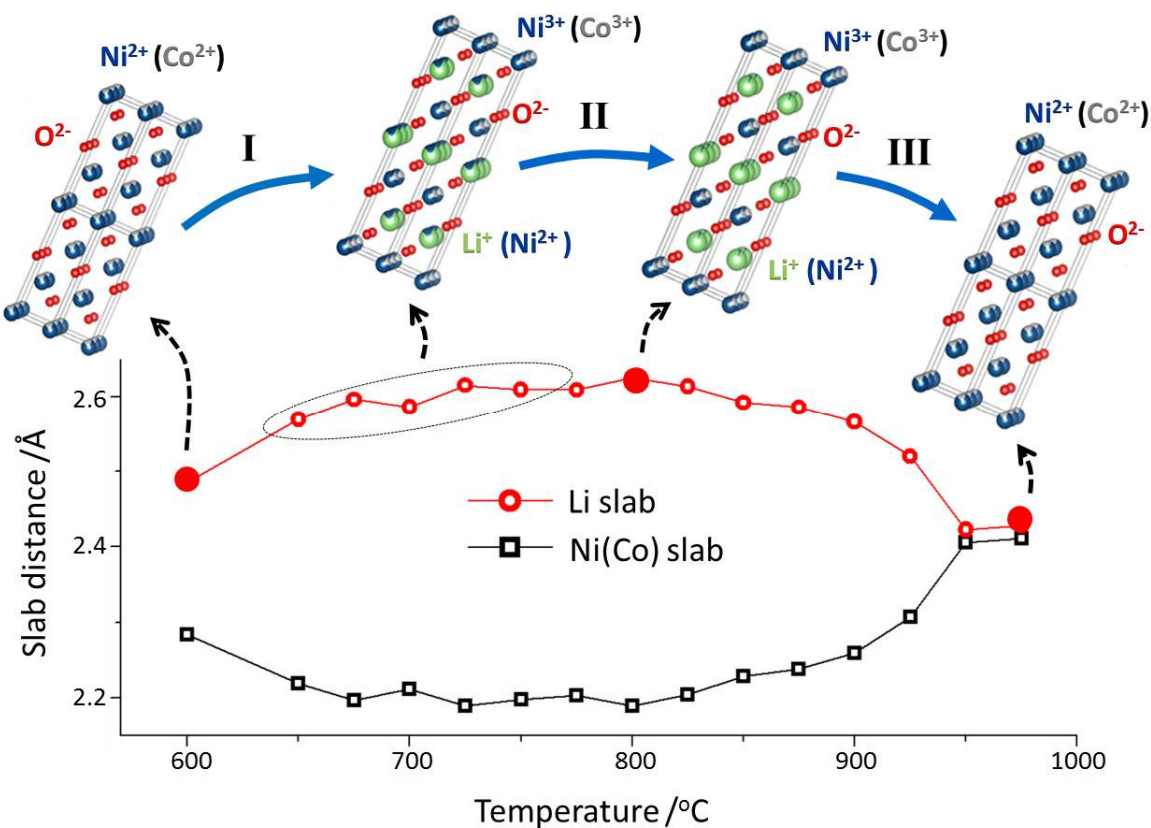


Figure V-89: Schematic illustration of the phase evolution and cationic ordering of the intermediates towards the final $\text{LiNi}_{0.8}\text{Co}_{0.2}\text{O}_2$ as a function of temperature (top), and the corresponding Li and Ni(Co) slab distances (bottom) during heat treatment

In situ Studies of Synthesis Reactions in Preparing $\text{LiNi}_{0.7}\text{Co}_{0.15}\text{Mn}_{0.15}\text{O}_2$ In a recent effort, time-resolved *in situ* high-energy X-ray diffraction (HEXRD) studies were conducted on the synthesis reactions in preparing quaternary system, $\text{LiNi}_{0.7}\text{Co}_{0.15}\text{Mn}_{0.15}\text{O}_2$ (NCM71515), to track the cationic ordering and corresponding kinetics during the synthesis process. Some of the results are given in Figure V-90, revealing a dynamically competing cationic ordering/disordering process, coupled with cationic oxidation and Li/O loss during heat treatment. Through kinetic control of the cationic ordering, highly ordered NCM71515 was synthesized in the air at a wide temperature range. Results from detailed structural and electrochemical characterization will be reported in the future.

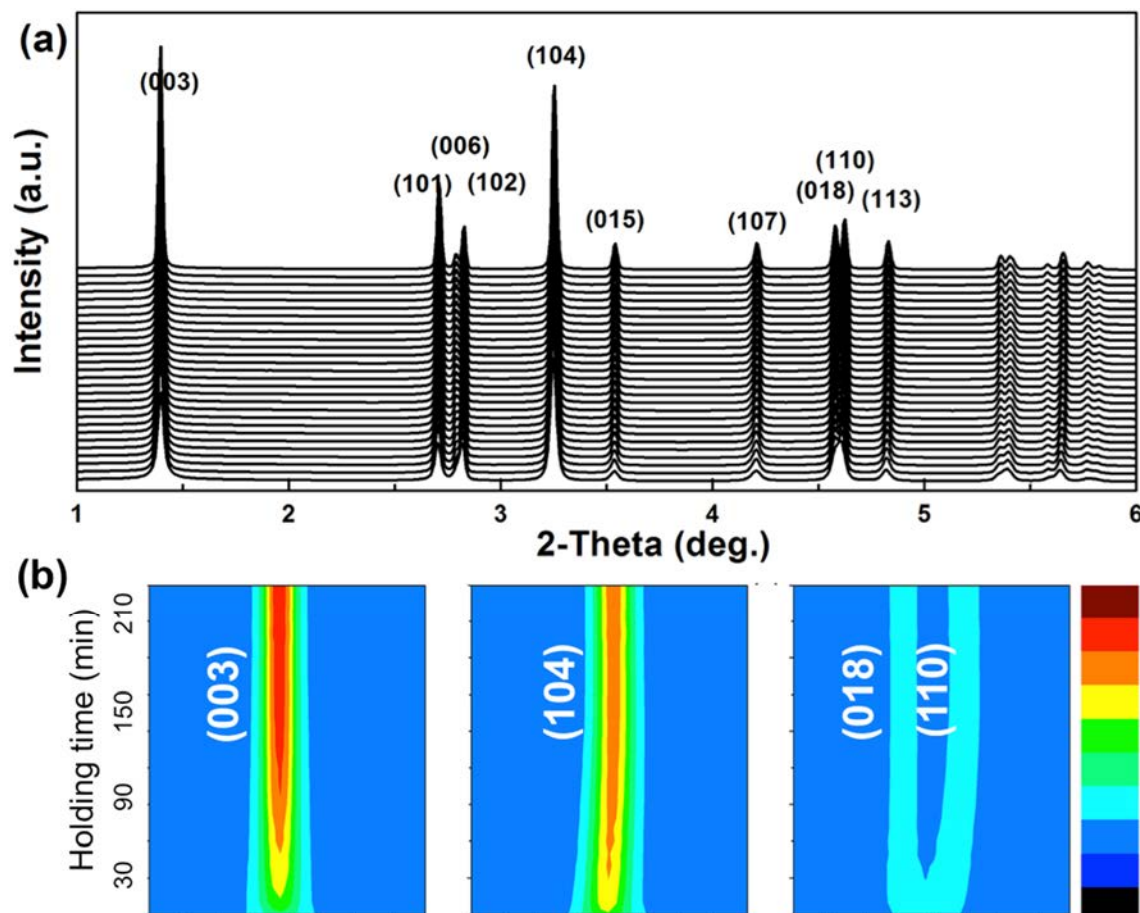


Figure V-90: *In-situ* tracking structural evolution of the intermediates during solid-state synthesis of $\text{LiNi}_{0.7}\text{Co}_{0.15}\text{Mn}_{0.15}\text{O}_2$ (NCM71515). (a) Time-resolved *in-situ* high-energy XRD (HEXRD) patterns recorded at 800 °C. (b) Contour plots in the selected angle regions containing (003), (104), (018), (110) reflections

Conclusions

New capabilities were developed under this project, enabling *real time* monitoring of synthesis parameters (P , T , pH values) during solvothermal synthesis. The structural evolution during synthesis and its dependence on the full set of parameters (T , P and pH) can now be investigated for mechanistic understanding of the formation of intermediates and the associated kinetic reaction pathways, providing new avenues for synthetic control of the structure and electrochemical properties of cathode materials.

A comprehensive investigation was made on the impact of synthesis conditions to the structural ordering and correlated electrochemical properties of Ni-rich layered oxide cathodes, via *in situ* X-ray diffraction, combined with TGA, NPD, (S)TEM-EELS and electrochemical measurements. Results from this study revealed a direct transformation of the intermediate from rock salt structure into a hexagonal phase, and during the process, Co substitution facilitates the nucleation of a Co-rich layered phase at low temperatures and subsequent growth and stabilization of solid solution $\text{Li}(\text{Ni}, \text{Co})\text{O}_2$ upon further heat treatment. Optimal conditions are identified from the *in situ* studies and utilized to obtain stoichiometric $\text{LiNi}_{0.8}\text{Co}_{0.2}\text{O}_2$ that exhibits high capacity (up to 200 mAh/g). The findings shed light on designing high performance Ni-rich layered oxide cathodes through synthetic control of the structural ordering in the materials, broadly in various NCM (*i.e.*, Li–Ni–Co(Mn)–O) materials. Some of the issues of $\text{LiNi}_{0.8}\text{Co}_{0.2}\text{O}_2$ for practical applications, such as cycling instability, may be alleviated by Mn substitution, which, however, introduces equivalent Ni^{2+} into the layered structure, and so may induce the undesirable $\text{Li}^+/\text{Ni}^{2+}$ cation mixing. In the future, *in situ* studies will be conducted on the synthesis processes in preparing Mn substituted NCM cathodes, thereby gaining synthetic control of their structure and electrochemical properties.

Products

Presentations/Publications/Patents

1. J. Zhao, J. Bai, and F. Wang, *Structure Stabilization of Ni-rich Layered Oxides as High-Energy Cathodes for Lithium-Ion Batteries*, **MRS 2016 fall meeting**, Nov. 29-Dec. 4, 2015, Boston, Massachusetts (oral).
2. J. Bai, L. Wang, Y-U. Park, W. Zhang, J.P. Looney, F. Wang, *in situ Solvothermal Synthesis of High-Energy Cathodes for Lithium-ion Batteries*, **MRS 2016 fall meeting**, Nov. 29-Dec. 4, 2015, Boston, Massachusetts (oral).
3. F. Wang, *Ternary Metal Fluorides as High-Energy Cathodes for Rechargeable Lithium Batteries*, **33rd Annual International Battery Seminar & Exhibits**, Fort Lauderdale, Florida, March 21-23, 2016 (invited).
4. F. Wang, Rational Design and Synthesis of New Battery Materials via *in situ* Studies, **Pacificchem 2015**, Honolulu, Hawaii, Dec. 15-20, 2015 (invited).
5. J. Bai, J. Zhao, A. Huq, W. Zhang, D. Wang, and F. Wang, *In situ* Tracking of the Structure Chemistry during the Synthesis of Ni-rich Layered Oxides as High-Energy Cathodes for Lithium-Ion Batteries, **IMLB 16**, Chicago, June 19-24, 2016.
6. F. Wang, S-W. Kim, D-H. Seo, K. Kang, L. Wang, D. Su, J. Vajo, J. Wang, J. Graetz, *Cu-Based Ternary Fluorides As High-Energy Cathodes for Rechargeable Lithium Batteries*, **IMLB 16**, Chicago, June 19-24, 2016.
7. F. Wang, *Designing Electrodes and Interfaces for Batteries: Insights from in situ Studies of Model Systems*, **Munich Battery Discussions 2016**, Electrode-Electrolyte Interface (EEI): from fundamentals to cell manufacturing, Garching, Germany, March, 14-15 2016 (Invited).
8. F. Wang, *Insights into Designing Electrodes and Interfaces for Lithium-ion Batteries from in situ Studies*, **XXV International Materials Research Congress (IMRC 2016)**, Cancun, Mexico, August 16-20, 2016.
9. J. Xu, F. Lin, D. Nordlund, E.J. Crumlin, F. Wang, J. Bai, M.M. Doeff, W. Tong, *Elucidation of the Surface Characteristics and Electrochemistry of High-Performance LiNiO₂*, **Chem. Commun.** 52, 4239 (2016).
10. H.D. Yoo, Y. Li, Y. Liang, Y. Lan, F. Wang, Y. Yao, Intercalation Pseudocapacitance of Exfoliated Molybdenum Disulphide for Ultrafast Energy Storage, **ChemNanoMat**. (accepted).
11. J. Zhao, W. Zhang, A. Huq, S.T. Mixture, B. Zhang, S. Guo, L. Wu, Y. Zhu, Z. Chen, K. Amine, F. Pan, J. Bai, F. Wang, *In situ Probing and Synthetic Control of Cationic Ordering in Ni-rich Layered Oxide Cathodes*, **Adv. Energy Mater.** 1601266, 2016 (in press).
12. F. Wang, X. Wang, J. Graetz, P. Khalifah, Nanostructured Copper Vanadium Oxides as High-Capacity Cathodes for Lithium-ion Batteries, **US patent** (filed in Sept. 2016).

V.D.5. Novel Cathode Materials and Processing Methods (ANL)

Michael M. Thackeray, Principal Investigator

Jason R. Croy, Co-Principal Investigator

Argonne National Laboratory

9700 South Cass Avenue

Lemont, IL 60439

Phone: 630-252-9184; Fax: 630-252-252-4176

E-mail: thackeray@anl.gov; croy@anl.gov

Tien Q. Duong, DOE Program Manager

U.S. Department of Energy

Advanced Battery Materials Research (BMR)

Vehicle Technologies Office

1000 Independence Avenue, SW

Washington, DC 20585

Phone: 202-586-7836

E-mail: Tien.Duong@ee.doe.gov

Start Date: October 1, 2015

End Date: September 30, 2018

Abstract

Objectives

- The primary objective of this project is to develop low-cost, high-energy and high-power Mn-oxide-based cathodes for lithium-ion batteries that will meet the performance requirements of PHEV and EV vehicles.
- A key goal is to improve the design, composition and performance of advanced electrodes with stable architectures and surfaces, facilitated by an atomic-scale understanding of electrochemical and degradation processes.

Accomplishments

- Systematic exploration of layered-layered-spinel compositional phase space for structural characterization and optimized electrochemical performance.
- Integration of surface spinel phases, as well as unique coating layers, into layered cathodes resulting in significant improvement of high voltage cycling for layered-spinel vs. layered electrodes.
- Identification of an optimized, baseline, layered-layered-spinel composition followed by scaled-up synthesis to the 0.5-1kg level in collaboration with Argonne National Laboratory's Materials Research Engineering Facility (MERF).

Future Achievements

- Complete full-cell testing of scaled-up, baseline layered-layered-spinel electrodes.
- Identify elemental and structural compositions yielding improved performance over the current layered-layered-spinel, baseline system.
- Identify unique materials and synthesis methods that enable cathode-surface modifications leading to improved electrode performance.

Technical Discussion

Background

This project is a comprehensively focused effort to stabilize high-capacity composite ‘layered-layered’ (LL) $x\text{Li}_2\text{MnO}_3 \cdot (1-x)\text{LiMO}_2$ ($M=\text{Mn, Ni, Co}$; $0 < x < 0.5$) electrode structures for lithium-ion batteries. This class of electrodes offers an excellent short-to-medium term opportunity to significantly improve the energy output and abuse tolerance of today’s commercial lithium-ion battery products in order to meet or exceed the 40-mile electric range of PHEVs and longer range EVs. For relatively low values of x ($x < 0.1$), these electrodes typically offer a capacity of 160-170 mAh/g at an average ~ 3.6 V when cycled between 4.3 and 2.5 V. For higher values of x ($0.3 < x < 0.5$), a significantly higher capacity (~ 250 mAh/g) can be accessed from the electrodes when charged to a higher potential (e.g., 4.6 V); however, these high-capacity electrodes suffer from severe structural and electrochemical decay, which has prevented their acceptance and use in commercial products. The project directly addresses the performance limitations of these high-capacity LL electrode structures.

Introduction

Lithium and manganese rich $y[x\text{Li}_2\text{MnO}_3 \cdot (1-x)\text{LiMO}_2] \cdot (1-y)\text{LiM}_2\text{O}_4$ ($M=\text{Mn, Ni, Co}$) “layered-layered-spinel” (LLS) materials have demonstrated improved electrochemical properties compared to their LL counterparts. It is believed that the embedded LiM_2O_4 spinel-like structures, containing transition metals (TMs) in the lithium layers, may act as stabilizing pillars at high states of charge. The strategy of embedding local, spinel-type structures provides a unique opportunity to address the atomic-scale issues associated with lithium-rich cathode materials including voltage fade and hysteresis. In addition, initial irreversible capacity loss, low rate performance, and surface instabilities have also been shown to benefit from integrated spinel domains. This project is an ongoing effort to understand the complex interplay between synthesis, composition, and electrochemical performance of integrated LLS electrode materials. A main outcome of the project will be the transfer of know-how to Argonne’s Materials Engineering Research Facility (MERF) for scale-up of promising electrode compositions and structures, followed by practical demonstration of electrode materials in full-cell, pouch-cell studies through collaborations with Argonne’s Cell Analysis, Modeling, and Prototyping Facility (CAMP).

Approach

The approach taken in this project is to 1) advance the performance of high-capacity, $x\text{Li}_2\text{MnO}_3 \cdot (1-x)\text{LiMO}_2$ electrodes by introducing a spinel component to stabilize the structure and minimize or eradicate the voltage-fade phenomenon; 2) explore processing routes in the laboratory and with MERF to prepare LLS composite electrode materials with acceptable capacity, power, and cycle life; and 3) design effective surface structures to protect the underlying metal oxide particles from the electrolyte and to improve their rate capability when charged at high potentials.

Results

Following the approach of embedding spinel domains in LL electrode materials, a series of model LLS compounds were studied as derived from a base, LL, $0.25\text{Li}_2\text{MnO}_3 \cdot 0.75\text{LiMn}_{0.375}\text{Ni}_{0.375}\text{Co}_{0.25}\text{O}_2$ composition. Precursor materials were synthesized by transition metal (TM) oxalate co-precipitation methods using the requisite proportions of Mn, Ni, and Co; a targeted spinel content, ranging between 0 and 25%, was introduced into the structure of the final electrode product during the firing process by systematically decreasing the Li:TM ratio of the lithium source (Li_2CO_3) and the TM oxalate precursor [1]. Cathode compositions were determined and confirmed using inductively coupled plasma spectroscopy (ICP-OES). Electrodes were cycled electrochemically in lithium half-cells (coin cells) at 30°C . Figure V-91(a) shows X-ray diffraction (XRD) patterns of the electrode series labeled according to the targeted spinel content, x . Peaks corresponding to a cubic phase, that are likely associated with TM ions in the lithium layer, evolve as the Li:TM ratio decreases. Plots of discharge capacities and first-cycle efficiencies (FCE) of the LLS electrodes, as a function of the targeted spinel content (not shown), indicate that the discharge capacity increases with x to reach a maximum

at $x=7.5\%$ with a FCE value close to 90%. Figure V-91(b) shows the variation of the charge/discharge capacity of the targeted $x=7.5\%$ electrode when subjected to an initial activation charge/discharge cycle between 4.6-2.0V and, thereafter, to cycling between 4.45-2.5V (15 mA/g, 30°C); the electrode delivers ~200 mAh/g during the early cycles. Characterization of this electrode system, which includes combined X-ray-diffraction, neutron diffraction, NMR and TEM studies, is in progress. These studies are expected to provide detailed information about atomic configurations in these complex structures and how the structures relate to synthesis parameters and electrochemical properties.

Parallel to the above efforts, studies are being conducted to understand the factors that control the large-scale synthesis of high tap density LLS powders using stirred tank reactors. A metal hydroxide precursor composition was selected to match the TM ratio in the base $0.25\text{Li}_2\text{MnO}_3 \cdot 0.75\text{LiMn}_{0.375}\text{Ni}_{0.375}\text{Co}_{0.25}\text{O}_2$ composition discussed above. Figure V-91(c) shows a SEM image of LLS particles from a ~0.5 kg production batch with a 15% targeted spinel content; they have an attractive tap density of 2.25 g/cc. The XRD patterns of scaled LLS products (not shown) provide evidence, like their oxalate-based counterparts, that a cubic phase is present with clear evidence of a (220) diffraction peak, characteristic of a spinel component for samples with the higher target spinel values.

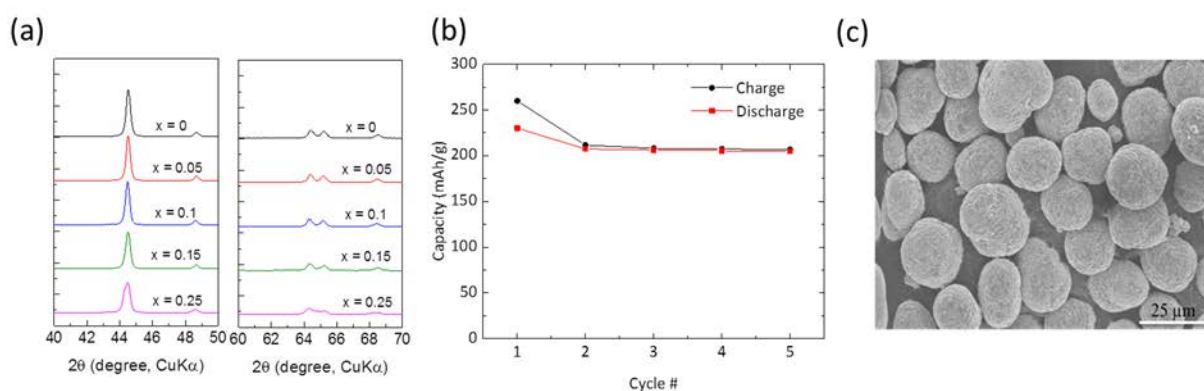


Figure V-91: (a) X-ray diffraction patterns of targeted LLS compositions, (b) Electrochemical properties of a $0.25\text{Li}_2\text{MnO}_3 \cdot 0.75\text{LiMn}_{0.375}\text{Ni}_{0.375}\text{Co}_{0.25}\text{O}_2$ cathode with a 7.5% targeted spinel content (activation: 4.6-2.0 V, subsequent cycles: 4.45-2.5 V), (c) SEM image of LLS powders from a ~0.5 kg scaled batch of metal hydroxide precursors

Past reports have emphasized the strategy of incorporating spinel and/or spinel-type local structures and defects in an attempt to mitigate the above-mentioned degradation mechanisms. Of particular concern is oxygen loss at the surface of particles at high SOCs. Large vacancy concentrations (e.g. Li) coupled with even small amounts of oxygen loss facilitate migration of the TMs that alters the structure of near-surface layers. Because spinel structures are more stable against oxygen loss and TM migration, and can share a compatible oxygen lattice with their layered counterparts, incorporation of a spinel component at the surface of oxide particles may be an attractive strategy to create more robust cathode surfaces. LiCoO_2 (LCO) is a model system for studying surface-related degradation of cathode electrodes because of its well-established electrochemical behavior. Here, the influence of a lithium-rich spinel coating with a targeted composition, $\text{Li}_{1.1}\text{Mn}_{1.9}\text{O}_4$, on the electrochemical properties of LCO was studied.

Figure V-92(a) shows the 1st charge/discharge cycles of a Li/LCO cell before and after wet-chemical treatments of the LCO electrode powder in acidic solutions of Li and Mn nitrates, targeting LCO/spinel concentrations of .95/.05 and .90/.10, followed by firing in air at ~500°C. Clearly observed in the 1st-cycle discharge is a plateau at ~2.7V for the treated samples, consistent with the formation of a spinel-type component at the electrode surface. Figure V-92(b) shows cycling data between 4.6-2.0V for the untreated and treated samples. A significant improvement in cell cycling stability was observed for the spinel-coated electrodes relative to the pure LCO electrode, with the 5% targeted spinel electrode delivering more than 200 mAh/g for 20 cycles. To stabilize the surface of the LCO electrode further, a ~0.5 nm coating of AlW_xF_y was deposited directly on the electrode laminates by atomic layer deposition (ALD); this approach to use W- and F-based coatings has been discussed in earlier reports [2]. Figure V-92(c) shows the capacity vs. cycle plot of the Li/0.95LiCoO₂•0.05Li_{1.1}Mn_{0.9}O₄ cell in which an AlW_xF_y coating had been applied to the cathode laminate. Cells were cycled between 4.5-3.0V at 15 mA/g and 30°C in Li half-cells. Figure V-92(c) shows that these

electrodes delivered an extremely constant capacity (~185 mAh/g) for 50 cycles. The dQ/dV plots, inset in Figure V-92(c), corresponding to cycles 1 and 50 show two distinct reversible redox peaks (starred), characteristic of a LCO electrode at high potentials; the data illustrate the excellent stability and reversibility of the coated, LS, LCO electrodes.

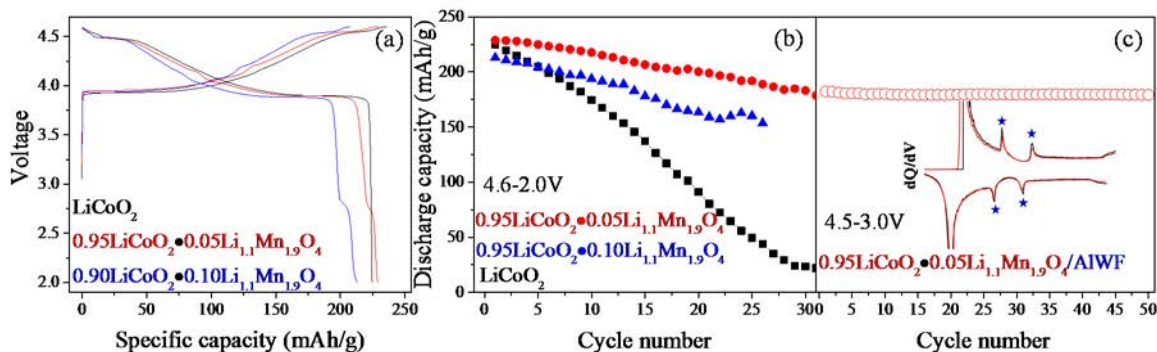


Figure V-92: (a) First-cycle voltage profiles of LiCoO_2 (black), $0.95\text{LiCoO}_2 \cdot 0.05\text{Li}_{1.1}\text{Mn}_{1.9}\text{O}_4$ (red), and $0.90\text{LiCoO}_2 \cdot 0.10\text{Li}_{1.1}\text{Mn}_{1.9}\text{O}_4$ (blue), (b) corresponding capacity vs. cycle data (4.6-2.0 V, 15 mA/g), (c) $0.95\text{LiCoO}_2 \cdot 0.05\text{Li}_{1.1}\text{Mn}_{1.9}\text{O}_4$ coated with $\sim 0.5\text{nm AIW}_x\text{F}_y$ cycled between 4.5-3.0 V. (All data vs. Li/Li^+ at 30°C , 15 mA/g). Inset shows dQ/dV plots of cycles 1 (black) and 50 (red). Stars indicate phase transitions in LCO

The energy and power density of lithium TM oxides is sensitive not only to atomic structure but also to particle morphology and size. This is because particle processing – especially by co-precipitation reactions to form industrially relevant cathode precursors – significantly influences electrode capacities and densities. Due to the importance of co-precipitation parameters on the final cathode specifications, and to demonstrate that LLS materials can be fabricated by existing cathode manufacturing processes, a study on the co-precipitation of hydroxide- and carbonate-based, LLS precursors was undertaken using stirred-tank reactors [3]. The results demonstrate that Mn-rich, LLS cathode powders can be synthesized from hydroxide precursors and that particle density and morphology can be tailored by varying the processing conditions.

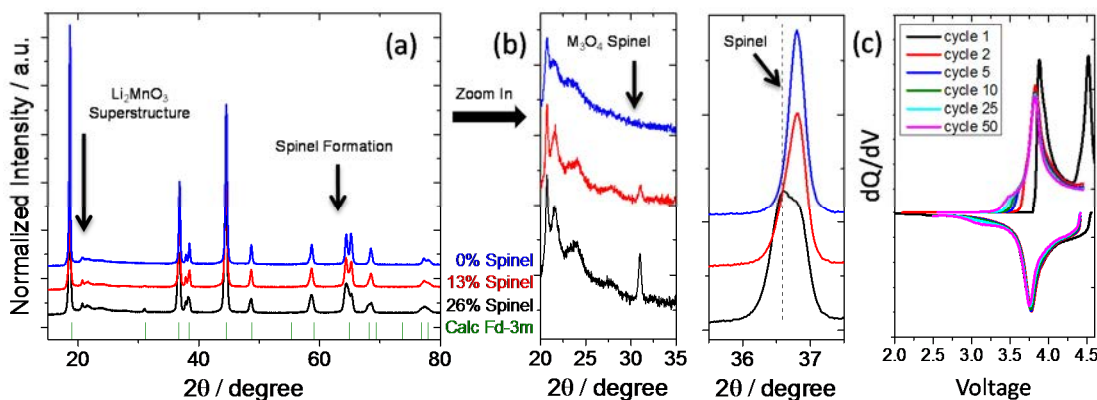


Figure V-93: (a) X-ray diffraction patterns of a $0.25\text{Li}_2\text{MnO}_3 \cdot 0.75\text{LiMn}_{0.375}\text{Ni}_{0.375}\text{Co}_{0.25}\text{O}_2$ LL material (0% spinel) with targeted spinel contents of 13% and 26%. Green bars along the bottom show calculated spinel peaks (Fd-3m symmetry). (b) Enlarged view of the $2\theta = 20\text{-}38^\circ$ region showing the formation of spinel-type phases. (c) dQ/dV plots of the 13% spinel LLS electrode during 50 cycles at 4.45-2.5 V (Li half-cells, 15 $\text{mA}\cdot\text{g}^{-1}$, room temperature)

Figure V-93(a) shows XRD patterns of a series of materials with increasing spinel contents. Clearly visible at $2\theta = \sim 32^\circ$, using a laboratory X-ray source, is the formation of a new peak as the spinel content increases. The position and intensity are consistent with the (220) plane of a cubic (Fd $\bar{3}m$) M_3O_4 spinel, in which M is a TM(s) together with, or excluding lithium, as shown by the calculated XRD pattern ($a = 0.81333\text{ nm}$) in Figure V-93(a). In addition, the peaks broaden at $2\theta = 36.5^\circ$ (Figure V-93(b)) while the doublet at $\sim 65^\circ$ begins to merge as the spinel content increases, indicating the formation of a spinel component. Note that throughout the series, even when the spinel content is 26%, the superstructure peaks from the ordering of Li_2MnO_3 -like

domains ($2\theta = 20\text{-}25^\circ$) are observed, and that the expected “activation” plateau of the first-cycle charge is clearly visible in Figure V-93(c). These electrodes deliver stable capacities of $\sim 180 \text{ mAh}\cdot\text{g}^{-1}$. Their excellent structural stability with cycling is highlighted in the dQ/dV plots of Figure V-93(c) for a LLS structure with a 13% spinel content.

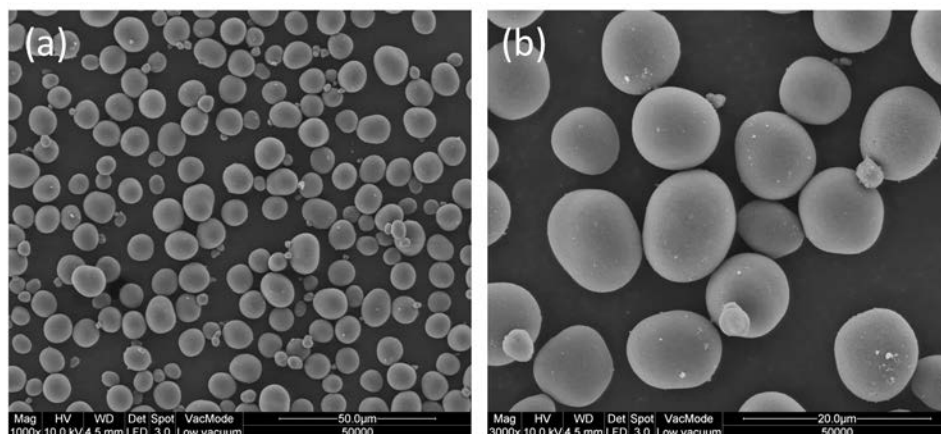


Figure V-94: Low (a) and high (b) magnification SEM images of lithiated LLS cathode powders produced at Argonne’s Materials Engineering Research facility (MERF). Particles deliver $\sim 205 \text{ mAh/g}$ between 4.45-2.50 V (15 mA/g, 30 °C) after a 1st-cycle formation between 4.6-2.0 V (not shown)

Following up on these initial synthesis studies, a baseline composition was chosen for larger-scale synthesis at MERF (ANL). A composition of $0.25\text{Li}_2\text{MnO}_3\cdot 0.75\text{LiMn}_{0.375}\text{Ni}_{0.375}\text{Co}_{0.25}\text{O}_2$, with a targeted $\sim 7\%$ spinel component was scaled to $\sim 1\text{kg}$ in a 20L stirred-tank reactor. Figure V-94(a) and (b) show SEM images of the final, carbonate-based, LLS baseline powders. The particles have an average size of $\sim 10\mu\text{m}$, a tap density of 2.0 g/cc, and deliver $\sim 205 \text{ mAh/g}$ between 4.45-2.50 V vs. Li/Li^+ (15 mA/g, 30°C) after a 1st-cycle formation between 4.6-2.0 V. The high capacities (e.g., $>200 \text{ mAh/g}$ at $<4.4\text{V}$ vs. graphite) delivered by these manganese-rich particles are promising. In addition, ongoing studies are realizing increased tap densities in similar compositions.

In order to better understand the role of composition on the formation and structure property-electrochemical-relationships of NMC-based LLS materials, and to improve on the baseline composition, a compositional study was performed over the region shown (red dots) in the ternary diagram of Figure V-95(a). Data points are labeled by their intended Li:Ni:Mn:Co molar ratios (with Ni+Mn+Co = 1). To ensure reliable and consistent comparisons between the materials, all $[\text{NiMnCo}](\text{OH})_2$ precursors were prepared in a 4L stirred-tank reactor with automated pH control.

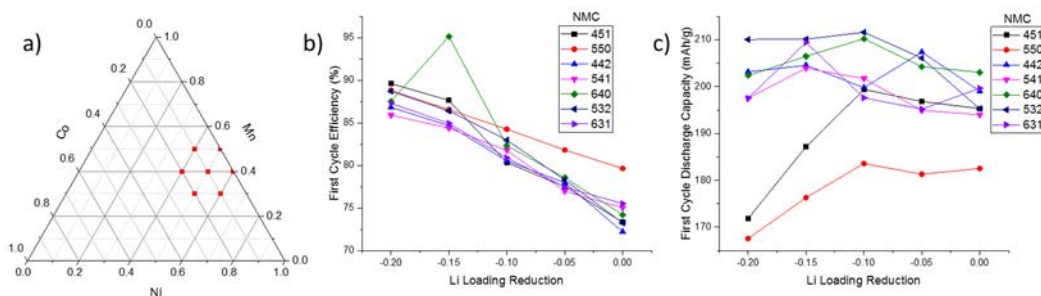


Figure V-95: a) Ternary diagram showing NMC compositions investigated. b) First-cycle efficiency as a function of Li loading compared to the baseline loading (0 on the x axis). c) First-cycle discharge capacity at varied Li loadings for the NMC materials studied

After synthesis of the NMC precursors, the materials were divided and fired with targeted lithium amounts to give the different, nominal Li:NMC ratios. Figure V-95(b) and (c) show the FCE and discharge capacities, respectively, of all materials. A clear trend appears where decreasing the lithium loading resulted in increasing the coulombic efficiency, consistent with prior observations of various other LLS materials synthesized using this method. The improved efficiencies result in better utilization of available capacity at lower lithium loadings.

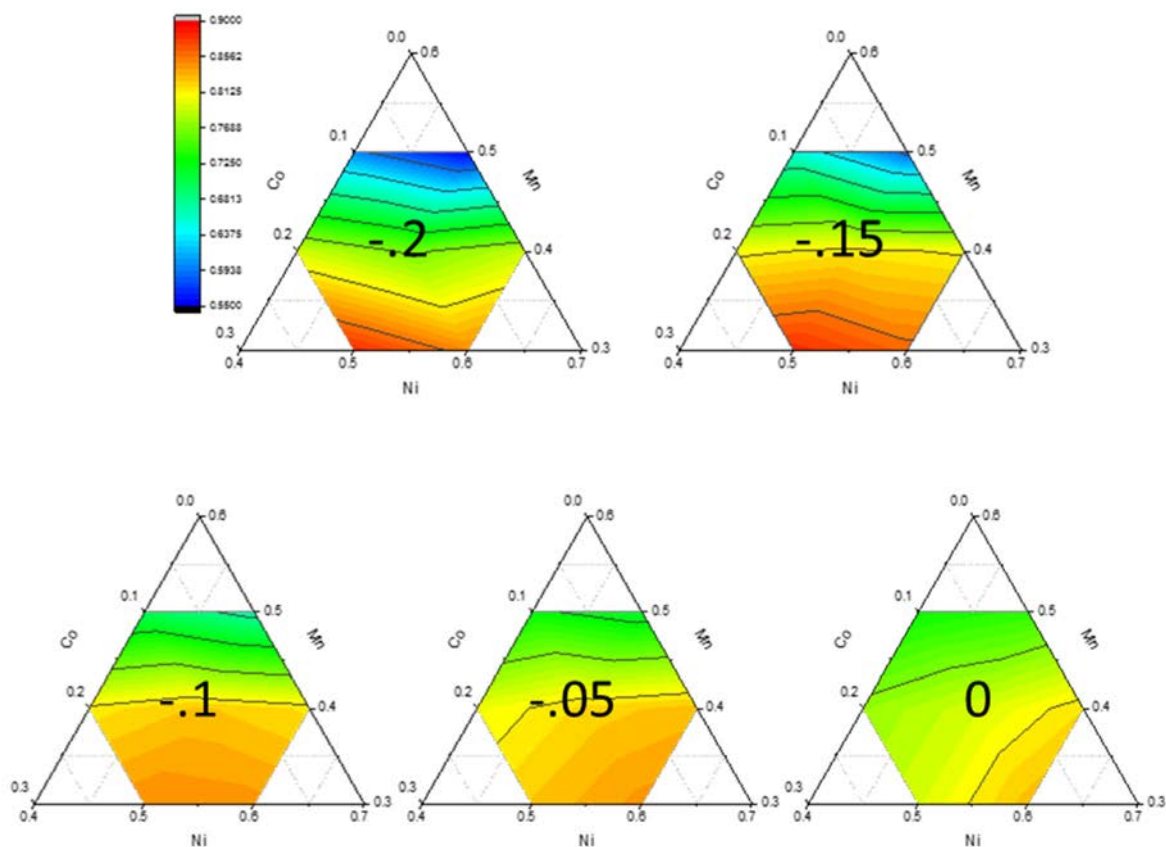


Figure V-96: Ternary contour plot of capacity retention (red=high, blue=low) over the NMC compositions studied. The numbers in the ternary plots denote the reduction of lithium loading from the baseline Li/NMC during synthesis

In Figure V-96, the rate retention of a 300 mA/g discharge cycle, compared to a 15mA/g cycle, is presented for the ternary phase space investigated. Capacity retention during higher rate testing increased at higher Ni loadings in the NMC-based cathodes. As the lithium loading decreases to -0.15 or -0.2 from the baseline loading (0), capacity retention becomes very poor for materials with 50% Mn. These same materials also showed the lowest first-cycle capacities, Figure V-95(c); likely the result of rocksalt-type impurities impeding Li diffusion as was evidenced in XRD data (not shown).

In summary, a systematic phase study of a portion of the NMC ternary space shows electrochemical improvements when a 'layered-layered-spinel' synthesis methodology (targeted lithium loadings) is applied. The large data set (35 samples) is being used to identify compositions of interest, and general electrochemical trends of NMC-based, LLS cathodes

Conclusions

Degradation mechanisms such as voltage fade and hysteresis are controlled by atomic-scale processes in lithium- and manganese-rich electrode materials. In order to combat these mechanisms, they must be addressed at the correct level. A strategy of embedding spinel and spinel-type local structures into lithium- and manganese-rich, LL electrode materials is being followed and has been shown to hold promise. A baseline

LLS composition has been identified and scaled-up to the ~1kg level at Argonne National Laboratory's Materials Engineering Research Facility. These materials can be produced by traditional methods to obtain good morphologies and high tap densities. The baseline composition delivers ~200 mA/g at less than 4.4 vs. graphite and is now being evaluated in full-cell studies. Furthermore, surface modifications, including the incorporation of surface spinel phases, and newly-developed fluoride-based materials, are improving the high-voltage stability of LS and LLS electrodes.

Products

Presentations/Publications/Patents

Presentations

1. J. S. Park, J. R. Croy, B. R. Long, E. Lee, M. M. Thackeray, *Composite "Layered-Layered-Spinel" Electrodes for High Energy Lithium-Ion Batteries*, 228th ECS Meeting, Phoenix, October, 2015.
2. J. S. Park, J. R. Croy, E. Lee, M. M. Thackeray, *Composite "Layered-Layered-Spinel" Electrodes for High Energy Lithium-ion Batteries*, Gordon Research Conference: Batteries, Ventura, CA, February 2016.
3. M. M. Thackeray, *Energy Storage: Challenges and Opportunities in an Evolving Lithium Economy*, IMDEA Energy Institute, Madrid, Spain, 7 March 2016 (Invited).
4. M. M. Thackeray, *Tapping and Taming the Potential of Lithium-Oxygen Electrochemistry*, Metal Air Battery International Congress - MaBIC 16, Santander, Spain, 9 March 2016 (Invited).
5. M. M. Thackeray, *Advances in the Structural Design of Cathodes for High Energy Lithium-ion Cells*, BMW Munich Battery Discussions, Garching, Germany, 14-15 March 2016 (Invited).
6. M. M. Thackeray, *Advances in the Structural Design of Cathodes for High Energy Lithium-ion Cells*, Helmholtz Institute, Ulm, Germany 5 April, 2016 (Invited).
7. M. M. Thackeray, *Advances in the Structural Design of Cathodes for High Energy Lithium-ion Cells*, U.S. Department of Energy – Daimler Battery Workshop, Ulm, Germany 7 April, 2016 (Invited).
8. J. R. Croy, *Challenges of High-Energy Cathode Materials*, BMR Cathode Workshop, Oak Ridge National Laboratory, Oak Ridge, TN, 15 March 2016
9. B. T. Yonemoto, Y. Shin, J. R. Croy, M. M. Thackeray, *Design and Processing of Advanced Lithium-ion Electrode Materials*, 18th International Meeting on Lithium Batteries, Chicago, IL, 20-24, June 2016.
10. M. M. Thackeray and J. R. Croy, *Processing and Characterization of High Capacity Composite Electrode Structures*, ES235, DOE Vehicle Technologies Program Annual Merit Review (Arlington, VA), 5-9, June 2016.
11. J. S. Park, J. R. Croy, E. Lee, J. Blauwkamp, M. M. Thackeray, *Structural, Compositional and Electrochemical Control of Integrated 'Layered-Layered-Spinel' Cathodes*, 18th International Meeting on Lithium Batteries, Chicago, IL, 20-24 June 2016.

Publications

1. J. R. Croy, J. S. Park, Y. Shin, B. T. Yonemoto, M. Balasubramanian, B. R. Long, Y. Ren, and M. M. Thackeray, *Prospects for Spinel-Stabilized, High-Capacity Lithium-Ion Battery Cathodes*, *J. Power Sources*, **334**, 213 (2016).

Patents and Patent Applications

1. M. M. Thackeray and S.-H. Kang, *Surface Protected Lithium Metal Oxide Electrodes*, US Patent 9,306,210 (5 April 2016).
2. M. M. Thackeray, J. R. Croy, B. R. Long, E. Lee, J. S. Park, *Layered-Spinel Electrodes for Lithium Batteries*, US Application 20160190577 (30 June 2016).

References

1. B. R. Long, J. R. Croy, J. S. Park, J. G. Wen, D. J. Miller, and M. M. Thackeray, *J. Electrochem. Soc.*, **161**, 2160 (2014).
2. J.S. Park, A. Mane, J.W. Elam, J.R. Croy, *Chem. Mater.*, **27**, 1917 (2015).
3. J. R. Croy, Joong Sun Park, Youngho Shin, Bryan T. Yonemoto, Mahalingam Balasubramanian, Brandon R. Long, Yang Ren, and Michael M. Thackeray, *J. Power Sources*, **334**, 213 (2016).

V.D.6. Lithium-bearing Mixed Polyanion Glasses as Cathode Materials (ORNL)

Jim Kiggans & Andrew Kercher, Principal Investigators

Oak Ridge National Laboratory
1 Bethel Valley Road
Oak Ridge, TN 37831-6124
Phone: 865-576-5252; Fax: 865-574-4357
E-mail: kercherak@ornl.gov

Tien Q. Duong, DOE Program Manager

U.S. Department of Energy
Advanced Battery Materials Research (BMR)
Vehicle Technologies Office
1000 Independence Avenue, SW
Washington, DC 20585
Phone: 202-586-7836
E-mail: Tien.Duong@ee.doe.gov

Start Date: June 2012
End Date: June 2016

Abstract

Objectives

- Synthesize mixed polyanion glasses for use as active cathode materials in lithium-ion batteries.
- Demonstrate enhanced electrochemical performance and physical properties by tailoring the glass composition (alkali, redox cation, and polyanion content).
- Produce mixed polyanion glasses that undergo multi-valent transitions in the transition metal cations during electrochemical testing.
- Through laboratory scale testing, demonstrate novel glasses with excellent overall cathode performance that are viable replacements for current cathode materials in electric vehicle applications.

Accomplishments

- Raman and infrared spectroscopy were used to identify key polyanion structures associated with improved cycling performance and 1st cycle irreversible loss.
- Compared to Cu-based glasses, Ag- and Ni-based glasses showed different trends between composition, polyanion structures, and electrochemical performance (cycleability, irreversible loss, and efficiency).
- An electrochemical version of the mixed polyanion effect was found to occur in glass cathodes, where small amounts of a 2nd alkali (5%) can improve the capacity retention.

Technical Discussion

Introduction

Polyanion glasses are a relatively unexplored class of cathode materials for lithium-ion batteries. Our prior work and limited other prior work have shown that polyanion glasses can undergo high-capacity glass-state conversion reactions and, in some cases, intercalation reactions (Refs. 1 and 2). We have demonstrated reversible conversion reactions in antimony, cobalt, copper, iron, nickel, and silver-based glasses (Ref. 3). The remarkable capacity of polyanion glass cathodes (200-500 mAh/g) exceeds currently used lithium-ion battery

materials (~145-170 mAh/g) and makes them attractive materials for further research. However, similar to crystalline conversion cathodes, the conversion reactions in glass cathodes exhibit high 1st cycle irreversible loss (often >25-50%), low energy efficiency, and/or large capacity fade (60-75% capacity loss in 75 cycles). These critical weaknesses must be overcome before glass cathodes will be practically implemented in vehicles or other commercial battery applications.

Glasses have a key advantage over crystalline materials, which may be utilized to address their electrochemical weaknesses: wide compositional variability. In conventional glass applications, glass composition is adjusted to achieve large changes in desired physical properties (such as electrical conductivity, ionic diffusivity, and density). Many glass systems can have large substitutions in their alkali, modifier, and glass former content. For example, binary phosphate glasses have been produced with up to 60 mol.% Li₂O (alkali), 64 mol.% ZnO (modifier), and 94 wt.% V₂O₅ (glass former) (Ref. 4).

Three particularly dramatic composition-property relationships may have particular benefit in glass cathodes: polaron hopping, the borate anomaly, and the mixed alkali effect. In polyanion glasses, polaron hopping is an electrically semiconducting behavior that typically requires a transition metal cation capable of at least two valence states (such as vanadium or molybdenum). Most of our reversible polyanion glasses have required vanadate substitution in order to promote polaron hopping and to obtain a sufficient electrical conductivity (for example, changing from <10⁻¹¹ S/cm to almost 10⁻⁷ S/cm in iron metaphosphate glasses with 0% and 50% vanadate substitution). The borate anomaly involves a sudden borate structure change from trigonal BO₃ to tetrahedral BO₄ that highly depends on alkali content. The borate anomaly can significantly alter density, mechanical properties, and ionic conductivity (Refs. 5 and 6). The mixed alkali effect is observed in glasses with multiple alkali cation types and affects the ionic diffusivity and chemical stability. These three composition-property relationships have been observed in many glass systems. However, the most desirable compositions for glass cathodes have not been extensively researched, and the effects of these three composition-property relationships on electrochemical reactions haven't been previously researched.

Research in 2016 has been primarily focused on determining whether polaron hopping, the borate anomaly, and the mixed alkali effect can improve the 1st cycle irreversible loss, energy efficiency, and capacity fade in polyanion glass cathodes in lithium-ion batteries.

Approach

Our glass cathode research involves: (1) glass processing, (2) glass structure and property characterization, and (3) electrochemical testing. Splat quenching between Cu plates has been used to produce the glass cathode materials. This common laboratory-scale processing technique has a quench rate of ~1,000°C/sec, which often has been required to avoid crystallization in our complex glass compositions. Commercially, this rapid quench rate could be achieved by roller quenching. Characterization techniques have been used to confirm the amorphous structure, to determine the polyanion structure, and to measure fundamental glass properties. Electrochemical testing has been performed on coin cells with slurry cast cathodes and a Li anode.

Results

Key performance metrics are sensitive to borate content

The polyanion composition of glass cathodes has been shown to strongly affect the key electrochemical metrics to evaluate improved glass cathode performance (1st cycle irreversible loss, energy efficiency, and capacity retention). For example, in FY15, we reported that a lithium copper phosphate vanadate glass with 10% borate (Li₂Cu(40P-10B-50V)) showed near-zero 1st cycle irreversible loss (2.7%), while the same glass without borate (Li₂Cu(50P-50V)) had a large 1st cycle irreversible loss (30%). During further studies in FY16, Li₂Cu(50P-50V) was found to have a higher capacity retention after 50 cycles than Li₂Cu(40P-10B-50V) (41% vs. 27%). Summary charts of the key electrochemical metrics for copper phosphate vanadate glasses with and without borate are shown in Figure V-97 as a function of cation content (Li per Cu).

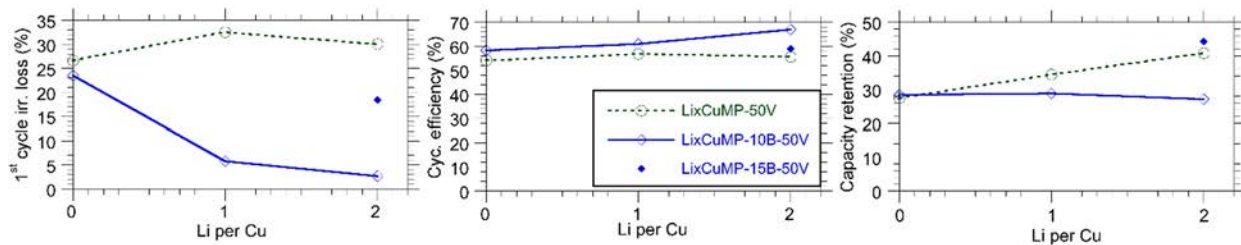


Figure V-97: Depending on borate content, borate can improve 1st cycle irreversible loss, cycling efficiency, and/or capacity retention (after 50 cycles)

While Figure V-97 does show strong trends as a function of cation content for a fixed polyanion composition, the key electrochemical metrics show a complex dependency on borate content. The addition of 5% more borate radically changes the performance according to all 3 metrics. A glass with additional borate substitution ($\text{Li}_2\text{Cu}(35\text{P}-15\text{B}-50\text{V})$) had the highest capacity retention after 50 cycles of any Cu-based glass cathode in the program (44%), but a higher 1st cycle irreversible loss than $\text{Li}_2\text{Cu}(40\text{P}-10\text{B}-50\text{V})$ (18% vs. 2.7%).

Correlating functional groups with electrochemical performance

Our electrochemical studies on borate substitution into copper phosphate vanadate glasses showed that borate content was not a good simple predictor of performance. Therefore, we focused on identifying what polyanion structures correlated with the key electrochemical metrics. Infrared and Raman spectroscopy were used to identify the polyanion content of this series of Cu-based glasses (Figure V-98).

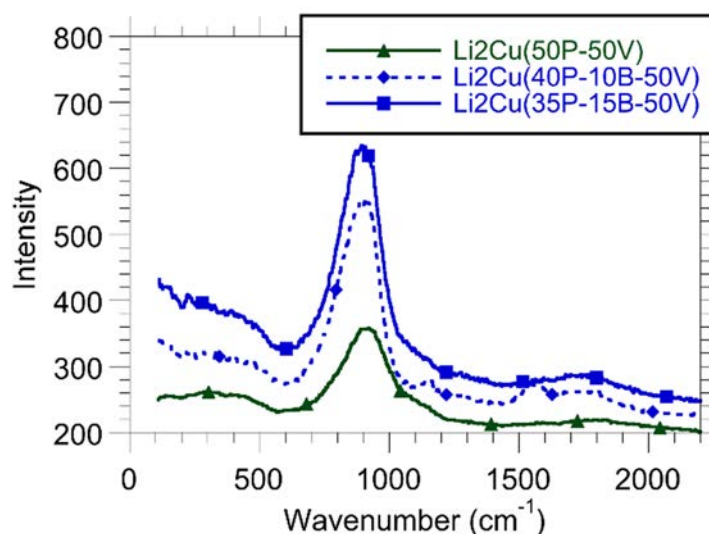


Figure V-98: Raman spectroscopy of lithium copper phosphate vanadate glasses with different amounts of borate (0%, 10%, and 15%)

Despite their similar compositions, the glasses with 10% and 15% borate had fundamentally different polyanion structures. The $\text{Li}_2\text{Cu}(40\text{P}-10\text{B}-50\text{V})$ glass exhibited a distinct Raman peak associated with trigonal BO_3 groups ($1490\text{-}1540\text{ cm}^{-1}$), but the $\text{Li}_2\text{Cu}(35\text{P}-15\text{B}-50\text{V})$ glass had tetrahedral BO_4 groups. The sudden transition from trigonal to tetrahedral borate at a certain alkali and borate content has been called the borate anomaly. This sudden polyanion transition typically causes a sharp change in physical properties, such as density, mechanical properties, and ionic conductivity (Refs. 5 and 6). Perhaps more importantly in glass cathodes, the tetrahedral BO_4 groups promote crosslinks in the glass former network, whereas the trigonal BO_3 groups appeared to promote clustering of the borate and phosphate in the glass (suggested by an IR peak at 1125 cm^{-1}) separate from the vanadate. The crosslinked structure of $\text{Li}_2\text{Cu}(35\text{P}-15\text{B}-50\text{V})$ glass had better capacity retention during cycling. Apparently, the more continuous vanadate structure of $\text{Li}_2\text{Cu}(40\text{P}-10\text{B}-50\text{V})$ has a very low first cycle irreversible loss. Understanding the relationship between polyanion structure and key electrochemical metrics is necessary in order to steadily improve glass cathode performance.

Extending the trend to other redox cations

Since basic correlations were found between polyanion structure and electrochemical performance in Cu-based glasses, nickel- and silver-based glasses with similar compositions were electrochemically tested and analyzed by Raman and IR spectroscopy. For lithium silver phosphate vanadate glasses, 10% borate addition reduced the 1st cycle irreversible loss from 52 mAh/g to 22 mAh/g. For lithium nickel phosphate vanadate glasses, 10% borate addition reduced the 1st cycle irreversible loss only slightly from 100 mAh/g to 83 mAh/g. The nickel-based glass with borate exhibited a distinct Raman peak associated with trigonal BO_3 groups, but the silver-based glass with borate did not (other distinctive IR peaks appeared instead).

In summary, the nickel- and silver-based glasses did not have the same strong correlations as the copper-based glasses. Comparing silver-based glasses with copper-based glasses, 10% borate addition did have a similar effect on 1st cycle irreversible loss, but the silver-based glass with borate did not show evidence of trigonal BO_3 groups (similar electrochemical effect, different polyanion structure). Comparing nickel-based glasses with copper-based glasses, 10% borate addition produced a distinct Raman peak for trigonal BO_3 groups in both, but the effect of borate addition on 1st cycle irreversible loss was much weaker (similar polyanion structure, much weaker electrochemical effect.).

Antimony borate & phosphate glasses with vanadate

Antimony phosphate and borate can theoretically have high capacity, multi-valent intercalation reactions (Sb^{5+} to Sb^{3+}) in a useful electrochemical window ($\leq 4.5\text{V}$) (Ref. 7). While only iron phosphate vanadate glasses have exhibited an intercalation reaction with full theoretical capacity, Sb-based glasses were tested because of their extraordinary theoretical properties. Lithium antimony phosphate and borate glasses with vanadate were produced by splat quenching.

Neither glass underwent an appreciable intercalation reaction. Both glasses showed high capacity conversion reactions at below 1.5V (Figure V-99). The phosphate/vanadate glass had a higher voltage conversion reaction than borate/vanadate glass by 0.2V, probably due to the higher inductive effect of phosphate.

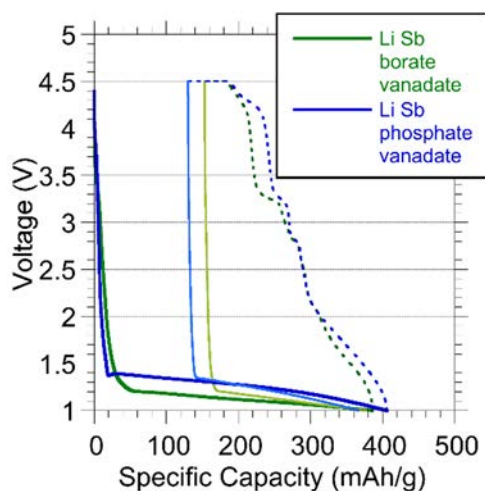


Figure V-99: The first & second discharges of lithium antimony phosphate vanadate and lithium antimony borate vanadate glasses

Mixed alkali effect in glass cathodes

The mixed alkali effect is an orders-of-magnitude effect in glass physical properties (such as electrical conductivity, alkali diffusion, and chemical durability) that occurs when a mixture of alkali cations is present. Only a few percent of a second alkali is needed to observe the property changes associated with the mixed alkali effect. A series of glass cathodes were tested to determine whether or not there is an electrochemical mixed alkali effect.

Electrochemical effects of sodium and lithium mixtures in copper phosphate vanadate glasses are shown in Figure V-100. A 5% Na content caused the largest changes to capacity retention and 1st cycle irreversible loss. The physical property change(s) that caused the sudden cathode performance changes are not known, but

mixing the alkali content has proven to be another route to improve electrochemical performance by adjusting the glass composition.

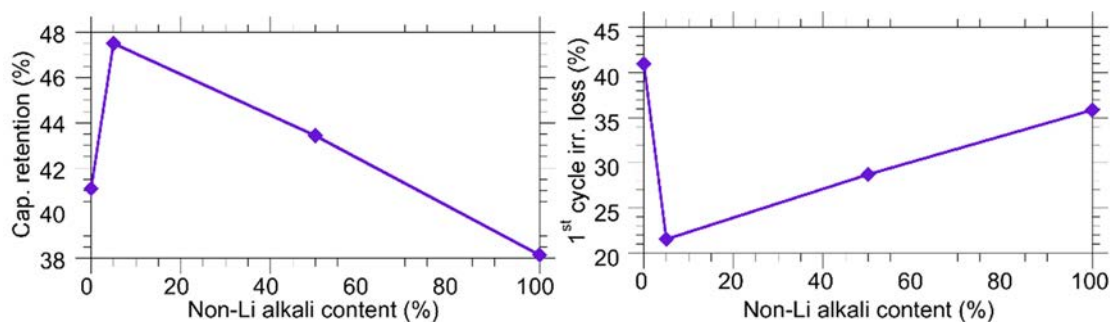


Figure V-100: The capacity retention (after 50 cycles) and 1st cycle irreversible loss of $\text{Na}_x\text{Li}_{(1-x)}\text{Cu}(50\text{P}-50\text{V})$ glasses

Conclusions

Tailoring the composition of glass cathodes has proven beneficial in improving the key metrics hindering the practical usage of glass cathodes: 1st cycle irreversible loss, energy efficiency, and capacity retention. Borate substitution into lithium-bearing copper phosphate/vanadate glasses had a strong effect on capacity retention and 1st cycle capacity loss, and the effect changed dramatically based on whether BO_3 or BO_4 groups were present. Mixed alkali content also was another compositional adjustment that was able to improve capacity retention and 1st cycle irreversible loss.

Products

Presentations/Publications/Patents

1. "Mixed polyanion glass cathodes: glass-state conversion reactions", A. K. Kercher, J. A. Kolopus, K. J. Carroll, R. R. Unocic, S. Kirklin, C. Wolverton, S. L. Stooksbury, L. A. Boatner, N. J. Dudney, *J. Electrochem. Soc.*, **163**(2), A131 (2016).
2. "Mixed polyanion glasses as Lithium-ion battery materials", A. K. Kercher, J. Kolopus, J. Ramey, K. Carroll, R. R. Unocic, S. Stooksbury, J. Kiggans, L. A. Boatner, N. J. Dudney, 2015 Fall MRS Meeting, Boston, MA, November 30th, 2015, oral presentation.
3. "Polyanion glass cathodes: a clearer picture", A. Kercher, J. A. Kolopus, R. L. Sacchi, R. E. Ruther, S. Chapel, K. J. Carroll, L. A. Boatner, N. J. Dudney, 230th Electrochemical Society conference / PRiME meeting, Honolulu, HI, October 6th, 2016, oral presentation.
4. "Mixed alkali effect in mixed polyanion glass cathodes", S. Chapel, A. Kercher, J. Kolopus, C. Davisson, 2016 ORISE Summer Student Poster Session, August 2016.

References

1. A. K. Kercher, J. O. Ramey, K. J. Carroll, J. O. Kiggans, N. J. Dudney, R. A. Meisner, L. A. Boatner, G. M. Veith, *J. Electrochem. Soc.*, **161**(14), A2210 (2014).
2. H. Yamauchi, G. Park, T. Nagakane, T. Honma, T. Komatsu, T. Sakai, A. Sakamoto, *J. Electrochem. Soc.*, **160**(10), A1725 (2013).
3. A. K. Kercher, J. A. Kolopus, K. J. Carroll, R. R. Unocic, S. Kirklin, C. Wolverton, S. L. Stooksbury, L. A. Boatner, N. J. Dudney, *J. Electrochem. Soc.*, **163**(2), A131 (2016).
4. H. Rawson, *Inorganic Glass-Forming Systems*, Academic Press, London (1967).
5. A. C. Wright, *Int. J. Appl. Glass Sci.*, **6**(1), 45 (2015).
6. F. Muñoz, L. Montagne, L. Pascual, A. Durán, *J. Non-Cryst. Solids*, **355**, 2571 (2009).
7. G. Hautier, A. Jain, S. P. Ong, B. Kang, C. Moore, R. Doe, G. Ceder, *Chem. of Mater.*, **23**(15), 3495 (2011).

V.D.7. Design of High Performance, High Energy Cathode Materials (LBNL)

Marca M. Doeff, Staff Scientist

Lawrence Berkeley National Laboratory
1 Cyclotron Road, M/S 62R0100
Berkeley, CA 94720
Phone: 510-486-5821
E-mail: mmdoeff@lbl.gov

Tien Q. Duong, DOE Program Manager

U.S. Department of Energy
Advanced Battery Materials Research (BMR)
Vehicle Technologies Office
1000 Independence Avenue, SW
Washington, DC 20585
Phone: 202-586-7836
E-mail: Tien.Duong@ee.doe.gov

Start Date: October 1, 2015
End Date: September 30, 2018

Abstract

Objectives

- Understand what limits electrochemical behavior of Ni-rich NMCs
 - Use an array of synchrotron techniques and microscopy to understand surface reactions.
 - Characterize changes in the bulk using synchrotron XRD and XAS.
 - Understand thermal behavior of charged materials.
- Use knowledge gained from studies above to design materials that can withstand cycling to high potentials and deliver ≥ 200 mAh/g.

Accomplishments

- Completed structural and surface characterization of NMC-622
 - Reactivity of O on surface is a driving force for surface reconstruction.
 - Phase behavior of NMC-622 resembles that of LiNiO_2 more than that of NMC-333.
- Synthesized compositionally-graded NMC-622 by spray pyrolysis
 - Established that surfaces are Ni-poor using transmission x-ray microscopy (TXM).
 - A comparison to a commercial NMC-622 material shows much less surface reactivity
 - Discharge capacity close to 200 mAh/g.

Future Achievements

- Thermal studies of NMC materials by TXM to understand details of phase conversion, oxygen loss
- Study effect of Ti-substitution on mitigating surface reactivity
- Extend studies to NMC-811

Technical Discussion

Background

Batteries for vehicular applications need improvements in energy density, ideally without compromising cost or safety. At present, cathodes are the limiting factor preventing achievement of this goal due to their relatively low specific capacities compared to graphite (~370 mAh/g) or silicon anodes (>4000 mAh/g). NMCs, which have the general formula $\text{Li}[\text{Ni}_x\text{Mn}_x\text{Co}_{1-2x}]\text{O}_2$, are a technologically important class of cathodes with particular relevance to electric vehicles because of the reduced quantity of expensive Co compared to LiCoO_2 , which is used in consumer batteries. The theoretical capacities of NMCs are ~280 mAh/g, but practical capacities range from ~160-200 mAh/g depending on Ni content. Higher Ni content is associated with greater practical capacities, but also poorer cycling behavior and thermal stability [1]. Other strategies to increase capacity include cycling NMCs to higher potentials, but this usually results in exacerbated capacity fading. Work on this project is directed towards development of higher capacity NMCs to improve energy density by attempting to understand the phenomena responsible for the capacity fade and using strategies to mitigate it such as partial Ti-substitution, elemental segregation, coatings, and improved electrolytic solutions. The PI on this project works closely with several other PIs in the Advanced Battery Materials Research program with a common goal of achieving a cathode that can cycle >200 mAh/g reliably and safely.

Introduction

Our previous work showed that NMC-442 cathodes suffer from surface reconstruction to a rock salt-like phase under a variety of conditions including storage in electrolytic solution, normal cycling, and high voltage cycling [2]. The surface reconstruction is probably responsible for the first cycle coulombic inefficiencies that are commonly observed, even when using conservative voltage limits. In addition, high voltage cycling results in the formation of an unfavorable cathode/electrolyte interface (CEI) layer that increases cell impedance [3]. It is this rise in cell impedance, rather than deterioration of the bulk material, that results in capacity fading during cycling to high potentials. Driving forces in both of these phenomena are the high reactivity of Ni ions, and the strong tendency for Ni-containing oxides to lose oxygen, particularly at high states-of-charge. Partial Ti substitution for Co in NMC-442 appears to ameliorate these tendencies, delaying loss of oxygen to higher levels of delithiation [4]. Improved cycling behavior is observed for Ti-substituted NMC materials when delithiated to the same level as unsubstituted NMC during high voltage cycling [5]. During FY15, it was also discovered that NMC-442 made by a simple and scalable spray pyrolysis method, exhibited a graded composition such that the Ni content was naturally lower on both the primary and secondary particle surfaces than in the bulk [6]. Materials made by this method exhibited better cycling behavior to high potentials and decreased amounts of surface reconstruction. In FY16, we turned our attention to Ni-rich NMCs, specifically NMC-622, with the goal of understanding what bulk and surface properties affect the electrochemical behavior and how similar or different it is compared to NMC-442. Once this understanding is in place, attempts to improve the cycling and thermal behavior, such as partial Ti-substitution and graded compositions may be applied, if deemed relevant.

Approach

We use a highly collaborative approach to understand what limits normal and high voltage cycling performance in Ni-rich NMC materials. A combination of synchrotron radiation and electron microscopy techniques (in collaboration with A. Mehta, D. Nordlund, T.-C. Weng, and Y. Liu at SSRL and H. L. Xin at BNL) and computational methods (with M. Asta at U.C. Berkeley) are used to understand the surface and bulk characteristics of baseline and Ti-substituted NMCs. Materials are synthesized either by classic co-precipitation methods or by spray pyrolysis. Electrochemical characterization is carried out in lithium half-cell configurations. Several physical techniques are used to characterize materials before and after electrochemical cycling under a variety of conditions. Nanotomographic imaging (Transmission x-ray microscopy, TXM) at SSRL is used to determine chemical gradients in particles and correlate this with electrochemical behavior. Soft x-ray absorption spectroscopy (XAS) experiments carried out at SSRL are used to probe oxidation states of transition metals at particle surfaces and in the bulk as a function of their electrochemical history. These results are correlated with scanning transmission electron microscopy (STEM) and electron energy loss

spectroscopy (EELS) experiments at Brookhaven National Laboratory to obtain a full understanding of what governs the behavior of NMCs as a function of composition and cycling history. For a full overview of the behavior of NMCs, the PI works closely with other PIs in the Advanced Battery Materials Research program, including R. Kostecki (interfacial characteristics using spectroscopy), W. Tong (novel materials), B. McCloskey (differential electrochemical mass spectroscopy to measure gas evolution), and C. Ban (NREL, atomic and molecular layer deposition for protective layers on cathode materials).

Results

In situ synchrotron X-ray diffraction was used to understand bulk structural changes in NMC-622 as it underwent delithiation and relithiation in a lithium half-cell (Figure V-101).

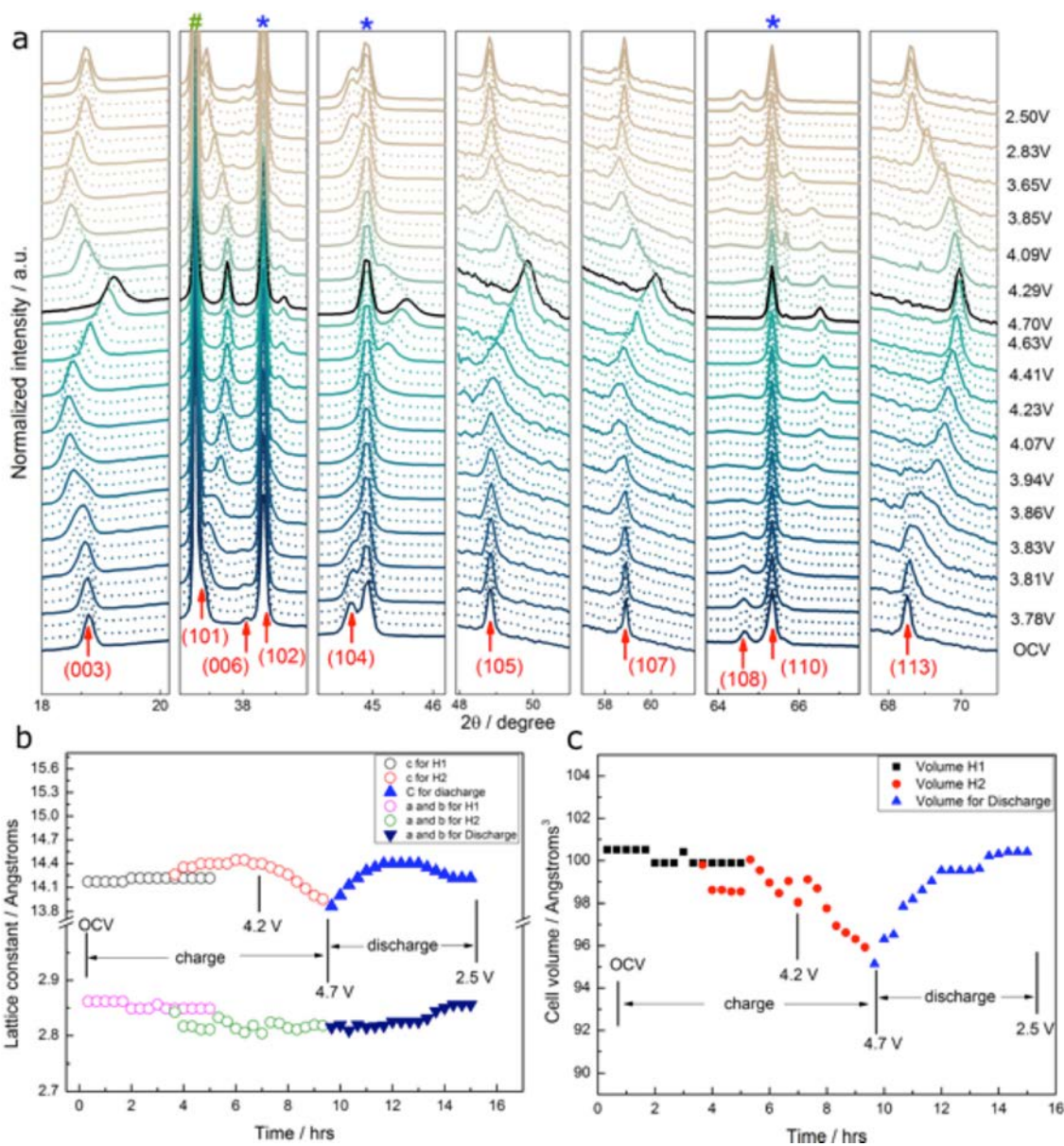


Figure V-101: a) *In situ* X-ray diffraction patterns for NMC-622 undergoing charge and discharge in a lithium half cell at C/10 rate; b) lattice constant changes as a function of state-of-charge; c) cell volume changes as a function of state-of-charge
Unpublished results

During the delithiation reaction, the *c*-axis first expands and then contracts, while the *a* and *b* lattice parameters contract slightly and then expand. A two-phase region is observed between 3.83 and 3.9V vs. Li^+/Li and another one close to 5V (not shown). This behavior is similar to that seen during the charging of LiNiO_2 [7]

and $\text{LiNi}_{0.8}\text{Co}_{0.15}\text{Al}_{0.05}\text{O}_2$ (NCA) [8] cathode materials, with the three phases designated H1, H2, and H3 in order of their appearance during charge. In contrast, NMCs with lower Ni contents or with balanced Ni and Mn content [9] show less distinctive and narrower phase transitions regions (in particular, the H2/H3 transition is less evident or missing completely). The total volume contraction for NMC-622 during charge is approximately 4% and the structural changes appear to be completely reversible between 4.7-2.5V.

Soft X-ray absorption spectroscopy was used to characterize the pristine NMC-622 material. Depending on the mode used, this experiment probes different depths of the sample: ~1-2 nm for Auger electron yield (AEY) mode, ~5 nm in total electron yield (TEY) mode, and ~50 nm for fluorescence yield (FY) mode. A comparison of the three modes for different element edges (Mn L-edge, Co L-edge, Ni L-edge, and O K-edge) is presented in Figure V-102.

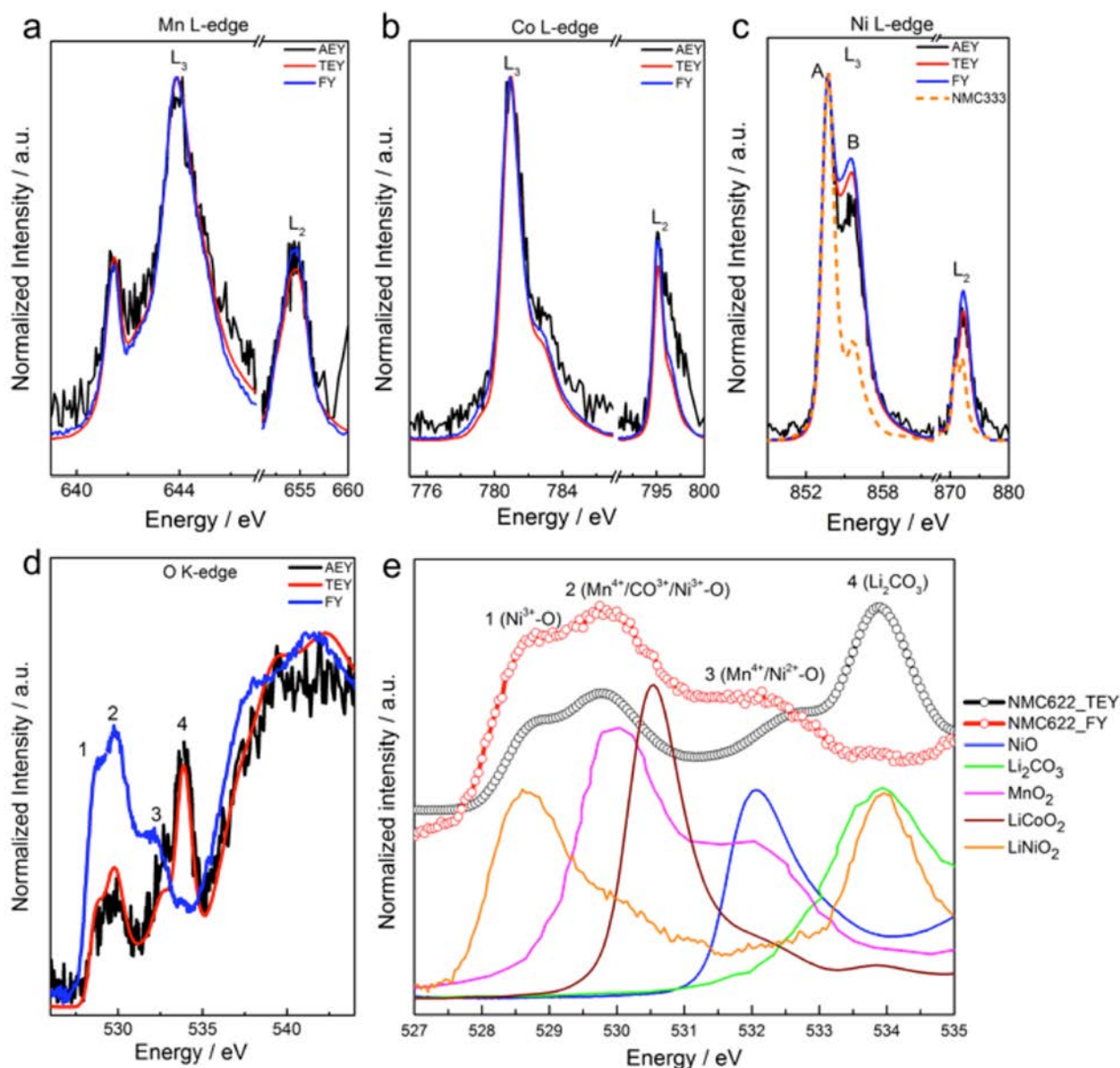


Figure V-102: Soft XAS spectra of pristine NMC-622 powder taken in three modes a) Mn L-edge, b) Co L-edge, c) Ni L-edge, d) O K-edge, and e) deconvoluted FY and TEY O K-edge data with assignments and reference samples
Unpublished results

The Mn and Co L-edge data are consistent with tetravalent and trivalent oxidation states of the metals, respectively, and show little variation as a function of sample depth. In contrast, the Ni L-edge data indicate that Ni on the surface of the pristine NMC-622 powder is slightly reduced in comparison to the bulk, determined from the relative ratios of peak A to peak B in the Ni L_3 region (data for NMC-333, in which all

the Ni is expected to be in the divalent state is given as a comparison). The O K-edge data shows significant variation as a function of sample depth. In particular, a peak near 534 eV, attributable to surface Li_2CO_3 , is evident in AEY and TEY modes and peaks attributable to lattice oxygen are less evident than in FY mode. This suggests that Li_2CO_3 is present on particle surfaces to a depth of < 5 nm. Similar observations showing surface rocksalt NiO phase and Li_2CO_3 on pristine LiNiO_2 particles have been published recently [10]. In that study, it was shown that the Li_2CO_3 content increased as the amount of excess Li-containing precursor was raised, with an inverse effect on the amount of rock salt phase formed. The surface properties of the LiNiO_2 samples had a strong effect on the electrochemistry, with materials with lower NiO content but higher amounts of Li_2CO_3 performing better.

Soft XAS results in TEY and FY mode as function of state-of-charge of NMC-622 electrodes are presented in Figure V-103.

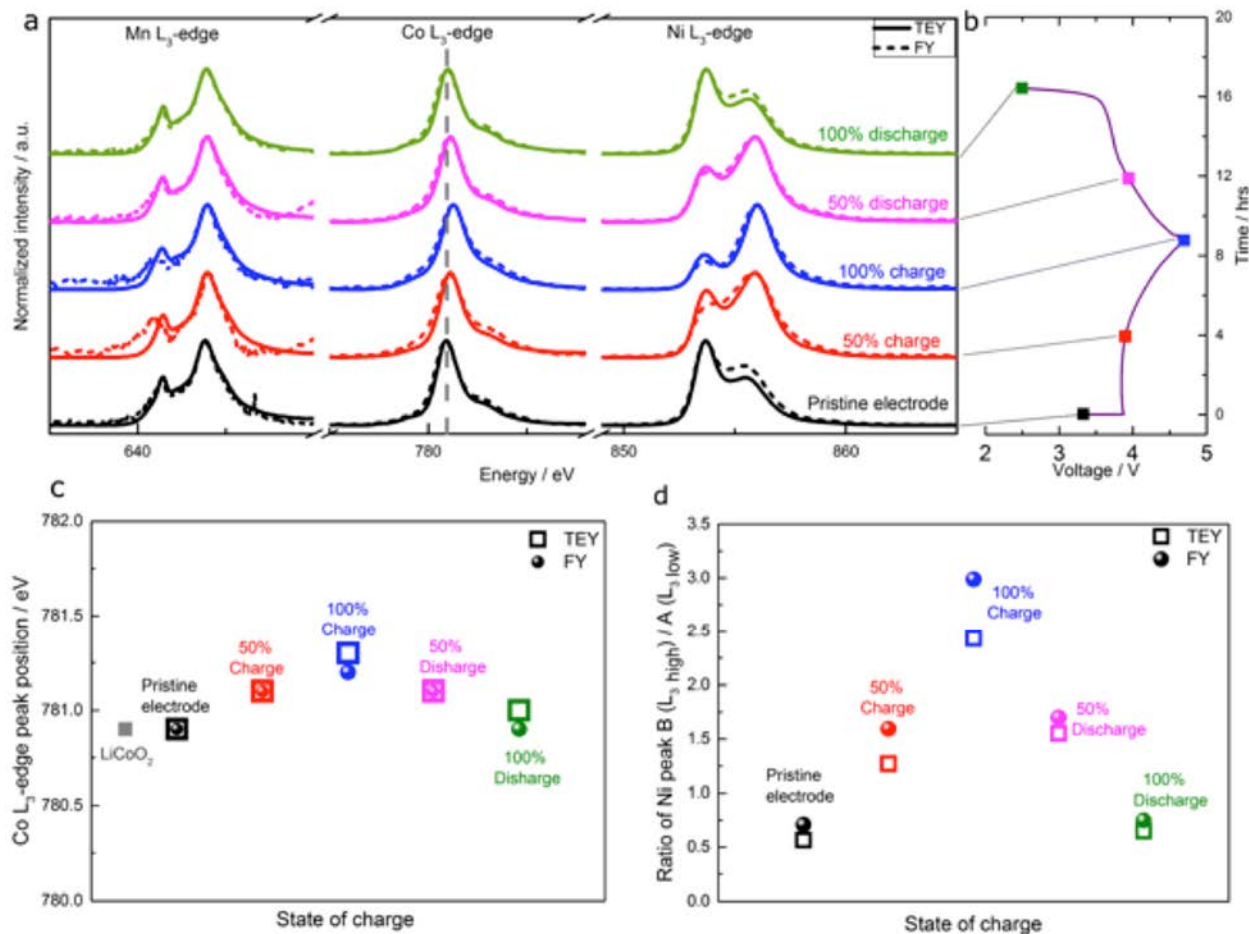


Figure V-103: a) Soft XAS data in TEY and FY modes on NMC-622 electrodes as a function of state-of-charge shown in b); c) Co L-edge peak positions as a function of state-of-charge and; d) Ni L-edge peak positions as function of state-of-charge

These results show that Mn is electrochemically inactive during cycling, as expected, although there appears to be some reduced Mn on surfaces during charge. Shifts in the Co L_3 -edge show that Co participates in redox during the charge and discharge processes, but the most dramatic changes are seen in the Ni L_3 edge, indicating that Ni is the main contributor to redox. At various points in the cycling process, there are significant discrepancies in relative peak heights between the TEY and FY modes, consistent with reduced Ni on particle surfaces relative to the bulk.

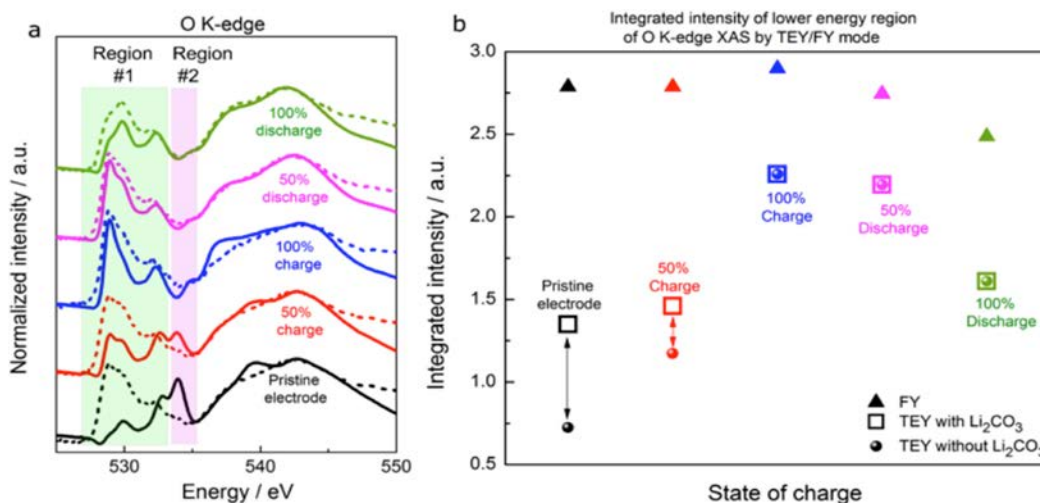


Figure V-104: a) O K-edge data on NMC-622 electrodes as a function of state-of-charge (solid line=TEY mode, dashed line-FY mode); b) integrated intensities of lower energy region peaks

Unpublished results

Figure V-104 shows the O K-edge data for electrodes as a function of state-of-charge (refer to Figure V-101 to Figure V-102 for peak assignments). Region 2 shows the evolution of the Li_2CO_3 peak during charge and discharge. While it was quite strong in the TEY spectra of the pristine and 50% charged electrodes, it disappeared in the spectra of the 100% charged and the discharged electrodes, indicating that it decomposed or dissolved upon charge to high potentials. TM3d-O2p hybridization peaks near 530 eV (region 1) are markedly stronger in FY mode than in TEY mode for the pristine and partially charged electrodes because of the presence of a thin layer of Li_2CO_3 on particle surfaces which obscures the signal from the lattice oxygen. As the Li_2CO_3 is removed, the FY and TEY spectra in region 1 become more similar for each electrode. As delithiation progresses, there is an increase in the number of unoccupied states in the TM3d-O2p hybridized orbitals, resulting in an increase in the integrated intensity of peaks in region 1 for the charged electrodes. The intensities are higher in FY mode than in TEY mode, indicating more TM3d-O2p unoccupied states in the bulk than on surfaces, consistent with the oxidation of Ni in the bulk. However, the changes in the integrated intensities are more dramatic in TEY mode (~68% compared to ~4% for FY mode), suggesting that surfaces undergo more dynamic changes of hole states in the TM3d-O2p hybridization. This indicates that surface oxygen is more active than that in the bulk. This is also consistent with first principle calculations reported last year that came to the conclusion that loss of oxygen from the surface is a driving force in formation of rock salt phases (surface reconstruction).

THE XAS studies are consistent with scanning transmission microscopy/electron energy loss spectroscopy (STEM/EELS) carried out on individual particles from electrodes cycled repeatedly between 2.5-4.7V (Figure V-105). For all three transition metals, there were consistent shifts of L_3 peaks towards higher energies as the EELS scanning moved from the surface to the bulk. On the other hand, the O K-edge peaks shifted to lower energies from the surface to the bulk because of higher TM3d-O2p unoccupied states in the bulk. In addition, the O pre-edge features associated with TM3d-O2p hybridization became stronger along the same scanning direction (Figure V-105b). These collectively showed that there was a significant buildup of reduced transition metals at the surfaces of the intensively cycled NMC particles. The STEM image (Figure V-105d) shows that in the surface region, the lithium channels were occupied by transition metals, indicating the tendency of a transition from the layered structure to a rock-salt structure, although the transition was not as complete as that seen in several other studies [2, 3, 11]. These observations are consistent with a build-up of reduced metals on particle surfaces due to reconstruction to a rock salt phase. After 50 cycles, however, the phase conversion has not propagated to the bulk (Figure V-105e). Soft XAS experiments, which probe a much larger ensemble of particles, show that all three transition metals are more reduced on particle surfaces (TEY) than in the bulk (FY) and that the difference is more apparent in the electrode cycled 50 times compared to the one cycled only once. The integrated peak intensities of the O K-edge data is significantly lower for the electrode after 50 cycles compared to the one after one cycle, and the effect is more pronounced on the surface than in the bulk. This would also be consistent with loss of oxygen on particle surfaces due to reconstruction to a rock salt phase.

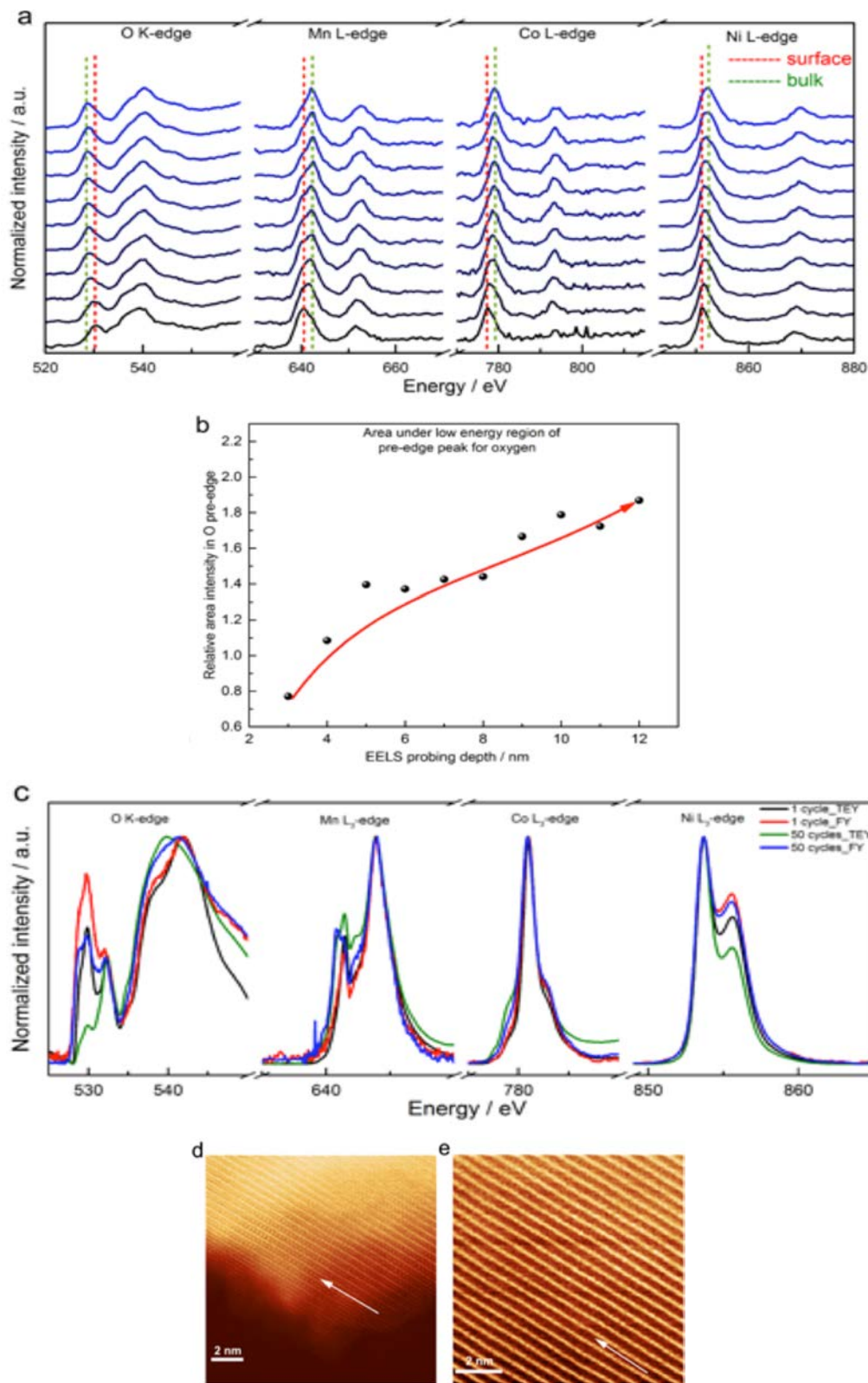


Figure V-105: a) EELS data from surface to the bulk on NMC-622 electrodes cycled 50 times between 4.7-2.5V.; b) integrated peak intensity of O pre-edge in the lower energy region as a function of EELS scanning depth; c) Soft XAS spectra of electrodes in the discharged state collected after 1 and 50 cycles (black= 1 cycle, TEY mode, red=1 cycle FY mode, green=50 cycles TEY mode, blue=50 cycles FY mode) and; d) and e) STEM images of NMC-622 particles after 50 cycles. White arrows show lithium channels

Unpublished results

Finally, transmission X-ray microscopy analysis of spray pyrolyzed NMC-622 shows that surfaces are Ni-poor (Figure V-106) as was the case with NMC-442 prepared by this method last year. The heterogeneity observed here and in NMC-442 appears to be quite general to this synthesis method, making this an attractive alternative to co-precipitation. The lower Ni content on particle surfaces should ameliorate reactivity and lead to improved electrochemical properties. Work next year will be directed towards understanding thermal properties of these materials as well as the electrochemical and structural characteristics.

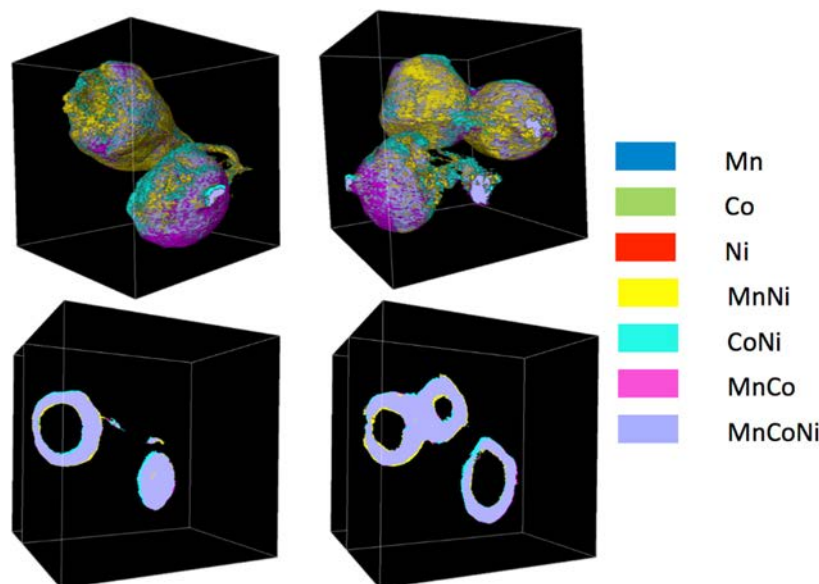


Figure V-106: Elemental association maps of NMC-622 particles prepared by spray pyrolysis, showing considerably heterogeneity of the particles (surfaces are Ni poor). Results were obtained using a synchrotron transmission X-ray microscopy technique

Unpublished results

Conclusions

Bulk changes to the NMC-622 structure are highly reversible although several phase transitions occur during delithiation/lithiation reactions, reminiscent of what occurs in LiNiO_2 and NCA materials. Volume changes of about 4% are modest and bode well for long-term cycling. The presence of a thin layer of Li_2CO_3 less than 5 nm thick on particle surfaces is also similar to what is seen in lithium nickelate electrodes, but this layer decomposes or is dissolved upon charging the electrode to 4.7V. Surface reconstruction to a rock salt phase is observed in cycled electrodes, similar to what occurs with NMC-442, studied in previous years. Analysis of O K-edge XAS data as well as computational results from last year, indicate that the driving force for this reconstruction is the high reactivity of surface oxygen compared to that in the bulk. These observations, taken together suggest that NMC-622 is intermediate in behavior between NMC-442 and LiNiO_2 . Spray pyrolyzed samples of NMC-622 show considerable heterogeneity in composition; in particular the surfaces are Ni-poor. This is also similar to what was found for spray-pyrolyzed samples of NMC-442, suggesting that the metal segregation is a general feature of this synthesis method. The lower Ni content on particle surfaces is expected to ameliorate reactivity with electrolytic solutions, reduce surface reconstruction, and result in better thermal properties.

Products

Presentations/Publications/Patents

1. "Design of High Performance, High Energy Cathode Materials" Marca M. Doeff 2016 DOE Annual Peer Review Meeting Presentation.

2. "Tailoring Transition-Metal Hydroxides and Oxides by Photon-Induced Reactions" Kai-Yang Niu, Liang Fang, Rong Ye, Dennis Nordlund, Marca M. Doeff, Feng Lin and Haimei Zheng, **Angew. Chemie Intl. Ed.** 55 (2016) DOI: 10.1002/anie.201606775.
3. "Facile Ethylene Glycol-Promoted Microwave-Assisted Solvothermal Synthesis of High-Performance LiCoPO₄ as a High-Voltage Cathode Material for Lithium-Ion Batteries" Jennifer Ludwig, Cyril Marino, Dominik Haering, Christoph Stinner, Dennis Nordlund, Marca Doeff, Hubert Gasteiger, and Tom Nilges, **RSC Advances**, DOI: 10.1039/C6RA19767A (2016).
4. "Atomic Insights into the Enhanced Surface Stability in High Voltage Cathode Materials by Ultrathin Coating" Xin Fang, Feng Lin, Dennis Nordlund, Matthew Mecklenburt, Mingyan Ge, Jieping Rong, Anyi Zhang, Chenfei, Shen, Yihang Liu, Yu Cao, Marca Doeff, and Chongwu Zhou, **Adv. Funct. Mater.** In press (2016).
5. "Experimental and Computational Investigation of Lepidocrocite Anodes for Sodium-Ion Batteries" Isaac Markus, Simon Engelke, Mona Shirpour, Mark Asta, and Marca Doeff, **Chem. Mater.** 10.1021/acs.chemmater.6b01074 (2016).
6. "Structural and Electrochemical Consequences of Al and Ga co-substitution in Li₇La₃Zr₂O₁₂ Solid Electrolytes" Daniel Rettenwander, Günther Redhammer, Florian Preishuber-Pflügl, Lei Cheng, Lincoln Miara, Reinhard Wagner, Andreas Welzl, Emmanuel Suard, Marca M. Doeff, Martin Wilkening, Jürgen Fleig, and Georg Amthauer, **Chem. Mater.** 28, 2384 (2016).
7. "Intermittent Contact Alternating Current Scanning Electrochemical Microscopy: A Method for Mapping Conductivities in Solid Li Ion Conducting Electrolyte Samples" Samantha Catarelli, Daniel Lonsdale, Lei Cheng, Jaroslaw Syzdek, and Marca M. Doeff, **Frontiers in Energy Research**, DOI: 10.3389/fenrg.2016.00014 (2016).
8. "Elucidating the Surface Characteristics and Electrochemistry of High-Performance LiNiO₂" J. Xu, F. Lin, D. Nordlund, E. J. Crumlin, F. Wang, J. Bai, M. M. Doeff, and W. Tong, **Chem. Commun.** 52, 4239 (2016).
9. "Metal Segregation in Hierarchically Structured Layered Cathode Materials with Improved Lithium Battery Performance" F. Lin, D. Nordlund, Y. Li, M. K. Quan, L. Cheng, T.-C. Weng, Y. Liu, H.L. Xin and M. M. Doeff, **Nature Energy** 1, 1 (2016).
10. "Synthesis, Crystal Chemistry, and Electrochemical Properties of Li_{7-2x}La₃Zr_{2-x}Mo_xO₁₂ (x=0.1-0.4): Stabilization of the Cubic Garnet Polymorph via Substitution of Zr⁴⁺ by Mo⁶⁺" D. Rettenwander, A. Welzl, L. Cheng, J. Fleig, M. Musso, E. Suard, M. M. Doeff, G. J. Redhammer and G. Amthauer, **Inorg. Chem.** 54, 10440 (2015).
11. "NMC Cathode and LLZO Electrolyte Studies" Marca M. Doeff, Feng Lin, Lei Cheng, Chixia Tian, Dennis Nordlund, and Huolin Xin, Molecular Foundry 2016 User Meeting, Lawrence Berkeley National Laboratory, Berkeley CA August 7-8, 2016.
12. "Understanding Interfacial Resistance of Al-Substituted Li₇La₃Zr₂O₁₂ Solid Electrolyte", Wei Chen, Lei Cheng, and Marca Doeff, 18th International Meeting on Lithium Batteries, Chicago, IL, June 19-24th, 2016.
13. "Sodiation Kinetics of Metal Oxide Conversion Electrodes: A Comparative Study with Lithiation" K. He, F. Lin, Y. Zhu, X. Yu, J. Li, R. Lin, D. Nordlund, T. C. Weng, R. M Richards, X. Q. Yang, M. Doeff, E.A. Stach, Y. Mo, H. Xin and D. Su, 18th International Meeting on Lithium Batteries, Chicago, IL, June 19-24th, 2016.
14. "Sodium Intercalation Mechanisms into Corrugated Titanate Structures for Na-ion Batteries" Isaac Markus, Mona Shirpour, Simon Engelke, Siaufung Dang, Mark Asta and Marca Doeff, 2016 Materials Research Society Meeting, Phoenix AZ, March 28th-April 1, 2016.
15. "A Comparative Study on Cubic Li_{6.4}Al_{0.2}La₃Zr₂O₁₂: Li_{6.4}Ga_{0.2}La₃Zr₂O₁₂ Garnet Solid Solution" D. Rettenwander, R. Wagner, L. Cheng, G. Amthauer, M. M. Doeff, G. J. Redhammer, and M. Wilkening, 2016 Materials Research Society Meeting, Phoenix, AZ, March 28th-April 1, 2016.
16. "First Principles Investigation of Sodium Intercalation Mechanisms into Corrugated Titanate Structures for Sodium-Ion Battery Anodes", Isaac Markus, Mona Shirpour, Simon Engelke, Mark Asta, and Marca Doeff, 8th International Conference on Advanced Lithium Batteries for Automobile Applications, Bilbao Spain, Sept. 30-Oct. 2, 2015.

17. "Structure, Ion Dynamics, and Stability of Cubic $\text{Li}_7\text{La}_3\text{Zr}_{2-x}\text{Mo}^{6+}_x\text{O}_{12}$ Garnets" D. Rettenwander, A. Welzl, P. Bottke, W. Schmidt, L. Cheng, G. Redhammer, M. Musso, M. M. Doeff, G. Amthauer, M. Wilkening and J. Fleig, 2015 Materials Research Society Meeting, Boston, MA Nov. 29-Dec. 4, 2015.
18. "Low Resistance in Bulk and Interface: A Study on Cubic $\text{Li}_7\text{Al}_{0.2-x}\text{Ga}_x\text{La}_3\text{Zr}_2\text{O}_{12}$ Garnets" D. Rettenwander, A. Welzl, L. Cheng, G. Amthauer, M. M. Doeff, and J. Fleig, 2015 Materials Research Society Meeting, Boston, MA Nov. 29-Dec. 4, 2015.
19. "Oxygen Activity Promoting the Surface Transformation of High Voltage Layered Oxide Cathodes for Lithium Ion Batteries" S. Hy, H. Liu, F. Lin, M. Doeff, D. Nordlund, H. Xin, and S. Meng, 228th meeting of the Electrochemical Society, Phoenix, AZ, October 2015.
20. "Layered Cathode Materials with Controlled Particle Assembly for High Energy Lithium-Ion Batteries" F. Lin, Y. Li, D. Nordlund, Y. Liu, T. C. Weng, H. Xin and M. Doeff, 228th meeting of the Electrochemical Society, Phoenix, AZ, October 2015.
21. "Synchrotron Studies of Battery Materials" Marca M. Doeff, 2016 SSRL/LCLS User's Meeting, Menlo Park, CA Oct. 5-7th, 2016. (invited).
22. "The Promise of Sodium Ion Batteries" Marca M. Doeff, 67th Annual Meeting of the International Society of Electrochemistry, The Hague, Netherlands, August 21st-26th, 2016. (invited).
23. "Preparation and Characterization of Garnet LLZO Solid Electrolytes for Lithium Batteries" Marca M. Doeff, Recent Advances in Solid State Electrolytes for Energy Storage Tutorial, Advanced Automotive Battery Conference 2016, Detroit MI June 13, 2016. (invited).
24. "LLZO Ceramic Electrolytes: A Path Forward to Solid-State Batteries?" Marca M. Doeff and Lei Cheng, 229th meeting of the Electrochemical Society, San Diego CA, May 29th-June 3rd, 2016. (invited).
25. "Recent Advances on Garnet LLZO Solid Electrolytes for Lithium Batteries" Marca M. Doeff, Guoying Chen, and Lei Cheng, Beyond Lithium Ion IX, Richland WA, May 24-26, 2016. (invited).
26. "Advances Towards Solid State Batteries Using Garnet LLZO Electrolytes" Marca M. Doeff and Lei Cheng, Materials Challenges in Alternative and Renewable Energy (MCARE2016), Clearwater, FL April 17-21, 2016. (invited).
27. "Interfacial Behavior of NMC Cathodes and LLZO Garnet Solid Electrolytes", Marca M. Doeff, 2016 Battery Workshop U.S. Department of Energy/Daimler A.G, Ulm Germany, April 7, 2016. (invited).
28. "Insights into the High Voltage Behavior of NMC Cathode Materials" Helmholtz Institute Ulm, Ulm Germany, April 5, 2016. (invited).
29. "Insights into the Structure and Performance of NMC Cathode Materials for Lithium-ion Batteries" Marca M. Doeff, 40th International Conference and Expo on Advanced Ceramics and Composites, Daytona Beach, FL, Jan. 24-29th, 2016. (invited).
30. "High Potential NMC Cathode Materials-a Route to High Energy Density Lithium-ion Batteries?" Marca M. Doeff and Feng Lin, 2015 Lithium Battery Power, Baltimore, MD, November 17-19, 2015. (invited).
31. "The Future of Energy Storage" Marca M. Doeff and Venkat Srinivasan, Energy Storage and Conversion Symposium, The Northern California Chapter of The American Vacuum Society, San Jose, CA November 13, 2015. (invited).
32. "Behavior of Layered Cathode Materials: A Route to Higher Energy Density for Lithium Ion Batteries" Marca M. Doeff, Feng Lin, and Isaac Markus, 62nd AVS International Symposium, San Jose, CA, Oct 19-23, 2015 Abstract #261. (invited).
33. "Advances in Sodium Ion Battery Chemistry" Marca M. Doeff, Mona Shirpour and Xiaowen Zhan, 2nd International Conference on Sodium Batteries, Phoenix AZ Oct. 7-9, 2015. (invited).

References

1. H.-J. Noh, S. Youn, C.S. Yoon, and Y.-K. Sun, *J. Power Sources*, **233**, 121 (2013).
2. Feng Lin, Isaac Markus, Dennis Nordlund, Tsu-Chien Weng, Mark Asta, Huolin L. Xin, and Marca M. Doeff, *Nature Commun.* **5**:3529, DOI: 10.1038/ncomms4529 (2014).
3. Feng Lin, Isaac M. Markus, Dennis Nordlund, Tsu-Chien Weng, Huolin L. Xin, and Marca M. Doeff, *Energy & Environ. Sci.* **7**, 3077 (2014).

4. Isaac Markus, Feng Lin, Kinson Kam, Mark Asta, and Marca Doeff, *J. Phys. Chem. Lett.* 5, 3649 (2014).
5. S. Wolff-Goodrich, F. Lin, I. Markus, D. Nordlund, H. Xin, M. Asta, and M. M. Doeff, *Phys. Chem. Chem. Phys.* 17, 21778 (2015).
6. F. Lin, D. Nordlund, Y. Li, M. K. Quan, L. Cheng, T.-C. Weng, Y. Liu, H.L. Xin and M. M. Doeff, *Nature Energy* 1, 1 (2016).
7. X. Yan, X. Sun, and J. McBreen, *Electrochem. Commun.* 1, 227 (1999).
8. W.-S. Yoon, K. Y. Chung, J. McBreen, and X.-Q. Yang, *Electrochem. Commun.* 8, 1257 (2006).
9. Thomas E. Conry, Apurva Mehta, Jordi Cabana, and Marca M. Doeff, *Chem. Mater.*, 24, 3307 (2012).
10. J. Xu, F. Lin, D. Nordlund, E. J. Crumlin, F. Wang, J. Bai, M. M. Doeff, and W. Tong, *Chem. Commun.* 52, 4239 (2016).
11. Feng Lin, Dennis Nordlund, Taijun Pan, Isaac Markus, Tsu-Chien Weng, Huolin Xin, and Marca M. Doeff, *J. Mater. Chem. A* 2, 19833 (2014).

V.D.8. Lithium Batteries with Higher Capacity and Voltage (UTA)

John B. Goodenough, Principal Investigator

The University of Texas at Austin
204 E. Dean Keeton Street
Austin, TX 78712
Phone: 512-471-1646; Fax: 512-471-7681
E-mail: jgoodenough@mail.utexas.edu

Start Date: January 2013
End Date: June 2017

Abstract

Objectives

- To increase cell energy density for a given cathode.
- To allow low-cost rechargeable batteries with cathodes other than insertion compounds.

Accomplishments

- Dendrite-free and reversible Li plating/stripping has been demonstrated where metallic lithium wets the electrolyte surface.
- Gold coating on a garnet pellet was useful to form Li-Au alloys and enable wetting of lithium.
- Temperature was shown to be crucial to prevent dendrite formation and penetration of a garnet ceramic electrolyte.
- LiF coating can protect garnet solid electrolytes from moisture and carbon dioxide, thereby reducing interfacial impedance.

Future Achievements

Solid ceramic and/or polymer electrolytes of high cation conductivity that are wet by an alkali-metal anode will be developed, and the anode/electrolyte bonding responsible for wetting will be shown to restrict the volume changes of the anode on cycling to the direction perpendicular to the electrode/electrolyte surface and allow a long cycle life of a symmetric A/electrolyte/A cell, A = Li or Na. In addition, we will explore the possibility of a rechargeable battery that transfers the lithium or sodium of the anode to a cathode of low potential, *e.g.* Cu, on which it is plated on discharge and stripped on charge.

Technical Discussion

Background

An alkali-metal anode (Li or Na) would increase the energy density for a given cathode by providing a higher capacity and cell voltage. However, lithium is not used as the anode in today's commercial lithium-ion batteries that use a flammable liquid electrolyte because electrochemical dendrite formation and growth during charge can induce a cell short-circuit and critical safety hazards.

Introduction

Commercial lithium-ion batteries are typically assembled with a transition-metal oxide host into which lithium has been inserted over a finite solid-solution range; the discharged anode is normally carbon and the electrolyte is a flammable organic liquid that is reduced by a charged anode unless ethylene carbonate is added to the electrolyte to provide formation of a solid-electrolyte-interphase (SEI) at the electrode/electrolyte interface to prevent chemical reduction of the electrolyte; the SEI is a lithium-ion conductor that, during the initial charge, takes Li^+ from the cathode irreversibly to lower the finite capacity of the cathode. Moreover, the SEI is a principal source of capacity fade that limits the cycle life of a cell. Metallic lithium is not wet by the liquid electrolyte, and dendrites (whiskers) form on the anode and grow during charge; the anode dendrites can grow across the electrolyte to the cathode to create an internal short-circuit with incendiary consequences. This safety problem has motivated the search for a non-flammable electrolyte, preferably a solid electrolyte. However, blocking anode electrolytes from reaching the cathode by a solid electrolyte is not a sufficient strategy, but we and others have shown that if an alkali-metal anode wets the surface of the electrolyte, dendrites do not form. Moreover, if the solid electrolyte is not reduced by the alkali-metal anode, the SEI layer does not form. Where an alkali-metal wets a solid electrolyte, it can be plated/stripped reversibly; symmetric A solid electrolyte/A cells (A = Li or Na) have been cycled over a thousand times at high rates provided the impedance to cation transfer across the anode/electrolyte interface is small.

Unfortunately, solid electrolytes with a sufficiently fast cation conductivity ($\sigma_i > 10^{-3} \text{ S cm}^{-1}$) have been difficult to find. We have identified glass, polymer, and ceramic solid electrolytes that are wet by an alkali-metal anode. We are also studying whether it is possible to transfer the alkali-metal to a copper-carbon anode from the anode during discharge and back during charge thus eliminating the finite capacitances of a cathode host oxide; the discharge voltage is limited by the difference between the alkali-metal and cathode-current-collector chemical potentials. This strategy would introduce a transformational change in the rechargeable battery.

Approach

1. Reduction of the cation conductivity of a dry block co-polymer-membrane containing pendants that extend into the interstitial spaces that contain very acidic terminal anions.
2. Demonstration of solid electrolytes that are wet by an alkali-metal anode and testing cycle life and the impedance of symmetric cells.
3. Where a solid electrolyte is wet by an alkali metal, exploring the concept of a reversible transfer of alkali-metal anodes to a cathode current collector on discharge and the limits of discharge voltage that can be obtained by using cathode current collectors of different chemical potential.
4. To reduce interfacial impedance of a garnet-structured solid electrolyte, the effect of a surface protective coating was tested.

Results

We have completed the following investigations:

Incorporating a low-melting-point Li^+ -electrolyte glass in the thiol-ene polymer for a solid electrolyte membrane

Test incorporating a low-melting-point Li^+ -electrolyte glass in the thiol-ene polymer for a solid electrolyte membrane has been performed with molten nitrate electrolytes. Molten nitrate electrolytes show low melting points especially at the eutectic points. For the test, LiNO_3 was mixed with NaNO_3 or KNO_3 . The eutectic temperatures for LiNO_3 - KNO_3 (42-58 mol%) and LiNO_3 - NaNO_3 (56-44 mol%) are 124 and 187°C, respectively.^[1] The molten nitrate electrolytes offer a high ionic conductivity and a chemical stability over a wide temperature range. Moreover, it has a low viscosity, so it is a good candidate for the incorporation test.

For the thiol-ene polymer membranes, we have fabricated (1) a tetrathiol-cross-linked ester (*divinyl adipate*) and (2) a di- and tetra-thiol(50-50 mol%)-cross-linked polyethylene oxide (*Poly(ethylene glycol) diacrylate*, $M_n \sim 700$) membranes.^[2] The second crosslinked PEO membrane was developed to enlarge the pore volume of

the membrane and thereby increase the chance of nitrate solution uptake. The mixed di- and tetra-thiol crosslinker can decrease the crosslinking density to less than that of the 100% tetrathiol crosslinker, and the PEO chain is longer in length than the ester monomer that was used in this study.

The two membranes were immersed in the nitrate eutectic solutions in an Ar-filled glove box as shown in Figure V-107. Immersion in the $\text{LiNO}_3\text{-NaNO}_3$ nitrate electrolyte at 187°C resulted in a rapid degradation of both of the membranes. Even after 10 minutes of storage, the membranes turned from transparent to black. The $\text{LiNO}_3\text{-NaNO}_3$ mixture also turned brown, which indicates a chemical reaction with the membranes. In the $\text{LiNO}_3\text{-KNO}_3$ nitrate electrolyte at 124°C , the membranes were much more stable, probably owing to the lower eutectic temperature. After 1 hour of storage, there was no color changes noticed, but both of the membranes did not absorb the nitrate electrolyte. However, after a prolonged storage for 10 hours, those membranes turned brown and were oxidized. After cooling down the electrolyte, the membranes were still transparent, but the electrolyte uptake did not occur during the experiment. From these experiments, it is obvious that the thiol-ene polymer membrane is not stable in a nitrate eutectic electrolyte at high temperature.

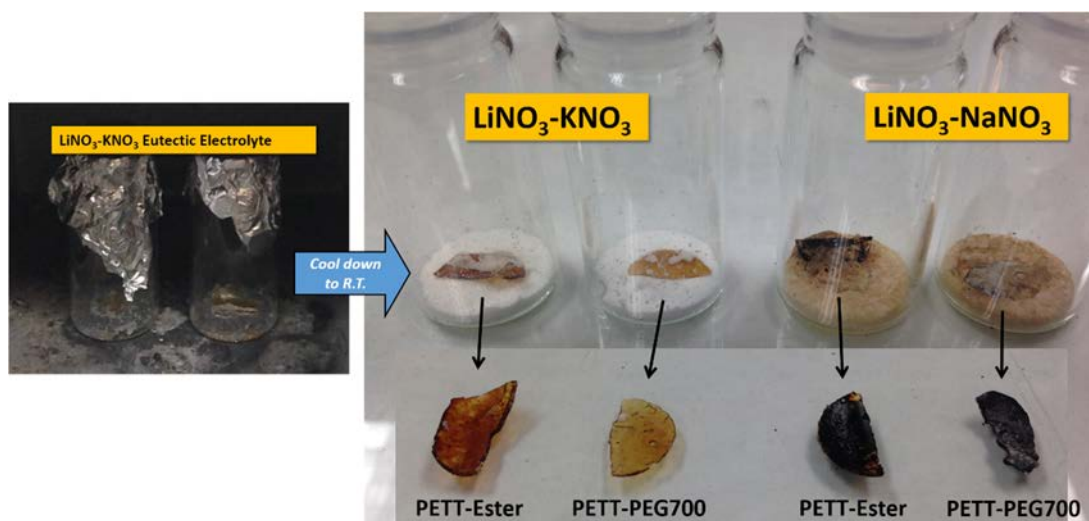


Figure V-107: (left) Polymer membrane immersion test in the $\text{LiNO}_3\text{-KNO}_3$ nitrate electrolyte at 124°C , (right) Photographs of the polymer membranes after the electrolyte soaking tests

Plating of a metallic lithium anode through a garnet-structured solid electrolyte

High-density $\text{Li}_7\text{La}_3\text{Zr}_2\text{O}_{12}$ (LLZO) pellets were prepared by sintering at 1150°C . Typical pellet density was $\sim 93\%$ in our experiment. Lithium-ion conductivity was measured to be $1.0 \times 10^{-4} \text{ S cm}^{-1}$ at room temperature. First, we checked the Li transport properties with $\text{Li}/\text{Au}/\text{LLZO}/\text{Au}/\text{Li}$ symmetric cells. To lower interfacial impedance, gold layers on both sides of the LLZO pellet were deposited before testing. Figure V-108(a) clearly demonstrates short circuits in 591 and 28 seconds at 0.1 and 0.5 mA cm^{-2} , respectively. Lithium dendrites can penetrate through open pores and grain boundaries at room temperature, as shown in Figure V-108(b). Cross-sectional area of the short-circuited LLZO turned black, and the SEM image for the corresponding area showed deposit of a secondary material that should be lithium metal. Since it is essential to get stable and reversible Li^+ transport properties across the LLZO electrolyte, we increased the cell temperature to 50°C . Figure V-109 shows charge/discharge voltage curves of a $\text{Li}/\text{Au}/\text{LLZO}/\text{Au}/\text{Li}$ symmetric cell. It shows reversible cycling at a current density of 0.1 mA cm^{-2} unlike the room-temperature test results. It suggests that a higher atomic mobility of Li atoms at a higher temperature can help reduce the surface area of the metastable dendrites and promote isotropic lithium growth.

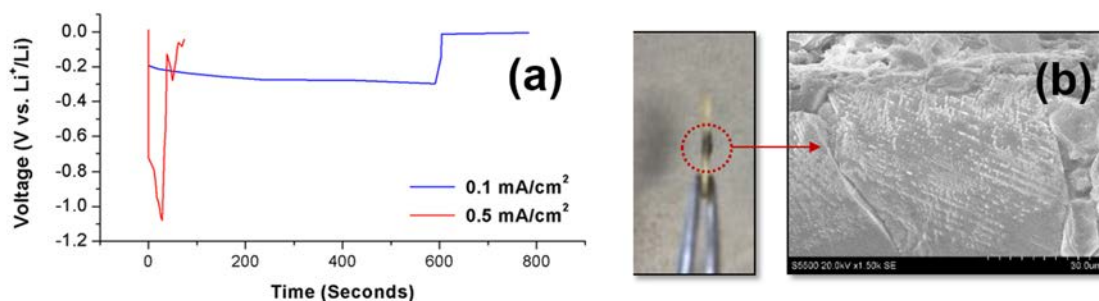


Figure V-108: (a) Li-plating voltage curves of Li/Au/LLZO/Au/Li symmetric cells at 0.1 and 0.5 mA cm⁻². (b) Cross-sectional photograph of LLZO after short-circuit (left) and the corresponding SEM image for the dark part (right)

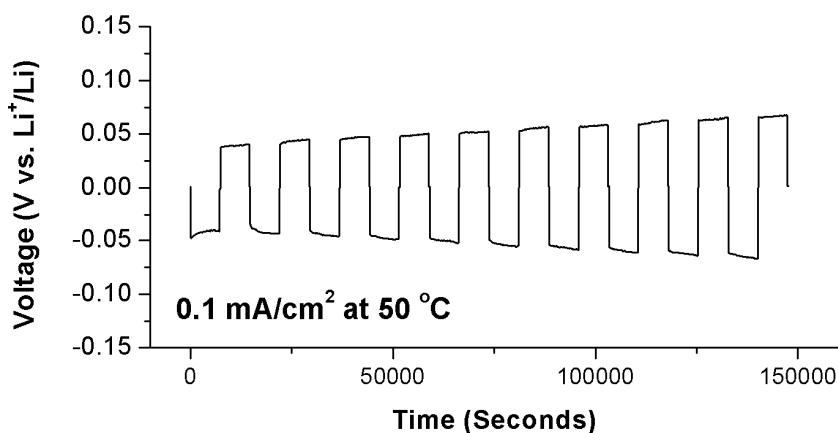


Figure V-109: Reversible charge / discharge voltage curves of Li/Au/LLZO/Au/Li symmetric cell at a current density of 0.1 mA cm⁻² and 50 °C

Garnet electrolyte with a small interfacial resistance

A garnet solid electrolyte reportedly has a high interfacial impedance. The origin of the large interfacial resistance is related to the garnet instability in air.^[3] The grains of garnet electrolyte reacts with moisture and carbon dioxide in air to form LiOH and Li₂CO₃ on the surface of LLZO grains; this reaction also occurs inside the pellets through the grain boundaries. Both LiOH and Li₂CO₃ are Li-ion insulators, which leads to a large interfacial resistance of the garnet electrolyte against lithium metal and other materials.

In addition to the gold coating and high-temperature cell operation strategies, we used LiF to increase the stability of the garnet electrolyte Li_{6.5}La₃Zr_{1.5}Ta_{0.5}O₁₂ (LLZT) against moisture and carbon dioxide. The XRD patterns of the as-prepared LLZT with different amounts of LiF are shown in Figure V-110(a); all the pellets crystallize in a cubic garnet structure with high purity and the lattice parameters of all the LLZT pellets calculated by the refinement with the Fullprof software are $a = 12.9340 \text{ \AA}$. The cubic lattice constant shows that LiF has little influence on the substitution of F⁻ for bulk O²⁻. LiF melts at 845°C and covers the surfaces of the LLZT particles and it appears to reduce the reaction between LLZT grains and moist air. The LiF on the grain surface of LLZT helps to stabilize the grain boundaries of LLZT by reducing the reaction of the Li-Al-O grain-boundary phase with moist air.^[3] A 2 wt% LiF was the best concentration to optimize the stability of LLZT against moist air and to keep the high total conductivity of LLZT. The densities of LLZT and LLZT fired with 2 wt% LiF (LLZT-2LiF) pellets are 93.2 and 92.2%, respectively. The ionic conductivities of LLZT with and without LiF were measured with Li-ion blocking electrodes; the impedance plots with typical semicircles are shown in Figure V-110(b). The LLZT pellets with and without LiF have the same bulk conductivities of 10⁻³ S cm⁻¹ at 25°C. The grain-boundary resistance of LLZT-2LiF pellet is a little larger than that of the pellet without LiF; the total conductivities of LLZT pellets and LLZT-2LiF are 5.5 and 5.2 × 10⁻⁴ S cm⁻¹ at 25°C, respectively. The impedance plots of the Li/Garnet/Li symmetrical cells at 25°C are shown in

Figure V-110(d); the interfacial resistance of the Li/LLZT-2LiF/Li was $345 \Omega \text{ cm}^{-2}$, which is far smaller than that of Li/LLZT/Li ($1260 \Omega \text{ cm}^{-2}$).

The LiF has a strong ionic bond and is insoluble in water; in a grain boundary of the garnet, it prevents diffusion of moisture and carbon dioxide into the pellet. The XPS data of the fresh LLZT sample is shown in Figure V-110(c); the two peaks in the C 1s spectrum located at 285.0 and 290.0 eV correspond to adventitious carbon and carbonate, respectively; and the ratio of Li_2CO_3 to the C peak of LLZT and LLZT-2LiF was 79.8 and 20.7 %, respectively. XPS results successfully demonstrate the importance of surface coating to enhance chemical stability of a solid electrolyte against moisture and carbon dioxide.

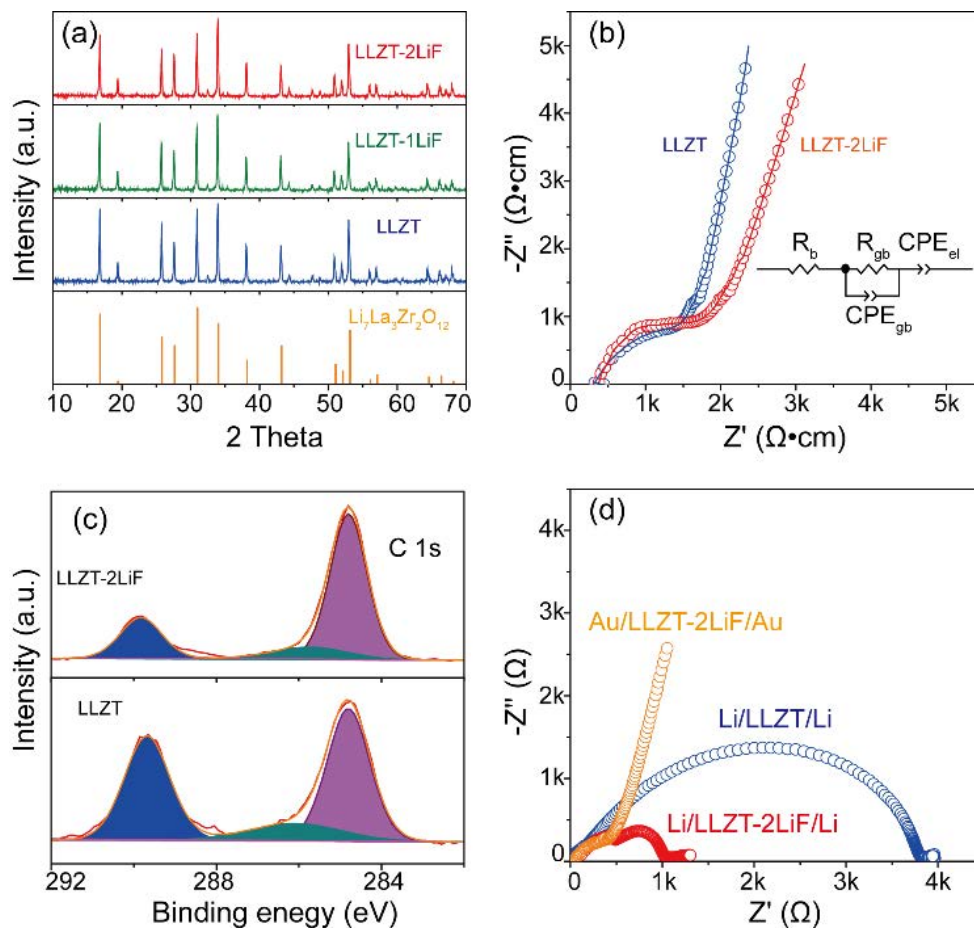


Figure V-110: (a) XRD patterns of LLZT with different amounts of LiF, (b) The impedance plots of LLZT and LLZT-2LiF with ion-blocking Au electrodes, (c) C 1s spectrum of LLZT and LLZT-2LiF, (d) The impedance plots of LLZT and LLZT-2LiF with Li electrodes, the pellets thickness and surface area are 0.12 cm and 0.69 cm^2 , respectively

Conclusions

In parallel with other support, we have demonstrated that alkali-metal anodes can be plated-stripped reversibly where the anode wets the surface of a solid (glass, polymer, ceramic) Li^+ or Na^+ electrolyte. Where the wetting is direct, the anode/electrolyte impedance is negligible; where the wetting is through a solid SEI layer, the SEI layer reduces the impedance significantly. In this project, we concentrated on ceramic and polymer solid electrolytes with a particular emphasis on the garnet Li^+ electrolyte. We have reduced the grain-boundary impedance by introducing LiF that blocks moist air from entering the grain boundaries where the Li instability in the garnet results in the formation of LiOH and Li_2CO_3 insulators in the grain boundaries. Nevertheless, we could conclude that other solid electrolytes showed greater promise. With the ability to plate an alkali metal reversibly on a current collector, we are exploring a radical new design of the cathode of a rechargeable battery that eliminates the use of an oxide host into which working cations are inserted.

Products

Presentations/Publications/Patents

1. K. Park, B. C. Yu, J. W. Jung, Y. Li, W. Zhou, H. Gao, S. Son, J. B. Goodenough, *Chem. Mater.* **2016**, 28, 8051–8059.
2. S. Xin, L. Yu, Y. You, H.P. Cong, H.P., Y.X. Yin, X.L. Du, Y-G. Guo, S.H. Yu, Y. Cui, and J.B. Goodenough, “The Electrochemistry with Lithium Versus Sodium of Selenium Confined to Slit Micropores” *Nano Letters* **2016**, 16, 4560-4568.
3. Y. Li, B. Xu, H. Xu, H. Duan, X. Lu, S. Xin, W. Zhou, L. Xue, G. Fu, A. Manthiram, and J.B. Goodenough, “Garnet Electrolyte with a Small Interfacial Resistance for Lithium-ion Batteries” *Angewandte Chemie.* **2016**, in press.

References

1. “Physical Properties Data Compilations Relevant to Energy Storage. 1. Molten Salts: Eutectic Data”, NSRDS-NBS 61, Pat 1, U.S. Department of Commerce, Issued March 1978.
2. K. Park, J. H. Cho, J. H. Jang, B. C. Yu, A. T. De La Hoz, K. M. Miller, C. J. Ellison, J. B. Goodenough, *Energy Environ. Sci.* **2015**, 8, 2389-2395.
3. a) Y. Li, J.-T. Han, S. C. Vogel, C.-A. Wang, *Solid State Ionics* **2015**, 269, 57-61; b) L. Cheng, E. J. Crumlin, W. Chen, R. Qiao, H. Hou, S. Franz Lux, V. Zorba, R. Russo, R. Kostecki, Z. Liu, K. Persson, W. Yang, J. Cabana, T. Richardson, G. Chen, M. Doeff, *Physical Chemistry Chemical Physics* **2014**, 16, 18294-18300.

V.D.9. Exploiting Co and Ni Spinels in Structurally-Integrated Composite Electrodes (ANL)

Michael M. Thackeray, Principal Investigator

Jason R. Croy, Co-Principal Investigator

Argonne National Laboratory

9700 South Cass Avenue

Lemont, IL 60439

Phone: 630-252-9184; Fax: 630-252-252-4176

E-mail: thackeray@anl.gov; croy@anl.gov

Tien Q. Duong, DOE Program Manager

U.S. Department of Energy

Advanced Battery Materials Research (BMR)

Vehicle Technologies Office

1000 Independence Avenue, SW

Washington, DC 20585

Phone: 202-586-7836

E-mail: Tien.Duong@ee.doe.gov

Start Date: October 1, 2015

End Date: September 30, 2018

Abstract

Objective

The objective of this project is to minimize or eliminate the voltage fade phenomenon in high capacity, structurally-integrated ‘layered-layered’ cathodes by introducing a stabilizing spinel component into the parent electrode with a particular emphasis on lithium-cobalt-oxide and lithium-nickel-oxide spinel components that accommodate lithium at ~3.5 V vs. metallic lithium.

Accomplishments

- Lithiated spinels in the system $\text{LiCo}_{1-x}\text{Ni}_x\text{O}_2$ ($0 \leq x \leq 0.2$) were prepared to obtain greater insight into their structural complexity and electrochemical properties as a first step to design, characterize, and tailor cobalt-rich spinel stabilizers for high-capacity $x\text{Li}_2\text{MnO}_3 \cdot (1-x)\text{LiMO}_2$ electrodes.
- Synthesis and electrochemical characterization of ‘layered-layered-spinel’ electrode materials containing lithium, nickel, manganese and cobalt (NMC) were initiated – these efforts are on-going.
- Synchrotron X-ray diffraction, transmission electron microscopy, and ^7Li magic angle spinning nuclear magnetic resonance spectroscopy were used to characterize the materials. Density functional theory (DFT) calculations complemented the information gathered from experiment.

Future Achievements

The electrochemical capacity of most lithium-metal-oxide electrodes is compromised by their structural instability and surface reactivity at high potentials. ‘Layered-layered-spinel’ NMC materials will be designed and developed to generate capacities of 200–220 mAh/g without structural or voltage decay. Most promising materials will be scaled up by Argonne’s Materials Engineering and Research Facility (MERF) for evaluation – both internally at Argonne and by industry.

Technical Discussion

Background

Despite their high specific capacity and low cost, the practical implementation of lithium- and manganese-rich ‘layered-layered’ (LL) electrodes, $x\text{Li}_2\text{MnO}_3 \bullet (1-x)\text{LiMO}_2$ ($M = \text{Ni}, \text{Mn}, \text{or Co}$), in lithium-ion cells has been thwarted by structural instability and voltage fade during cycling, poor electrical conductivity, and a low first-cycle efficiency [1]. A strategy to incorporate a spinel component into layered (L) or LL materials to form complex, structurally integrated ‘layered-spinel’ (LS) or ‘layered-layered-spinel’ (LLS) electrode materials was therefore adopted in an attempt to stabilize and enhance the electrochemical properties of high-capacity $x\text{Li}_2\text{MnO}_3 \bullet (1-x)\text{LiMO}_2$ electrodes [2-5]. In this project, attention was focused primarily on evaluating the family of lithiated, cobalt-rich electrode materials, $\text{LiCo}_{1-x}\text{Ni}_x\text{O}_2$ ($0 \leq x \leq 0.2$) with a spinel-related structure, which operate at approximately 3.5 V vs. Li^0 . The overall strategy is discussed more comprehensively in a recent publication that has emanated from this project: E. Lee et al., *Exploring Lithium-Cobalt-Nickel-Oxide Spinel Electrodes for ≥ 3.5 V Lithium-ion Cells*, ACS Appl. Mater. & Interfaces, **8**, 27720 (2016) [5].

Introduction

The strategy of embedding a lithiated cobalt-rich spinel rather than a stoichiometric, manganese-based spinel such as $\text{Li}_{1+y}\text{Mn}_{2-y}\text{O}_4$ or $\text{LiNi}_{0.5}\text{Mn}_{1.5}\text{O}_4$ as a stabilizer for high-capacity $x\text{Li}_2\text{MnO}_3 \bullet (1-x)\text{LiMO}_2$ electrode structures is attractive for the following reasons: (1) Lithiated spinels $\text{LiCo}_{1-x}\text{Ni}_x\text{O}_2$ ($0 \leq x \leq 0.2$) (alternatively, $\text{Li}_2[\text{Co}_{2-2y}\text{Ni}_{2y}]\text{O}_4$ ($0 \leq y \leq 0.4$)), such as $x\text{Li}_2\text{MnO}_3 \bullet (1-x)\text{LiMO}_2$ materials, have close-packed structures with a rock-salt stoichiometry, making them compositionally and potentially structurally compatible with one another; (2) Relative to that of manganese and nickel, cobalt has a lower propensity to migrate during electrochemical $\text{Co}^{3+/4+}$ redox reactions of LiMO_2 electrodes at high potentials[6], thereby offering the possibility of mitigating voltage fade with cycling; and (3) Lithium extraction from a lithiated cobalt-rich spinel component, $\text{Li}_{2-x}\text{Co}_{2-2y}\text{Ni}_{2y}\text{O}_4$ ($0 \leq x \leq 1$), occurs at a potential (~ 3.6 V) [7,8] significantly higher than that of its lithiated manganese-oxide spinel analogue, $\text{Li}_2\text{Mn}_2\text{O}_4$ (~ 2.9 V) [9,10].

Approach

The approach is to design, synthesize and characterize new spinel-related materials, compositions and structures that operate between 3 to 4 V and to determine their structural/electrochemical property relationships. This information will be used to identify the most promising spinel components that can be used, in low concentration, to stabilize high capacity $x\text{Li}_2\text{MnO}_3 \bullet (1-x)\text{LiMO}_2$ ($M = \text{Ni}, \text{Mn}, \text{Co}$) electrode structures.

Results

‘Layered-Spinel’ (LS) Lithium-Cobalt-Nickel-Oxide Electrodes

$\text{LiCo}_{1-x}\text{Ni}_x\text{O}_2$ materials, when synthesized at low-temperature ($\sim 400^\circ\text{C}$), have a cubic structure that resembles a lithiated spinel; they are of interest for stabilizing high capacity, lithium- and manganese-rich metal oxide electrodes. For materials synthesized at intermediate temperature ($600\text{--}800^\circ\text{C}$), both cubic and layered phases were detected by powder X-ray diffraction and their electrochemical signatures. The use of a local Co-based spinel component within a layered or layered-layered electrode structure is one of the key features that is being targeted to optimizing the capacity and cycling stability of structurally-integrated LLS composite cathodes; for this reason, $\text{LiCo}_{1-x}\text{Ni}_x\text{O}_2$ materials synthesized at intermediate temperatures have been studied in detail to determine the structural and electrochemical property relationships of stabilizing layered-spinel components. Figure V-111a and b show, respectively, HR-TEM and STEM-HAADF images of a typical nanocomposite, ‘layered-spinel’ $\text{LiCo}_{0.9}\text{Ni}_{0.1}\text{O}_2$ product prepared at 600°C . The images clearly indicate that the spinel and layered domains within the composite structure are atomically aligned with one other. These images strongly suggest that, on increasing the firing temperature, the phase transition from spinel to a layered configuration occurs at distinct phase boundaries and, therefore, that the layered-to-spinel ratio can be tailored by temperature control. This observation provides compelling evidence to support the strategy of using a Co-based spinel component to stabilize layered and ‘layered-layered’ electrode structures. The results also

emphasize the need to accurately control synthesis conditions while fabricating these complex nanocomposite materials.

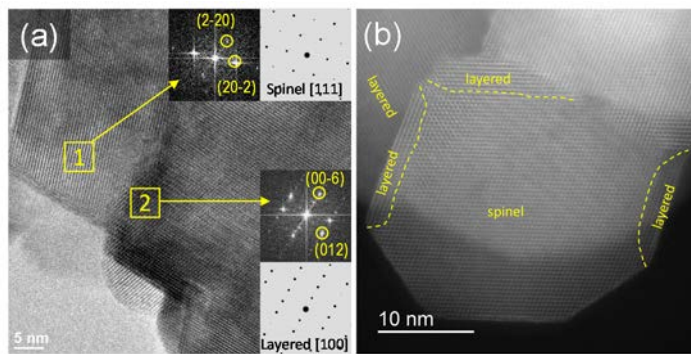


Figure V-111: (a) HR-TEM and (b) STEM-HAADF images of $\text{LiCo}_{0.9}\text{Ni}_{0.1}\text{O}_2$ (600 °C) showing atomically integrated 'layered-spinel' nano-composite crystals

Relatively little is known about 'low-to-intermediate temperature' lithiated-spinel- and composite layered-spinel $\text{LiCo}_{1-x}\text{Ni}_x\text{O}_2$ materials because prior studies of these compositions have focused predominantly on their high-temperature ($\sim 900^\circ\text{C}$) layered analogues, such as LiCoO_2 (LCO) and $\text{LiNi}_{0.80}\text{Co}_{0.15}\text{Al}_{0.05}\text{O}_2$ (NCA) electrode materials that are of greater technological and commercial significance. In order to probe the structural and electrochemical features of $\text{LiCo}_{1-x}\text{Ni}_x\text{O}_2$ materials synthesized at intermediate temperatures, a series of $\text{LiCo}_{1-x}\text{Ni}_x\text{O}_2$ ($0 \leq x \leq 0.5$) materials, when synthesized at 700 and 800 °C, was revisited; their electrochemical properties have been assessed in the context of the expected signatures of layered- and spinel-type structures. Figure V-112a shows the X-ray diffraction patterns of $\text{LiCo}_{1-x}\text{Ni}_x\text{O}_2$ samples prepared at 700 °C. Although weak peaks of a $\text{Li}_6\text{Ni}_{1-6}\text{O}$ rock salt impurity phase were observed in these samples for $x \geq 0.3$, the solid solution behavior of Co and Ni in the residual $\text{LiCo}_{1-x}\text{Ni}_x\text{O}_2$ structure was confirmed by a linearly increasing lattice volume as a function of Ni content, x (data not shown). The normalized voltage profiles and dQ/dV plots of the $\text{Li}/\text{LiCo}_{1-x}\text{Ni}_x\text{O}_2$ cells in Figure V-112b and c, respectively, clearly indicate the development of two electrochemical processes, one at ~ 3.9 V, that was attributed to a Co-rich layered structure and the other at ~ 3.5 V, attributed either to a Ni-rich layered structure or a lithiated-spinel structure, $\text{Li}_2[\text{Co}_{2-2y}\text{Ni}_{2y}]_2\text{O}_4$ (or both). What is particularly noteworthy about the data is that, for $y \geq 0.3$ in Figure V-112b and c, the electrochemical profile adopts that of a nickel-rich electrode, while a lower nickel content $0 < y \leq 0.2$ appears to maintain some spinel-like character in the structure, and therefore some transition metal ions in the lithium layers, even when fired at 700 °C. The data highlight the possibility of tailoring the spinel character of the structure by controlling composition as well as synthesis conditions.

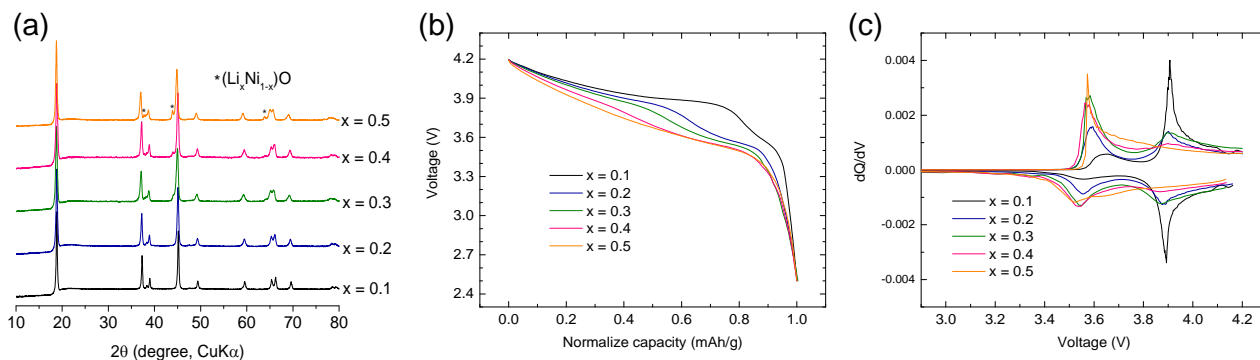


Figure V-112: (a) XRD patterns, (b) normalized discharge profiles, and (c) differential capacity plots of $\text{LiCo}_{1-x}\text{Ni}_x\text{O}_2$ materials synthesized at 700 °C

Layered $\text{Li}[\text{Co}_{1-x-y}\text{Ni}_x\text{Mn}_y]\text{O}_2$ and ‘Layered-Spinel’ $\text{Li}_2\text{MnO}_3 \bullet \text{Li}[\text{Co}_{1-x}\text{Ni}_x]\text{O}_2$ Electrodes

Encouraged by the finding that structurally integrated spinel configurations, characterized by the presence of cobalt (and nickel) in the lithium-rich layers, were formed by solid-state reactions at intermediate temperatures (700 - 800°C), synthesis efforts were expanded to prepare LS composite materials containing Ni, Mn, Co and excess Li (i.e., Li-rich NMC).

A series of $\text{Li}[\text{Co}_{1-2x}\text{Ni}_x\text{Mn}_x]\text{O}_2$ compositions ($x=0.025, 0.05, \text{ and } 0.1$) electrode materials were prepared at various synthesis temperatures between 500 and 900°C. Figure V-113a shows normalized voltage profiles of lithium cells with a $\text{Li}[\text{Co}_{0.9}\text{Ni}_{0.05}\text{Mn}_{0.05}]\text{O}_2$ electrode ($x=0.05$) that had been synthesized at various temperatures. The 3.5 V plateau, attributable to the lithiated spinel structure, is clearly observed in the sample fired at 500°C. Although the length of the 3.5 V plateau decreases significantly for cells with electrodes synthesized at higher temperatures, this reaction is still clearly visible when the electrodes were prepared at 600°C. Corresponding differential capacity (dQ/dV) plots in Figure V-113(b-d) reveal a weak oxidation peak at ~ 3.7 V for $x = 0.05$ and 0.1 electrodes prepared at 900°C, indicating that the reaction mechanism on charge differs slightly from the discharge process. It is also noteworthy that the dQ/dV plots reflect more stable cycling behavior as the degree of Ni and Mn substitution, x , in these NMC electrodes increases.

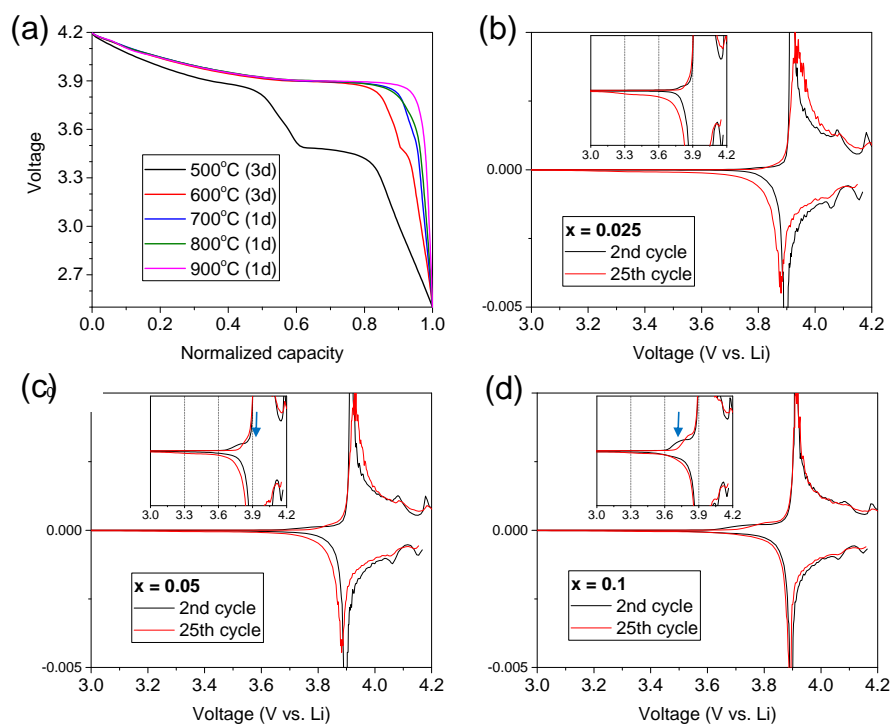


Figure V-113: (a) Normalized 1st discharge profile of $\text{Li}[\text{Co}_{0.9}\text{Ni}_{0.05}\text{Mn}_{0.05}]\text{O}_2$ synthesized at various temperatures between 500 and 900 °C, (b-d) differential capacity plots of a $\text{Li}[\text{Co}_{1-2x}\text{Ni}_x\text{Mn}_x]\text{O}_2$ electrode ($x=0.025; 0.05; 0.10$) prepared at 900 °C

In a parallel study of LS NMC electrodes, $x\text{Li}_2\text{MnO}_3 \bullet (1-x)\text{Li}[\text{Co}_{1-y}\text{Ni}_y]\text{O}_2$ materials were synthesized at temperatures between 500 and 900°C. The XRD patterns of samples fired at 600°C are shown in Figure V-114a. All samples clearly exhibit merged (018)/(110) peaks at $\sim 65^\circ 2\theta$, suggesting the presence of a cubic, lithiated-spinel structure. The low-intensity diffraction peaks at $\sim 22^\circ 2\theta$, due to Li/Mn ordering, are broad as a result of the intermediate temperature synthesis. However, first-cycle voltage profiles (not shown) reveal an irreversible plateau at ~ 4.5 V consistent with the electrochemical activation of Li_2MnO_3 regions in the electrode structures. Figure V-114(b-d) show the electrochemical data of lithium half cells, when cycled between 2.5 and 4.2 V. After the initial charge, the voltage profiles in Figure V-114b show two electrochemical events that were assigned to lithium insertion into localized layered regions (~ 3.9 V) and into spinel regions (3.6 V). With increasing Li_2MnO_3 content, x , the capacity retention on cycling improves (Figure V-114c) while the specific capacity decreases (Figure V-114d). In addition, a comparison between samples having the same Li_2MnO_3 content reveal an enhancement of cycling stability as nickel is substituted for cobalt (Figure V-114d).

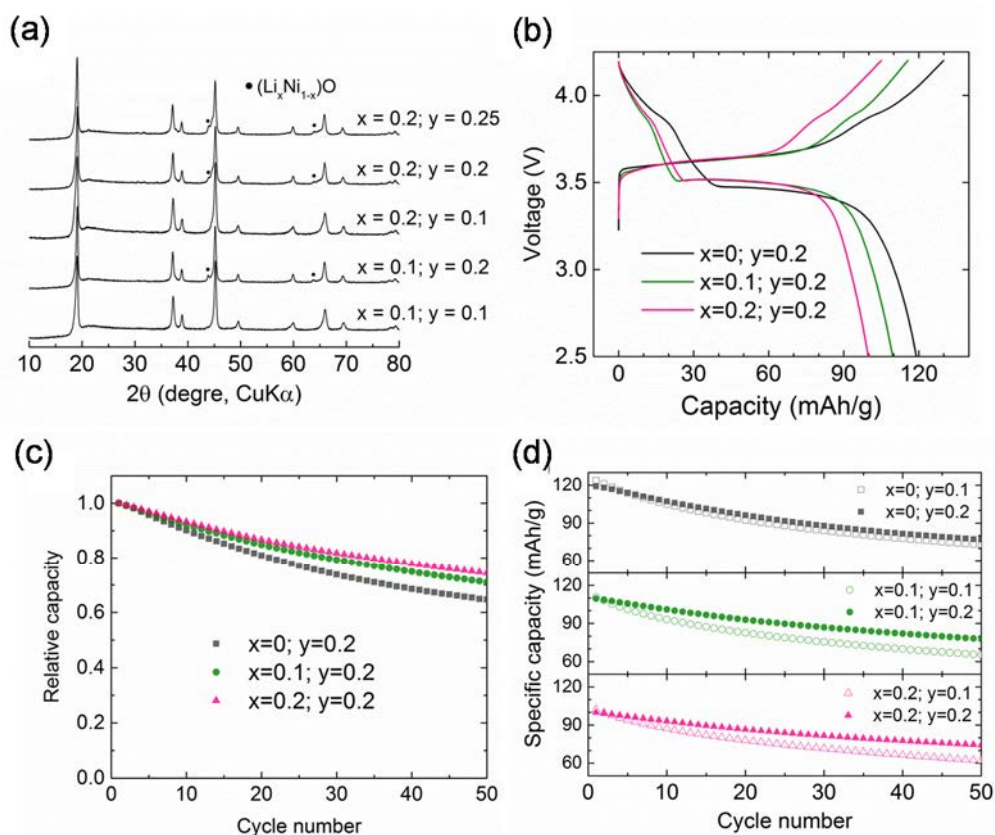


Figure V-114: (a) XRD patterns, (b) initial voltage profiles, (c) relative capacity retention, and (d) cycle performance comparison of $x\text{Li}_2\text{MnO}_3 \cdot (1-x)\text{LiCo}_{1-y}\text{Ni}_y\text{O}_2$ electrode materials synthesized at 600°C

Conclusions

- Considerable progress has been made in synthesizing and understanding the structural and electrochemical complexity of cobalt- and nickel-substituted lithiated spinel structures that are typically prepared at moderately low temperatures ($400\text{--}500^\circ\text{C}$).
- Preliminary studies were initiated to explore the possibility of using lithiated cobalt-nickel-oxide spinels as stabilizing components in layered-spinel NMC electrodes. These studies, and encouraging results therefrom, have opened the door to the exploitation of a wide phase and compositional space that deserves further attention.

Products

Presentations/Publications/Patents

Presentations

1. M. M. Thackeray, *Energy Storage: Challenges and Opportunities in an Evolving Lithium Economy*, Victor Pretorius Memorial Lecture, University of Pretoria, South Africa, 6 October 2015. (Invited.)
2. E. Lee, J. R. Croy and M. M. Thackeray, *Novel Cathode Materials and Process Methods*, BMR Program Review Meeting, LBNL, Berkeley, California, 20 January 2016.
3. M. M. Thackeray, J. R. Croy, E. Lee, J.-S. Park, J. Blauwkamp, B. Yonemoto, R. Benedek, F. Dogan, M. Balasubramanian, C. Wang, V. P. Dravid, C. Wolverton, *Tailoring Spinel Electrodes for High Capacity Lithium-ion Cells*, DOE Annual Merit Review, Vehicle Technologies Program, Washington DC, 8-12 June, 2016.

4. M. M. Thackeray, *Strategies and Advances in the Structural Design of Lithium Metal Oxide Electrodes for Lithium-ion Batteries*, 18th International Meeting on Lithium Batteries, Chicago, Illinois, 19-24 June 2016. (Invited).
5. E. Lee, J. Blauwkamp, J. S. Park, J. Wu, F. Dogan, R. Benedek, J. R. Croy, V. P. Dravid, and M. M. Thackeray, *Structure and Electrochemistry of Lithium-Cobalt-Oxide Spinel and their Role in 'Layered-Spinel' Composite Cathodes*, 18th International Meeting on Lithium Batteries, Chicago, Illinois, 19-24 June 2016.

Publications

1. E. Lee, J. Blauwkamp, F. C. Castro, J. Wu, V. P. Dravid, P. Yan, C. Wang, S. Kim, C. Wolverton, R. Benedek, F. Dogan, J. S. Park, J. R. Croy, and M. M. Thackeray, *Exploring Lithium-Cobalt-Nickel-Oxide Spinel Electrodes for ≥ 3.5 V Lithium-ion Cells*, ACS Appl. Mater. & Interfaces, **8**, 27720 (2016).

Patent Applications

1. M. M. Thackeray, J. R. Croy, B. R. Long, J. S. Park and E. Lee, *Cobalt-Stabilized Electrodes for Lithium Batteries*, US Application 20150318546 (5 November 2015).

References

1. J. R. Croy, M. Balasubramanian, K. G. Gallagher, A. K. Burrell, Acc. Chem. Res. **48**, 2813 (2015).
2. S.-H. Park, S.-H. Kang, C. S. Johnson, K. Amine and M. M. Thackeray, Electrochem. Comm. **9**, 262 (2007).
3. D. Kim, G. Sandi, J. R. Croy, K. G. Gallagher, S.-H. Kang, E. Lee, M. D. Slater, C. S. Johnson and M. M. Thackeray, J. Electrochem. Soc. **160**, A31-A38 (2013).
4. B. R. Long, J. R. Croy, J. S. Park, J. Wen, D. J. Miller, and M. M. Thackeray, J. Electrochem. Soc., **161** (14) A2160-A2167 (2014).
5. E. Lee, J. Blauwkamp, F. C. Castro, J. Wu, V. P. Dravid, P. Yan, C. Wang, S. Kim, C. Wolverton, R. Benedek, F. Dogan, J. S. Park, J. R. Croy, and M. M. Thackeray, ACS Appl. Mater. & Interfaces, **8**, 27720 (2016).
6. J. Reed and G. Ceder, Chem. Rev. **104**, 4513 (2004).
7. R. J. Gummow, M. M. Thackeray, W. I. F. David and S. Hull, Mater. Res. Bull. **27**, 327(1992).
8. R. J. Gummow and M. M. Thackeray, J. Electrochem. Soc. **140**, 3365 (1993).
9. M. M. Thackeray, W. I. F. David, P. G. Bruce and J. B. Goodenough, Mater. Res. Bull. **18**, 461 (1983).
10. J. M. Tarascon and D. Guyomard, J. Electrochem. Soc. **138**, 2864 (1991).

V.D.10. Discovery of High-Energy Lithium-Ion Battery Materials (LBNL)

Wei Tong, Principal Investigator

Lawrence Berkeley National Laboratory
Energy Storage and Distributed Resources Division
1 Cyclotron Road, MS62R0203
Berkeley, CA 94720
Phone: 510-486-7084
E-mail: weitong@lbl.gov

Tien Q. Duong, DOE Program Manager

U.S. Department of Energy
Advanced Battery Materials Research (BMR)
Vehicle Technologies Office
1000 Independence Avenue, SW
Washington, DC 20585
Phone: 202-586-7836
E-mail: Tien.Duong@ee.doe.gov

Start Date: October 2015
End Date: September 2018

Abstract

Objectives

- Develop a cathode that can cycle > 200 mAh/g while exhibiting minimal capacity and voltage fade. Target at the compositions in Li-TM-O chemical space that utilizes Ni²⁺/Ni⁴⁺ redox to enable high capacity and integrates a second transition metal to improve structural stability.
- Gain fundamental understanding of the composition, structure, and electrochemical property relationships to further guide the material design.

Accomplishments

- Synthesized phase pure LiNiO₂ by solid-state reaction that delivered an initial capacity of 200 mAh/g.
- Elucidated the critical role of Li excess in the surface characteristics of LiNiO₂ and its impact on electrochemical performance.
- Identified optimal synthetic condition for Li₂NiO₂ by solid-state reaction, a high initial capacity of 330 mAh/g was achieved.
- Developed a comprehensive understanding of the key contributing factors to the performance decay of LiNiO₂ and Li₂NiO₂ on the basis of Ni³⁺/Ni⁴⁺ and Ni²⁺/Ni⁴⁺ redox through in-depth studies on the crystal and electronic structure change in the bulk and at the surface.

Future Achievements

- Design Li-excess metal oxide compositions that are composed of Ni and a second transition metal to serve as electrochemical redox and structural stabilizer.
- Develop the synthesis that can be used to screen the second transition metals for Li-excess Ni-based metal oxides. Perform the synthesis and initial electrochemical characterization of the designed compositions.
- Identify promising compositions that demonstrate good electrochemical performance with an initial capacity > 200 mAh/g for detailed studies on phase transformation and charge compensation during the electrochemical reaction.

Technical Discussion

Background

Rechargeable lithium-ion batteries are considered the most promising energy storage devices for electrical vehicles (EVs). Of the commonly used cathode materials in lithium-ion batteries, layered lithium transition metal oxides (LiTMO₂, TM is a transition metal) are the most promising candidates for EVs because of their high theoretical capacity (~ 270 mAh/g) and relatively high average operating voltage (~ 3.6 V vs. Li+/Li). Continuous search for better cathodes with higher energy and power density, as well as long cycle life, good safety characteristics and lower cost, has led to some promising materials, e.g., LiNi_{1-x-y}Mn_xCo_yO₂ (0 < x, y < 1) (NMC) and LiNi_{0.8}Co_{0.15}Al_{0.05}O₂ (NCA). However, a practical capacity is limited to about 180 mAh/g to minimize the possible phase transformation at low Li concentration, extend the cycle life, and improve the safety characteristics. In order to achieve the mass adoption of EVs, energy density needs to be doubled in order to meet the performance requirements of EVs with a 300 to 400 mile range. Our current efforts are directed towards the development of new high-energy cathodes that can cycle > 200 mAh/g while exhibiting minimal capacity and voltage fade. The emphasis is on the compositions in Li-Ni-O composition space that utilizes Ni²⁺/Ni⁴⁺ redox to enable high capacity and integrates a second transition metal to serve as structural stabilizer.

Introduction

The recent discovery of high-capacity materials with lithium excess provides new insights into design principles for potential high-capacity cathode materials. According to the percolation theory, lithium excess is required in order to access 1 lithium exchange capacity in LiTMO₂ compounds. This seems to be independent of transition metal species, therefore, could open up a composition space for the search of new materials with high capacity. This project proposes to use this theory as the material design principle to determine a winning composition. Of all the transition metals in periodic table, Ni is an interesting element as its Ni²⁺/Ni⁴⁺ redox couple may provide a solution to overcome the capacity limitation caused by the usual limit of one electron per transition metal within an acceptable voltage range. Within this composition space, one of the two interesting compounds is LiNiO₂, a compound within layered oxide family demonstrating a similar electrochemical properties to LiCoO₂. Another one is Li₂NiO₂, which, in principal, enables the full utilization of the Ni²⁺/Ni⁴⁺ redox couple with two lithium per formula unit, providing a high theoretical capacity of 513 mAh/g. Both materials have a layered structure but belong to different space group with different Ni coordination in the structure. The search of new materials will initiate within the known phase space of these two compounds and extend to composition design of Li-excess nickel based oxides.

Approach

This project integrates material design, synthesis, physical and electrochemical evaluation to search for new high capacity cathodes within Li-Ni-O chemical space. We initiated our material synthesis efforts with the known LiNiO₂ and Li₂NiO₂ compounds to gain good understanding of the synthesis structure electrochemical property relationships for Ni-based layered oxide compounds. Both materials were synthesized via a facile solid-state reaction and subjected to a variety of synchrotron based radiation and spectroscopy techniques to characterize the bulk and surface properties in the pristine and cycled states. Both the crystal and electronic structural changes of the as-produced materials during the electrochemical reaction were investigated to understand the degradation mechanism of Ni-containing layered oxides.

Results

LiNiO₂ samples were prepared by a solid-state method using both commercial and precipitated Ni(OH)₂ precursors. 2% and 10% excess LiOH precursor was used along with precipitated Ni(OH)₂ to prepare LiNiO₂ samples, denoted as “solution_2exLi” and “solution_10exLi”, respectively. “solid_10exLi” sample was synthesized following a general solid state reaction protocol by milling Li₂CO₃ and Ni(OH)₂ precursors with 10% excess Li. Figure V-115a shows the synchrotron X-ray diffraction (SXRD) patterns of the as-synthesized LiNiO₂ powders. The high intensity ratios between (003)/(104) and clear peak splits between (108) and (110)

suggest good phase crystallinity and cation ordering. Based on the Rietveld refinement results, the occupancies of 3a sites by Ni ions are less than 2% for all three samples.

Electrochemical test was performed between 4.3 and 2.7 V at C/10. The 1st cycle voltage profiles are shown in Figure V-115b. Solution_2exLi delivered a capacity of 223 mAh/g in the 1st charge, and 190 mAh/g in the 1st discharge. The 1st cycle electrochemical behaviors of LiNiO₂ prepared with 10% excess Li (solution_10exLi and solid_10exLi) were quite similar, suggesting the negligible effect of Ni(OH)₂ precursor. These two samples delivered a charge capacity of 240 mAh/g (equivalent to 0.85 Li deintercalation) and a discharge capacity of 206 mAh/g (equivalent to 0.73 Li re-intercalation). These differences among the samples were repeatable and beyond what would be expected from cell-to-cell variation (< 5 mAh/g) within our experiments, thus, can be considered to result from the active material. The higher capacity and lower polarization for the samples with 10% excess Li compared to the solution_2exLi sample indicated that the amount of excess Li in the synthesis had a much larger effect on the electrochemical properties than the source of the Ni precursor. Not only did the larger excess of Li have positive effects on the 1st cycle capacity, but also better capacity in the subsequent cycles was observed (Figure V-115d). Scanning electron microscopy (SEM) images illustrate that all three samples have a similar morphology with a secondary particle size of about a few microns. Given the similar bulk properties, such differences observed in the electrochemical performance of the samples synthesized with different amounts of excess Li and different types of Ni(OH)₂ precursor must originate from the surface characteristics.

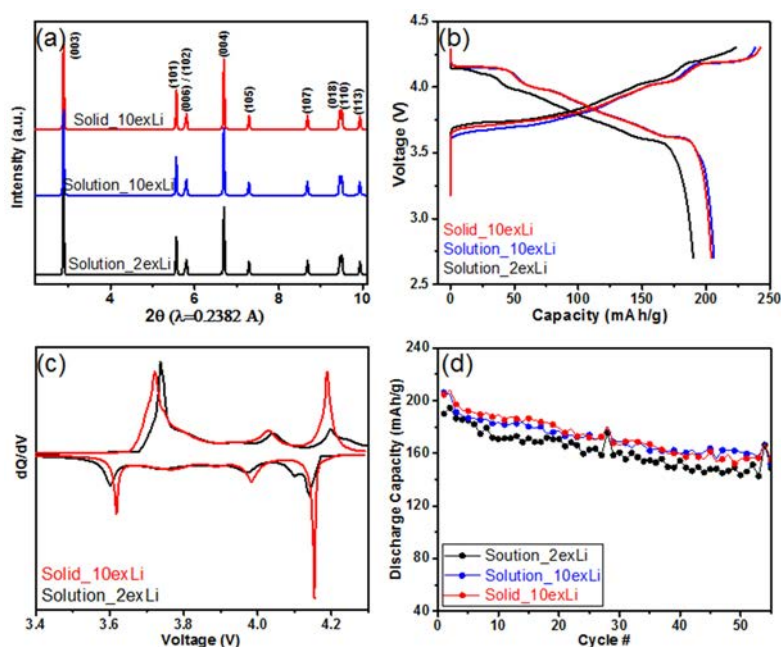


Figure V-115: (a) Synchrotron X-ray diffraction patterns, (b) the 1st cycle voltage profiles, (c) dq/dV plots, and (d) cycling performances of the as-produced LiNiO₂. Cells were cycled between 4.3 and 2.7 V at C/10, capacity at 1 C was defined as 180 mAh/g

To understand these further, surface-sensitive soft X-ray Absorption Spectroscopy (XAS) technique was employed. The Ni L₃-edge soft XAS spectra of the three pristine powders are shown in Figure V-116. Three detection modes, Auger electron yield (AEY), Total electron yield (TEY), and Fluorescence yield (FY), were collected simultaneously to probe 1 - 2 nm, 2 - 5 nm, and ~ 50 nm from the sample surface towards the bulk, respectively. For LiNiO₂, the most salient electronic structure can be qualitatively obtained through the deconvolution of the Ni L₃-edge into high-energy (L₃_{high}) and low-energy (L₃_{low}) features. The ratio between L₃_{high} and L₃_{low} is in a positive relationship with Ni oxidation state. The three modes (AEY, TEY, and FY) of Ni L₃-edge for each sample shown in Figure V-116a-c are normalized with respect to the L₃_{low} feature. It can be clearly seen that the variation in the Ni oxidation state follows a similar trend from the very surface to the sub-surface for all three of the samples. As evidenced by the increased L₃_{high}/L₃_{low} ratios from AEY to FY mode, Ni is more oxidized in the sub-surface and bulk region of the LiNiO₂ samples compared to their surfaces; in other words, there is an oxidation state gradient. When comparing each mode across the three samples (Figure V-117d), it can be seen that the solution_2exLi has the lowest Ni oxidation state in all three

modes, while the $L3_{\text{high}}/L3_{\text{low}}$ ratios for the other two samples with 10% excess Li are very close to each other, indicating similar Ni oxidation states and gradients.

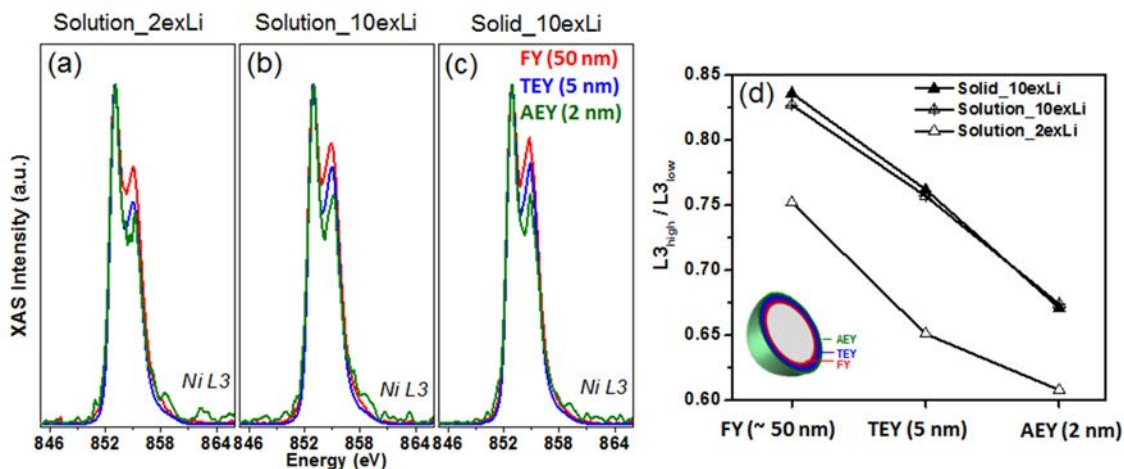


Figure V-116: Soft XAS spectra for the three pristine LiNiO_2 samples. (a) Ni L3-edge spectra from three detection modes with different probing depths (AEY: 1 - 2 nm; TEY: 2 - 5 nm; FY: ~ 50 nm). Note: all the spectra are normalized with respect to the low energy Ni L3-edge. (b) $L3_{\text{high}}/L3_{\text{low}}$ ratios of all three samples at different modes shown in (a) - (c)

Despite a high initial discharge capacity of 205 mAh/g, the capacity still faded relatively fast and only 160 mAh/g was remained at the end of the 45th cycle, corresponding to 78% capacity retention with respect to the 1st cycle (Figure V-115d). *Ex situ* synchrotron X-ray diffraction (SXRD) at the end of charge and discharge states for the selected cycles were collected to further investigate the phase evolution of LiNiO_2 over the extended cycles. After the first charge, (003) diffraction peak shifted to lower 2θ value, which can be attributed to the H2 phase formation. At the end of 2nd charge, another set of diffraction peaks was observed (as highlighted by the green dash line). This is an indication of H3 phase formation. Afterwards, H3 phase repeatedly occurred at the end of charge in the subsequent cycles (10th and 45th). However, it can be clearly seen that the intensity of H3 (003) diffraction peak gradually decreased, suggesting the less H3 phase formation. In addition to the structural change at the charged states, the pristine structure was not completely resumed after the 1st discharge. As shown in Figure V-116b, the (003) peak slightly shifted to the lower angle region, compared to its pristine state, suggesting the lattice expansion along c direction likely due to the irreversible Li loss. In the subsequent cycles, the variations were fairly small, indicated by the similar peak positions and intensities in the XRD patterns.

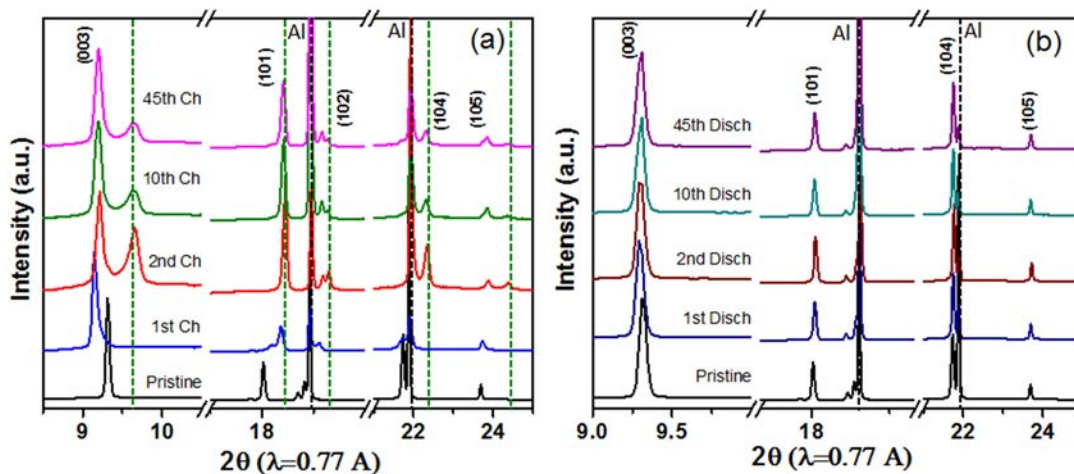


Figure V-117: SXRD of LiNiO_2 at (a) 4.3 V charge states, and (b) 2.7 V discharge states for the selected cycles. Diffraction peaks related to Al current collectors and H3 phases are highlighted by black and green dash lines, respectively

In parallel with the phase evolution tracked by SXRD, hard XAS was also performed at the Ni K-edge (8333 eV) to elucidate the charge compensation mechanism and local environments around Ni ions (Figure V-118). In the X-ray absorption near edge structure (XANES) (Figure V-118a), the Ni edge shifted to higher energy after each selected charge state (dash lines) compared to the edge in the pristine electrode (black solid line), owing to the oxidation of Ni ions during the charge processes. Close examination of the edge positions on the derivative plots in Figure V-118b revealed the highest Ni valence state at the end of the 2nd charge (red dash line), which is in accordance with the most prominent H3 phase formation (Figure V-117a). It further confirmed that more Li ions were extracted during the 2nd charge than the 1st charge. At the 10th and 45th cycle, the Ni edge at the charging states slightly moved to lower energy than that at the 2nd charge. The discharge states (solid lines) upon cycling show a different trend, where a continuous shift to higher energy indicates less reduced Ni after repeated discharges. These two changes lead to the conclusion that the amount of electrons from Ni redox was getting smaller after cycling and the decrease in Ni redox change resulted from both the charge and discharge states.

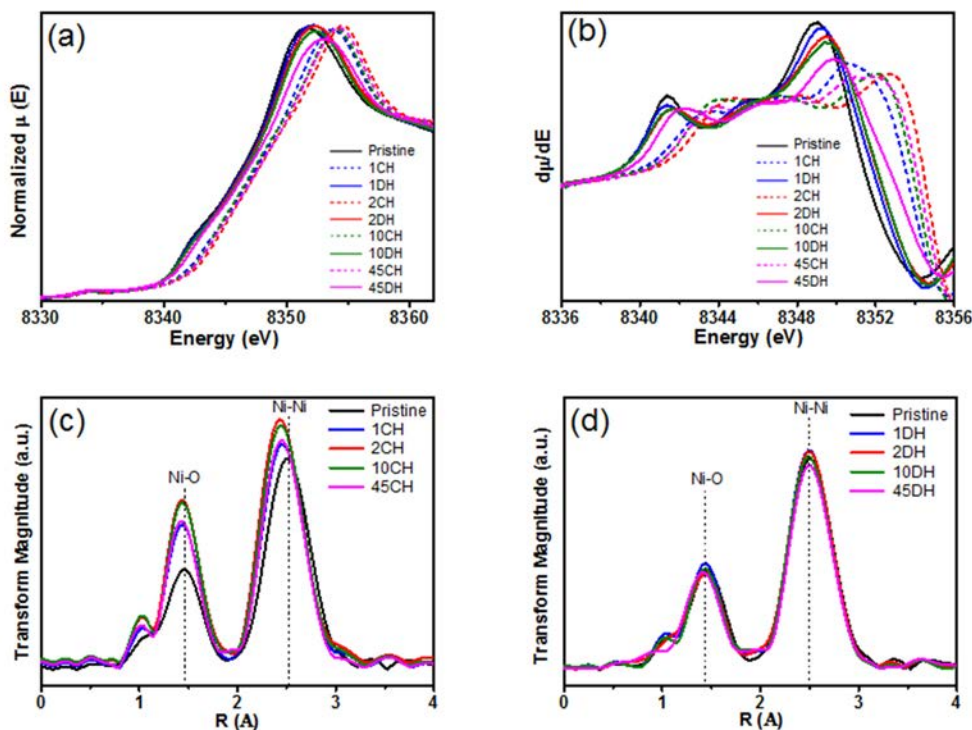


Figure V-118: (a) XANES, (b) XANES derivative plots for selected states, and Fourier transform radial distribution function for the Ni K-edge EXAFS at (c) charge, and (d) discharge states

Soft XAS spectra were collected at various cycled states to investigate the variation of surface properties over the extended cycles (Figure V-119). A pair of total electron yield (TEY) and fluorescence yield (FY) were collected to probe the variation of Ni oxidation at 2 - 5 nm and ~ 50 nm from the surface towards the bulk. Again, the ratio of Ni L-edge at high-energy and low-energy states ($L_{3\text{high}}/L_{3\text{low}}$) shows a positive relationship with the Ni valence state. The FY and TEY modes of Ni L₃-edge for electrodes at various states shown in Figure V-119 are normalized with respect to the $L_{3\text{low}}$ feature. In the pristine state (Figure V-119a), the $L_{3\text{high}}/L_{3\text{low}}$ ratio is smaller in TEY mode (blue) than that in FY mode (red), indicating more reduced Ni ions at the surface. After charge processes (Figure V-119b-e), the $L_{3\text{high}}/L_{3\text{low}}$ ratio systematically increased compared to the pristine electrode owing to the Ni oxidation. Interestingly, the $L_{3\text{high}}/L_{3\text{low}}$ ratios in TEY mode at charged states gradually decreased from the 1st to 45th cycle, indicating that the degree of Ni oxidation was reduced at the surface over the extended cycles. After the 1st discharge, the surface characteristics were similar to that in the pristine state. However, the $L_{3\text{high}}/L_{3\text{low}}$ ratio in TEY mode increased after the 10th discharge and further enlarged after the 45th discharge, revealing that the Ni reduction after the discharge over long-term cycling was not complete, i.e., the Ni redox reaction was not fully reversible at the surface. Variation of Ni oxidation state in the bulk detected by hard XAS and at the surface by soft XAS showed that reversible Ni redox within each cycle was getting smaller both in the bulk and at the surface. This is direct evidence of the electronic structure changes that underpin the reversible capacity loss.

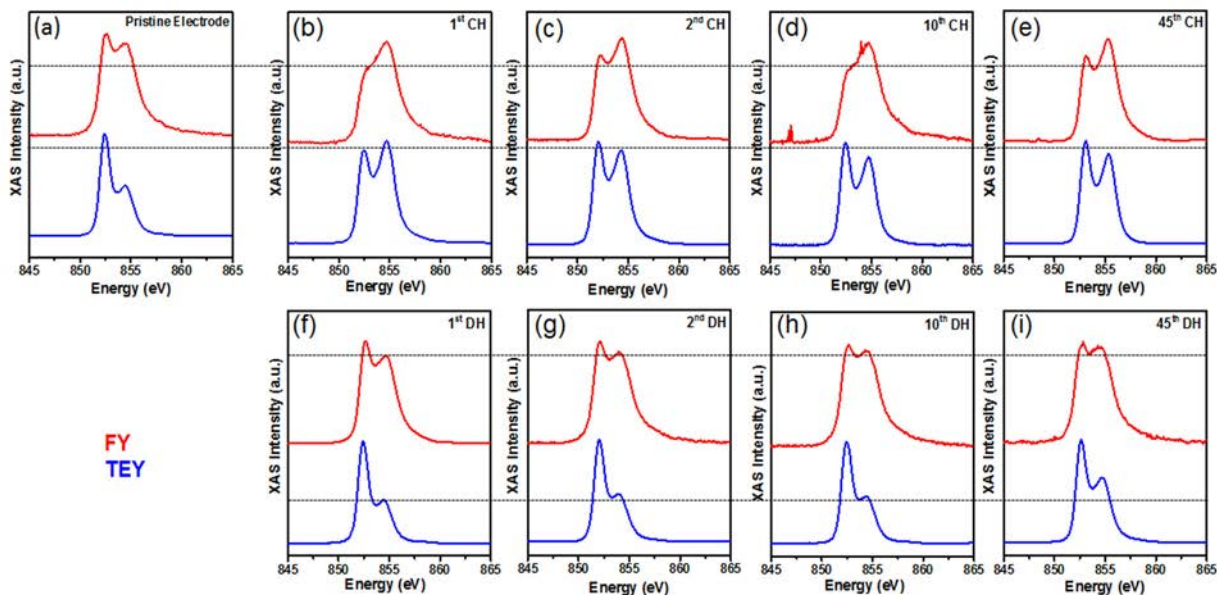


Figure V-119: Soft XAS spectra of Ni L3-edge at: (a) pristine state, (b) 1st charge, (c) 2nd charge, (d) 10th charge, (e) 45th charge, (f) 1st discharge, (g) 2nd discharge, (h) 10th discharge, (i) 45th discharge. The dash lines provide guidance for comparison of Ni L3-edge between the 1st cycle and later cycles

Li_2NiO_2 and a series of $\text{Li}_2\text{Ni}_{1-x}\text{Cu}_x\text{O}_2$ ($0 < x < 1$) samples were prepared by a solid state method. Figure V-120a shows the XRD patterns of the four samples with Ni content ranging from 1 to 0.4. Overall, all the major XRD peaks in these samples could be indexed to *Immm* space group. Close examination of the XRD patterns revealed a small amount of NiO impurity in the final product of Li_2NiO_2 , whereas, Cu substitution removed the NiO impurity and facilitated the formation of pure *Immm*-type phase. In addition, shifts of the XRD diffraction peaks were observed with increasing Cu content (dash lines) due to the substitution of a larger Cu ion on the Ni site.

The 1st cycle voltage profiles are displayed in Figure V-120b. Li_2NiO_2 delivered a capacity of 380 mAh/g during the first charge and 330 mAh/g during the first discharge. With Cu substituted, both charge and discharge capacities increased; the total charge capacity increased up to ~ 440 mAh/g at 0.2 Cu and showed little change with Cu content. This was presumably ascribed to the removal of electrochemically inactive NiO impurity in the Cu substituted samples. On the other hand, the Cu substitution resulted in a substantial change in the charge profiles, which progressively decomposed into two distinguishable plateaus around 3.2 and 3.6 V. As shown in Figure V-120c, the dQ/dV of Li_2NiO_2 during the charge was featured by several peaks around 3.2, 3.5, 3.7, and 4.0 V. With 0.2 Cu substitution, oxidation peaks around 3.7, and 4.0 V remained, suggesting the retaining of Li_2NiO_2 features. But the oxidation peak around 3.2 V appeared to grow at the expense of 3.5 V peak. Further increasing Cu content to 0.6 led to only sharp peaks at 3.2 and 4.0 V. Therefore, we can conclude that the oxidation peak at 3.2 V was associated with Cu substitution, and 4.0 V peak was a common feature of Li_2NiO_2 and Li_2CuO_2 .

Meanwhile, the discharge capacity increased with Cu content and reached 380 mAh/g at 0.6 Cu. The discharge profile of Li_2NiO_2 was featured by three reduction peaks around 3.6, 2.0, and 1.8 V, resembling with that of electrochemically lithiated LiNiO_2 and suggesting the formation of layered LiNiO_2 after the 1st charge. The absence of reduction peaks at > 3 V indicated an irreversible phase transformation in the high voltage region. Changes in the discharge profiles varied with Cu content. At 0.6 Cu, the 3.6 and 2.0 V plateaus gradually diminished and was replaced by a new 2.9 V plateau, suggesting the Cu-related phase transformation. All these changes implied Cu substitution influenced the phase transformation mechanism of Li_2NiO_2 during the charge process. On the other hand, although the Cu substitution improved the initial capacity, the capacity retention (Figure V-120d) was not effectively enhanced within the tested voltage window (4.6 – 1.5 V). Of all the four materials, an intermediate composition, $\text{Li}_2\text{Ni}_{0.8}\text{Cu}_{0.2}\text{O}_2$, was chosen for the electrochemical mechanism studies considering a substantial change in the 1st charge profile, preserved discharge features, and relatively good capacity and retention.

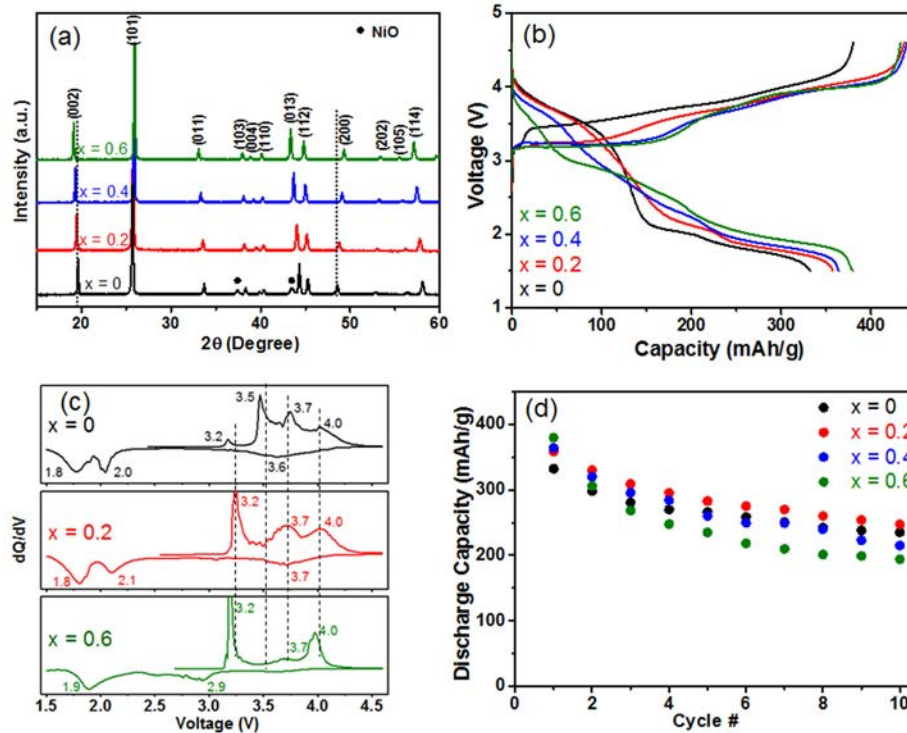


Figure V-120: (a) X-ray diffraction patterns, (b) the 1st cycle voltage profiles, and (c) selected 1st cycle dQ/dV plots, (d) cycling performance of $\text{Li}_2\text{Ni}_{1-x}\text{Cu}_x\text{O}_2$ ($x = 0, 0.2, 0.4, 0.6$) solid solutions. Cells were cycled at 12 mA/g between 4.6 and 1.5 V

In order to elucidate the structural evolution, *Ex situ* XRD patterns were collected at various states of charge. As shown in Figure V-121a-b, a new set of diffraction peaks represented by the dash lines developed upon charge to 3.8 V, which could be indexed as $\text{Li}_{1+\delta}\text{CuO}_2$ ($0 \leq \delta \leq 0.5$). Meanwhile, another set of broad diffraction peaks (solid circles) showed a match with phases belonging to *Fm3m* space group (e.g., NiO and $\text{Li}_{1-x}\text{Ni}_x\text{O}$). When further charging the electrode to 4.6 V (Figure V-121c), changes in the XRD peaks of *Fm3m* NiO were almost negligible and an increase in the amount of Li_2CO_3 was revealed. The main features of $\text{Li}_{1+\delta}\text{CuO}_2$ (marked by dash lines) were mostly preserved through the rest of the 1st cycle upon discharge to

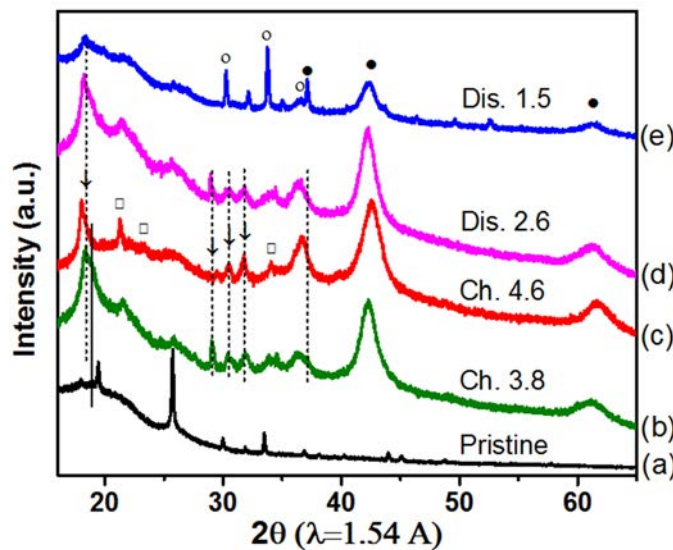


Figure V-121: *Ex situ* XRD patterns of $\text{Li}_2\text{Ni}_{0.8}\text{Cu}_{0.2}\text{O}_2$ electrodes at (a) pristine state, (b) 3.8 V charge, (c) 4.6 V charge, (d) 2.6 V discharge, and (e) 1.5 V discharge, respectively. Dash lines represent $\text{Li}_{1+\delta}\text{CuO}_2$ phases ($0 \leq \delta \leq 0.5$). NiO, Li_2O , and Li_2CO_3 are indicated by solid circles, open circles, and open squares, respectively

2.6 V. On the other hand, the original *Immm* structure was not recovered after discharged to 1.5 V (Figure V-121e). Instead, $\text{Li}_{1+\delta}\text{CuO}_2$ phase dismissed after further discharging $\text{Li}_2\text{Ni}_{0.8}\text{Cu}_{0.2}\text{O}_2$ electrode to 1.5 V and the formation of Li_2O crystalline phase was revealed.

Conclusions

In conclusion, optimal synthesis of both Ni^{2+} - and Ni^{3+} -based layered oxides was identified via a solid-state reaction. Stoichiometric LiNiO_2 and phase pure Li_2NiO_2 with superior electrochemical performance enabled in-depth studies on the performance degradation mechanism using synchrotron XRD and XAS techniques. LiNiO_2 experienced reversible phase transition from original hexagonal phase (H1) to another two hexagonal phases (H2, H3), however, gradual loss of H3 phase features was revealed over extended cycles. And Li_2NiO_2 phase, even with Cu substitution, irreversibly degraded to layered oxide and NiO .

Our future work will mainly focus on the design of Li-excess layered oxides on the basis of Ni redox, the key design of which lies in the selection of a second transition metal that ideally enables better utilization of Ni redox and structural stabilization while demonstrating high energy density without sacrificing other performance metrics. Optimal synthesis of the as-designed compositions will be guided by the synthesis-structure-electrochemical property relationships built upon Ni^{2+} - and Ni^{3+} -based LiNiO_2 and Li_2NiO_2 compounds. Phase transformation and charge compensation of transition metals will be continuously monitored by synchrotron radiation and absorption characterization techniques. In addition, the oxygen reactivity in all these Ni-based compounds will be closely monitored by differential electrochemical mass spectrometry to elucidate the intrinsic properties of Ni-O chemical bonding and the effect of other transition metals.

Products

Presentations/Publications/Patents

1. I. Villaluenga, K. H. Wujcik, W. Tong, D. Devaux, D. H. C. Wong, J. M. DeSimone, and N. P. Balsara, "Compliant glass-polymer hybrid single ion-conducting electrolytes for lithium batteries," *PNAS*, 113, 52-57 (2015).
2. J. Xu, F. Lin, D. Nordlund, E. J. Crumlin, F. Wang, J. Bai, M. M. Doeff, and W. Tong, "Elucidation of the surface characteristics and electrochemistry of high-performance LiNiO_2 ," *Chemical Communications*, 52, 4239 (2016).
3. J. Xu, W. Tong, "Investigating Synthetic Effects on Ni-Based Oxide as a Cathode Material for Lithium-ion Batteries," Presented at the Electrochemical Society, 228th Meeting, Phoenix AZ (October 2015).
4. J. Xu, W. Tong, "Discovery of High-Energy Lithium-ion Battery Materials *via* Combinatorial Materials Approach," Poster presented at Bay Area Battery Summit, Berkeley CA (November 2015).
5. J. Xu, W. Tong, "High-Capacity Ni-Based Layered Oxide Cathode for Lithium-ion Batteries," Poster presented at Industry Day and Open House, Berkeley CA (May 2016).

V.E. Diagnostics

V.E.1. Design and Synthesis of Advanced High-Energy Cathode Materials (LBNL)

Guoying Chen, Principal Investigator

Lawrence Berkeley National Laboratory
1 Cyclotron Road, MS 62-203
Berkeley, CA 94720
Phone: 510-486-5843
E-mail: gchen@lbl.gov

Tien Q. Duong, DOE Program Manager

U.S. Department of Energy
Advanced Battery Materials Research (BMR)
Vehicle Technologies Office
1000 Independence Avenue, SW
Washington, DC 20585
Phone: 202-586-7836
E-mail: Tien.Duong@ee.doe.gov

Start Date: October 2012

End Date: September 2016

Abstract

Objectives

- Obtain fundamental understanding on structural, chemical and morphological instabilities during Li extraction/insertion and extended cycling.
- Establish and control the interfacial chemistry between the cathode and the electrolyte at high operating potentials.
- Determine transport limitations at both particle and electrode levels.
- Rationally design and develop next-generation electrode materials.

Accomplishments

- Revealed facet-dependent nature of pristine LMR surface properties, including elemental, chemical and structural properties. Recommended careful characterization of pristine particles in studies that investigate cycling-induced changes on the cathode.
- Established the relationships among surface chemical composition, facet reactivity, cathode structural, cycling and thermal stabilities. Recommended the use of reduced TM content on pristine surface as an indicator for LMR cathode reactivity.
- Demonstrated improved structure and cycling stabilities on oxide particles with maximized expression of surface facets resistant to TM reduction. Recommended particle engineering for better-performing LMR cathodes.
- Revealed the effect of synthesis conditions in manipulating LMR particle surface facets and surface transition-metal reduction.
- Assessed the strategy of enabling high-energy LiVPO_4F cathode material by introducing substituents to narrow the voltage gap in the two-electron redox process in the $\text{Li}_2\text{VPO}_4\text{F}$ - LiVPO_4F - VPO_4F system.

Future Achievements

This project ended on September 30, 2016.

Technical Discussion

Background

For automotive applications such as PHEV and EV, lithium batteries are handicapped by low energy density, low power density, poor cycle life, poor safety and high cost. Much of the limitation comes from the poor performance of current electrode materials. Furthermore, high cell potentials and demanding cycling requirements lead to chemical and mechanical instabilities, all of which are important issues must be understood and addressed before battery scale-up and commercial development activities.

Introduction

To meet the DOE targets for lithium-ion batteries intended for vehicular applications, electrode materials with high-energy density and high stability are needed. Critical performance issues, such as structural and morphological instabilities, side reactions with the electrolyte, and transport limitations, are sensitive to material's chemical compositions, crystal structures, surface facets, and particle sizes. Advances in materials development, therefore, require a better understanding of the relationships between their properties and functions. This project addresses these issues in a systematic way, by synthesizing single-crystal version of the commercially promising yet complex electrode materials, obtaining new insights into the materials by utilizing state-of-the-art analytical techniques that are mostly inapplicable on conventional, aggregated secondary particles, and subsequently establishing the relationships between structure and function. The goal is to use these findings to rationally design and synthesize advanced electrode materials with improved performance.

Approach

Prepare single crystals of Li-rich layered oxides and high-voltage Ni/Mn spinels with well-defined physical attributes. Perform advanced diagnostic and mechanistic studies at both bulk and single-crystal levels. Global properties and performance of the samples will be established from the bulk analyses, while the single-crystal based studies will utilize time- and spatial-resolved analytical techniques to probe material's redox transformation and failure mechanisms.

Results

In FY16, we continued to investigate the correlation in pristine surface properties, cycling-induced changes, and stability of Li- and Mn-rich (LMR) layered oxide cathodes. Facet-dependent surface properties on pristine LMR particles were directly visualized on our crystal samples. Figure V-122a shows a selected area electron diffraction (SAED) pattern collected on a small polyhedron-shaped $\text{Li}_{1.2}\text{Mn}_{0.13}\text{Mn}_{0.54}\text{Co}_{0.13}\text{O}_2$ crystal (labeled as S-Poly, ~200 nm in size), recorded by using an aperture covering the entire particle in a transmission electron microscope. In addition to the reflections from the three variants of monoclinic $C2/m$ structure, a second set of reflections (highlighted in green circles) was also observed. Comparison with the simulated SAED pattern reveals that the secondary phase belongs to a spinel structure. The dark-field image collected by using the spinel reflections only allowed us to locate the spinel's exclusive presence on particle surface, as shown by the bright contrast in Figure V-122b. The extent of spinel formation is non-uniform throughout the surface which reveals the facet-dependent nature. When the spinel slab was parallel to the electron beam, Co and Ni enrichment were also observed on the surface, suggesting facet-dependent elemental composition. Structural transformation on pristine surface was further confirmed by scanning transmission electron microscope/electron energy loss spectroscopy (STEM/EELS) studies. Figure V-122c shows the high angle annular dark field (HAADF) STEM image where a thin surface layer (about 2 nm) with a different atomic arrangement from that of the bulk is clearly shown. Atomic simulation of the surface layer (Figure V-122c inset) shows that some lithium sites are occupied by the transition metals to form a spinel phase with antisite defects. Electron energy loss spectra including O K-edge, Mn, Ni and Co L-edges were collected from the bulk to the surface and the results are shown in Figure V-122d, with the expanded regions of Ni, Co, Mn and O also

shown on the left. Ni was found to remain at 2+ while the spectra of both Mn and Co show a gradual increase in the L3/L2 ratio when going from the bulk towards the surface, corresponding to a decrease in oxidation state of both transition metals (TMs). The reduction in the TM oxidation state is also supported by the lower O pre-peak intensity observed on the surface, where the collected O profile resembles that of a spinel. EELS Li K-edge imaging in the low-loss region confirms the presence of Li where Mn and Co are reduced, providing clear evidence that all three transition metals as well as Li are present in the surface layer. These results are consistent with the sXAS data previously reported on these samples, with further particle-level evidence that instead of the layered structure, the reduced TMs reside in a defective spinel on the pristine surface suggesting the similarity to what was reported on the cycled conventional secondary particles in the literature. It is therefore imperative that in order to determine the effect of battery cycling on structural transformations of the cathode surface, one has to ensure that the same crystalline orientation is examined for both pristine and cycled particles. These studies should also be performed in multiple zone axes to avoid the misinterpretations based on a particular two-dimensional projection.

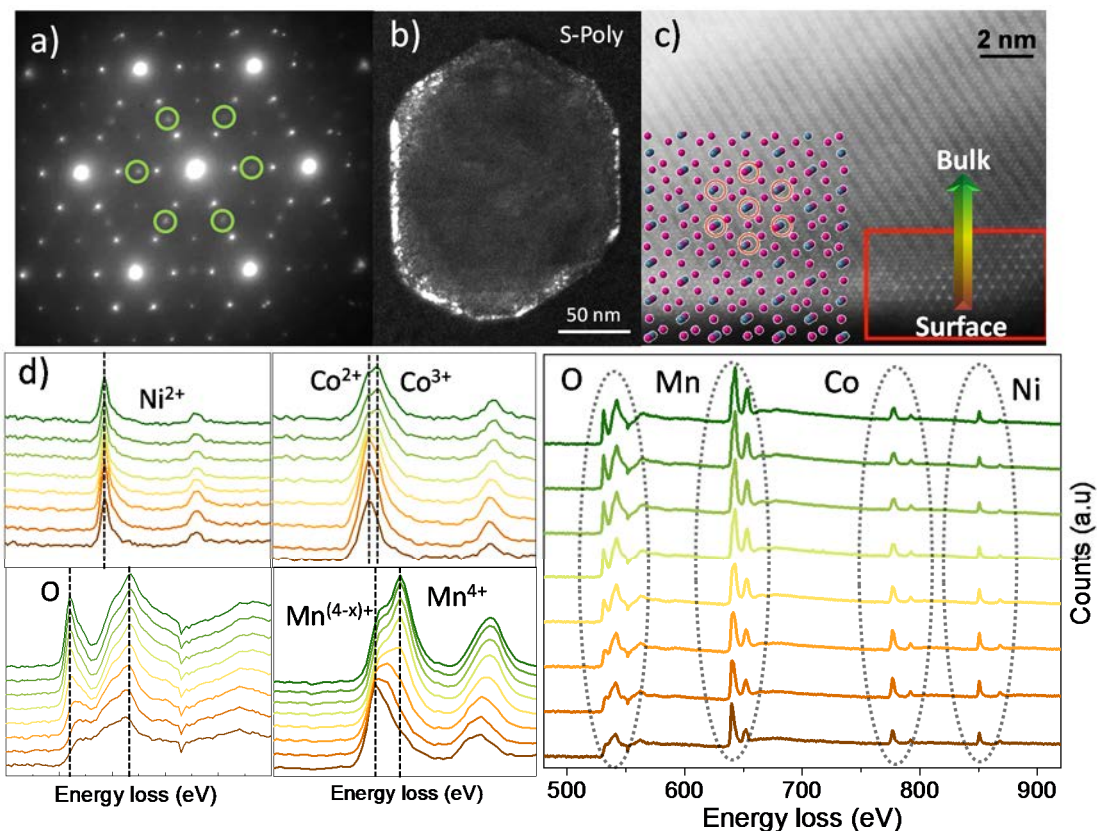


Figure V-122: a) SAED pattern collected on a S-Poly crystal, b) contrast image taken with one of the reflections shown in green in Figure a, c) high-resolution HAADF STEM image collected on the crystal sample and d) EELS data collected from the surface-to-bulk region shown in the HAADF image in Figure c, with the expanded views shown on the left

Studies were then carried out to evaluate the changes in TM oxidation states on the surface, dissolution and subsequent precipitation of TMs during the cycling of LMR oxides. Composite electrodes of $\text{Li}_{1.2}\text{Mn}_{0.13}\text{Mn}_{0.54}\text{Co}_{0.13}\text{O}_2$ crystal samples with six different morphologies previously synthesized in our lab, namely plate, needle, S-Poly, L-Poly, box and octahedron, were prepared by mixing 80 wt% oxide crystals, 10 wt% carbon additive and 10 wt% PVdF binder. Coin cells with the composite cathodes, lithium foil counter and reference electrodes, Celgard 2400 polypropylene separator, and 1 M LiPF_6 in EC-DEC (1:1, v/v) electrolyte were charge/discharged between 2.5 and 4.6 V at 20 mA/g and then disassembled to recover the separator, the electrolyte and the cathode crystals. Figure V-123a to Figure V-123c show the Mn, Co and Ni soft XAS spectra (L edge, TEY mode) collected on the pristine electrodes as well as the separators recovered after either 30 or 45 cycles. All three TMs were detected on the separators which had a black appearance on the side facing the Li metal anode, revealing the participation of a TM dissolution, migration and deposition mechanism during cycling. While Mn, Co and Ni were at 4+, 3+ and 2+ on the fresh electrodes, respectively, the oxidation state of the TMs on the separators was found to be at 2+ universally. The amount of deposited

TMs increases with cycling but it is morphology dependent, with the most deposits found in the cell containing the box sample and the least with the L-Poly sample. Significant reduction of Mn and Co was also observed on the cathode particles recovered after 45 cycles, as evidenced by the soft XAS spectra collected on the cycled electrodes. The low energy/high energy Co L3 peak ratios in three different detection modes of Auger electron yield (AEY), total electron yield (TEY) and fluorescence yield (FY), which have an approximate probing depth of 1-2, 2-5 and 50 nm, respectively, are shown in Figure V-123d. The monotonous increase in oxidation state from AEY, TEY to FY suggests that Co reduction progressed from the surface to the bulk. The highest ratio, corresponding to most Co^{3+} reduction, was found on the box sample whereas the lowest ratio was found on the L-Poly sample. TM concentration in the recovered electrolyte was also analyzed by ICP and the results are shown in Figure V-123e. Compared to the plate, needle and L-Poly samples, significantly more TM dissolution was observed on the S-Poly sample with the highest surface area and the box sample with the most reactive surface facets, suggesting the effects of both particle morphology and surface area on the reactivity at particle surface. These results corroborate well with the trend observed in cell capacity retention (Figure V-123f) and provide clear evidence for the correlation between cycling stability, cycling-induced TM reduction and dissolution in the electrolyte. The use of the intricate electrochemical protocols, high-resolution microscopy/spectroscopy techniques and high throughput ensemble-averaged spectroscopy on crystal samples with various morphologies allowed us to further correlate the pristine surface properties, their changes during cycling and cathode stability. It was found that particle morphology determines the extent of TM reduction during both synthesis and cycling, which directly correlates to cathode rate performance and stability. Oxide structure and cycling stabilities improve with maximum expression of surface facets stable against TM reduction.

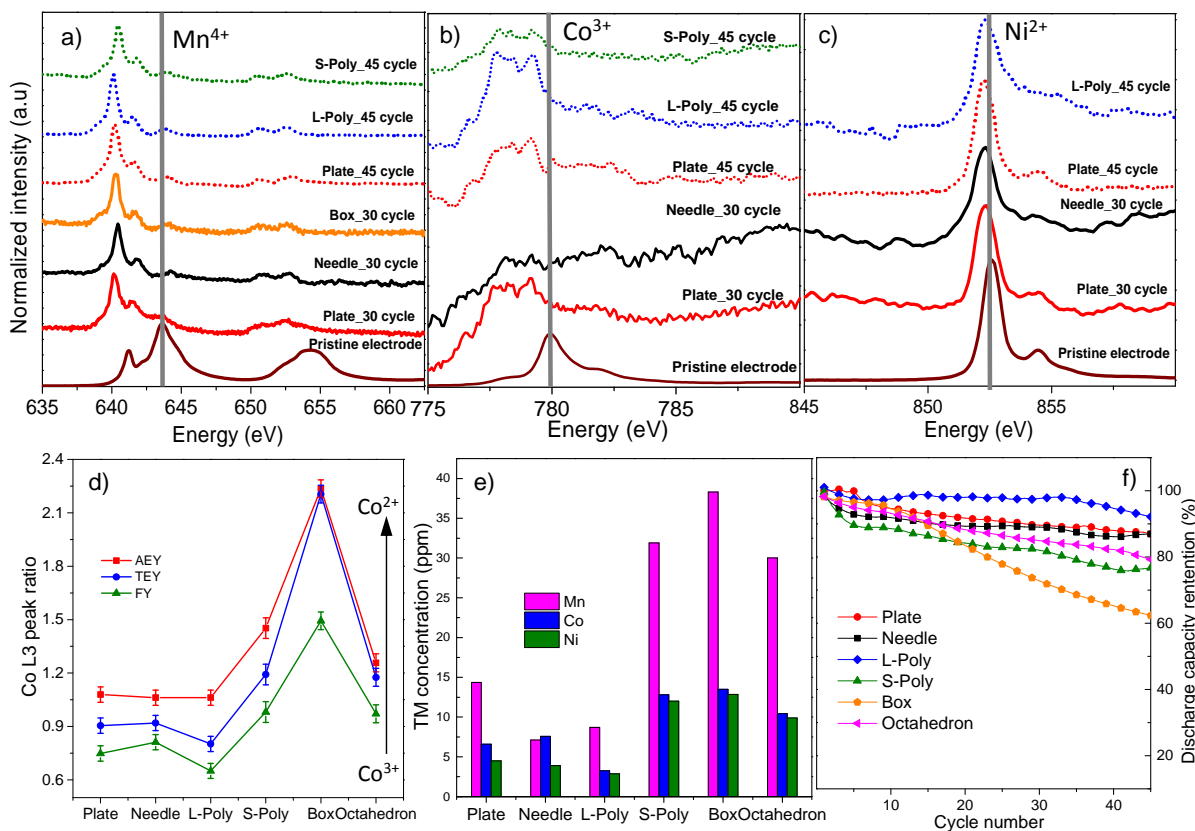


Figure V-123: a) Mn, b) Co and c) Ni L-edge soft XAS spectra collected on recovered separators and the pristine electrodes, d) Co low/high L3 peak ratio determined from the soft XAS spectra (AEY, TEY and FY modes) of the crystals recovered after 45 cycles, e) TM concentration in the electrolytes recovered after 45 cycles, and f) capacity retention of the various $\text{Li}_{1.2}\text{Ni}_{0.13}\text{Mn}_{0.54}\text{Co}_{0.13}\text{O}_2$ half-cells cycled between 2.5 and 4.6 V at 20 mA/g

In an effort to maximize the preferred facets for performance as well as to better understand the relationships among synthesis conditions, composition, morphology, and surface properties, a systematic study on the effect of heating and cooling conditions was performed. Four samples, designated as 3°C/3°C, 3°C/15°C, 3°C/Q and 15°C/3°C to indicate the heating and cooling rates used in each case (Q refers to quenching), were synthesized

at 900°C in a composition of $\text{Li}_{1.2}\text{Mn}_{0.13}\text{Mn}_{0.54}\text{Co}_{0.13}\text{O}_2$. Figure V-124a shows the X-ray diffraction (XRD) patterns of the samples which are consistent with our previous report that our crystals synthesized by the molten-salt method adopt a single-phase monoclinic structure ($C2/m$) with random domains of [100], [110] and [1-10] variants. All samples showed good crystallinity and phase purity, but the intensity of the diffraction peaks from 20° to 23° (2θ) is noticeably higher in the 3°C/3°C sample, suggesting larger domain size. Scanning electron microscopy (SEM) studies (Figure V-124b) showed that all samples were discrete crystals exhibiting a plate shape with an average size of 1 μm . The thickness of the 3°C/3°C and 3°C/15°C plates are similar at about 200 nm, whereas the 3°C/Q and 15°C/3°C crystals are much thicker at about 300 and 350 nm, respectively. This corresponds to an increase in surface contribution from facets other than the large (001)_m planes in the latter two samples.

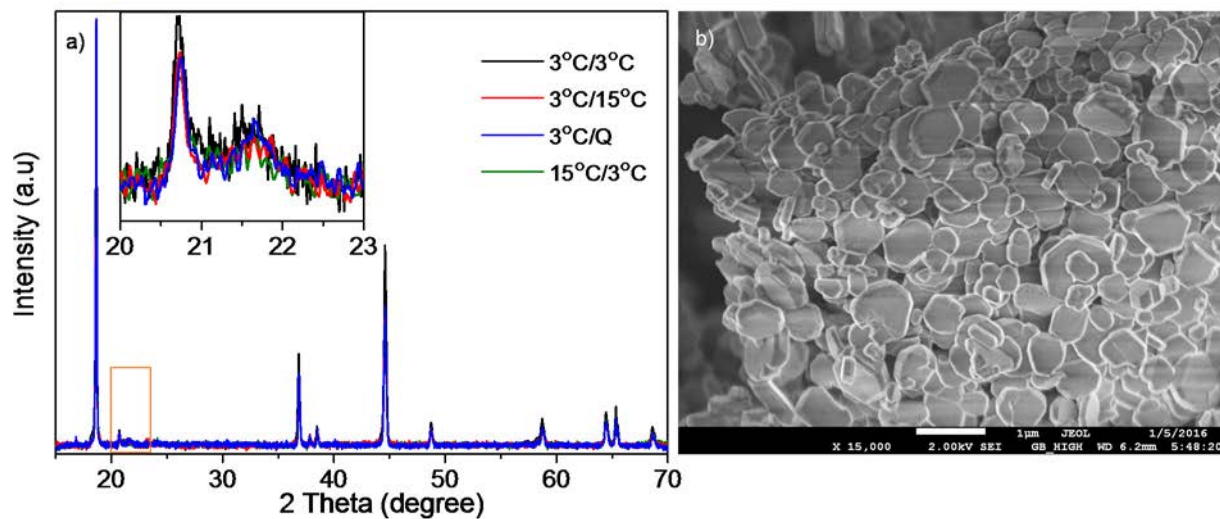


Figure V-124: a) XRD patterns of the crystals synthesized under different conditions and b) SEM image of the 3 °C/3 °C sample

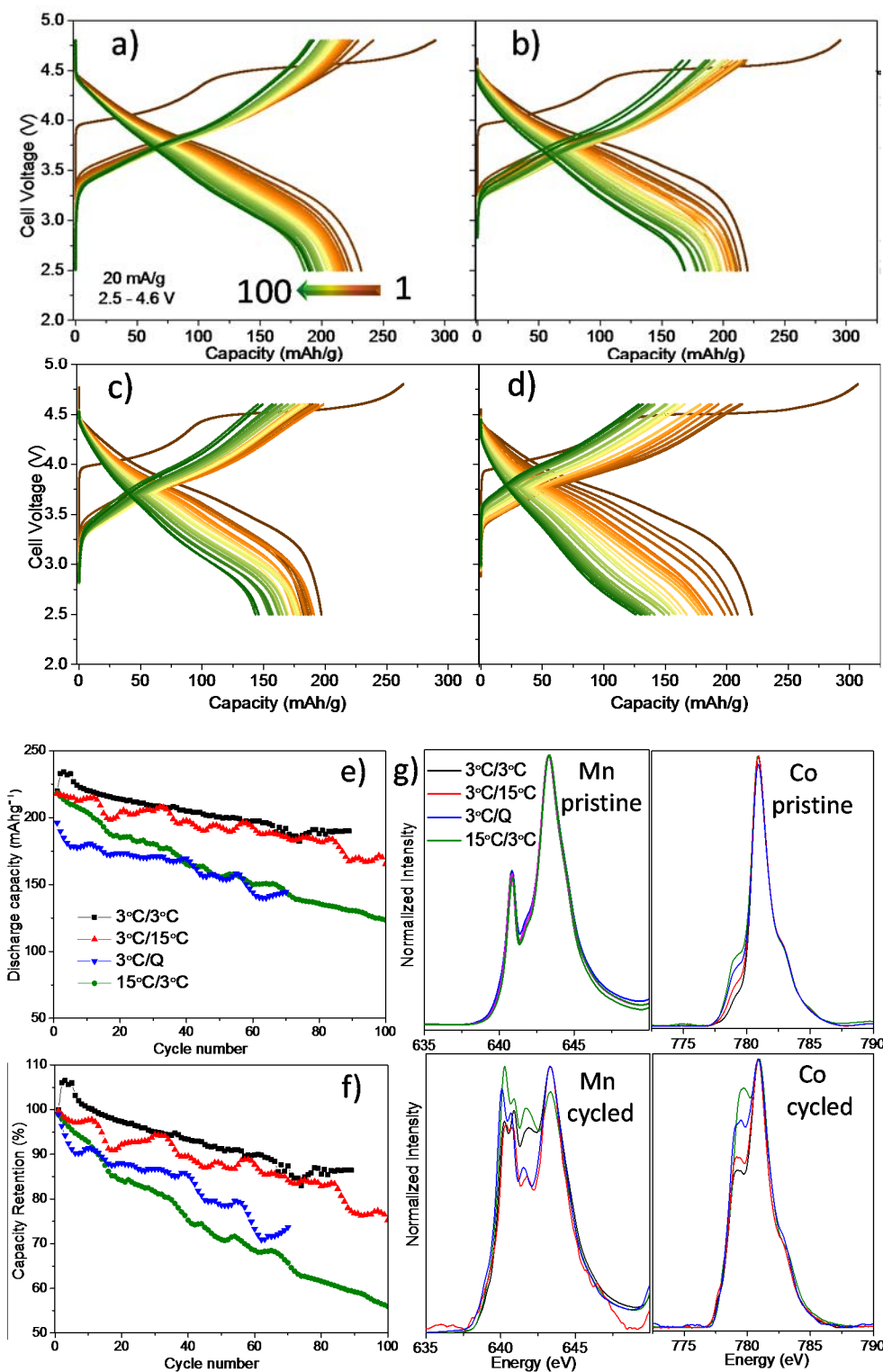


Figure V-125: a) Galvanostatic charge-discharge profiles of the crystal electrodes: a) 3 °C/3 °C, b) 3 °C/15 °C, c) 3 °C/Q and d) 15 °C/3 °C, e) discharge capacities and f) capacity retention of the cells, and g) Soft XAS TEY spectra of Mn and Co L3-edges before and after 45 cycles

The voltage profiles from half-cell cycling of the crystal composite electrodes are shown in Figure V-125a - Figure V-125d. At a current density of 20 mA/g, similar first charge profiles were obtained which includes a sloping region and a plateau region. The discharge capacity gradually decreased during the first 100 cycles, but the 3°C/3°C sample had the best performance in both discharge capacity and capacity retention, which was closely followed by the 3°C/15°C sample. Inferior performance was observed on both 3°C/Q and 15°C/3°C

samples (Figure V-125e and Figure V-125f). Figure V-125g shows the Mn and Co soft XAS TEY spectra collected before and after 45 cycles. At pristine, Mn and Ni remain at 4+ and 2+ on all samples. The intensity of the low-energy shoulder peak at the Co L3 edge, closely associated with the reduced Co^{2+} content in the sample, increases following the order of $3^\circ\text{C}/3^\circ\text{C} < 3^\circ\text{C}/15^\circ\text{C} < 3^\circ\text{C}/\text{Q} < 15^\circ\text{C}/3^\circ\text{C}$. This is consistent with the increase in sample thickness, suggesting that thicker plates have more reactive surface. After 45 cycles, the intensity of both lower-energy shoulder peaks at the Mn and Co L3 edges increased drastically, corresponding to extensive Mn and Co reductions during cycling. The reduction progressed from the surface towards the bulk, as evidenced by depth-profiling soft XAS in AEY, TEY and FY modes. Samples with more cycling-induced Mn and Co reductions were found to have worse electrochemical performance. The study provides further evidence that synthesis conditions impact particle surface crystalline orientation and transition-metal reduction, which subsequently impact chemical and cycling stabilities of the LMR-NMC cathodes.

In the context of pursuing high-energy cathodes capable of delivering more than 200 mAh/g, we also initiated an effort to explore alternative cathode materials in FY16. One of the recognized strategies to improve the energy density of cathode materials is to increase the number of cyclable Li^+ in the compound by introducing multi-electron redox couples. Among the common transition metals, vanadium exhibits several stable oxidation states (+2, +3, +4 and +5) so the $\text{V}^{n+}/\text{V}^{(n-1)+}$ redox couples present a rare opportunity to cycle more than one Li^+ per formula unit. Tavorite-type LiVPO_4F with a triclinic space group $P\bar{1}$ has a three-dimensional framework of distorted $[\text{VO}_4\text{F}_2]$ octahedra and $[\text{PO}_4]$ tetrahedra that form different types of tunnels. The corner-shared chains of Li polyhedra and interconnected interstitial space make the compound a potential fast ionic conductor while the high ionicity of the M-(O, F) bonds raises operating voltages. This fluorophosphate was initially reported by J. Barker in 2005 as a promising 4 V cathode material, but later studies demonstrated the extraction/reinsertion of one Li^+ at a voltage plateau of ~ 4.25 V ($\text{V}^{3+}/\text{V}^{4+}$ redox process) and another one at a much lower plateau of 1.8 V ($\text{V}^{3+}/\text{V}^{2+}$ redox process), yielding theoretical capacities of 156 and 312 mAh/g for one and two removed Li^+ , respectively. As the utilization of two voltage plateaus with such a large gap of 2.4 V presents a major challenge for control electronics in battery systems, most studies on LiVPO_4F so far have been limited to the 4 V region.

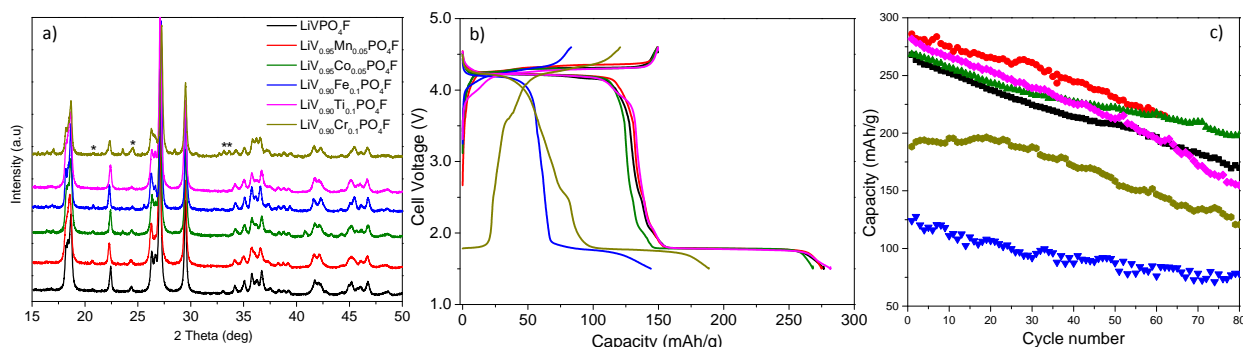


Figure V-126: a) XRD patterns of the synthesized $\text{LiM}_x\text{V}_{(1-x)}\text{PO}_4\text{F}$ samples, b) first-cycle voltage profiles during galvanostatic charge-discharge at 16 mA/g, and c) long-term cycling performance of the $\text{LiM}_x\text{V}_{(1-x)}\text{PO}_4\text{F}$ cathodes. * indicates peaks from the $\text{Li}_3\text{V}_2(\text{PO}_4)_3$ phase

Our research aimed to find out whether metal substitution can reduce the voltage gap by manipulating the two-plateau voltage profile into a more sloping one and/or improve the overall cycling stability of the $\text{Li}_2\text{VPO}_4\text{F}$ - LiVPO_4F - VPO_4F system. A series of $\text{LiM}_x\text{V}_{(1-x)}\text{PO}_4\text{F}$ ($\text{M} = \text{Mn}, \text{Co}, \text{Cr}, \text{Fe}$ and Ti , $x=0, 0.05$ or 0.1) compounds were prepared by a two-step carbothermal reduction reaction where $\text{M}_x\text{V}_{(1-x)}\text{PO}_4/\text{C}$ intermediates were first prepared and then reacted with LiF to form the final products. As shown in the XRD patterns (Figure V-126a), all samples were phase pure except $\text{LiV}_{0.9}\text{Cr}_{0.1}\text{PO}_4\text{F}$ where a small amount of the common impurity of monoclinic $\text{Li}_3\text{V}_2(\text{PO}_4)_3$ was also present. Preliminary electrochemical performance was evaluated in 2032-type coin cells with a $\text{LiM}_x\text{V}_{(1-x)}\text{PO}_4\text{F}$ composite cathode, a Li metal anode, and a 1.0 M LiPF_6 EC: DEC (1:1) electrolyte. Figure V-126b shows the first-cycle voltage profiles during galvanostatical charge and discharge between 1.5 and 4.5 V at a current density of 16 mA/g. The presence of two plateaus at 4.25 and 1.8 V in LiVPO_4F is consistent with the reported two-phase topotactic reactions, involving significant lattice contractions/expansions and an overall symmetry shift from triclinic $P\bar{1}$ in LiVPO_4F to monoclinic $\text{C}2/c$ in VPO_4F and $\text{Li}_2\text{VPO}_4\text{F}$. Mn, Co and Ti substitution resulted in little change in voltage profiles and overall capacity. Although the introduction of Fe or Cr resulted in a more sloping voltage profile which suggests

possible involvement of solid solution phases, the discharge capacity was substantially reduced compared to that of the parent LiVPO_4F . The new electrochemical signal around 2.5 V in the Cr substituted version may be attributed to the $\text{Cr}^{3+}/\text{Cr}^{2+}$ redox activity. The long-term cycling performance comparison shows stability improvement in both $\text{LiV}_{0.90}\text{Mn}_{0.05}\text{PO}_4\text{F}$ and $\text{LiV}_{0.90}\text{Co}_{0.05}\text{PO}_4\text{F}$ electrodes (Figure V-126c), however, the overall impact of transition metal substitution on the voltage profile and cycling stability of LiVPO_4F was rather trivial. Further work on the $\text{Li}_2\text{VPO}_4\text{F}$ - LiVPO_4F - VPO_4F system was not justified and a No-Go decision was made.

Conclusions

In conclusion, we demonstrated the effective use of single-crystal based diagnostic studies for comprehensive understanding of structure-property-performance-stability relationships and for performance optimization of the LMR cathode materials. We found that surface properties of the LMR oxide particles differ from that of the ideal bulk. Furthermore, crystal structure, elemental and chemical compositions of the surface are facet dependent. The nature of the surface facets determine material's tendency in TM reduction, both during synthesis and cycling. The extent of surface TM reduction on pristine material, therefore, is an indicator for surface reactivities, with the reduction increases with cycling and progresses from the surface to bulk. We further reveal that oxide structural and cycling stabilities improve with maximum expression of surface facets stable against TM reduction. An effort to synthesize oxide particles with desired physical properties, especially desired surface features that will enable stable cycling, was also carried out and synthesis-structure-electrochemical property relationships in the LMR oxides was investigated. Our study recommends morphology engineering as an important revenue for material optimization and provides important strategies in addressing some of the critical issues facing the family of LMR cathode materials.

Products

Presentations/Publications/Patents

1. P. Yan, J. Zheng, J. Zheng, Z. Wang, G. Teng, S. Kuppen, J. Xiao, G. Chen, F. Pan, J.-G. Zhang, and C.-M. Wang, "Ni and Co Segregations on Selective Surface Facets and Their Composition Dependence in Layered Lithium Transition-Metal Oxide Cathodes," *Advanced Energy Materials*, 6, 1502455 (2016).
2. A. K. Shukla, Q. Ramasse, C. Ophus, H. Duncan, and G. Chen, "Unraveling structural ambiguities in Li and Mn rich transition metal oxides," *Nature Communications*, 6, 8711 (2015).
3. P. Yan, J. Zheng, S. Kuppen, Q. Li, D. Lv, J. Xiao, G. Chen, J.-G. Zhang, and C.-M. Wang, "Phosphorus Enrichment in Solid Electrolyte Interphase Layer on High Voltage Cathodes for Lithium Ion Battery," *Chemistry of Materials*, 27 (21), 7447 (2015).
4. R. Ruther, H. Zhou, C. Dhital, S. Kuppen, A. Kercher, G. Chen, A. Huq, F. Delnick, and J. Nanda, "Synthesis, Structure, and Electrochemical Performance of High Capacity $\text{Li}_2\text{Cu}_{0.5}\text{Ni}_{0.5}\text{O}_2$ Cathodes," *Chemistry of Materials*, 27 (19), 6746 (2015).
5. W.-H. Kan, S. Kuppen and G. Chen, "Advanced High-energy Cathode Materials for Lithium-ion Batteries," UC-Industry Battery Workshop, Berkeley, CA, September 2016.
6. S. Kuppen, A. K. Shukla and G. Chen, "Crystal-based Microscopy and Spectroscopy Diagnostics for Lithium-ion Battery Cathode Development," 2016 Molecular Foundry Users Meeting, Berkeley, CA, August 2016 (invited).
7. P. Yan, J. Zheng, S. Kuppen, X. Zhang, K. Amine, J. Xiao, G. Chen, J.-G. Zhang, and C.-M. Wang, "Investigating Side Reactions and Coating Effects on High Voltage Layered Cathodes for Lithium Ion Batteries", 2016 Microscopy and Microanalysis, Columbus, OH, July 2016.
8. G. Chen, "Design and Synthesis of Advanced High-Energy Cathode Materials," DOE Hydrogen Program and Vehicle Technologies Program Annual Merit Review and Peer Evaluation Meeting, Washington, DC, June 2016.
9. G. Chen, "Li-and Mn-rich NMCs and Ni/Mn spinels," 2016 DOE Battery Materials Research Cathode Workshop, Knoxville, TN, March 2016 (invited).

10. G. Chen, "Design and Synthesis of Advanced High-Energy Cathode Materials," 2016 DOE BMR Program Review Meeting, Berkeley, CA, January 2016.
11. S. Kuppan and G. Chen, "Development of Advanced High-Energy Density Cathode Materials," Bay Area Battery Summit, Berkeley, CA, November 2015.
12. S. Kuppan, A. K. Shukla and G. Chen, "Crystal Diagnostic Studies for Optimizing Critical Properties of Lithium-ion Battery Cathodes," The 228th ECS Meeting, Phoenix, AZ, October 2015.
13. S. Kuppan, A. K. Shukla and G. Chen, "Crystal Diagnostics of Lithium-ion Battery Cathode Materials Using Complementary Microscopy and Spectroscopy Techniques," 2015 ALS User Meeting, Berkeley, CA, October 2015 (invited).

V.E.2. Interfacial Processes – Diagnostics, Lawrence Berkeley National Laboratory (LBNL)

Robert Kostecki

Lawrence Berkeley National Laboratory
1 Cyclotron Road
Berkeley, CA 94720
Phone: 510-486-6002; Fax: 510-486-5454
E-mail: r_kostecki@lbl.gov

Tien Q. Duong, DOE Program Manager

U.S. Department of Energy
Advanced Battery Materials Research (BMR)
Vehicle Technologies Office
1000 Independence Avenue, SW
Washington, DC 20585
Phone: 202-586-7836
E-mail: Tien.Duong@ee.doe.gov

Start Date: October 1, 2015
End Date: September 30, 2018

Abstract

Objectives

- Provide critical understanding of basic principles that govern the function and operation of active materials, composite electrodes and lithium-ion battery cells that is necessary for successful implementation of high energy density materials in lithium-ion cells for PHEVs and EVs. Establish direct correlations between electrochemical performance, interfacial phenomena, surface chemistry, morphology, topology and degradation mechanisms of ABMR baseline materials, electrodes and cells.
- Propose and evaluate remedies to interfacial and materials instability e.g., artificial surface coatings (e.g., ALD) and/or structures, novel electrode architectures, electrolyte additives etc.
- Develop, adapt and employ unique experimental techniques and methodologies to guide development of novel electrochemical energy storage materials, electrodes and battery systems. Obtain detailed insight into the dynamic behavior of molecules, atoms, and electrons at electrode/electrolyte interfaces at resolution that is adequate to the size and function of basic chemical or structural building blocks.

Accomplishments

- Determined the mechanism of transition metal dissolution and it offered a unique insight into the complex and interrelated mechanism of interfacial phenomena at high-voltage cathodes and anodes.
- Demonstrated feasibility of *in situ* near-field FTIR microscopy and spectroscopy to study interfacial phenomena at Li-battery electrodes. Near-field spectroscopy was established for the first time as a technique for identifying functional components of the SEI film on a Si electrode. Results establish new information (spatial localization of compounds) unachievable by other methods.

Future Achievements

- The lithium-ion cathode is a major determinant of cost and energy density in lithium-ion batteries. To realize further gains, the specific energies of cathodes must be improved.
 - Cathode structural disorder, interfacial instability and the tendency to convert to spinel or rock salt phases during cycling need to be remedied to achieve energy density, lifetime and safety goals.

- These failure modes must be addressed through diagnostic studies to guide development of next generation robust cathode materials
- Apply advanced characterization techniques to obtain detailed insight into detrimental processes at electrode/electrolyte interfaces of high voltage Ni-rich NMC-type cathode materials.
- Determine and remedy electrochemical performance limiting factors and degradation mechanisms under cycling conditions.
 - Determine origins of structural instabilities of the high Ni content electrodes, particularly formation of inert spinel and rock salt phases during cycling, oxygen loss, transition metal dissolution, and formation of resistive interphases and surface films at cathode electrolyte interfaces (CEI).
- Work closely with ABMR PIs to establish clear connections between diagnostics, theory/modelling, materials synthesis, and cell development efforts.
- Develop and apply novel innovative experimental methodologies to study and understand the basic function and mechanism of operation of materials, composite electrodes, and lithium-ion cells for PHEV and EV applications.

Technical Discussion

Background

This project addresses the key technical barriers related to the battery technology development effort of the DOE Office of Vehicle Technologies:

- Low lithium-ion battery energy density, and calendar/cycle lifetimes (related to cost) for PHV and EV applications.
- Inadequate cell/electrode impedance that limits power and affects system safety
- Need for new advanced battery materials and composite electrodes with acceptable specific energy, durability, costs, and safety characteristics.

This work constitutes an integral part of the concerted effort within the BMR Program and it attempts to establish clear connections between diagnostics, theory/modelling, materials synthesis, and cell development efforts. The main objective of this task is to obtain detailed insight into the dynamic behavior of molecules, atoms, and electrons at electrode/electrolyte interfaces of high voltage Ni/Mn-based materials such as $\text{Li}[\text{Ni}_x\text{Mn}_y\text{Co}_z]\text{O}_2$ compounds (NMCs) in lithium-ion cells for PHEVs and EVs.

Introduction

Lithium-ion batteries are inherently complex and dynamic systems. Although often viewed as simple devices, their successful operation relies heavily on a series of complex mechanisms, involving thermodynamic instability in many parts of the charge/discharge cycle and the formation of metastable phases. This paradigm of lithium-ion system operation usually drives the battery toward irreversible physical and chemical conditions that lead to battery degradation and failure.

The requirements for a long-term stability of lithium-ion batteries are extremely stringent and necessitate control of the chemistry at a wide variety of temporal and structural length scales. Progress towards identifying the most efficient mechanisms for electrical energy storage and the ideal material depends on a fundamental understanding of how battery materials function and what structural/electronic properties limit their performance. This in turn necessitates the development and use of new characterization tools to monitor these processes.

The design of the next generation of lithium-ion batteries requires a fundamental understanding of the physical and chemical processes that govern these complex systems. Although some significant advances have been made to prepare and utilize new materials efforts towards the understanding of their operation mechanisms and degradation modes have been insufficient and/or unsuccessful.

Approach

The main objective of this task is to obtain detailed insight into the dynamic behavior of molecules, atoms, and electrons at electrode/electrolyte interfaces of high voltage $\text{Li}[\text{Ni}_x\text{Mn}_y\text{Co}_z]\text{O}_2$ materials at a spatial resolution that corresponds to the size of basic chemical or structural and chemical building blocks [1-4]. In coordination with other PIs in the High-Energy Cathode Thrust, this task focuses on high Ni content NMC compositions such as 523 and 622, which are expected to achieve high discharge capacities even within conservative electrode potential limits. The pristine and cycled NMC powders and electrodes are probed using a variety of surface- and bulk-sensitive techniques, including FTIR, ATR-FTIR, near-field IR and Raman spectroscopy and microscopy and scanning probe microscopy to identify and characterize changes in materials structure and composition. Novel *in situ/ex situ* far- and near-field optical multifunctional probes in combination with standard electrochemical and analytical techniques are developed to unveil the structure and reactivity at interfaces and interphases that determine materials electrochemical performance and failure modes.

The *in situ/ex situ* investigations of the surface reconstruction into rock salt on NMC samples of different morphology and composition are carried out in sync with similar studies by X-ray techniques (M. Doeff, LBNL) and directly linked with investigations interfacial reactivity toward organic electrolytes. The objective is to unveil the role of the metal dissolution on the surface reconstruction and/or vice versa and their effect on the battery performance and failure modes in NMC/graphite and NMC/Si battery systems. To achieve rigorous surface structure-interfacial property relationships, *in situ* AFM, and spectroscopic ellipsometry as well as *ex situ* Raman and near-field IR spectroscopy/imaging, FTIR and XPS are carried out to investigate the surface layer (re)formation process and composition on NMC model single particle electrodes. The effect of electrolyte composition, additives and protective coatings is explored, to determine the mechanism and kinetics of surface phenomena and their possible implications for long-term electrochemical performance of the NMC cathodes in high-energy lithium-ion systems. far- and near-field IR microscopy and spectroscopy.

In close collaboration with the BMR Cathode Group, NSOM, FTIR-ATR and environmental XPS are used to monitor surface reactions and identify their intermediates and end-products on binder and carbon-free Si single crystals with different surface crystal orientation are used to investigate the spatial-chemical composition of surface layers. We embark in a collaborative effort with the LBNL ALS IR beam line 5.4.1 scientists to adopt and employ a synchrotron-based tunable IR source to overcome spectral range limitation of the tunable lasers and/or inadequate intensity of the glow bar IR source. We expect that this new and unique experimental setup will constitute a major breakthrough in the diagnostics of electrochemical interfaces, and lithium-ion systems in particular.

The PI of this project will receive pristine NMC powders and composite electrodes tested under different cycling regimes from M. Doeff (LBNL). C. Ban (NREL) will supply NMC samples with protective ALD coatings. The diagnostic studies will be carried out in sync with differential electrochemical mass spectrometry analysis by B. McCloskey (LBNL) and other diagnosticians in the BMR program. He will also work closely with V. Battaglia (LBNL) to obtain samples from full cell cycling experiments.

Results

We have achieved the following progress:

1. Interfacial Activity of High-Voltage Cathodes

We evaluated interfacial phenomena at NMC using fluorescence spectroscopy. In our previous report we have demonstrated that surface reactivity of LMNO lithium-ion positive electrode materials toward the electrolyte strongly depends on the surface crystalline orientation and local defects. We have shown that this results in electrochemical oxidation of DEC and EC at the electrode at potentials > 4.2 V, leading to the formation of fluorescent Ni^{II} and $\text{Mn}^{\text{II/III}}$ complexes with β -diketonate ligands, which have detrimental impact on the on Li^+ transport.

We demonstrated the universality of this mechanism by using the same systematic approach on high energy density materials such as (NMCs). The model single particle, binder- and carbon-free baseline NMC-111 electrodes were prepared using a standard procedure described in the previous report. We also extended our

investigations to thin-film NMC-532 model cathodes deposited by pulse laser deposition (PLD) on Au/stainless steel substrates (collaboration with Dr. Wang's group at TAMU. X-ray diffraction (XRD) data indicate that these films are highly crystalline, whereas atomic force microscope (AFM) images show film thickness ca. 200 nm with ~20 nm roughness.

Ex situ fluorescence signal of aged binder- and carbon- free baseline NMC-111 electrodes cycled in coin cells confirmed the deposition of metal complexes with β -keto esters Ligands at the NMC surface (Figure V-127a). The presence of Co(II), Mn(II) and Ni(II) complexes within the SEI of a NMC (111)/graphite cell was also confirmed by XANES experiments (Figure V-127b-d).

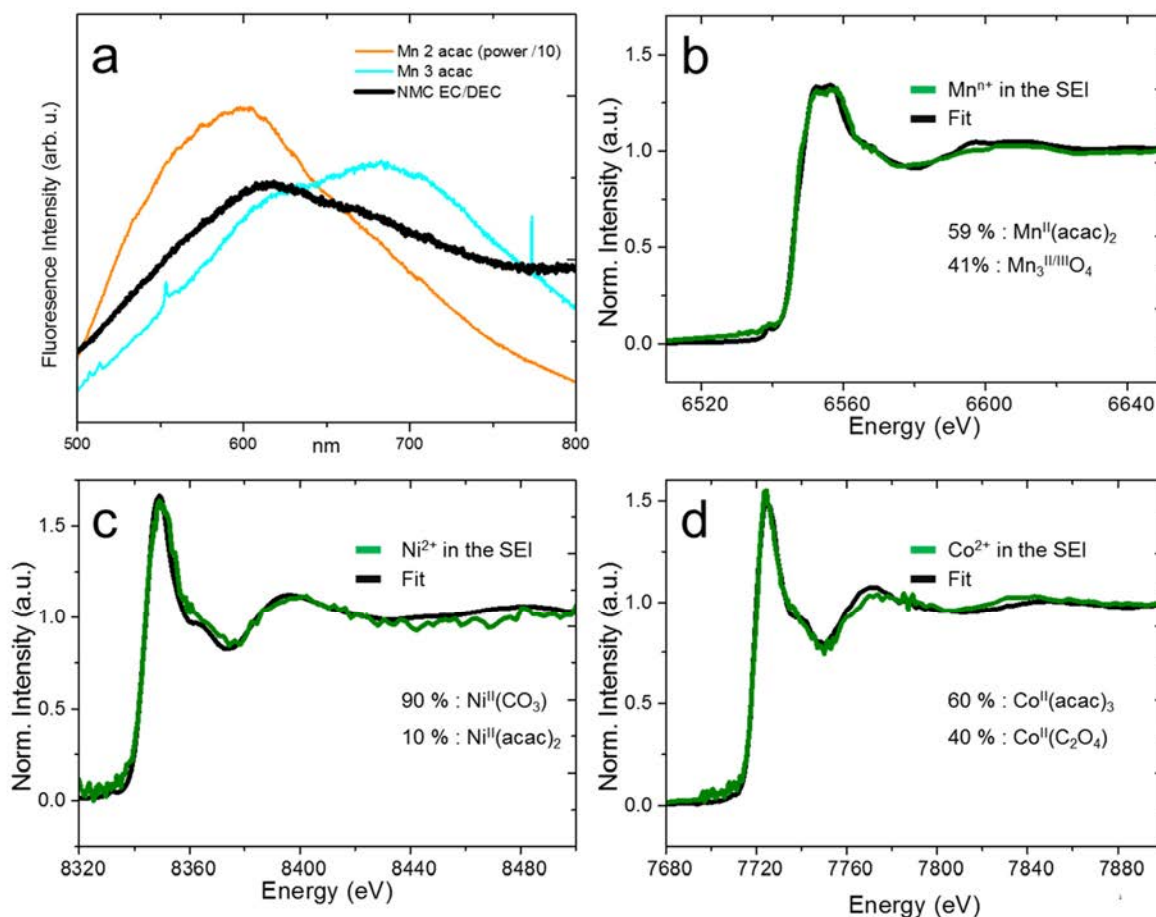


Figure V-127: Fluorescence spectra of model NMC-111 electrode after two cycles, and reference spectra of Mn(II) and Mn(III)(acac) complexes (a), X-ray absorption spectra of graphite anodes from NMC/graphite coin cells cycled 850 times (b-d)

The onset of the fluorescence signal at the surface of NMC electrode coincides with Li^+ removal and results in solvent oxidation and Ni, Mn and Co dissolution. To further understand the mechanisms of metal dissolution in NMC-111 the model cathodes were cycled at 0.05 mV/s in three different electrolytes: 1 M LiPF_6 , EC:DEC 1:2, 1 M LiPF_6 , EC, and 1 M LiPF_6 , DEC. The fluorescence signal from NMC electrode in 1 M LiPF_6 , DEC electrolyte was substantially higher than in the other two, indicating that DEC oxidation is mainly responsible for metal dissolution and formation of metal(β -diketone) fluorescent complexes with short side chains, which dissolve in the electrolyte. EC oxidation produces higher molecular weight metal^{II}(β -diketone) complexes, which contribute to the build-up of a surface film at the NMC cathode surface and prevent further dissolution. ICP analysis of the electrolyte from cycled NMC/graphite cells also revealed that the rate of metal dissolution was twice as fast in DEC-based electrolyte than in pure EC. Similar results were obtained for cells containing NMC-532 thin-film electrodes.

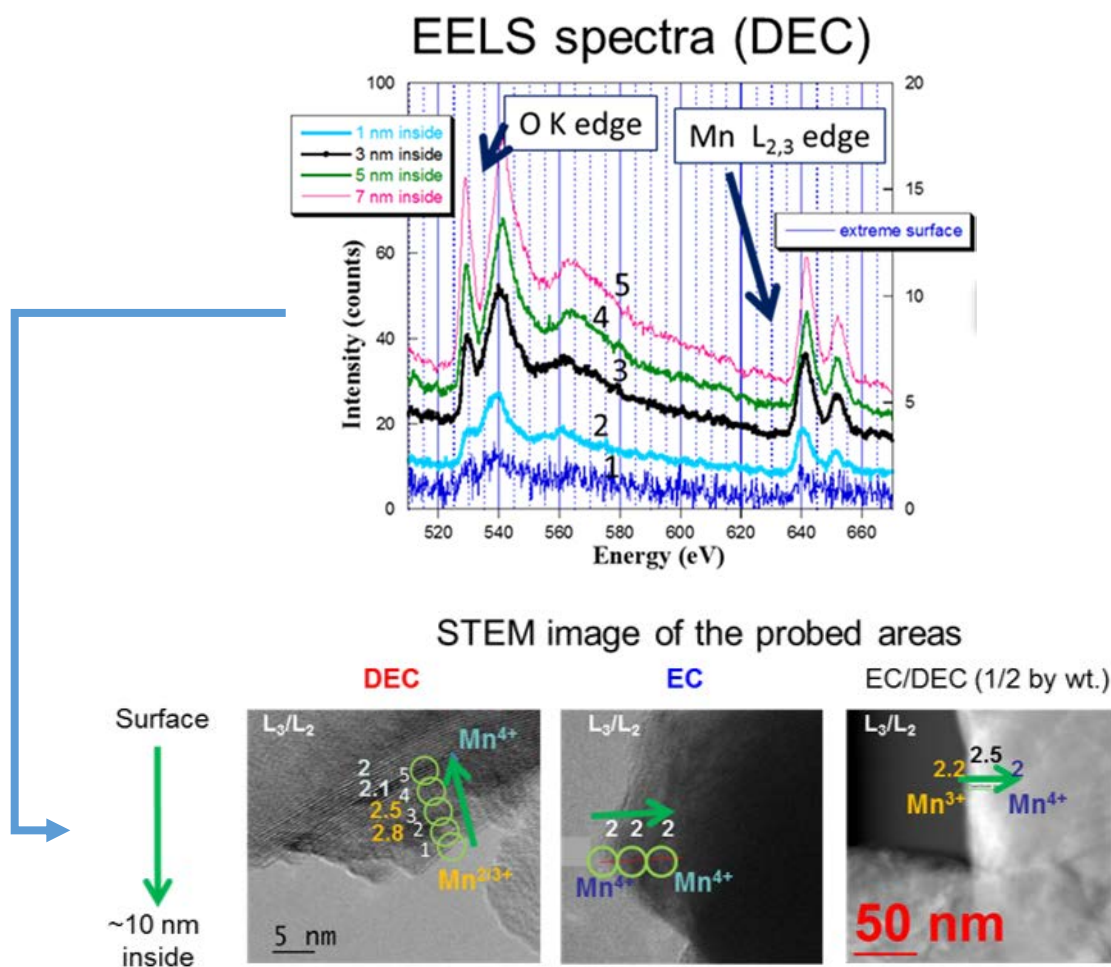


Figure V-128: EELS spectra and STEM images of cycled NMC electrode in three 1M LiPF₆-based electrolytes

To further understand the interfacial reactivity of NMC electrodes toward organic carbonate electrolytes, we performed EELS experiments at low temperature, using a vacuum transfer sample holder, on non-washed binder- and carbon-free NMC electrodes cycled in a Swagelok cell vs. Li-foil anode between 4.4 and 2.8 V in 1 M LiPF₆, EC, DEC or EC/DEC (1/2 wt.) electrolytes (Figure V-128). Surface reconstruction in NMC is usually associated with Mn, Ni and/or Co reduction at the surface and the corresponding depletion of oxygen environment. Both phenomena can be probed using EELS by analyzing the Mn L₃/L₂ edge ratio to determine Mn oxidation state. As illustrated in Figure V-128, the Mn oxidation state decreases at the surface of NMC during cycling and is associated with an electronic structure change evidenced at the O K-edge. While these structural changes are easily identifiable in DEC electrolyte, with EC almost no variation of the transition metal oxidation state is observed at the surface.

These results are consistent with the literature data and they support the general idea of simultaneous Ni, Mn, and Co dissolution from NMC cathodes and surface structure reconstruction from layered to rock salt during cycling. Using the difference observed with EC or DEC, these results suggest a direct correlation between, surface film formation, metal dissolution and the corresponding fluorescence emission and surface reconstruction. The early formation of a surface film in the EC-based electrolyte during cycling limits the surface reconstruction by inhibiting EC oxidation and subsequent metal dissolution. As stronger fluorescence signal was associated with more surface reconstruction, the intensity of fluorescence from the electrolyte oxidation and metal dissolution products can be used to assess quantitatively the extent of surface structure transformation. Further investigations are underway to evaluate the role of rock salt surface layer formation on the battery performance and failure modes in NMC/graphite and NMC/Si battery systems.

2. Interfacial Activity of Silicon Anodes

We exploited the exceptional spatial resolution (ca. 20 nm), surface sensitivity and chemical selectivity of near-field FTIR microscopy and spectroscopy to identify individual chemical building blocks of the SEI film on a silicon model electrode. We looked at the influence of LiBOB as an additive in the standard electrolyte on the SEI film chemical composition, morphology and individual component distribution. LiBOB is an effective electrolyte additive known for its positive effect on the interfacial properties of the anode in lithium-ion batteries via the formation of $\text{Li}_x\text{B}_y\text{C}_n\text{O}_{2n}$ ($n>3$) oligomers. $\text{Li}_2\text{C}_2\text{O}_4$ and $\text{Li}_x\text{B}_y\text{C}_n\text{O}_{2n}$ compounds form and get incorporated in the SEI layer upon LiBOB electroreduction during the initial cycles.

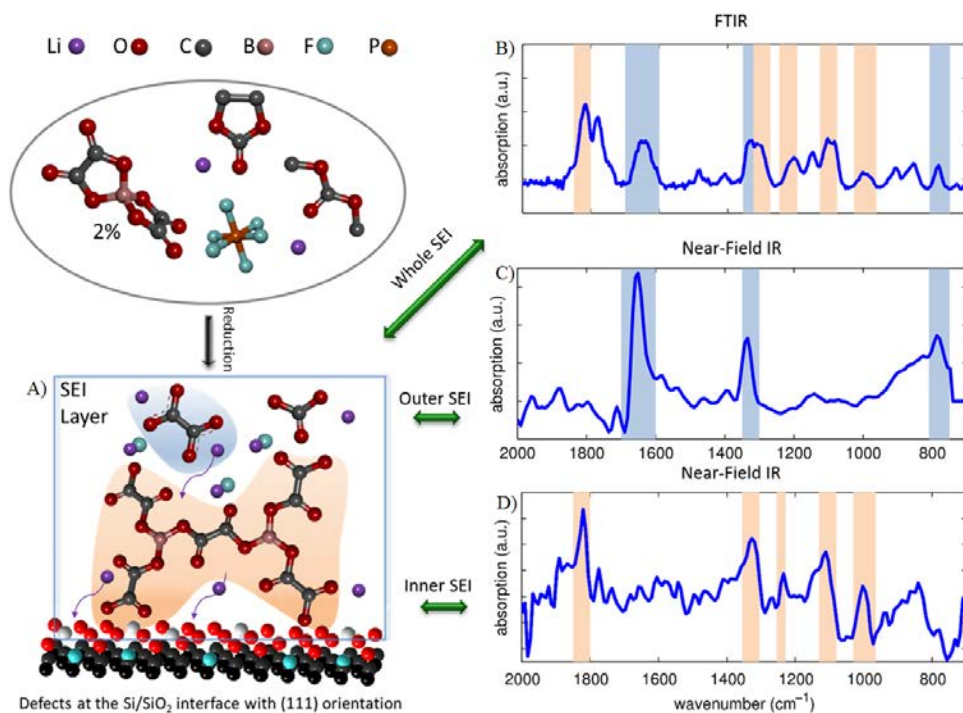


Figure V-129: Illustration of the SEI layer structure and chemical composition (A), *ex situ* ATR-FTIR spectrum (B), and SINS spectra of the Si(111) electrode after the initial cathodic scan to 1.5 and 0.5 V in 1 M LiPF₆ + 2% LiBOB, EC:DMC (1:1 wt) electrolyte

We used these compounds as spectroscopic markers to map the SEI layer chemical composition because of their very distinguishable spectroscopic signatures in infrared that are easily identifiable by synchrotron infrared near-field spectroscopy (SINS). Varying LiBOB content in the electrolyte and probing the corresponding SEI films formed on Si with SINS in combination with other techniques can help to unravel the correlation between the function and chemical composition of an effective SEI layer. The samples were characterized by near-field IR spectroscopy using the Advanced Light Source Synchrotron (ALSS) beamline 5.4.1. Figure V-129 shows the conclusive SINS identification of $\text{Li}_2\text{C}_2\text{O}_4$ and $\text{Li}_x\text{B}_y\text{C}_n\text{O}_{2n}$ in the surface film on Si (111) wafer electrode swept to 1.5 and 0.5 V in 1 M LiPF₆ + 2% LiBOB in EC:DMC 1:2, by comparison to a standard average ATR-FTIR spectrum. We were able to correlate for the first time the improved passivating properties of silicon in the presence of LiBOB with the formation and incorporation of $\text{Li}_x\text{B}_y\text{C}_n\text{O}_{2n}$ ($n>6$) in the inner part of the SEI layer. Further investigations are underway to evaluate the influence of rock salt surface layer formation on the battery performance in high Ni content NMC based battery systems

Conclusions

- X-ray absorption, optical fluorescence spectroscopy and imaging experiments demonstrated that solvent oxidation at transition metal oxide surface is enhanced by surface defects such as oxygen vacancies and results in metal dissolution via the formation of fluorescent Metal(β -diketone) complexes.

- We have demonstrated that formation of fluorescent species is a common phenomenon observed in transition metal oxides cathodes during cycling at high potentials.
- Fluorescence signal originates from oxidation of linear carbonate esters. Oxidation of EC results in the formation of a surface film containing species with longer side chains which inhibit further metal dissolution.
- Surface reconstruction in $\text{LiNi}_{0.33}\text{Mn}_{0.33}\text{Co}_{0.33}\text{O}_2$ surface and rock salt structure formation is more pronounced in linear carbonate ester-based electrolytes.
- Formation of $\text{Mn}^{\text{III}}/\text{Mn}^{\text{II}}$, Co^{II} and Ni^{II} complexes on transition metal oxide cathodes in organic carbonate electrolytes is responsible for Mn, Co and Ni dissolution as well as surface reconstruction and relates to the observed failure modes in lithium-ion batteries.
- A combination of traditional (cyclic voltammetry, FTIR) and next-generation (near-field IR, LIBS) techniques were used to identify the role of LiBOB additive in stabilizing the SEI on Si electrodes
 - An oligomeric “inner SEI” composed of $\text{LiB}_2\text{C}_{10}\text{O}_{20}$ forms early (>1.5 V) and is responsible for passivating the Si surface.
 - The “outer SEI” consists of compounds including LiF and $\text{Li}_2\text{C}_2\text{O}_4$ which do not clearly contribute to SEI functionality.
- Near-field spectroscopy established for the first time as a technique for identifying functional components of the SEI film. Results are in accordance with data provided by other methods and establish new information (spatial localization of compounds) unachievable by other methods.

Products

Presentations/Publications/Patents

1. Maurice Ayache, Dongyoun Jang, Jaroslaw Syzdek, and Robert Kostecki, “Near-Field IR Nanoscale Imaging of the Solid Electrolyte Interphase on a HOPG Electrode”, *Journal of The Electrochemical Society*, 162 (13) A7078-A7082 (2015); DOI:10.1149/2.0101513jes
2. Martin Winter, Ulrike Vogl, Simon Lux, Adam Weber, Prodib Das, and Robert Kostecki. “The mechanism of SEI formation on/at single crystal Si (110) and (111) electrodes”, *Journal of Electrochemical Society*, 2015, 162, A2281-A2288 10.1149/2.0361512jes
3. L. Cheng, W.H. Wu, A. Jarry, W. Chen, Y. Ye, J. Zhu, R. Kostecki, K. Persson, J. Guo, M. Salmeron. G. Chen and M. Doeff, “Interrelationships among Grain Size, Surface Composition, Air Stability and Interfacial Resistance of Al-substituted $\text{Li}_7\text{La}_3\text{Zr}_2\text{O}_{12}$ Solid Electrolytes”, *ACS Appl. Mater. Interfaces*, 2015, 7 (32), pp 17649–17655, DOI:10.1021/acsami.5b02528
4. Y. S. Yu, C. Kim, D. Shapiro, M. Farmand, R. Kostecki, D. Qian, S. Meng and J. Cabana, “Advanced X-Ray Transmission Microscopy for Chemical and Fracture Imaging of Single Li_xFePO_4 Particles at High Resolution”, 227th ECS Meeting, Chicago, IL, May 24-28, 2015
5. R. Kostecki, A. Jarry, S. Gottis, and J. B. Kerr, “Mechanism of Formation of Metal Acetylacetonates at the $\text{Li}_x\text{Ni}_{0.5}\text{Mn}_{1.5}\text{O}_4\text{-S/Carbonate Ester Electrolyte Interface}$ ” 227th ECS Meeting, Chicago, IL., May 24-28, 2015
6. L. Terborg, Y. Park, S. Venkatachalam, P. Hernandez and R. Kostecki, “Interfacial Reactivity of a High Capacity Manganese Rich (HCMRTM) Lithium-ion Positive Electrode”, 227th ECS Meeting, Chicago, IL, May 24-28, 2015
7. M. Ayache, D. Jang, and R. Kostecki, “Nanoscale IR Near-Field Imaging of the SEI Layer on an HOPG Electrode”, 227th ECS Meeting, Chicago, IL, May 24-28, 2015
8. Robert Kostecki, “Battery Characterization and Diagnostics Across Length and Time Scales”, 10th China-U.S. Electric Vehicle and Battery Technology Workshop, Beijing P.R.China, March 29-30, 2015 (invited talk)
9. Robert Kostecki, Maurice Ayache, Simon Lux, Ivan Lucas, “Near-field optical imaging of the SEI layer on a Sn anode”, 249th ACS National Meeting & Exposition March 22-26, 2015, Denver, CO, USA (invited talk)

10. Robert Kostecki, Maurice Ayache, Angelique Jarry, Ivan Lucas, "Chemical Imaging of Interfaces and Interphases in Lithium-ion Anodes", International Battery Association (IBA) and Pacific Power Source Symposium, January 5-9, 2015, Waikoloa Village, Hawaii, USA (invited talk)
11. M. Ayache, J. Syzdek, I. Lucas, N. Norberg and R. Kostecki, "Interfacial Studies of the SEI Layer on a Tin Electrode", 2014 ECS and SMEQ Joint International Meeting Cancun, Mexico, October 5-9, 2014
12. Maurice Ayache, Simon Lux, and Robert Kostecki, "Nanoscale Chemical Mapping of the Solid Electrolyte Interphase in Lithium-ion Systems", SciX Conference, September 29, 2014, Reno, NV (invited talk)
13. Robert Kostecki, Maurice Ayache, Angelique Jarry, Ivan Lucas, Alexander McLeod, Richard Russo, Jaroslaw Syzdek, Vasileia Zormpa, "*In situ/in operando* characterization of electrical energy storage systems", 65th Annual Meeting of the International Society of Electrochemistry, August 31 – September 5, 2014, Lausanne, Switzerland (keynote lecture)
14. Jarry, Y. Fu, M. Ayache, V. Battaglia, and R. Kostecki, "Interfacial Phenomena and Chemical Cross-talk in LiNi_{0.5}Mn_{1.5}O₄/Graphite Lithium-ion Battery System", 248th ACS National Meeting and Exposition, August 10-14, 2014, San Francisco, CA (invited talk)

References

1. A. Jarry et al., JACS, 2015, **137**, 3533-3539.
2. N. S. Norberg et al., Electrochem. Commun. **34**, 29-32, (2013).
3. M. Moshkovich et al., J. Electroanal. Chem., 2001, **497**, 84-96.
4. S. E. Sloop et al., *J. Power Sources*, 2003, **119–121**, 330-337.

V.E.3. Advanced *in situ* Diagnostic Techniques for Battery Materials (BNL)

Xiao-Qing Yang, Principal Investigator

Brookhaven National Laboratory
Chemistry Division
Bldg. 555
Upton, NY 11973
Phone: 631-344-3663; Fax: 631-344-5815
E-mail: xyang@bnl.gov

Xiqian Yu, Co-Principal Investigator

Brookhaven National Laboratory
Chemistry Division
Bldg. 555
Upton, NY 11973
Phone: 631-344-4142; Fax: 631-344-5815
E-mail: xyu@bnl.gov

Tien Q. Duong, DOE Program Manager

U.S. Department of Energy
Advanced Battery Materials Research (BMR)
Vehicle Technologies Office
1000 Independence Avenue, SW
Washington, DC 20585
Phone: 202-586-7836
E-mail: Tien.Duong@ee.doe.gov

Start Date: September 1, 2015

End Date: August 30, 2016

Abstract

Objectives

- To determine the contributions of electrode materials changes, interfacial phenomena, and electrolyte decomposition to the cell capacity and power decline.
- To develop and apply synchrotron based *in situ* X-ray techniques such as x-ray diffraction (XRD) and x-ray absorption spectroscopy (XAS) to study materials in an environment that is close to the real operating conditions.
- To search new approaches on how to improve the thermal stability of cathode materials including doping and surface modification techniques.
- To develop new diagnostic tools for battery studies.

Accomplishments

- By collaborating with Dr. Yijin Liu at Stanford Synchrotron Radiation Lightsource, SLAC National Accelerator Laboratory and other collaborators, designed, synthesized Fe substituted high voltage spinel $\text{LiNi}_{0.5-x}\text{Mn}_{1.5-x}\text{Fe}_{2x}\text{O}_4$ (LNMFO) cathode materials and carried out thermal stability studies these materials. The optimized $\text{LiNi}_{1/3}\text{Mn}_{4/3}\text{Fe}_{1/3}\text{O}_4$ materials showed outstanding thermal stability.
- By collaborating with Prof. Lin Gu at Institute of Physics, Chinese Academy of Sciences, through a systematic study of $\text{LiNi}_{1/3}\text{Co}_{1/3}\text{Mn}_{1/3}\text{O}_2$ (NCM) cathode materials cycling at different charge-discharge rates, using *in situ* synchrotron based XRD and XAS, as well as using atomic resolution *ex situ* STEM after high rate cycling, intermediate phase formation at high rate cycling was discovered.

The results of these studies would provide important guidance for designing new cathode materials for high power usage of lithium-ion batteries, such as for HEV and PHEV.

- By collaborating with beamline scientists at X-ray powder diffraction (XPD) and hard x-ray nano-probe (HXN) beamlines at NSLSII, new *in situ* and *ex situ* studies of battery materials using the unique capability of these two beamlines have been designed and carried out. The preliminary results are promising.

Future Achievements

- The synchrotron based *ex situ* and *in situ* x-ray pair distribution function (PDF) technique will be developed and applied for battery material research, especially on the high energy density cathode materials.
- The full field transmission x-ray microscopy (TXM) technique as well as micro- and nano- probe scanning TXM techniques will be developed and applied for lithium-ion battery research.
- Using the unique capability of the new Hard x-ray nano-probe (HXN) beamline at NSLSII to do both *in situ* and *ex situ* studies of battery materials
- The collaborative research with US academic research institutions and industrial partners will be further expanded and strengthened.

Technical Discussion

Background

This project has been focused on developing advanced diagnostic characterization techniques to investigate these issues, obtaining in-depth fundamental understanding of the mechanisms governing the relationship between the structure and the performance, and providing guidance and approaches to solve these problems. The unique approach of this project is the development and application of combined synchrotron based *in situ* X-ray techniques (x-ray diffraction, hard and soft x-ray absorption) with other imaging and spectroscopic tools such as high resolution transmission electron microscopy (HRTEM), Scanning transmission electron microscopy (STEM), mass spectroscopy (MS), X-Ray fluorescence microscopy (XRF) and transmission x-ray microscopy (TXM). For advanced lithium-ion battery technologies, the revolutionary approaches using new generation of materials for cathode, anode, electrolyte, and separator are in the horizon. The new generation of cathode materials such as high voltage spinels ($\text{LiMn}_{2-x}\text{Ni}_x\text{O}_4$) and/or Li-rich high energy density $\text{Li}_{1+x}(\text{NiMnCo})\text{O}_2$ composite materials together with high energy density Si-based anode materials will significantly increase the energy density of the LIB cells. However, there are many technical barriers must be overcome before the large scale commercialization of these new materials can be realized. This project has been using the time-resolved x-ray diffraction TR-XRD and absorption (TR-XAS) developed at BNL to study the kinetic properties of these materials with structural sensitivity (TR-XRD) and elemental selectivity (TR-XAS). This project will develop and apply the HRTEM and TXM to study the mechanism of capacity fading of cathode and anode materials. Another important issue is the thermal stability of new cathode materials which is closely related to the safety of the batteries. This problem will be studied using the combined TR-XRD, TR-XAS with mass spectroscopy (MS). This project also proposes to develop a novel *in situ* X-ray fluorescence (XRF) microscopy combined with X-ray absorption spectroscopy (XAS) technique, which will enable us to track the morphology and chemical state changes of the electrode materials during cycling. We will further develop this novel technique utilizing the new unique capability of TES beamline at NSLS II, with better signal/noise ratio and spatial resolution to do diagnostic studies of the cathode and anode materials of advanced lithium-ion batteries. In summary, this project supports the goals of VTO, the Energy Storage team, and BMR program by developing new diagnostic technologies and applying them to the advanced lithium-ion battery systems to provide guidance for new material development.

Introduction

Genuine Previously, oxygen release mechanism has been studied¹ for the high voltage spinel^{2,3} $\text{LiNi}_{0.5}\text{Mn}_{1.5}\text{O}_4$ (LNMO), a cathode with high energy density due to high operating voltage at around 4.7 V. When heated at fully charged state, the highly oxidized Ni^{4+} has the tendency to be reduced to lower valence states^{1,4}; while at the same time, structural transition requires manganese to migrate from octahedral sites to tetrahedral sites which can only be realized after manganese is reduced from Mn^{4+} to Mn^{2+} . Both of these reductions will cause oxygen release and poor thermal stability problem for this material. Therefore, the solution we proposed to suppress the oxygen release is to lower nickel's concentration by introducing some more stable cations, which also has the tendency to migrate to tetrahedral sites from octahedral sites during heating without paying the price of reduction. Indeed, Delmas et al^{5,6} found that Al^{3+} , which doesn't need to be reduced to migrate, plays a positive role in improving the thermal stability of nickel-based layered material. Therefore, Al became a necessary component in the commercialized cathode material $\text{LiNi}_{0.8}\text{Co}_{0.15}\text{Al}_{0.05}\text{O}_2$. Here, we proposed to use transition metal cations as substitution candidates because they can be electrochemically active and therefore contribute to the capacity. In order to see the tendency of migration from octahedral sites to tetrahedral site, octahedral site stabilization energy (OSSE)^{7,8} is plotted as a function of the electronic structure of 3d transition metal cations in Figure V-130b. OSSE is used because it is the energy difference between an octahedron and a tetrahedron and therefore a good indicator of the tendency of migration. Generally speaking, higher OSSE corresponds to stronger tendency to migrate. Among cations with the greatest migrating tendency (e.g., Ti^{4+} , V^{5+} , Cr^{6+} , Fe^{3+} , Zn^{2+} etc.), Fe^{3+} is considered as the most promising candidate with the following reasons. Firstly, Fe is environmentally benign and naturally abundant. Secondly, Fe^{3+} is stable in air and therefore easy to be handled during synthesis process. Thirdly, $\text{Fe}^{3+}/\text{Fe}^{4+}$ electrochemically active redox couple can be utilized at the high voltage region (>4.7 V), as reported by Ohzuku^{9,10} and Manthiram¹¹. This means that Fe^{3+} can potentially play the dual roles of both in keeping high energy density and in stabilizing the structure against oxygen release. Manthiram *et al*¹¹ has reported that low concentration Fe doping can improve the electrochemical performance of high voltage spinel and explained the mechanism behind the improvement. In this paper, we go beyond the low concentration doping level and use Fe to simultaneously substitute Ni and Mn to the greatest possible extent, aiming to obtain an optimized transition metal stoichiometry that delivers both excellent electrochemical performance and excellent thermal stability by suppressing oxygen release.

The other Important studies of this project is the structural changes of cathode materials during high rate charging and discharging, which are quite critical for the vehicle application. It is well known that layer structured cathode materials LiMO_2 (M = Ni, Co, Mn) have better rate capability comparing with olivine LFP systems^{12,13}, due to their higher electronic conductivity, higher lithium ion diffusion coefficient and two-dimensional diffusion paths. However, to the best of our knowledge, not much systematic studies have been reported on the phase transition behavior of the layer structured cathode materials during high current rate charging. In the present work, the structural changes of NMC in a wide range of current rates (from 0.1C to 60C) charging are systematically studied using synchrotron based time-resolved *in situ* XRD. The contribution from each transition metal ions (Ni, Mn, Co) to charge compensation on charging is obtained by *in situ* Q-XAS. The details of atomic arrangement and local phase distributions for NMC samples harvested from half-way charged cell at 30C rate are studied by the aberration-corrected STEM technique. An intermediate phase is observed using *in situ* time resolved XRD during the first charging cycle when current rates higher than 10C are applied.

Approach

- A combination of time resolved X-ray diffraction (TR-XRD) and mass spectroscopy (MS), together with *in situ* soft and hard X-ray absorption (XAS) during heating and transmission electron microscopy (TEM) to study the thermal stability of the electrode materials, especially the high voltage spinel $\text{LiNi}_{1/3}\text{Mn}_{4/3}\text{Fe}_{1/3}\text{O}_4$ with Fe substitution.
- Using *in situ* XRD and XAS, as well as TEM to study the new concentration gradient cathode materials to improve the cycle life of lithium-ion batteries.
- Using quick x-ray absorption spectroscopy and time resolved x-ray diffraction techniques to study the kinetic properties and the structural changes of $\text{Li}_{1-x}\text{Ni}_{1/3}\text{Co}_{1/3}\text{Mn}_{1/3}\text{O}_2$ cathode material from $x=0$ to $x=0.7$ during high rate charge process for high rate capability of lithium-ion batteries.

- Extended collaboration with other US and international academic institutions and US industrial partners.

Results

1: The effect of Fe substitution on thermal stability in $\text{LiNi}_{0.5-x}\text{Mn}_{1.5-x}\text{Fe}_{2x}\text{O}_4$ ($2x = 0, 0.2, 0.33$)

In FY2016, BNL has been focused on the studies of thermal stability studies of Fe substituted high voltage spinel cathode materials $\text{LiNi}_{1/3}\text{Mn}_{4/3}\text{Fe}_{1/3}\text{O}_4$ in comparison with un-substituted $\text{LiNi}_{0.5}\text{Mn}_{1.5}\text{O}_4$ using *in situ* time-resolved x-ray diffraction (XRD) and mass spectroscopy techniques. In order to study the effect of Fe substitution on the structural evolution and oxygen release during heating the charged cathode, *in situ* XRD-Mass Spectroscopy (MS) experiments were carried out for the $\text{LiNi}_{0.5-x}\text{Mn}_{1.5-x}\text{Fe}_{2x}\text{O}_4$ ($2x = 0, 0.2, 0.33$) samples. It can be seen from Figure V-130 that Fe substitution clearly improves the thermal stability of charged cathode by suppressing the oxygen release and maintaining the structure. Charged $\text{LiNi}_{0.5}\text{Mn}_{1.5}\text{O}_4$ releases oxygen at around 250°C and this threshold is pushed to around 380°C for the $2x=0.2$ sample. Further improvement is achieved in the $2x=0.33$ sample which showed no oxygen release up to 500°C . Correlating with suppressed oxygen release is the integrity of the structure as seen in the right panel of Figure V-130.

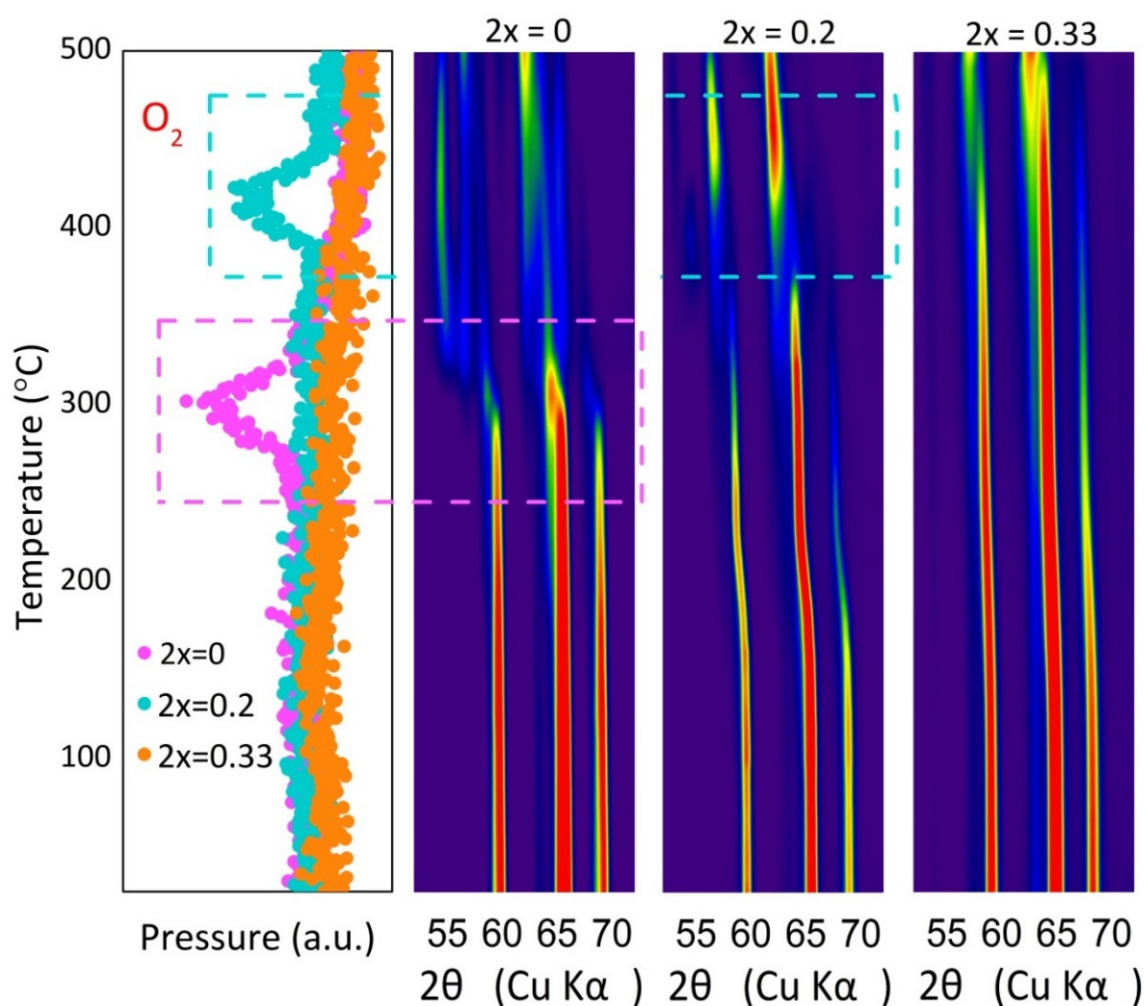


Figure V-130: Effect of Fe substitution on the structural evolution and oxygen release during heating the charged samples of $\text{LiNi}_{0.5-x}\text{Mn}_{1.5-x}\text{Fe}_{2x}\text{O}_4$ ($2x=0, 0.2, 0.33$). The left panel is the *in situ* MS data for oxygen and the right three panels are the *in situ* XRD data for $\text{LiNi}_{0.5-x}\text{Mn}_{1.5-x}\text{Fe}_{2x}\text{O}_4$ ($2x=0, 0.2, 0.33$). X.-Q. Yang *et. al.* *Adv. Energy Mater.*, (December 2015), DOI: 10.1002/aenm.201501662

2: (TXM) investigation on new concentration gradient NCM cathode materials

In FY2016, BNL also carried out the energy resolved transmission X-ray microscopic (TXM) investigation on new concentration gradient NCM cathode materials in a noninvasive manner with 3D reconstructed by images through tomography scans to study the 3D Ni, Co, and Mn elemental distribution from surface to the bulk. In the left panel of Figure V-131, the 3-D distribution of Ni, Mn, and Co are clearly displayed using red, blue and green colors. On the right panel, using the same color code, the concentrations of Ni, Mn, and Co as functions of distance from surface (0 μm) toward the core (up to $-5\mu\text{m}$) are plotted. It can be seen clearly that the concentration gradient nature of the material is well demonstrated (higher Mn concentration at surface than in the bulk; lower Ni concentration at surface than in the bulk, to get both better thermal stability and higher capacity).

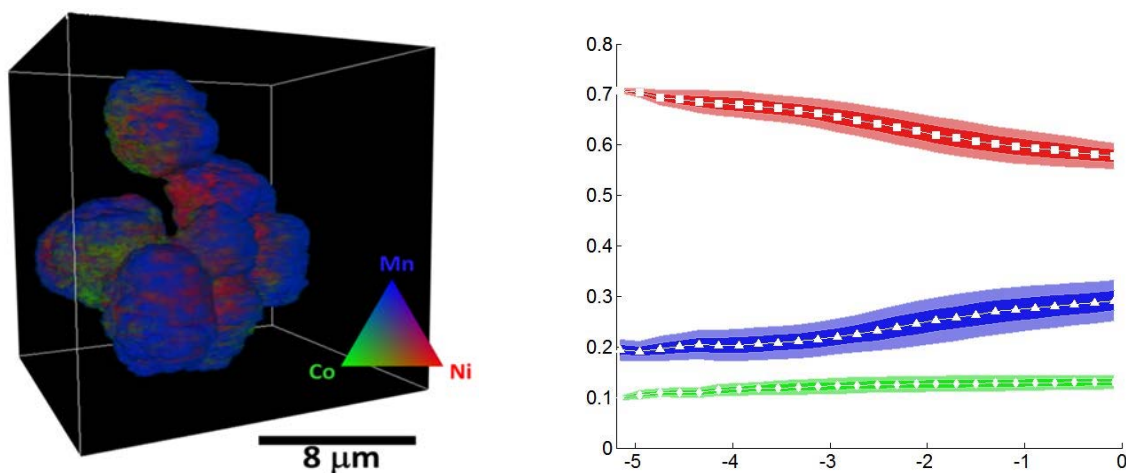


Figure V-131: The reconstructed 3D TXM image of a particle cluster of fully concentration gradient $\text{LiNi}_{0.6}\text{Mn}_{0.2}\text{Co}_{0.2}\text{O}_2$ sample (left panel) with the color legend indicating the elemental distribution over the investigated 3D volume. By regrouping the voxels as a function of the shortest distance from the corresponding voxel to the outer surface, we plot the normalized elemental concentration versus the voxel depth. As shown in the right panel, the different slopes in the concentration gradient were clearly observed. It worth to mention that the elemental concentration over tens of millions of voxels were retrieved in this experiment, which provides good statistic of the depth profile as indicated by the color band in right panel

3: Structural changes of $\text{LiNi}_{1/3}\text{Mn}_{1/3}\text{Co}_{1/3}\text{O}_2$ (NMC) cathode during high rate charge-discharge cycling using time resolved XRD and XAS as well as TEM

In FY2016, BNL also studied the structural changes of widely used $\text{LiNi}_{1/3}\text{Mn}_{1/3}\text{Co}_{1/3}\text{O}_2$ (NMC) cathode during high rate charge-discharge cycling (from 10C to 60C) by using ultrafast time-resolved *in situ* X-ray diffraction (XRD). Intermediate phases were observed when the current rates were increased to 10C, and became more pronounced at 30C and 60C, as shown in Figure V-132.

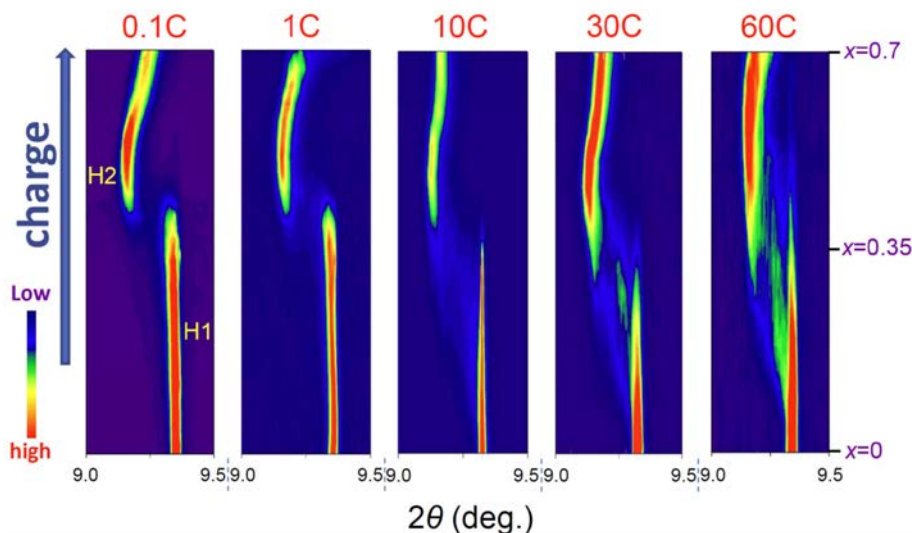


Figure V-132: *In situ* XRD of NMC during the first charge. Contour plot of the 003 diffraction peak of $\text{Li}_{1-x}\text{Ni}_{1/3}\text{Co}_{1/3}\text{Mn}_{1/3}\text{O}_2$ with increasing x between $x = 0$ and $x = 0.7$ during the first charge process at different C rates (0.1 C, 1 C, 10 C, 30 C, 60 C). Data were collected at X14A at NSLS with a wavelength of 0.7747 Å

X.-Q. Yang et al., *Adv. Energy Mater.*, (August, 2016), DOI: 10.1002/aenm.201600597.

BNL also carried out the studies of *in situ* time resolved TR- XAS on a $\text{LiNi}_{1/3}\text{Mn}_{1/3}\text{Co}_{1/3}\text{O}_2$ (NMC) cathode material during high rate cycling at 30C. The valence state and local environment of each transition metal element in NMC are monitored by *in situ* quick X-ray absorption technique. Figure V-133a-c shows the changes of the X-ray absorption near edge spectroscopy (XANES) at the Ni, Co and Mn K-edges during 30C charge, respectively. The K-edge of Ni shifts continuously to higher energy, indicating the oxidation of Ni ions from Ni^{2+} to Ni^{4+} during the charging process. In contrast, the K-edges of Co and Mn exhibit almost no energy shift. The Co and Mn K-edge features change shape, indicating that the local environment changes around Co and Mn ions, but Co and Mn do not contribute much to the charge compensation. Same results are obtained at 1C and 10C rates. These results suggest that charge compensation during charging mainly arises from Ni.

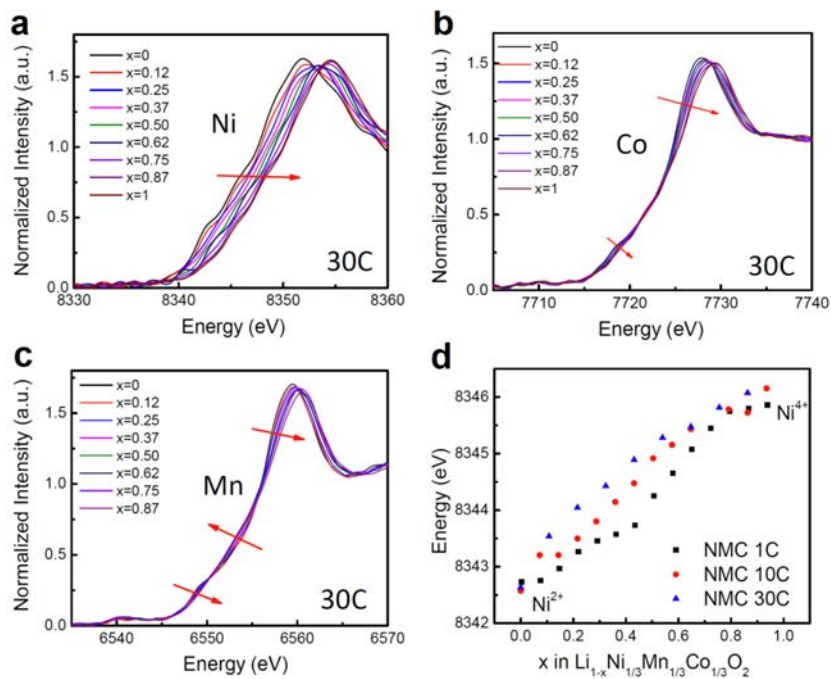


Figure V-133: *In situ* Quick XAS of NMC during the first charge. The x-ray absorption near edge spectroscopy (XANES) results of NMC at (a) Ni, (b) Co and (c) Mn K-edges during 30C charge, respectively. (d) The Ni K-edge energy shift as a function of nominal lithium content x in NMC during initial charge process at the current rates of 1C, 10C and 30C

X.-Q. Yang et al., *Adv. Energy Mater.*, (August, 2016), DOI: 10.1002/aenm.201600597.

In collaboration with scientists at Institute of Physics (IOP), Chinese Academy of Sciences (CAS), the TEM studies of a half-way charged $\text{LiNi}_{1/3}\text{Mn}_{1/3}\text{Co}_{1/3}\text{O}_2$ (NMC) cathode material after 30C charging was studied using high resolution TEM. The results in Figure V-134 shown that some regions (marked by red square) with different lattice sites of Li occupation (tetrahedral vs octahedral in normal case) were observed after high rate charging, relating to the intermediate phase observed in XRD.

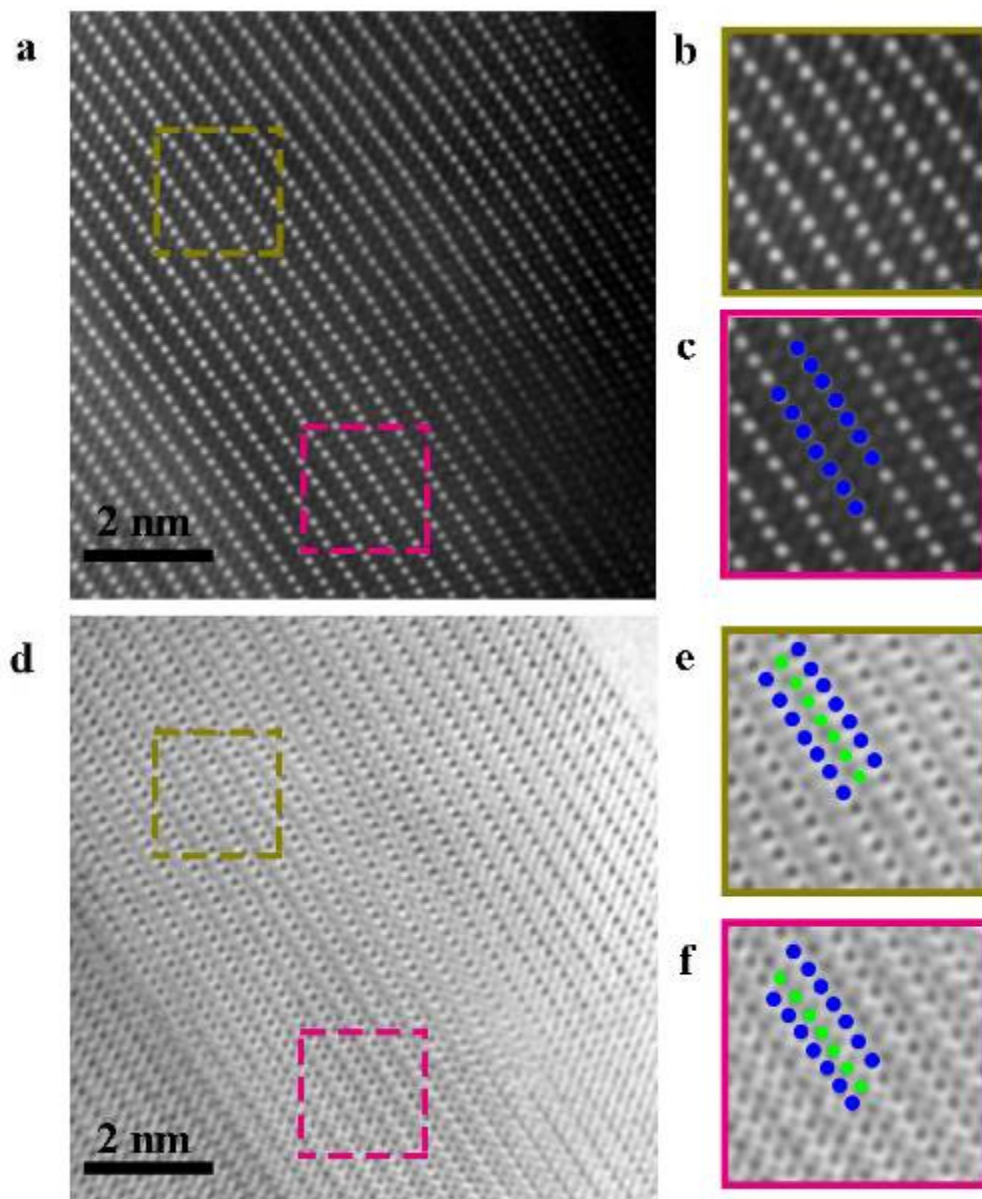


Figure V-134: Structure of half charged NMC at 30C rate. a) Typical HAADF image taken along the [110] zone axis of the NMC electrode after 55 s charging at the current rate of 30C. b,c) The zoom-in image of the areas marked with orange and pink squares, respectively. d) Corresponding ABF images of NMC electrode after 55 s charging. e,f) The zoom-in image of the areas marked with orange and pink squares, respectively. The blue and green dots indicate the TM ions and Li ions, respectively

Conclusions

Based on the fundamental understanding of the interplay between oxygen release and crystal structural change which is further related to the electronic structure of transition metal cations, we proposed using Fe as a major component for the high voltage spinel system in designing thermally stable and high-performance cathode. The synthesized $\text{LiNi}_{0.5-x}\text{Mn}_{1.5-x}\text{Fe}_{2x}\text{O}_4$ ($2x = 0.33$) material delivers both satisfactory thermal stability and

competitive electrochemical performance. These results highlight the importance of fundamental studies in advancing the battery chemistry.

The exploratory studies of the non-equilibrium phase transition behavior in layer structured NMC cathode system during high rate cycling carried out by BNL have important indications. It provides direct evidence for the different phase transition behaviors than those during low rate charging. Intermediate phases were observed at high rate charging at 10C, 30C, and 30C by *in situ* XRD. In contrast, such intermediate phase formation was not observed during low rate charging. Since the formation of intermediate phases is strongly related to the larger over-potential generated by high rate charging, during the low rate charge, the over-potential may not be high enough to facilitate the formation of intermediate phases. Phase coexistence heterogeneities and tetrahedral occupation of Li in the Li-poor phase, which could be one of the intermediate phases were observed in the half-way charged NMC using *ex situ* STEM. By using the *in situ* quick X-ray absorption technique, we find that the charge compensation contribution by Ni ions is faster and more effective at the higher C rate, suggesting the benefit of higher Ni content in NMC for rate capability. These results show that the high rate induced intermediate phase formation process reported in the literature for olivine structured LFP system, also exist in layer structured NMC system. This, raises the question about the presence of such intermediate states in other systems, such as layer structured LiCoO₂ and cubic spinel structured LiMn₂O₄. These important results will further inspire theoretical and experimental studies on the high rate induced structural changes for a wide spectrum of cathode materials and thereby provide valuable guidance for the development of cathode materials for lithium-ion batteries with better rate capability.

Products

Presentations/Publications/Patents

1. Arthur von Wald Cresce*, Mallory Gobet, Oleg Borodin, Jing Peng, Selena M. Russell, Emily Wikner, Adele Fu, Libo Hu, Hung-Sui Lee, Zhengcheng Zhang, Xiao-Qing Yang, Steven Greenbaum, Khalil Amine, and Kang Xu, “Anion Solvation in Carbonate-Based Electrolytes”, *J. Phys. Chem. C*, 2015, 119 (49), pp 27255–27264, DOI: 10.1021/acs.jpcc.5b08895, November, 2015.
2. X. Yu, E. Hu, S. Bak, Y. Zhou, X.-Q. Yang, 5. “Strategies to curb structural changes of lithium/transition metal oxide cathode materials & the changes’ effects on thermal & cycling stability”, *Chin. Phys. B* Vol. 25, No. 1 (December 2015) 018205, DOI: 10.1088/1674-1056/25/1/018205.
3. Enyuan Hu, Seong-Min Bak, Yijin Liu, Jue Liu, Xiqian Yu, Yongning Zhou, Zhou, Peter Khalifah, Kingo Ariyoshi, Kung-Wan Nam, and Xiao-Qing Yang, “Utilizing Environmental Friendly Iron as a Substitution Element in Spinel Structured Cathode Materials for Safer High Energy Lithium-Ion Batteries” *Adv. Energy Mater.*, (December 2015), DOI: 10.1002/aenm.201501662.
4. Hyun-Kyung Kim, Seong-Min Bak, Suk Woo Lee, Myeong-Seong Kim, Byeongho Park, Su Chan Lee, Yeon Jun Choi, Seong Chan Jun, ung Tark Han, Kyung-Wan Nam, Kyung Yoon Chung, Jian Wang, Jigang Zhou, Xiao-Qing Yang, Kwang Chul Roh, and Kwang-Bum Kim, “Scalable Fabrication of Micron-Scale Graphene Nanomeshes for High-Performance Supercapacitor Applications”, *Energy & Environmental Science* (2016), DOI: 10.1039/c5ee03580e, published on the web 27th January 2016.
5. Kai He, Sen Zhang, Jing Li, Xiqian Yu, Qingping Meng, Yizhou Zhu, Enyuan Hu, Ke Sun, Hongseok Yun, Xiao-Qing Yang, Yimei Zhu, Hong Gan, Yifei Mo, Eric A. Stach, Christopher B. Murray & Dong Su, “Visualizing non-equilibrium lithiation of spinel oxide via *in situ* transmission electron microscopy” *Nature Communications*, May (2016) 7, Article number: 11441 doi: 10.1038/ncomms11441.
6. Fang-Chao Liu, Zulipiya Shadik, Xiao-Fang Wang, Si-Qi Shi, Yong-Ning Zhou, Guo-Ying Chen, Xiao-Qing Yang, Lin-Hong Weng, Jing-Tai Zhao, and Zheng-Wen Fu, “A Novel Small-Molecule Compound of Lithium Iodine and 3-Hydroxypropionitrile as a Solid-State Electrolyte for Lithium–Air Batteries”, *Inorg. Chem.*, 2016, 55 (13), pp 6504–6510, DOI: 10.1021/acs.inorgchem.6b00564, Publication Date (Web): June 16, 2016.
7. Jigang Zhou, Jian Wang, Jeffrey Cutler, Enyuan Hu, and Xiao-Qing Yang, “Imaging the surface morphology, chemistry and conductivity of LiNi_{1/3}Fe_{1/3}Mn_{4/3}O₄ crystalline facets using scanning

transmission X-ray microscopy”, *Phys. Chem. Chem. Phys.*, 2016, 18, 22789-22793, DOI: 10.1039/C6CP03511F, published date (web) July 2016.

8. Yong-Ning Zhou, Ji-Li Yue, Enyuan Hu, Hong Li, Lin Gu, Kyung-Wan Nam, Seong-Min Bak, Xiqian Yu, Jue Liu, Jianming Bai, Eric Dooryhee, Zheng-Wen Fu, Xiao-Qing Yang, “High-Rate Charging Induced Intermediate Phases and Structural Changes of Layer-Structured Cathode for Lithium-Ion Batteries”, *Adv. Energy Mater.*, (August, 2016), DOI: 10.1002/aenm.201600597.
9. Xiqian Yu, Enyuan Hu, Xiao-Qing Yang*, Seong-Min Bak, Yongning Zhou, Hung-Sui Lee, Paul Northrup, Kyung-Wan Nam, Yijin Liu, Jie Xiao, Jun Liu, Huiming Wu and Khal Amine, “Using Synchrotron Based X-ray Diffraction and Absorption as Well as TXM to Study the New Electrode Materials for Lithium-ion and Li-S Batteries”, presented at 2015 ALS User Meeting, October 6 to 10, 2015, Berkeley, California, USA, **Invited**.
10. Xiqian Yu, Enyuan Hu, Jue Liu, Seongmin Bak, Hung Sui Lee, Xiao-Qing Yang*, Zhizhen Zhang, Lin Gu, Yong-Sheng Hu, Hong Li, Xuejie Huang, and Liquan Chen “Structural characterization studies of advanced electrode and solid electrolyte materials for Lithium-ion and sodium batteries using synchrotron based x-ray techniques and TEM”, presented at the Conference of International Battery Frontier 2016 (CIBF2016), May 24-26, 2016, Shenzhen, China. **Invited**.
11. Enyuan Hu, Xiao-Qing Yang*, Xiqian Yu, Yongning Zhou, Seong-Min Bak, Hung-sui Lee, Zhaoxiang Wang and Yijin Liu, “Using Synchrotron Based *in situ* X-ray Diffraction and Absorption and TXM Techniques to Study the New Electrode Materials for Next Generation of Batteries”, presented at the Seminar at Energy Sciences Institute, Yale University New Haven, September 14, 2016, **Invited**.

References

1. Hu, E. Y.; Bak, S. M.; Liu, J.; Yu, X. Q.; Zhou, Y. N.; Ehrlich, S. N.; Yang, X. Q.; Nam, K. W. *Chem. Mater.* 2014, 26, 1108.
2. Zhong, Q. M.; Bonakdarpour, A.; Zhang, M. J.; Gao, Y.; Dahn, J. R. *J. Electrochem. Soc.* 1997, 144, 205.
3. Amine, K.; Tukamoto, H.; Yasuda, H.; Fujita, Y. *J. Electrochem. Soc.* 1996, 143, 1607.
4. Whittingham, M. S. *Chem. Rev.* 2004, 104, 4271.
5. Guilmard, M.; Croguennec, L.; Denux, D.; Delmas, C. *Chem. Mater.* 2003, 15, 4476.
6. Guilmard, M.; Croguennec, L.; Delmas, C. *Chem. Mater.* 2003, 15, 4484.
7. Choi, S.; Manthiram, A. *J. Electrochem. Soc.* 2002, 149, A1157.
8. Kurihara, L. K.; Suib, S. L. *Chem. Mater.* 1993, 5, 609.
9. Ohzuku, T.; Ariyoshi, K.; Takeda, S.; Sakai, Y. *Electrochim. Acta* 2001, 46, 2327.
10. Ohzuku, T.; Takeda, S.; Iwanaga, M. *J. Power Sources* 1999, 81, 90.
11. Liu, J.; Manthiram, A. *J. Phys. Chem. C* 2009, 113, 15073. J.H. Karchmer, “Analytical Chemistry of Sulfur and its Compounds, Part 1”, Wiley-Interscience, 1970.
12. Jo, M.; Hong, Y. S.; Choo, J.; Cho, J. *J. Electrochem. Soc.* 2009, 156, A430.
13. Wu, S. L.; Zhang, W.; Song, X.; Shukla, A. K.; Liu, G.; Battaglia, V.; Srinivasan, V. *J. Electrochem. Soc.* 2012, 159, A438.

V.E.4. NMR and Pulse Field Gradient Studies of SEI and Electrode Structure (University of Cambridge)

Clare Grey, Principal Investigator

University of Cambridge
Department of Chemistry
Lensfield Road
Cambridge, CB2 1EW
Phone: +44(1223)336509; Fax: +44(1223)336362
E-mail: cpg27@cam.ac.uk

Tien Q. Duong, DOE Program Manager

U.S. Department of Energy
Advanced Battery Materials Research (BMR)
Vehicle Technologies Office
1000 Independence Avenue, SW
Washington, DC 20585
Phone: 202-586-7836
E-mail: Tien.Duong@ee.doe.gov

Start Date: January 2013
Projected End Date: December 2016

Abstract

Objectives

- Identify major solid electrolyte interphase (SEI) components, their spatial proximity, and how they change with cycling.
- Explore how additives modify the SEI.
- Develop new nuclear magnetic resonance (NMR)-based methods for identifying different components in the SEI and their spatial proximities within the SEI, which will be broadly applicable to the study of SEI formation on a much wider range of electrodes.
- Use *in situ* NMR/magnetic resonance imaging (MRI) metrologies to investigate Li and Na dendrite formation and the role that additives and various electrolytes play in controlling Li/Na morphology.
- Compare Na and Li metal anodes.
- Develop methods for the determination of local structure in Na anode and cathode materials.

Accomplishments

- Completed SEI study of Si nanoparticles by NMR spectroscopy
 - Identified organics in SEI on Si electrodes.
 - Established mechanism for capacity loss in Si as a function of cycle number.
- Developed a new design of a NMR probe for real-time investigation of Li- and Na-ion batteries with *in situ* NMR spectroscopy using an Automatic Tuning Matching Cyclor (ATMC).
- Observed transition from mossy to dendritic Li growth via MRI
 - Verified Sand's time model for Li dendrite formation based on concentration gradient of ions in electrolyte.
 - Observed dendrite formation before Sand's time.
- Identified the species present after reduction of electrolyte additives, fluoroethylene carbonate (FEC) and vinylene carbonate (VC).

- Characterized electrolyte decomposition products and effect of iodide redox mediators in Li air battery.
- Characterized new Na electrode materials
 - Determined the role of Mg-doping in high rate P2-Na_{2/3}Mn_{1-y}Mg_yO₂ Na-ion battery cathodes.

Future Achievements

- Determine the effect of voltage and additives (e.g. FEC) on the composition of the Si SEI. Synthesize ¹³C-enriched FEC.
- Synthesize and test new inorganic coatings to increase the Coulombic efficiency seen on cycling SEI.
- Identify correlations between SEI structure and thickness and Li metal dendrite formation.
- Determine the short- and long-range structures formed on cycling Na and Li anode materials, focusing on Sn and hard carbons.

Technical Discussion

Background

The ability to cycle a battery for the multiple cycles required for transportation applications requires that a SEI is formed on the electrodes of a lithium-ion battery. Without such a stable SEI, breakdown of the electrolyte continues unhindered, removing electrolyte (and Li) from the cell, and results in increased resistance of the cell. Stable SEI formation on the anode is critical, because a battery operates outside the stability of the electrolyte (below approx. 1.3 - 0.8 V vs. Li). Although electrolytes have been optimized to form a stable SEI on graphite, the commercial anode material, the push to utilize very high energy density anodes such as Si, Sn and Li metal results in new and significant challenges. For example, lithiation of Sn and Si involves significant volume expansion (e.g. 300% for Si), due to the large volume occupied by the lithium in the Li_xSi and Li_xSn alloys. Cracks develop, exposing fresh surface for SEI formation. Practically, this means that the composite phase that makes up the SEI must be flexible and able to accommodate these expansions and contractions. Risk reduction strategies exploited to develop commercial Si/Sn-based anodes generally involve mixing graphitic carbon with Si/Sn, to make use of reversible capacity from both graphite and Si/Sn. In practice, this actually accentuates the SEI problem because the electrode must be cycled to low potentials so as to access the full graphite capacity. This results in even more severe SEI formation, either due to the formation of more heavily reduced Li_xM species (e.g. Li_{15+x}Si₄) or due to more severe volume expansion, which may result in the exposure of fresh surface. Strategies for SEI stabilization have been proposed but without a detailed understanding of SEI structure and composition a rational path forward is not obvious.

In principle, Li metal is a promising anode material due to its exceptionally high energy density, with a specific capacity > 3800 mAh g⁻¹. Much effort has been made to use metallic Li anodes in rechargeable lithium-ion batteries and its use is fundamental to the high energy densities quoted for Li-air and Li-sulfur battery technologies. However, the practical application of Li metal to rechargeable batteries has been prevented due to serious drawbacks associated with morphological change of the Li metal following continuous stripping and plating. In particular, dendrite growth causes severe safety concerns and eventual cell failure. Continual SEI formation on the Li microstructures consumes Li⁺. Furthermore, the nature and thickness of the SEI appears to affect the mechanism of microstructure formation on the Li metal anode. Thus, it is important to understand the nature of the SEI that forms on Li and to determine how this affects dendrite formation.

In addition, Na-ion batteries are an attractive option for low-cost and environmentally benign energy-storage technologies. While a number of Na cathode materials have now been identified,^[1,2] hard carbons represent the best materials identified to date as anode materials^[3,4] since graphite shows almost no ability to store Na electrochemically. Extremely high capacity is also observed for Sn-based materials, but they suffer from capacity fade, in part due to uncontrolled SEI formation. Furthermore, the composition of the SEI that forms on these anodes is poorly understood. Na-ion batteries are a more sustainable alternative to the existing lithium-ion technology and could alleviate some of the stress on the global Li market as a result of the growing electric car and portable electronics industries.

Fundamental research focused on understanding the structural and electronic processes occurring on electrochemical cycling is key to devising rechargeable batteries with improved performance.

Introduction

This report describes four studies, the first on the SEI that forms on Si. The major technique used in this work is NMR and our surface (SEI) studies are complemented by studies that focus on elucidating the short range changes that occur within the electrodes themselves. Chemical reduction of fluoroethylene carbonate (FEC) and vinylene carbonate (VC) are then studied so as to provide spectral fingerprints and insights into the decomposition products that may form on cycling in lithium-ion batteries.

In situ MRI studies of lithium-ion dendrites are then investigated linking dendrite formation with Li^+ concentration in the electrolyte. Finally, the extension of our NMR methods to Na electrodes is investigated.

Approach

Perform multinuclear NMR, IR and X-ray photoelectron spectroscopy (XPS) of SEI composition. NMR and MRI studies of dendrite formation. ^{23}Na *in situ* and *ex situ* NMR studies of Na battery materials.

Results

We have completed a detailed investigation of the SEI passivating layer that grows on Si nanoparticles, employing multinuclear ^1H , ^7Li , ^{19}F and ^{13}C NMR solid state NMR (ssNMR) spectroscopy. A binder-free Si electrode (with 50 nm particles) was used in the first study so as to remove the variable of common binders such as carboxymethylcellulose (CMC) often used in electrode formulation, which may also inhibit SEI growth, and to simplify the NMR analysis. Both the conductive carbon and mixed Si/C composite electrodes were studied separately. SEI growth was observed by ^1H ssNMR as a function of voltage, with electrochemical experiments demonstrating SEI forming on both C and Si surfaces. One consequence of the long lithiation process on Si at approximately 150 mV vs. Li is that substantial SEI is formed below this voltage. Using selective ^{13}C labelling, the decomposition products of electrolyte solvents ethylene carbonate (EC) and dimethyl carbonate (DMC) were detected independently (Figure V-135). ^1H - ^{13}C and ^7Li - ^{13}C cross-polarization (CP) experiments were performed to identify species close to protons and Li ions, respectively. To aid our assignments of the ^{13}C spectra, chemical shifts of predicted SEI decomposition products were determined. The density functional theory (DFT) calculations of relevant small molecules provided useful trends regarding the chemical shifts, guiding the low sensitivity experiments and assignments.

EC decomposition products are present in higher concentrations and are dominated by PEO-type oligomer species. ssNMR applied to both rinsed and unrinsed electrodes show that the organics are easily rinsed away, suggesting they are located on the outer layer of the SEI. A CH_3R or $\text{R}'\text{CH}_2\text{R}$ environment was formed below 40 mV; while many oligomeric species cannot be ruled out, the experimental results are consistent with an assignment of these carbon functionalities to those present in the theoretically predicted SEI decomposition products, lithium butylene dicarbonate (LBDC) and lithium ethyl carbonate (LEC). RCO_2Li species in low relative abundance were also detected, the majority being assigned to HCO_2Li . ROCO_2Li EC decomposition products were confirmed by correlation (two dimensional NMR) experiments, showing a chemical signature consistent with lithium ethylene dicarbonate (LEDC). Lithium methyl carbonate (LMC) was the dominant DMC decomposition product. The binder-free system resulted in a very dry electrode system and LiOH was detected. Furthermore, LiF and LiPF_6 were the only F-containing species. The results of this comprehensive NMR study have been used to analyze the NMR spectra of electrodes acquired after multiple cycles.

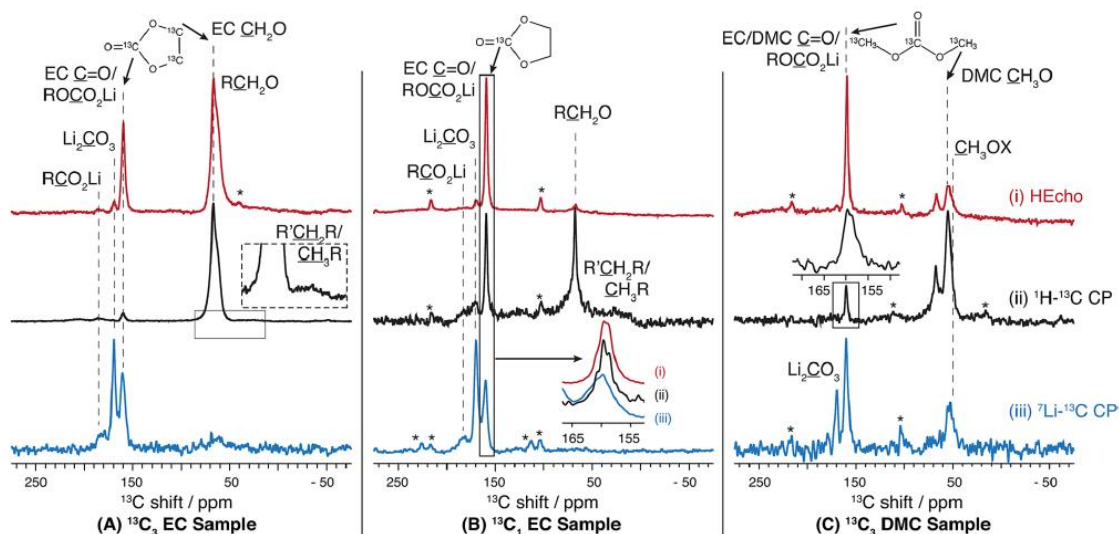


Figure V-135: Coin cells cycled using (A) $^{13}\text{C}_3$ EC (B) $^{13}\text{C}_1$ EC and (C) $^{13}\text{C}_3$ DMC labelled electrolytes. ^{13}C spectra were acquired with (i) a Hahn echo (HEcho) (ii) ^1H - ^{13}C CP and (iii) ^7Li - ^{13}C CP

SEI Growth and Capacity Loss in Si Electrodes

Following the work on binder-free Si/C electrodes described above, we have now performed extended cycling studies of Si/C/CMC electrodes (Figure V-136) that show their capacity dropping steadily with cycling. The growth of the SEI was monitored by using ^7Li , ^{19}F and ^{13}C -enriched EC and DMC, with the organics dominating the SEI. LiF formation was primarily seen in the 1st cycle, the solid organic phases growing noticeably in concentration between cycles 1 and 30 (Figure V-137).

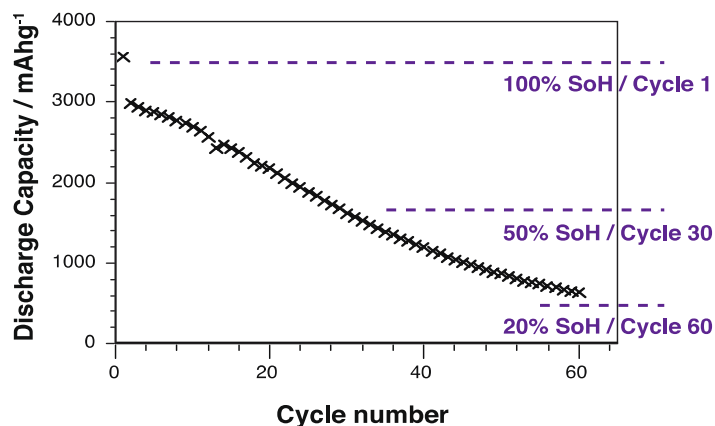


Figure V-136: Discharge capacity of Si as a function of cycle number

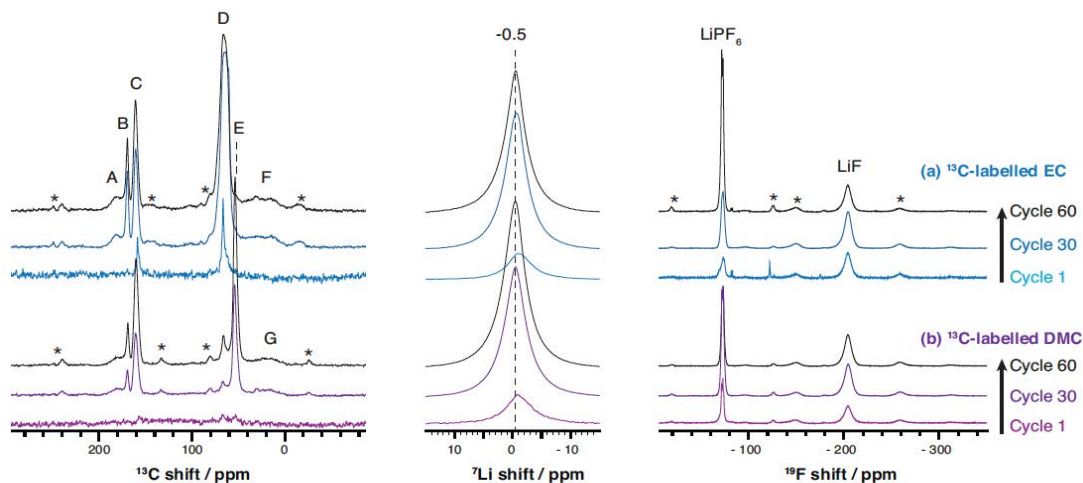


Figure V-137: ^{13}C , ^7Li and ^{19}F NMR of electrode samples prepared with ^{13}C (a) EC (blue) and (b) DMC (purple) labeled electrolytes following cycling

Homonuclear ^{13}C NMR correlation experiments were used to identify the organic fragments in the sample extracted after 30 cycles, and in particular identify components involving more extensive radical reactions to form molecules such as LBDC and LEC (giving rise to peaks such as F in Figure V-137). No significant growth of solid organic SEI components was observed between 30 and 60 cycles, with SEI formation correlating with increasing electrode tortuosity as observed with focused-ion beam and scanning electron microscopy. A 2-stage model for lithiation capacity loss was developed (Figure V-138): initially, the lithiation capacity steadily decreases, and parasitic reactions and pronounced SEI growth are seen. Later, below 50% of the initial lithiation capacity, less Si is (de)lithiated resulting in less volume expansion and contraction; the rate of parasitic reactions declines, and the Si SEI thickness stabilizes. The decreasing discharge capacity is primarily attributed to kinetics, with the increased electrode tortuosity severely limiting Li^+ ion diffusion through the bulk of the electrode. The resulting restricted diffusion is consistent with the changes in the lithiation processes seen in the electrochemical capacity curves.

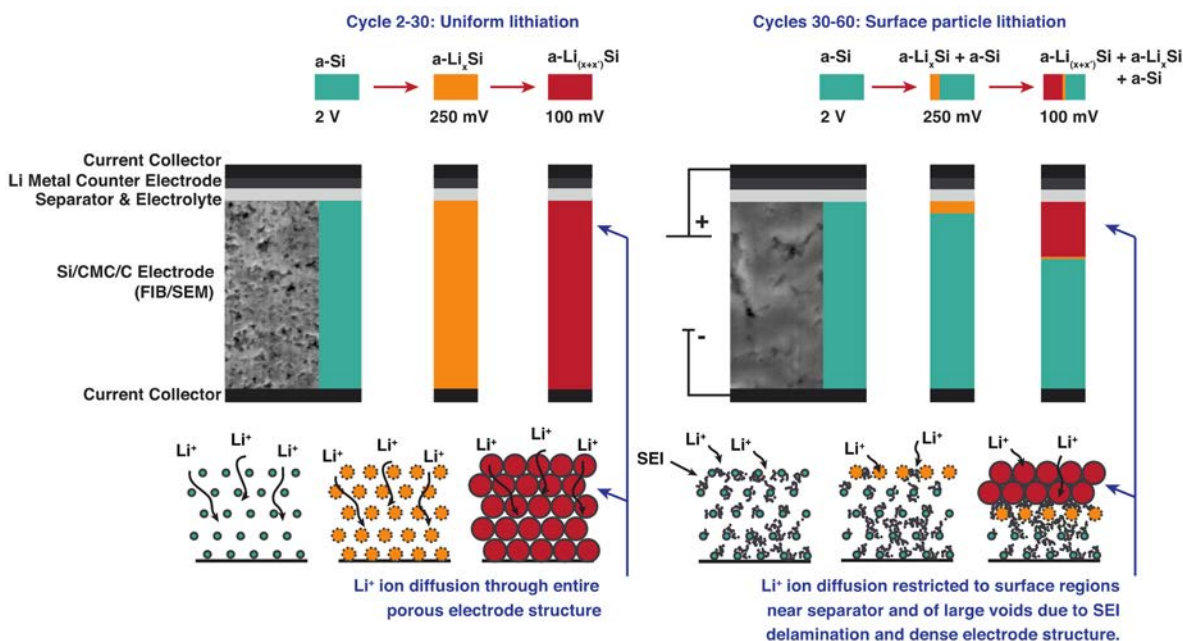


Figure V-138: Schematic showing microscale processes: electrode pore structure becomes more dense with cycling, restricting Li^+ diffusion to surface regions near the separator and to surface regions of large pores. The FIB/SEM electrode cross sections show the increasing density of the electrode pore structure

Understanding the Role of FEC and VC additives in SEI Formation

In collaboration with Prof. B. Lucht (U. Rhode Island), we have directly synthesized the reduction products of fluoroethylene carbonate (FEC) and vinylene carbonate (VC) via lithium naphthalene reduction in order to (a) identify which products are formed and (b) provide spectral fingerprints of these species, which can then be used to search for/identify similar products in the SEI formed in the presence of these additives. (Deuterated lithium naphthalene was used so as to separate the decomposition products from the reductant in the ^1H - ^{13}C CP ssNMR experiments).

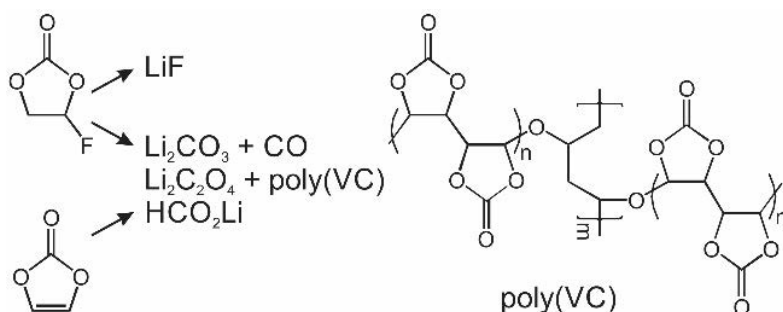


Figure V-139: Proposed FEC/VC reduction products and possible structure for crosslinking site of poly(VC)

Analysis of the resulting solid precipitates formed from both VC and FEC and gas evolution with multinuclear ssNMR, XPS, Fourier transform infrared spectroscopy (FTIR), and gas chromatography mass spectrometry (GC-MS) reveals that both FEC and VC decomposition products include HCO_2Li , $\text{Li}_2\text{C}_2\text{O}_4$, Li_2CO_3 , and polymerized VC (Figure V-139), albeit in different relative quantities. For example, in the case of VC reduction (Figure V-140 (b), (d) and (f)), greater quantities of Li_2CO_3 , $\text{Li}_2\text{C}_2\text{O}_4$, HCO_2Li were seen compared to FEC reduction (Figure V-140 (a), (c) and (e)) in both ssNMR and XPS. The data were consistent with prior work which proposed a possible reaction mechanism to form poly(VC) from both VC and FEC.^[5]

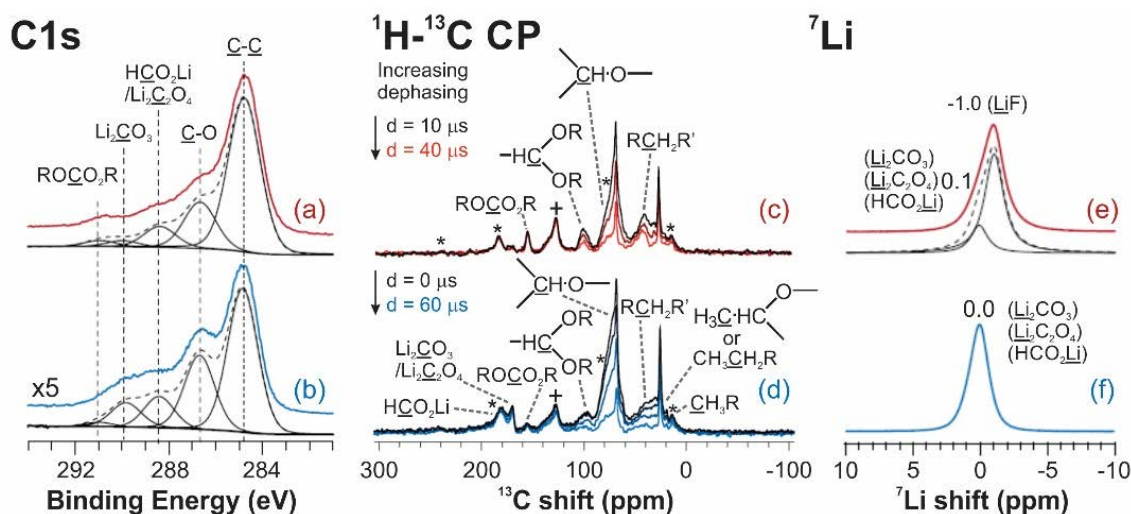


Figure V-140: $\text{C}1\text{s}$ XPS spectra (a, b), ^1H - ^{13}C CP dipolar dephasing ssNMR (c, d, MAS = 10 kHz), and ^7Li single pulse ssNMR (e, f, MAS = 60 kHz) of FEC (red) and VC (blue) precipitates obtained after reduction with deuterated naphthalene. In c and d, asterisks indicate spinning sidebands and crosses represent deuterated naphthalene

For FEC, the experimental data supports a reduction mechanism where FEC reduces to form VC and LiF, followed by subsequent VC reduction and polymerization. In the FEC reduction product, HCO_2Li , $\text{Li}_2\text{C}_2\text{O}_4$, and Li_2CO_3 were found in smaller quantities than in the VC reduction product, with no additional fluorine environments, other than LiF, detected by ^{19}F ssNMR or F1s XPS (Figure V-141). This is contrary to previous reports where fluorinated organic products are proposed.

FEC and VC are used in higher (FEC) and lower (VC) concentrations in the base electrolytes of lithium-ion batteries. Our findings suggest that the different relative ratios of the inorganic and organic reduction products

formed by their decomposition are relevant to the chemical composition and morphology of the SEI formed in their presence and likely impact Li^+ transport in systems containing FEC and VC additives. Experiments are now in progress to compare these reduction products with those found in the SEIs formed in Si anodes with FEC additives.

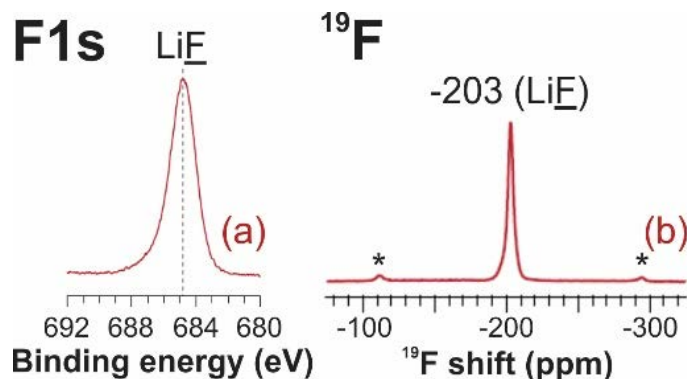


Figure V-141: F1s XPS spectrum (a) and ^{19}F Hahn echo ssNMR (b) of FEC precipitates after reduction with deuterated naphthalene

Using ^7Li MRI to Understand Microstructural Li Metal Growth

Li dendrite growth in lithium-ion and Li rechargeable batteries is associated with severe safety concerns. To overcome these problems, a fundamental understanding of the growth mechanism of dendrites under working conditions is needed. We have used *in situ* ^7Li MRI on both the electrolyte and Li metal electrodes in symmetric Li cells, allowing the behavior of the electrolyte concentration gradient to be studied and correlated with the type and rate of microstructure growth on the Li metal electrode. A standard EC/DMC/ LiPF_6 electrolyte was used. Chemical shift (CS) imaging was used because we have shown that it we can resolve different types of Li microstructures, with the mossy types of microstructure growing close to the surface of the anode from the beginning of charge in every cell studied, from high to low currents, while dendritic growth is triggered much later (Figure V-142).

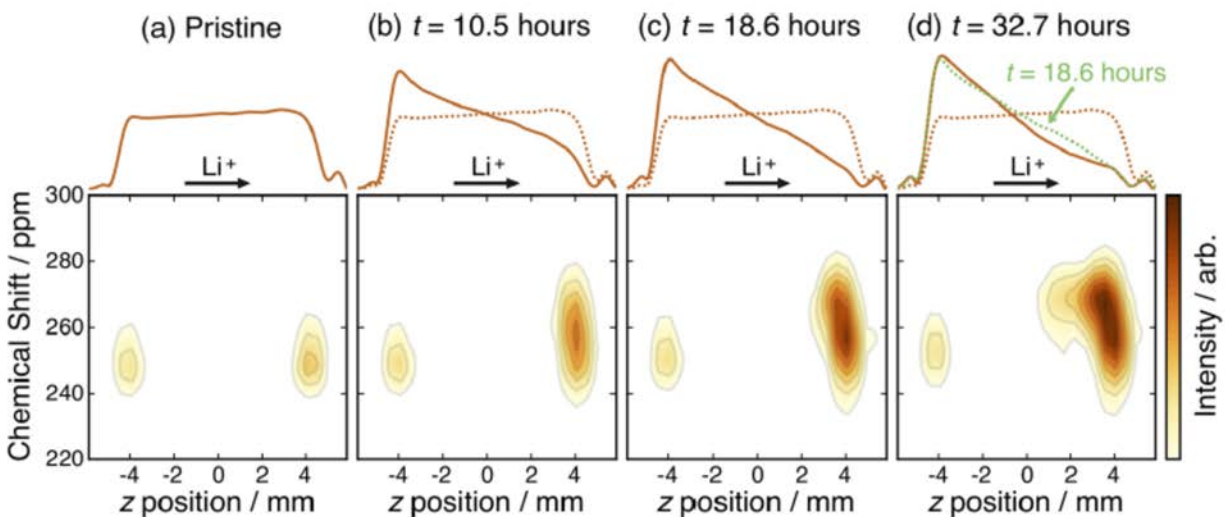


Figure V-142: MRI time series showing the evolution of the ^7Li electrolyte concentration profile (top) and the ^7Li chemical shift image of the metal (bottom) for the cell charged at 0.76 mA cm^{-2} . The two Li metal electrodes are located at z-positions of approximately, $\pm 4 \text{ mm}$. The intensity increase on the right hand side (RHS) electrode, seen on passing current indicates the growth of Li microstructure. The onset of dendrite formation is seen in (c) (18.6 hours)

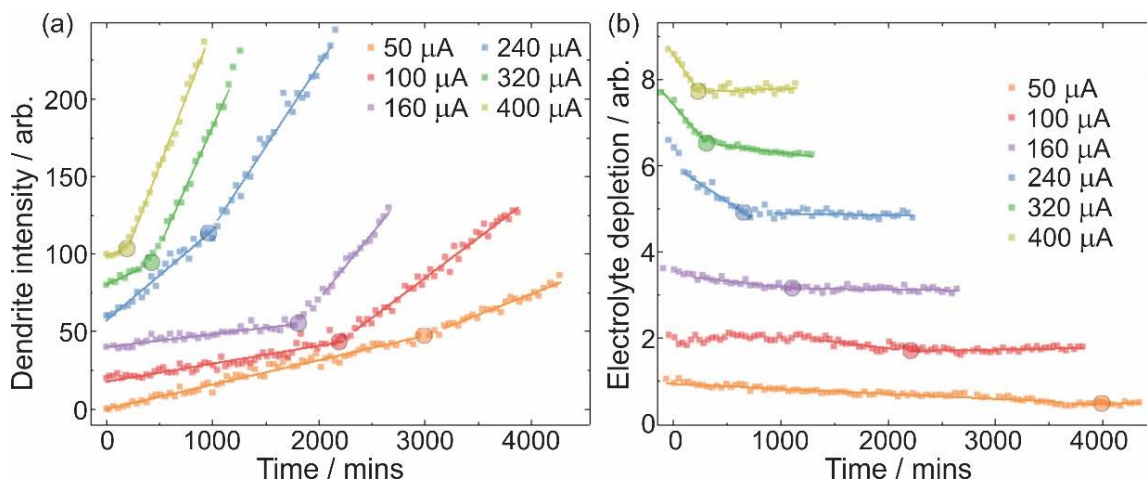


Figure V-143: (a) Dendrite intensity and (b) electrolyte depletion near the RHS Li electrode as a function of current (for 0.31 cm^{-1} electrodes). Arbitrary offsets have been applied to the data in the y direction

Simple metrics have been developed to interpret the MRI data sets and compare results from a series of cells charged at different current densities (Figure V-143). The results show that at high charge rates, there is a strong correlation between the onset time of dendrite growth and the local depletion of the electrolyte at the surface of the electrode observed both experimentally and predicted theoretically (via the Sand's time model) (Figure V-144). A separate mechanism of dendrite growth is observed at low currents, which is not governed by salt depletion in the bulk liquid electrolyte. Experiments are in progress to correlate the onset of dendrite formation with SEI formation.

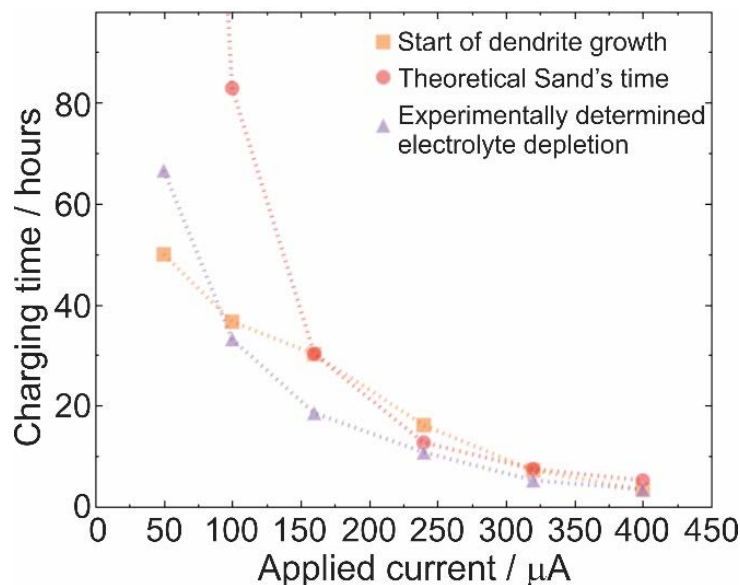


Figure V-144: Comparison between the Sand's time and onset of dendrite formation/electrolyte depletion

^{23}Na NMR studies of Na microstructures

Parallel *in situ* ^{23}Na NMR studies have been performed on the Na dendrites that form on Na metal anodes. Quantification of the NMR signal indicates that Na metal deposits with a morphology associated with an extremely high surface area, the deposits continually accumulating, even in the case of galvanostatic cycling at low currents. Two regimes for the electrochemical cycling of Na metal are seen that have implications for the use of Na anodes: at low currents (0.5 mA cm^{-2}), the Na deposits are partially removed on reversing the current, while at high currents (1 and 2 mA cm^{-2}) there is essentially no removal of the deposits in the initial stages. At longer times, high currents show a significantly greater accumulation of deposits during cycling, again indicating a much lower efficiency of removal of these structures when the current is reversed. Analysis

of the current–time transients performed in a separate experiment were interpreted in terms of a change in the mechanism of nucleation from a progressive (time dependent) nucleation mechanism at the overpotentials observed for the lower current density of 0.5 mA cm^{-2} to instantaneous at higher currents. We proposed that the different and fewer microstructures that are formed at lower currents are more readily removed on cycling. Unfortunately, despite differences in the nucleation and growth process, both mechanisms yield microstructures that continue to grow as cycling progresses.

^{23}Na NMR studies of layered sodium cathode materials

We have investigated a series of different layered Na cathode materials, focusing on questions such how does cation substitution of nominally inert ions such as Mg and Li affect the structural transformations that occur at high voltages (when most of the Na-ions are removed), and differences in Na-mobility in these phases. An in-depth investigation of the effect of Mg doping on the electrochemical performance and structural stability of $\text{Na}_{2/3}\text{MnO}_2$ with a P2 layer stacking was performed by comparing three compositions: $\text{Na}_{2/3}\text{Mn}_{1-y}\text{Mg}_y\text{O}_2$ ($y = 0.0, 0.05, 0.1$). Mg substitution leads to smoother electrochemistry, with fewer distinct electrochemical processes, improved rate performance and better capacity retention (Figure V-145). These observations were attributed to the more gradual structural changes upon charge and discharge, as observed with synchrotron, powder X-ray, and neutron diffraction. Mg doping reduces the number of Mn^{3+} Jahn-Teller centers and delays the high voltage phase transition occurring in P2- $\text{Na}_{2/3}\text{MnO}_2$. The local structure was investigated using ^{23}Na ssNMR spectroscopy. The ssNMR data provides direct evidence for fewer oxygen layer shearing events, leading to a stabilized P2 phase, and an enhanced Na^+ ion mobility up to 3.8 V vs. Na^+/Na upon Mg doping. By comparing the ^{23}Na NMR spectra of the $x = 0, 0.05$ and 0.1 phases (Figure V-146), it is clear that much less complex spectra with fewer resonances are observed on Mg substitution. The $x = 0.1$ sample, for example, contains only a single resonance for Na contents of between 0.67 and 0.4, consistent with rapid mobility in between the layers. A weak signal centered at around 1100 ppm forms (highlighted with a blue box) due to the OP4 phase, a phase containing alternating octahedral and prismatic environments for Na in the Na-metal layers. The relative concentration of this phase (which is formed by layer shearing) decreases with increasing Mg content. The 5% Mg-doped phase exhibits one of the best rate performances reported to date for Na-ion cathodes with a P2 structure, with a reversible capacity of 106 mAh g^{-1} at the very high discharge rate of 5000 mA g^{-1} . In addition, its structure is highly reversible and stable cycling is obtained between 1.5 and 4.0 V vs. Na^+/Na , with a capacity of approximately 140 mAh g^{-1} retained after 50 cycles at a rate of 1000 mA g^{-1} .

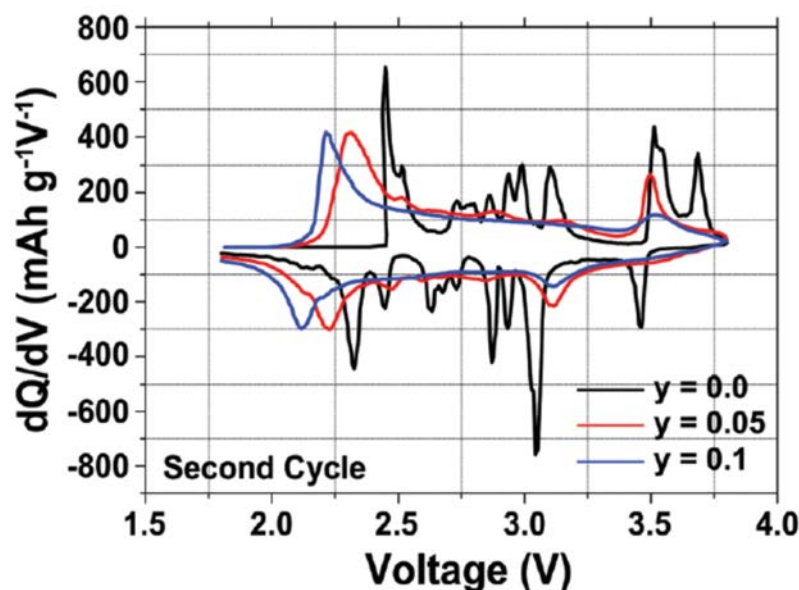


Figure V-145: Differential capacity vs. voltage plots of the $\text{Na}_{2/3}\text{Mn}_{1-y}\text{Mg}_y\text{O}_2$ ($y = 0.0, 0.05, 0.1$) compositions

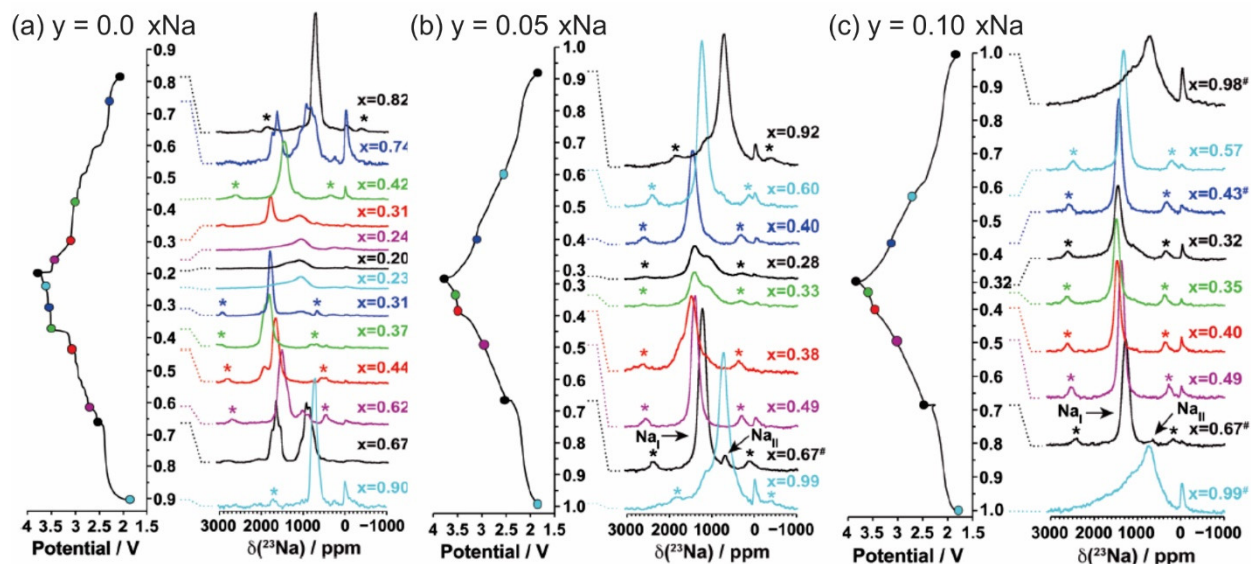


Figure V-146: *Ex situ* ^{23}Na MAS ssNMR spectra collected on cells stopped at different points along the first electrochemical charge/discharge cycle of $\text{Na}_{2/3}\text{Mn}_{1-y}\text{Mg}_y\text{O}_2$, where $y = 0.0, 0.05, 0.1$ for (a), (b), and (c), respectively. Spectra are scaled according to the number of scans collected during the experiment, the amount of sample in the rotor, and the NMR signal decay obtained from T_2 relaxation time measurements. Hashes indicate samples for which a lack of experimental data prevent proper scaling of the spectrum. Asterisks indicate spinning sidebands

Conclusions

In the first project, we provided an in-depth multinuclear NMR study of the chemical composition of the SEI on Si/C electrodes in the absence of binder. By employing selective ^{13}C labelling of both electrolyte solvents, EC and DMC, specific organic and Li-containing species of the SEI were identified and determined to originate from individual solvents. These findings provide the clarity necessary to correlate discrete electrolyte components with the resulting species present in the SEI - insight that is important to understanding the relationship between electrolyte composition and SEI structure, stability, and morphology.

Following up on the first study, we also provided a detailed characterization of SEI growth on Si/C electrodes in the presence of binder (CMC). Organic decomposition products dominated the SEI and grew substantially between cycles 1-30. Interestingly, little to no growth of solid organic SEI species was observed between cycles 30-60, yet decreases in capacity were continually observed. We discovered that the additional depletion in capacity could be attributed to increased electrode tortuosity and subsequently developed a 2-stage model for lithiation capacity loss. In the first stage, lithiation capacity decreases and is associated with parasitic reactions and pronounced SEI growth. In the second stage, less Si is (de)lithiated, allowing conditions for SEI thickness to stabilize. After this point, decreasing discharge capacity was primarily attributed to kinetics, with increased electrode tortuosity severely limiting lithium ion diffusion through the bulk of the electrode.

Finally, to better understand how additives influence SEI composition and stability, the reduction products of FEC and VC were directly synthesized via chemical reduction with Li naphthalene. Here, we identified and quantified the relative ratios of semicarbonates and polymers that form when FEC and VC are reduced. This work provides spectral fingerprints of relevant species that may be found in the SEI when FEC and VC are employed as additives in electrolytes. These spectral features can aid in identifying interfacial species formed in the presence of additives and their influence on SEI stability and Li transport.

In the second project on Li metal anodes, we used *in situ* ^7Li MRI to understand the chemical processes underpinning dendrite formation in Li metal anodes. We found that at high charge rates there is a strong correlation between the onset time of dendrite growth and local depletion of the electrolyte at the surface of the electrode, consistent with theoretical models that describe electrochemical dendrite growth (the Sand's time model). Conversely, deviation from theoretical predictions is observed at low currents, suggesting alternative

mechanisms as a function of current. Work to understand the relationship between SEI and the onset of dendrite growth is ongoing in our laboratory.

Finally, a series of ^{23}Na NMR experiments have been performed to characterize both the anodes and cathodes of Na-ion batteries. Na dendrite formation appears to be more severe for Na metal anodes in comparison to Li metal anodes, significant dendrite/microstructure formation occurring at low current densities, as probed by *in situ* NMR experiments. However, the microstructures that form at low currents can be partially removed on reversing the current, which is not the case for the dendrites formed at higher currents. Differences in the mechanisms of nucleation of dendrites may account for some of these differences. In addition, ^{23}Na NMR was shown to be a highly useful tool to investigate local structure and Na-ion dynamics in Na cathode materials. A high rate material was identified $\text{Na}_{2/3}\text{Mn}_{1-y}\text{Mg}_y\text{O}_2$ ($y = 0.5$), which maintains a moderately high capacity (106 mAh g^{-1}) even at high rates of 5000 mA g^{-1} .

Products

Presentations/Publications/Patents

1. Clément, R. J.; Bruce, P. G.; Grey, C. P. "Review-Manganese-Based P2-Type Transition Metal Oxides as Sodium-Ion Battery Cathode Materials" *J. Electrochem. Soc.*, **2015**, *162*, A2589.
2. Liu, T.; Leskes, M.; Yu, W. J.; Moore, A. J.; Zhou, L. N.; Bayley, P. M.; Kim, G.; Grey, C. P. "Cycling Li-O₂ batteries via LiOH formation and decomposition" *Science*, **2015**, *350*, 530.
3. Chang, H. J.; Ilott, A. J.; Trease, N. M.; Mohammadi, M.; Jerschow, A.; Grey, C. P. "Correlating Microstructural Lithium Metal Growth with Electrolyte Salt Depletion in Lithium Batteries Using Li-7 MRI" *J. Am. Chem. Soc.*, **2015**, *137*, 15209.
4. Michan, A. L.; Leskes, M.; Grey, C. P. "Voltage Dependent Solid Electrolyte Interphase Formation in Silicon Electrodes: Monitoring the Formation of Organic Decomposition Products" *Chem. Mater.*, **2016**, *28*, 85.
5. Bayley, P. M.; Trease, N. M.; Grey, C. P. "Insights into Electrochemical Sodium Metal Deposition as Probed with *in situ* ^{23}Na NMR" *J. Am. Chem. Soc.*, **2016**, *138*, 1955.
6. Michan, A. L.; Divitini, G.; Pell, A. J.; Leskes, M.; Ducati, C.; Grey, C. P. "Solid Electrolyte Interphase Growth and Capacity Loss in Silicon Electrodes." *J. Am. Chem. Soc.*, **2016**, *138*, 7918.
7. Pecher, O.; Bayley, P. M.; Liu, H.; Liu, Z.; Trease, N. M.; Grey, C. P. "Automatic Tuning Matching Cycler (ATMC) *in situ* NMR spectroscopy as a novel approach for real-time investigations of Li- and Na-ion batteries" *J. Mag. Reson.*, **2016**, *265*, 200.
8. Clément, R. J.; Billaud, J.; Armstrong, A. R.; Singh, G.; Rojo, T.; Bruce, P. G.; Grey, C. P. "Structurally stable Mg-doped P2- $\text{Na}_{2/3}\text{Mn}_{1-y}\text{Mg}_y\text{O}_2$ sodium-ion battery cathodes with high rate performance: insights from electrochemical, NMR and diffraction studies" *Energy Environ. Sci.*, **2016**, *9*, 3240.
9. Seymour, I. D.; Middlemiss, D. S.; Halat, D. M.; Trease, N. M.; Pell, A. J.; Grey, C.P. "Characterizing oxygen local environments in paramagnetic battery materials via O-17 NMR and DFT calculations" *J. Am. Chem. Soc.*, **2016**, *138*, 9405.
10. Ilott, A. J.; Mohammadi, M.; Chang, H. J.; Grey, C. P.; Jerschow, A. "Real-time 3D imaging of microstructure growth in battery cells using indirect MRI" *Proc. Nat. Ac. Sci. USA*, **2016**, *113*, 1077.
11. Michan, A. L.; Parimalam, B. S.; Leskes, M.; Kerber, R. N.; Yoon, T.; Grey, C. P.; Lucht, B. L. "Fluoroethylene carbonate and vinylene carbonate reduction: Understanding lithium-ion battery electrolyte additives and solid electrolyte interphase formation" *Chem. Mater.*, **2016**, Article ASAP, DOI: 10.1021/acs.chemmater.6b02282.
12. C. P. Grey, LMU Munich, talk to the Chemistry Department, January 2016.
13. C. P. Grey, 17th International Materials Engineering Conference (IMEC 17), Israel, February 2016.
14. C. P. Grey, International Battery Association Meeting, Nantes, March 2016.
15. C. P. Grey, Electrochemical Society Meeting, San Diego, May 2016.
16. C. P. Grey, NSF Ceramics Workshop, San Diego, May 2016.

17. C. P. Grey, IMLB, Chicago, June 2016.
18. C. P. Grey, Euromar, Aarhus, Denmark, July 2016.
19. C. P. Grey, Smarter Conference, Bayreuth, September 2016.
20. C. P. Grey, Challenges and Prospects for Solid State Chemistry, Seville, September 2016.

References

1. Yabuuchi, N.; Kubota, K.; Dahbi, M.; Komaba, S. *Chem. Rev.*, **2014**, *114*, 11636.
2. Clément, R. J.; Bruce, P. G.; Grey, C. P. *J. Electrochem. Soc.*, **2015**, *162*, A2589.
3. Stevens D. A.; Dahn, J. R. *J. Electrochem. Soc.*, **2000**, *147*, 1271.
4. Irisarri, E.; Ponrouch A.; Palacin, M. R. *J. Electrochem. Soc.*, **2015**, *162*, A2476.
5. Zhang, B.; Metzger, M.; Solchenbach, S.; Payne, M.; Meini, S.; Gasteiger, H. A.; Garsuch, A.; Lucht, B. L. *J. Phys. Chem. C*, **2015**, *119*, 11337.

V.E.5. Optimization of Ion Transport in High-Energy Composite Electrodes (University of California, San Diego)

Ying Shirley Meng, Principal Investigator

University of California San Diego
9500 Gilman Drive
La Jolla, CA 92093
Phone: 858-822-4247; Fax: 858-534-9553
E-mail: shmeng@ucsd.edu

Tien Q. Duong, DOE Program Manager

U.S. Department of Energy
Advanced Battery Materials Research (BMR)
Vehicle Technologies Office
1000 Independence Avenue, SW
Washington, DC 20585
Phone: 202-586-7836
E-mail: Tien.Duong@ee.doe.gov

Start Date: April 2013
End Date: March 2017

Abstract

Objectives

This project aims to probe and control the atomic-level kinetic processes that govern the performance limitations in terms of rate capability and voltage stability in high-energy composite electrodes. Using a suite of powerful analytical tools such as atomic resolution scanning transmission electron microscopy (a-STEM) & electron energy loss spectroscopy (EELS), neutron, soft X-ray adsorption spectroscopy (XAS), X-ray photoelectron spectroscopy (XPS), and first principles (FP) computation will elucidate approaches to optimize ion transport. Ultimately, this will hone in on the optimum bulk compositions and surface characteristics to improve the mechanistic rate and cycling performance of high-energy composite electrodes. Moreover, it aims to develop the large-scale synthesis efforts in order to produce materials with consistent performance. The surface-sensitive characterization tools will be extended to diagnose various silicon anode types.

Accomplishments

- Established *operando* neutron diffraction technique to observe lattice oxygen evolution in Li-rich layered oxides.
- Established a suite of surface and interface characterization tools, such as soft XAS and XPS, probing the surface oxygen activities of Li-rich layered oxides.
- Obtained the optimum nanoscale uniform crystalline LLTO surface coating in Li-rich layered oxides when charged up to 4.8 V.
- Investigated the effect of SEI morphology on electrochemical performance of Si nanocomposite by using STEM/EELS and XPS.
- Established a nano-size probe electron diffraction (NEBD) to measure the strain evolution of Si upon cycling.

Future Achievements

- Bulk substitution/doping effect on preventing oxygen vacancies formation in Li-rich layered oxides.

- Investigation of continuous effect of nanoscale uniform crystalline LLTO surface coating on Li-rich layered oxides during long-term cycling.
- Establish ALD surface modification method to improve the cyclability of Si.
- Probing the surface and interface of ALD coated Si using STEM/EELS and XPS techniques.

Technical Discussion

Background

Li-rich layered oxides, either as a solid solution or as a nano-composite of layered Li_2MnO_3 and Li(TM)O_2 (TM=Ni, Co, Mn), draw significant attention as the next-generation cathode materials for high-energy-density lithium-ion batteries in electric vehicles (EVs) [1, 2]. While the research has continued to push the limit of the available capacity of the materials throughout the years, these composites suffer from poor rate capabilities and a limited cycle life. When the material is charged over transition metal redox reaction region (above 4.4 V for most of Li-rich material), lattice oxygen removal result in oxygen vacancies formation on the surface, which further triggers surface phase transformation from layered to spinel-like phase [3, 4]. This irreversible phase transformation finally results in voltage degradation and lower Li mobility during extended cycles. This work will provide a fundamental understanding of oxygen anions electrochemical activity in the class of high energy density cathode material for lithium-ion batteries. Moreover, the studies on oxygen electrochemical activity will guide us on engineering of surface coatings and bulk material compositions to suppress oxygen gas generation and promote lithium ion transport of lithium-rich material.

Si anode is a promising candidate for next generation lithium-ion batteries because of high theoretical capacity, which is ten times higher than that of graphite anodes. However, Si electrodes suffer from rapid capacity fade during electrochemical cycling, which can be attributed to the large volume expansion (300%) and the formation of an unstable solid electrolyte interphase (SEI) layer. One way to prevent the large stress and strain that occurs from the volume expansion is to use Si nanoparticles with less than 150 nm in size. One of the more successful strategies for dealing with the capacity loss and continuous electrolyte decomposition on Si electrodes, has been the use of battery electrolyte additives such as fluoroethylene carbonate (FEC). It is found that FEC stabilizes SEI layer formation; therefore, improve the capacity retention of Si anode by altering the SEI chemistry and thickness. In this work the composition and interface structure of Si electrodes with FEC containing electrolyte and with the traditional electrolyte upon cycling will be compared [5-8].

Introduction

Recently, anionic activity, such as oxygen redox reaction, has been discovered in the electrochemical processes, providing extra reversible capacity for certain transition-metal (TM) oxides. When the material is charged over transition metal redox reaction region (above 4.4 V for most of Li-rich material), reversible oxygen redox process ($2\text{O}^{2-} \rightarrow \text{O}_2^{n-}$, where $n=1, 2, \text{ or } 3$) dominates in the bulk to compensate charge changes during delithiation. At the same time, the lattice oxygen removal in terms of O_2 gas, or LiO_2 , Li_2O_2 , Li_2O solids result in oxygen vacancies formation on the surface and subsurface (5-10nm range from the surface). A large fraction of the TM ions in these regions therefore are in under-coordinated octahedral sites which are not stable and spontaneously migrate to the fully-coordinated octahedral sites nearby in the Li layer. On the other hand, the Li in the TM layer migrates to the shared tetrahedral site in the opposite site, forming a Li-Li dumbbell. The above two migrations cause the spinel-like phase to create on the surface. This surface phase transformation from layered to spinel-like is irreversible upon the following cycles, accompanying the increased percentage of microstrain within the particles and finally results in voltage degradation and lower Li mobility during extended cycles. However, compared to TM cations, oxygen anions electrochemical activity is more challenging to be experimentally proved and quantified with a single characterization technique alone. Therefore, a multi-modal experimental approach (including neutron, soft XAS, XPS, STEM/EELS, FP computation) must be established for capturing oxygen activity. If successful, this research will provide a major breakthrough in commercial applications of the class of high energy density cathode material for lithium-ion batteries. Additionally, it will provide in-depth understanding of the role of surface modifications and bulk substitution in the high voltage composite materials. The diagnostic tools developed here can also be leveraged to study a wide variety of cathode and anode materials for rechargeable batteries.

Approach

The above mentioned objectives will be achieved by uniquely combining neutron diffraction, soft XAS, XPS, STEM/EELS, FP computation to elucidate the oxygen activity as well as dynamic changes of the bulk and surface structural in the complex oxide materials during electrochemical cycling. A systematic study with powerful analytical tools is necessary to guide us on engineering of surface coatings and bulk material compositions for high rate and long life cathode materials. Additionally, alternative synthesis methods will be explored to produce materials in large scale with consistently good performance. Finally, the developed advanced characterization tool will be extended to better understand the degradation mechanism of silicon anode to further improve the longevity of the material.

Combining several advanced characterization tools and synthesis techniques will be used to accomplish the objectives of this effort:

1. Identify the path-specific Li dynamics, lattice dynamics and lattice oxygen evolution in Li-rich layered oxides.
2. Identify the surface oxygen activities in Li-rich layered oxides via soft XAS and XPS.
3. Obtain the optimum surface coating and substitution compositions in lithium rich layered oxides when charged up to 4.8 V (or 5.0 V).
4. Identify the appropriate SEI characteristics and microstructure for improving first cycle irreversible capacity of silicon anode.
5. Identify the mechanisms of ALD and MLD coated silicon anode for their improved chemical stability upon long cycling.

Results

The following progress has been achieved:

Lattice dynamics and lattice oxygen evolution in Li-rich layered oxide during battery charge and discharge via *operando* neutron diffraction

Neutron diffraction was used to investigate the lattice dynamics and oxygen evolution of two distinct Li-rich materials, $\text{Li}[\text{Li}_{x/3}\text{Ni}_{(3/8-3x/8)}\text{Co}_{(1/4-x/4)}\text{Mn}_{(3/8+7x/24)}\text{O}_2$ ($x=0.6$, HLR) and $\text{Li}[\text{Li}_{x/3}\text{Ni}_{(1/3-x/3)}\text{Co}_{(1/3-x/3)}\text{Mn}_{(1/3+x/3)}\text{O}_2$ ($x=0.24$, LLR), respectively. These materials contain various degrees of oxygen activation at high voltage. The lattice parameter changes and oxygen position were measured by *operando* battery cycling, where the LLR exhibits larger oxygen movement and higher lattice contractions compared to the HLR. Figure V-147 (a) demonstrates that both HLR and LLR maintain relatively constant oxygen position during the high voltage plateau, until the end of charge. Moreover, the DFT calculations show that in the presence of oxygen vacancy during the high voltage plateau, the changes in the lattice parameters and oxygen positions are consistent with the experimental observations.

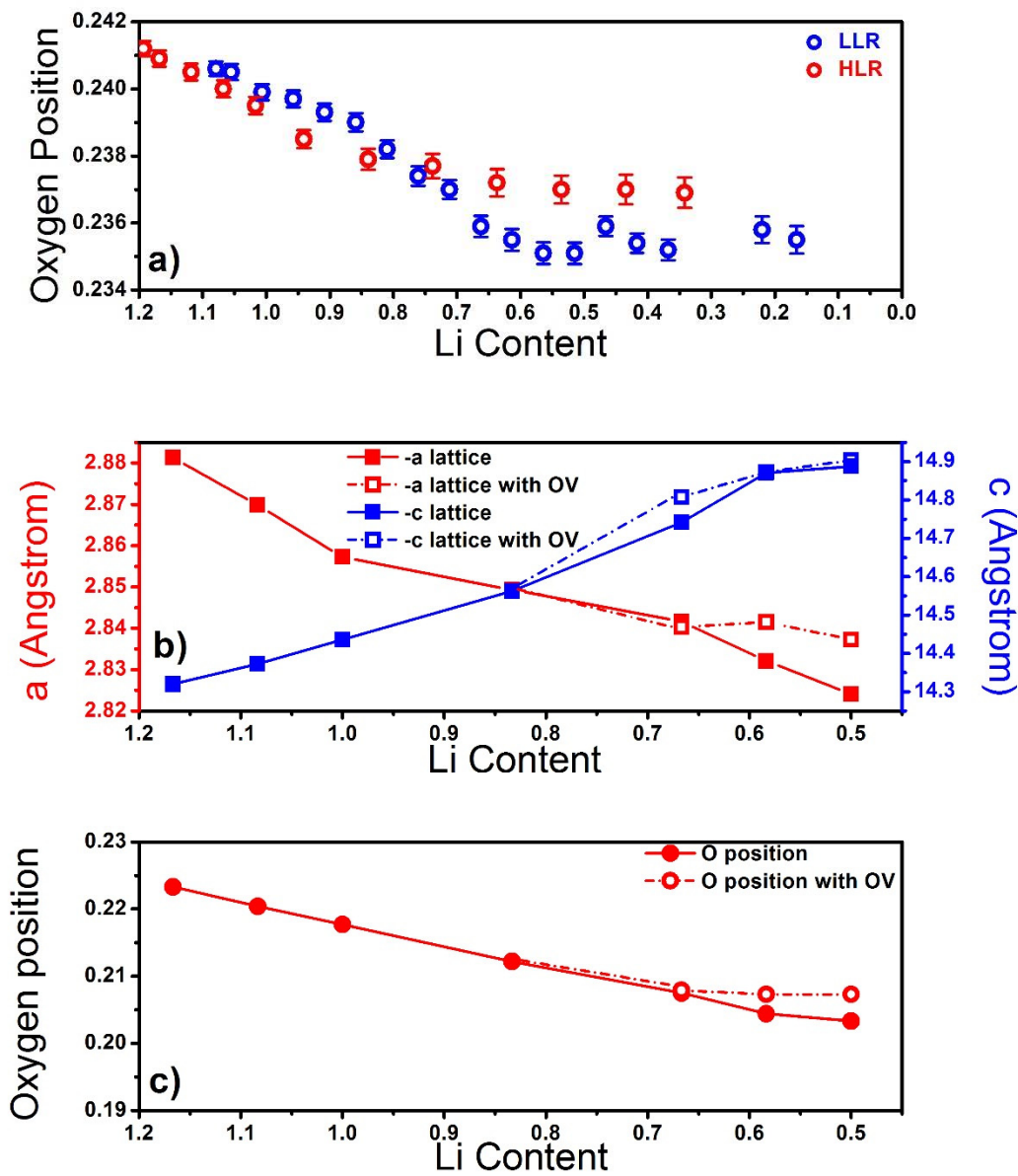


Figure V-147: a) Oxygen position from refinement results, b) DFT results of the evolution of the lattice parameters and c) oxygen position with and without oxygen vacancy

Probing the surface oxygen activities of Li-rich layered oxides cathode via soft XAS and XPS

Soft XAS is a powerful characterization tool that can determine local atomic and electronic structures. Total electron yield (TEY) mode is applied to investigate the oxygen activities on the surface of $\text{LiNi}_{0.4}\text{Mn}_{0.4}\text{Co}_{0.2}\text{O}_2$ (NMC 422) and $\text{Li}_{1.2}\text{Ni}_{0.13}\text{Mn}_{0.53}\text{Co}_{0.13}\text{O}_2$ (Li-rich) at different states of charge. The broad structures above 534 eV correspond to the transition of O 1s to the hybridized states, consisting of metal 4sp and oxygen 2p orbitals. The pre-edge structure below 534 eV corresponds to the transition to the states of metal 3d and oxygen 2p orbitals. The 3d band can further be separated with the lower energy peak corresponding to the t_{2g} orbitals and the higher energy peak corresponding to the e_g orbitals. The intensity ratio of the 3d to 4sp band represents the amount of unoccupied 3d orbitals in the metal ions and a change in the local environment of oxygen, such as oxygen vacancies and peroxo-/superoxo-like species. As shown in Figure V-148, the 3d/4sp NMC 422 ratio increased during charge, indicating a larger amount of unoccupied 3d orbitals from the transition metal ion oxidation. The decrease of 3d/4sp ratio after one cycle suggests that the change of bond covalency between oxygen and the neighboring transition metals are due to the formation of Co-O like rock-salt structure on the surface of NMC 422 material. While the decrease of 3d/4sp ratio of Li-rich during charge comes from the dramatic change in the local environment of oxygen, such as bond length and oxygen vacancies formation.

More interestingly, this 3d/4sp ratio goes back to some extent after discharge, implying that the involved oxygen activities on the surface of Li-rich can be partially reversible.

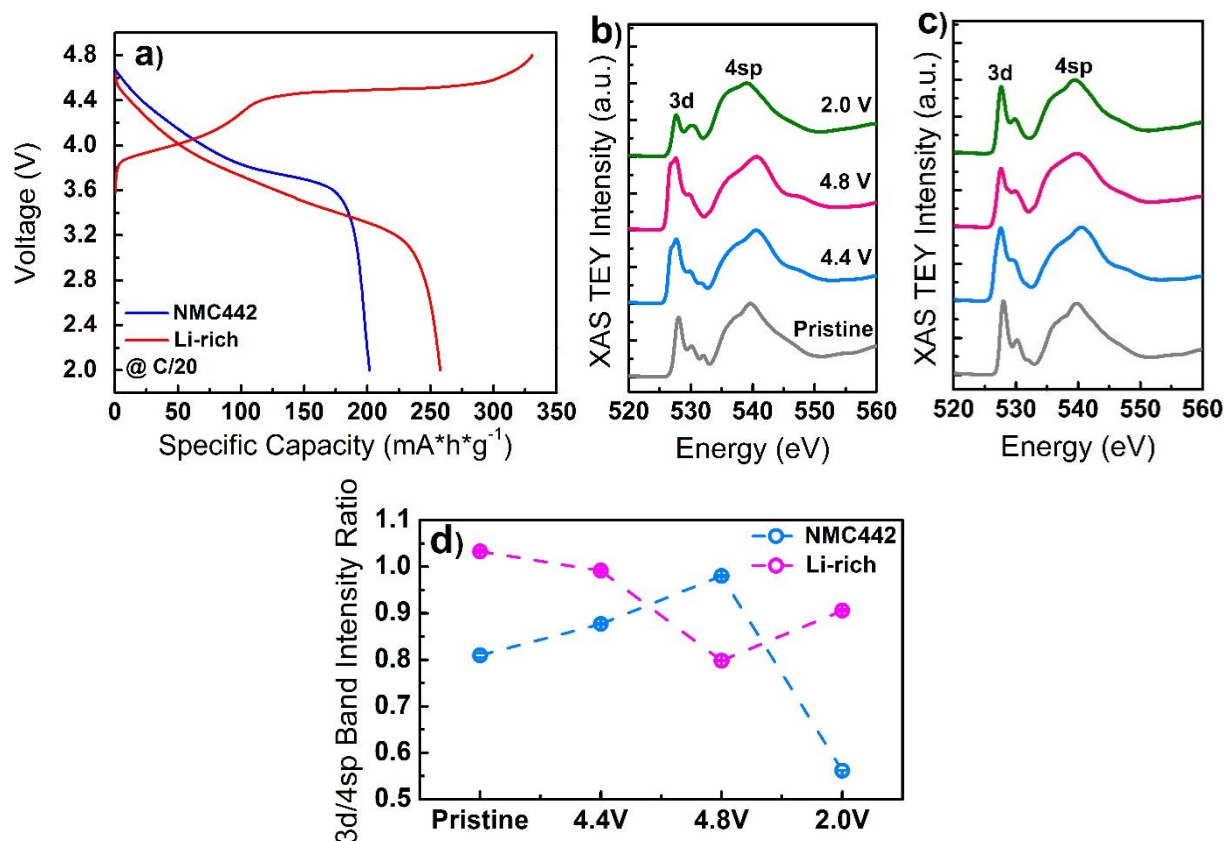


Figure V-148: (a) First cycle voltage profile of NMC 442 and Li-rich, where the voltage range is 2.0 – 4.8 V, at C/20 = 12.5 mA g⁻¹. Soft XAS results (TEY mode) at various states of charge in the first cycle of O K-edge (b) NMC442 and (c) Li-rich NMC. (d) Comparison of O 3d/4sp band intensity ratios between NMC442 and Li-rich NMC

XPS is a powerful surface sensitive characterization tool that can determine chemical species and oxidation state of the transition metals. In order to study the surface chemistry including redox process of transition metal and oxygen activities of Li-rich oxides, XPS data was collected from electrodes at different charge/discharge states. Figure V-149 shows the resulting XPS spectra for the Ni 3p, Mn 3p and O1s region. The pristine Ni 3p shows a binding energy ~67.6 eV. After charged to 4.4 V, where the Ni²⁺/Ni⁴⁺ redox occurs, the peak shifts to a higher binding energy of ~68.6 eV. When further charged to 4.8V, the peak slightly shifts back to a lower binding energy, which is caused by the oxygen oxidation at high voltage. The peak shifts back to 67.6 eV when discharged to 3.3 V and remains unchanged upon fully discharged. Mn 3p region shows a major peak at 49.8 eV corresponding to Mn⁴⁺, a minor peak at 48.6 eV ascribed to Mn³⁺. At pristine state, not all of the Mn ions are in Mn⁴⁺, indicating Mn on the surface is reduced to some extent after contact with electrolyte. During the charging/discharging process, Mn ions experience Mn³⁺/Mn⁴⁺ redox reaction, contributing certain amount of capacity. For the O 1s spectra, at pristine state, the two main peaks at ~529.1 and ~531.5 eV are assigned to O²⁻ anions in the crystal lattice and carbonate species on the surface, respectively. The minor component at ~533.0 eV is ascribed to adsorbed species from the electrolyte. Another peak component at ~530.5 eV, which is associated with peroxy-like species (O₂)ⁿ⁻ or under-coordinated oxygen atoms, is dramatically increased after charged to high voltage (larger than 4.4 V). More interestingly, this component corresponding to peroxy-like species gradually reduced back to the pristine state after one cycle. This oxygen activity observed by XPS clearly indicates oxygen anion redox reversibly contributes to the overall capacity of Li-rich layered oxides.

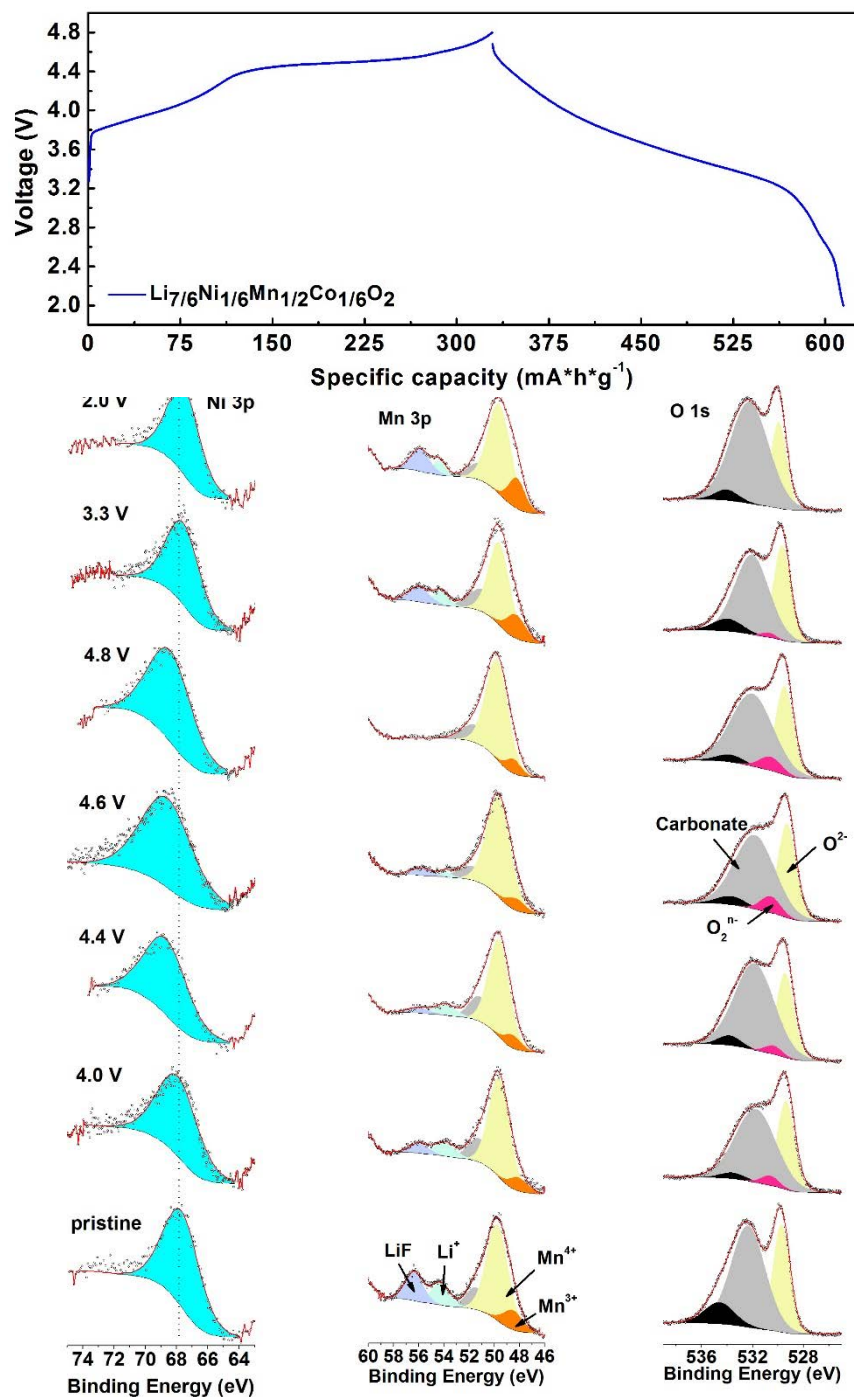


Figure V-149: (up) First cycle voltage profile of Li-rich material, where the voltage range is 2.0 – 4.8 V, at C/20 = 12.5 mA g⁻¹. (down) Ni 3p, Mn 3p and O 1s XPS spectra at various charge/discharge states in the first cycle

Nanoscale LLTO (lithium lanthanum titanium oxide) surface coating for Li-rich LNMO (Li_{1.13}Ni_{0.3}Mn_{0.567}O₂) material

The surface of Li-rich LNMO was coated with LLTO to enhance the electrochemical performance. XRD determined that crystallized LLTO existed in the coated Li-rich material. In order to identify the uniformity of the LLTO coating, bright field STEM coupled with EELS were applied to the uncoated and coated LLTO Li-rich material. Figure V-150 (a) and (b) compares the STEM images of the uncoated and coated Li-rich material. The uncoated particles have a clean surface with Li and TM layers extending to the outermost

surface. After LLTO coating, there is a uniform nanoscale layer (less than 1 nm in thickness) found on the particle surface. The EELS experiments were carried out on both bulk and surface region of LLTO coated Li-rich (Figure V-150 c). The data points are aligned with the BF image (Figure V-150 b) to indicate where each spectrum was taken (shown in red and black). There is a clear Ti-L edge peak in the spectra obtained on the surface region, where Ti-L3 and Ti-L2 were induced by the electron transitions from $2p^{3/2}$ and $2p^{1/2}$, respectively, to unoccupied 3d orbitals. This Ti-L edge disappears in the bulk region of the material, which indicates LLTO is only the surface. It should be noted that the La-M edge was not detected since it overlaps with Ni-L edge. Both materials were cycled at a slow rate of 25 mA g^{-1} (C/10) between 2-4.8 V. The uncoated Li-rich material shows only 74.2% capacity retention after 190 cycles, while the LLTO coating improves the capacity retention to 82.3%. In addition, the LLTO coated Li-rich delivers higher coulombic efficiency than the uncoated upon the long term cycling. The results indicate that nanoscale uniform crystalline LLTO surface coating could improve the cycling stability significantly.

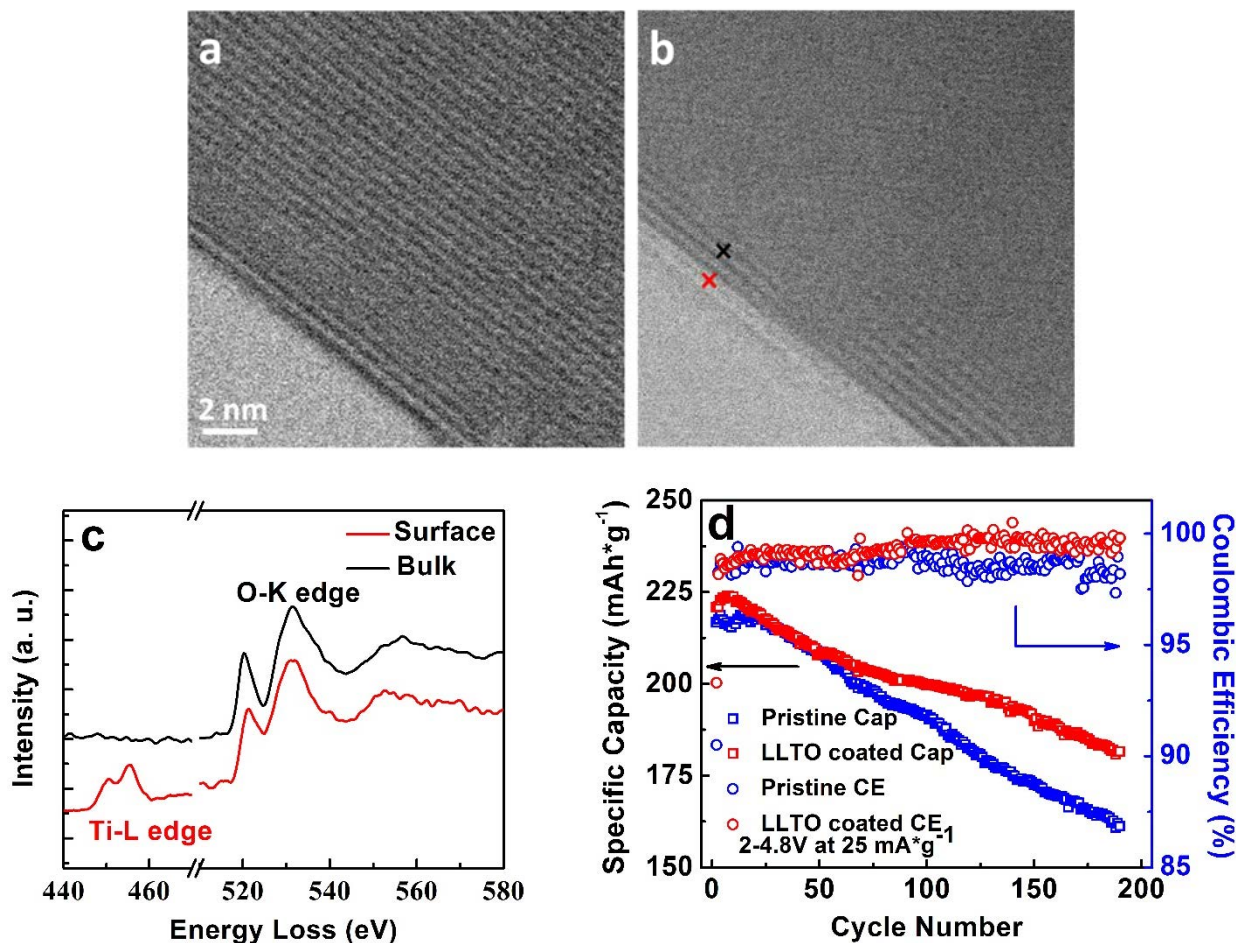


Figure V-150: STEM/ABF images of (a) uncoated Li-rich material and (b) 1wt% LLTO coated Li-rich. (c) EELS spectra of 1wt% LLTO coated Li-rich at different regions. (d) Comparison of capacity and coulombic efficiency for uncoated and LLTO coated Li-rich over the course of 190 cycles

Direct visualization of the SEI morphology on Si using STEM EELS

For the first time we present the direct visualization on how FEC affects the SEI morphology throughout electrochemical cycling. Figure V-151 shows the ADF-STEM images of SEI with progressive cycling, where the electrode cycled in EC/DEC after the first delithiation forms an inhomogeneous porous SEI. Moreover, this SEI is intermixed with the silicon nanoparticles as the cycle number increases (up to 100 cycles). Conversely, the electrode cycled in EC/DEC/FEC is covered with a dense and uniform SEI layer. The silicon nanoparticles preserved its morphology and are covered in a homogenous, dense SEI which was first hypothesized. Surprisingly, after 100 cycles the electrode cycled in EC/DEC/FEC had similar SEI morphology to that of the SEI generated by EC/DEC.

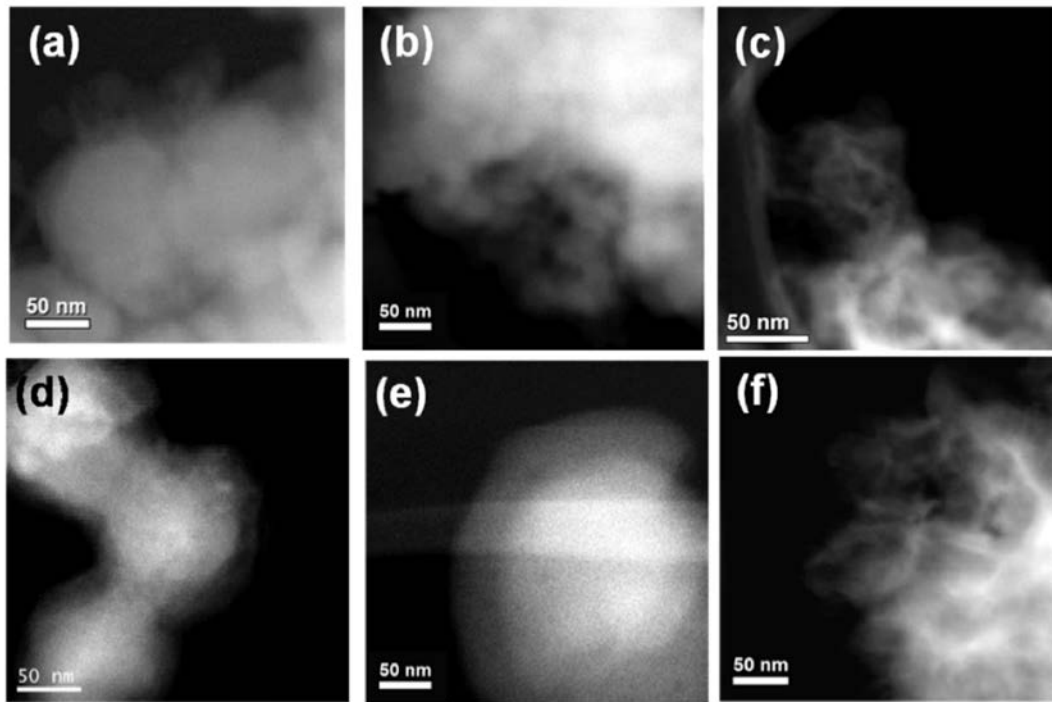


Figure V-151: ADF-STEM images of the Si in conventional electrolyte (a) after 1 cycle, (b) after 5 cycles, (c) after 100 cycles and the Si in electrolyte containing FEC, (d) after 1 cycle, (e) after 5 cycles and (f) after 100 cycles

Nano-scale strain mapping and amorphization evolution of Si anodes upon lithiation using TEM

Si anode undergoes large volume expansion upon cycling, resulting in massive mechanical strain in the electrode. Therefore, it is important to measure the strain evolution upon cycling and correlate it with the electrochemical performance of the material. Herein, the crystallinity mapping and strain mapping of the partially lithiated Si are presented using electron diffraction. The diffraction information can be generated by scanning a nano-size probe (NBED) across a sample. Figure V-152(a) shows a BF-TEM image of the partially lithiated silicon. Figure V-152 (b,c) illustrates color-coded two dimensional orientation and strain maps at 1 nm spatial resolution and 0.5° precession. Based on the color-coded orientation map (Figure V-152(b)), the orientation of the crystalline particles can be determined clearly. The amorphous regions can be distinguished by having small spots (Figure V-152(b)) implying the formation of amorphous Li_xSi alloy upon the lithiation of silicon. In addition, the lithiation of crystalline silicon is accompanied by large strain formation shown in Figure V-152(c). The center of the grain was used as a reference and considerable strain variation from -1% to 2% (from the lower left to the upper right corner of the grain) was observed.

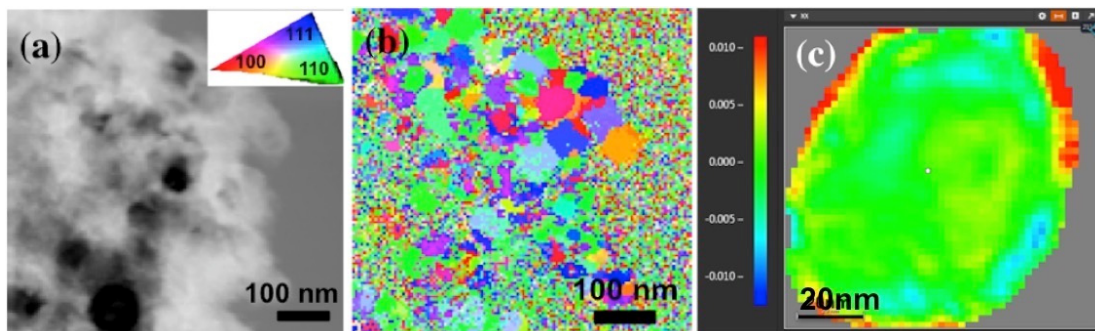


Figure V-152: (a) BF-TEM image of the partially lithiated Si and color-code (insert), (b) corresponding orientation map, (c) strain map from a partially lithiated grain

Aluminum hydroquinone coated Si nanoparticles using Molecular Layer Deposition (MLD)

One of the successful strategies for stabilizing the Si surface chemistry has been surface modification. Herein, Si surface modification has been applied via MLD of alucone in order to improve the interfacial chemistry of Si anode upon cycling. The electrochemical performance of the coated Si is shown in Figure V-153, which does not demonstrate significant changes in comparison with the bare Si anode. The coated and the bare Si electrodes cycled in $\text{LiPF}_6/\text{EC}/\text{DEC}$ at C/10 within the potential window of 0.05-1V. The major difference of our work from the literature is that we use CMC based binder. We suspect that the alucone coating may have more significant effect on the electrode made from the PVDF type of binder than the electrode made from CMC binder. This indicates the importance of understanding the effect of surface coating on binder chemistry.

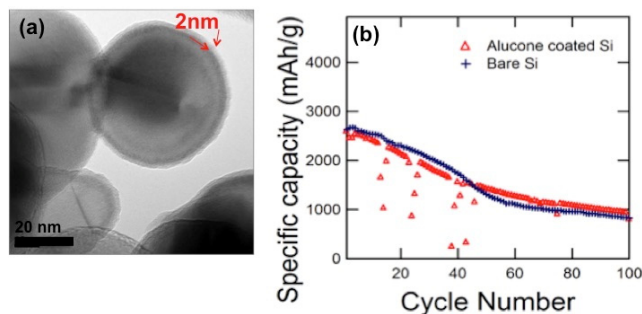


Figure V-153: Cycling performance of Si coated compared to the bare Si

Conclusions

A multi-modal characterization toolset has been established to quantify the electrochemical activities of oxygen anions in Li-rich layered oxides. Neutron diffraction and FP computation indicate the presence of oxygen vacancy in the bulk of Li-rich layered during the high voltage plateau. Soft XAS and XPS results show that involved oxygen activities on the surface reversibly contribute to the overall capacity of Li-rich layered oxides. In addition, LLTO surface coating was explored to improve the voltage/ capacity stability of LNMO as well as initial CE. Future investigation is underway including: (1) investigation of continuous effect of nanoscale uniform crystalline LLTO surface coating during long-term cycling; (2) bulk substitution/doping effect on preventing oxygen vacancies formation in Li-rich layered oxides; (3) correlation between structure defects (dislocations, grain boundary) and oxygen activity evolution. Furthermore, a comprehensive study of the effect of SEI evolution on Si electrochemical performance has been performed using STEM/EELS and XPS, which shown the critical role of Si surface and interface effects in long term electrochemical cycling.

Products

Presentations/Publications/Patents

1. H. D. Liu, Y. Chen, S. Hy, K. An, S. Venkatachalam, D. Qian, M. Zhang, and Y. S. Meng, "Operando Lithium Dynamics in the Li-Rich Layered Oxide Cathode Material via Neutron Diffraction", *Adv. Energy Mater.* 2016, 1502143.
2. M. Zhang, H. D. Liu, Y.S. Meng, "Lithium Excess Cathode Material and Co-precipitation Formation Method", provisional US Patent.
3. H. D. Liu, J. Huang, D. Qian, S. Hy, C. Fang, J. Luo, and Y. S. Meng, "Communication-Enhancing the Electrochemical Performance of Lithium-Excess Layered Oxide $\text{Li}_{1.13}\text{Ni}_{0.3}\text{Mn}_{0.57}\text{O}_2$ via a Facile Nanoscale Surface Modification", *J. Electrochem. Soc.* 2016, 163 (6), A971.
4. S. Hy, H. D. Liu, M. Zhang, D. Qian, B.-J. Hwang, Y. S. Meng, "Performance and design considerations for lithium excess layered oxide positive electrode materials for lithium-ion batteries", *Energy Environ. Sci.* 2016, 9, 1931.
5. B. Qiu, M. Zhang, L. Wu, J. Wang, Y. Xia, D. Qian, H. D. Liu, S. Hy, Y. Chen, K. An, Y. Zhu, Z. Liu, Y. S. Meng, "Gas-solid interfacial modification of oxygen activity in layered oxide cathodes for lithium-ion batteries", *Nat. Commun.* 2016, 7.

6. H. Liu, Y. Chen, S. Hy, K. An, S. Venkatachalam, D. Qian, M. Zhang, and Y. S. Meng, "Operando Lithium Dynamics in the Li-Rich Layered Oxide Cathode Material Via Neutron Diffraction" 229th ECS Meeting, 2016, San Diego, U.S., Oral presentation.
7. H. Liu, Y. Chen, S. Hy, K. An, S. Venkatachalam, D. Qian, M. Zhang, and Y. S. Meng, "Investigate the lithium Dynamics in Li-Rich Layered Oxide Cathode Material Via Operando Neutron Diffraction" 18th International Meeting on Lithium Batteries, 2016, Chicago, U.S., Poster.
8. Y. S. Meng, "Making the Invisible Visible-Advanced Diagnosis Methods for Lithium Ion Rechargeable Battery Materials" 18th International Meeting on Lithium Batteries, 2016, Chicago, U.S., Invited talk.
9. M. Sina, J. Alvarado, H. Shobukawa, Y. S. Meng, "Visualizing the Solid Electrolyte Interphase Layer Evolution in Silicon Electrodes" 229th ECS Meeting, 2016, San Diego, U.S., Oral presentation.
10. Alvarado, K. W. Schroder, T. A. Yersak, Y. S. Meng, "Understanding the Factors That Improve the Cycling Performance of Silicon Anode for Lithium-ion Batteries" 229th ECS Meeting, 2016, San Diego, U.S., Oral presentation.
11. J. Alvarado, M. Sina, H. Shobukawa, Y. S. Meng, "Interface Optimization Principles of Si Anode for Lithium-ion Batteries" International Battery Association, 2016, Nantes, France, Invited Talk.
12. M. Sina, J. Alvarado, H. Shobukawa, K. W. Schroder, K. Stevenson, Y.S. Meng, "Direct Visualization of the Solid Electrolyte Interphase and Its Effects on Silicon Electrochemical Performance" Advanced Materials Interfaces, 2016, DOI: 10.1002/admi.201600438.
13. M. Sina, J. Alvarado, H. Shobukawa, Y. S. Meng, "Morphological and chemical evolution of silicon nanocomposite during cycling" M&M Meeting, 2016, Columbus, OH, Invited talk.

References

1. Q. Xia, X. Zhao, M. Xu, Z. Ding, J. Liu, L. Chen, D. G. Ivey, W. Wei, "A Li-rich Layered@Spinel@Carbon heterostructured cathode material for high capacity and high rate lithium-ion batteries fabricated via an *in situ* synchronous carbonization-reduction method", J. Mater. Chem. A 2015, 3, 3995.
2. Y.-P. Deng, F. Fu, Z.-G. Wu, Z.-W. Yin, T. Zhang, J.-T. Li, L. Huang, S.-G. Sun, "Layered/spinel heterostructured Li-rich materials synthesized by a one-step solvothermal strategy with enhanced electrochemical performance for Lithium-ion batteries", J. Mater. Chem. A 2016, 4, 257.
3. C. R. Fell, D. Qian, K. J. Carroll, M. Chi, J. L. Jones, Y. S. Meng, "Correlation between oxygen vacancy, microstrain, and cation distribution in lithium-excess layered oxides during the first electrochemical cycle", Chem. Mater. 2013, 25, 1621.
4. B. Xu, C. R. Fell, M. Chi, Y. S. Meng, "Identifying surface structural changes in layered Li-excess nickel manganese oxides in high voltage lithium-ion batteries: A joint experimental and theoretical study", Energy Environ. Sci. 2011, 4, 2223.
5. B. Philippe, R. Dedryvere, M. Gorgoi, H. Rensmo, D. Gonbeau, K. Edstrom, "Role of the LiPF₆ salt for the long-term stability of silicon electrodes in Lithium-ion batteries – A photoelectron spectroscopy study", Chem. Mater. 2013, 25, 394.
6. C. Xu, F. Lindgren, B. Philippe, M. Gorgoi, F. Bjorefors, K. Edstrom, T. Gustafsson, "Improved performance of the silicon anode for Lithium-ion batteries: understanding the surface modification mechanism of fluoroethylene carbonate as an effective electrolyte additive", Chem. Mater. 2015, 27, 2591.
7. M. T. McDowell, I. Ryu, S. W. Lee, C. M. Wang, W. D. Nix, Y. Cui, "Studying the kinetics of crystalline silicon nanoparticle lithiation with *in situ* transmission electron microscopy", Adv. Mater. 2012, 24, 6034.
8. K. Schroder, J. Alvarado, T. A. Yersak, J. C. Li, N. Dudney, L. J. Webb, Y. S. Meng, K. J. Stevenson, "The effect of fluoroethylene carbonate as an additive on the solid electrolyte interphase on silicon lithium-ion electrodes", Chem. Mater. 2015, 27, 5531.

V.E.6. Analysis of Film Formation Chemistry on Silicon Anodes by Advanced *In Situ* and *Operando* Vibrational Spectroscopy (UC Berkeley, LBNL)

Gabor A. Somorjai

University of California, Berkeley
Department of Chemistry
D54 Hildebrand Hall
Berkeley, CA 94720
Phone: 510-642-4053; Fax: 510-643-9668
E-mail: somorjai@berkeley.edu

Philip N. Ross

Lawrence Berkeley National Laboratory
Materials Sciences Division
1 Cyclotron Road
Berkeley, CA 94720
Phone: 510-642-4053; Fax: 510-643-9668
E-mail: pnross@lbl.gov

Tien Q. Duong, DOE Program Manager

U.S. Department of Energy
Advanced Battery Materials Research (BMR)
Vehicle Technologies Office
1000 Independence Avenue, SW
Washington, DC 20585
Phone: 202-586-7836
E-mail: Tien.Duong@ee.doe.gov

Start Date: October 1, 2012
End Date: September 30, 2016

Abstract

Objectives

- Understand the composition, structure and formation / degradation mechanisms of the solid electrolyte interface (SEI) on the surfaces of Si anodes during charge / discharge cycles by applying advanced *in situ* vibrational spectroscopies.
- Determine how the properties of the SEI contribute to failure of Si anodes in lithium-ion batteries in vehicular applications. Per se this understanding to develop electrolyte additives and / or surface modification methods to improve Si anode capacity loss and cycling behavior.

Accomplishments

- Here we show by sum frequency generation (SFG) vibrational spectroscopy, which is a non-linear optical technique that yields vibrational spectra of molecules at interfaces that in an ethylene carbonate (EC) : fluoroethylene carbonate (FEC) solution, new vibrational peaks arise that can only be associated with EC reorientation, induced by FEC, on silicon surfaces.
- We have found that the beneficial effect of FEC as a common electrolyte additive is associated to the formation of a crystalline-like EC interface even at open circuit potential.
- We have found that the beneficial crystalline-like surface coverage diminishes with the increase of FEC.

Future Achievements

- We intend to apply the same methodology presented herein to investigate whether vinyl carbonate (VC) has the same reconstruction effect on other common electrolytes.
- We intend to explore the composition, structure and formation / degradation mechanisms of the solid electrolyte interface (SEI) on the surfaces of metallic lithium anodes during charge / discharge cycles by applying advanced *in situ* vibrational spectroscopies.

Technical Discussion

Background

Lithium-ion batteries are one of the most common forms of energy storage devices. In a battery, electrical energy is generated by conversion of chemical energy via redox reactions at the anode and cathode. The battery's chemistry dictates the amount of charge that can be stored. The type of anode and cathode employed in lithium-ion batteries exhibit a typical open current potential (OCP) of ~4 volts and rigorous research is conducted to increase it to 5 volts and above. The common anode today in portable electronic appliances is graphite based. Graphite has a theoretical capacity of 372 mAh/g (1 Li per 6 carbon atoms). However, for electric vehicles where higher capacity is needed, the silicon based anodes are attractive candidates to replace graphite based anodes. Silicon stores 3.75 Li atoms per one Si atom yielding a theoretical capacity of 4008 mAh/g.

However, the Si lattice expands up to three times its volume, which results in irreversible capacity loss and short cycling lifetime due to continued cracking and electrolyte consumption on the exposed Si surface. The key factor in long-term use (cyclability and stability) of such devices is the formation of an electrically insulating layer that allows lithium ion transport at a reasonable rate while hindering electrolyte consumption on the Si anode surface, and is termed the solid electrolyte interface (SEI).

Previous studies from Prof. Somorjai's laboratory have indicated that the nature of the electrolyte consuming reactions in lithium batteries is electrode material dependent. Specifically, a study using *ex situ* infrared vibrational spectroscopy observed two different SEI compositions on Sn and Ni electrodes even though the same electrolyte solution was used. Therefore, we may expect the electrolyte consuming reactions on Si may be unique to this surface, and that the nature of the reactions may be a critical factor in determining the functioning of the surface layer formed, i.e. whether it functions as an SEI. The successful replacement of graphite by Si may require detailed understanding of these surface reactions and the ability to manipulate them by surface or electrolyte modification.

Introduction

In a battery, electrical energy is generated by conversion of chemical energy via redox reactions at the anode and cathode. During the charge / discharge cycles, in the presence of lithium ions the liquid electrolyte solution (mainly carbonates) is being consumed on the electrodes surfaces. If continued uninterrupted this will lead to capacity loss and finally render the lithium-ion battery useless. The key factor in long-term use (cyclability and stability) of such devices is the formation of an insoluble electrical insulating layer that allows lithium ion transport at a reasonable rate while hindering electrolyte consumption on the anode surface, and is termed the solid electrolyte interphase (SEI). In an attempt to increase the capacitance of the lithium-ion batteries silicon anode various compositions of electrolytes (solvent and lithium salt) were tested. However, due to the silicon volume expansion as a result of lithiation and delithiation the carbonate based SEI fails to maintain its integrity. The addition of fluoroethylene carbonate (FEC) remarkably improves discharge capacity retention and coulombic efficiency regardless of the silicon anode form. However, the property that makes FEC a desirable additive to electrolytes is unclear rendering Si high capacity useless. Here we show by sum frequency generation (SFG) vibrational spectroscopy, which is a non-linear optical technique that yields vibrational spectra of molecules at interfaces that in an ethylene carbonate (EC) : FEC solution, new vibrational peaks arise that can only be associated with EC reorientation, induced by FEC, on silicon surfaces. Our finding can now initiate additive design to not only act as a sacrificial compound but also induce tighter EC, crystalline-

like surface alignment of other electrolyte candidates leading to a resilient SEI, consequently enabling the use of silicon anodes in the lithium-ion vehicular industry.

Approach

Amorphous Si anode thin films, e-beam deposited on optical windows, are studied using baseline electrolyte and promising electrolyte variations. *In situ* sum frequency generation (SFG) vibrational spectroscopy is used to directly monitor the composition and structure of electrolyte reduction compounds formed on the Si anodes. Different SFG polarization combinations allow us to detect the adsorption angle of the electrolyte molecules at the liquid-solid interface. Pre-natal and post-mortem chemical composition is identified using X-ray photoelectron spectroscopy (XPS). The Si films and nanostructures are imaged using scanning and transmission electron microscopies, as well as atomic force microscopy (AFM). (See Figure V-154.)

Results

We have synthesized the following electrolyte solutions: 1.0 M LiClO₄ in ethylene carbonate (EC), 1.0 M LiClO₄ : in fluoroethylene carbonate (FEC) and their mixtures EC:FEC at ratios of: 9:1, 7:3, and 6:4 w/w, and pure EC in order to investigate the effect of fluorinated additives (FEC) on the surface ordering of the electrolyte molecules at electrolyte / amorphous silicon (a-Si) interface. Our main conclusion is that at open circuit potentials FEC induces ordering of adsorbed EC molecules on the a-Si anode leading to a tighter packing of EC molecules at the anode surface, consequently yielding a better SEI in lithium-ion batteries. By tuning the SFG polarization configuration to ssp we have enhanced the SF signal sensitivity to adsorbates with a perpendicular dipole orientation in respect to the electrode's surface. In Figure V-155, we present the a-Si / EC and EC:FEC based electrolyte interphases at open circuit potential (OCP) at the C=O stretch range. No prominent SFG features corresponding to pure FEC solutions were detected from the interface. The main broad peak of EC (black curve) is ~ 1820 cm⁻¹ (fundamental stretching, yellow bar) with a shoulder around 1780 cm⁻¹ (Fermi resonance, green bar). Noticeably, upon adding FEC, e.g., EC:FEC 9:1 (red curve) the

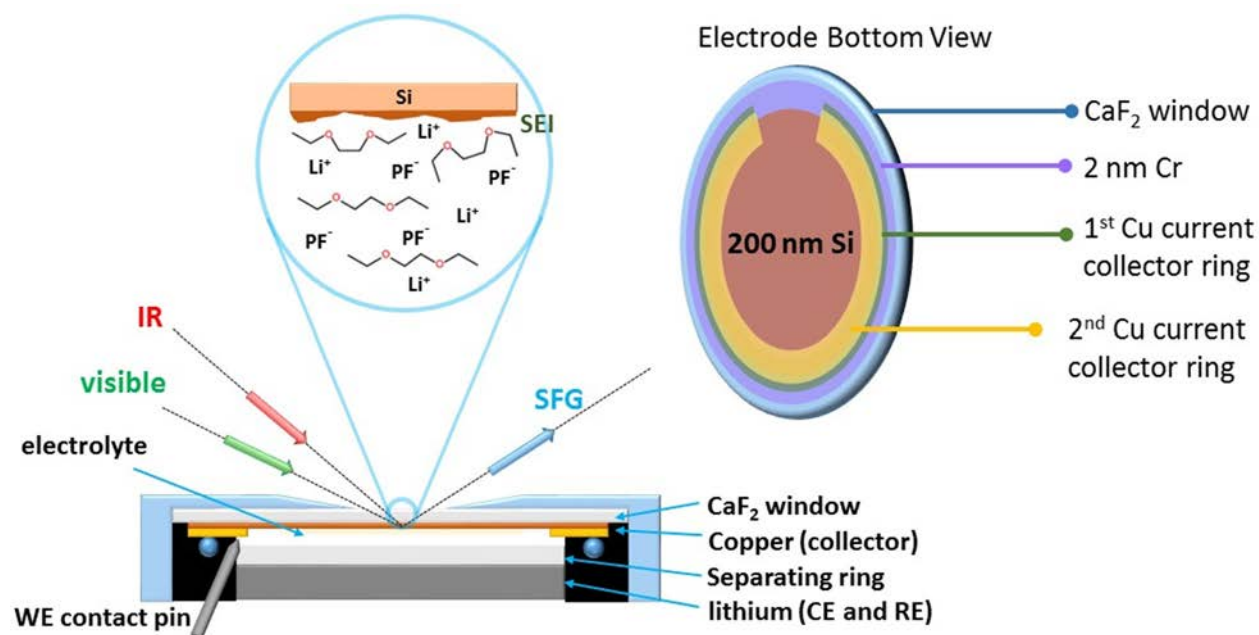


Figure V-154: (a) General illustration of the electrochemical half-cell used in our SFG measurements. (b) The layered amorphous Si anode and its copper current collectors deposited sequentially on a CaF₂ window. By depositing the copper rings and amorphous Si directly on the CaF₂ window we enable the visible and IR beams to propagate through the window and through the a-Si anode reaching the a-Si / electrolyte interface. The SFG signal then propagates upwards (back reflection). This design also ensures good electrical conductivity

Fermi resonance at 1780 cm^{-1} intensifies. This trend continues with the addition of more FEC to form EC:FEC 7:3 (blue curve). This trend suggests a solid-like EC packing at the anode surface presumably due to better dipole-dipole stacking.

In Figure V-155a we show the resulting SFG spectra in open circuit potential (OCP) in the C-H stretch region and in Figure V-155b the carbonyl stretch of 1.0 M LiClO_4 in: pure EC and three mixtures of EC : FEC 9:1, 7:3, and 6:4 (w/w) electrolyte solutions. The addition of FEC to EC yields new vibrational peaks that we associate with EC reorienting since pure FEC has no features in both ranges and no redox electrochemical processes can take place. The vibration at 1780 cm^{-1} is associated to EC – EC interactions in the solid crystalline phase, therefore we suggest that its intensification after the addition of FEC is due to a crystalline-like coverage on the a-Si anode. Moreover, under SSP polarization combination, we observed higher SFG intensities meaning the addition of FEC has realigned the ethylene carbonate molecules to assume a more perpendicular adsorption angle.

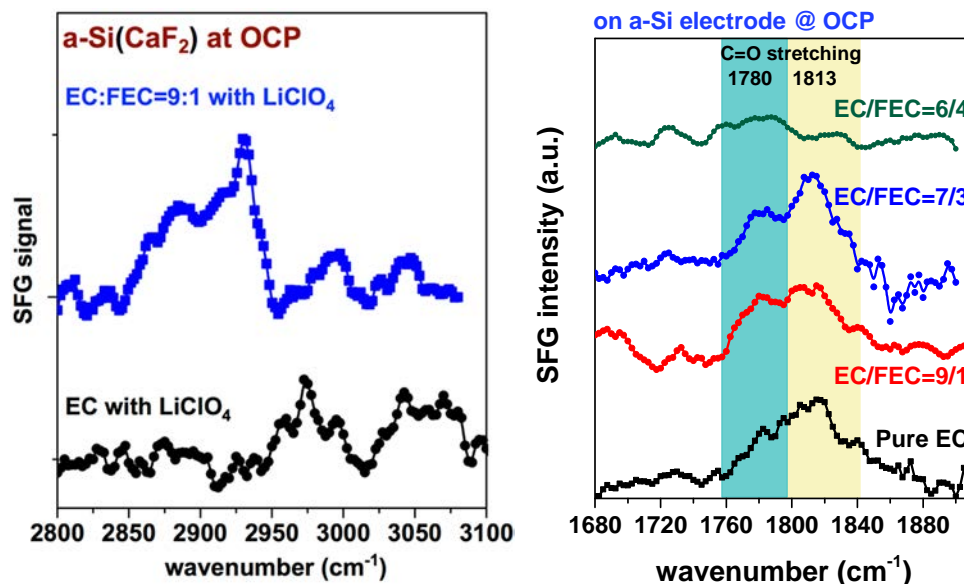


Figure V-155: We present the reorientation effect of FEC on EC at open circuit potentials as probed by SFG. Left – SFG at the midIR, EC (black curve) has a two peak profile (2980 cm^{-1} and 3050 cm^{-1}) the addition of FEC at 9:1 (w/w) ratio yields a new strong peak at 2920 cm^{-1} with a shoulder at 2880 cm^{-1} . Right – SFG at the farIR, EC solution shows a peak at 1820 cm^{-1} and one at 1780 cm^{-1} . Upon adding FEC a more organized crystalline-like EC surface arrangement takes place as evident by the increase of the 1780 cm^{-1} peak. However, above 7:3 (w/w) ratio the ordered EC interface becomes disordered as the SFG profile broadens

In Figure V-156, we show the trend of EC ring opening frequencies (s-CH₂, ~ 2880 cm^{-1}) arising from EC:FEC 9:1 (w/w) mixture in contact with a-Si anode after the first lithiation / delithiation (right) and the second cycle (left) at the C-H stretch region. By dividing the SFG spectra (SFGGA/SFGOCP) we emphasize the appearance (or trend) of vibrational peaks that are less clear in a regular SFG scan since in most cases the SFG from the a-Si/SEI interferes with the SFG generated from the Si substrate. In Figure V-156 (left), the shoulder around 2880 cm^{-1} (s-CH₂) suggests that EC undergoes a ring opening but still its products are tightly packed upon (black dots). Upon discharge (open red squares) most of the EC molecules are converted to linear moieties such as $-\text{OCH}_2\text{CH}_2\text{O}-$ expressed by the major peak at 2950 cm^{-1} . In Figure V-156 (right), no major trend features are detectable and so we presume that the SEI first layer consists of mainly R-OCH₂-CH₂O-R'.

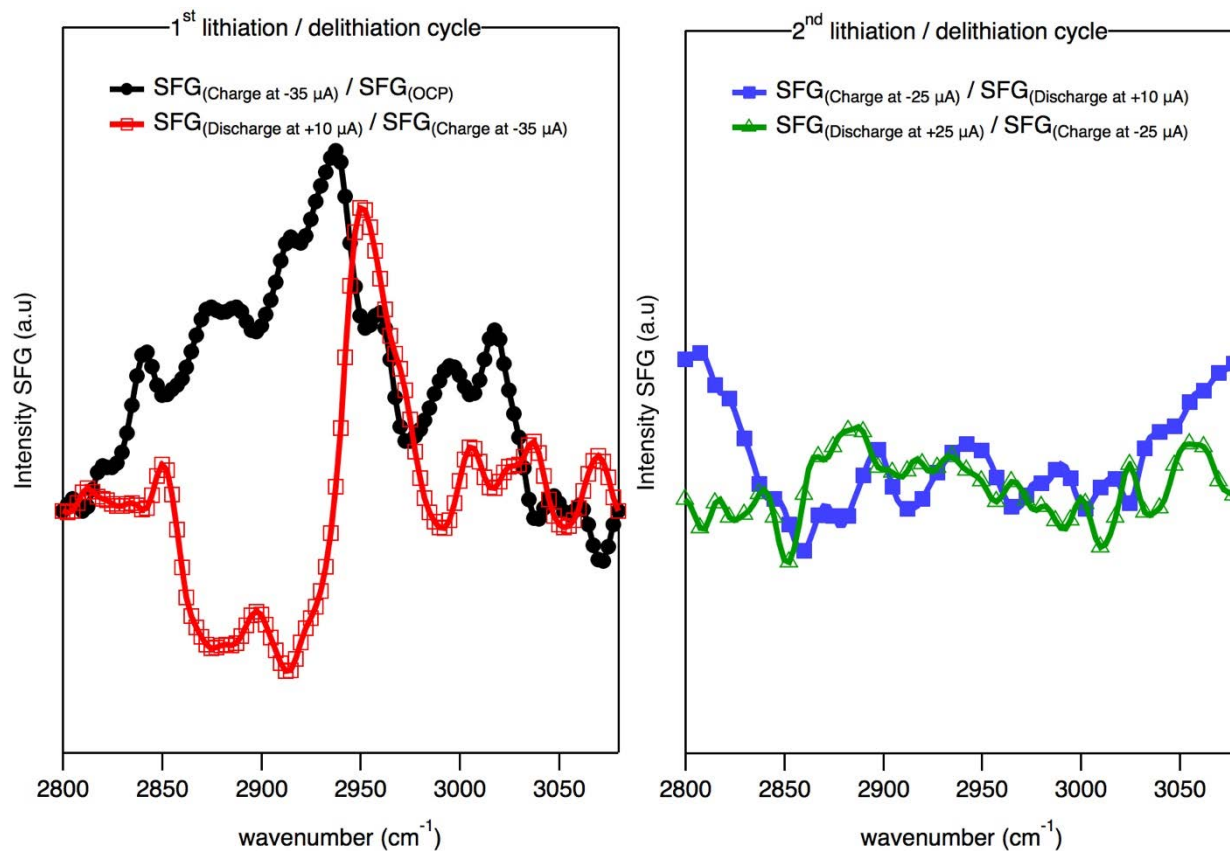


Figure V-156: We show the evolution of SFG (ssp) signal associated with EC:FEC (9:1, w/w) in contact with a-Si (s-CH₂) vibrations under reaction conditions by dividing the SFG spectra by their former potentials

Conclusions

In conclusion, we have observed that FEC on a-Si induces better ordering of the adsorbed EC on the silicon anode. The C-H stretch range suggests that the SEI does not change in chemistry after the first delithiation but maintains a tightly packed layer of linear products.

Products

Presentations/Publications/Patents

1. Shi, F.; Zhao, H.; Komvopoulos, K.; Somorjai, G.; Ross, P. N., Tailoring the Desired Surface Chemistry in Silicon-Based Lithium-Ion Batteries with Electrolyte Additives. Meeting Abstracts 2015, MA2015-01 (2), 410.
2. Shi, F.; Song, Z.; Ross, P. N.; Somorjai, G. A.; Ritchie, R. O.; Komvopoulos, K., Failure mechanisms of single-crystal silicon electrodes in lithium-ion batteries. Nature Communications 2016, 7, 11886.
3. Horowitz, Y.; Han, H. L.; Ross, P. N.; Somorjai, G. A., *In Situ* Potentiodynamic Analysis of the Electrolyte/Silicon Electrodes Interface Reactions - A Sum Frequency Generation Vibrational Spectroscopy Study. Journal of the American Chemical Society 2016, 138 (3), 726-729.
4. Horowitz, Y.; Han, H. L.; Somorjai, G. A., Fluoroethylene carbonate aligns ethylene carbonate on amorphous silicon anodes starting at open circuit potential to produce better solid electrolyte interphase as probed by sum frequency generation vibrational spectroscopy under reaction conditions – submitted.

V.E.7. Microscopy Investigation on the Fading Mechanism of Electrode Materials (PNNL)

Chong-Min Wang, Chief Scientist

Pacific Northwest National Laboratory
902 Battelle Boulevard, Mail Stop K8-93
Richland, WA 99352
Phone: 509-371-6268; Fax: 509-371-7866
E-mail: Chongmin.wang@pnnl.gov

Tien Q. Duong, DOE Program Manager

U.S. Department of Energy
Advanced Battery Materials Research (BMR)
Vehicle Technologies Office
1000 Independence Avenue, SW
Washington, DC 20585
Phone: 202-586-7836
E-mail: Tien.Duong@ee.doe.gov

Start Date: July 1, 2015

End Date: September 30, 2018

Abstract

Objectives

The overall objective of this work is microscopy investigation of the fading mechanism of electrode materials for rechargeable batteries. The focus of the work will be on using *Ex situ*, *in situ* and operando high-resolution transmission electron microscopy (TEM) and spectroscopy to probe the structural evolution of electrodes and interfaces between the electrode and electrolyte and correlate this structural and chemical evolution with battery performance, therefore guiding the designing and discovery of new materials for enhanced performance.

Accomplishments

- *In situ* TEM study clarified the effect of coating layer on lithiation behavior of Si, leading to strategy of optimized designing of a coating layer on Si anode.
- Captured SEI structure and chemistry of layer structured cathode; gained key insights on the voltage and capacity fading/failure mechanism of cathode and potential method for mitigating the fading.
- Captured atomic level information on how Ni, Co, and Mn mix with the Li layer in the layer structured cathode.
- Discovered the selective surface plane segregation of Ni and Co in the layer structured cathode.
- Developed *in situ* liquid SIMS for direct capturing molecular information at solid-liquid interphase and integration with *in situ* TEM results.

Future Achievements

- Atomic to electrode scale diagnosis for both cathode, anode, and SEI.
- Focus on probing secondary particle behavior for cathode, lattice stability, interfacial interaction between electrode and electrolyte and their correlation with capacity fading.
- A combination of *in situ* TEM and SIMS can lead to both morphological and true chemical information of the SEI layer and its evolution. These research will guide optimized synthesis and modification of electrode materials for enhanced battery performance.

Technical Discussion

Background

Both *ex situ* and *in situ* TEM have been demonstrated to be critical for probing the structure and chemistry of electrode and SEI layer (1). Recently, we have developed new operando characterization tools to characterize SEI formation and electrode/electrolyte interaction using practical electrolyte that are critical for making new breakthroughs in the battery field (2, 3). The success of this work will increase the energy density of lithium-ion batteries and accelerate market acceptance of electrical vehicles (EV), especially for plug-in hybrid electrical vehicles (PHEV).

Introduction

For layer structured cathode materials, it is generally believed that that high Co content in the NCM material enhances the rate performance; high Ni content gives rise to higher lithium utilization and presence of Mn⁴⁺ improves the structural stability and thermal stability (4). However, the detailed fundamental roles of each transition metal cation e.g. Ni, Co and Mn, especially at the high voltages are still unclear, not mentioning the possible synergistic effects among these three cations during the electrochemical process. Furthermore, dopants such as Sn and Si have been noticed affect the fading characteristics dramatically (5). Understanding the different contributions of Ni, Co, and Mn and their movements during cycling, if any, not only help optimize the electrochemical performances of NCM at high cutoff voltages, it also unravels the structural evolution pathway of NCM, providing guidance for the further modification on the original NCM from the point of view of synthesis.

Approach

Extend and enhance the unique *ex situ* and *in situ* TEM methods for probing the structure of lithium-ion batteries, especially for developing a biasing liquid electrochemical cell that uses a real electrolyte in a nano-battery configuration. Use various microscopic techniques, including *ex situ*, *in situ*, and especially the operando TEM system, to study the fading mechanism of electrode materials in batteries. This project will be closely integrated with other research and development efforts on high-capacity cathode and anode projects in the BMR Program to 1) discover the origins of voltage and capacity fading in high-capacity layered cathodes and 2) provide guidance for overcoming barriers to long cycle stability of electrode materials.

Results

1. How does Al₂O₃ coating layer on cathode function to mitigate capacity fading

Surface coating of cathode has been identified as an effective approach for enhancing the capacity retention of layered structure cathode. However, the underlying operating mechanism of such thin coating layer, in terms of surface chemical functionality and capacity retention, remains unclear. Aberration corrected scanning transmission electron microscopy and high efficient spectroscopy to probe the delicate functioning mechanism of Al₂O₃ coating layer on Li_{1.2}Ni_{0.2}Mn_{0.6}O₂ cathode. It is discovered that in terms of surface chemical function, the Al₂O₃ coating suppresses the side reaction between cathode and the electrolyte upon the battery cycling. At the same time, the Al₂O₃ coating layer also eliminates the chemical reduction of Mn from the cathode particle surface, therefore avoiding the dissolution of the reduced Mn into the electrolyte. In terms of structural stability, the Al₂O₃ coating layer can mitigate the layer to spinel phase transformation, which otherwise will initiate from the particle surface and propagate towards the interior of the particle with the progression of the battery cycling (Figure V-157). The atomic to nanoscale effects of the coating layer observed here provide insight for optimized design of coating layer on cathode to enhance the battery properties.

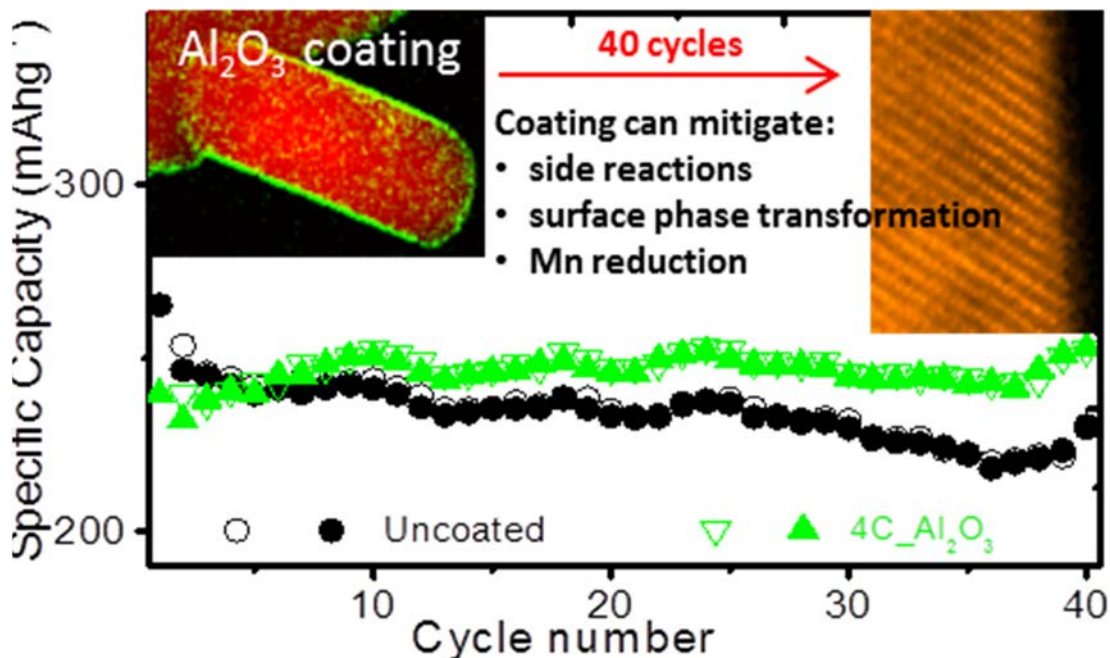


Figure V-157: Correlation of STEM imaging of structure, EDS mapping of chemical composition and electrochemical property measurement help to identify the effect of Al_2O_3 coating effect for improved battery performance

2. Surface plane selective segregation of Ni and Co in layer structured cathode

Through intensive aberration corrected STEM investigation on ten layered oxide cathode materials, two important observations have been made. Firstly, Ni and Co show strong plane selectivity when building up their respective surface segregation layers (SSL). Specifically, Ni-SSL is exclusively developed on (200) facet in Li-Mn-rich oxides (monoclinic $C2/m$ symmetry) and (012)h facet in Mn-Ni equally rich oxides (hexagonal $R-3m$ symmetry), while Co-SSL has a strong preference to (20-2)m plane with minimal Co-SSL also developed on some other planes in Li-Mn-rich cathodes. Structurally, Ni-SSLs tend to form spinel-like lattice while Co-SSLs are in a rock-salt-like structure. Secondly, by increasing Ni concentration in these layered oxides, Ni and Co SSLs can be suppressed and even eliminated. These observations indicate that Ni and Co SSLs are tunable through controlling particle morphology and oxide composition, which opens up a new way for future rational design and synthesis of cathode materials. (See Figure V-158.)

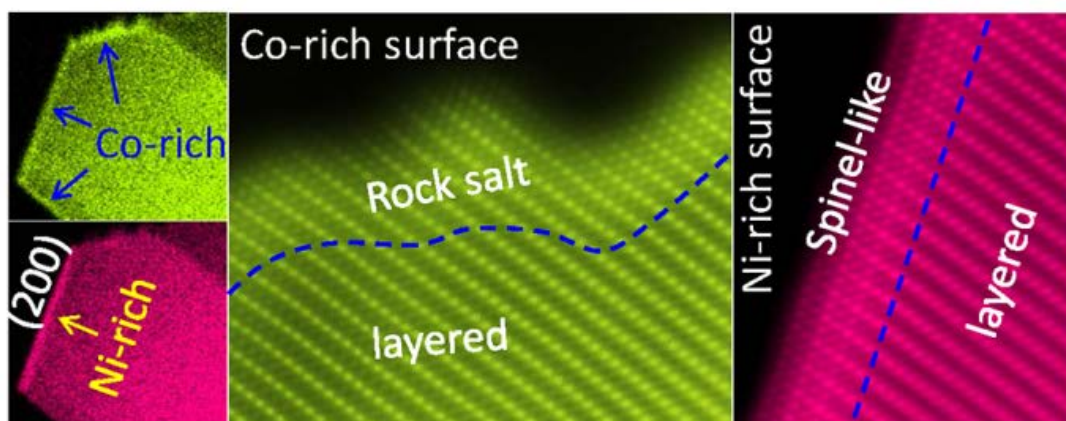


Figure V-158: STEM-HAADF image revealing the distinctive surface plane selective segregation of Ni and Co in Li-Mn-rich oxide cathodes. Ni exclusively segregates on the (200) type planes and forming a layer of spinel structure, while Co has a strong preference to segregate on (20-2)m plane with minimal on other planes and forms rock salt structure

3. Development of *in situ* liquid SIMS for probing SEI chemistry

Dynamic structural and chemical evolution at solid–liquid electrolyte interface is always a mystery for a rechargeable battery due to the challenge to directly probe a solid–liquid interface under reaction conditions. We have *in situ* liquid secondary ion mass spectroscopy (SIMS) for the first time to directly observe the molecular structural evolution at the solid–liquid electrolyte interface for a lithium (Li)-ion battery under dynamic operating conditions. We have discovered that the deposition of Li metal on copper electrode leads to the condensation of solvent molecules around the electrode. Chemically, this layer of solvent condensate tends to be depleted of the salt anions and with reduced concentration of Li^+ ions, essentially leading to the formation of a lean electrolyte layer adjacent to the electrode and therefore contributing to the overpotential of the cell. This observation provides unprecedented molecular level dynamic information on the initial formation of the solid electrolyte interphase (SEI) layer. (See Figure V-159.)

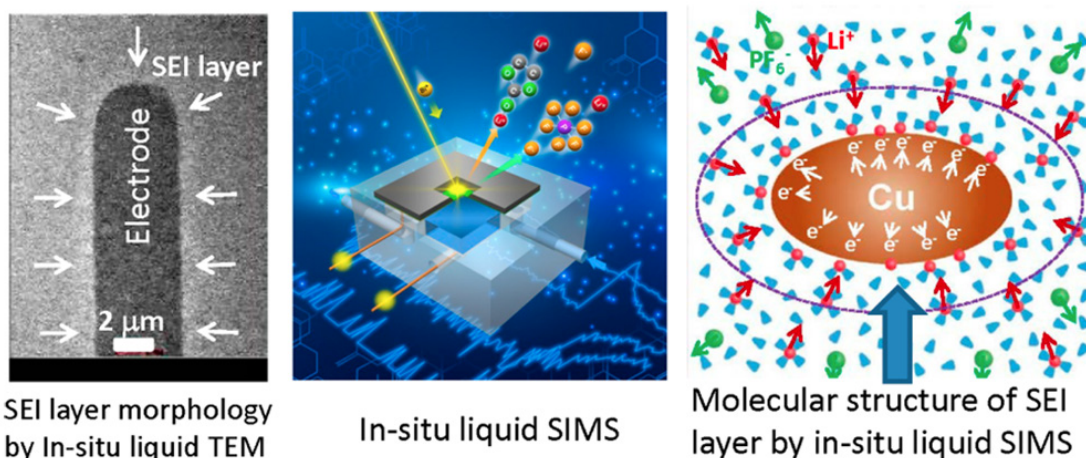


Figure V-159: STEM bright field image showing the formation of SEI layer on Pt electrode (left image), the schematic drawing to illustrate the *in situ* liquid SIMS device for probing the SEI layer (middle), and the schematic drawing to illustrate the SEI layer chemistry at the electrode as captured based on *in situ* liquid SIMS

Conclusions

Over the last year, we have made great progress on understanding the fading mechanism of both anode and cathode materials as well the developing of new tools for capturing molecular information of SEI layers. For anode, we focused on Si based materials and investigated the artificial SEI on the Si lithiation behavior. We discovered that a too strong coating layer may lead to the retardation of lithiation and self-discharging of the battery. Therefore, a proper selection of coating materials is paramount importance. For the cathode materials, we focused on the layer structured materials. We concluded that solid-electrolyte reaction leads to the decomposition of electrolyte, dissolution of transition metal into the electrolyte, which all contributes to the capacity and voltage fading. Therefore, a thin layer of coating on cathode will be essential for mitigating this solid-liquid reaction, which leads to enhanced battery performance. We discovered that Ni and Co shows selective surface plane segregation characteristics, which can lead to the optimized design of particle with certain crystallographic facet and correspondingly to control the Ni and Co segregation. In terms of new capability, the development of *in situ* liquid SIMS for probing SEI layer for rechargeable battery represents a milestone achievement. This capability allows unprecedented probing of molecular structural information of SEI layer under the battery operating condition.

Products

Presentations/Publications/Patents

1. Pengfei Yan, Jianming Zheng, Saravanan Kuppam, Qiuyan Li, Dongping Lv, Jie Xiao, Guoying Chen, Ji-Guang Zhang, and Chong-Min Wang, “Phosphorus Enrichment as a New Composition in the Solid Electrolyte Interphase of High-Voltage Cathodes and Its Effects on Battery Cycling”, *Chem. Mater.* 2015, 27, 7447–7451.

2. Qiangfeng Xiao, Meng Gu, Hui Yang, Bing Li, Cunman Zhang, Yang Liu, Fang Liu, Fang Dai, Li Yang, Zhongyi Liu, Xingcheng Xiao, Gao Liu, Peng Zhao, Sulin Zhang, Chongmin Wang, Yunfeng Lu, and Mei Cai, "Inward lithium-ion breathing of hierarchically porous silicon anodes", *Nature Communications*, 2015, 6, 8844.
3. Zihua Zhu, Yufan Zhou, Pengfei Yan, Rama Sesha Vemuri, Wu Xu, Rui Zhao, Xuelin Wang, Suntharampillai Thevuthasan, Donald R. Baer, and Chong-Min Wang, "*In situ* Mass Spectrometric Determination of Molecular Structural Evolution at the Solid Electrolyte Interphase in Lithium-Ion Batteries", *Nano Lett.*, 2015, 15, 6170.
4. Pengfei Yan, Jianming Zheng, Xiaofeng Zhang, Rui Xu, Khalil Amine, Jie Xiao, Ji-Guang Zhang, and Chong-Min Wang, "Atomic to Nanoscale Investigation of Functionalities of an Al₂O₃ Coating Layer on a Cathode for Enhanced Battery Performance", *Chem. Mater.* 2016, 28, 857–863.
5. Yang He, Meng Gu, Haiyan Xiao, Langli Luo, Yuyan Shao, Fei Gao, Yingge Du, Scott X. Mao, and Chongmin Wang, "Atomistic Conversion Reaction Mechanism of WO₃ in Secondary Ion Batteries of Li, Na, and Ca", *Angew. Chem. Int. Ed.* 2016, 55, 6244–6247.
6. Jiangwei Wang, Hao Luo, Yang Liu, Yang He, Feifei Fan, Ze Zhang, Scott X. Mao, Chongmin Wang, and Ting Zhu, "Tuning the Outward to Inward Swelling in Lithiated Silicon Nanotubes via Surface Oxide Coating", *Nano Lett.* 2016, 16, 5815–5822.
7. Pengfei Yan, Jianming Zheng, Jiabin Zheng, Zhiguo Wang, Gaofeng Teng, Saravanan Kuppan, Jie Xiao, Guoying Chen, Feng Pan, Ji-Guang Zhang, and Chong-Min Wang, "Ni and Co Segregations on Selective Surface Facets and Rational Design of Layered Lithium Transition-Metal Oxide Cathodes", *Adv. Energy Mater.* 2016, 6, 1502455.
8. Zhaofeng Gan, Meng Gu, Jianshi Tang, Chiu-Yen Wang, Yang He, Kang L. Wang, Chongmin Wang, David J. Smith, and Martha R. McCartney, "Direct Mapping of Charge Distribution during Lithiation of Ge Nanowires Using Off-Axis Electron Holography", *Nano Lett.* 2016, 16, 3748–3753.
9. Chongmin Wang, Pengfei Yan, Langli Luo, Jianming Zheng, Jie Xiao, and Ji-Guang Zhang, "Mitigating Capacity Fading of Lithium ion Battery by Surface Coating of Electrode Materials: the Beneficial and Detrimental Effect", Presented at 2016 MRS Spring Meeting, Phoenix, AZ, 03/29/2016.

References

1. Wang Chongmin, "*In situ* Transmission Electron Microscopy and Spectroscopy Studies of Rechargeable Batteries Under Dynamic Operating Conditions: A Retrospective And Perspective View", *J. Mater. Res.* 2015, 30, 326-334.
2. Genc, A., Kovarik, L., Gu, M., Cheng, H.K., Plachinda, P., Pullan, L., Freitag, B., and Wang, C.M., "XEDS STEM Tomography for 3D Chemical Characterization of Nanoscale Particles", *Ultramicroscopy*, 2013, 131, 24-32.
3. Gu M., Parent, L. R., Mehdi, L., Unocic, R., McDowell, M., Sacci, R., Xu, W., Connell, J., Xu, P., Abellan, P., Chen, X., Zhang, Y. H., Perea, D., Lauhon, L., Zhang, J., Liu, J., Browning, N. D., Cui, Y., Arslan, I., Wang, C. M. "Demonstration of an Electrochemical Liquid Cell for Operando Transmission Electron Microscopy Observation of the Lithiation/Delithiation Behavior of Si Nanowire Battery Anodes", *Nano Lett.* 2013, 13, 6106-6112.
4. Thackeray M. M., Johnson C. S., Vaughey J. T. Li, N., Hackney S. A., "Advances In Manganese-Oxide 'Composite' Electrodes for Lithium-Ion Batteries", *J. Mater. Chem.* 2005, 15, 2257–2267.
5. Lin F., Markus I. M., Nordlund D., Weng T. C., Asta M. D., Xin H. L., Doeff M. M., Surface Reconstruction and Chemical Evolution of Stoichiometric Layered Cathode Materials for Lithium-Ion Batteries", *Nat. Commun.* 2014, 5, 3529.

V.E.8. Characterization Studies of High-Capacity Composite Electrode Structures (ANL)

Michael M. Thackeray, Principal Investigator

Jason R. Croy, Co-Principal Investigator

Argonne National Laboratory

9700 South Cass Avenue

Lemont, IL 60439

Phone: 630-252-9184; Fax: 630-252-4176

E-mail: thackeray@anl.gov; croy@anl.gov

Tien Q. Duong, DOE Program Manager

U.S. Department of Energy

Advanced Battery Materials Research (BMR)

Vehicle Technologies Office

1000 Independence Avenue, SW

Washington, DC 20585

Phone: 202-586-7836

E-mail: Tien.Duong@ee.doe.gov

Start Date: October 1, 2015

End Date: September 30, 2018

Abstract

Objectives

- The primary objective of this project is to broaden the scope of studies of electrode materials relevant to the BMR program, using DOE and international user facilities through collaborative efforts.
- More specifically, the goal is to use a range of X-ray techniques, including *in situ* methods, such as X-ray diffraction (XRD) and X-ray absorption (XAS) at the Advanced Photon Source (APS); high-resolution transmission electron microscopy (HRTEM) at Argonne's Electron Microscopy Center (EMC) and elsewhere; and neutron scattering at the ISIS facility, Rutherford Appleton Laboratory (RAL), UK and/or ORNL's Spallation Neutron Source (SNS).

Accomplishments

- Initiated simulations describing the structural stability of model, layered-layered-spinel compositions.
- Characterized the onset of spinel formation in a baseline layered-layered-spinel composition and the associated electrochemistry.
- Identified the coherent, crystallographic integration of layered and spinel phases in manganese-based composite structures.
- Elucidation of cation migration and mechanisms in novel, model lithium-rich compounds

Future Achievements

- Precisely describe, via combined neutron and X-ray techniques, the distribution of transition-metal cations in the lithium layers of layered-layered and layered-layered-spinel counterparts, and relate the results to the observed electrochemical performance.
- Characterize surface-modified layered-layered-spinel compositions and structures, including the effects of surface-integrated spinel components.

Technical Discussion

Background

Multi-component electrodes, $y[x\text{Li}_2\text{MnO}_3 \bullet (1-x)\text{LiMO}_2] \bullet (1-y)\text{LiM}_2\text{O}_4$ ($M=\text{Mn, Ni, Co}$), are currently among the most promising class of cathodes for next-generation lithium-ion batteries [1-4]. However, the degradation mechanisms of these cathodes are not yet well understood. This lack of understanding is due to the complexity of the pristine materials, control over their synthesis, and the complex atomic-level processes that occur on cycling. In order to create more robust structures, an in-depth understanding of the structure-electrochemical properties of this new class of materials is required.

Introduction

Embedding spinel (S), and spinel-type, local configurations within a composite matrix of layered (L), and layered-layered (LL) structures provides a unique opportunity to address several drawbacks associated with cathode materials including voltage fade, initial irreversible capacity loss, low rate performance, and surface instabilities. To optimize the synergistic effects of structurally integrated components, it is critically important to obtain a deeper knowledge of the compositional constitution of structures that can be formed under various synthesis conditions. Structurally-integrated $y[x\text{Li}_2\text{MnO}_3 \bullet (1-x)\text{LiMO}_2] \bullet (1-y)\text{LiM}_2\text{O}_4$ “layered-layered-spinel” (LLS) electrodes are extremely complex; as a result, the systematic understanding of the interplay between targeted composition, the resulting structures and electrochemical performance is a non-trivial task.

Approach

The approach taken in this project is to 1) exploit DOE’s user facilities and beyond to gain fundamental insights into complex $y[x\text{Li}_2\text{MnO}_3 \bullet (1-x)\text{LiMO}_2] \bullet (1-y)\text{LiM}_2\text{O}_4$ electrode materials; 2) combine data sets from multiple, advanced characterization techniques to enable a more complete understanding of complex structures across multiple length scales; 3) combine experimental results with computational predictions to advance the design of robust cathode structures; and 4) establish national and international collaborations with experts in the field to foster innovation and provide solutions to scientific and technological challenges.

Results

A key feature of LLS composite materials is the presence of transition-metal (TM) ions in the Li-rich layers [1-4]. Recent results have shown that the Co content plays an important role in the overall performance of LLS electrodes when synthesized by “underlithiation” of parent, LL precursors [3]. Simulations have been performed to elucidate the effect of Co in the Li layer on structural stability during the first-charge voltage plateau. The simulations address two structures with composition $0.4\text{Li}_2\text{MnO}_3 \bullet 0.6\text{LiCoO}_2$; in one case, the LiCoO_2 component is set up with the lithiated spinel $\text{Li}_2\text{Co}_2\text{O}_4$ (rocksalt) structure [i.e., ‘low temperature’ LT- LiCoO_2 [5-7] to form a LS composite [Figure V-160a, top]; the other case is a LL composite of layered LiCoO_2 and Li_2MnO_3 components (not shown). First principles molecular dynamics simulations were performed for a state of charge corresponding to the removal of all Li from the Li layer (in both LS and LL systems). The selected simulation temperature of 1000K is higher than battery operating temperatures, but illustrates the trends at acceptable computational cost. The dynamical simulations (Figure V-160a) illustrate the relative stability of the selected structures. Figure V-160b shows the density of O-O “pairs” (defined as pairs of oxygen with bond lengths less than 1.7 Å) that are formed on complete delithiation of the lithium layer. The LS composite shows a higher density of O-O pairs toward the end of the first-charge voltage plateau than the LL composite. Moreover, the density of Mn ions (from the Li_2MnO_3 component) that have migrated to the Li layer [not shown in the plot] is also higher in the LS composite than in the LL composite. Figure V-160a (bottom) shows a snapshot of the delithiated LS structure at simulation times of several picoseconds.

The present simulations suggest that Co ions in the Li layer, in $\text{Li}_2\text{Co}_2\text{O}_4$ -type domains, do not stabilize a LS composite electrode structure during the first charge compared with the behavior of LL electrodes. This finding does not necessarily contradict the experimental observation of relatively low voltage fade in LLS

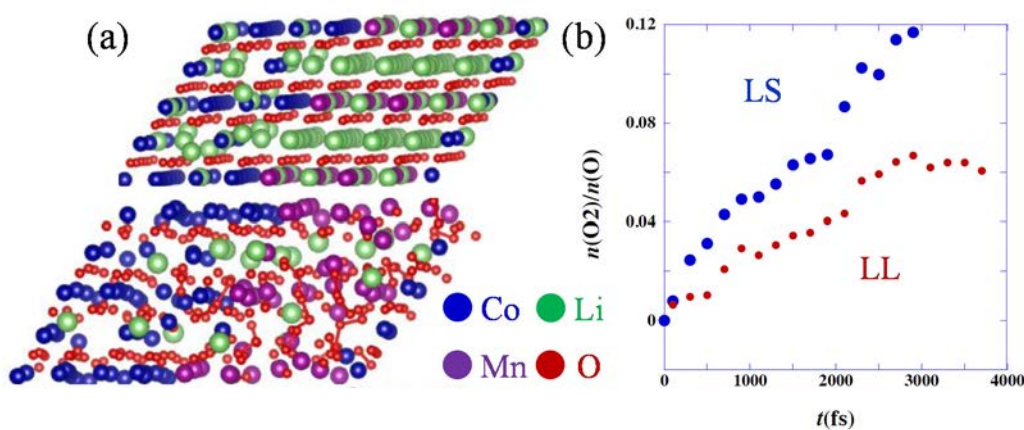


Figure V-160: Modeling of LL and LS Structures: Atomic structure in computational unit cell for the LS 0.4Li₂MnO₃•0.6LiCoO₂ system shortly before the onset of the voltage plateau (a, top) and towards the end of the plateau (a, bottom). (b) Density of O-O pairs with bond lengths less than 1.7 Å as a function of simulation time for delithiated LL (red) and LS (blue) structures

systems. For example, LLS electrodes and their LL counterparts generally achieve similar first-cycle charge capacities, while the LLS electrodes generally achieve a higher first-cycle discharge capacity, coulombic efficiency and cycling stability. In addition, previous reports have shown that a small amount of nickel substitution in lithiated spinel Li₂Co_{2-x}Ni_xO₄ enhances the electrochemical cycling stability of the spinel phase [6, 7]. These observations may be related to local structures that form after the first charge and subsequent transformations that occur during cycling, rather than during the first charge. It is speculated that the presence of spinel domains may inhibit oxygen (or oxygen-vacancy) transport during cycling, thereby slowing the diffusion of transition metal ions to the lithium layer during electrochemical cycling and, consequently, voltage fade. It is possible, however, that the structurally-integrated lithiated-spinel Li₂Co₂O₄ – layered Li₂MnO₃ materials investigated in this work, both with rock salt structures, may differ in their electrochemical behavior relative to complex nickel-containing compositions of practical LLS electrodes. Further work is being conducted required to validate this hypothesis.

In order to gain further insight into the structural relationships of integrated LS materials, a series of lithium-manganese-oxide, model materials having the general formula, Li_{2-z}MnO_{3-δ} (0 ≤ z ≤ 1.5), lying along the layered Li₂MnO₃ and spinel LiMn₂O₄ tie-line of Li-Mn-O phase diagram, were selected for a detailed structural study. Laboratory X-ray diffraction spectra (Figure V-161a) and electrochemical charge-discharge voltage profiles (data not shown) confirmed that the samples with z=0.5, 0.75, and 1.0 have integrated structures consisting of a layered Li₂MnO₃ (z=0) component and a spinel component in the Li_{2-z}MnO_{3-δ} series. For z=0.25, the electrochemical signature of a spinel phase was not distinguishable; however, a detailed investigation of the corresponding XRD provided evidence of a trace amount of a spinel phase (Figure V-161b). The results emphasize the complex relationship between the integrated structures and their electrochemical response. The coherent crystallographic relationship between the layered and spinel components was also confirmed. In Figure V-161c (z=1.0 sample), synchrotron high-resolution XRD data shows distinct L and S peaks as well as a single peak shape for the (111)S/(001)L and (222)S/(002)L reflections, the (001)L and (111)S reflections corresponding to the oxygen close packed planes in each structure. The overlap of the two main peaks therefore indicates almost identical close-packed interlayer distances in the two (layered and spinel) components. The crystallographic coherency between the layered and spinel components was confirmed by high-resolution electron microscopy and diffraction (Figure V-161d).

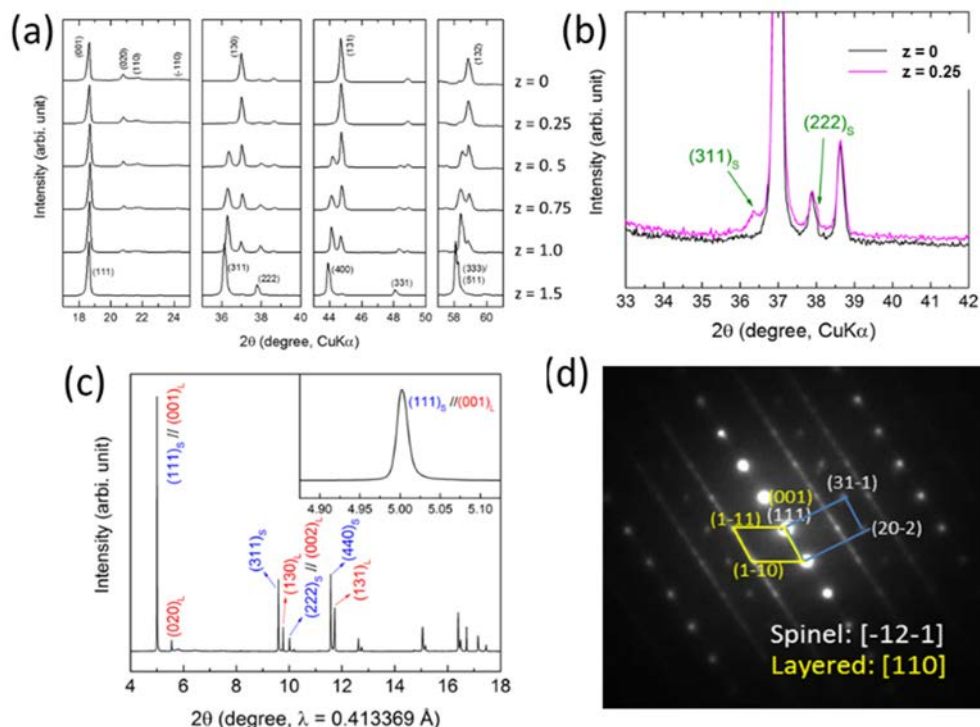


Figure V-161: Characterization of $\text{Li}_{2-z}\text{MnO}_{3-\delta}$ LS Structures: (a and b) Laboratory XRD of $\text{Li}_{2-z}\text{MnO}_{3-\delta}$ powder samples; (c) high-resolution synchrotron XRD spectrum of a structurally-integrated LS $\text{Li}_{2-z}\text{MnO}_{3-\delta}$ ($z=1.0$) sample; and (d) corresponding HRTEM electron diffraction image

To better understand the relationship between integrated spinel domains and Li-layer TM content in more practical compositions, a systematic study of structure and electrochemistry was initiated on a series of LLS materials as a function of Li:TM ratios by keeping the TMs constant and varying the Li content. Nominally, in complex LLS notation, samples with various, targeted spinel contents were synthesized according to the series $(1-x)[0.25\text{Li}_2\text{MnO}_3 \bullet 0.75\text{LiNi}_{0.375}\text{Mn}_{0.375}\text{Co}_{0.25}\text{O}_2] \bullet x[\text{Li}_{0.5}\text{Ni}_{0.28}\text{Mn}_{0.53}\text{Co}_{0.18}\text{O}_2]$, with $x=0, 0.025, 0.05, 0.075, 0.1$. Figure V-162a shows a comparison of the targeted and ICP-measured elemental compositions for the series. Excellent agreement was obtained and the targeted Li:TM ratios confirmed. Figure V-162b shows the XRD patterns of the series. Even though a limited range of lithium content was targeted, differences in the XRD patterns appeared as a function of x (Figure V-162a), e.g., the line broadening at $\sim 44^\circ 2\theta$ (particularly for the $x=0.1$ sample) indicating the presence of a second phase. Interestingly, this sample provided a stable capacity of ~ 200 mAh/g and a first-cycle efficiency of $\sim 90\%$. Neutron diffraction data of this series have recently been acquired at SNS (ORNL) and are currently being analyzed to determine the distribution of TM cations in alternating TM-rich and Li-rich layers as a function of targeted spinel content, a parameter that is believed to strongly influence electrochemical behavior.

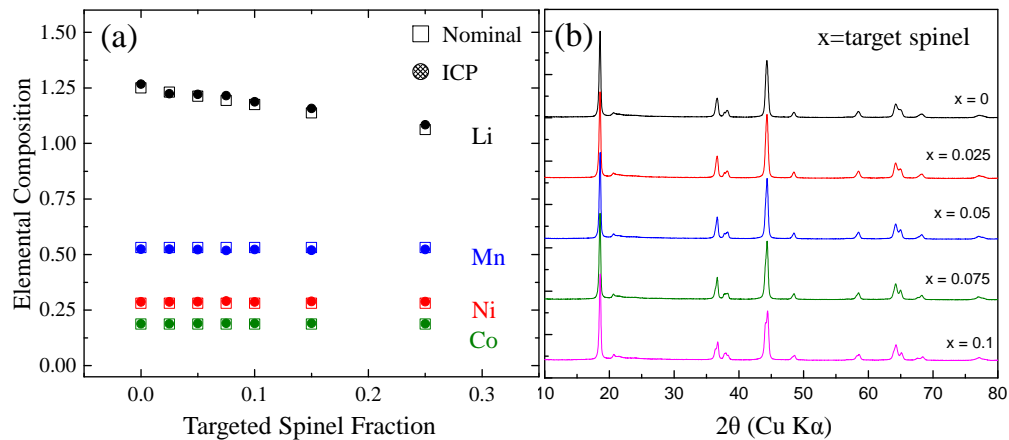


Figure V-162: Onset of “Spinel” Signatures in LLS Compositions: (a) Nominal (open symbols) and ICP-measured (closed symbols) compositions of $\text{Li}_{1.25-2z}(\text{Ni}_{0.28}\text{Mn}_{0.53}\text{Co}_{0.19})\text{O}_y$ layered-layered-spinel, cathode powders, and (b) XRD patterns of the samples in (a) as a function of targeted spinel content, x

As discussed, LLS electrodes have shown promise for improving first-cycle efficiencies, rate capability, and possibly structural stability compared to their LL counterparts, particularly at low values of excess lithium (e.g., $\leq 25\%$ Li_2MnO_3). However, to fully optimize useable capacity, it is desirable to maximize the excess lithium content, x in $x\text{Li}_2\text{MnO}_3 \bullet (1-x)\text{LiMO}_2$, while simultaneously stabilizing lithium-excess regions (e.g., Li_2MO_3 -ordered structures). One such strategy is to incorporate a completely inactive $\text{Li}_2\text{M}'\text{O}_3$ component where M' may consist of, for example, Ti^{4+} . Octahedral Ti^{4+} (d^0) will not oxidize and is expected to be robust against oxygen loss. However, when incorporated into materials at the nanoscale, unique behavior might be expected from lithiated compounds. For example, bulk LiCrO_2 is not particularly active as a cathode material but when synthesized as nanoparticles becomes highly active for Li de-intercalation/intercalation. Furthermore, $\text{Cr}^{3+/6+}$ activity induces facile migration of Cr cations into tetrahedral sites of the lithium layers, disrupting the local structure around migrated cations. In order to study the behavior of this unique combination of materials, $\text{Li}_{1.2}\text{Ti}_{0.4}\text{Cr}_{0.4}\text{O}_2/\text{Li}$ pouch-cells were studied by X-ray absorption spectroscopy (XANES/EXAFS), *in situ*, during first-cycle delithiation to 4.8V.

Figure V-163a shows high-resolution synchrotron X-ray diffraction pattern of a high purity $\text{Li}_{1.2}\text{Ti}_{0.4}\text{Cr}_{0.4}\text{O}_2$ sample (i.e., $0.5\text{Li}_2\text{TiO}_3 \bullet 0.5\text{LiCrO}_2$) in which the signature peaks related to Li-Ti ordering (inset), similar to Li-Mn ordering found in Li_2MnO_3 are clearly observed. EXAFS data (not shown) confirmed that the local structure around Ti is similar to that of a reference Li_2TiO_3 sample (e.g., Li-Ti ordering) while the Cr EXAFS shows that Cr is fully coordinated in the second shell (Cr-M coordination = 6). Therefore, the overall structure is similar to that of LL compositions such as $\text{Li}_{1.2}\text{Mn}_{0.4}\text{Co}_{0.4}\text{O}_2$ where the tetravalent and trivalent TM cations strongly charge order to create distinct local environments. Figure V-163b shows the *in situ* development of the Cr K-edge XANES as a function of lithium content, x . As expected for active Cr^{3+} compounds, Cr^{3+} is immediately oxidized to Cr^{6+} and migrates to tetrahedral sites as clearly indicated by the large increase in the pre-edge region (inset). Figure V-163c shows the evolution of the Ti K-edge during delithiation. Interestingly, the main edge changes in a somewhat ambiguous way similar to the Mn edge of Mn-rich, LL materials. However, the pre-edge region shows a large increase in intensity and a shift to lower energies (inset). EXAFS analysis also shows that the Ti-O coordination decreases by $\sim 10\%$ during the first-cycle charge. This shift in Ti pre-edge energies, along with increased intensities, is known to occur in Ti compounds as the Ti-O coordination goes from 6 (octahedral) to 4 (tetrahedral). Although Li_2TiO_3 is inactive to Li deintercalation/intercalation reactions, this property does not preclude instabilities and Ti migration associated with the local domain structures that appear in complex, lithium-rich materials. These findings suggest that the mechanisms of voltage fade and hysteresis, related to oxygen activity and TM migration, may not be unique to the lithium- and manganese-rich class of electrodes and, therefore, that the design of more robust high-capacity lithium-rich materials requires a rational design based on a better understanding of structure-composition-electrochemical property relationships, which is an ongoing aspect of this project.

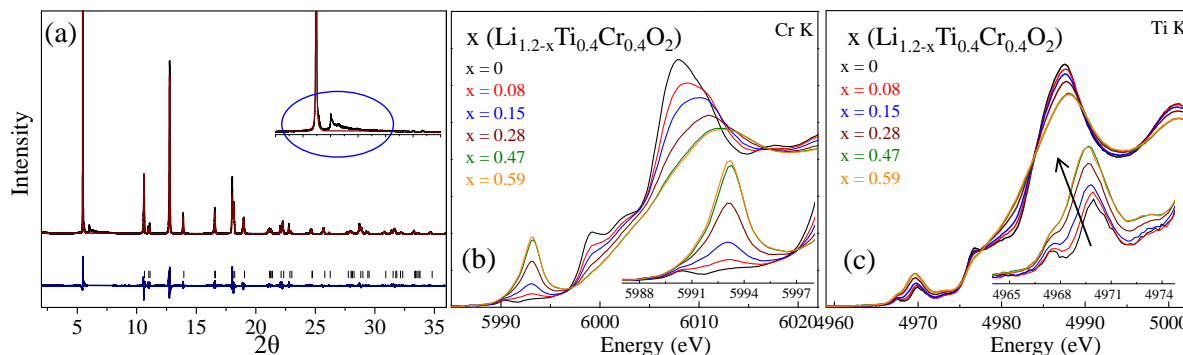


Figure V-163: X-ray Characterization of Model Systems: (a) HR-XRD patterns of $\text{Li}_{1.2-x}\text{Ti}_{0.4}\text{Cr}_{0.4}\text{O}_2$; and (b),(c) *in situ* Cr- and Ti K-edge XANES data. Insets in (b) and (c) show magnified views of respective pre-edge regions

Conclusions

The complex phase space encompassed by the $y[\text{xLi}_2\text{MnO}_3 \bullet (1-x)\text{LiMO}_2] \bullet (1-y)\text{LiM}_2\text{O}_4$, LLS class of materials offers both exciting and daunting opportunities and challenges. Next generation electrodes will almost certainly incorporate different structural motifs in either LL or LLS configurations. These structurally-integrated electrodes show considerable promise; the incorporation of embedded spinel and/or “spinel-type” atomic arrangements appears to be a viable path forward for mitigating challenges associated with structural instabilities. By selective engineering of local domain structures, new and technologically-relevant properties are emerging. However, the complexity of the domain structures, and the correlation between local structures and macroscopic electrochemical performance, requires a deeper understanding of atomic-scale, structure-property-electrochemical relationships. This project has shown that even slight modifications of LL materials, via the incorporation of local spinel-type configurations, can have positive impacts on overall electrode performance. Systematic studies have been, and will continue to be, pursued in order to better understand materials design criteria (e.g., synthesis conditions, elemental and structural composition) relevant to the rational design of more robust, high-capacity electrodes for lithium-ion batteries.

Products

Presentations/Publications/Patents

1. Jason R. Croy, *The Next Generation of Lithium-ion Batteries for Transportation Applications: Perception, Promises and Problems*, University of Illinois Chicago, Topics in Energy and Sustainability (Chicago, IL) Nov. 24, 2015. **(Invited)**.
2. Jason R. Croy, K.G. Gallagher, M. Balasubramanian, J.S. Park, E.J. Lee, A.K. Burrell and M.M. Thackeray, *Lithium- and Manganese-Rich Cathodes: A Deep Dive and A Look Forward*, International Battery Association Meeting, Nantes, France, 24 March 2016. **(Invited)**.
3. M.M. Thackeray and J.R. Croy, *Processing and Characterization of High Capacity Composite Electrode Structures*, Presentation to BASF, Argonne National Laboratory, Lemont, IL, 3, March, 2016.
4. Jason R. Croy, Atomic-Scale Degradation Mechanisms in High-Capacity, Lithium- and Manganese Rich Cathode Materials, Energy Materials Nanotechnology, Orlando, FL, 24 February 2016. **(Invited)**.
5. Jason R. Croy and M.M. Thackeray, Processing and Characterization of High Capacity, Composite Electrode Structures, BMR Program Review, Berkeley, CA, 20 January 2016.
6. M.M. Thackeray and J.R. Croy, *Processing and Characterization of High Capacity Composite Electrode Structures*, ES235, DOE Vehicle Technologies Program Annual Merit Review (Arlington, VA), 5-9, June 2016.

References

1. S. H. Park, S. H. Kang, C. S. Johnson, K. Amine, and M. M. Thackeray, *Electrochem. Comm.*, **9**, 262 (2007).
2. D. Kim, G. Sandi, J. R. Croy, K. G. Gallagher, S.-H. Kang, E. Lee, M. D. Slater, C. S. Johnson, and M. M. Thackeray, *J. Electrochem. Soc.*, **160**, A31 (2013).
3. B. R. Long, J. R. Croy, J. S. Park, J. G. Wen, D. J. Miller, and M. M. Thackeray, *J. Electrochem. Soc.*, **161**, 2160 (2014).
4. J. R. Croy, J. S. Park, Y. Shin, B. T. Yonemoto, M. Balasubramanian, B. R. Long, Y. Ren, M. M. Thackeray, *J. Power Sources*, **334**, 213 (2016).
5. R. J. Gummow, M. M. Thackeray, W. I. F. David, and S. Hull, *S. Mater. Res. Bull.* **27**, 327 (1992).
6. R. J. Gummow, M. M. Thackeray, *J. Electrochem. Soc.* **140**, 3365 (1993).
7. E. Lee, J. Blauwkamp, F. C. Castro, J. Wu, V. P. Dravid, P. Yan, C. Wang, S. Kim, C. Wolverton, R. Benedek, F. Dogan, J. S. Park, J. R. Croy, and M. M. Thackeray, *ACS Appl. Mater. & Interfaces* **8**, 27720 (2016).